# INDUCTION AND PERMANENT-MAGNET SYNCHRONOUS GENERATORS FOR SMALL-SCALE POWER SYSTEM APPLICATIONS

by

**Tze-Fun Chan**

This thesis is submitted for the Degree of

**Doctor of Philosophy**

at

**City University**

School of Engineering and Mathematical Sciences

March 2004

# TABLE OF CONTENTS

# LIST OF FIGURES

# LIST OF TABLES

## ACKNOWLEDGMENTS

The author would like to thank Dr. L.L. Lai of City University, London, for his continuous guidance and supervision throughout this research project. His unfailing advice and encouragements, especially at times when research publication was both slow and difficult, have been one of the major supports that kept the project going.

Thanks are given to Prof. S.L. Ho for being my local supervisor at the Department of Electrical Engineering, the Hong Kong Polytechnic University. The encouragements from Prof. A.K. David and Prof. Kit-Po Wong, former and present Heads of the same Department, are deeply appreciated.

The author is indebted to Mr. Lie-Tong Yan, retired Associate Professor of Tsinghua University, Beijing, China, for his assistance in procuring the prototype generators and the development of finite element analysis programs. The author is privileged to have collaborated with Mr. Yan in the past few years.

The financial support from the Hong Kong Polytechnic University, mainly in the form of research grants (Reference Codes 353/067, A-PA49, and A-PD56) is gratefully acknowledged. These grants have enabled experimental and prototype generators to be designed and acquired, and have supported the development of the finite element analysis programs. The Department of Electrical Engineering, the Hong Kong Polytechnic University, also provided the computing and testing facilities.

Thanks are due to Prof. O.J.M. Smith, Professor Emeritus in Electrical Engineering and Computer Sciences, University of California in Berkeley, for his correspondence on the SEMIHEX (or Smith) connection for three-phase induction motors. This has led to the development of the SMIG and SMSEIG schemes by the author.

Thanks are also due to Dr. K.A. Nigim, presently the Program Coordinator of an MEng Course in Electric Power at the Department of Electrical and Computer Engineering, University of Waterloo, Ontario, Canada, for his input to the development of the SESRIG scheme in Chapter 5.

The author would also like to thank two of his former undergraduate students at the Department of Electrical Engineering, the Hong Kong Polytechnic University, for their contributions. Mr. Chi-Sing Li (BEng, 2001) assisted in the implementation of the closed-loop controller for the SESRIG and in obtaining the dynamic test results. Mr. Yan-Wing Lam (BEng, 2002) assisted in the implementation of the microcontroller-based capacitor switching system for multi-mode operation of the SMIG.

The author is grateful to Mr. C.K. Cheung, Technician-in-Charge of the Electrical Machines Laboratory, Department of Electrical Engineering, the Hong Kong Polytechnic University, for his technical support.

The warmest thanks are given to the author's wife Anna for her understanding and tolerance throughout the research project, and to his sons Chung Ming and Chung Kwong, in whose company he always finds pleasure and relief.

## DECLARATION

The author hereby grants powers of discretion to the Librarian of City University, London, to allow this thesis to be copied in whole or in part without further reference to the author. This permission covers only single copies made for study purposes, subject to the normal conditions of acknowledgment.

## ABSTRACT

This thesis presents two types of alternating current (ac) generators that are becoming popular for use in small-scale distributed generation and in autonomous (or stand-alone) power systems. For the induction generator (IG), two modes of operation are identified, namely operation on the power grid and operation in the isolated mode. Single-phase operation is emphasized due to its applicability in remote rural regions where electrification is both costly and difficult to carry out. In the case of grid-connected operation, a number of practical phase-balancing schemes for a three-phase IG are proposed and analyzed. The method of symmetrical components is found to be a versatile tool for analyzing all the circuit configurations to be studied, including the Smith connection. Microcontroller-based multi-mode operation of an IG with the Smith connection is also investigated.

When operated in the stand-alone mode, the IG is more commonly known as the self-excited induction generator (SEIG). In this thesis, a unified approach that combines the method of symmetrical components and the pattern search method of Hooke and Jeeves is used to analyze a three-phase SEIG which supplies asymmetrical or single-phase loads. Its applicability is tested on various SEIG schemes, including the Steinmetz connection, modified Steinmetz connection (MSC), the simplified Steinmetz connection (SSC), the self-regulated self-excited induction generator (SRSEIG), and SEIG with the Smith connection (SMSEIG). For certain studies, the above approach is used in association with an iterative procedure in order to obtain the solution.

A coupled circuit and field approach based on a two-dimensional finite element method (2-D FEM) is proposed for analyzing a grid-connected IG with the Steinmetz connection. The technique of coupling the single-phase circuit equations to the field

domain equations is set forth and a rotor circuit model that accounts for the non-uniform current distribution in the rotor winding is also presented.

A voltage and frequency control scheme that employs an SEIG with slip-ring rotor, namely the SESRIG, is also proposed and investigated. The feasibility of using an external rotor resistance as a control parameter is demonstrated theoretically and experimentally.

The study on the permanent-magnet synchronous generator (PMSG) is focused on autonomous power system applications. A PMSG with inset rotor, which possesses an inverse saliency characteristic, is found to give satisfactory performance when supplying isolated loads. Zero voltage regulation and other extremum conditions are deduced based on the two-axis model. A saturated two-axis model that gives a more accurate prediction of the load characteristic is developed. For a more rigorous analysis, a coupled circuit and field, time-stepping 2-D FEM is also proposed.

# Chapter 1

# INTRODUCTION

## 1.1 Background of Research

Conservation of energy resources, environmental protection and sustainable development are the three major challenges that the world faces in the new millennium [1]. One important issue is to satisfy the energy needs of people without causing rapid depletion of the natural energy resources and degradation of the environment. A general consensus among countries of the world is that greater emphasis should be placed on the use of renewable energy resources for electric power generation. Many developing countries, e.g., China, Nepal, Mexico, and others, have abundant renewable energy resources, but these resources are invariably located in remote regions, thereby creating a number of obstacles for their deployment. The problem can readily be solved if the region is already served by a three-phase grid. Local power systems that employ three-phase generators may be developed. The generators could be conventional wound-field synchronous generators, but over the past few decades increasing use is made of squirrel-cage type induction generators (IGs), particularly in wind energy systems and micro-hydro power systems. In the latter case, the grid provides frequency and voltage regulation, as well as the reactive power required by the IG. Due to the distributed nature of the energy resources, these power systems are usually small-scale in terms of rating. They may not be as efficient as central bulk power systems, but this disadvantage is offset by the reduction or even elimination of the transmission losses over long distances. The global trend of privatization and deregulation is a further

impetus to the development of small scale distributed or (embedded) generation systems [2], [3].

Even in developed countries, energy conservation and environmental protection can be achieved by extensive renewable energy programs and more widespread use of waste heat utilization and cogeneration [4]. For such applications, the low cost and flexibility of using induction generators result in their increasing popularity.

In remote regions of some developing countries, rural electrification is often based on single-phase generation and transmission/distribution systems [5]. This approach has the advantage that, for a given amount of capital investment, a wider area can be provided with electricity. There is thus a great need for the development of single-phase IGs. Although single-phase induction motors may be adapted for generator operation, it is often more economical, for ratings above 3 kW, to use standard three-phase induction machines [6]. With a suitable phase-balancing scheme, the three-phase IG can operate satisfactorily on a single-phase grid. A practical phase-balancing scheme invariably employs passive circuit elements, such as capacitance, inductance, or resistance.

In countries and regions where a grid connection is difficult and expensive to provide, a more cost effective solution is to develop stand-alone, or autonomous power systems [7], [8] which may consist of one or more induction generators and a small number of loads to be served, comprising typically lighting, heating, and water pumping. The absence of the grid implies that the reactive power has to be furnished locally by capacitors, and an induction machine operating in this mode is often referred to as the self-excited induction generator (SEIG). Both the output voltage and frequency depend upon the connected load and will vary greatly when the load or the speed of the prime-mover is changed. Frequency control and voltage control are two important operational

aspects for autonomous power systems. Both three-phase systems and single-phase systems may be developed. Besides, the choice of appropriate values of excitation capacitances to secure successful voltage build-up and to sustain the voltage when the generator is supplying load, is of paramount importance.

Single-phase operation of a three-phase IG, with or without a phase balancer, renders the machine operating with phase imbalance. For the grid connected IG, the voltage and frequency are constant, hence the analysis can be carried out by using the method of symmetrical components [9]. With the SEIG, however, the performance analysis is complicated by the variation of frequency as well as the magnetizing reactance, both being dependent on the speed and loading conditions.

The method of symmetrical components is basically a linear analysis and the principle of superposition applies. In an induction generator, the air gap voltage is higher for a given terminal voltage, meaning that the machine operates at a higher magnetic saturation level compared with that when the machine is run as a motor. To account for the effects of magnetic nonlinearity, an electromagnetic field analysis, such as the finite element method [10], may be more appropriate. Although the field approach may not guarantee superior results, it nevertheless involves less simplifying assumptions in the modeling and hence is theoretically more rigorous.

Phase-balancing methods have formerly been applied successfully to three-phase induction machines with symmetrical, star- or delta-connected stator windings. Recently, however, a new class of high-efficiency induction motors based on asymmetrically-connected stator windings has been proposed. The connection, which is commonly known as SEMIHEX connection or the Smith connection [11]-[13], has found applications in pump motor drives in rural areas where only a single-phase

supply is available. The peculiar feature of the Smith connection is the use of three capacitors in association with the asymmetrical stator winding. Under favorable conditions the phase voltages and currents of the induction machine may be perfectly balanced. This interesting winding connection may be applied for generator applications as well.

Great advances in permanent-magnet (PM) technology [14] have taken place in the past two decades. Powerful rare-earth PM materials, such as neodymium-iron-boron (NdFeB), have emerged and the price is becoming more affordable. A direct impact on the electric motor industry is the rapid development of high-performance drives, such as the brushless PM dc motor drive and PM synchronous motor drive. At the same time, the PM synchronous generator (PMSG) has been considered as a contender with the induction generator, mainly in autonomous power system applications. Compared with the IG, the PMSG also has such advantageous features as brushless rotor construction, no need for dc excitation, and less maintenance. Furthermore, the absence of rotor loss implies that very high efficiencies could be realized. These advantages, however, are at the expense of lack of field control, and voltage regulation is a major issue to be resolved.

It should be pointed out that other electric machines may also be employed for ac power generation. The variable reluctance machine, for example, has been rigorously researched as a contender with the SEIG [15]-[19]. However, the inherent low power factor of the reluctance machine is a major disadvantage, and special rotor designs, such as the axially-laminated anisotropic (ALA) rotor [18], need to be used in order to secure a large power-to-weight ratio.

The switched reluctance motor (SRM) has received great attention in the past two decades, mainly for use in traction and high-speed drive [20]. It can readily be adapted for power generation [21], [22], but two factors render the machine a less viable option. First, the machine requires a dedicated electronic drive and control circuit. Second, the power output is inherently dc and a dc/ac converter is required for supplying an ac load or interfacing with the grid, which increases the system cost and may produce additional harmonics.

## 1.2 Literature Survey

### 1.2.1 Three-Phase IGs and SEIGs

The principle and operation of grid-connected three-phase IGs are well understood and are discussed in detail in many textbooks [23]. Performance analysis is based on the induction motor equivalent circuit, negative values of slip being used since the rotor speed is higher than the synchronous speed. The SEIG, on the other hand, involves more complicated analysis and has received considerable attention. Pioneering work of the SEIG dated back to the twenties and thirties of the last century [24], [25] when it was discovered that an induction machine with capacitance connected to the stator terminals might stay excited after being disconnected from the grid. The significance of such a phenomenon for generator application was apparent, but since then very little has been written on the subject and the synchronous generator dominates the role for large-scale power generation.

Towards the late seventies and early eighties of the last century, however, interest on SEIGs revived as witnessed by the numerous research publications. Murthy *et al.* [26] and Malik and Hague [27] analyzed the SEIG using the loop impedance method, based on the per-phase equivalent circuit model. The Newton-Raphson method was employed

for simultaneously determining the per-unit frequency and magnetizing reactance. Ouazene and McPherson [28], on the other hand, proposed the nodal admittance method, also based on the equivalent circuit. This approach resulted in a high-order polynomial in the per-unit frequency which could be solved to yield the generator performance. The generalized induction machine model has been used by Elder *et al.* [29], Grantham *et al.* [30] and Wang [31] for analysis of voltage build-up and transient operation of the SEIG.

The capacitor sizing problem for a three-phase SEIG was studied by Malik and Mazi [32], Jabri and Alolah [33], and Chan [34], while performance of an SEIG driven by regulated and unregulated turbines was investigated by Bonert and Hoops [35], Chan [36] and Alghuwainem [37]. Wind turbine driven SEIGs were studied by Ammassaigounden *et al.* [38], Watson *et al.* [39] and Raina and Malik [40].

Voltage compensation using the long-shunt connection was first investigated by Bim *et al.* [41] with a view to improving the voltage regulation characteristic of the SEIG. This method, together with the short-shunt configuration, was subsequently analyzed by Chan [42] and Wang and Su [43]. Application of the compensated SEIG for supplying an induction motor load has recently been reported [44].

Voltage and frequency control of the three-phase SEIG has also been studied recently [45]-[50]. Voltage control invariably involves the regulation of effective capacitance across the stator terminals, and a variety of control methods, such as the fixed-capacitor thyrister-controlled reactor (FC-TCR) [27], might be employed. Frequency control for SEIG, on the other hand, is more difficult and involves expensive and sophisticated equipment, such as an ac/dc/ac converter [45], [50].

### 1.2.2 Single-phase IGs and SEIGs

Analysis and performance of a grid-connected single-phase IG with main and auxiliary windings were reported by Boardman *et al.* [51]. It was found that the generator efficiency was higher if the rotor was driven to give reverse rotation (i.e., the rotor rotates against the air gap traveling field). This principle was also applicable to a three-phase IG connected to a single-phase power grid [52]. When a three-phase IG operates on a single-phase power system, the currents are generally unbalanced and the rated three-phase power output cannot be developed. Other adverse effects include thermal overload, mechanical vibration, noise, poor efficiency and low power factor. Various phase-balancing schemes for a three-phase IG have been investigated [6], [53]-[54]. In the method proposed by Durham and Ramakumar [6], an artificial third line is created, using a capacitance and an inductance of equal reactances, for supplying the IG whose power factor has been corrected to unity. The disadvantage of such a scheme is that, in the event that the supply is removed, severe overvoltages will be produced as a result of series resonance between the capacitance and inductance. In the phase-balancing schemes proposed by Smith [53], capacitors were used exclusively and there was no danger of resonance effect. The analysis, however, was confined to the case when the induction machine was exactly balanced. Most of the circuits introduced require a ground-wire in the supply system, which may not be feasible in some regions. More recently, Chan [54] investigated phase balancing for an IG using the Steinmetz connection, and it was demonstrated that perfect phase balance could be achieved over a wider range of generator impedance angle by the use of dual phase converters.

Anther important contribution of Smith is the introduction of the Smith (or SEMIHEX) connection [11]-[13], devised primarily to enable a three-phase motor to be operated on

a single-phase supply. Capacitances were employed exclusively for achieving phase balance. The principle of the circuit was explained in considerable detail by Smith [11], but no formal analysis was carried out.

The study on single-phase SEIGs was conducted by Murthy [55], Murthy *et al.* [56], Rahim [57], Chan [58] and Singh and Shilpkar [59]. Two-phase symmetrical component method was applied to an SEIG with main and auxiliary windings in quadrature. Ojo [60] presented a transient analysis of single-phase SEIGs using the d-q equivalent circuit model. Application of single-phase SEIG for heating and lighting loads in remote regions was proposed by Singh *et al.* [61] and microprocessor control of single-phase SEIG was reported by Watson and Watson [62]. Ojo *et al.* also investigated the operation of a single-phase SEIG using a pulse-width modulated inverter with a battery supply [63].

Analysis of a three-phase SEIG supplying single-phase loads was reported by Al-Bahrani and Malik [64] and Rahim [65]. Fukami *et al.* [66] developed a self-regulated single-phase SEIG by introducing series capacitance compensation. The machine configurations analyzed in [64]-[66], however, were essentially the single-phasing mode of operation. Since only two phases are involved in the energy conversion process, the winding utilization is poor and the phase imbalance is severe.

With a view to minimizing the phase imbalance, Chan [67] investigated the performance of a three-phase SEIG with the Steinmetz connection, i.e., one in which the load impedance and the excitation capacitance are connected across different stator phases. It was found, however, that perfect phase balance could not be achieved with unity-power-factor loads.

### 1.2.3 Permanent-Magnet Synchronous Generators

Research work on the PMSG has been reported in the past few decades [68]-[79]. Early PMSGs employed low-cost ceramic magnets [68], [69], but recently high-energy materials such as neodymium-iron-boron (NdFeB) [76], [77] have become more popular. Binns *et al.* [69] reported the analysis and applications of a PMSG with multi-stacked, imbricated rotor. Modeling and analysis of the PMSG has been discussed by Chalmers [71] and Rahman *et al.* [73]. There has also been rigorous research interest in the axial-flux PM generator for wind-turbine applications [70], [72], [77], [78]. Due to the larger diameter to axial-length ratio, axial-flux machines are more suitable for multi-pole, low-speed, direct-drive applications than radial-flux machines.

It is well known that the excitation of a PMSG cannot be varied, and hence the terminal voltage varies with the load current. Attempts have been made for improving the voltage regulation of the PM generator. One method to control the terminal voltage is to use shunt capacitance compensation [69], [73], [74], but the capacitors will occupy additional space and extra capital costs are incurred. A more attractive solution is to employ a special generator design that imparts an inherent voltage compensation characteristic to the machine. Chalmers [71] has shown that a generator with an interior-magnet rotor exhibits interesting load characteristics when supplying an isolated load. In this type of generator, the direct-axis (d-axis) synchronous reactance $X_d$ is less than the quadrature-axis (q-axis) synchronous reactance $X_q$, i.e., the generator possesses an inverse saliency feature. The voltage regulation may be reduced if the generator has the proper value of inverse saliency ratio $r$ ($= X_q/X_d$). It has also been proved that, if the armature resistance is neglected, a voltage rise will result when the load current is increased from zero, provided that $r$ is larger than 2.

For practical applications, it is desirable that the generator voltage regulation be as small as possible. This requires a careful machine design in order to give the appropriate combination of generator parameters, such as the no-load generated e.m.f., armature resistance and the synchronous reactances.

A synchronous machine with the inset PM rotor construction [14] also exhibits inverse saliency and hence an improved load characteristic might be obtained for generator operation. The inset rotor construction involves less complicated rotor stampings and hence is easier to fabricate than the interior-type rotor.

The synchronous reactances used in the two-axis model can be computed from FEM analysis [76]. FEM is also useful for analysis of PMSGs with unconventional rotor configurations [72], [78]. The application of a coupled circuit and field method to PMSG was recently reported by Zhou *et al.* [79].

## 1.3 Research Objectives

This thesis aims to achieve the follow research objectives:

1) An investigation on various phase-balancing schemes for a three-phase IG operating on a single-phase power grid, including the Smith connection that involves asymmetrical phase windings and phase converters.

2) A detailed 2-D FEM analysis on a grid-connected IG with the Steinmetz connection.

3) An investigation on various three-phase SEIG circuit configurations suitable for supplying unbalanced / single-phase loads.

4) Implementation of a frequency and voltage controller for a slip-ring SEIG.

5) A detailed analysis of a PMSG with inset rotor for autonomous power system applications, using both the two-axis model and a time-stepping FEM.

## 1.4 Organization of the Thesis

The previous sections in this chapter have provided the justification for the proposed research and the main research objectives have been set forth. This thesis may broadly be divided into three parts. Chapters 2 and 3 investigate the performance of a three phase IG when operating on a single-phase power system. Chapters 4 and 5 are devoted to SEIGs with cage and slip-ring rotors. Chapter 6 discusses exclusively the PMSG with inset rotor for autonomous power system applications. Chapter 7 gives a summary of the major accomplishments and discusses further work that might be pursued.

## 1.5 Statement of Originality

The original contributions and important developments of this thesis are given in the following statements:

- Various phase-balancing schemes for a three-phase IG connected to a single-phase power system, including the novel Smith connection, are analyzed by using the method of symmetrical components.
- Various SEIG schemes are analyzed by using a search method in association with the method of symmetrical components. The SRSEIG and SMSEIG schemes are proposed and analyzed for the first time.
- Analysis of a grid-connected IG with the Steinmetz connection using a coupled circuit 2-D finite element method is proposed.
- Microcontroller-based operation of a three-phase IG with the Smith connection is proposed and implemented.
- A voltage and frequency control scheme for an IG with slip-ring rotor is investigated.
- A PMSG with inset rotor for achieving a reduced voltage regulation when supplying an autonomous power system is proposed and its performance is analyzed by using

the two-axis model. A saturated two-axis model is also developed based on the results of an FEM analysis.

- A coupled circuit, time-stepping finite element method is proposed for the analysis of the PMSG with an inset rotor.
- Experimental work on various IG and SEIG schemes as well as the PMSG with inset rotor is undertaken.

# Chapter 2

# THREE-PHASE IG OPERATING ON A SINGLE-PHASE POWER SYSTEM

## 2.1 Introduction

In this chapter, the general principle of phase balancing for a three-phase IG operating on a single-phase power system is investigated and several practical phase-balancing schemes are proposed, including those that involve dissipative elements and current injection transformers. It is demonstrated that the IG-converter system can be analyzed by using the method of symmetrical components. A phasor diagram approach enables the conditions of perfect phase balance to be deduced. Performance analysis of a three-phase IG with the Smith connection is also possible using the same approach. The feasibility of the phase-balancing schemes is verified by laboratory experiments on a small induction machine. A microcontroller-based control scheme for an IG with the Smith connection is also proposed to give efficient control at low cost.

## 2.2 Phase-Balancing Using Passive Circuit Elements

### 2.2.1 Analysis of IG with Phase Converters

Plain single-phase operation of a three-phase machine is an extreme case of unbalanced operation. This stems from the fact that the line current flowing into the 'free' terminal of the stator winding is forced to be zero. To reduce the phase imbalance, an effective remedy is to inject a line current artificially into the 'free' terminal by using phase converters which comprise passive circuit elements. Fig. 2.1 illustrates the principle of phase balancing for an induction machine operating on a single-phase power system [5], [54], [80]. The rotor is assumed to be rotating in such a direction that it traverses the stator winding in the sequence A-B-C. For generator operation, the rotor speed must be

slightly higher than the positive-sequence rotating field. Although special reference is made to a delta-connected machine in the following discussion, the principle is also applicable to a star-connected machine. Phase A of the IG is connected to the single-phase power system of voltage $V$, while the phase converters $Y_1$ and $Y_2$ are respectively connected across phase C and phase B. The current $I_{L2}$ that results from the currents $I_1$ and $I_2$ through the phase converters constitutes the line current into the 'free' terminal of the generator. Apparently the phase balance is improved and indeed, by appropriate choice of the values of $Y_1$ and $Y_2$, perfect phase balance may be achieved.

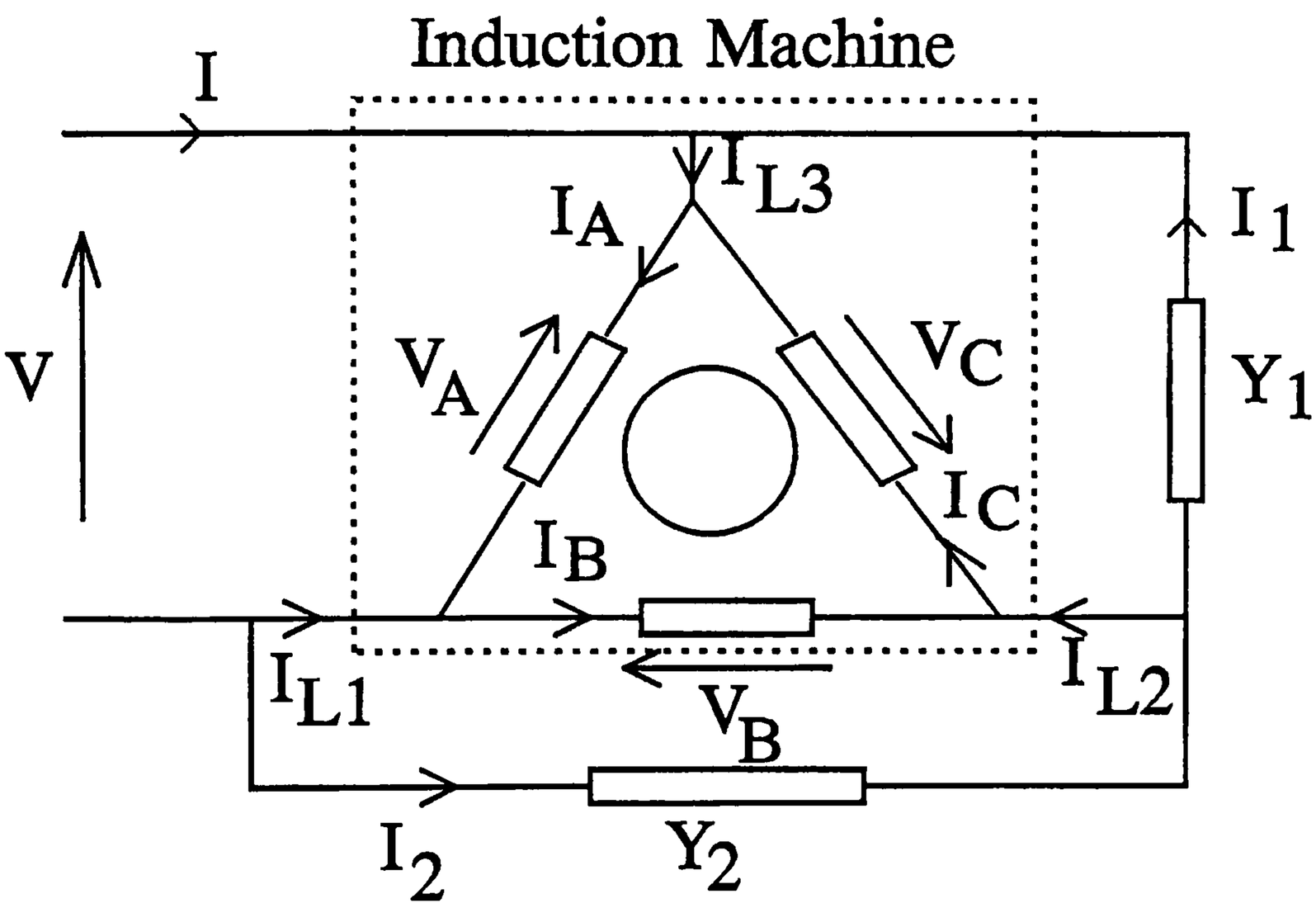


Fig. 2.1 Single-phase operation of three-phase IG with phase converters.

Referring to Fig. 2.1 and adopting the *motor* convention for the induction machine, the following 'inspection equations' [9] may be written:

$$V = V_A \tag{2.1}$$

$$V_A + V_B + V_C = 0 \tag{2.2}$$

$$I_1 = V_C Y_1 \tag{2.3}$$

$$I_2 = V_B Y_2 \tag{2.4}$$

$$I_1 = I_B - I_C + I_2 \tag{2.5}$$

The above equations can be solved by using the method of symmetrical components. The derivation is outlined in Appendix A.3, from which the positive-sequence voltage $V_p$ and negative-sequence voltage $V_n$ are determined:

$$V_p = \sqrt{3}V \cdot \frac{Y_n + \frac{e^{-j\pi/6}}{\sqrt{3}} Y_1 + \frac{e^{j\pi/6}}{\sqrt{3}} Y_2}{Y_1 + Y_2 + Y_p + Y_n} \tag{2.6}$$

$$V_n = \sqrt{3}V \cdot \frac{Y_p + \frac{e^{j\pi/6}}{\sqrt{3}} Y_1 + \frac{e^{-j\pi/6}}{\sqrt{3}} Y_2}{Y_1 + Y_2 + Y_p + Y_n} \tag{2.7}$$

where $Y_p$ and $Y_n$ are, respectively, the positive-sequence and negative-sequence admittances of the IG as shown in Fig. A.1 and Fig. A.2.

For perfect phase balance, the negative-sequence voltage component $V_n$ given by (2.7) should be equal to zero, hence

$$Y_p + \frac{e^{j\pi/6}}{\sqrt{3}} Y_1 + \frac{e^{-j\pi/6}}{\sqrt{3}} Y_2 = 0 \,. \tag{2.8}$$

By selecting values of $Y_1$ and $Y_2$ that satisfy (2.8), balanced operation of the IG may be achieved.

### 2.2.2 Phase-Balancing Schemes

Based on the theory outlined in Section 2.2.1, four practical phase-balancing schemes for a three-phase IG operating on a single-phase power system have been developed and

investigated. Figs. 2.2(a)-(d) show the details of the circuit connections. For convenience of discussion, each phase-balancing scheme is designated by the phase converter elements used, suffix 1 denoting a phase-C converter element while suffix 2 denoting a phase-B converter element. For example, a $R_1$-$C_2$ scheme will have a resistance connected across phase C and a capacitance connected across phase B.

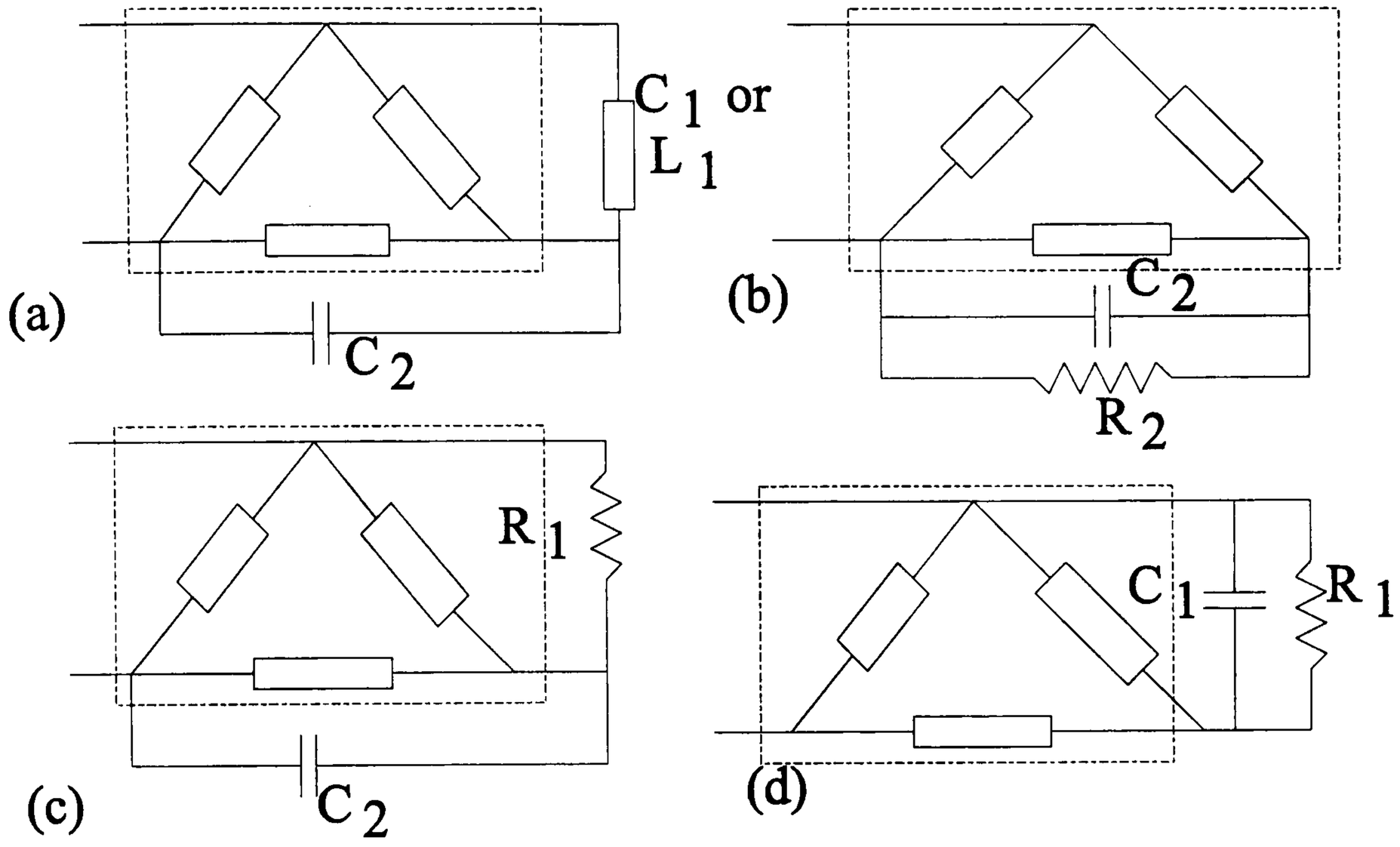


Fig. 2.2 Phase-balancing schemes for three-phase IG:
(a) $C_1(L_1)$-$C_2$ scheme; (b) $R_2$-$C_2$ scheme;
(c) $R_1$-$C_2$ scheme; (d) $R_1$-$C_1$ scheme.

The $C_1(L_1)$-$C_2$ scheme shown in Fig. 2.2(a) employs only energy storage elements, while the remaining schemes employ dissipative (or lossy) elements in addition to energy storage elements. For IG applications, the phase converter resistances can take the form of storage heating elements, auxiliary loads, or battery chargers. From the IG system's point of view, the power dissipated in these loads may be regarded as useful output as far as efficiency evaluation is concerned.

Using (2.8), it is possible to determine the values of the phase converters that result in perfect phase balance. As an illustration, consider the $C_1(L_1)$-$C_2$ scheme shown in Fig.

2.2(a). Assuming that $Y_1$ and $Y_2$ to be pure *capacitances* (i.e. $Y_1 = 0 + jB_1$; $Y_2 = 0 + jB_2$), (2.8) may be written as:

$$Y_p e^{-j\phi_p} + \frac{1}{\sqrt{3}} B_1 e^{j2\pi/3} + \frac{1}{\sqrt{3}} B_2 e^{j\pi/3} = 0 \tag{2.9}$$

where $Y_p$ is the positive-sequence admittance of the generator and $\phi_p$ is the positive-sequence impedance angle. Both $Y_p$ and $\phi_p$ are functions of the rotor speed.

Equating real and imaginary parts respectively to zero in (2.9), the values of the phase converter susceptances $B_1$ and $B_2$ are given by:

$$B_1 = \sqrt{3} G_p + B_p = 2 Y_p \sin(2\pi/3 - \phi_p) \tag{2.10}$$

$$B_2 = -\sqrt{3} G_p + B_p = 2 Y_p \sin(\phi_p - \pi/3) . \tag{2.11}$$

At the rotor speed such that $\phi_p = 2\pi/3$ rad, $B_1 = 0$ and $B_2 = \sqrt{3} Y_p$, Fig. 2.2(a) is reduced to the well-known Steinmetz connection [81].

Table 2.1 summarizes the values of phase converter elements to give perfect phase balance for various phase-balancing schemes. It is observed that the values of the phase converter elements are functions of the conductances and susceptances (or alternatively, the admittance and impedance angle) of the positive-sequence IG equivalent circuit.

To check the feasibility of the above phase-balancing schemes, experiments were performed on a 2.2-kW, 220-V, 50-Hz, 4-pole, delta-connected induction machine IG1 whose parameters are given in Appendix D.1. It was found that exact phase balance could in general be obtained with appropriate choice of values of phase converters, subject to the limitations inherent in each phase-balancing scheme. Figs. 2.3 to 2.6 show the variation of the phase converter conductances/susceptances that result in perfect phase balance when the IG is operating on a 220-V single-phase power system. Very

good agreement between the computed and experimental results is observed, thus verifying the theory developed in Section 2.2.1.

TABLE 2.1
CONDUCTANCES AND SUSCEPTANCES OF PHASE CONVERTERS FOR PERFECT PHASE BALANCE OF THREE-PHASE IG

| Scheme | Conductance (S) | Susceptance# (S) |
|---|---|---|
| $C_1(L_1)$-$C_2$ | $G_1 = 0$<br>$G_2 = 0$ | $B_1 = 2Y_p.sin(2\pi/3-\phi_p)$<br>$B_2 = 2Y_p.sin(\phi_p-\pi/3)$ |
| $R_2$-$C_2$ | $G_1 = 0$<br>$G_2 = \sqrt{3}Y_p.sin(\phi_p-2\pi/3)$ | $B_1 = 0$<br>$B_2 = \sqrt{3}Y_p.cos(\phi_p-2\pi/3)$ |
| $R_1$-$C_2$ | $G_1 = 2\sqrt{3}Y_p.sin(\phi_p-2\pi/3)$<br>$G_2 = 0$ | $B_1 = 0$<br>$B_2 = 2\sqrt{3}Y_p.sin(5\pi/6-\phi_p)$ |
| $R_1$-$C_1$ | $G_1 = \sqrt{3}Y_p.cos(5\pi/6-\phi_p)$<br>$G_2 = 0$ | $B_1 = \sqrt{3}Y_p.sin(5\pi/6-\phi_p)$<br>$B_2 = 0$ |

#Capacitive susceptances defined to be positive; inductive susceptances defined to be negative

### 2.2.3 Discussion of Results

The performance, limitation and application of each phase-balancing scheme are discussed as follows.

*$C_1(L_1)$-$C_2$ scheme*

As shown in Fig. 2.3, perfect phase balance can be achieved over the practical operating speed range of the IG (1500 r/min to 1570 r/min). The susceptance $B_2$ increases approximately linearly with speed and remains capacitive over the whole speed range. On the other hand, $B_1$ decreases with speed. At speeds below 1539 r/min, $B_1$ is capacitive and above this speed $B_1$ is inductive. At 1539 r/min, phase balance can be achieved with a single capacitance across phase B.

*$R_2$-$C_2$ scheme*

Using this scheme, perfect phase balance is possible at rotor speeds for which the positive-sequence impedance angle $\phi_p$ exceeds $2\pi/3$ rad (which results in positive values of the phase converter conductance $G_2$). Both $G_2$ and $B_2$ increase with increase in rotor speed. This scheme is useful when a large percentage of the input power need to be delivered to the power system.

*$R_1$-$C_2$ scheme*

As in the previous scheme, perfect phase balance is possible at rotor speeds for which $\phi_p$ exceeds $2\pi/3$ rad. The conductance $G_1$ increases with speed, but the susceptance $B_2$ remains substantially constant (Fig. 2.5).

*$R_1$-$C_1$ scheme*

As shown in Fig. 2.6, perfect phase balance over the normal generator speed range is possible with this scheme. Since $G_1$ has a much larger value compared with conductances in the previous two schemes, a larger amount of power is dissipated in the phase converter. This scheme is useful when a large percentage of the prime mover power is to be consumed by the local loads.

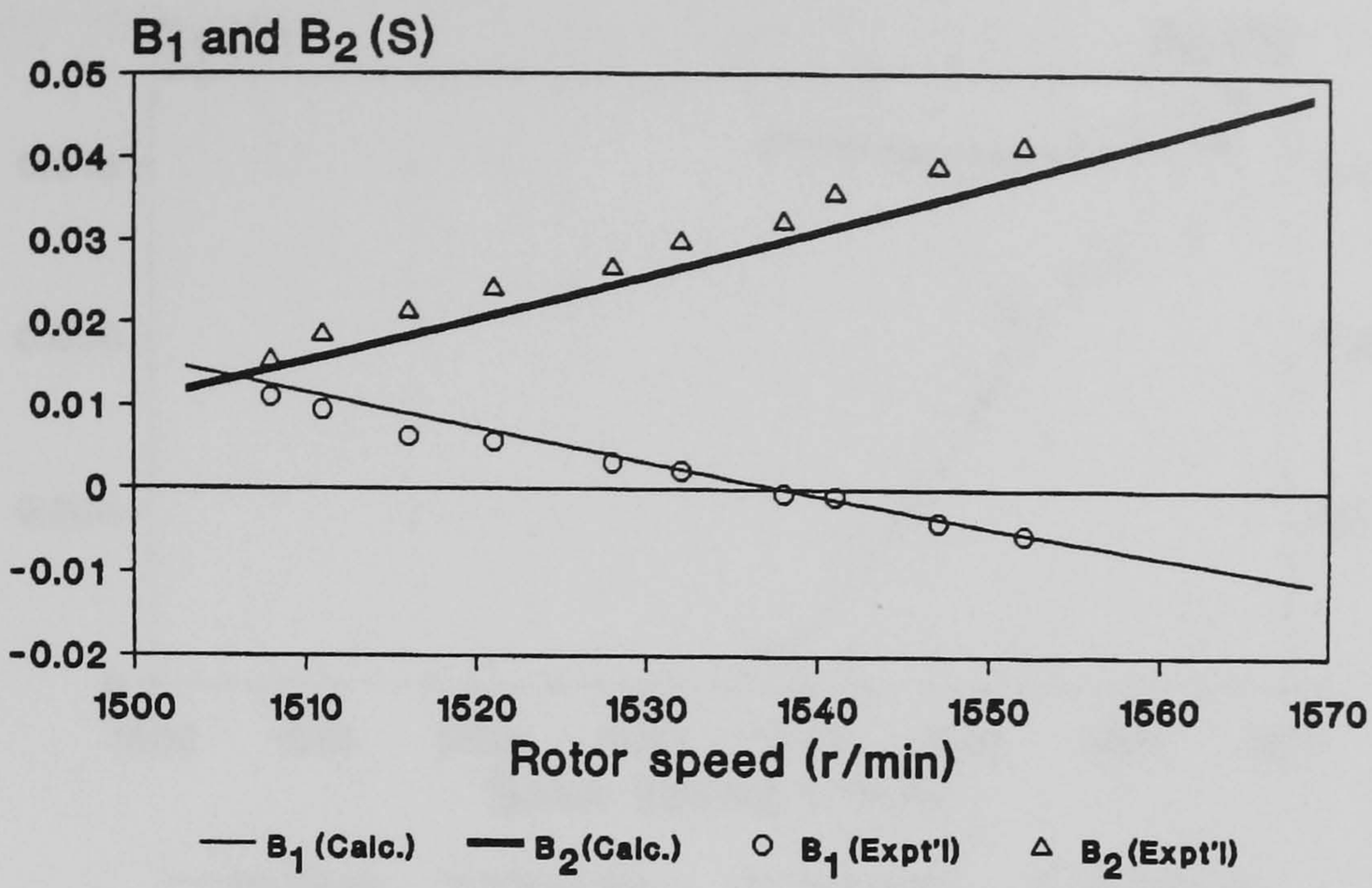


Fig. 2.3 Values of $B_1$ and $B_2$ to give phase balance at different speeds in $C_1(L_1)$-$C_2$ scheme.

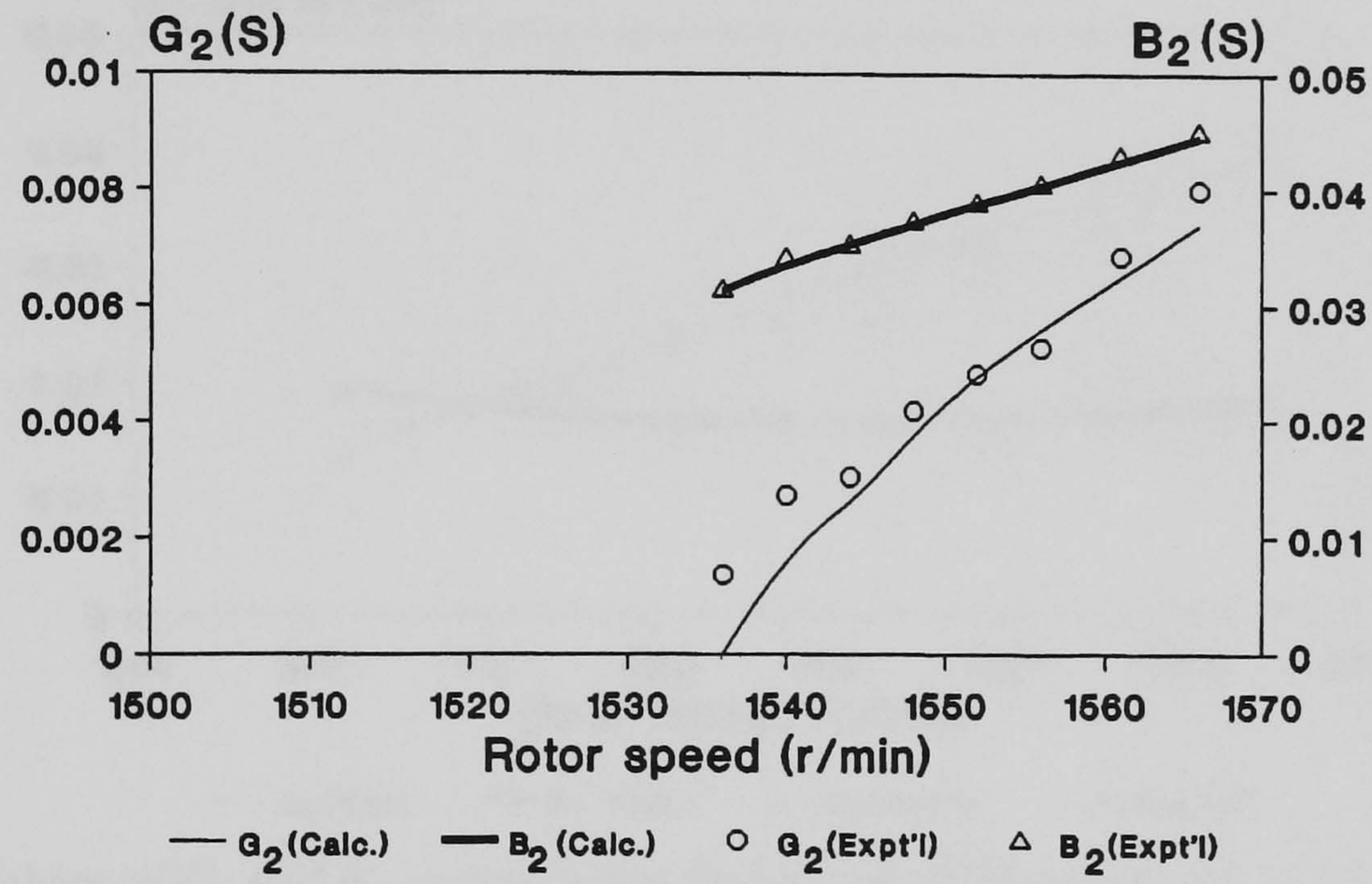


Fig. 2.4 Values of $G_2$ and $B_2$ to give phase balance at different speeds in $R_2$-$C_2$ scheme.

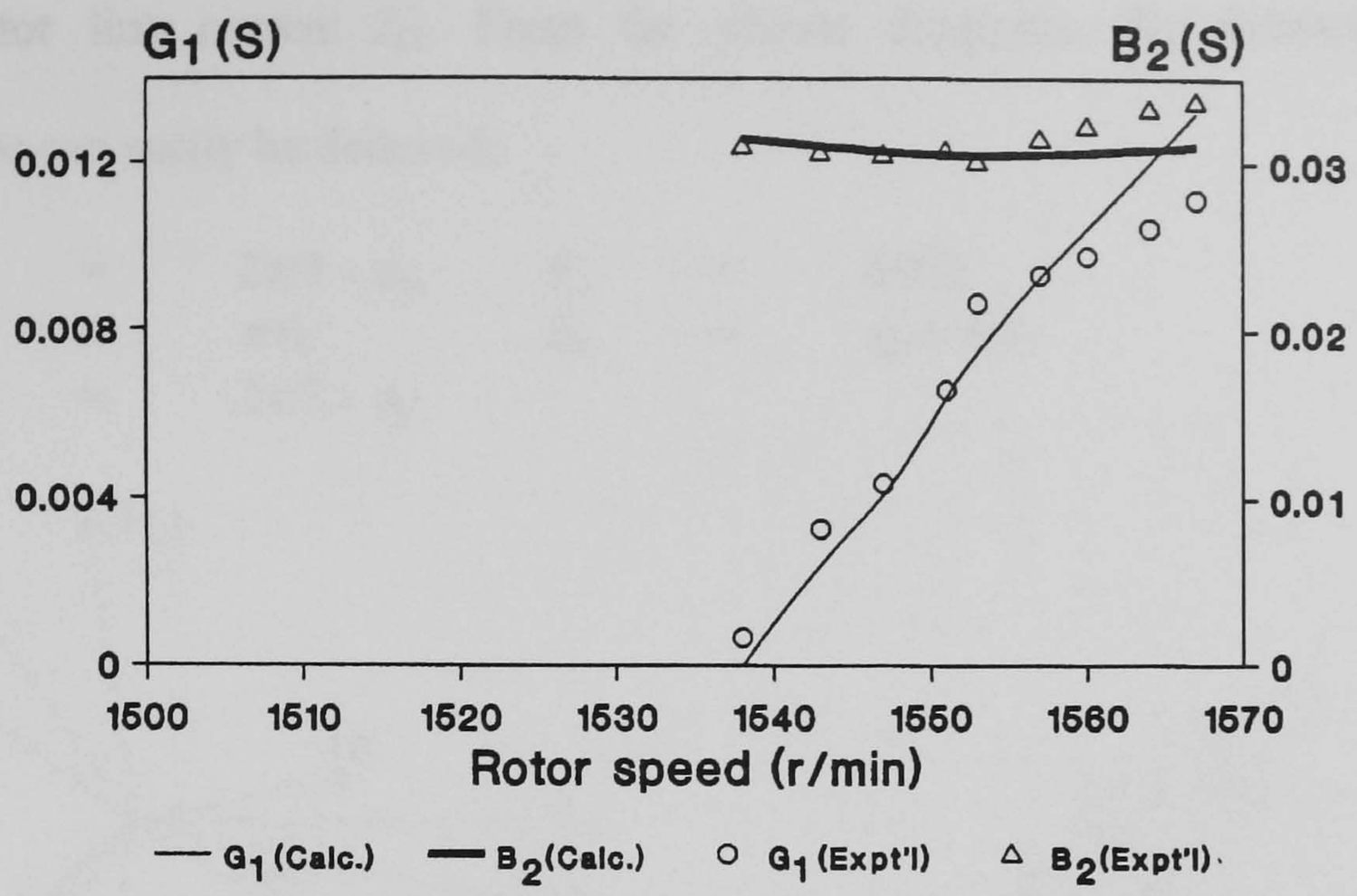


Fig. 2.5 Values of $G_1$ and $B_2$ to give phase balance at different speeds for $R_1$-$C_2$ scheme.

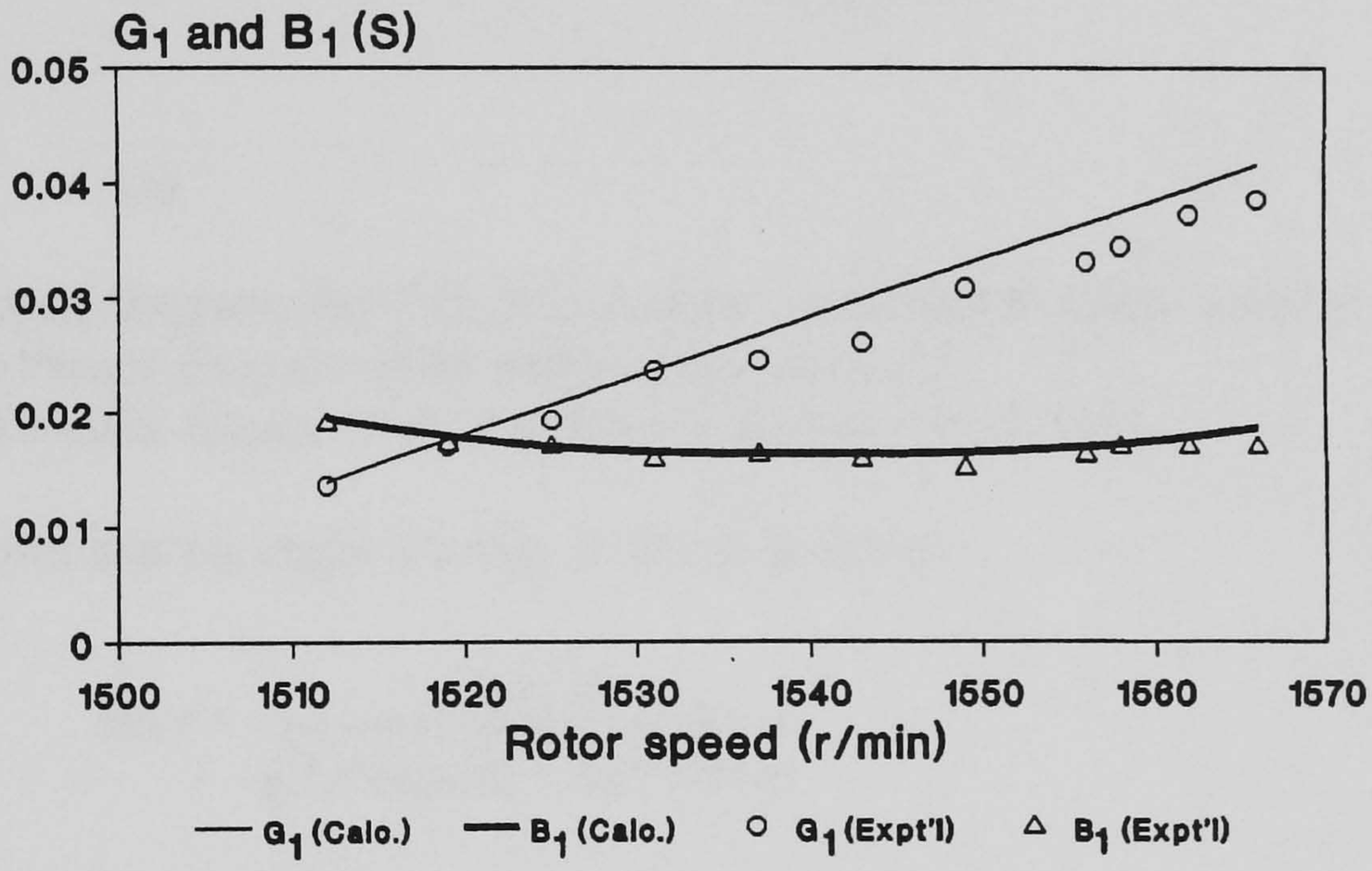


Fig. 2.6 Values of $G_1$ and $B_1$ to give phase balance at different speeds for $R_1$-$C_1$ scheme.

### 2.2.4 System Power Factor

The output power factor of the IG system can in general be computed using the equations presented in Section 2.2.1. For perfect phase balance, however, a closed form expression for the system power factor can be deduced from the voltage-current relationship in the phasor diagram. As an illustration, Fig. 2.7(a) shows the phasor diagram for the $C_1(L_1)$-$C_2$ scheme, assuming that the phase voltages and currents are balanced and $\phi_p$ is less than $2\pi/3$ rad, while Fig. 2.7(b) shows the relationship between the system input current $I$ and

the generator line current $I_{L1}$. From the phasor diagrams, the following angular relationships can easily be deduced:

| | | | | | | | |
|---|---|---|---|---|---|---|---|
| $\theta_1$ | = | $2\pi/3 - \phi_p$; | $\theta_2$ | = | $2\pi/3$; |
| $\theta_3$ | = | $\pi/6$; | $\theta_4$ | = | $\phi_p + \pi/6$; |
| $\theta_5$ | = | $2\pi/3 - \phi_p$ | | | |

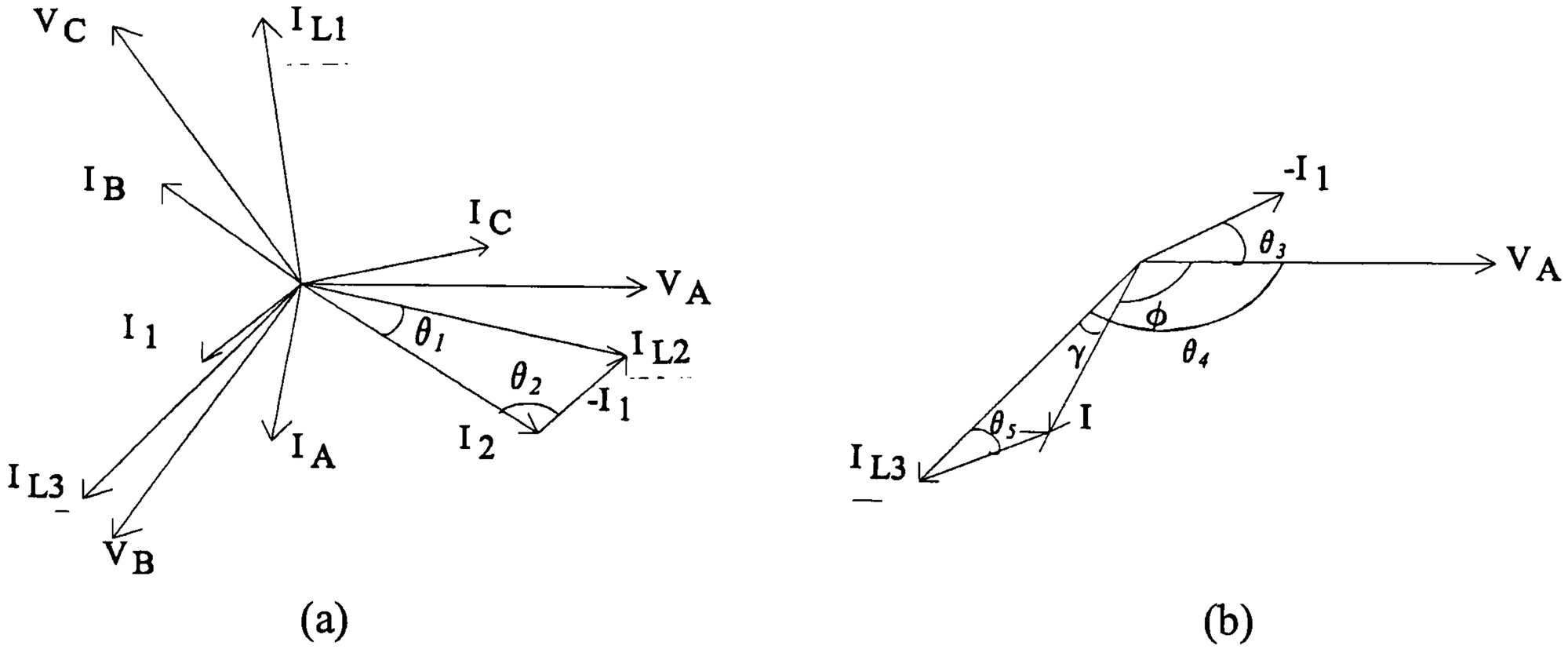


Fig. 2.7 Phasor diagrams for $C_1(L_1)$-$C_2$ scheme under perfect phase balance:
(a) Phasor diagram under perfect phase balance;
(b) Phasor diagram showing detailed angular relationships.

It can be shown that the angle $\gamma$ in Fig. 2.7(b) is given by

$$\sin\gamma = \frac{2\sin^2\alpha}{\sqrt{3+4\sin^2\alpha - 2\sqrt{3}\sin 2\alpha}} \tag{2.12}$$

where

$$\alpha = 2\pi/3 - \phi_p\,. \tag{2.13}$$

The derivation of (2.12) is given in Appendix A.4.

Hence the power factor angle $\phi$ is

$$\phi = \theta_4 - \gamma = \phi_p + \pi/6 - \gamma\,. \tag{2.14}$$

The power factor under balanced condition thus depends only on the positive-sequence impedance angle of the IG. The system power factors of the phase-balancing schemes are summarized in Table 2.2.

TABLE 2.2
SYSTEM POWER FACTORS OF PHASE-BALANCING SCHEMES UNDER PERFECT PHASE BALANCE

| Scheme | System power factor (p.u.) |
|---|---|
| $C_1(L_1)$-$C_2$ | $cos(\phi_p + \pi/6 - \gamma)$<br>where $\gamma = sin^{-1}\{2sin^2\alpha/(3+4sin^2\alpha-2\sqrt{3}sin2\alpha)\}$.<br>(For $\phi_p<2\pi/3$, $\alpha=2\pi/3-\phi_p$; for $\phi_p>2\pi/3$, $\alpha=\phi_p-2\pi/3$) |
| $R_2$-$C_2$ | $cos(\phi_p + \pi/6)$ |
| $R_1$-$C_2$ | $cos(3\pi/2 - \phi_p)$ |
| $R_1$-$C_1$ | $cos(\phi_p - \pi/6)$ |

Fig. 2.8 shows the variation of system power factor with speed for various phase-balancing schemes. It is observed that above 1539 r/min, the $C_1(L_1)$-$C_2$ and $R_2$-$C_2$ schemes have practically the same power factor, which is well over 0.9. The power factor of the $R_1$-$C_2$ scheme is slightly lower but is quite acceptable. The power factor of the $R_1$-$C_1$ scheme, however, is very low and becomes zero at a rotor speed of 1543 r/min. Below this speed, power is drawn from the power system in order to furnish the power to the phase converter resistance. A line-side power factor correction capacitor may thus be necessary for this phase-balancing scheme.

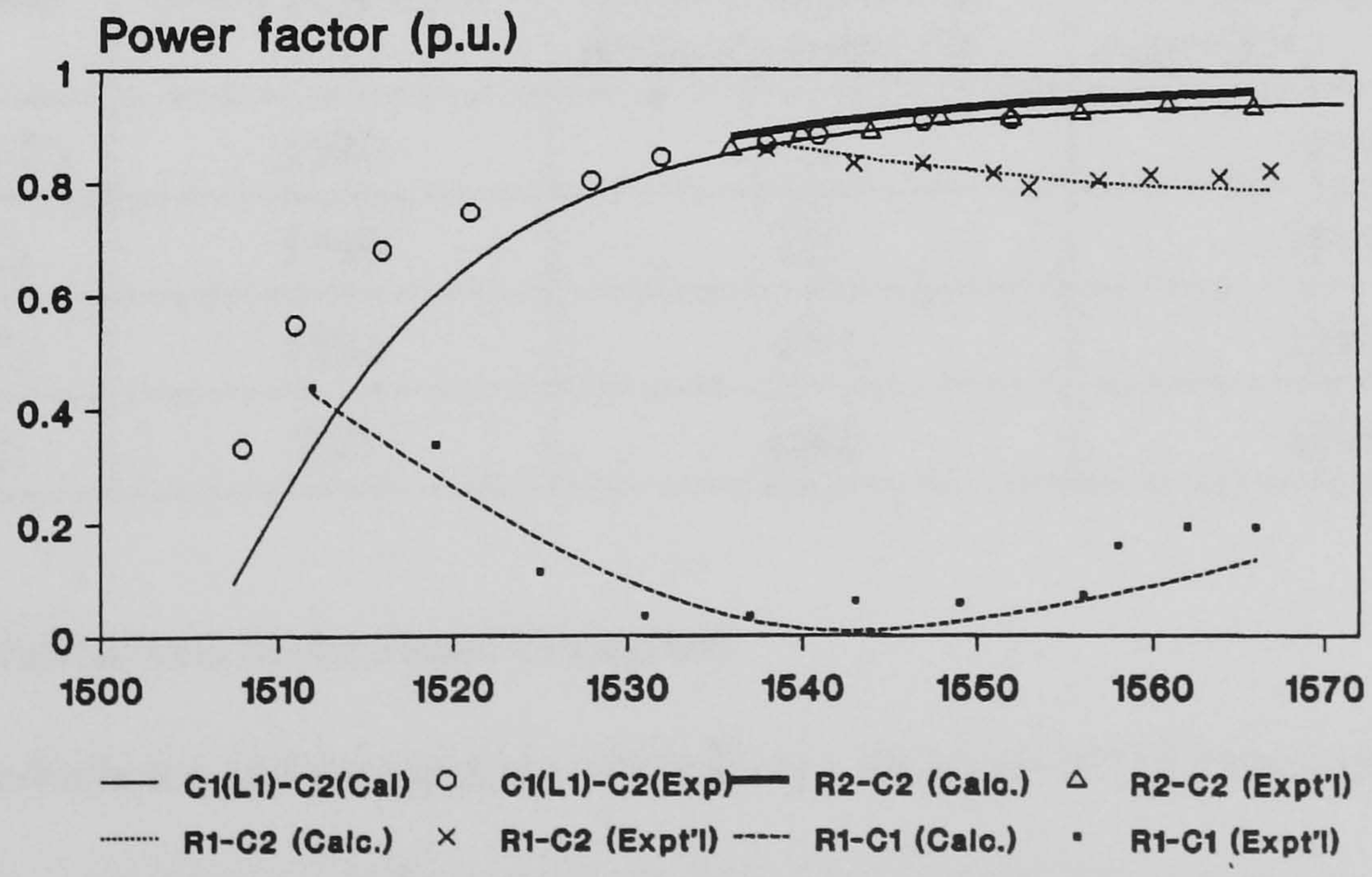


Fig. 2.8 System power factor under perfect phase balance.

### 2.2.5 Power and Efficiency

With perfect phase balance achieved by the use of phase converters, the IG operates as if it were operating under a balanced three-phase voltage supply. If the power dissipated in the phase converter resistance is regarded as useful power output, the system efficiency under single-phase operation is identical to the generator efficiency under balanced three-phase operation. For the experimental machine, a full-load efficiency of 0.82 was obtained with various phase balancing schemes.

Table 2.3 shows the experimental values of output power to grid, power dissipated in the phase converters, and developed electrical power for different phase-balancing schemes at a rotor speed of 1552 r/min and a stator current of 5.0 A. In all cases the developed power approaches the rated power of the induction machine. In the $R_1$-$C_1$ scheme, however, 86% of the net output electrical power is dissipated in the phase converter resistance, which is consistent with the observation made in Section 2.2.4.

TABLE 2.3
POWER TO GRID, POWER DISSIPATED IN PHASE CONVERTER AND NET ELECTRICAL OUTPUT

| Scheme | Power to grid (W) | Power dissipated in phase converter (W) | Net electrical power output (W) |
|---|---|---|---|
| $C_1(L_1)$-$C_2$ | 1910 | 0 | 1910 |
| $R_2$-$C_2$ | 1740 | 233 | 1973 |
| $R_1$-$C_2$ | 1564 | 420 | 1984 |
| $R_1$-$C_1$ | 270 | 1606 | 1876 |

### 2.2.6 Operation with Fixed Phase Converters

Both the conductance and susceptance of the IG are functions of the rotor speed. In order to achieve phase balance at different speeds, the values of the phase converters need to be varied accordingly. This can be accomplished using switched capacitors, thyristor-

controlled reactors, and chopper-controlled resistors. The increased circuit complexity and extra cost incurred may make the phase-balancing scheme unattractive. If, however, the load variation is limited to a narrow range using some form of turbine speed control, satisfactory machine performance may be achieved with fixed values of phase converters. Fig. 2.9 to Fig. 2.11 show the performance of the $R_2$-$C_2$ scheme in which the phase converters are fixed at the experimental values that give perfect phase balance at full load current. From Fig. 2.9, it is observed that the phase-B voltage increases when the speed is decreased from the rated value while the phase-C voltage decreases. The percentage over-voltage, however, is relatively small. At a speed of 1520 r/min, the experimental phase-B voltage is only 7% above the rated value.

Fig. 2.10 shows the variation of phase and line currents with speed. Again a slight overcurrent occurs in phase B as the speed is decreased from the rated value. Nevertheless, the increase in copper loss in phase B is more than offset by the reduction in copper losses in the other two phases, implying that the thermal performance of the generator is satisfactory.

Fig. 2.11 shows the variation in power factor and efficiency with speed. As the rotor speed is decreased from the rated value, the IG becomes over-compensated, causing a rise in the system power factor. But as the speed further decreases, the power delivered to the power system is smaller and the power factor drops rapidly. An efficiency close to 0.8 is obtained at speeds above 1550 r/min.

### 2.2.7 Summary

The feasibility of phase-balancing for a three-phase IG operating on a single-phase power system has been investigated. A general analysis for the IG generator with phase converters is presented, and expressions for determination of the phase converter

elements are given. Effects of phase-balancing on the output power, system power factor, and efficiency are discussed. It is also demonstrated that satisfactory generator performance is obtained with fixed phase converter elements if the speed variation is limited by turbine control. The theoretical analysis is verified by experiments on a small induction machine.

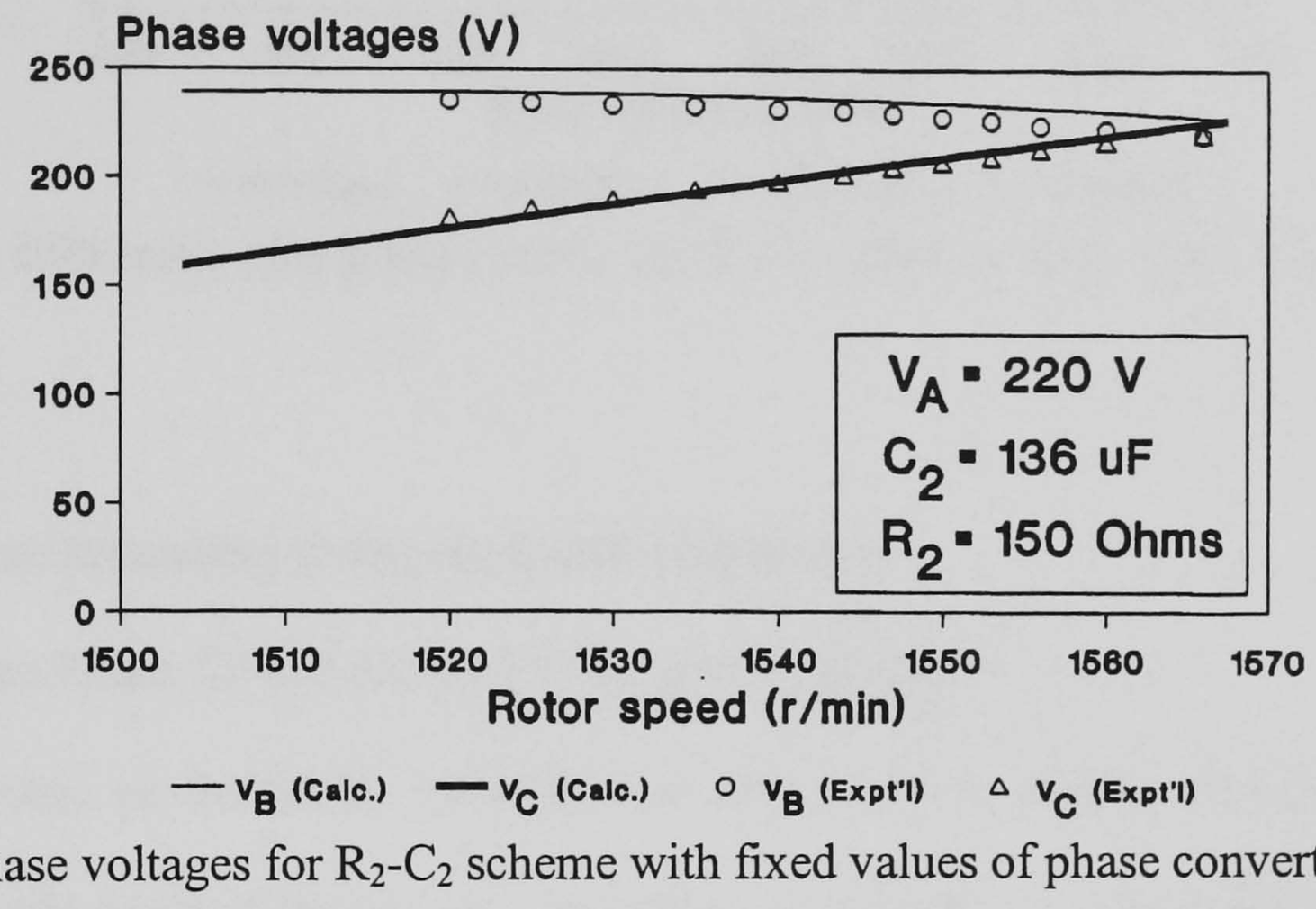


Fig. 2.9 Phase voltages for $R_2$-$C_2$ scheme with fixed values of phase converters.

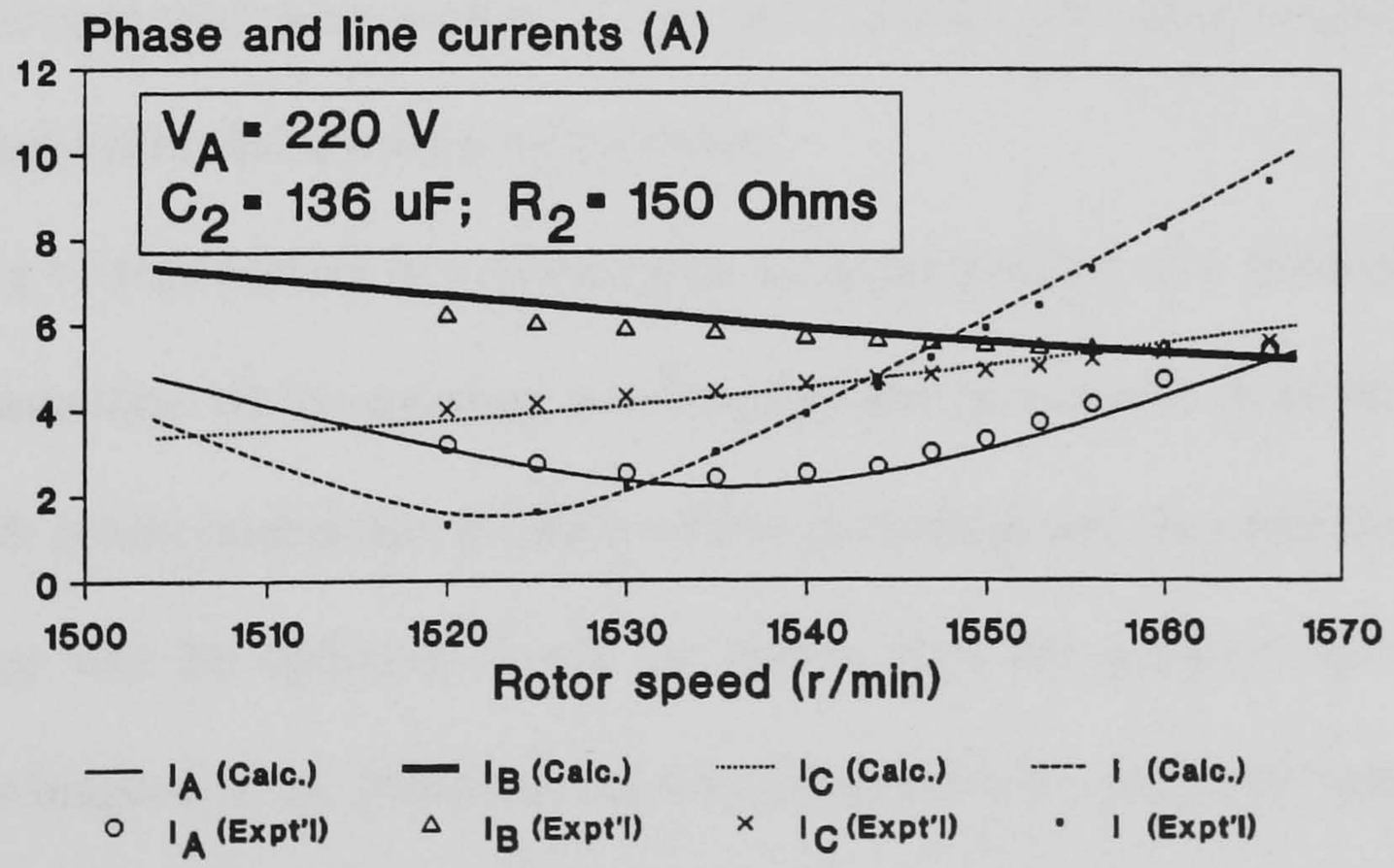


Fig. 2.10 Phase and line currents for $R_2$-$C_2$ scheme with fixed values of phase converters.

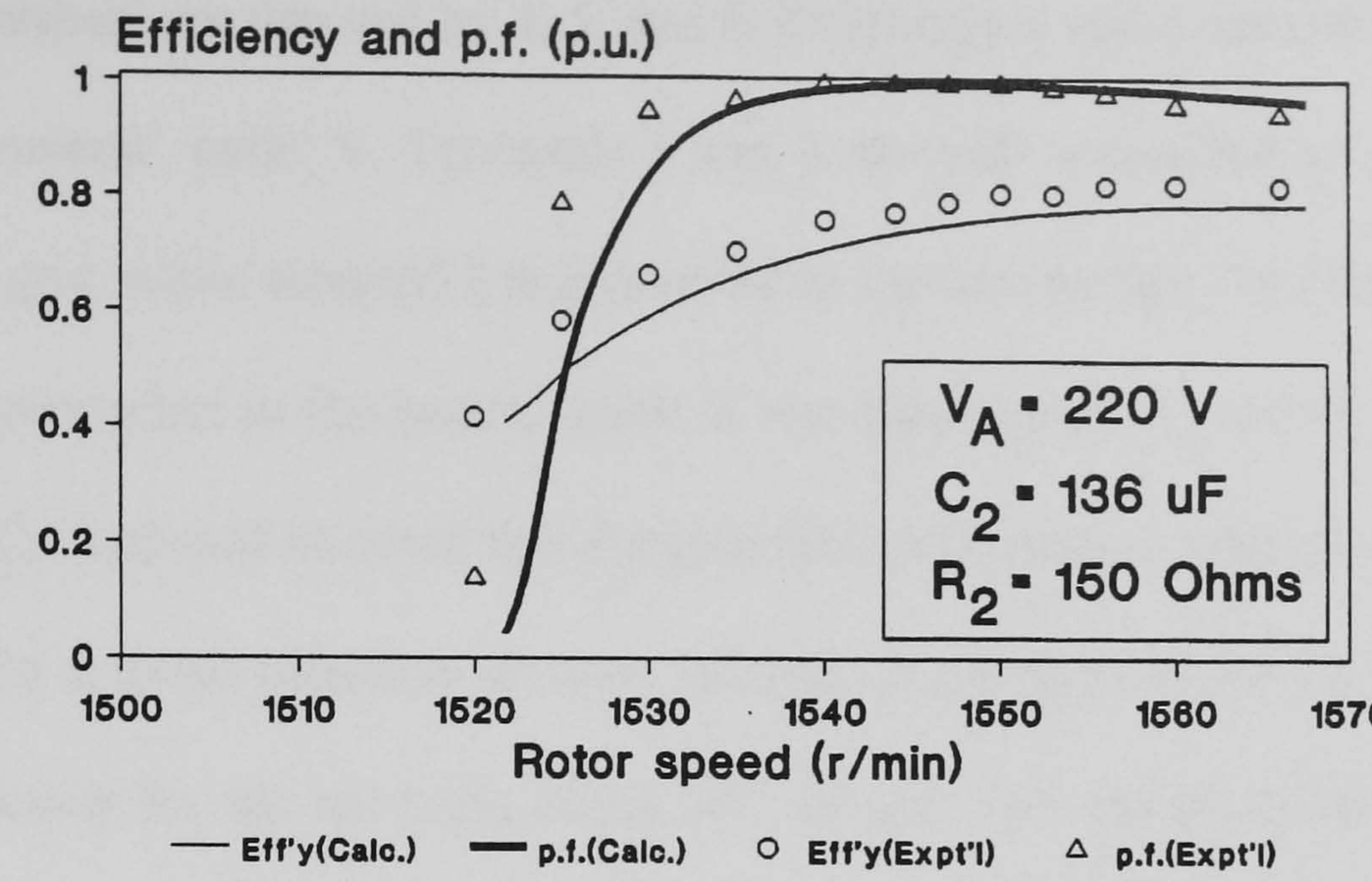


Fig. 2.11 Efficiency and power factor for $R_2$-$C_2$ scheme with fixed values of phase converters.

## 2.3 Phase Balancing Using the Smith Connection

### 2.3.1 Three-Phase IG with the Smith Connection (SMIG)

Published work on the Smith connection to date has been mainly concerned with the motoring mode of operation and the operational aspects such as selection of capacitances for perfect balance and motor starting. Chan and Lai [82], [83] have recently proposed a method of analysis on these modes of operation.

The objective of this section is to investigate the performance of a three-phase IG with the Smith connection when operating on a single-phase power grid. A systematic analysis of the IG with Smith connection (SMIG) will be presented, and the conditions for perfect phase balance will be deduced. It will be shown that, for medium and heavy loads, perfect phase balance in the induction machine is possible by using only capacitive phase converters. A method to give satisfactory operation over the normal speed range is proposed. Experimental results will be used to validate the theoretical analysis.

Fig. 2.12 shows the Smith connection for a three-phase IG operating on a single-phase power system. The 'starts' of the stator phases A, B and C are denoted by 1, 2, and 3

while the 'finishes' are denoted by 4, 5, and 6. Terminals 4 and 6 are common and form the 'pseudo-neutral' point N. Terminals 1 and 2 are both connected to one line of the single-phase grid, while terminal 3 is connected to the second line. Terminal 5 (the 'free' terminal) is connected to the neutral point N via capacitance $C_1$, and to terminal 3 via capacitance $C_2$. It should be noted that the generator performance is sensitive to the phase connection for a given direction of rotor rotation. A comparison of Fig. 2.12 with the Smith connection for the motoring mode [82] reveals that phases B and C have been interchanged, a condition necessary for proper phase balancing as will be explained in the following section.

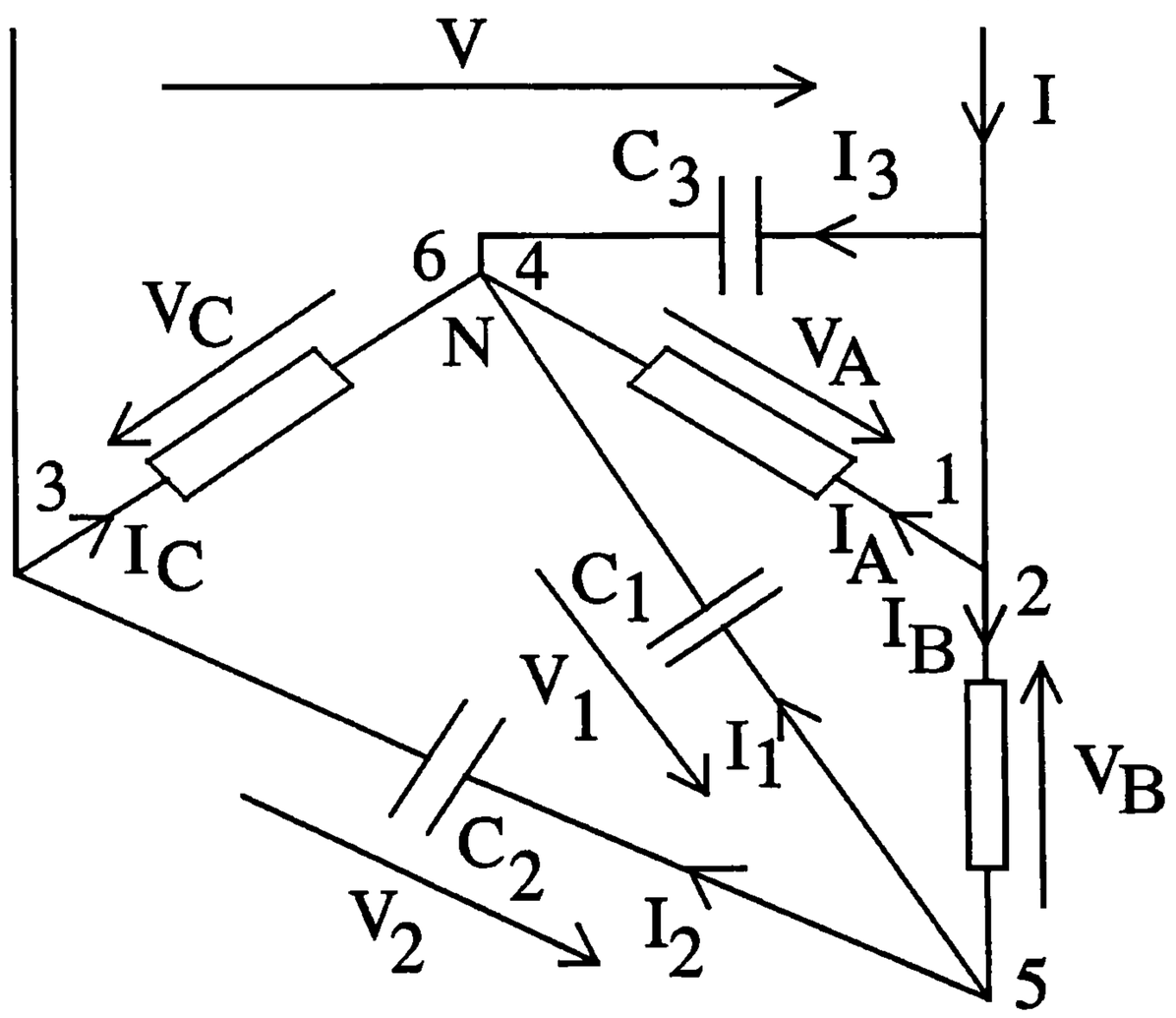


Fig. 2.12 Smith connection for three-phase IG operating on a single-phase grid.

The Smith connection is essentially an asymmetrical winding connection. But, with an appropriate choice of the terminal capacitances, it is possible for the IG to operate with balanced phase currents and phase voltages. As shown in Fig. 2.12, the phase-B current is the sum of the capacitor currents $I_1$ and $I_2$. Consider the phasor diagram in Fig. 2.13(a), drawn for the special case for perfect phase balance. The current $I_1$ leads $V_1$ (or $V_{AB}$) by

$\pi/2$ rad and hence lags $V_B$ by $2\pi/3$ rad. The voltage $V_2$ (which is equal to $V_{AB}$ - $V_C$), is equal to $2V_A$. The capacitor current $I_2$ leads $V_2$ by $\pi/2$ rad and hence it lags $V_B$ by $5\pi/6$ rad. For generator impedance angles between $2\pi/3$ rad and $5\pi/6$ rad, the phase current $I_B$ can be synthesized with the required magnitude and phase angle to give phase balance, by using suitable values of $C_1$ and $C_2$.

Under perfect phase balance conditions, the phase currents of the IG must sum to zero. This requires that the currents $I_2$ and $I_3$ to be equal, implying that $C_3$ must be equal to twice of $C_2$.

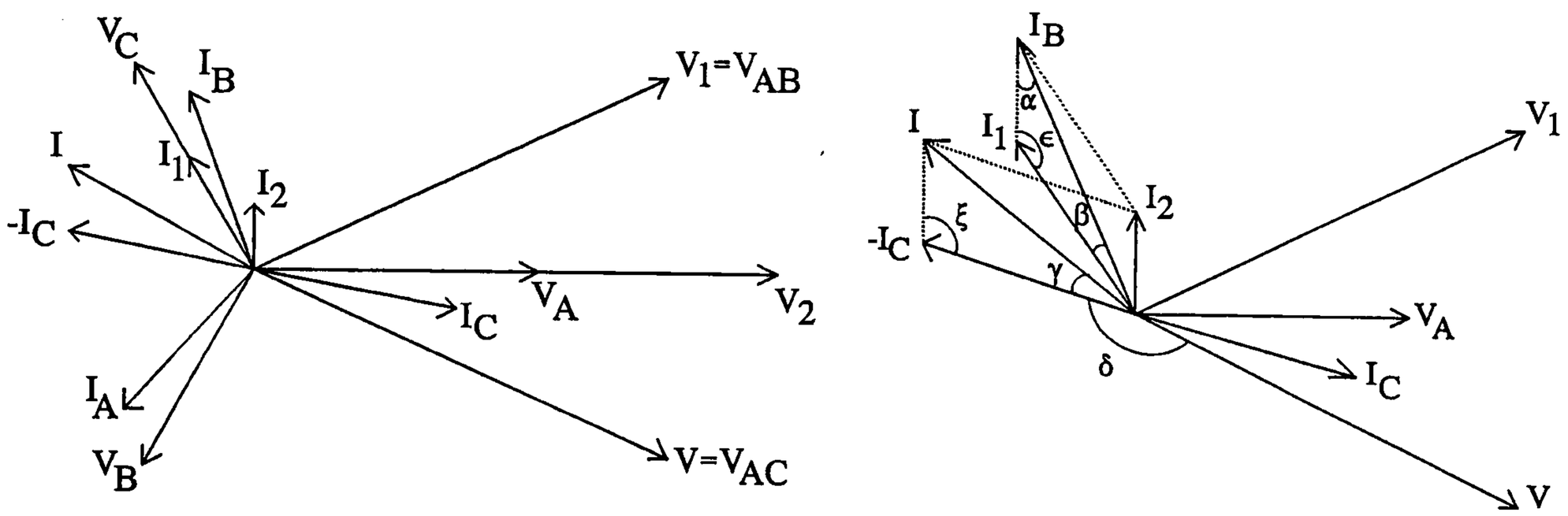


(a) (b)

Fig. 2.13 SMIG under perfect phase balance:
(a) Phasor diagram;
(b) Phasor diagram showing angular relationship between currents.

With balanced currents flowing in the stator phases, a perfect rotating magnetic field is produced. The air gap voltages per phase, and hence the phase voltages, will also be balanced. The generator operates as if it were supplying a balanced three-phase load, hence the efficiency is the same as that obtaining when the generator operates on a balanced three-phase grid.

Balanced conditions are valid for a given set of capacitance values as long as the rotor speed remains constant. When the rotor speed changes, the circuit conditions are disturbed and a new set of capacitance values is required to balance the generator again.

### 2.3.2 Performance Analysis

Performance analysis of the three-phase SMIG for the general off-balance operation can be carried out using the method of symmetrical components, the circuit being considered as a special case of winding asymmetry. Referring to Fig. 2.12 and adopting the *motor* convention for the induction machine, the following inspection equations may be established:

$$V = V_A - V_C \tag{2.15}$$

$$I_B = I_1 + I_2 \tag{2.16}$$

$$I_A + I_C + I_1 + I_3 = 0 \tag{2.17}$$

$$I_1 = V_1 . Y_1 = (V_A - V_B) . Y_1 \tag{2.18}$$

$$I_2 = V_2 . Y_2 = (V_A - V_B - V_C) . Y_2 \tag{2.19}$$

$$I_3 = V_A . Y_3 \tag{2.20}$$

$$I = I_2 - I_C \tag{2.21}$$

$$Y_3 = 2 . Y_2 \tag{2.22}$$

where $Y_1 = jB_1 = j\omega C_1$, $Y_2 = jB_2 = j\omega C_2$, and $Y_3 = jB_3 = j\omega C_3$.

The symmetrical component equations given in Appendix A.1 are written for a star-connected system as follows:

$$\begin{bmatrix} V_A \\ V_B \\ V_C \end{bmatrix} = \frac{1}{\sqrt{3}} \begin{bmatrix} 1 & 1 & 1 \\ 1 & h^2 & h \\ 1 & h & h^2 \end{bmatrix} \begin{bmatrix} V_0 \\ V_p \\ V_n \end{bmatrix} \tag{2.23}$$

$$\begin{bmatrix} I_A \\ I_B \\ I_C \end{bmatrix} = \frac{1}{\sqrt{3}} \begin{bmatrix} 1 & 1 & 1 \\ 1 & h^2 & h \\ 1 & h & h^2 \end{bmatrix} \begin{bmatrix} I_0 \\ I_p \\ I_n \end{bmatrix} \tag{2.24}$$

where $h$ is the complex operator $\exp(j2\pi/3)$.

From (2.16) and (2.17),

$$I_A + I_B + I_C - I_2 + I_3 = 0 \tag{2.25}$$

Using (2.19), (2.23) and (2.24), (2.25) can be rewritten as:

$$\frac{3I_0}{\sqrt{3}} - (V_A - V_B - V_C).Y_2 + V_A.Y_3 = 0 \tag{2.26}$$

From (2.22), (2.23) and (2.26), the following equation is obtained:

$$\frac{3I_0}{\sqrt{3}} + \frac{3V_0}{\sqrt{3}}.Y_2 = 0 \tag{2.27}$$

Since $I_0 = V_0.Y_0$, where $Y_0$ is the zero-sequence admittance of the motor, (2.27) may be written as:

$$V_0.(Y_0 + Y_2) = 0 \tag{2.28}$$

The sum of admitttances $Y_0$ and $Y_2$ is non-zero, hence the zero-sequence voltage $V_0$ must vanish according to (2.28).

Hence, if the condition prescribed by (2.22) is satisfied, zero-sequence voltage and current are absent in the SMIG. There are thus no zero-sequence losses, and the phase imbalance is contributed solely from negative-sequence quantities.

Eqns. (2.15) to (2.22) can now be solved in association with (2.23) and (2.24) to yield the positive-sequence and negative-sequence voltage components:

$$V_p = \frac{\sqrt{3}V}{h(1-h)} \cdot \frac{hY_n - 2Y_2 - (1-h)Y_1}{Y_p + Y_n + 3Y_1 + 2Y_2} \tag{2.29}$$

$$V_n = \frac{\sqrt{3}V}{h(1-h)} \cdot \frac{(1-h^2)Y_1 + 2Y_2 - h^2 Y_p}{Y_p + Y_n + 3Y_1 + 2Y_2} \tag{2.30}$$

where $Y_p$ and $Y_n$ are the positive- and negative-sequence admittances of the three-phase IG.

For a given single-phase grid voltage $V$ and speed (or per-unit slip), $Y_p$ and $Y_n$ are known and both $V_p$ and $V_n$ can be computed. The currents $I_p$ and $I_n$ can then be calculated from the positive- and negative-sequence equivalent circuits. The generator performance, such as phase voltages, phase currents, electromagnetic torque, power factor and efficiency, can subsequently be obtained.

### 2.3.3 Balanced Operation

*A) Susceptances for perfect phase balance*

It is of interest to investigate the values of susceptances that will result in balanced operation in the three-phase induction machine. Since negative-sequence voltage is absent when the generator is balanced, one obtains, from (2.30),

$$(1-h^2)Y_1+2Y_2-h^2Y_p=0\,. \tag{2.31}$$

Assuming that $Y_1$ and $Y_2$ to be pure *capacitive* admittances, i.e. $Y_1 = jB_1$ and $Y_2 = jB_2$, (2.31) may be rewritten as two simultaneous algebraic equations:

$$\frac{1}{2}B_1+B_2=-\frac{Y_p}{\sqrt{3}}\cos\phi_p \tag{2.32}$$

$$\frac{3}{2}B_1+B_2=Y_p\sin\phi_p \tag{2.33}$$

where $\phi_p$ is the positive-sequence impedance angle of the IG.

The capacitive susceptances that result in perfect phase balance are obtained by solving (2.32) and (2.33):

$$B_1=\frac{2}{\sqrt{3}}Y_p\sin\left(\frac{5\pi}{6}-\phi_p\right) \tag{2.34}$$

$$B_2=Y_p\sin\left(\phi_p-\frac{2\pi}{3}\right) \tag{2.35}$$

$$B_3 = 2Y_p \sin\left(\phi_p - \frac{2\pi}{3}\right). \tag{2.36}$$

The values of phase-converter susceptances required thus depend on $Y_p$ and $\phi_p$ which are both functions of the rotor speed. Depending upon the generator impedance angle, one or more of the susceptances may assume negative values, implying that inductances may have to be used for perfect phase balance. Table 2.4 summarizes the nature of the phase converter susceptances for different values of $\phi_p$. When $\phi_p$ lies between $2\pi/3$ rad and $5\pi/6$ rad, $B_1$, $B_2$, and $B_3$ all have positive values, implying that perfect phase balance can be achieved by using capacitances only. When $\phi_p$ is less than $2\pi/3$ rad, $B_1$ is positive but $B_2$ and $B_3$ are negative, hence one capacitance and two inductances are required for perfect phase balance.

TABLE 2.4
SUSCEPTANCES FOR PERFECT PHASE BALANCE IN THREE-PHASE IG

| Range of $\phi_p$ | $B_1$ | $B_2$ | $B_3$ |
|---|---|---|---|
| $\phi_p < 2\pi/3$ | Capacitive | Inductive | Inductive |
| $\phi_p = 2\pi/3$ | Capacitive | Zero | Zero |
| $2\pi/3 < \phi_p < 5\pi/6$ | Capacitive | Capacitive | Capacitive |
| $\phi_p = 5\pi/6$ | Zero | Capacitive | Capacitive |
| $\phi_p > 5\pi/6$ | Inductive | Capacitive | Capacitive |

It is interesting to note that, when $\phi_p = 2\pi/3$ rad, $B_2$ and $B_3$ are both equal to zero, hence the capacitances $C_2$ and $C_3$ are not required. Under this condition, the Smith connection is equivalent to the Steinmetz connection for a star-connected IG. When $\phi_p = 5\pi/6$ rad, however, $B_1$ is equal to zero and only capacitances $C_2$ and $C_3$ need to be used for achieving perfect phase balance.

*B) Line current and power factor*

Referring to the phasor diagram of the SMIG shown in Fig. 2.13(b), the following angular relationships may be deduced:

$\alpha = 5\pi/6 - \phi_p$; $\beta = \phi_p - 2\pi/3$; $\varepsilon = 5\pi/6$;
$\delta = \phi_p + \pi/6$; $\xi = \phi_p - 5\pi/6$.

From the current phasor triangles, it can be shown that the line current $I$ and the generator phase current $I_{ph}$ are related by

$$I = I_{ph}\sqrt{1 + 8\sin^2\left(\phi_p - \frac{2\pi}{3}\right)}. \tag{2.37}$$

The angle $\gamma$ between $I$ and $I_C$ in Fig. 2.13(b) is given by

$$\gamma = \sin^{-1}\left[\frac{\sin 2(\phi_p - 2\pi/3)}{\sqrt{1 + 8\sin^2(\phi_p - 2\pi/3)}}\right]. \tag{2.38}$$

If the *input* power factor angle $\phi$ is defined to be positive when the line current $I$ lags the supply voltage $V$, then

$$\phi = \delta + \gamma = \phi_p + \frac{\pi}{6} + \gamma. \tag{2.39}$$

Eqns. (2.38) and (2.39) indicate that the input power factor angle of the SMIG under perfect phase balance is a function of the generator impedance angle only. Fig. 2.14 shows the variation of the line power factor angle $\phi$ with the positive-sequence impedance angle $\phi_p$. It is observed that the line power factor angle is $180^0$e (i.e., line power factor is equal to unity) when $\phi_p$ is equal to $130.89^0$e. At higher values of $\phi_p$, the SMIG delivers power at lagging power factor to the single-phase grid.

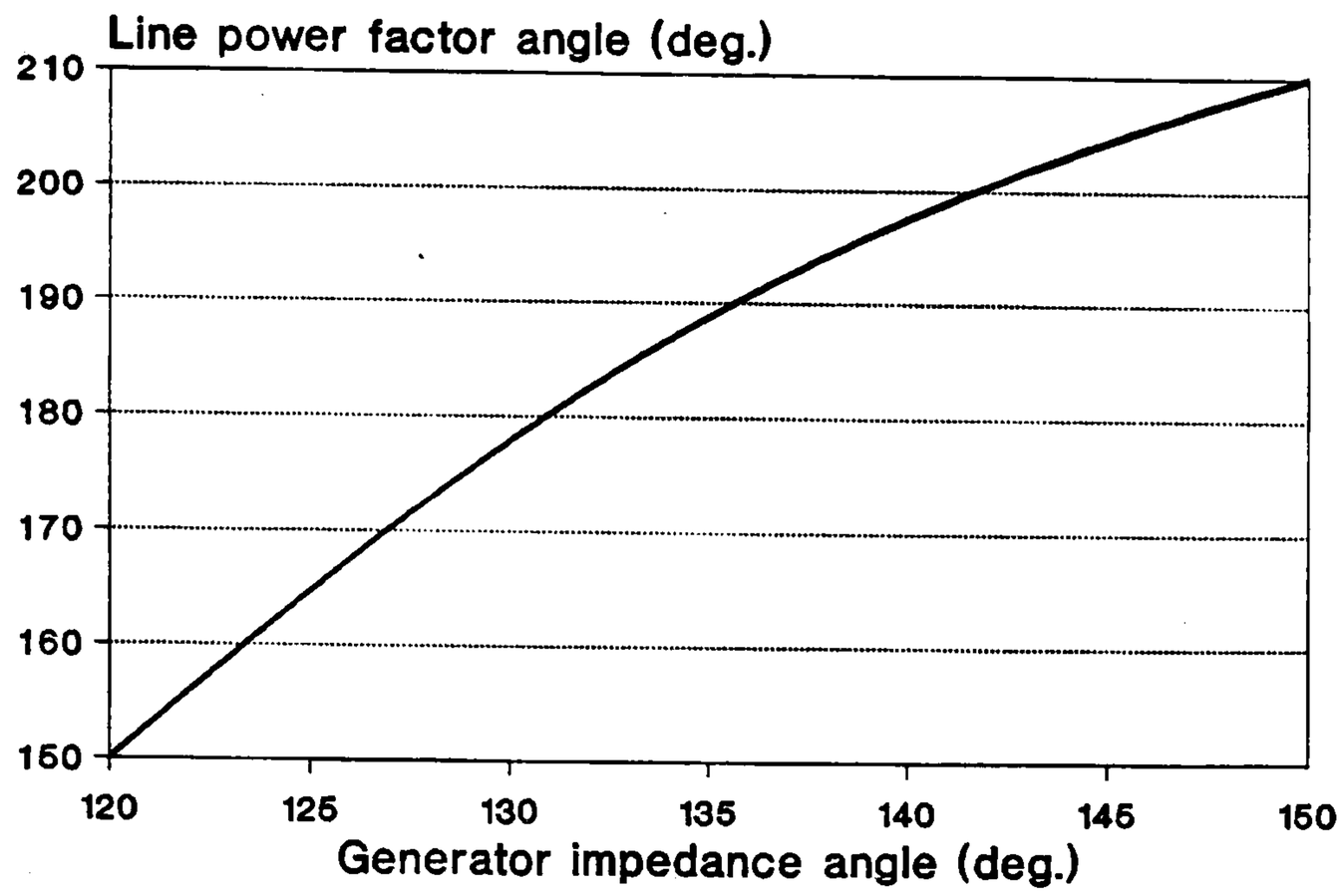


Fig. 2.14 Variation of line power factor angle with generator impedance angle.

### 2.3.4 Results and Discussion

To verify the above analysis, a phase-balancing experiment was performed with the machine IG1 (reconnected as the SMIG) whose parameters are given in Appendix D.1. With the single-phase grid voltage maintained constant at 380 V, the rotor speed of the SMIG was controlled by a separately-excited dc motor and the capacitances were varied until the phase voltages and currents were balanced. Fig. 2.15 shows the computed and experimental values of susceptances $B_1$ and $B_2$ that give perfect balanced operation in the three-phase machine. For speeds above 1539 r/min, both $B_1$ and $B_2$ are positive (i.e., capacitive). As the rotor speed increases, $B_1$ decreases slightly while $B_2$ increases almost linearly, meaning that more and more reactive power is being furnished by the capacitances $C_2$ and $C_3$. Good correlation between the experimental and computed performance characteristics is observed. The results confirm that perfect phase balance in the three-phase IG can be achieved at different speeds using the Smith connection.

A load test was next conducted on the experimental machine with the following values of capacitances: $C_1 = 27$ μF, $C_2 = 16$ μF, and $C_3 = 32$ μF. These capacitances enabled the

IG to be balanced at a rotor speed of 1568 r/min and at a phase current of 5.25 A (0.97 of rated value). For convenience, this speed will be denoted by $N_b$ in the subsequent discussion. Due to additional power losses produced by the negative-sequence rotating field, the 'cut-in' speed $N_{cut\text{-}in}$ (i.e., the speed at which the SMIG starts to deliver power to the grid) was 1515 r/min, which is considerably higher than the synchronous speed. Fig. 2.16 to Fig. 2.20 show the experimental and computed performance characteristics of the SMIG. Fig. 2.16 shows that, with fixed values of capacitances, the phase-A voltage increases as the speed decreases from $N_b$, while both the phase-B and phase-C voltages decrease. At speeds above $N_b$, overvoltage occurs in phase C. The voltage stress in phase A and phase C thus imposes a limit on the speed range over which the given set of capacitances could be left in the circuit. If the phase voltage is not to exceed 110 per cent of the rated value, then satisfactory generator operation from $N_{cut\text{-}in}$ up to 1600 r/min is possible.

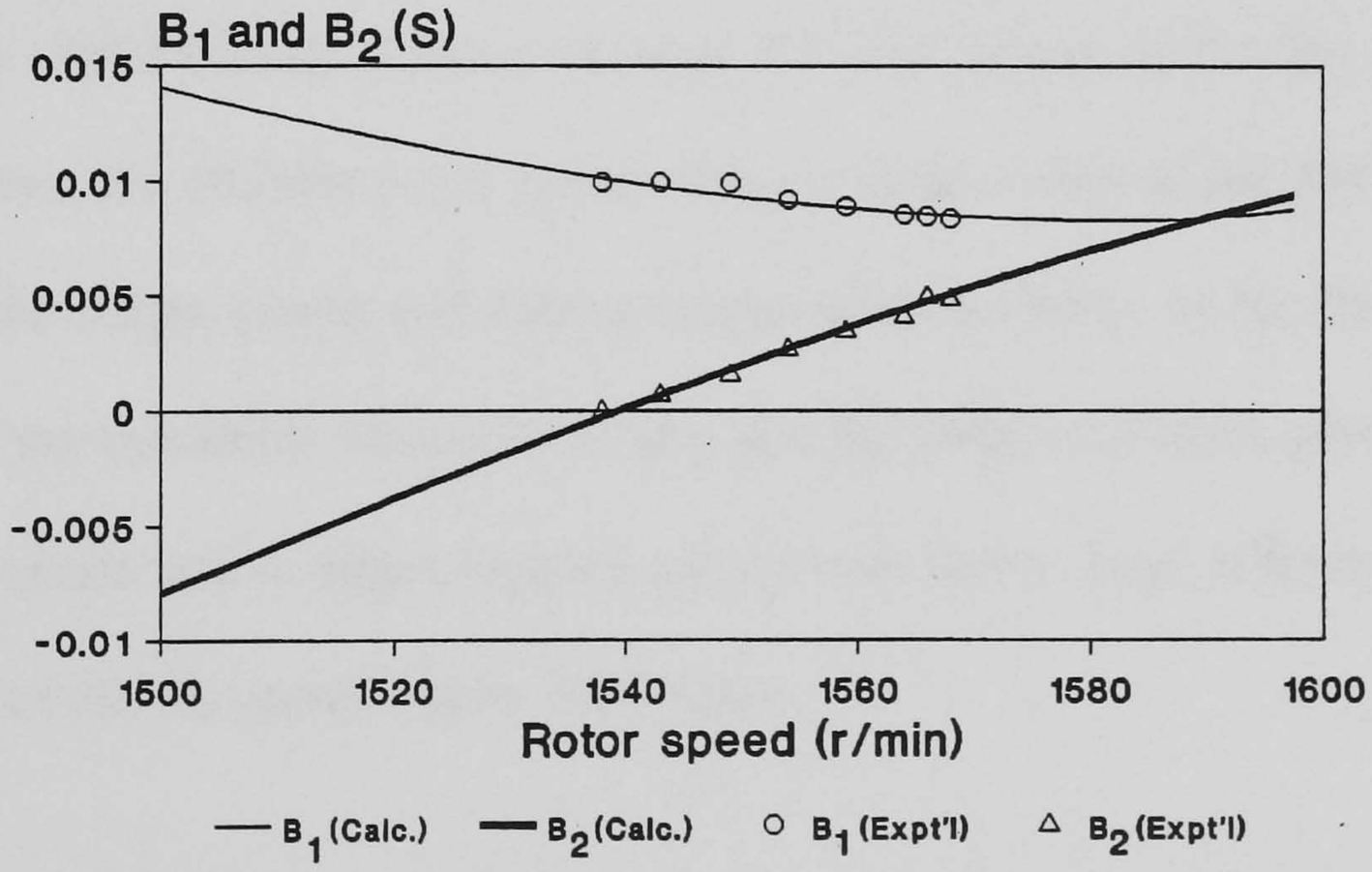


Fig. 2.15 Susceptances of phase converters to give perfect phase balance in experimental SMIG ($B_3 = 2B_2$).

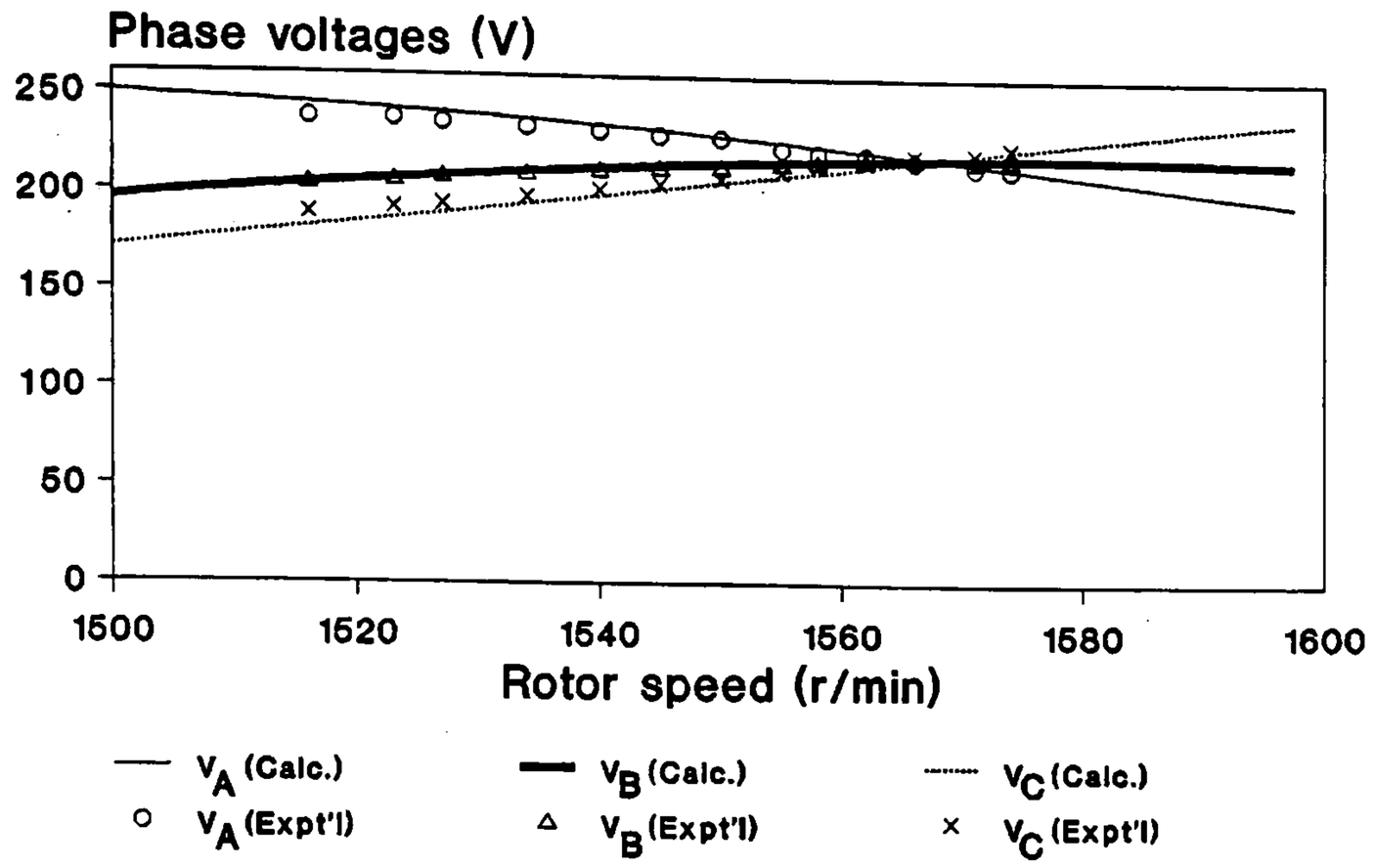


Fig. 2.16 Phase voltage variations of SMIG.

Fig. 2.17 shows the variation of phase and line currents of the SMIG with speed. Both $I_A$ and $I_C$ exhibit a concave-upward characteristic, but $I_A$ is much higher at low speeds. At synchronous speed, $I_A$ is equal to 7.1 A, or 131% of the rated value. Starting from 1520 r/min, $I_C$ increases very rapidly, eventually exceeding both $I_A$ and $I_B$ for speeds above $N_b$. On the contrary, the phase-B current is relatively insensitive to changes in rotor speed. At speeds below 1540 r/min, $I_B$ is almost constant at 6 A (110% of rated value).

Fig. 2.18 shows the efficiency and power factor characteristics of the SMIG while Fig. 2.19 shows the output power and driving torque characteristics. At $N_b$, the efficiency is very close to the maximum value of 0.78 p.u. and the SMIG delivers a power of 2320 W to the single-phase grid at approximately unity power factor. High efficiency and power factor are observed for speeds above 1540 r/min.

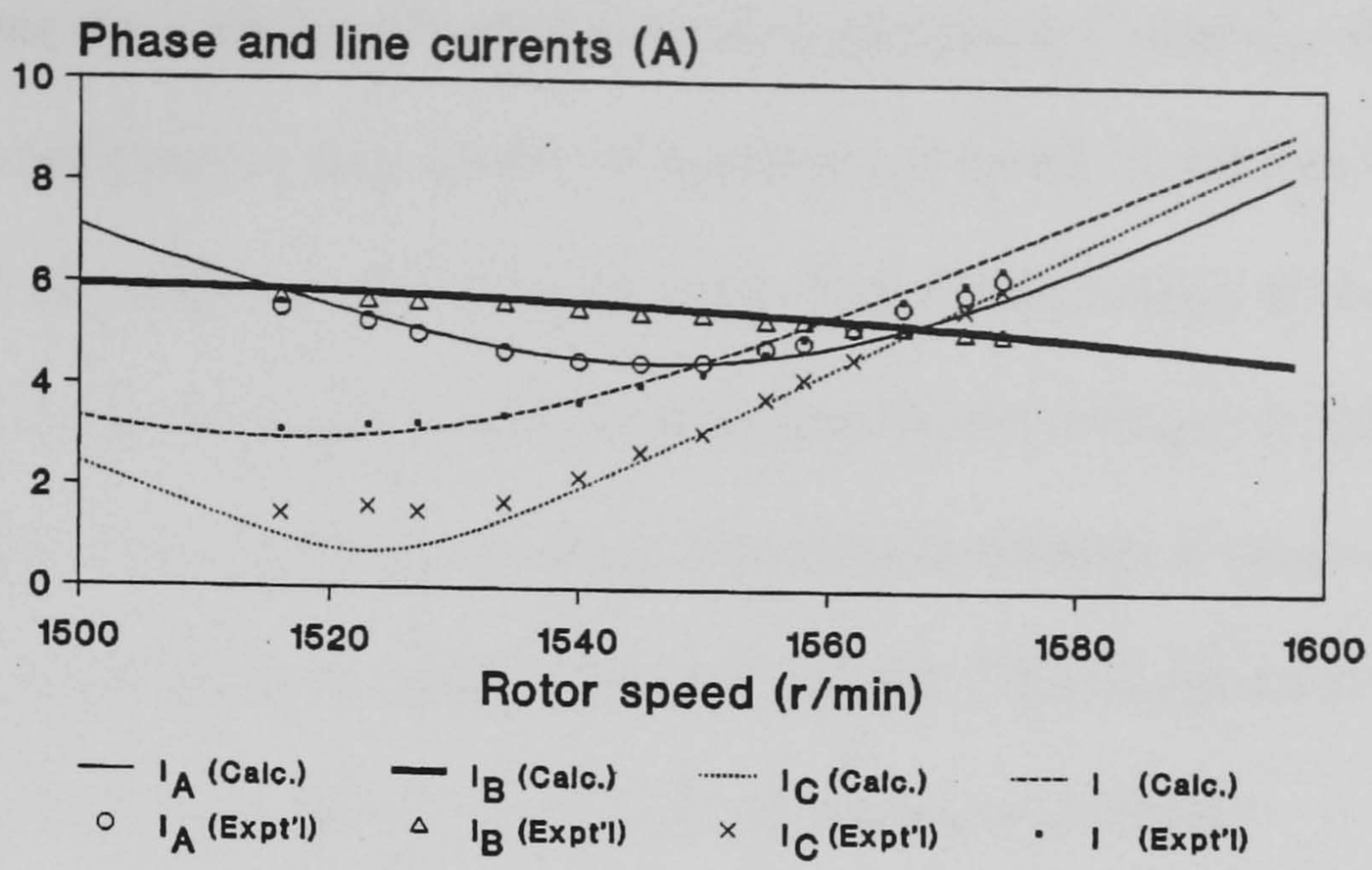


Fig. 2.17 Phase and line current variations of SMIG.

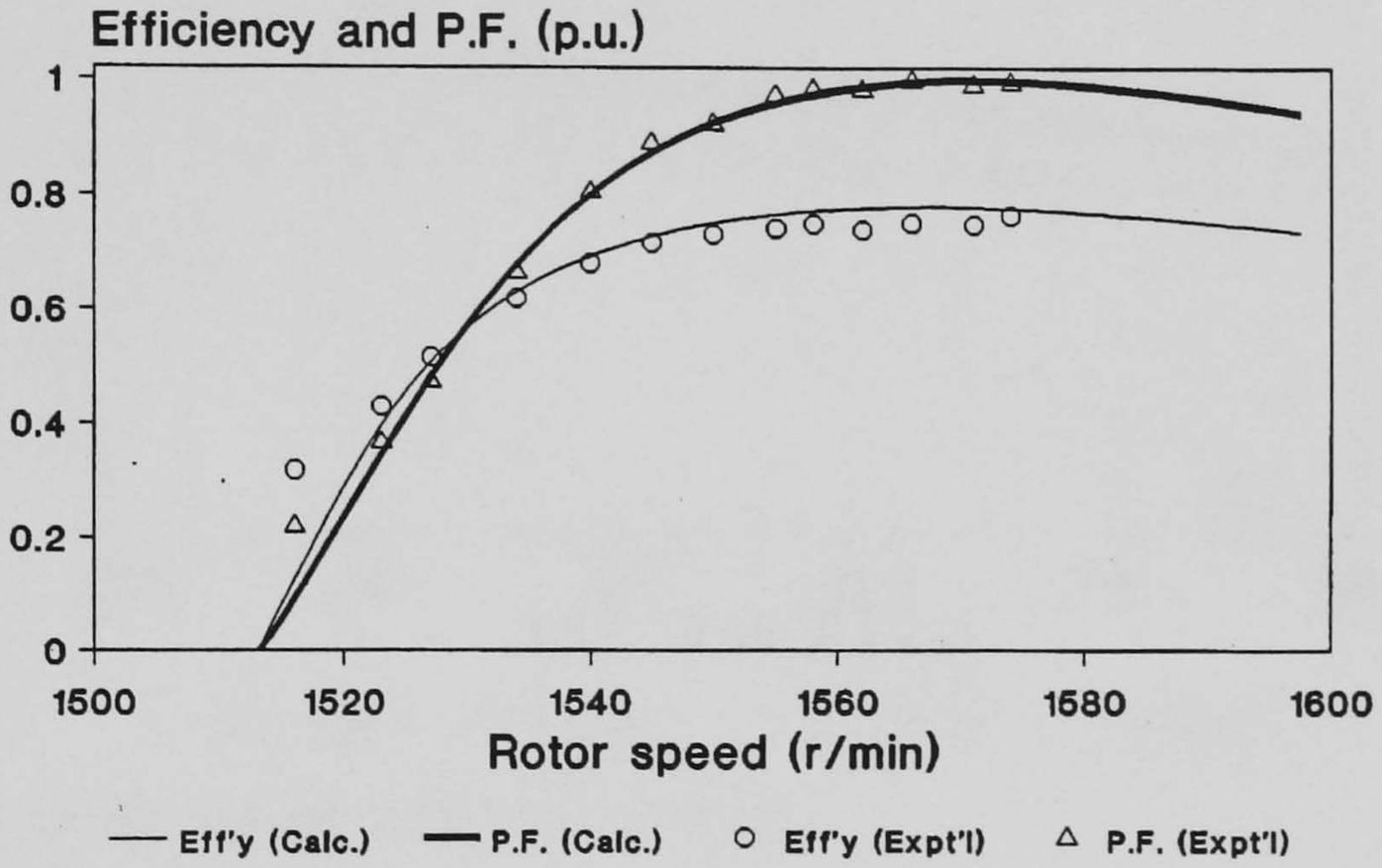


Fig. 2.18 Efficiency and power factor characteristics of SMIG.

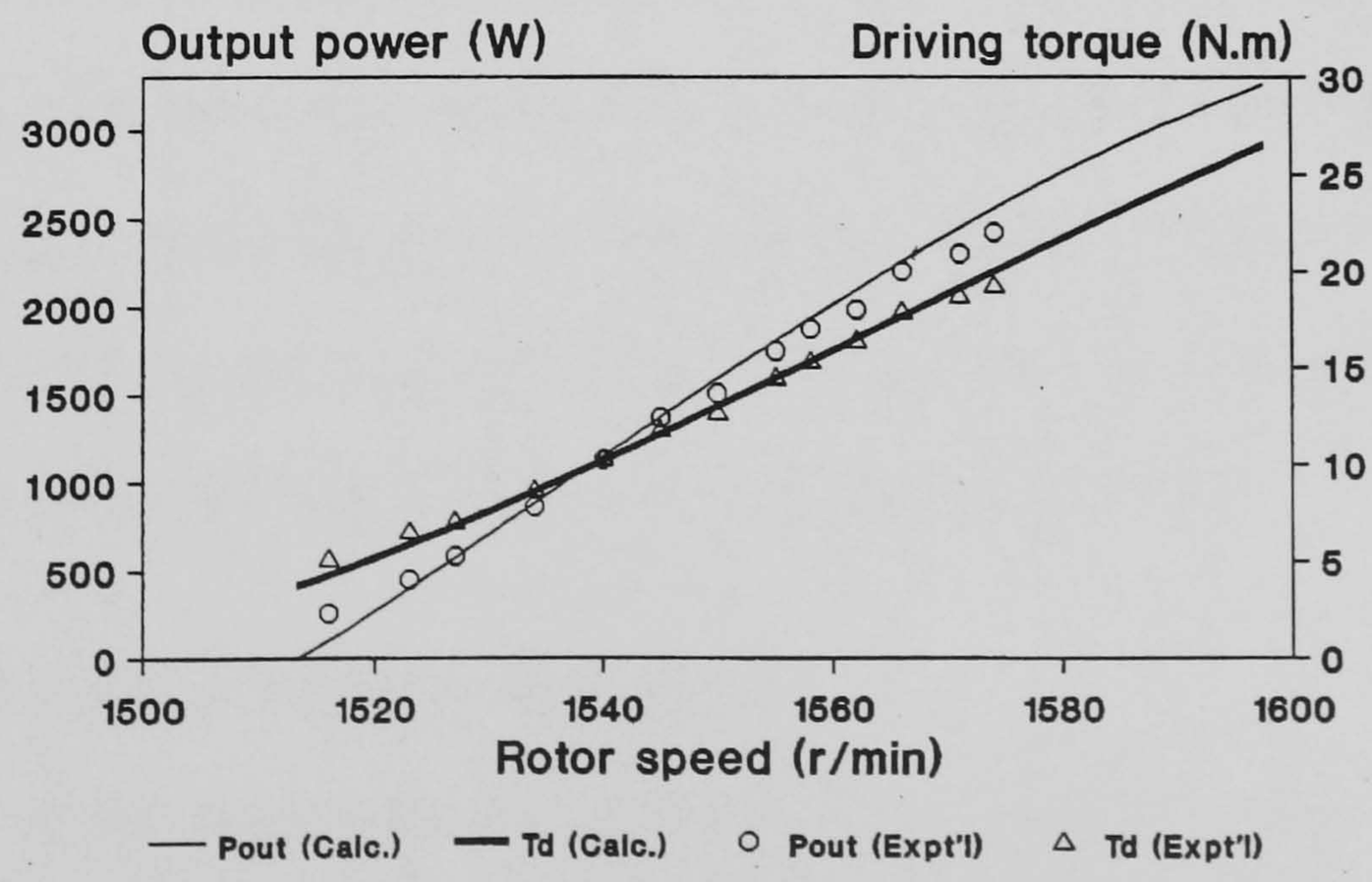


Fig. 2.19 Output power and driving torque characteristics of SMIG.

Fig. 2.20 shows the variation of voltages across capacitances $C_1$ and $C_2$. Both $V_1$ and $V_2$ increase with reduction in rotor speed. At synchronous speed, $V_1$ reaches 135% of rated value while $V_2$ is equal to 109% of rated value. The voltage ratings of the capacitances should thus be properly chosen in order to withstand the overvoltages at light load.

Good agreement between the experimental and theoretical results is observed in Fig. 2.16 to Fig. 2.20, showing that the steady-state performance of the single-phase SMIG can be accurately determined using the method of symmetrical components.

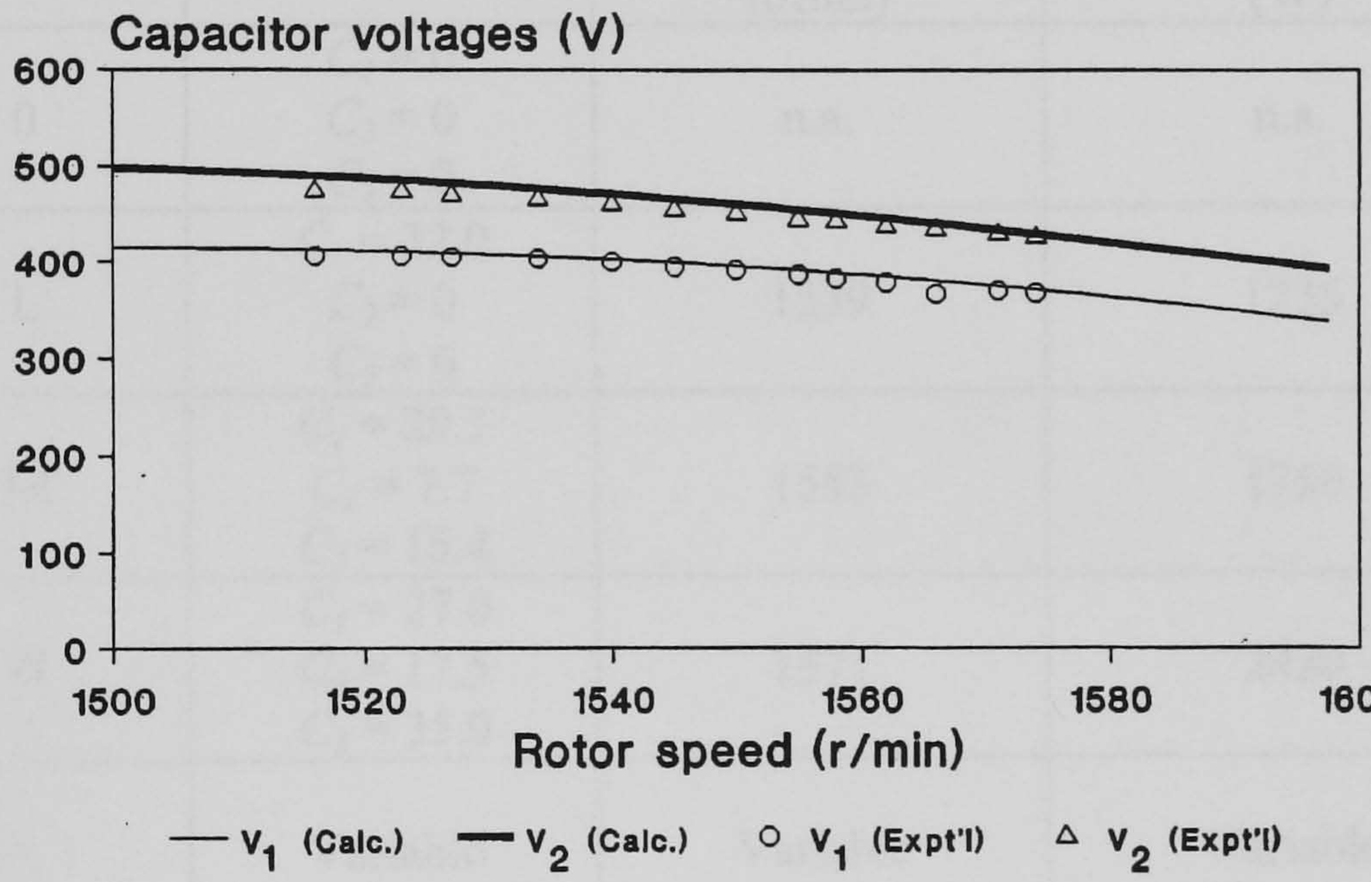


Fig. 2.20 Capacitor voltage variations of SMIG.

Despite the overcurrent in phase A and phase B (at low speeds), the total losses in the SMIG are less than those corresponding to $N_b$, even at speeds down to $N_{cut\text{-}in}$. The rotor copper loss may exceed the rated value at low speeds, due to the more predominant negative-sequence voltage. To avoid excessive temperature rise in the rotor, the SMIG should not be left in the 'idling' mode for a prolonged period of time.

### 2.3.5 Effect of Phase-Balancing Capacitances

The effects of the phase-balancing capacitances on generator performance will be discussed in the following sections with reference to the experimental machine. Referring

to Table 2.5, Mode L, Mode M and Mode H denote operation with capacitances that result in perfect phase balance at light load, medium load and heavy load, respectively. For comparison, single-phasing operation (Mode 0) and operation with perfect phase balance (Mode V) are also investigated.

TABLE 2.5
OPERATING MODES OF SMIG AND THE CORRESPONDING PHASE-BALANCING CAPACITANCES

| Mode | Capacitances (μF) | Speed at perfect phase balance (r/min) | Power output at perfect balance (W) |
|---|---|---|---|
| 0 | $C_1 = 0$<br>$C_2 = 0$<br>$C_3 = 0$ | n.a. | n.a. |
| L | $C_1 = 32.0$<br>$C_2 = 0$<br>$C_3 = 0$ | 1539 | 1235 |
| M | $C_1 = 29.1$<br>$C_2 = 7.7$<br>$C_3 = 15.4$ | 1553 | 1750 |
| H | $C_1 = 27.0$<br>$C_2 = 17.5$<br>$C_3 = 35.0$ | 1571 | 2430 |
| V | Variable | Variable | Variable |

*A) Output power*

Fig. 2.21 shows the computed output power characteristics of the SMIG. The speed $N_{cut\text{-}in}$ at which the generator begins to deliver power varies slightly depending on the phase-balancing capacitances being used. At 1568 r/min, the power outputs of the SMIG for various modes are approximately equal, except for Mode 0 (single-phasing mode). The diagram also shows that, with the phase-balancing capacitances, the IG can deliver 40% more power than the single-phasing mode of operation at rated speed.

*B) Power factor and efficiency*

Fig. 2.22 shows the power factor characteristics of the single-phase SMIG. With single-

phasing mode, the power factor is very low, reaching only 0.5 (leading) at a speed of 1570 r/min. With Mode L capacitances, the power factor is much higher, exceeding 0.8 (leading) at speeds above 1525 r/min. It is interesting to find that with Mode H capacitances, the power factor reaches unity at 1575 r/min. Below this speed, the power factor is lagging, implying that lagging reactive power is supplied to the grid. A similar trend is observed for Mode M, but unity power factor now occurs at a lower speed. For Mode V, the line power factor angle is constrained by the positive-sequence impedance angle of the IG (Fig. 2.14), and power is delivered at a leading power factor when the rotor speed is below 1565 r/min.

The phase-balancing capacitances are effective in suppressing the negative-sequence losses, with a consequent improvement in generator efficiency over the single-phasing mode of operation. As illustrated in Fig. 2.23, the efficiencies for Modes L, M and H are maximum when the generator is balanced, i.e., when the corresponding characteristic touches the Mode V curve. With the generator balanced at a large power output, however, the efficiency at low speeds is reduced due to a more severe phase imbalance.

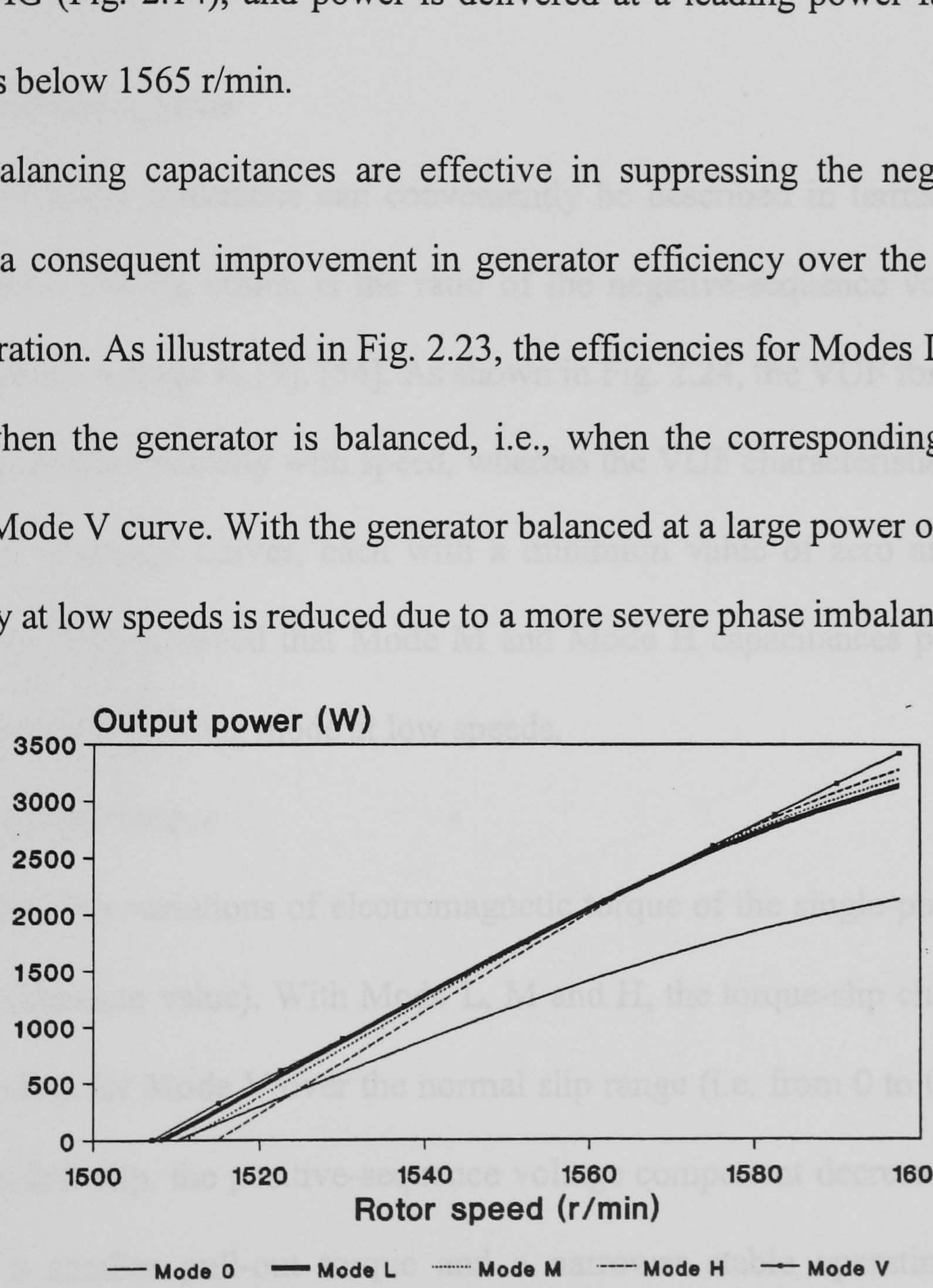


Fig. 2.21 Effect of capacitances on output power.

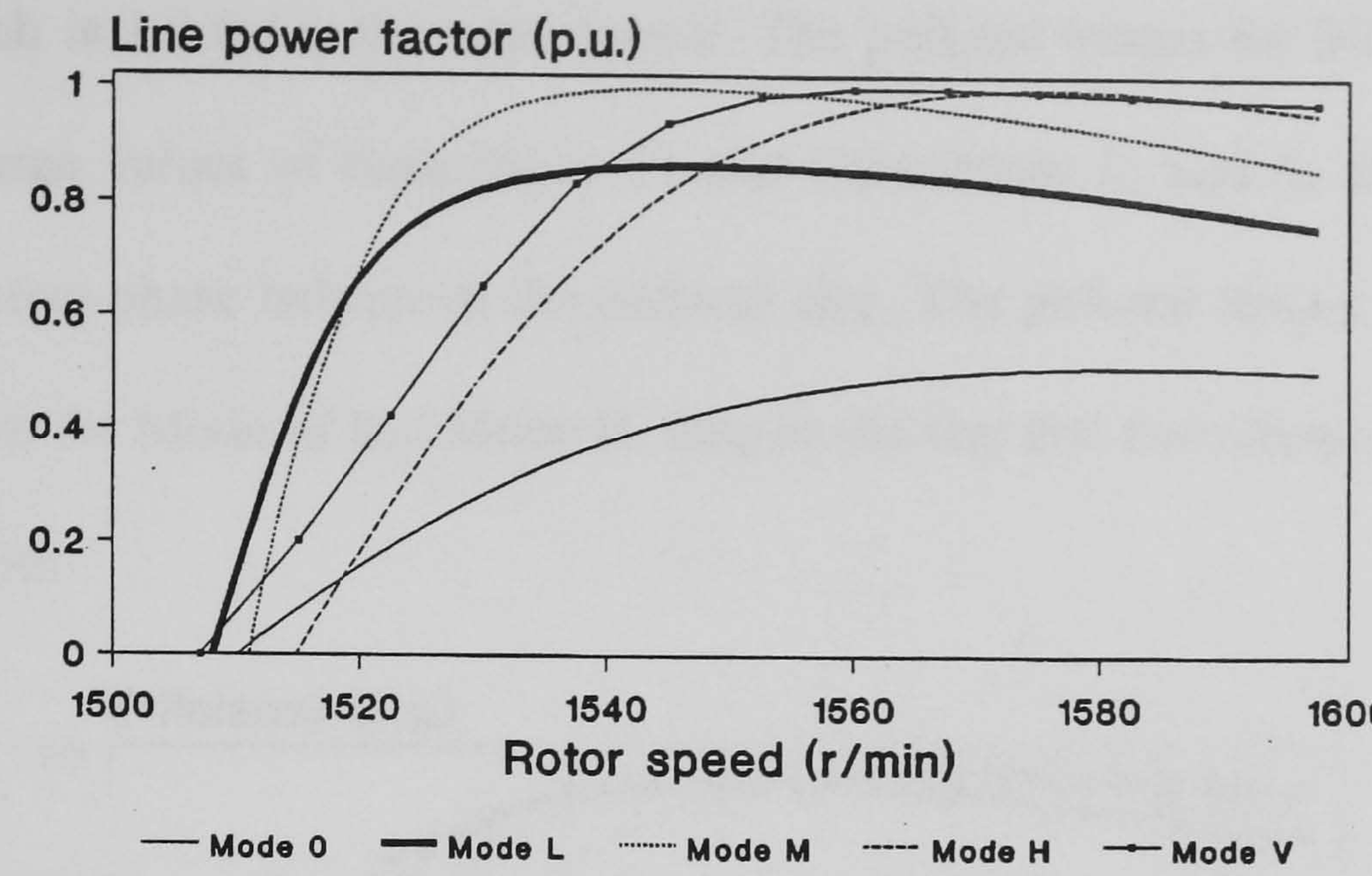


Fig. 2.22 Effect of capacitances on line power factor.

*C) Voltage unbalance factor*

The degree of phase imbalance can conveniently be described in terms of the voltage unbalance factor (VUF), which is the ratio of the negative-sequence voltage $V_n$ to the positive-sequence voltage $V_p$ [9], [54]. As shown in Fig. 2.24, the VUF for single-phasing mode increases monotonically with speed, whereas the VUF characteristics for Modes L, M and H are V-shaped curves, each with a minimum value of zero at the respective balance points. It is observed that Mode M and Mode H capacitances produce a larger VUF than the single-phasing mode at low speeds.

*D) Electromagnetic torque*

Fig. 2.25 shows the variations of electromagnetic torque of the single-phase SMIG with per-unit slip (absolute value). With Mode L, M and H, the torque-slip characteristics are very close to that for Mode V over the normal slip range (i.e. from 0 to 0.06). At higher values of per-unit slip, the positive-sequence voltage component decreases significantly, resulting in a smaller pull-out torque and a narrower stable operating region. It is observed that the pull-out torques for Mode L, M and H occur at values of per-unit slip from 0.12 to 0.14, as compared with 0.25 for Mode V. The pull-out torque for Mode H is

38 N.m, which is 1.9 times the rated torque. The pull-out torque for Mode V is much higher, but large values of capacitance $C_1$ and inductances $L_2$ and $L_3$ are required for achieving perfect phase balance at the pull-out slip. The pull-out torque for Mode L is larger than that for Mode M and Mode H, despite the fact that the values of capacitances used are smaller.

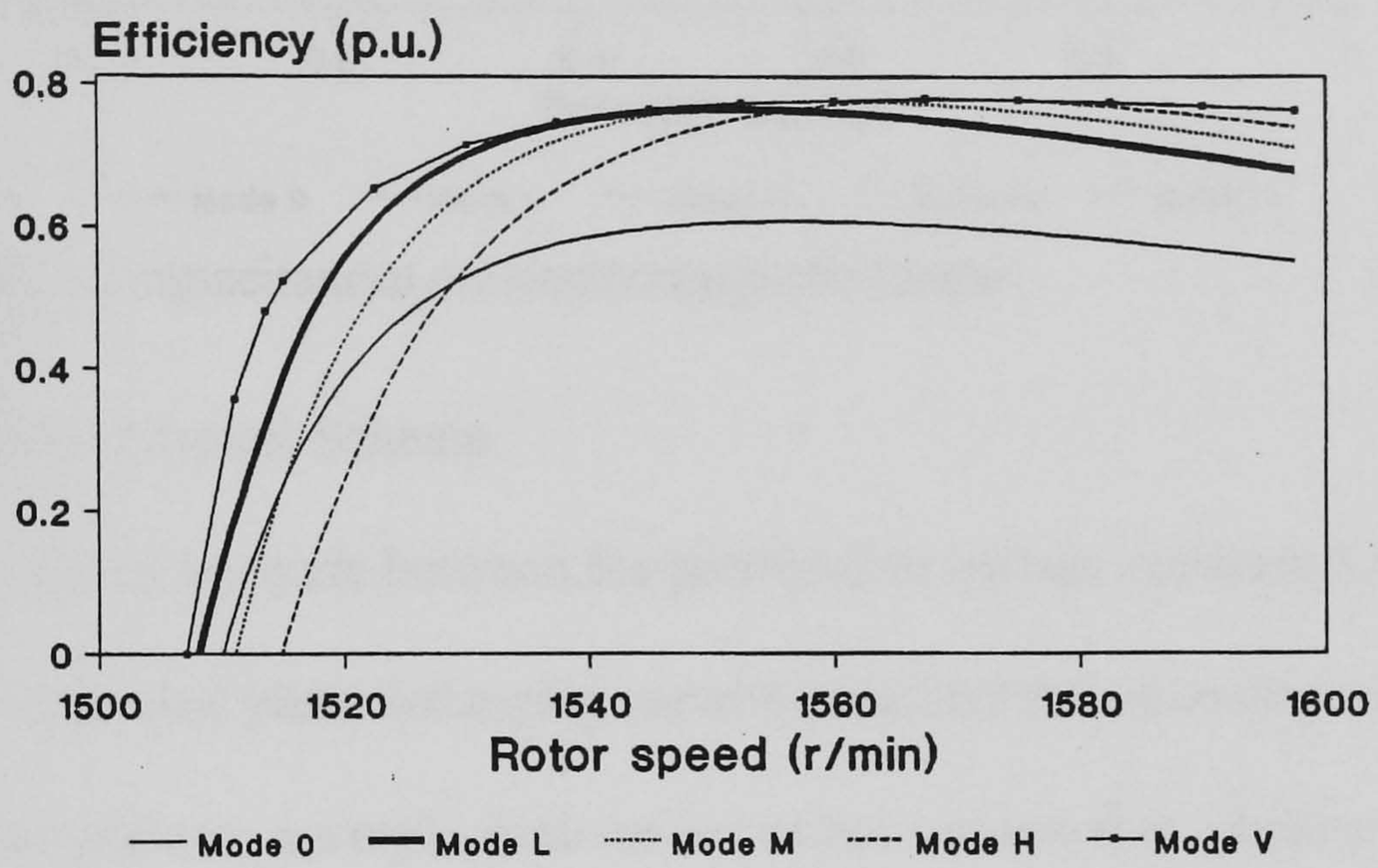


Fig. 2.23 Effect of capacitances on efficiency.

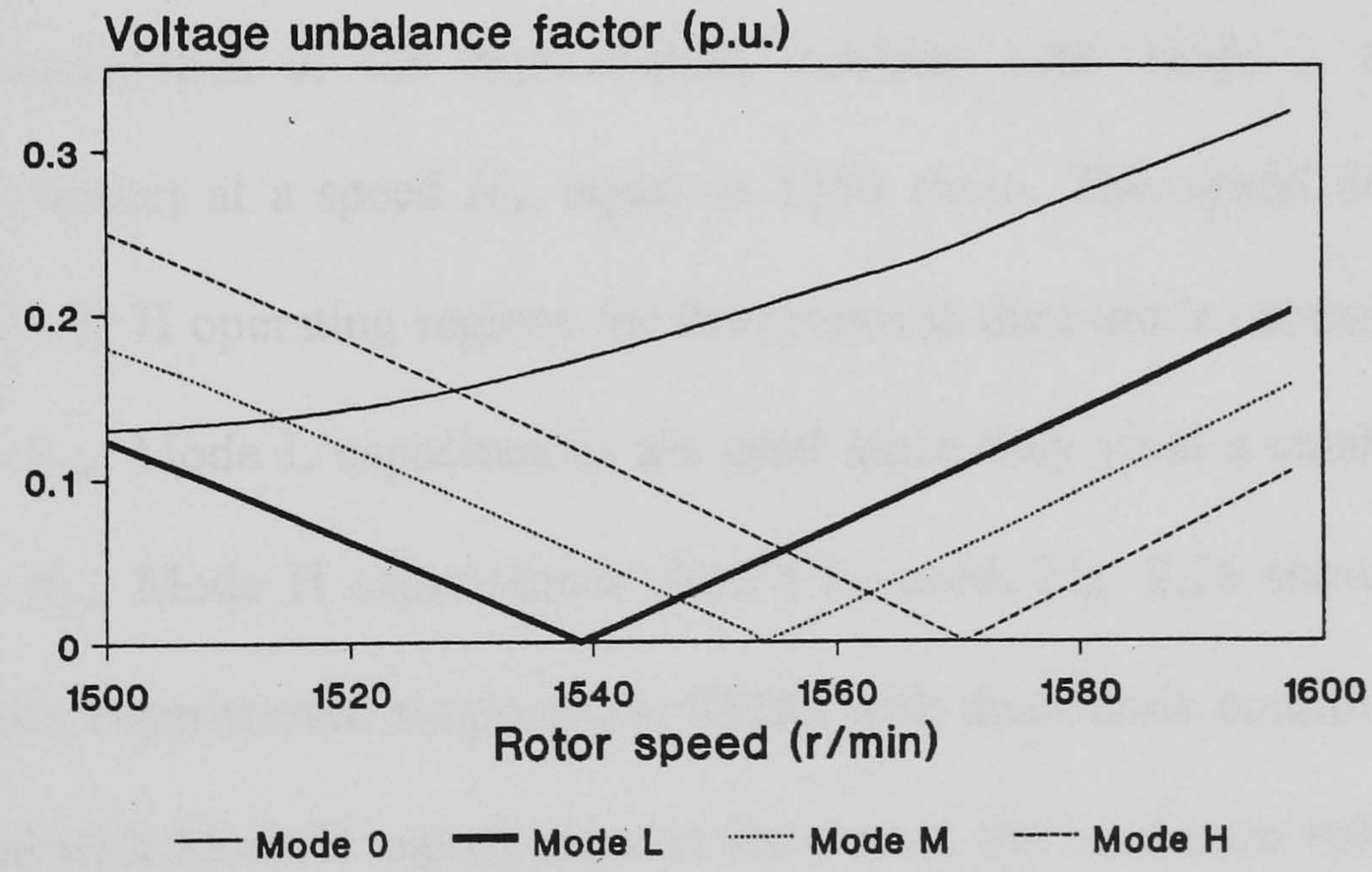


Fig. 2.24 Effect of capacitances on voltage unbalance factor.

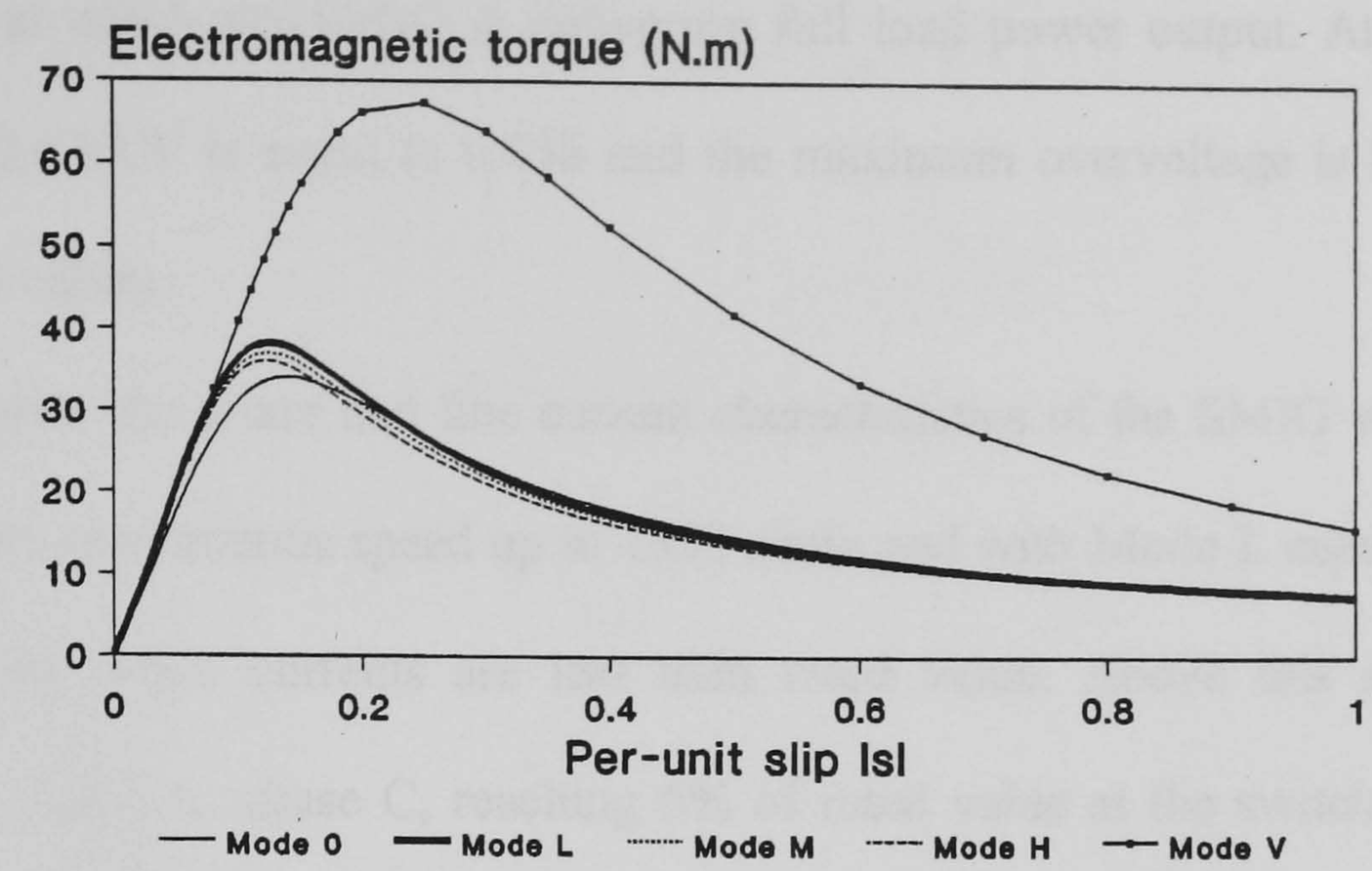


Fig. 2.25 Effect of capacitances on electromagnetic torque.

### 2.3.6 Dual-Mode Control Scheme

A compromise has to be made between the permissible voltage imbalance and the cost in providing the additional phase-balancing capacitances and the associated switches. From economic considerations, a simple dual-mode control scheme that employs only two sets of capacitances, e.g., Mode L and Mode H, may be implemented. Referring to Fig. 2.24, the VUF characteristics of the experimental machine with Mode L and Mode H capacitances intersect at a speed $N_{sw}$ equal to 1556 r/min. This speed demarcates the Mode L and Mode H operating regions for the proposed dual-mode control scheme. For speeds below $N_{sw}$, Mode L capacitances are used since they yield a smaller VUF. For speeds above $N_{sw}$, Mode H capacitances should be used. Fig. 2.26 shows the voltage variations of the experimental single-phase SMIG with dual-mode control. From $N_{sw}$ to 1590 r/min and with Mode H capacitances in the circuit, the maximum voltage occurs in phase C and is equal to 13 V (5.9% of rated value). At speeds below $N_{sw}$, the maximum overvoltage occurs in phase A and is equal to 15 V (6.8% of rated value). Also shown in Fig. 2.26 is the variation in the VUF, which is now a W-shaped curve. Perfect phase balance is obtained at 1539 r/min at which the SMIG is delivering half load and again at

1571 r/min at which the SMIG is delivering full load power output. At the switching speed $N_{sw}$, the VUF is equal to 0.056 and the maximum overvoltage is less than 11 V (5% of rated value).

Fig. 2.27 shows the phase and line current characteristics of the SMIG with dual-mode control. From synchronous speed up to 1553 r/min and with Mode L capacitances in the circuit, all the phase currents are less than rated value. Above this speed, a slight overcurrent occurs in phase C, reaching 6% of rated value at the switching speed $N_{sw}$. After changeover to Mode H capacitances, a small overcurrent occurs in phase B, but both phase-A and phase-C currents are now less than the rated value.

The experimental results shown in Fig. 2.26 and Fig. 2.27 suggest that satisfactory operation of the single-phase SMIG over a wide range of power output can be achieved by using a simple dual-mode control scheme.

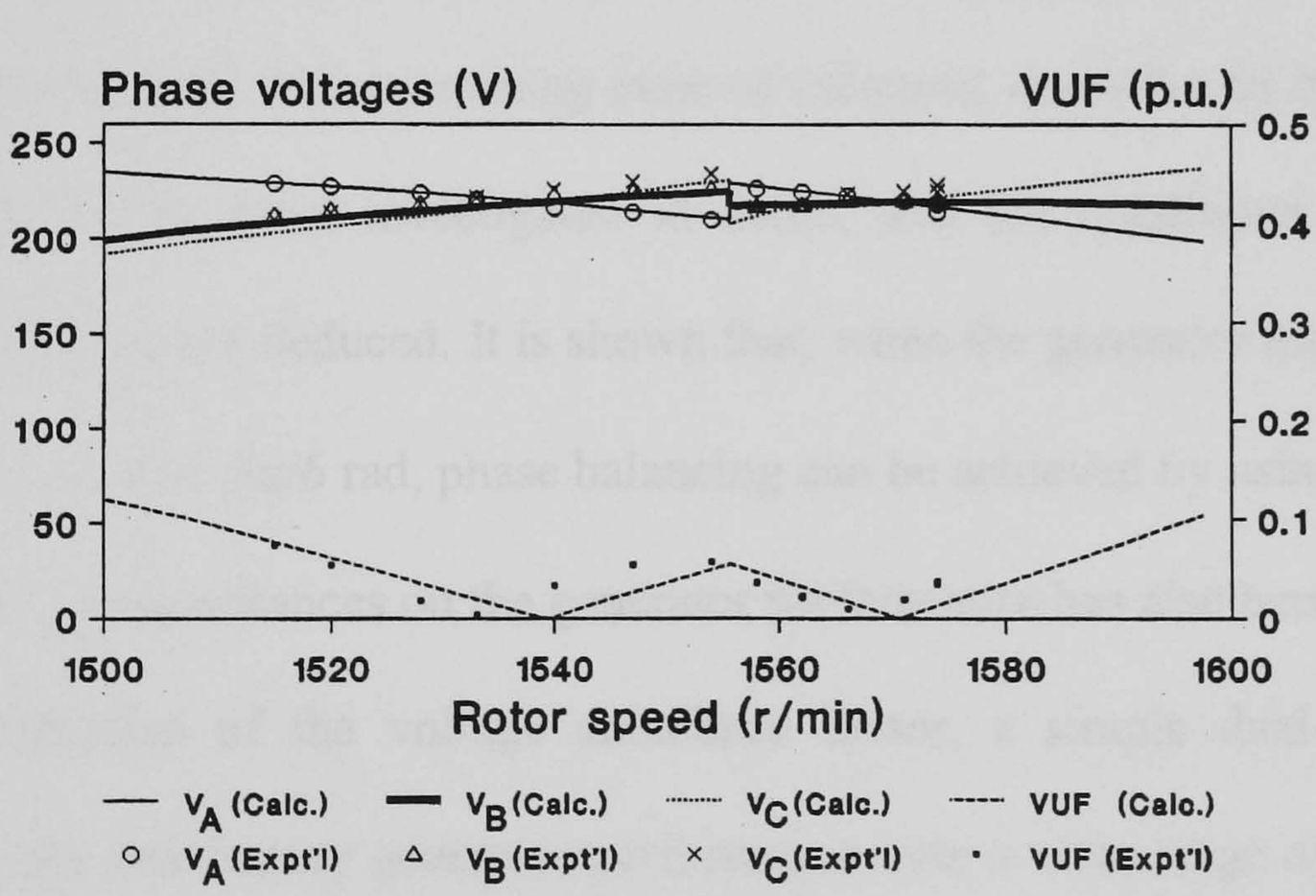


Fig. 2.26 Phase voltages and VUF of SMIG with dual-mode control.

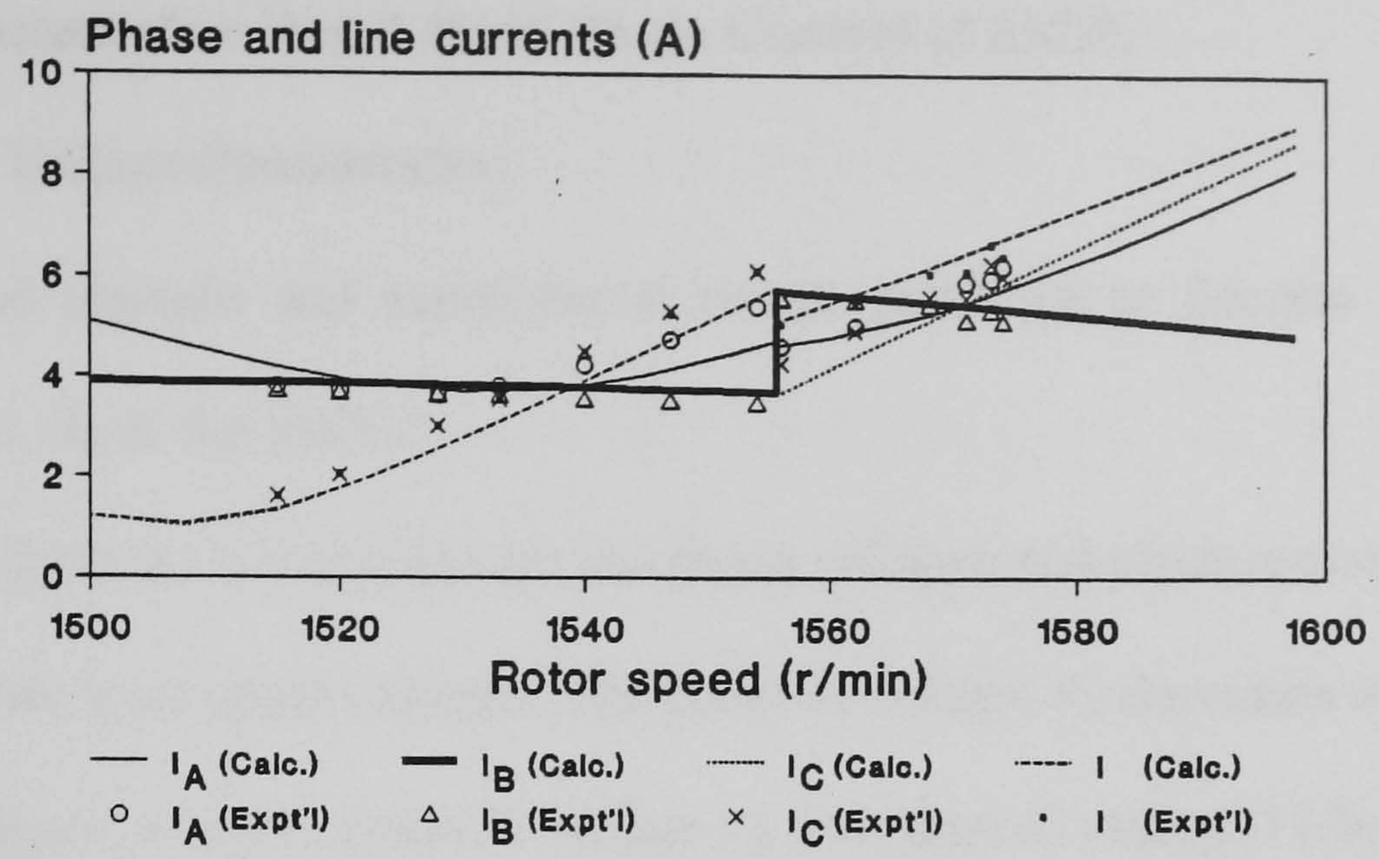


Fig. 2.27 Phase and line currents of SMIG with dual-mode control.

### 2.3.7 Summary

The feasibility of a grid-connected single-phase IG system based on the Smith connection has been demonstrated in this section. A systematic analysis using the method of symmetrical components has been presented for evaluation of the generator performance at different rotor speeds. The interesting case of balanced operation in the three-phase induction machine has been investigated in detail, and the conditions necessary for perfect phase balance are deduced. It is shown that, when the generator impedance angle is between $2\pi/3$ rad and $5\pi/6$ rad, phase balancing can be achieved by using capacitances only. The effect of capacitances on the generator performance has also been investigated. From a consideration of the voltage unbalance factor, a simple dual-mode control strategy that gives satisfactory generator performance over a wide range of power output is proposed. The theoretical analysis is validated by experiments performed on a small induction machine.

## 2.4 Microcontroller-Based Multi-Mode Control of SMIG

### 2.4.1 Phase Voltage Consideration

The theoretical analysis and experimental results presented in Section 2.3 reveal the following facts about the SMIG:

1) For a given set of capacitances, the phase voltages and phase currents will change when the rotor speed changes. The phase-A voltage $V_A$ decreases with increase in rotor speed, whereas phase-B voltage $V_B$ and phase-C voltage $V_C$ both increase.

2) The greater the deviation of rotor speed from that corresponding to perfect balance, the greater the deviation of the phase voltages from the value corresponding to perfect phase balance.

3) $V_C$ is more sensitive to rotor speed change than $V_B$.

4) $V_C$ varies almost linearly with the rotor speed.

The above observations suggest that, instead of the rotor speed signal, the phase-C voltage $V_C$ may be exploited for controlling the switching of capacitances for multi-mode operation of the IG. An advantage of this approach is that an expensive speed sensor need not be used.

### 2.4.2 Control System

For practical design, a compromise has to be made between the phase imbalance permissible and the cost of the controller system. Previous studies have indicated that a dual-mode or three-mode controller will suffice to yield satisfactory machine performance. In this section, the implementation of a three-mode controller will be described. For easy reference, the three modes are referred to as L-mode (low load), M-mode (medium load) and H-mode (heavy load), respectively.

To reduce the circuit complexity and to improve the system reliability, a digital approach based on the microcontroller technology has been adopted. A microcontroller may be viewed as a compact computer manufactured on a single chip. The built-in input/output (I/O) and memory systems enable the chip to be interfaced with the hardware system to be controlled. At present, microcontrollers of the 8051 family [84] are widely used for implementing stand-alone, embedded control systems.

Fig. 2.28 shows the schematic diagram of the proposed controller. The phase-C voltage $V_C$ is input to a signal conditioning circuit which consists of a two-winding step-down transformer, a diode rectifier and a sample-and-hold circuit. The sampled dc signal is next input to an analog-to-digital converter (ADC). The digital control signal is input to an 8052 microcontroller (an enhanced member of the 8051 family) which functions as a voltage comparator and a mode selector. The control functions are executed by an Assembly language program that has previously been developed, compiled and linked using an Assembler, and 'burned in' the read only memory (ROM) of the microcontroller chip [85]. The output from the microcontroller is then used to drive a relay/contactor circuit that effects capacitor switching. The system cost is low because of the well-established microcontroller technology and the small component count.

It should be noted that the 8052 chip cannot be programmed by the user. In other words, the control program has to be supplied to the manufacturer for producing the microcontroller. This approach is not economical for prototyping, so in practice an enhanced version of the chip with erasable and programmable read only memory (EPROM) will be used. Program development and debugging can now be undertaken under the personal computer (PC) environment and the final program can be written into the EPROM.

The proposed control strategy can be explained by referring to Fig. 2.29 which shows the variation of $V_C$ with rotor speed for the three sets of capacitances. For this example, the balance points are LB, MB and HB, at which $V_C$ is equal to the rated value of 130 V. The threshold value ΔV has been assigned to be ±5 V as indicated by the two dashed horizontal lines at 125 V and 135 V. The IG is allowed to operate in its present mode provided that the change in $V_C$ does not exceed the specified voltage threshold. A mode change or an alarm will be initiated, however, when the change in $V_C$ reaches or exceeds the threshold value. The latter provision is necessary as the phase imbalance will be too large.

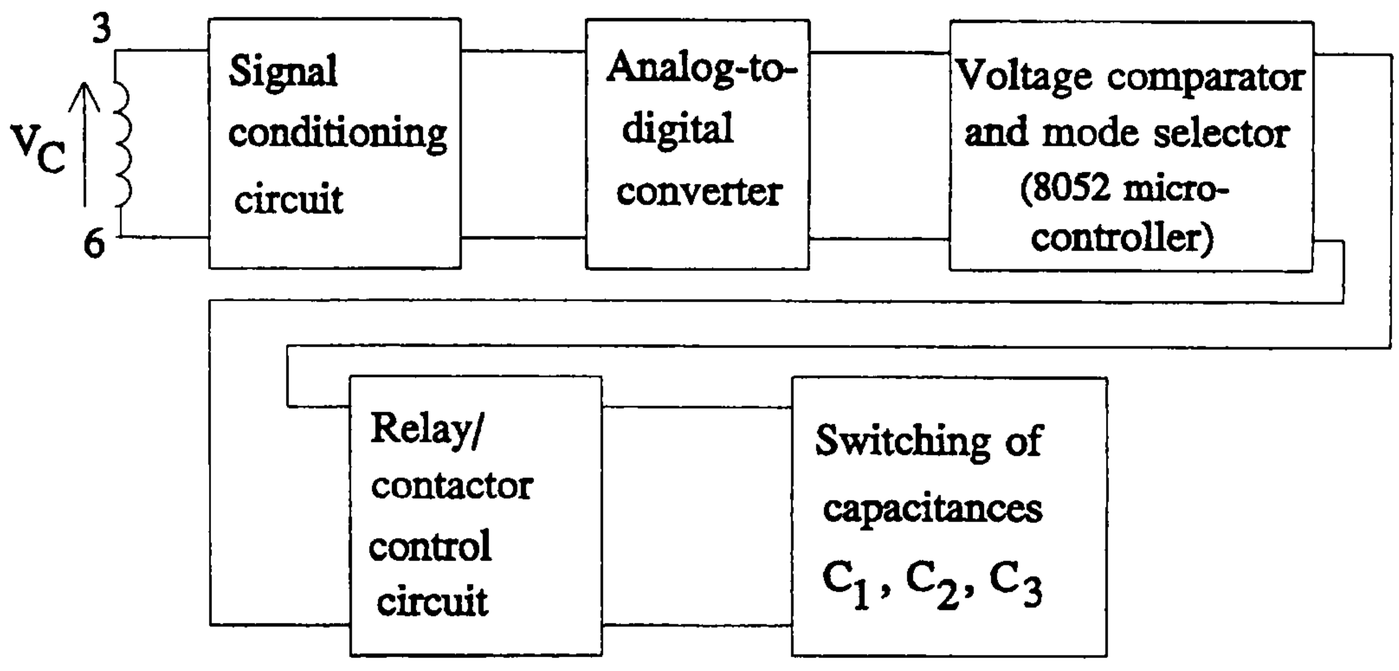


Fig. 2.28 Schematic diagram of proposed microcontroller based mode selection system.

Assume that the induction generator is initially operating at perfect phase balance with L-mode capacitances in the circuit. As the rotor speed increases, $V_C$ will vary according to the L-mode characteristic (thin solid curve in Fig. 2.29) from point LB towards LU. At point LU the threshold voltage is reached and a mode change is initiated. M-mode capacitances are switched into the circuit and $V_C$ will then vary according to the M-mode characteristic (thick solid curve in Fig. 2.29). Further increase in rotor speed will cause $V_C$ to reach point MU at which the H-mode capacitances are switched in. If the rotor speed continues to increase, the point HU on the H-mode characteristic (dotted curve in

Fig. 2.29) will finally be reached and further mode change is not possible. An alarm signal will be issued to caution the operator for appropriate action.

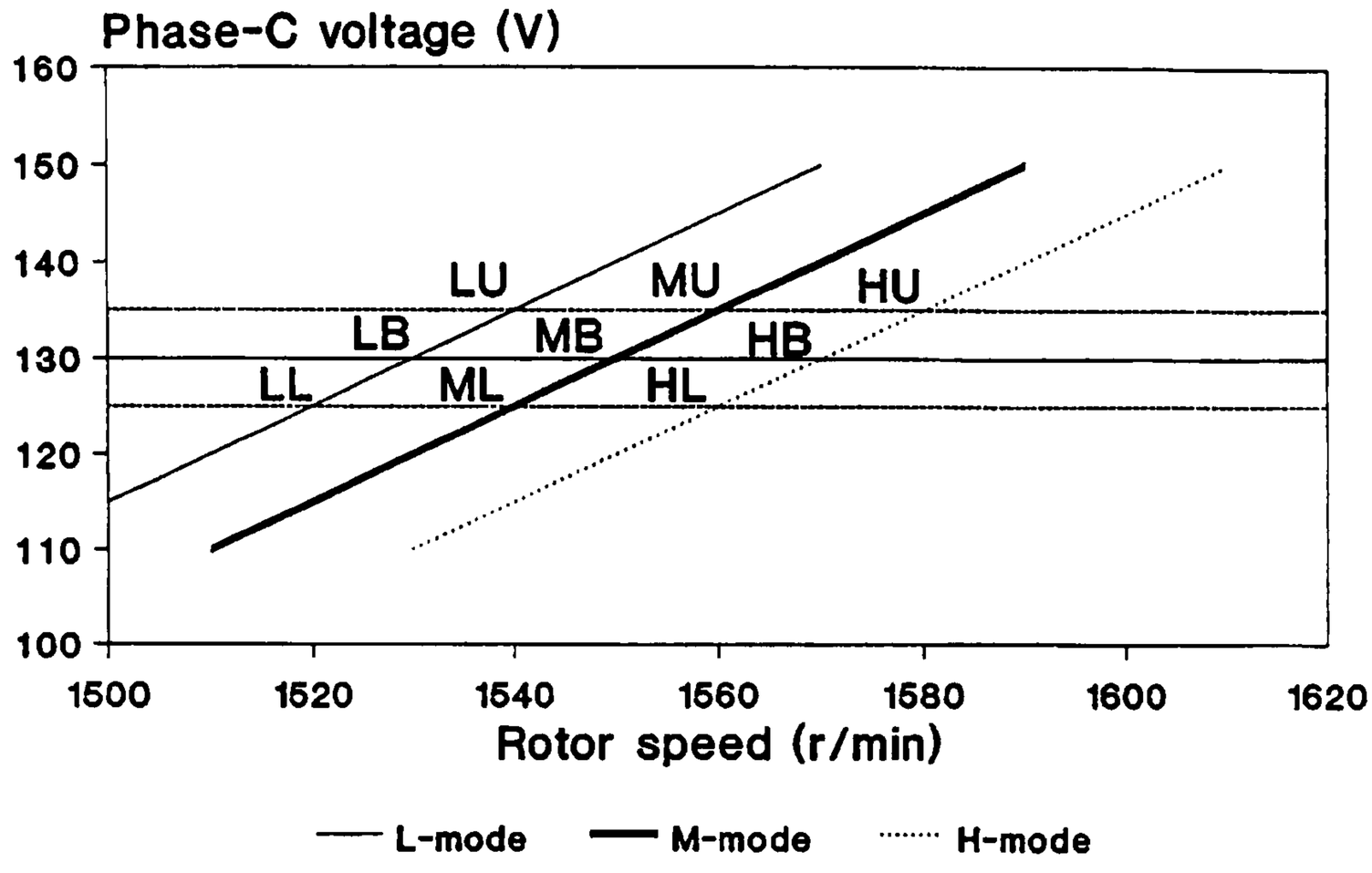


Fig. 2.29 Variation of phase-C voltage with speed for L-mode, M-mode and H-mode capacitances.

Change of mode in the reverse sequence takes place in a similar manner when the rotor speed decreases. The transition from H-mode to M-mode occurs at point HL while the transition from M-mode to L-mode occurs at point ML. For proper mode change operation, the voltage threshold should be chosen such that, in Fig. 2.29, HL is on the left of MU along the speed axis, and ML is on the left of LU.

Fig. 2.30 shows the flowchart of the voltage comparison routine of the Assembly program in the microcontroller. The function of this routine is to keep track of the present operating mode of the IG and to determine whether a mode change is necessary. The program reads the $V_C$ signal from the ADC continuously and compares it against the following voltages:

$V_b =$ voltage of $V_C$ at perfect balance;

$V_L =$ minimum value of $V_C$ permissible;

$V_U =$ maximum value of $V_C$ permissible.

As long as the condition $V_L < V_C < V_U$ prevails, no action is taken and the controller continues to read the sampled $V_C$ signal. When $V_C > V_U$ or $V_C < V_L$, however, a mode change will be initiated. To avoid rapid mode changes back and forth due to transient disturbances, the sampled signal is read twice before initiating a mode change and a time delay is introduced after each mode change.

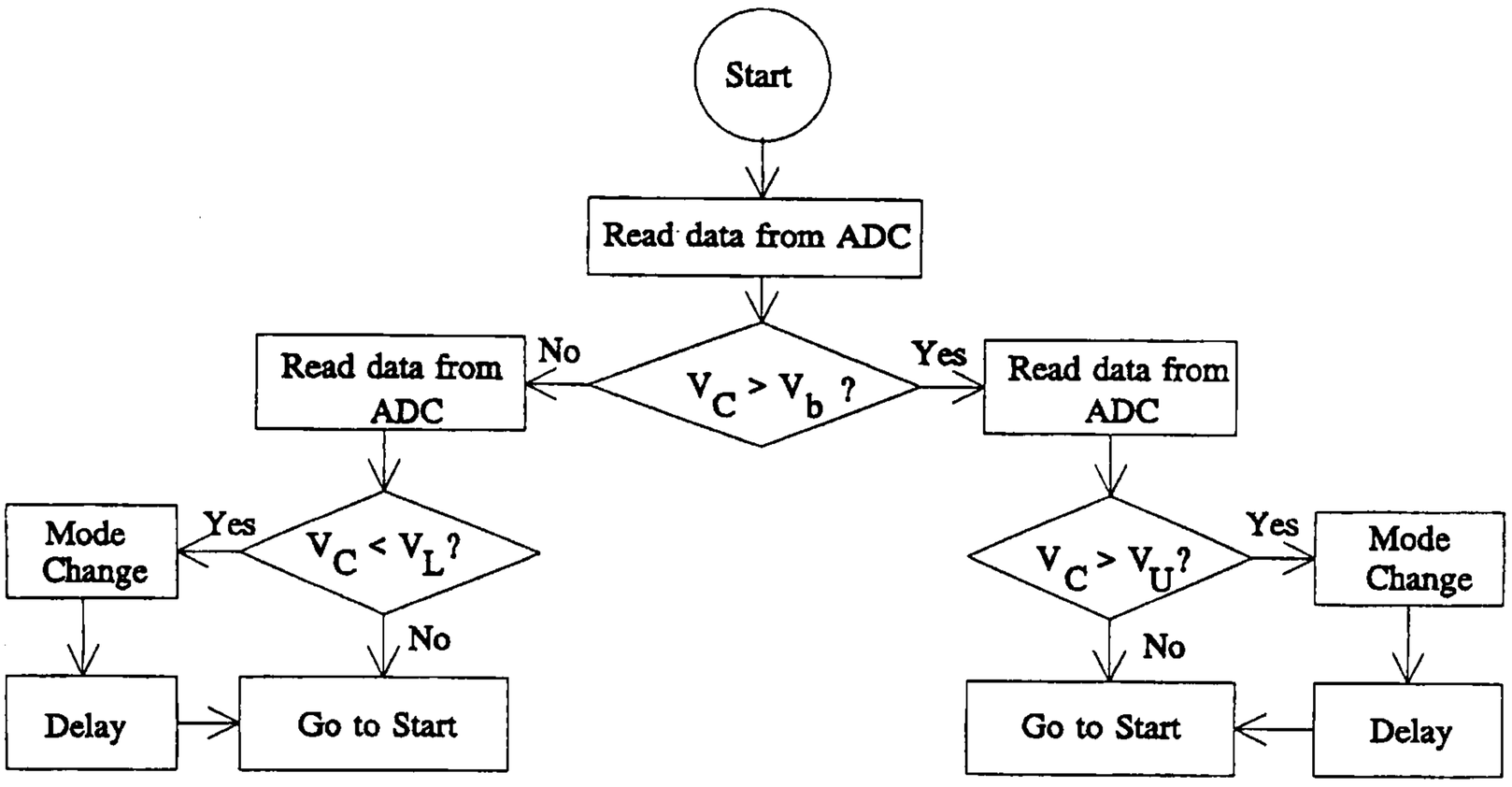


Fig. 2.30 Flowchart of the voltage comparison routine of the control program.

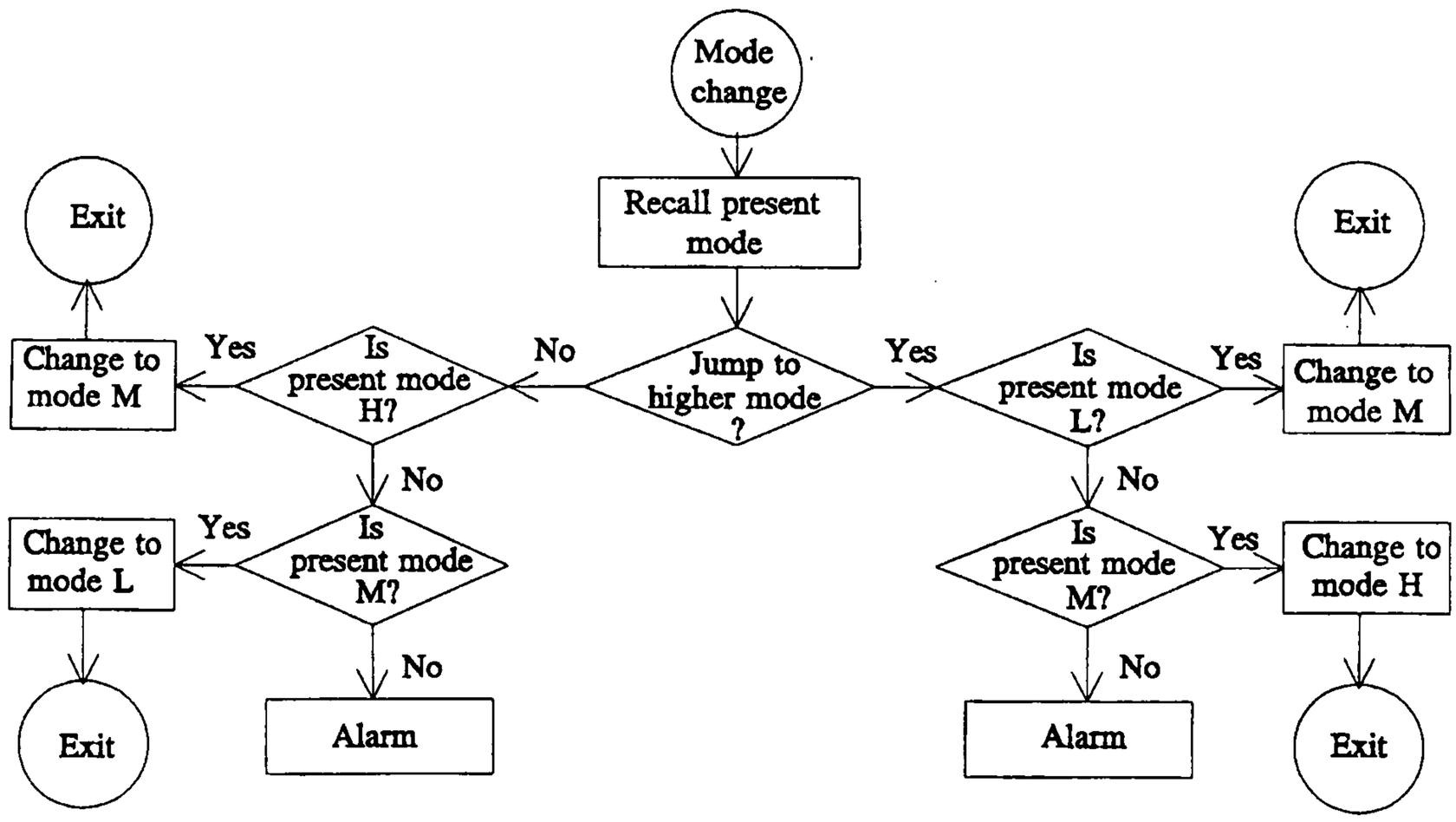


Fig. 2.31 Flowchart of mode selection routine of the control program.

Fig. 2.31 shows the flowchart of the mode selection routine. When the 'Mode change' command is issued from the voltage comparison routine, the present operating mode is

recalled and the appropriate mode is selected accordingly. An alarm signal will be flagged when no further mode change is possible.

### 2.4.3 Practical Implementation

Tests performed on a 50-Hz, four-pole, 130 V (phase), 5.2 A (phase) experimental machine gave the sets of capacitances for perfect phase balance as shown in Table 2.6. Based on these results, the capacitor switching arrangement shown in Fig. 2.32 was designed and the Assembly language control program was developed. Table 2.7 shows how the six switches S1 to S6 should be controlled in order to give the capacitance values in Table 2.6. The system would be initialized to L-mode immediately after the controller was energized. Thereafter the appropriate mode would be selected based on the measured $V_C$ signal.

The 89C52 microcontroller from ATMEL [86], which is one of the enhanced members of the 8052 family, was selected for hardware implementation. This chip is a high-performance CMOS 8-bit microcontroller with 8 kbytes of EPROM and 256 kbytes of random access memory (RAM), and is compatible with the 8051/8052 instruction set. There are four parallel I/O ports. In the prototype system, port P1 was used for digital signal input from the ADC. Port P0 was used for control of the relay/contactor circuit, while port P2 was used for control of the mode and alarm indication circuit.

Calibration of the sampled dc signal against the phase-C voltage $V_C$ was necessary for software program development. Fig. 2.33 shows the calibration curve obtained on the experimental system. Due to the voltage drop in the diode rectifier of the signal conditioning circuit, nonlinearities occur when $V_C$ is small. Over the practical operating range (from 120 V to 140 V), however, the sampled dc signal is approximately proportional to $V_C$.

Heavy-current relays were used for switches S1 to S6 in the prototype system. Voltage amplification of the digital output from the microcontroller was required for energizing the relays. For larger machines, the use of zero-crossing solid-state relays [11] is preferred in order to minimize the transient switching currents.

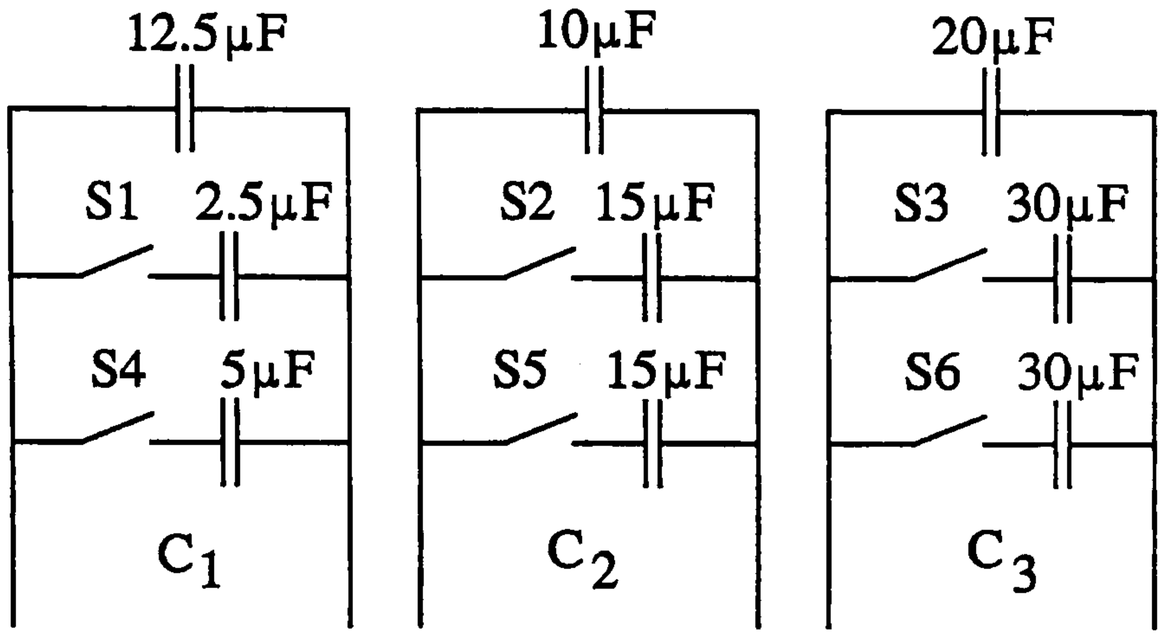


Fig. 2.32 Capacitor switching arrangement of single-phase induction generator with the Smith connection.

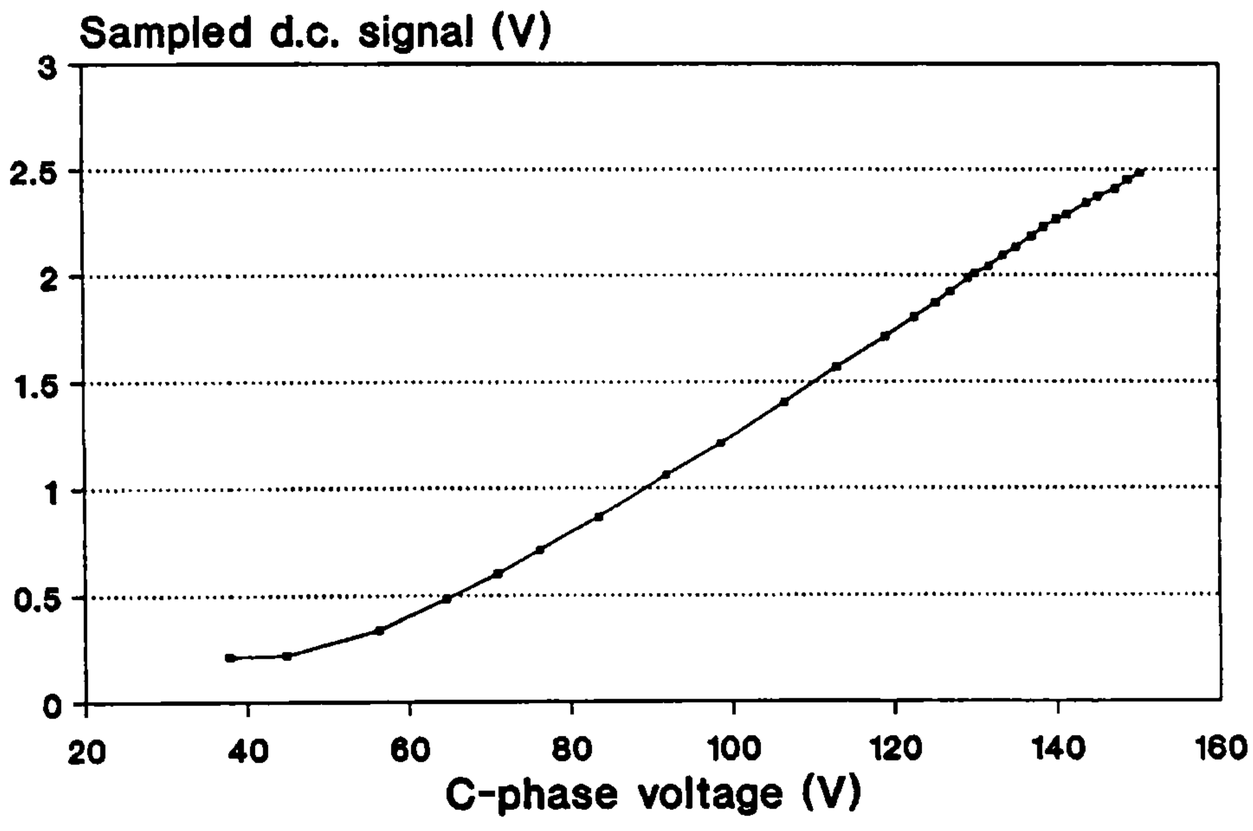


Fig. 2.33 Variation of the sampled dc signal against $V_C$.

TABLE 2.6
CAPACITANCES FOR PERFECT PHASE BALANCE IN EXPERIMENTAL MACHINE

| Mode | $C_1$ ($\mu$F) | $C_2$ ($\mu$F) | $C_3$ ($\mu$F) | Rotor speed at balance (r/min) |
|---|---|---|---|---|
| L | 20 | 10 | 20 | 1533 |
| M | 15 | 25 | 50 | 1552 |
| H | 12.5 | 40 | 80 | 1574 |

TABLE 2.7
SWITCH CONTROL FOR PHASE BALANCING CAPACITANCES

| Mode | $C_1$ | $C_2$ | $C_3$ |
|---|---|---|---|
| L | S1 closed<br>S4 closed | S2 open<br>S5 open | S3 open<br>S6 open |
| M | S1 closed<br>S4 open | S2 closed<br>S5 open | S3 closed<br>S6 open |
| H | S1 open<br>S4 open | S2 closed<br>S5 closed | S3 closed<br>S6 closed |

### 2.4.4 Experimental Results and Discussion

Fig. 2.34 shows the phase voltage variations obtained from a load test on the experimental SMIG system with the multi-mode controller, the rotor speed being increased monotonously from synchronous value (1500 r/min). It is observed that the phase voltages vary within close limits about the rated value (130 V) throughout the normal speed range. Switching over from L-mode to M-mode occurs at a rotor speed of 1541 r/min, and switching from M-mode to H-mode occurs at a rotor speed of 1563 r/min. Fig. 2.34 has further confirmed that $V_C$ is an appropriate control signal for mode selection.

Fig. 2.35 shows the corresponding variations of the phase and line currents of the IG. For rotor speeds close to the balance points, the phase current imbalance is quite small. At very light loads, however, the imbalance becomes more severe. The phase currents under this condition, however, are much lower than the rated value (due to the use of L-mode capacitances) and hence the motor losses are acceptable. Within each mode, the phase-B current $I_B$ decreases only slightly with increase in rotor speed, but its magnitude is larger when the next higher mode is selected. $I_A$ and $I_C$, on the other hand, vary considerably

within the same mode, but the two currents are approximately equal for operation in the H-mode.

Fig. 2.36 shows the efficiency and power factor characteristics of the SMIG. Despite the mode changes, the efficiency characteristic is quite smooth and the efficiency is acceptable at rotor speeds above 1530 r/min. The power factor characteristic, on the other hand, exhibits marked discontinuities due to the mode changes. Over the practical speed range, however, the output line power factor exceeds 0.8 (leading) while at speeds corresponding to perfect phase balance, the line power factor is above 0.9 (leading).

Similar performance characteristics were obtained when the rotor speed was reduced from that corresponding to heavy load. Switching from H-mode to M-mode was found to occur at a rotor speed of 1567 r/min and switching from M-mode to L-mode at a rotor speed of 1542 r/min.

The response of the micro-controller to transient speed changes was also studied. For a moderate increase or decrease in rotor speed, switching between modes was accomplished in about 1.5 s.

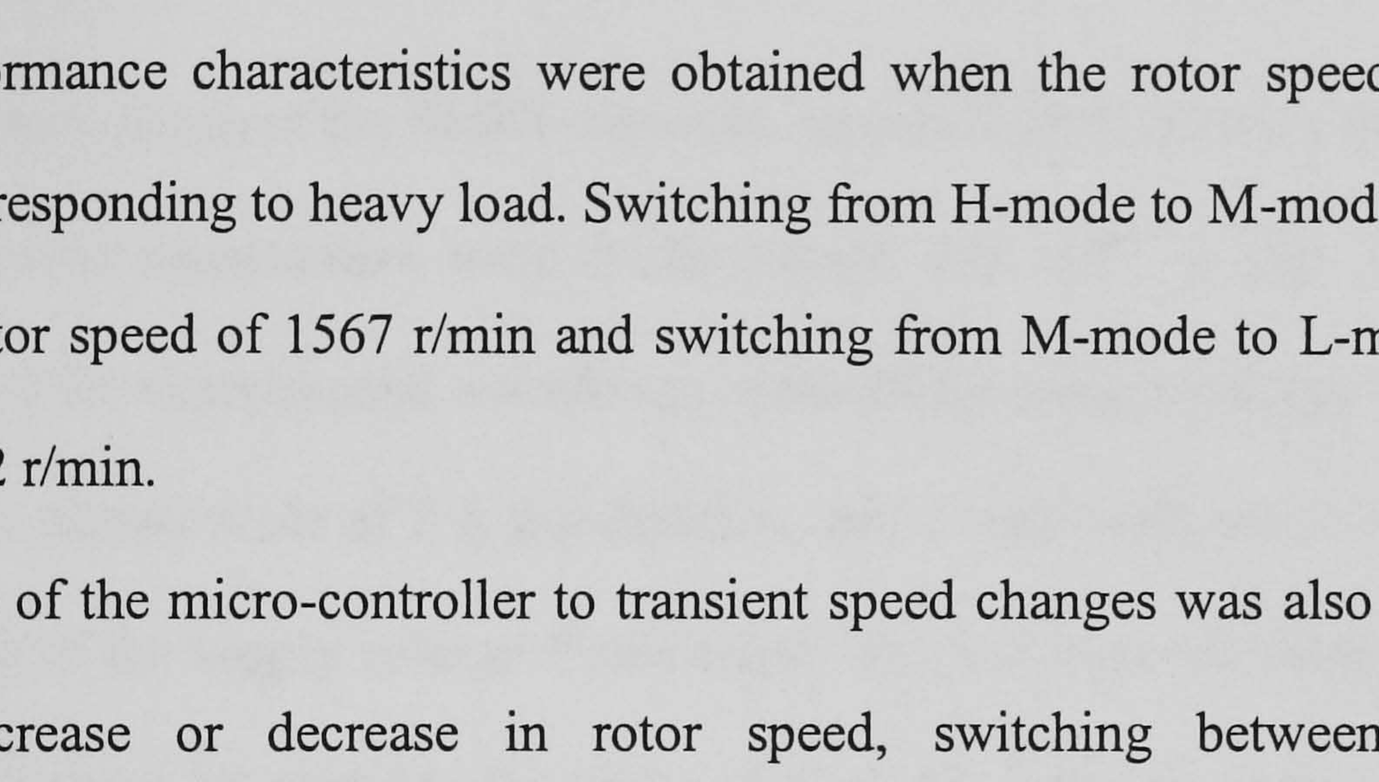


Fig. 2.34 Phase voltage variations of SMIG under multi-mode operation.

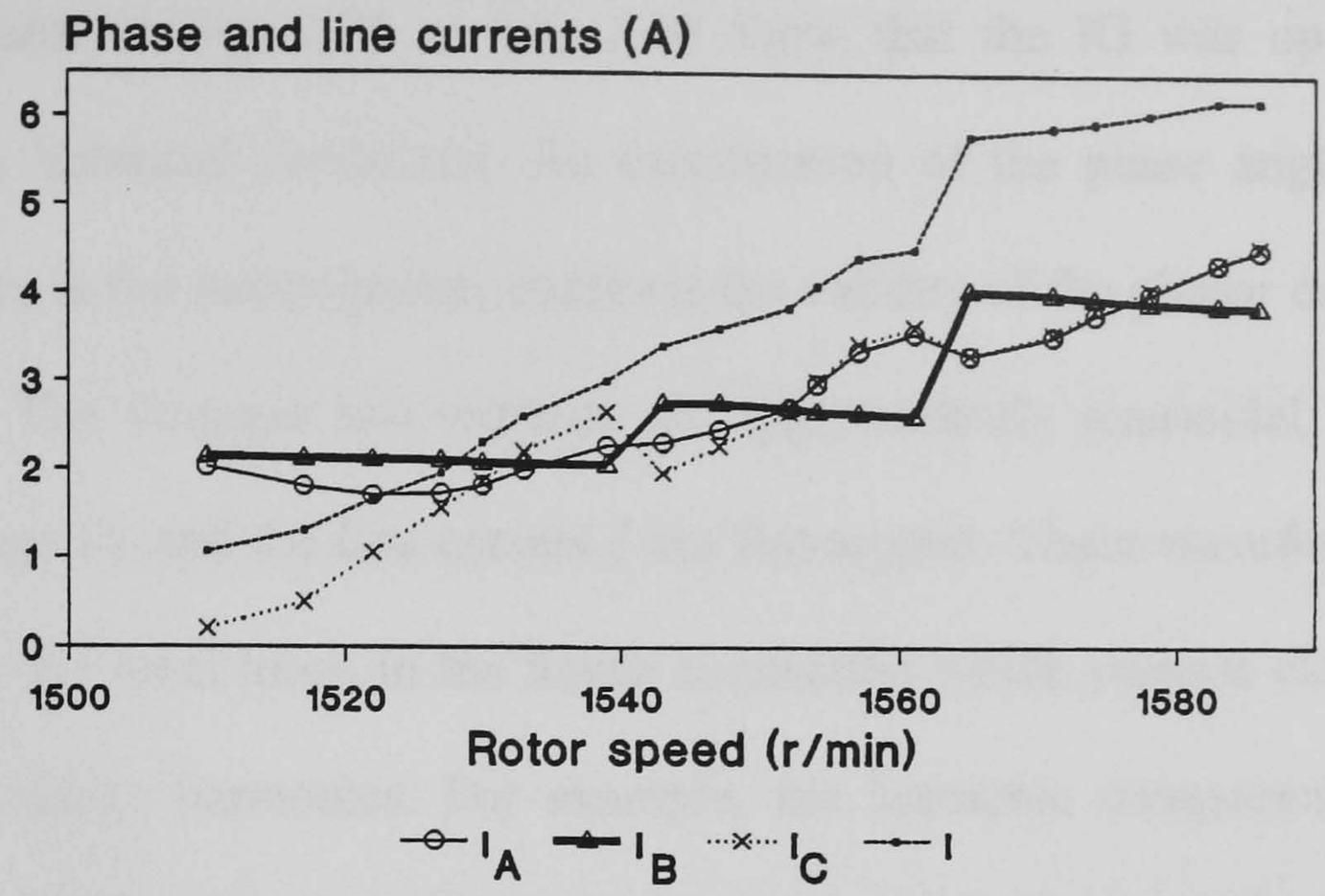


Fig. 2.35 Phase and line current variations of SMIG under multi-mode operation.

Experimental waveforms of the SMIG were also recorded when the rotor speed was 1533 r/min and L-mode capacitances were in the circuit. Fig. 2.37 to Fig. 2.39 show the oscillograms of the experimental waveforms obtained by using a voltage scale of 200 V per division, a current scale of 2 A per division, and a time scale of 5 ms per division. The waveform of the supply voltage $V$ (the upper trace) in each oscillogram provides a convenient reference for studying the phase relationship between various voltages and currents.

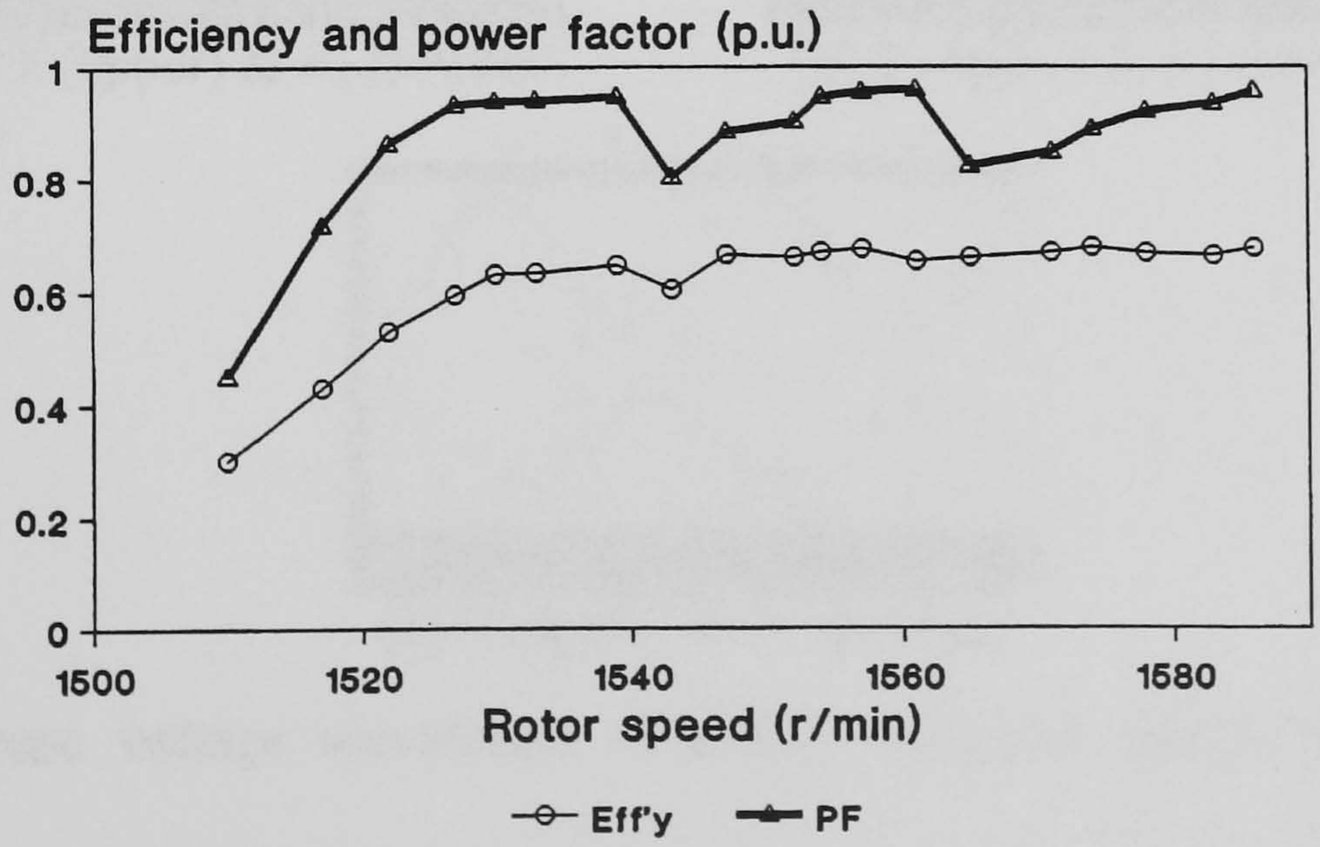


Fig. 2.36 Efficiency and power factor variations of SMIG under multi-mode operation.

The oscillograms in Fig. 2.37 to Fig. 2.39 show that the IG was operating under approximately balanced conditions. An examination of the phase angles (using the vertical cursors in the oscillograms) confirms the validity of the phasor diagram shown in Fig. 2.13. The voltages and currents are approximately sinusoidal, but both the phase-C voltage $V_C$ and the line current $I$ are flat-topped. These waveform distortions are caused by the local loops in the Smith connection which provide closed paths for the flow of current harmonics. For example, the harmonic components in $V_C$ will circulate the corresponding harmonic currents through capacitances $C_1$ and $C_2$ in loop 3453 of Fig. 2.12. Similarly, harmonic currents will flow in capacitance $C_3$ due to harmonics in the phase-A voltage $V_A$. This phenomenon is confirmed by the waveforms of capacitor currents shown in Fig. 2.39. Third harmonic distortion, for example, can be observed from the waveform of $I_1$ in Fig. 2.39(a).

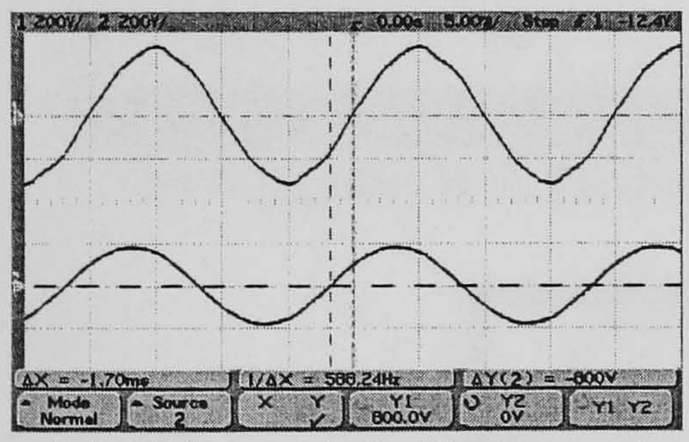


(a) $V$ (upper) & $V_A$ (lower)

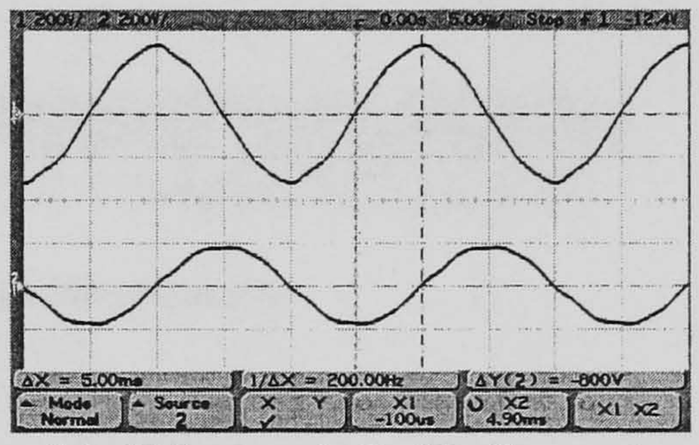


(b) $V$ (upper) & $V_B$ (lower)

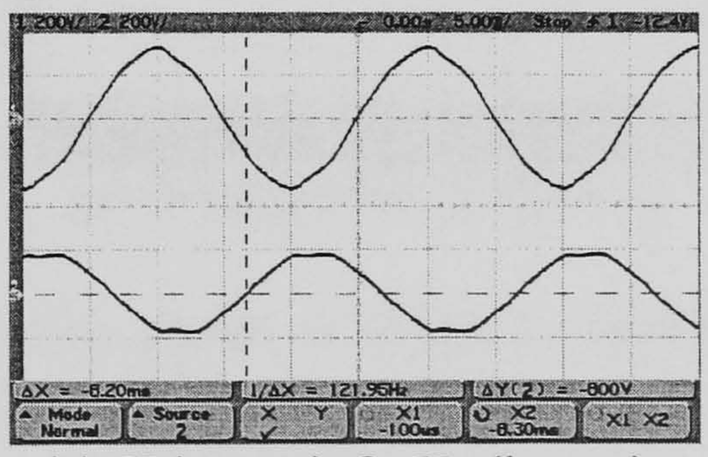


(c) $V$ (upper) & $V_C$ (lower)

Fig. 2.37 Phase voltage waveforms of SMIG: balanced operation with L-mode capacitances.

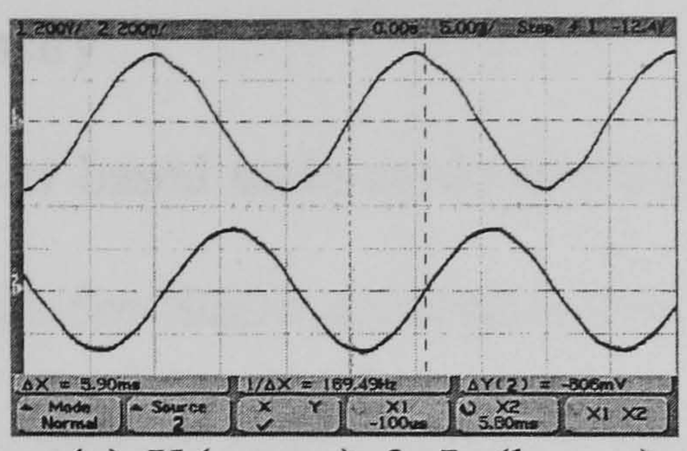


(a) $V$ (upper) & $I_A$ (lower)

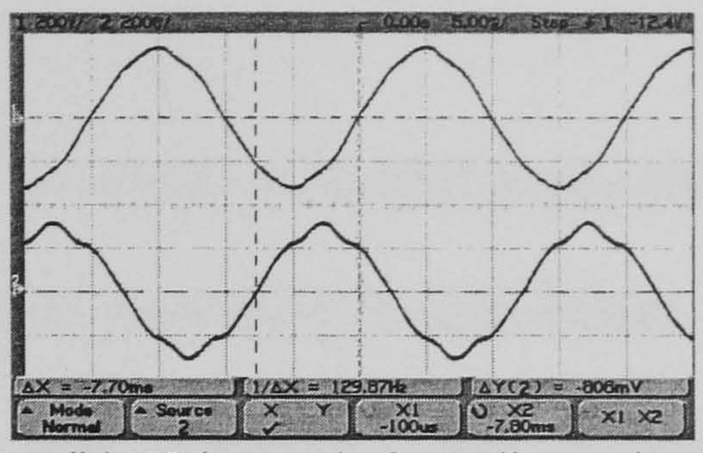


(b) $V$ (upper) & $I_B$ (lower)

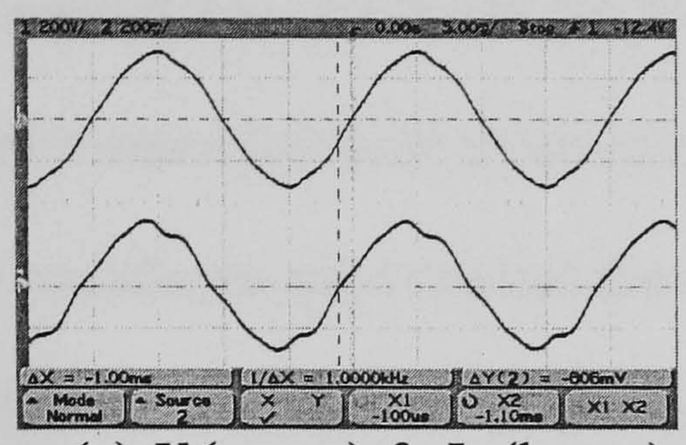


(c) $V$ (upper) & $I_C$ (lower)

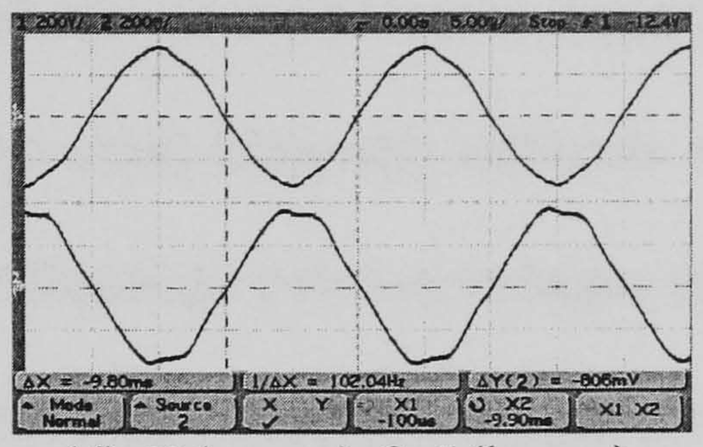


(d) $V$ (upper) & $I$ (lower)

Fig. 2.38 Phase and line currents waveforms of SMIG: balanced operation with L-mode capacitances.

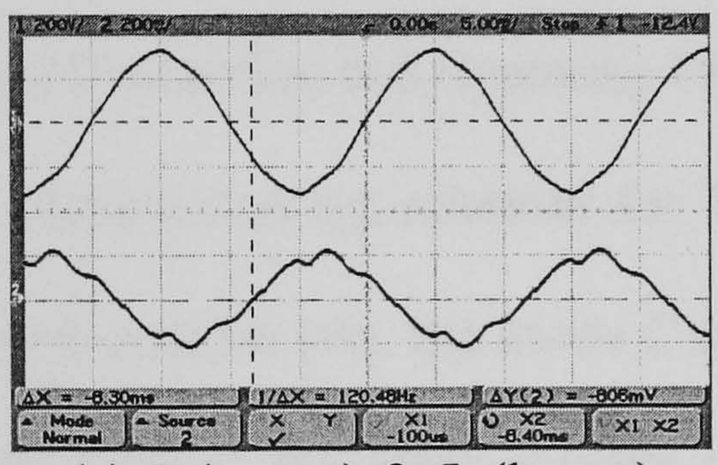


(a) $V$ (upper) & $I_1$ (lower)

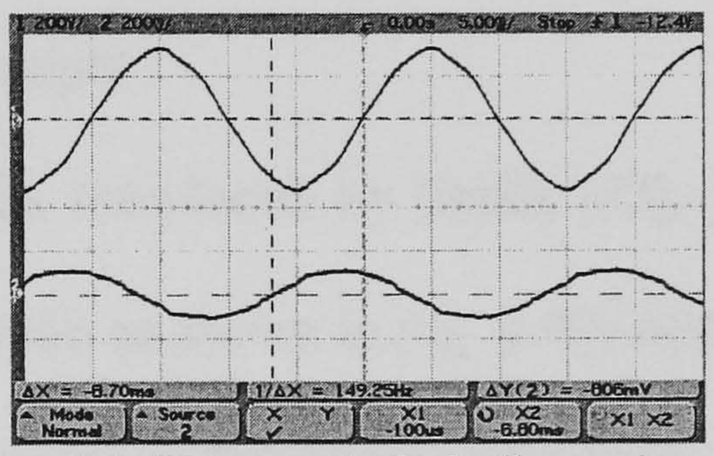


(b) $V$ (upper) & $I_2$ (lower)

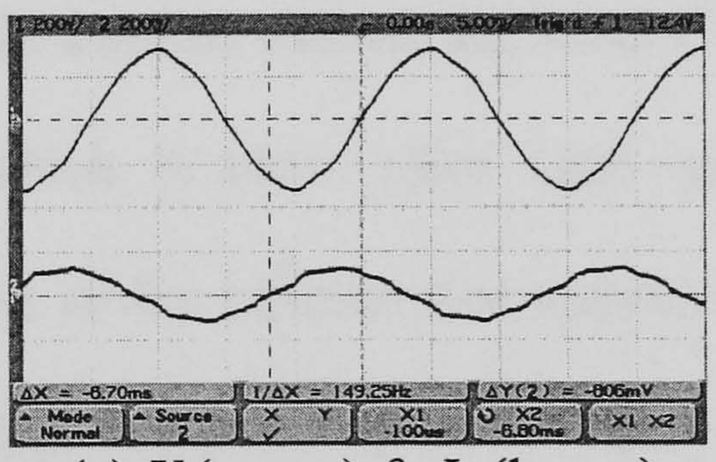


(c) $V$ (upper) & $I_3$ (lower)

Fig. 2.39 Capacitor current waveforms of SMIG: balanced operation with L-mode capacitances.

### 2.4.5 Summary

Microcontroller based multi-mode operation of a grid-connected single-phase induction generator with the Smith connection has been presented in this section. The control system and mode switching strategy have been described. The prototype controller system implemented has confirmed the feasibility of the proposed design. Satisfactory generator performance has been obtained on a small laboratory induction machine. The experimental waveforms have verified the relationships between voltages and currents in the SMIG. This section has also demonstrated that a low-cost, reliable practical single-phase IG system could be realized using the microcontroller approach.

## 2.5 Phase-Balancing Using a Line-Current Injection Method

### 2.5.1 Circuit Connection and Operating Principle

Among the phase-balancing schemes for IGs introduced by Smith [53], a novel line current injection method (viz. the Mode C circuit as shown in Fig. 2.40) deserves special attention. Whereas all the other circuits require a three-wire, two-level single-phase voltage supply for providing the injected current, the Mode C circuit requires only a two-wire single-phase supply (which is more often used universally) and employs a transformer for furnishing one of the injected line current components. Perfect phase balance could be achieved when the generator power factor angle is between $2\pi/3$ rad and $5\pi/6$ rad. In [53], the current injection transformer is assumed to have a unity primary/secondary turns ratio.

In this section, a systematic analysis on the above Mode C circuit for single-phase operation of a three-phase IG will be presented. The effect of non-unity transformer turns ratio on machine performance and the conditions of phase balance will also be investigated.

Fig. 2.40 shows the Mode C circuit for single-phase operation of a three-phase delta-connected IG. Phase A (the reference phase) is connected across the single-phase grid of voltage $V$ while a capacitance $C_2$ is connected across phase B (the lagging phase). The primary winding of the current-injection transformer is connected across phase A. The secondary winding voltage $V_A'$, together with the phase-B voltage $V_B$, causes a current $I_5$ to flow through the capacitance $C_5$. The capacitor currents $I_2$ and $I_5$ thus constitute the line current $I_{L2}$ that flows into terminal 2 of the IG.

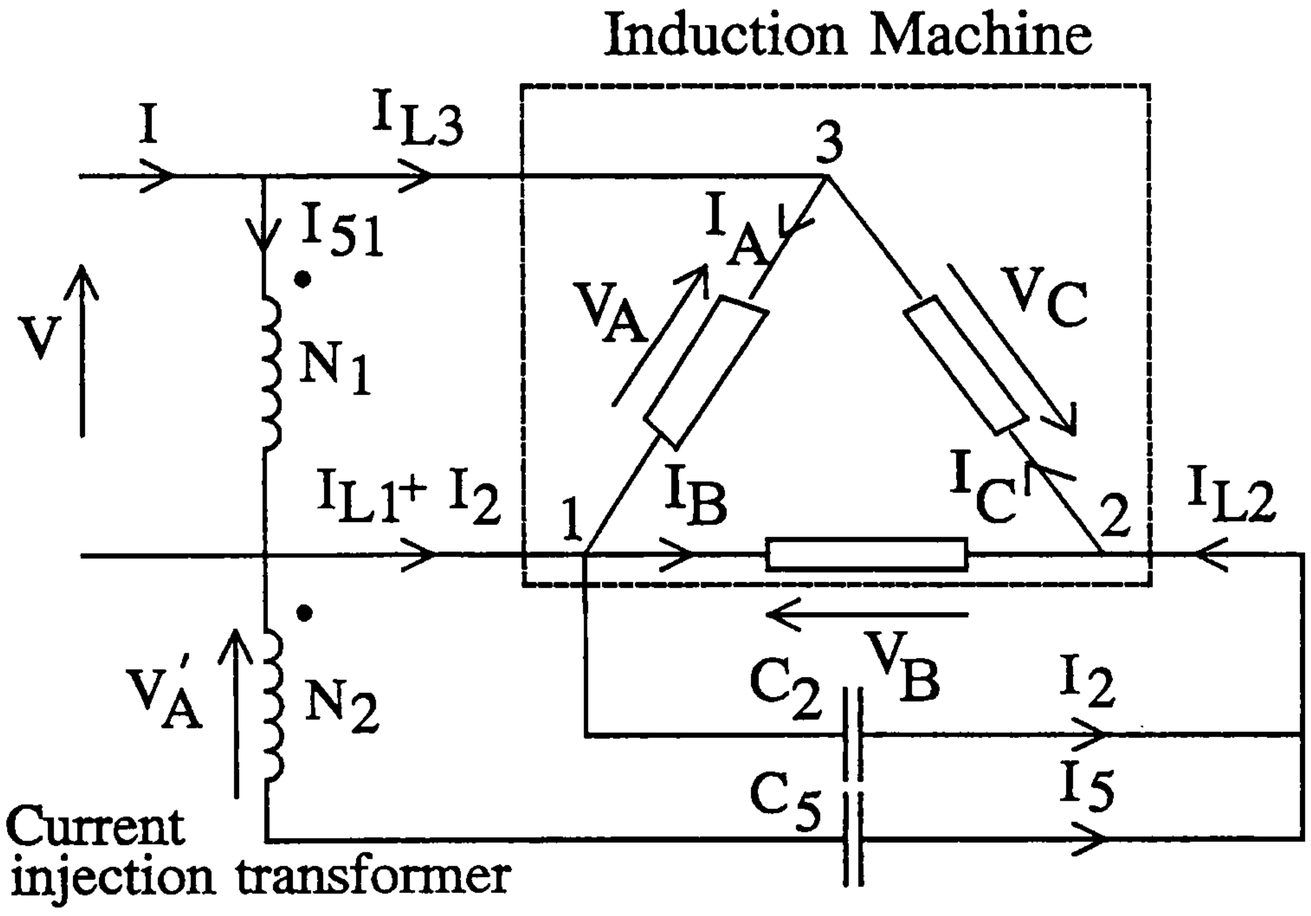


Fig. 2.40 Mode C circuit for single-phase operation of a delta-connected three-phase IG.

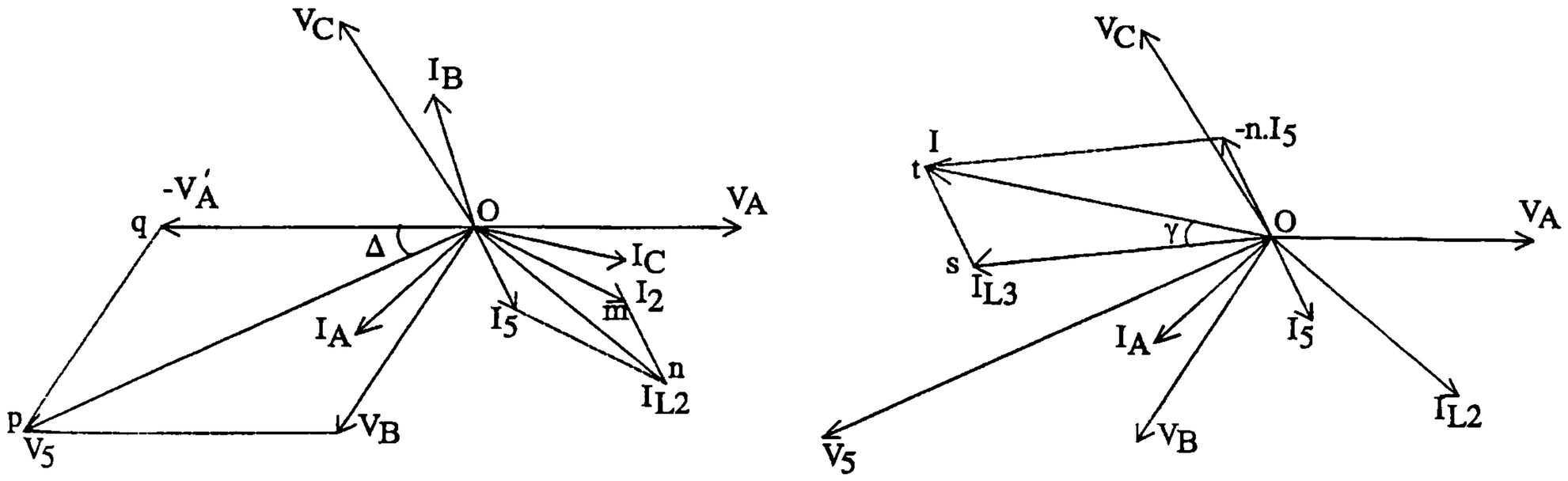


(a) (b)

Fig. 2.41 Phasor diagrams for the Mode C circuit:
(a) Phasor diagram showing components of $I_{L2}$;
(b) Phasor diagram showing components of grid current $I$, the transformer no-load current having been neglected.

Consider the phasor diagram in Fig. 2.41(a), drawn for the special case of perfect phase balance. The line current $I_{L2}$ lags the phase-C voltage $V_C$ by ($\phi_p$ + $\pi$/6) rad, while the current $I_2$ lags $V_C$ by 5$\pi$/6 rad. Provided $\phi_p$ is greater than 2$\pi$/3 rad, $I_{L2}$ can always be formed from appropriate values of $I_2$ and $I_5$ and perfect phase balance can be obtained. The maximum value of generator impedance angle $\phi_{p,max}$ below which perfect phase balance is possible depends on the angle $\Delta$ which varies as the turns-ratio of the current injection transformer.

Fig. 2.41(b) shows the components of the supply line current $I$, the transformer no-load current having been neglected. It is noticed that both active power and reactive power are delivered to the line voltage $V$ via the current injection transformer (by virtue of the voltage $V_A$ and the current component -$n.I_5$). The IG delivers balanced three phase power from the stator winding terminals 1, 2 and 3 as shown in Fig. 2.40. Most of this power is transmitted conductively to the single-phase line via terminals 1 and 3 (by virtue of the voltage $V_A$ and the line current $I_{L3}$). The remaining power output is delivered to the line inductively through the transformer coupling mechanism. Fig. 2.41(b) also suggests that the line power factor of the IG system is high and the transmission losses associated with the reactive power supply are reduced.

### 2.5.2 Performance Analysis

Performance analysis of the phase-balancing scheme shown in Fig. 2.40 can also be carried out using the method of symmetrical components [9]. Adopting the *motor* convention for the induction machine and neglecting the leakage impedance drop of the current injection transformer, the following inspection equations may be established:

$$V = V_A \tag{2.40}$$

$$V_A + V_B + V_C = 0 \tag{2.41}$$

$$I_2 = V_B \cdot Y_2 \tag{2.42}$$

$$I_5 = (V_B - V_A') \cdot Y_5 \tag{2.43}$$

$$I_{L3} = I_A - I_C \tag{2.44}$$

$$I_{L2} = I_2 + I_5 \tag{2.45}$$

$$I_{L2} = I_C - I_B \tag{2.46}$$

$$I = I_{L3} + I_{51} \tag{2.47}$$

where $Y_2 = j\omega C_2$, $Y_5 = j\omega C_5$ and $\omega$ is the angular frequency of the supply voltage.

The primary and secondary quantities of the current injection transformer are related by

$$I_{51} = I_{t0} - n.I_5 \tag{2.48}$$

$$V_A' = n.V_A \tag{2.49}$$

where $n$ is the secondary-to-primary turns-ratio $N_2/N_1$ and $I_{t0}$ is the no-load current of the transformer.

Solution of the above equations using the method of symmetrical components gives the positive-sequence voltage $V_p$ and the negative-sequence voltage $V_n$:

$$V_p = \sqrt{3}V \cdot \frac{Y_n + (Y_2 + Y_5)/(1-h) - n.Y_5/(h-h^2)}{Y_p + Y_n + Y_2 + Y_5} \tag{2.50}$$

$$V_n = \sqrt{3}V \cdot \frac{Y_p - h.(Y_2 - Y_5)/(1-h) + n.Y_5/(h-h^2)}{Y_p + Y_n + Y_2 + Y_5} \tag{2.51}$$

where $Y_p$ and $Y_n$ are the positive-sequence and negative-sequence admittances of the three-phase IG and $h$ is the unit complex operator $\exp(j2\pi/3)$.

For a given single-phase grid voltage $V$ and speed (or per-unit slip), $Y_p$ and $Y_n$ are known and both $V_p$ and $V_n$ can be computed. The currents $I_p$ and $I_n$ can then be calculated from

the positive-sequence and negative-sequence equivalent circuits. The generator performance, such as phase voltages, phase currents, electromagnetic torque, power factor and efficiency, can subsequently be obtained.

### 2.5.3 Balanced Operation

*A) Conditions for Balanced Operation*

Since negative-sequence voltage must be absent when the generator is balanced, one obtains, from (2.51),

$$Y_p - h.(Y_2 - Y_5)/(1-h) + n.Y_5/(h-h^2) = 0\,. \tag{2.52}$$

Eqn. (2.52) may be solved to give the capacitive admittances that result in perfect phase balance. Alternatively, the phasor diagram under balanced conditions can be used. Referring to Fig. 2.41(a), the voltage $V_5$ across $C_5$ is given by:

$$V_5 = k_n \cdot V_{ph} \tag{2.53}$$

where

$$k_n = \sqrt{1+n+n^2} \tag{2.54}$$

and $V_{ph}$ is the phase voltage.

The angle $\Delta$ in phasor triangle Oqp is given by:

$$\sin\Delta = \frac{\sqrt{3}}{2.k_n}\,. \tag{2.55}$$

Applying Sine Rule to the phasor triangle Omn yields:

$$I_2 = \frac{\sqrt{3}\,I_{ph}.\sin(\pi - \Delta - \phi_p)}{\sin(2\pi/3 + \Delta)} \tag{2.56}$$

$$I_5 = \frac{\sqrt{3}\,I_{ph}.\sin(\phi_p - 2\pi/3)}{\sin(2\pi/3 + \Delta)} \tag{2.57}$$

where $I_{ph}$ is the phase current and $\phi_p$ is the positive-sequence impedance angle of the IG.

The admittances $Y_2$ and $Y_5$ that result in perfect phase balance are thus given by

$$Y_2 = \sqrt{3}\, Y_p \cdot \frac{\sin(\pi - \Delta - \phi_p)}{\sin(2\pi/3 + \Delta)} \tag{2.58}$$

$$Y_5 = \frac{\sqrt{3}\, Y_p}{k_n} \cdot \frac{\sin(\phi_p - 2\pi/3)}{\sin(2\pi/3 + \Delta)} . \tag{2.59}$$

Eqn. (2.58) implies that admittance $Y_2$ is positive when $\phi_p$ is less than $\pi$ - $\Delta$. It is obvious that both $Y_2$ and $Y_5$ (and hence $C_2$ and $C_5$) depend on $Y_p$ and $\phi_p$, as well as the transformer turns-ratio $n$.

Fig. 2.42 shows the variations of $Y_2$ and $Y_5$ for balanced operation of the experimental IG whose technical data are given in Section 2.5.4. For a given value of $\phi_p$, an increase in $n$ results in an increase of $Y_2$ but a decrease of $Y_5$. This feature may be exploited for design of a practical system. Use of values of $n$ exceeding 2, however, is not recommended as the effect on $Y_2$ and $Y_5$ is less pronounced.

*B) Line Current and Power Factor*

If the no-load current of the current injection transformer is neglected, the line current $I$ and the angle $\gamma$ can be computed from the phasor triangle Ost in Fig. 2.41(b), as follows:

$$I = \sqrt{(n.I_5)^2 + {I_{L3}}^2 - 2\,(n.I_5)\, I_{L3} \cos(\phi_p - \pi/3 + \Delta)} \tag{2.60}$$

$$\sin\gamma = \frac{n.I_5}{I} . \sin(\phi_p - \pi/3 + \Delta) . \tag{2.61}$$

If the *input* power factor angle $\phi$ is defined to be positive when the line current $I$ lags the grid terminal voltage $V$, then

$$\phi = \phi_p + \frac{\pi}{6} + \gamma . \tag{2.62}$$

Fig. 2.43 shows the variation of the line power factor angle $\phi$ as $n$ is varied from unity to

2. For a given value of $\phi_p$, $\phi$ increases almost linearly with $n$. When $\phi_p = 125^0$e, $\phi$ is less than $180^0$e and the *output* line power factor of the system is leading. The line power factor therefore becomes higher as $n$ increases. When $\phi_p = 130^0$e, the line power factor is very close to unity, but a transition from leading to lagging power factor occurs when $n$ = 1.2. At larger values of $\phi_p$, the system exports reactive power to the grid.

From (2.59), it is observed that when the turns-ratio $n$ is equal to unity and $\phi_p = 2\pi/3$ rad, $Y_5$ is equal to zero, hence the capacitance $C_5$ is not required and the circuit is reduced to the Steinmetz connection for a delta-connected IG. When $\phi_p = 5\pi/6$ rad, however, $Y_2$ is equal to zero in accordance with (2.58). This is the maximum value of the generator positive-sequence impedance angle for which perfect phase balance can be achieved.

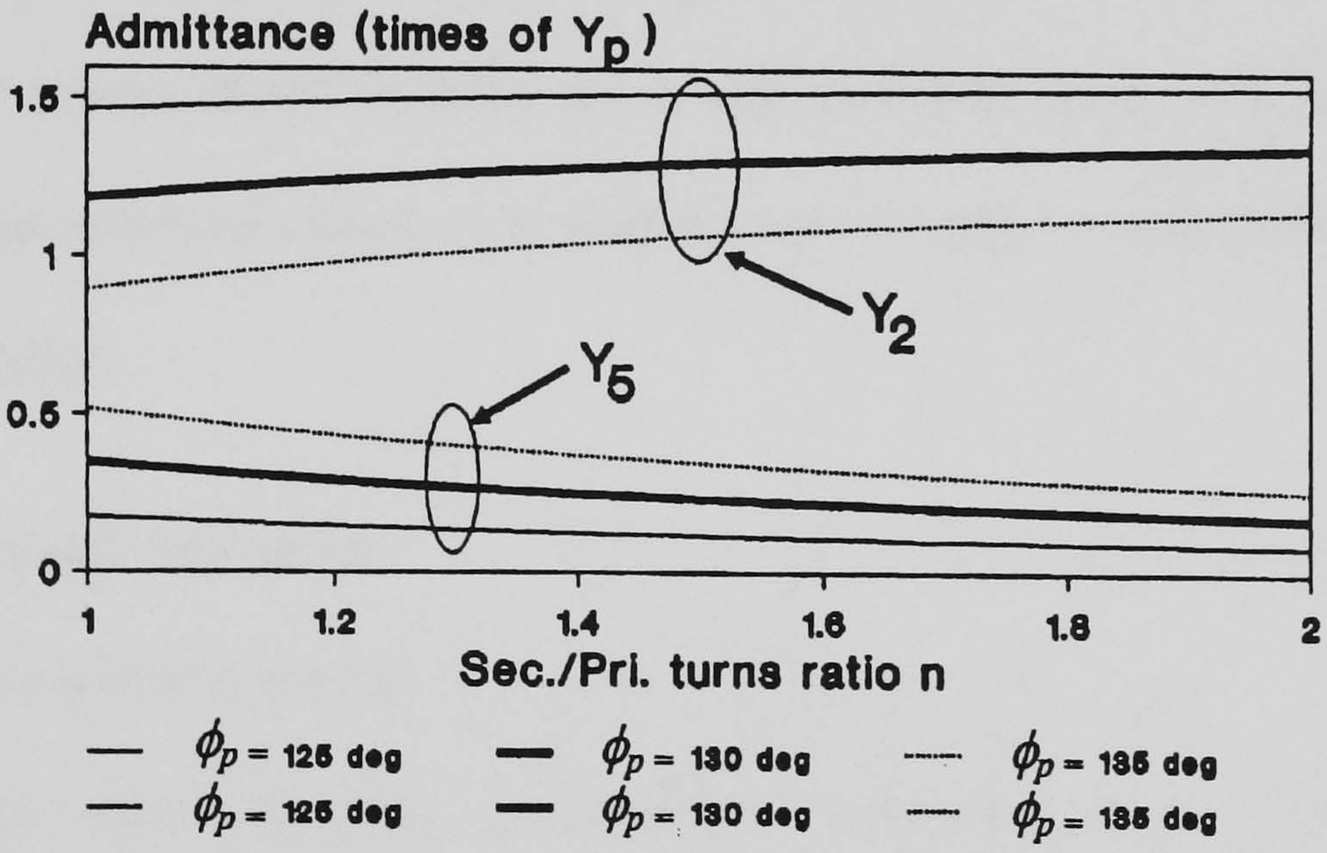


Fig. 2.42 Effect of transformer turns ratio $n$ on the values of $Y_2$ and $Y_5$ for balanced operation of IG.

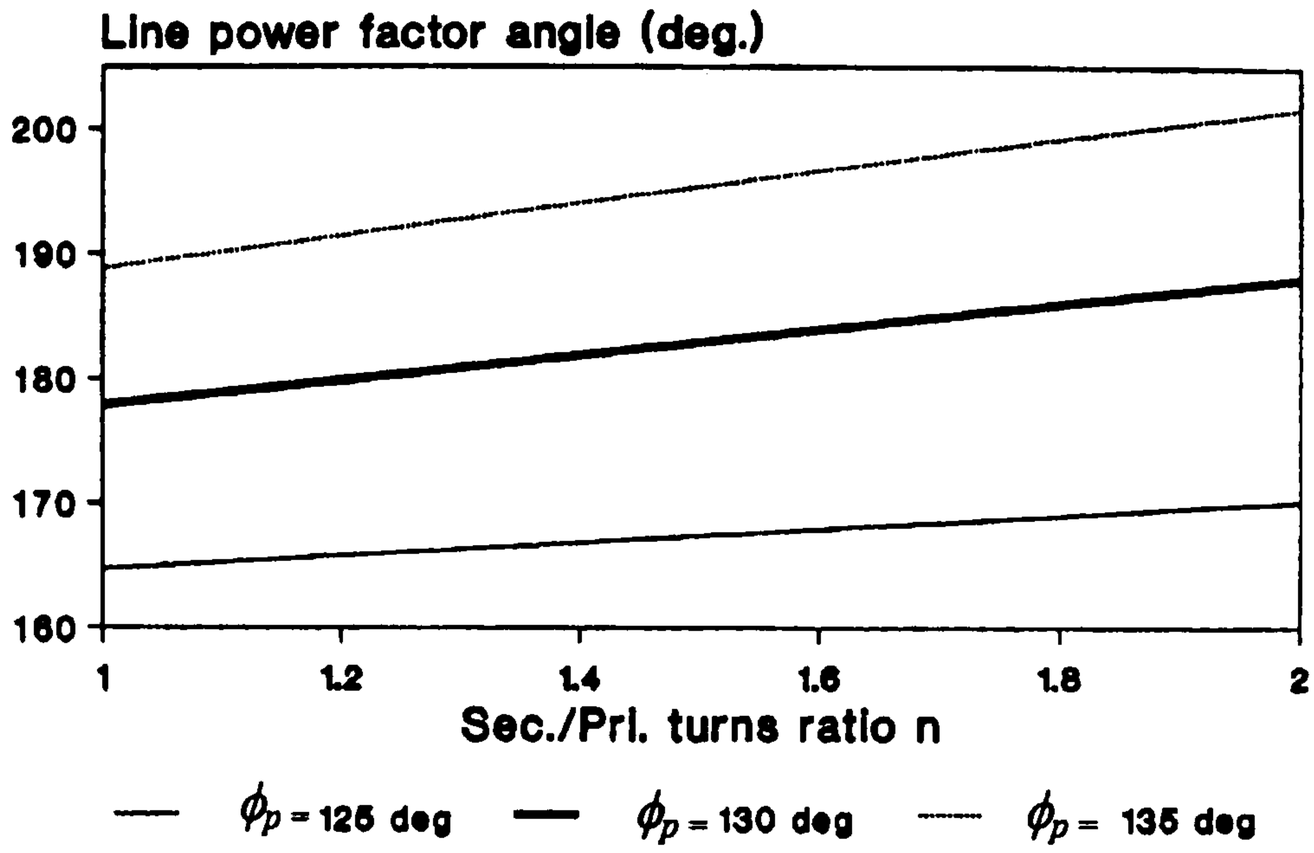


Fig. 2.43 Effect of transformer turns ratio $n$ on the line power factor angle $\phi$.

By choosing a value of $n$ greater than unity and using the correct values of capacitances, balanced operation can be achieved for values of $\phi_p$ exceeding $5\pi/6$ rad. When $n$ is increased to 1.2, for example, $Y_2$ is equal to zero when $\phi_p = 0.85\pi$ rad. This corresponds to a generator power factor of 0.89, achievable probably for a very large IG. In most cases, a current injection transformer with $n$ close to unity would suffice for achieving balanced operation.

### 2.5.4 Results and Discussion

*A) Computation of Performance*

To verify the above analysis, performance computations and experiments were performed on a 2.0-kW, 200-V, 9.4-A, 50-Hz, four-pole, delta-connected induction machine. Fig. 2.44 shows the variations of $Y_p$ and $\phi_p$ with rotor speed, determined experimentally by operating the induction generator on a balanced three-phase supply at a constant voltage $V_p^*$. Fig. 2.45 shows the corresponding variations of positive-sequence electromagnetic torque $T_p^*$. For a specific rotor speed, the positive-sequence torque was computed from the following equation:

$$T_p = T_p^* \times \left(V_p / V_p^*\right)^2 \tag{2.63}$$

where $V_p$ is the computed positive-sequence voltage, while $V_p^*$ and $T_p^*$ are the corresponding values as given by Fig. 2.44 and Fig. 2.45.

The negative-sequence quantities were determined in a similar manner. For the experimental machine, the negative-sequence admittance $Y_n$ was determined as $0.1\angle -59^0$ S and could be regarded as constant over the normal speed range. The negative-sequence electromagnetic torque $T_n$ was also insensitive to the rotor speed but depended on the applied voltage. For a given rotor speed, $T_n$ was computed as:

$$T_n = T_n^* \times \left(V_n / V_n^*\right)^2 \tag{2.64}$$

where $T_n^*$ is the negative-sequence torque determined with an applied negative-sequence voltage of $V_n^*$. For the experimental machine, $T_n^*$ = 1.9 N.m when $V_n^*$ = 54 V.

The driving torque $T_d$ of the IG was computed as:

$$T_d = T_p + T_n + T_{fw} \tag{2.65}$$

where $T_{fw}$ is the torque for overcoming the friction and windage losses.

The current injection transformer used was rated at 50-Hz, 200/210.5 V and 1-kVA. It had a no-load current of $(0.107 - j0.259)$ A and an equivalent leakage impedance of $(1.4 + j2.89)$ Ω, both referred to the primary side. The leakage impedance drop was neglected in the performance computations, but the copper losses were included when evaluating the system efficiency.

*B) Computed and Experimental Results*

A phase-balancing experiment was next performed at different rotor speeds. The grid voltage was maintained at rated value and the capacitances were varied until balanced generator operation was obtained. Fig. 2.46 shows the computed and experimental values of capacitances $C_2$ and $C_5$ that result in balanced operation of the three-phase IG. It is

observed that perfect phase balance is possible for speeds above 1533 r/min. As the rotor speed increases, $C_5$ increases approximately linearly while $C_2$ remains substantially constant over most of the rotor speed range.

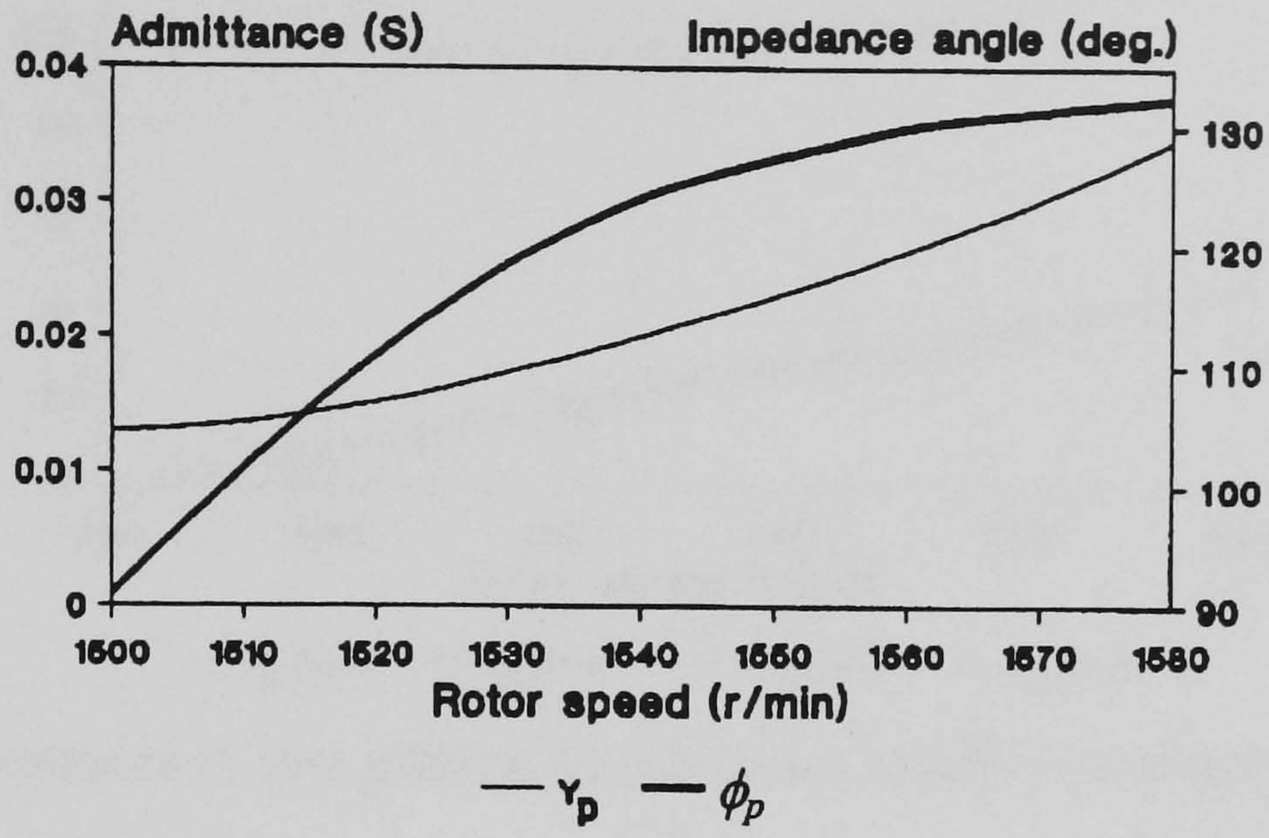


Fig. 2.44 Experimental variations of positive-sequence admittance $Y_p$ and positive-sequence impedance angle $\phi_p$ with rotor speed, determined at $V_p^* = 200$ V.

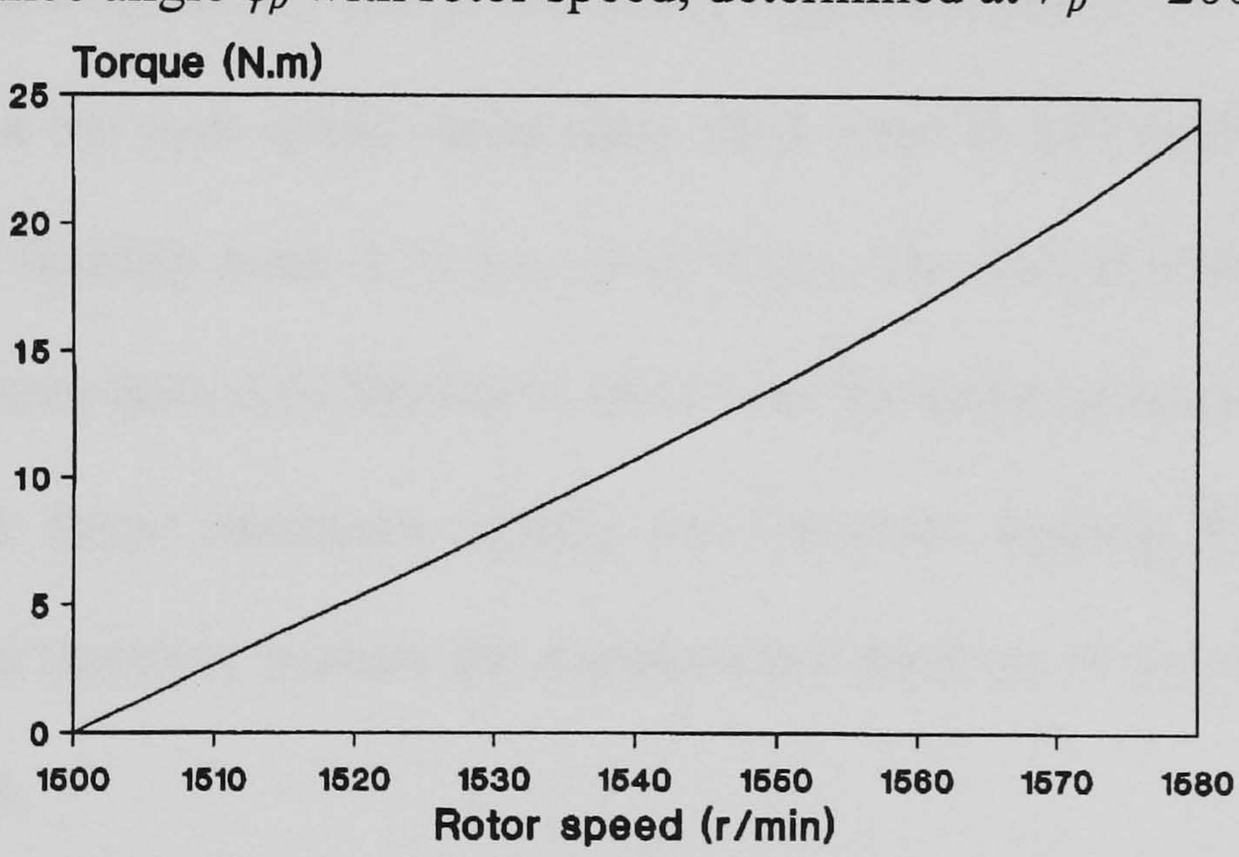


Fig. 2.45 Experimental variation of positive-sequence electromagnetic torque of IG with rotor speed, determined at $V_p^* = 200$ V.

Fig. 2.47 shows the variations of phase current, line current and output power when the IG operates under perfect phase balance. At a speed of 1562.5 r/min (which corresponds to operation with approximately rated phase current), the generator delivers a power of 2.09 kW to the single-phase grid. Due to the injected current component $I_5$, the ratio of input current to the phase current at full load is 1.92. This is higher than the ratio of $\sqrt{3}$ in

the case of a single-phase IG with the Steinmetz connection, and may be attributed to the primary current $I_{51}$ of the current injection transformer.

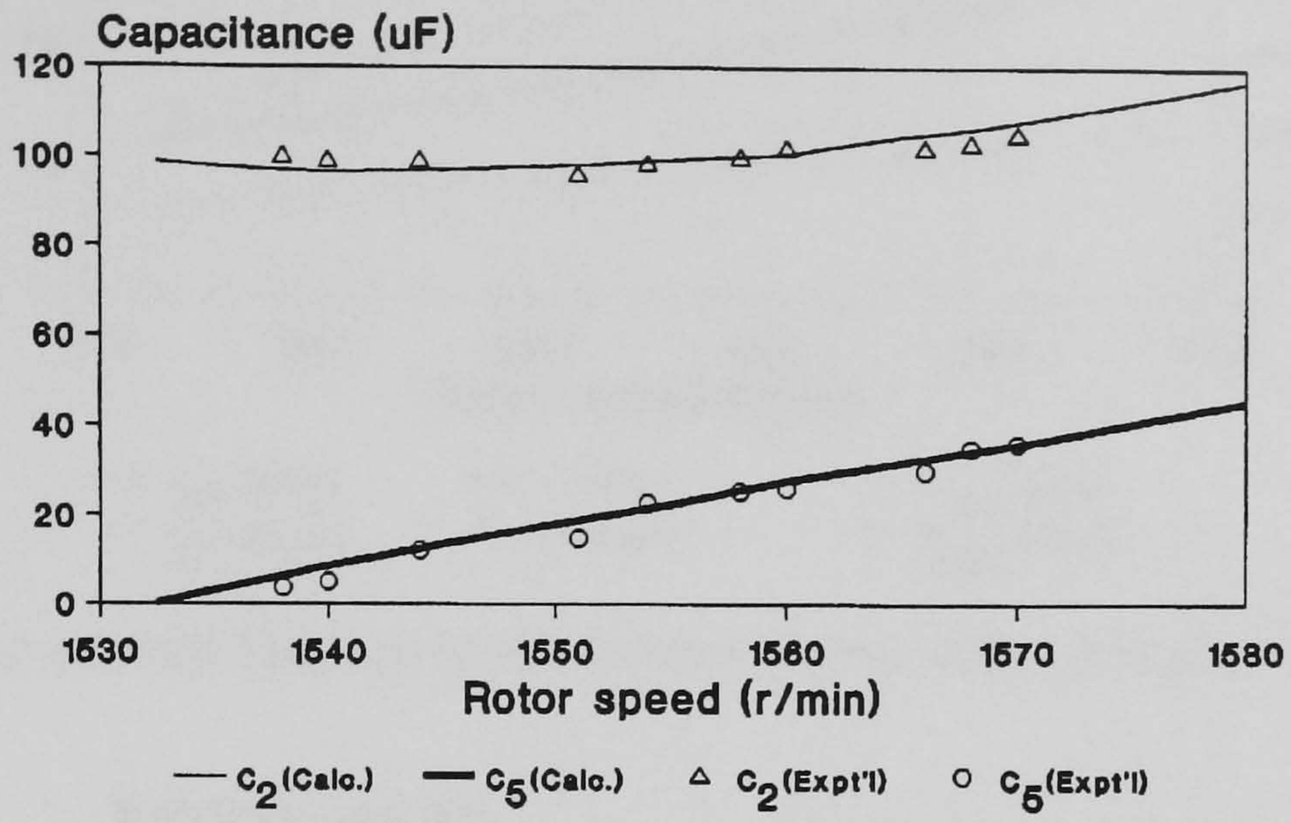


Fig. 2.46 Capacitances to give perfect phase balance at different speeds.

Fig. 2.48 shows the efficiency and power factor characteristics of the IG under perfect phase balance. As the rotor speed varies from 1533 r/min to 1570 r/min, the efficiency decreases almost linearly from 0.74 p.u. to 0.70 p.u. The output power factor, on the other hand, increases from 0.85 leading to unity over the same speed range. Above 1570 r/min, the power factor decreases slightly and becomes lagging. This novel phase-balancing method therefore enables the experimental machine to operate with excellent line power factors.

The close agreement between the computed and experimental results in Fig. 2.46 through Fig. 2.48 confirms the principle of phase balancing as explained in Section 2.5.1.

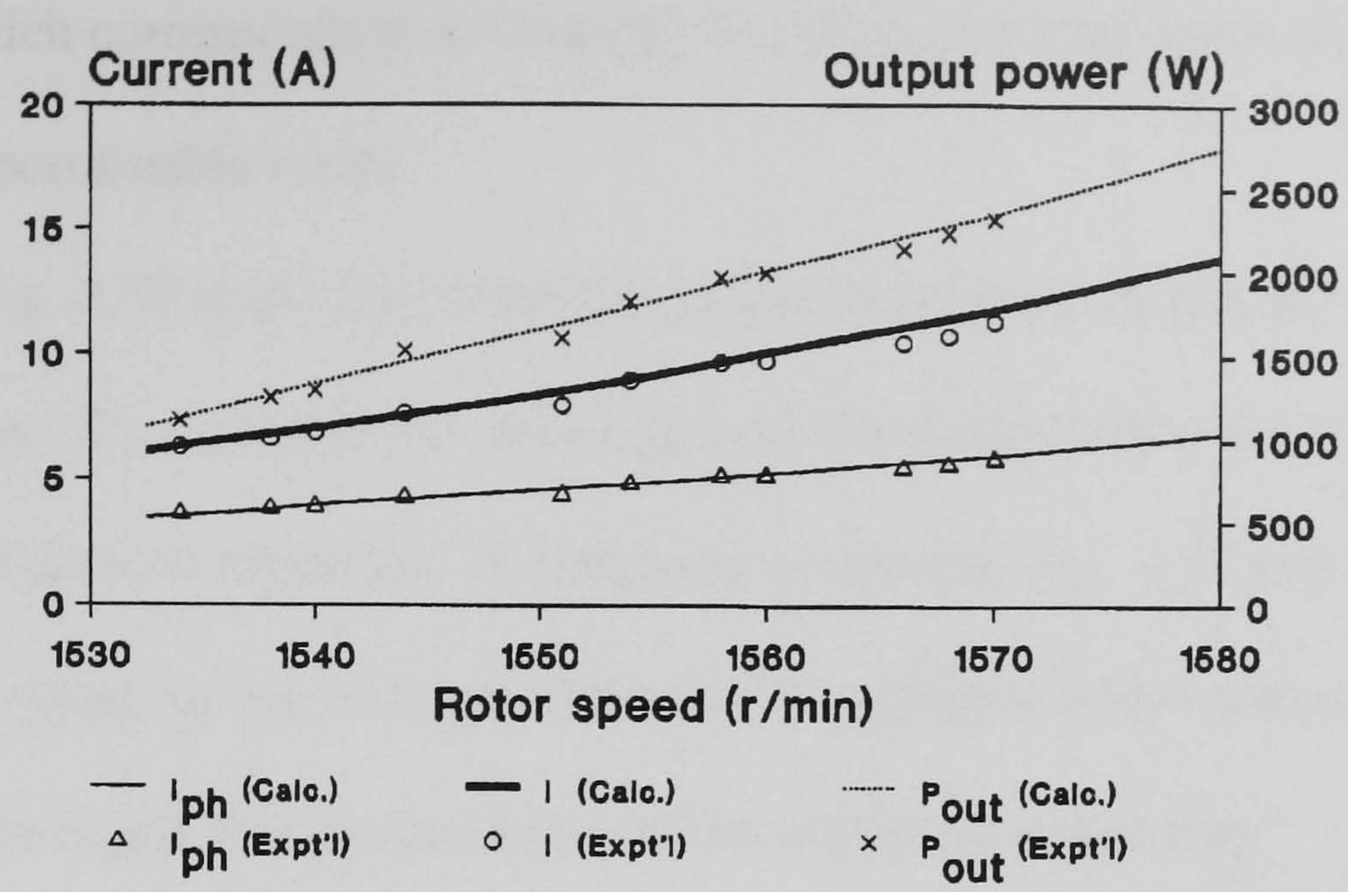


Fig. 2.47 Phase current, line current and output power at perfect phase balance.

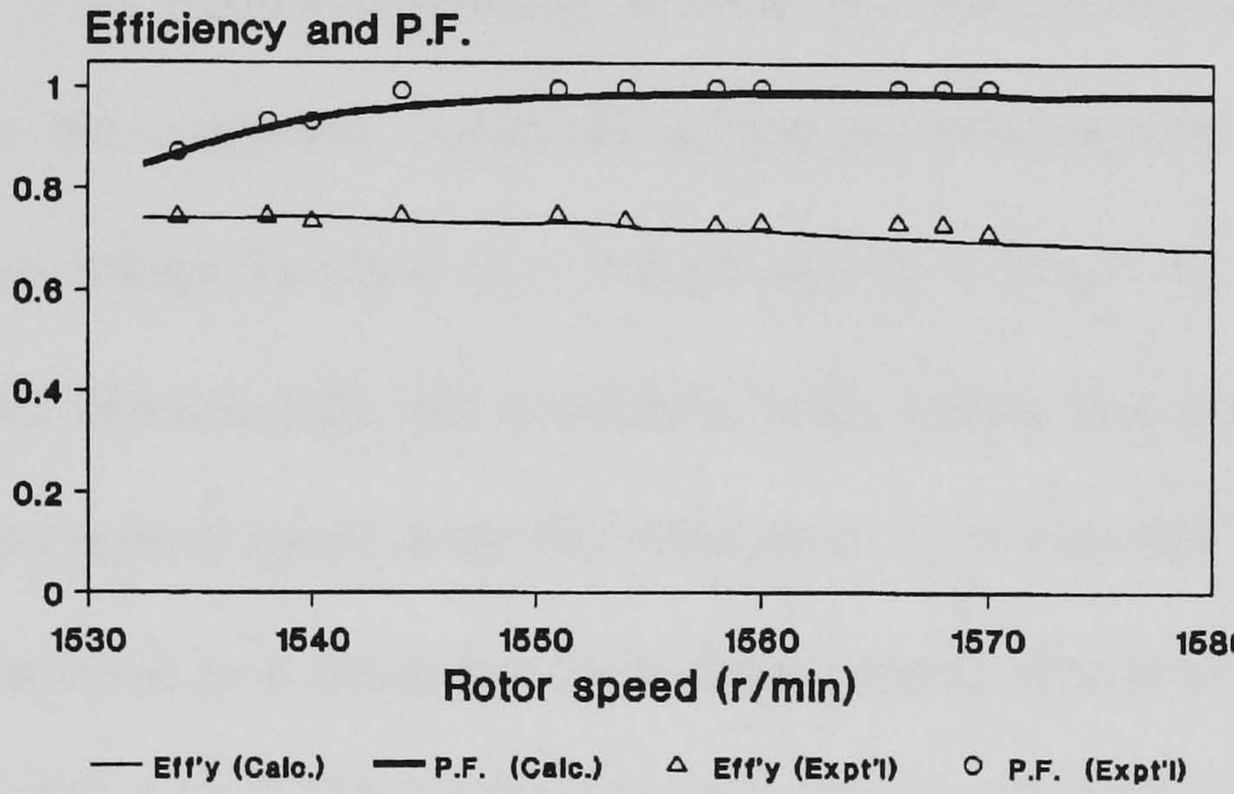


Fig. 2.48 Efficiency and output power of IG at perfect phase balance.

A load test was conducted on the experimental machine with $C_2$ = 102 μF and $C_5$ = 30 μF. It was found that the IG was balanced at a rotor speed of 1566 r/min and at a phase current of 5.5 A. Fig. 2.49 through Fig. 2.52 show the computed and experimental performance characteristics obtained. As shown in Fig. 2.49, the phase-B voltage $V_B$ increases as the rotor speed decreases from that corresponding to the balance point, whereas the phase-C voltage $V_C$ decreases. Fig. 2.50 shows that overcurrent occurs in phase B at rotor speeds below 1550 r/min. $I_A$ and $I_C$, on the other hand, are less than the rated value and hence offset the effect of the overcurrent in phase B. At a rotor speed of

1510 r/min, which corresponds to a 'floating' condition, the total stator copper losses are still within the permissible limits.

Fig. 2.51 and Fig. 2.52 show that, when the capacitances are constant, the efficiency, the power factor, and the output power are in general lower than when the capacitances are varied to give balanced operation. A comparison between Fig. 2.47 and Fig. 2.52 also shows that the output power is lower when the IG operates with constant capacitances. This is due to the negative-sequence losses under unbalanced operation.

Very good agreement between the computed and experimental results is observed in Fig. 2.49 through Fig. 2.52, thereby confirming the validity of the method of analysis.

Fig. 2.53 shows the computed variations of the positive-sequence voltage $V_p$ and negative-sequence voltage $V_n$ when $C_2$ = 102 μF and $C_5$ = 30 μF. $V_p$ exhibits a slightly convex downward characteristic: the maximum value occurs at a rotor speed of 1545 r/min, but over the normal speed range the variation in $V_p$ is less than 5%. The variation of $V_n$, on the other hand, is in the form of a V-shaped curve, with zero value occurring at a rotor speed of 1562.5 r/min. The variation of the voltage unbalance factor VUF (which is the ratio of magnitudes of $V_p$ and $V_n$), is thus also a V-shaped curve.

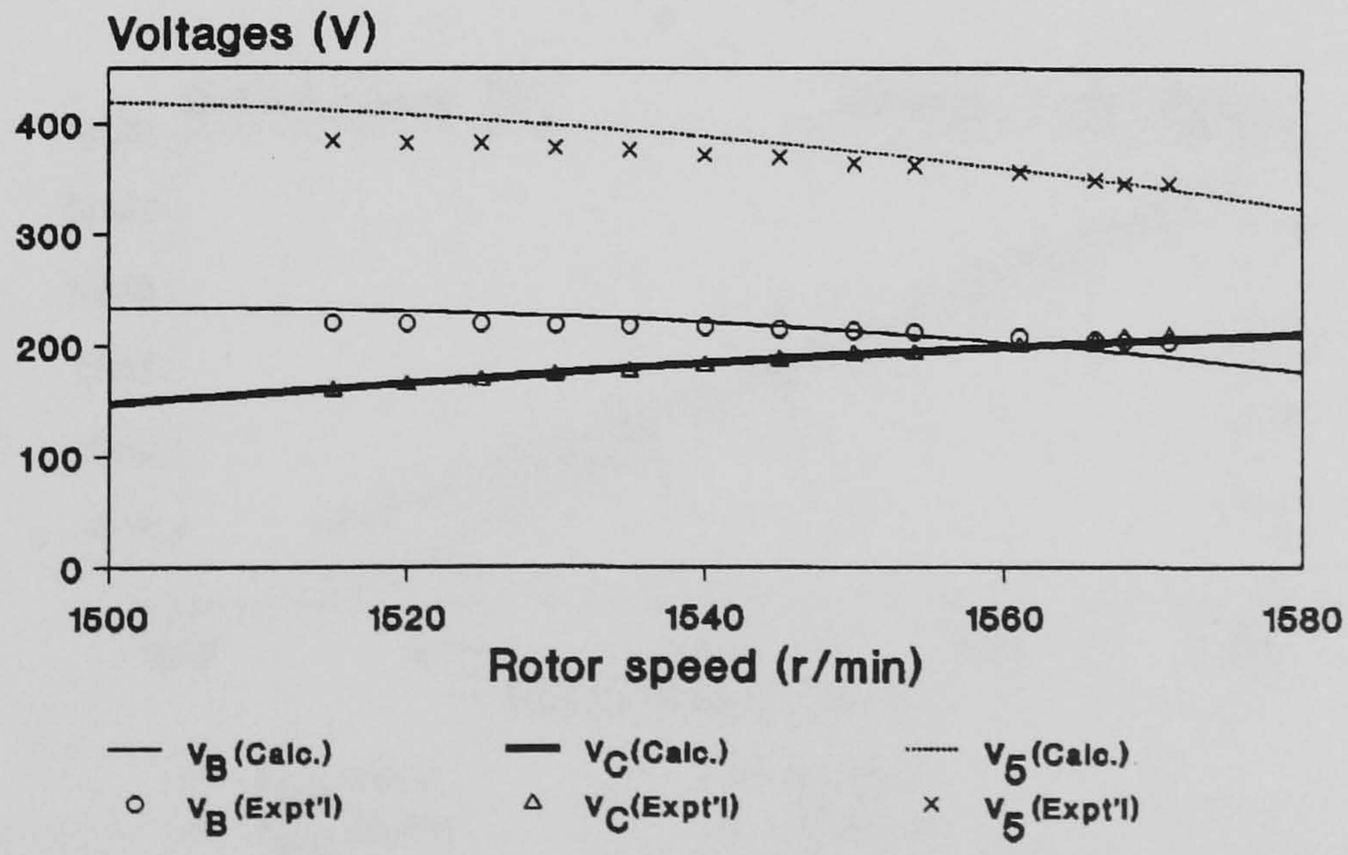


Fig. 2.49 Variations of voltages $V_B$, $V_C$ and $V_5$ when the IG operates with constant capacitances.

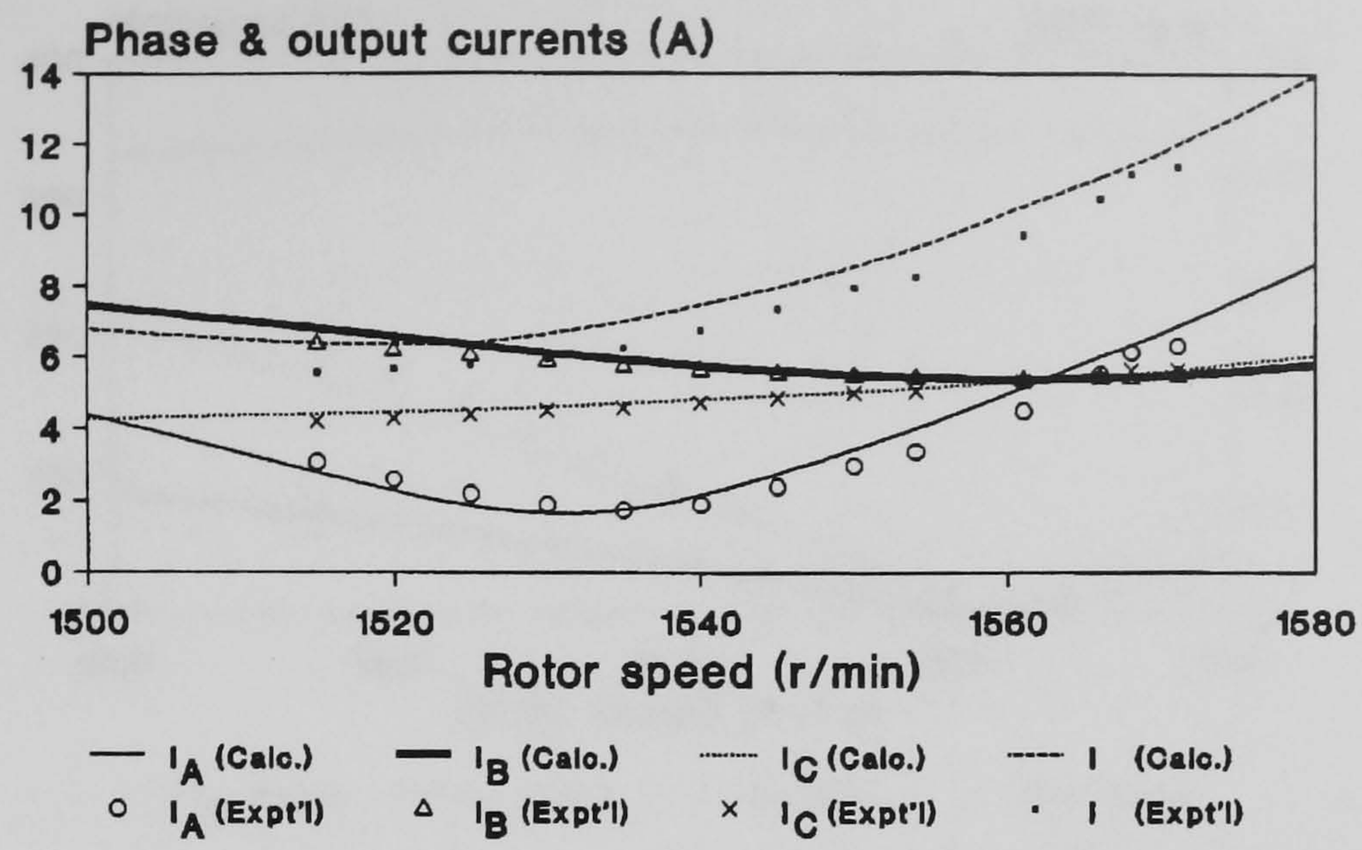


Fig. 2.50 Variations of phase and output currents when the IG operates with constant capacitances.

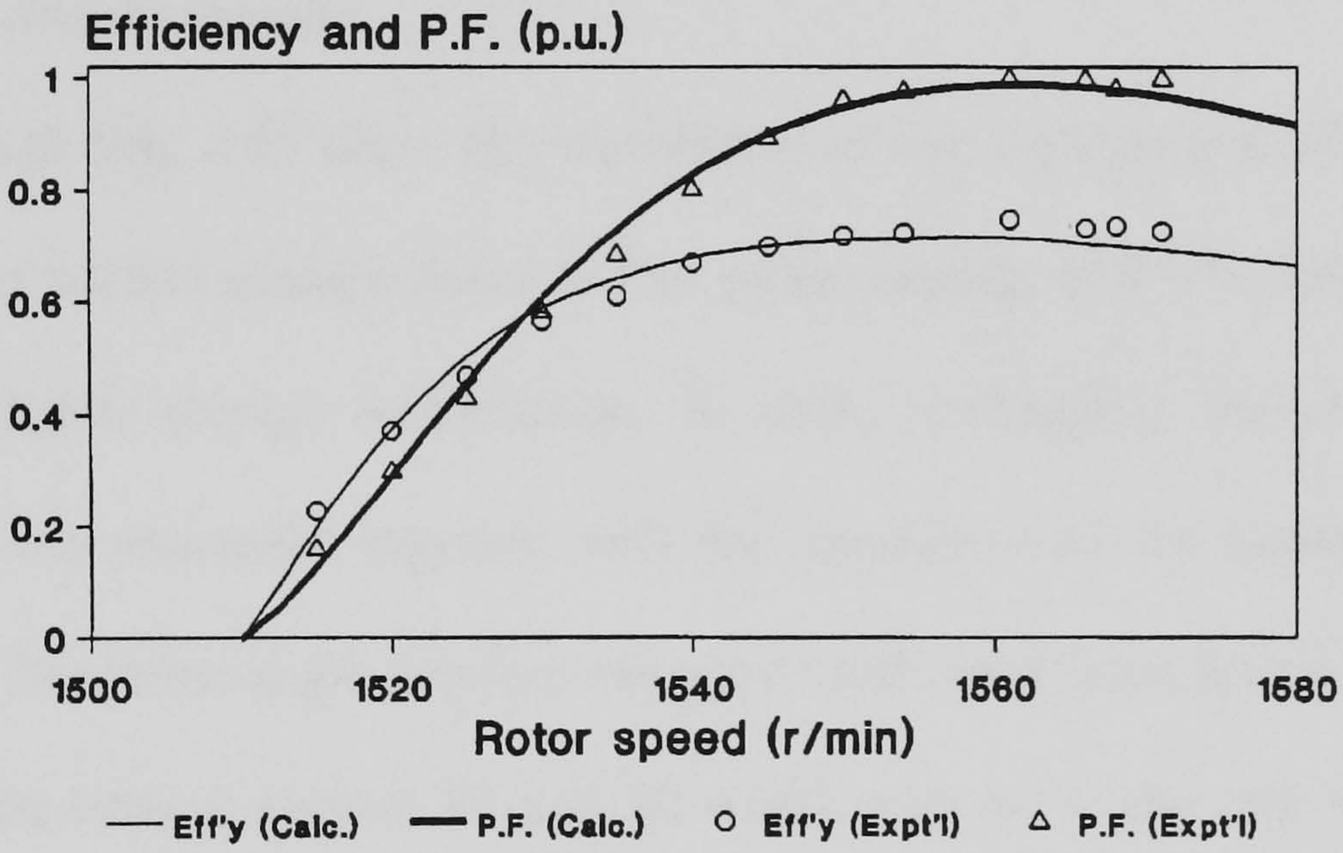


Fig. 2.51 Variations of efficiency and power factor when the IG operates with constant capacitances.

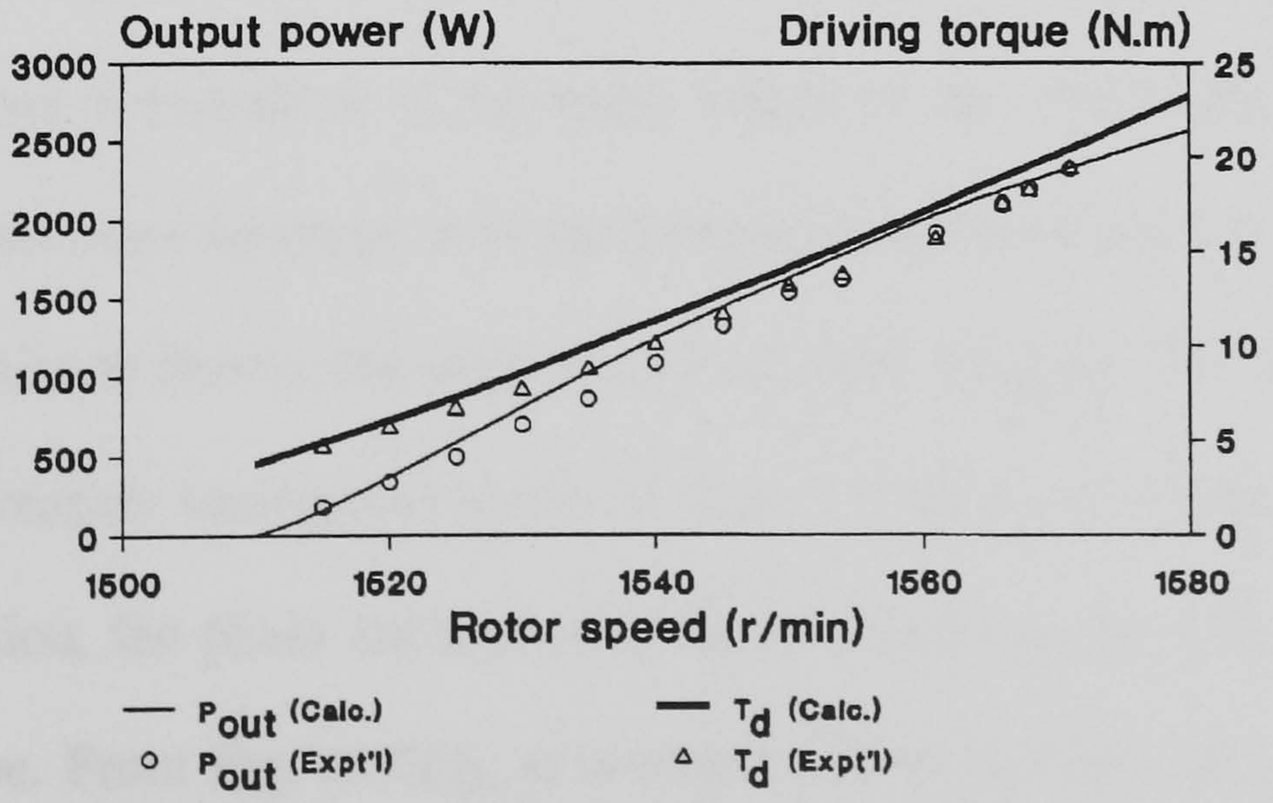


Fig. 2.52 Variations of output power and driving torque when the IG operates with constant capacitances.

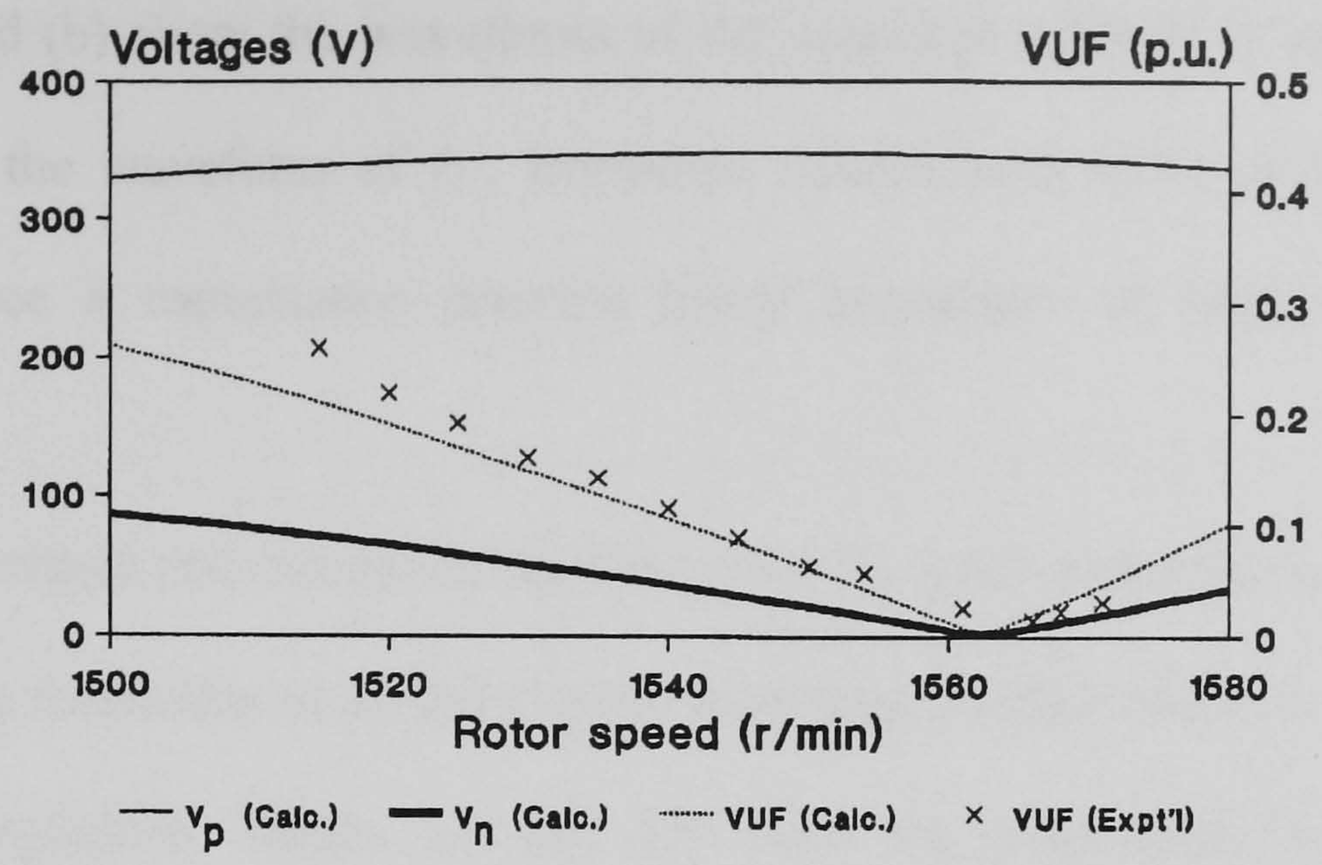


Fig. 2.53 Variations of $V_p$, $V_n$ and voltage unbalance factor (VUF) when the IG operates with constant capacitances.

*C) Waveforms and Harmonics*

Fig. 2.54 through Fig. 2.56 show the waveforms of the experimental IG system when operating under perfect phase balance with a phase current of 5.0 A, measured using a dual-channel digital storage oscilloscope. In each oscillogram, the phase-A voltage (upper trace) was measured together with the waveform of the quantity of interest (lower trace). The phase angle between the upper and lower waveforms is given by the separation of the vertical cursors X1 and X2 which were set to the zero crossings of the two waveforms.

The waveforms in Fig. 2.54(a) and (b) show that the phase voltages of the IG are quite sinusoidal. A close examination of the phase angles of the waveforms confirmed that the phase voltages were balanced. The third-harmonic induced e.m.f.s, however, cause a circulating current to flow in the delta-connected stator winding. This can be observed from the phase current waveforms shown in Fig. 2.55(a) to (c). Except for the third-harmonic distortion, the phase currents are balanced and they have approximately the same wave shape. From Fig. 2.55(d), it is observed that the line current $I$ and $V_A$ are almost in anti-phase, which implies that the output power factor is very close to unity.

Fig. 2.56(a) and (b) show the waveforms of the capacitor currents $I_2$ and $I_5$ while Fig. 2.56(c) shows the waveform of $I_{51}$. Harmonic distortion is more prominent in these waveforms since a capacitance presents lower impedance to higher order current harmonics.

The principal voltage and current harmonics of the IG were measured using a harmonic analyzer. It was found that in all the system waveforms, harmonics of the 9th order and above were negligible. Tables 2.8 and 2.9 show the magnitudes of the principal harmonics in the voltages and currents. The results in Table 2.8 confirm the sinusoidal waveforms obtained in Fig. 2.54. It is seen that third harmonic distortion in the phase voltages is quite small, but the 7th harmonic is more prominent. The results in Table 2.9, on the other hand, show that the harmonic distortion in the phase currents is mainly due to the third harmonic, which is consistent with the observed waveforms in Fig. 2.55. The capacitor currents $I_2$ and $I_5$ are rich in 7th harmonic. In the case of $I_5$, the higher 7th harmonic content may be due to the smaller effective capacitive reactance since $C_5$ is in series with the transformer equivalent leakage reactance. The phase currents of the IG, on the other hand, contain very little 7th harmonic. The primary current $I_{51}$ of the current injection transformer has the most severe harmonic distortion due to the 7th harmonic reflected from the secondary winding and the third harmonic component in the no-load current. In the experimental IG system, however, the magnitude of $I_{51}$ is small compared with the line current. The line current waveform is therefore quite sinusoidal, with a total harmonic distortion (THD) of 7.5% approximately.

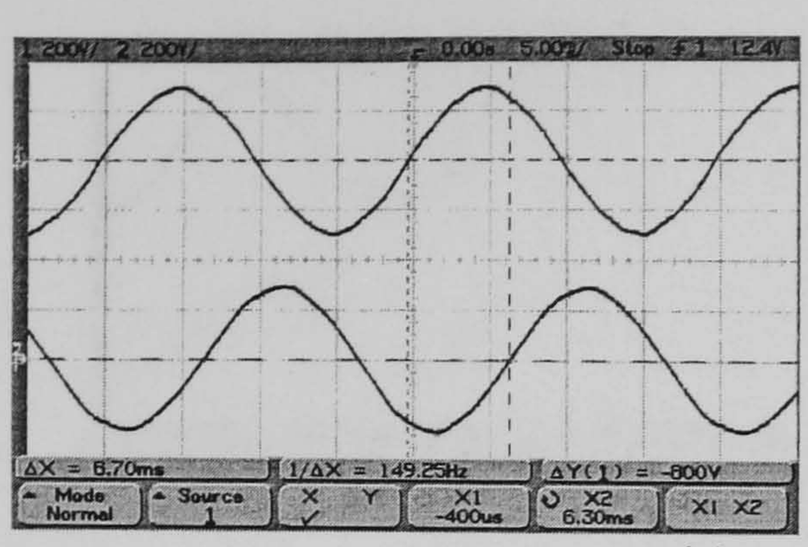


(a)

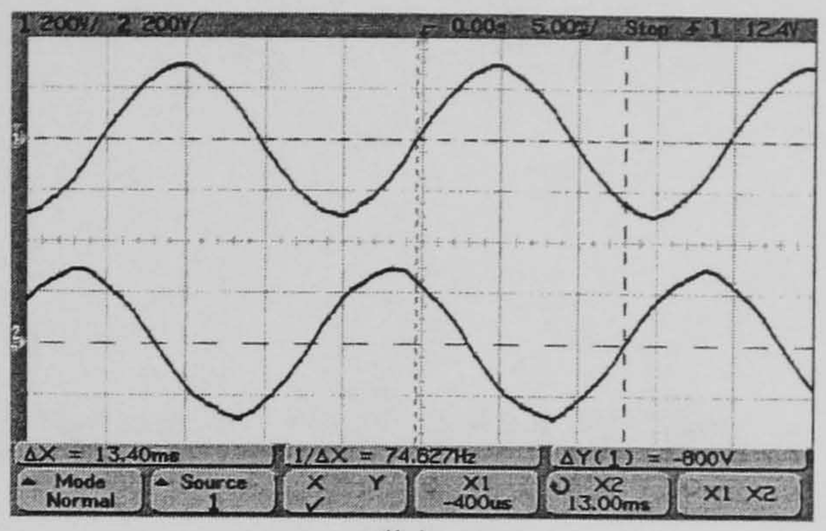


(b)

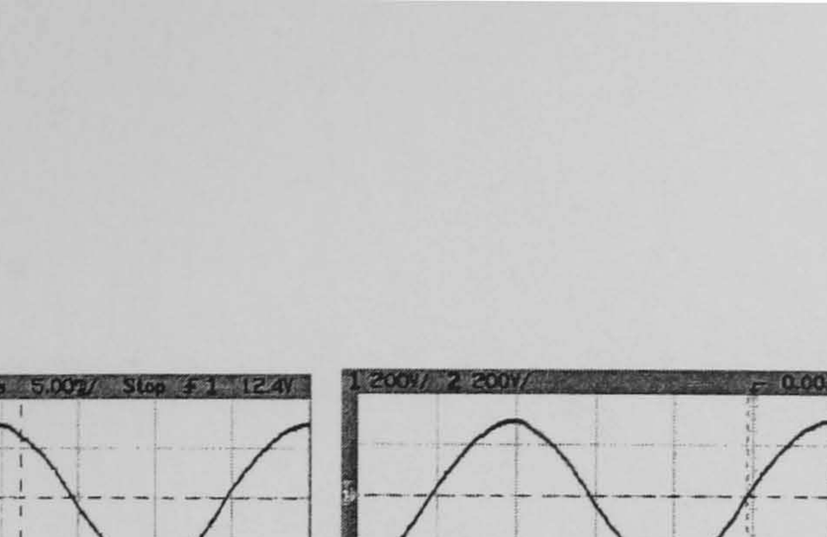


(c)

Fig. 2.54 Voltage waveforms of experimental IG at full load: (a) $V_A$ and $V_B$; (b) $V_A$ and $V_C$; (c) $V_A$ and $V_5$ (Scale for $V_A$, $V_B$, and $V_C$: 200 V/div; scale for $V_5$: 500 V/div; time scale: 5 ms/div).

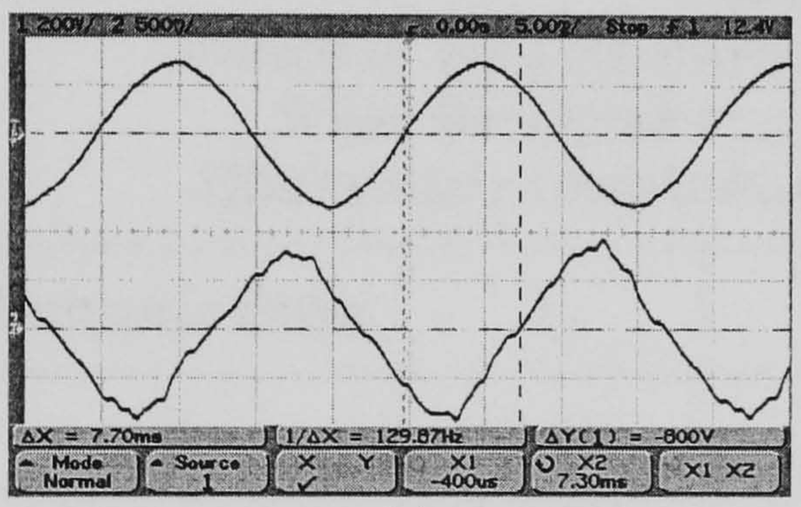


(a)

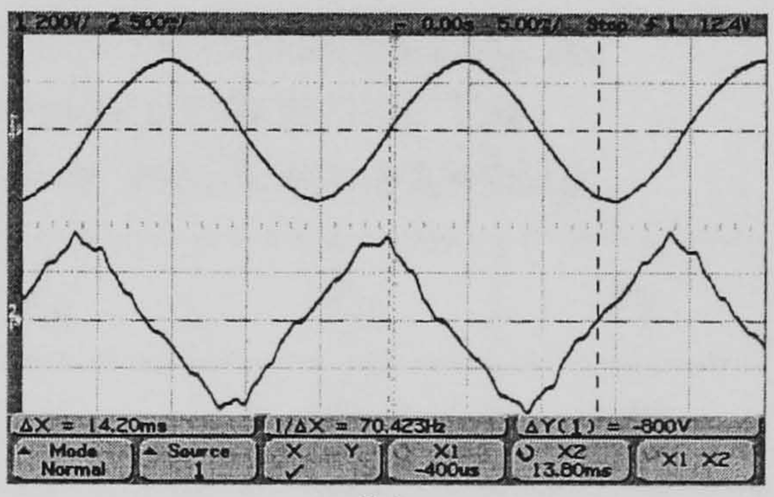


(b)

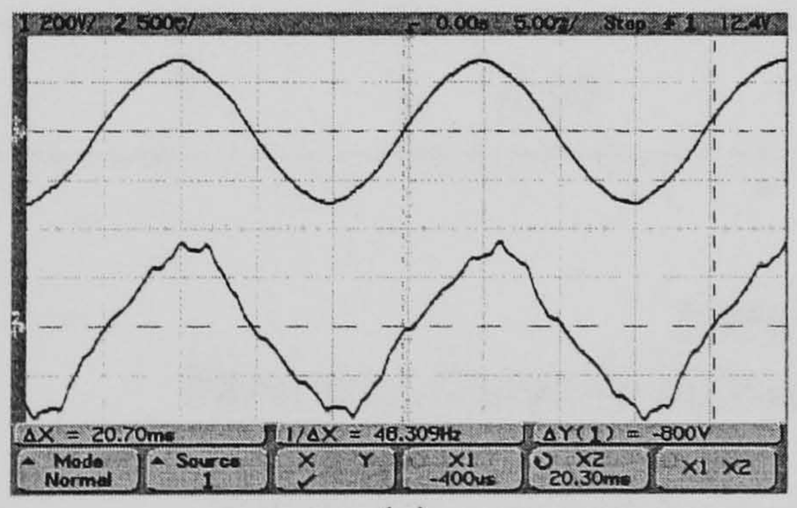


(c)

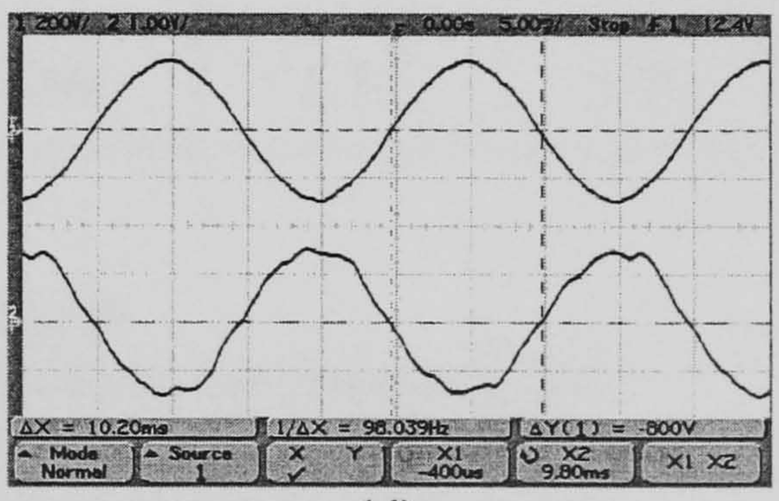


(d)

Fig. 2.55 Phase and line current waveforms of experimental IG at full load: (a) $V_A$ and $I_A$; (b) $V_A$ and $I_B$; (c) $V_A$ and $I_C$; (d) $V_A$ and $I$ (Scale for phase currents: 5 A/div; scale for line current: 10 A/div; time scale: 5 ms/div).

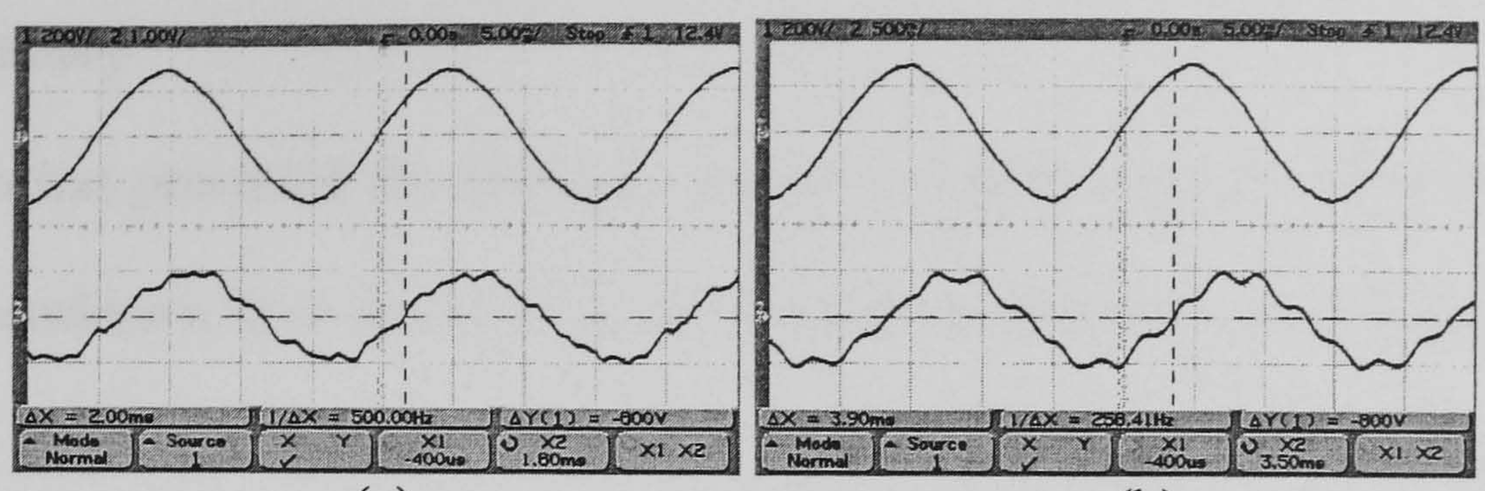


(a) (b) (c)

Fig. 2.56 Waveforms of capacitor currents and transformer primary current: (a) $V_A$ and $I_2$; (b) $V_A$ and $I_5$; (c) $V_A$ and $I_{51}$ (Scale for $I_2$: 10 A/div; scale for $I_5$ and $I_{51}$: 5 A/div; time scale: 5 ms/div).

TABLE 2.8
PRINCIPAL VOLTAGE HARMONICS IN EXPERIMENTAL IG
WHEN BALANCED AT A PHASE CURRENT OF 5 A
(EXPRESSED AS PERCENTAGE OF THE FUNDAMENTAL)

| Harmonic Order | $V_A$ | $V_B$ | $V_C$ | $V_5$ |
|---|---|---|---|---|
| 3 | 0.29 | 1.0 | 0.84 | 1.03 |
| 5 | 1.17 | 0.55 | 1.51 | 0.73 |
| 7 | 2.03 | 1.98 | 3.72 | 3.76 |

TABLE 2.9
PRINCIPAL CURRENT HARMONICS IN EXPERIMENTAL IG
WHEN BALANCED AT A PHASE CURRENT OF 5 A
(EXPRESSED AS PERCENTAGE OF THE FUNDAMENTAL)

| Harmonic Order | $I_A$ | $I_B$ | $I_C$ | $I$ | $I_2$ | $I_5$ | $I_{51}$ |
|---|---|---|---|---|---|---|---|
| 3 | 8.63 | 10.84 | 9.7 | 4.42 | 3.34 | 2.2 | 7.1 |
| 5 | 1.77 | 1.33 | 2.8 | 2.79 | 2.68 | 3.07 | 1.9 |
| 7 | 1.55 | 1.77 | 0.0 | 5.35 | 12.9 | 25.4 | 29.0 |

### 2.5.5 Summary

This section has presented the principle and performance analysis of Smith's Mode C circuit that enables a three-phase IG to be operated satisfactorily on a single-phase grid. The circuit employs a transformer and two capacitances for phase balancing. A phasor diagram approach enables analytic expressions for the values of capacitances to be deduced. A general performance analysis is developed by applying the method of symmetrical components. Experimental results obtained on a small induction machine have confirmed the accuracy of analysis and feasibility of the circuit configuration. The advantageous features of this phase-balancing scheme include simplicity of the circuit configuration, low cost, high efficiency and excellent system power factor.

# Chapter 3

# FINITE ELEMENT ANALYSIS OF GRID-CONNECTED IG WITH THE STEINMETZ CONNECTION

## 3.1 Introduction

Among the various phase-balancing schemes in use, the Steinmetz connection [81] is particularly suitable for adapting a three-phase induction machine for single-phase operation due to the extremely simple circuit configuration. The method is applicable to an induction machine with a star-connected winding or a delta-connected stator winding. It can be shown that, for a given value of phase-balancing capacitance, there exists a speed or load at which the voltage unbalance factor is a minimum [54]. Furthermore, if the value of the capacitance and speed are properly chosen, a perfect phase balance condition can be achieved. With the aid of the Steinmetz connection, three-phase induction machines could conveniently be used as non-utility generators in distributed single-phase generation systems in remote or rural regions.

In Chapter 2, the performance analysis of an induction generator with asymmetrical winding connection or unbalanced phase voltages is carried out using the method of symmetrical components. Since the method is based on the principle of superposition, the assumption of circuit linearity has to be made. When the induction machine operates in the generator mode, the higher air gap voltage leads to more severe magnetic saturation, consequently the assumption of a linear magnetic circuit is less valid. The accuracy of the symmetrical component method is also affected by the variation in the values of the equivalent circuit parameters, in particular the rotor resistance which depends on the rotor slip and thermal conditions. In order to account for the complex magnetic field distribution in the IG and the dependence of rotor

parameters on speed, detailed modeling and solution of the machine variables in the magnetic field domain will be more appropriate.

Electromagnetic field analysis of three-phase induction motor drives using the finite element method (FEM) has been a subject of rigorous research in the past two decades [87]-[92]. The major advantage of the FEM is the accurate modeling of the machine's magnetic circuit. Magnetic nonlinearity, material non-homogeneity and the effect of discrete winding layouts can easily be accounted for. Another advantage of the FEM is that it permits direct modeling in phase quantities, hence the analysis implicitly includes the effects of space and time harmonics. The third advantage of the FEM is its ability to deal with both steady-state and transient machine operations, without requiring simplifying assumptions as those made in classical machine theory, e.g., the d-q machine model as used in the Electromagnetic Transients Program (EMTP) [93], [94]. The machine performance can be obtained directly from the field solution, without the need to use the equivalent circuit parameters. A feature of the FEM, however, is the relatively long computing time and the large memory requirement.

Most of the publications on FEM have been devoted to three-phase induction motor drives under balanced operating conditions [87], [89], [90]. To the best knowledge of the author, FEM analysis of a three-phase IG with the Steinmetz connection has not been reported before.

In this chapter, the performance analysis of a single-phase grid-connected IG with the Steinmetz connection will be conducted using a coupled circuit and field approach, based on a two-dimensional (2-D) FEM. Emphasis will be placed on the phase-balancing capability of the IG circuit configuration under steady-state conditions. The generator performance computed by the proposed method will be compared with that

computed by the method of symmetrical components and that obtained from experiments on a 2.2-kW induction machine.

## 3.2 Steinmetz Connection and Symmetrical Component Analysis

Analysis of the Steinmetz connection shown in Fig. 3.1 is quite straightforward and involves the following steps:

1) Establish the 'inspection equations' based on Kirchhoff's Laws.

2) Solve the 'inspection equations' in association with the symmetrical component equations to obtain the positive-sequence voltage $V_p$ and negative sequence voltage $V_n$.

3) Compute the positive-sequence current $I_p$ and negative sequence current $I_n$ from the equivalent circuits of the IG.

4) Compute the performance of the IG.

It is well known that the output power factor of an IG is leading, which implies that the air gap voltage is considerably higher than the corresponding value when the machine operates as a motor. Magnetic saturation is more severe and hence it is very difficult to choose the proper value of magnetizing reactance that truly reflects the magnetic saturation conditions in the machine. The magnetic field distribution is further complicated by the presence of the negative-sequence rotating field, which in turn depends upon the rotor speed or output power. Skin effect in the rotor conductors also causes a discrepancy between the effective value of rotor resistance and that determined from standard locked-rotor and dc resistance tests. Due to the above uncertainties, computations based on the method of symmetrical components are subject to errors. In order to account for the complex magnetic conditions in the machine, a field approach will be attempted as detailed in the following sections.

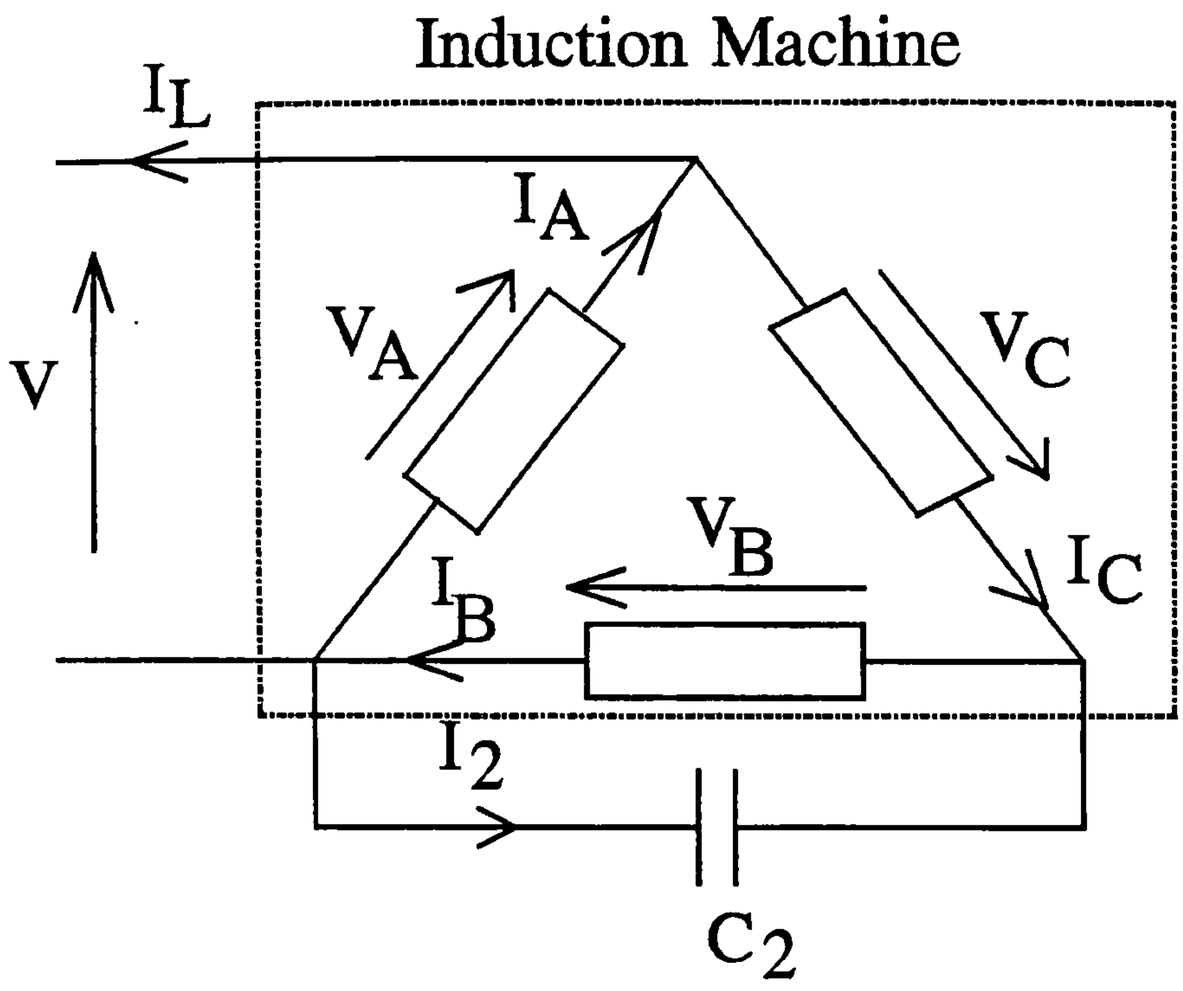


Fig. 3.1 Single-phase operation of three-phase, delta-connected induction generator with Steinmetz connection.

## 3.3 Machine Model

A coupled circuit and field approach is adopted for performance analysis of a three-phase IG with the Steinmetz connection. Fig. 3.2 shows the cross-sectional view of the experimental machine chosen for the investigation. Pertinent technical data of the induction machine are given in Appendix D.2. To reduce the complexity of the problem and solution time, the following assumptions and solution techniques will be used:

1) Two-dimensional (2-D) finite element method (FEM) is used for the magnetic field computation, with the complex magnetic vector potentials as the variables. Rectangular (*x*-*y*) coordinates are used in the FEM model, hence each magnetic vector potential *A* has only an axial or *z*-component [88].

2) First-order triangular elements and linear interpolation functions are used.

3) Stator end-winding leakage reactance is ignored.

4) The rotor speed is constant.

5) The nominal magnetization curve is used for both stator and rotor iron core, i.e., hysteresis effect is neglected.

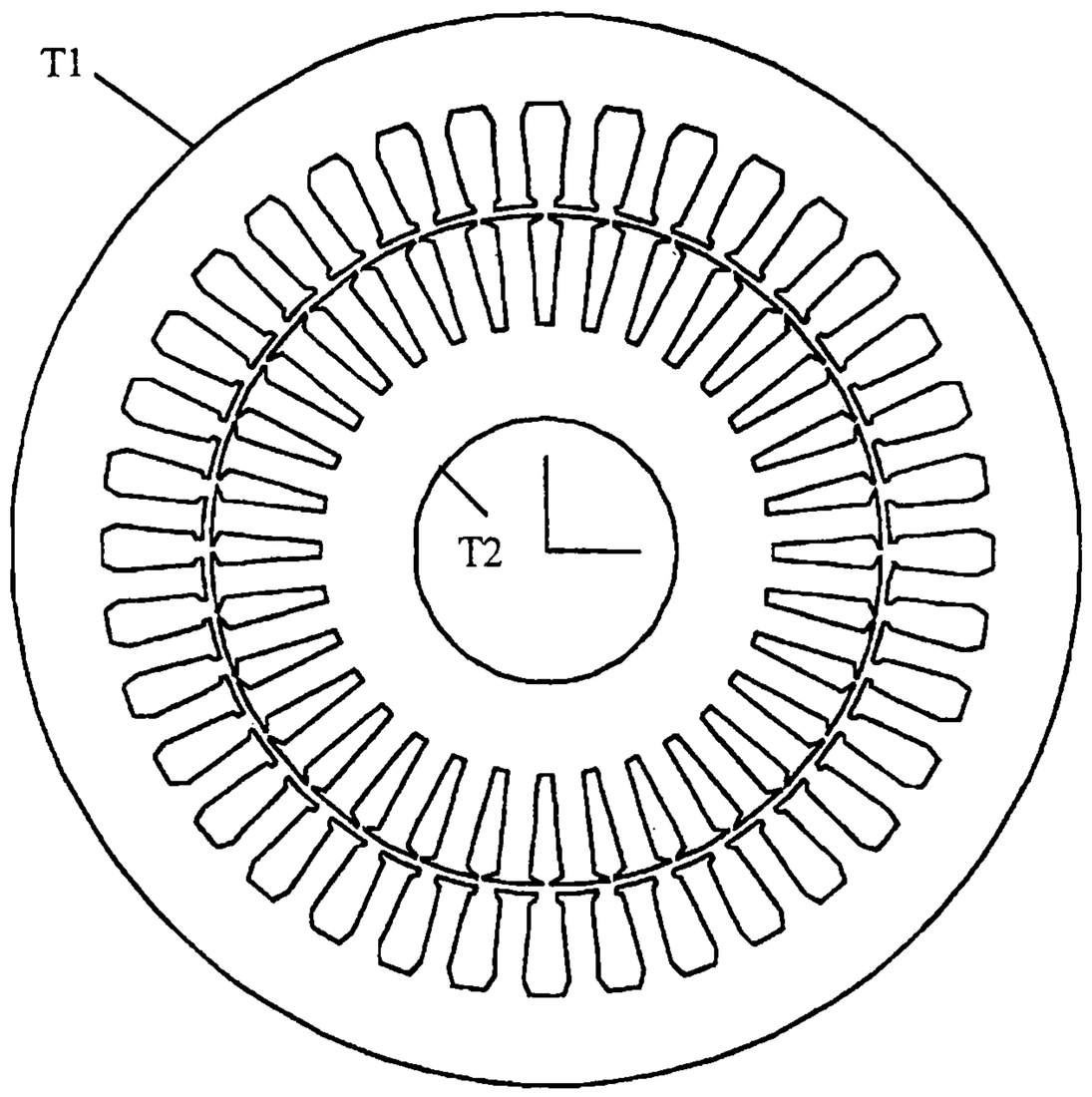


Fig. 3.2 Cross-section of experimental induction generator.

## 3.4 Finite Element Analysis

Since the stator winding connection is asymmetrical, the electromagnetic quantities such as voltage, current and flux density, are all time varying but may not be sinusoidal. Accordingly, it is not possible to use the complex form of the field equation. A time-stepping finite element field formulation coupled with external circuit equations is therefore adopted in the solver. Besides, the solution region has to be extended to the entire cross-section of the induction machine.

### 3.4.1 Basic Field Equations

Using the assumptions made in Section 3.3 and with reference to Fig. 3.2, the basic field equation and boundary conditions are formulated as follows [10], [95]:

$$\frac{\partial}{\partial x}\left(\frac{1}{\mu}\cdot\frac{\partial A}{\partial x}\right)+\frac{\partial}{\partial y}\left(\frac{1}{\mu}\cdot\frac{\partial A}{\partial y}\right)=-J \tag{3.1}$$

$$A|_{T1}=A|_{T2}=0 \tag{3.2}$$

where

$A$ = magnetic vector potential;

$J$ = externally impressed current density;

$\mu$ = magnetic permeability;

$T1$ = outer periphery of the stator iron core;

$T2$ = inner periphery of the rotor iron core.

The energy functional is

$$E(A) = \iint_{\Omega} \left( \int_0^B \frac{B}{\mu} .dB - A.J \right) dx.dy \tag{3.3}$$

where $\Omega$ denotes the field solution region and $B$ is the flux density.

After discretization and functional minimization, the following matrix equation is obtained:

$$[K].[A] = [R] \tag{3.4}$$

where

$[K]$ = coefficient matrix;

$[A]$ = column vector of nodal magnetic vector potentials;

$[R]$ = right-hand-side column vector containing known terms.

The derivation of (3.4) is given in Appendix C. This matrix equation is subsequently modified due to the application of boundary conditions and the coupled circuit and field approach adopted in the solution. Details of the circuit formulation will be given in the following sections.

### 3.4.2 Stator Circuit Equations

Fig. 3.3 shows the stator circuit model for single-phase operation of the IG with the Steinmetz connection. $E_A$, $E_B$ and $E_C$ are the internal e.m.f.s induced in stator phases A,

B and C, respectively. The generator convention will be adopted in the formulation of the circuit equations.

Neglecting the stator end-winding leakage reactance, the following equation may be written for phase A:

$$V_A = E_A - I_A R_1 . \tag{3.5}$$

To facilitate easy coupling with the FEM field domain, (3.5) is rewritten as

$$I_A - \frac{E_A}{R_1} = -\frac{V_A}{R_1} = -\frac{V}{R_1} . \tag{3.6}$$

Since the impressed voltages across phase B and phase C are not explicitly known, they have to be expressed in terms of other circuit parameters, available after the computation for the previous time-step. For phase-B,

$$V_B = E_B - I_B R_1 \tag{3.7}$$

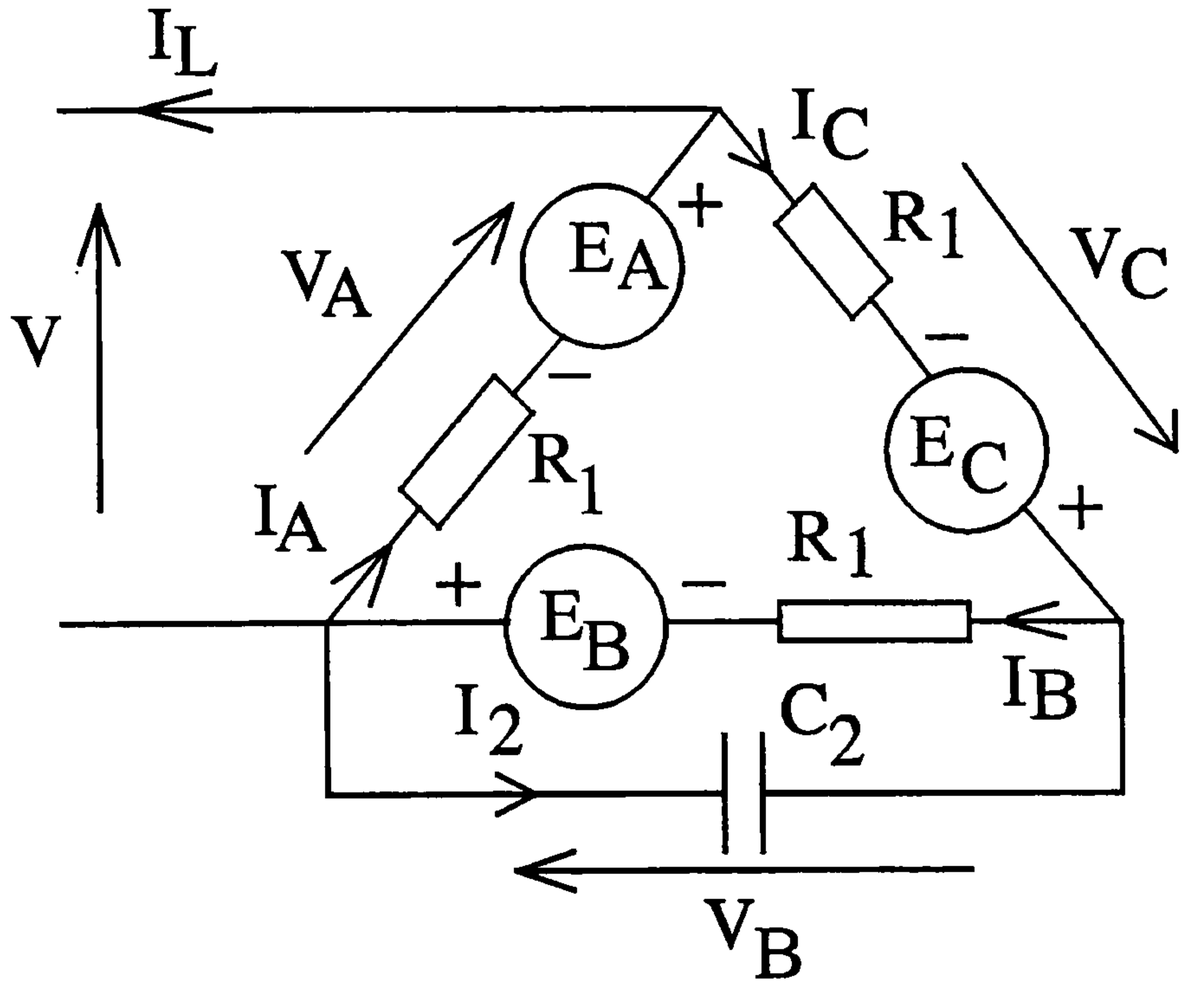


Fig. 3.3 Stator circuit model for delta-connected IG with Steinmetz connection.

The phase-B and phase-C currents are related by

$$I_C + I_2 = I_B . \tag{3.8}$$

The capacitor current $I_2$ can be written as:

$$I_2 = C_2 \frac{dV_B}{dt} \approx C_2 . \frac{V_B - V_B'}{\Delta t} \tag{3.9}$$

where

$V_B'$ = value of phase-B voltage in the previous time step;

$\Delta t$ = incremental time step.

Substituting (3.8) and (3.9) into (3.7) and simplifying, the following equation may be written:

$$\left(1 + \frac{\Delta t}{R_1 C_2} I_B\right) - \frac{\Delta t}{R_1 C_2} I_C - \frac{E_B}{R_1} = \frac{V_B'}{R_1} . \tag{3.10}$$

For phase C,

$$V_C = E_C - I_C R_1 . \tag{3.11}$$

Sum of the phase voltages must be equal to zero for a delta circuit, hence

$$V_A + V_B + V_C = 0 . \tag{3.12}$$

Eliminating $V_C$ from (3.11) and (3.12),

$$-V_A - V_B = E_C - I_C R_1 . \tag{3.13}$$

Eliminating $V_B$ from (3.9) and (3.13),

$$V_A + \frac{\Delta t}{C_2} I_2 + V_B' + E_C - I_C R_1 = 0 . \tag{3.14}$$

Finally, eliminating $I_2$ from (3.8) and (3.14),

$$-\frac{\Delta t}{R_1 C_2} I_B + \left(1 + \frac{\Delta t}{R_1 C_2}\right) I_C - \frac{E_C}{R_1} = \frac{V_A + V_B'}{R_1} . \tag{3.15}$$

It should be noted that (3.6), (3.10) and (3.15) have been expressed in a form suitable for coupling with the matrix equation (3.4). All the additional circuit variables are grouped on the left-hand side of each equation, while the known terms are placed on the right-hand side.

### 3.4.3 Stator E.m.f.s

From the FEM solution, the average value of magnetic vector potential in an element *e* is

$$A_e = \frac{1}{S}\int\int_{\Delta} A.dx.dy = = \frac{1}{S}\int\int N_i.A_i.dx.dy = \frac{1}{S}\sum_{i=1}^{3}\frac{\Delta_e}{3}.A_i \tag{3.16}$$

where $N_i$ = shape function, $S$ = cross-sectional area of coil side, and $\Delta_e$ = area of triangular element.

The stator internal e.m.f. $E_{ph}$ ($ph$ = A, B, and C) can next be computed by applying Faraday's Law, using the fact that flux density is the time derivative of the magnetic vector potential $A$:

$$\begin{aligned} E_{ph} &= -\sum_{e=1}^{n_{ph}}\left(-\frac{\partial}{\partial t}A_e\right).l_{fe}.\frac{N_c}{2}.k_e = -\sum_{e=1}^{n_{ph}}\left(\frac{\Delta A_e}{\Delta t}\right).l_{fe}.\frac{N_c}{2}.k_e \\ &= \frac{N_c.l_{fe}}{2\Delta t}\left(\sum_{e=1}^{n_{ph}}k_e A_e - \sum_{e=1}^{n_{ph}}k_e A_e'\right) \end{aligned} \tag{3.17}$$

where $A_e'$ = average value of vector potential of element computed in the previous time step, $N_c$ = turns per coil, $l_{fe}$ = axial length of iron core, $n_{ph}$ = number of elements in the conductor regions of stator phase $ph$, and $k_e = \pm 1$, depending on the position of the coil side (i.e., whether it is at the starting end or finishing end of the coil).

### 3.4.4 Rotor Circuit Model

Under normal operating conditions, the frequency of the positive-sequence rotor e.m.f. and current is very low, typically 2 to 3 Hz. This implies that the effective rotor resistance is much smaller than that deduced from a standard locked-rotor test conducted at rated frequency. On the contrary, the negative-sequence rotor current is approximately equal to twice the rated frequency, hence the effective negative-sequence rotor resistance is higher than the locked-rotor value. Due to the uncertainties in the value of rotor resistance, solution using the method of symmetrical components is subject to appreciable error.

Rotor end-winding leakage reactance is neglected in some FEM programs for balanced operation of a symmetrical three-phase induction machine. Such an assumption, however, cannot be used for the present problem as this would lead to very large pulsation in the computed rotor current and non-convergence.

A rotor circuit model is therefore introduced to overcome the above difficulties. Fig. 3.4 shows the sectional view of the rotor conductor bar and end ring of the experimental machine. To account for the frequency effect, each rotor bar is partitioned into 6 layers, each with two triangular elements. The current density in each layer is assumed to be constant during the field solution. Each end ring is likewise partitioned into 6 layers. For each layer, the resistance of the rotor conductor $R_{21}$, the cross-sectional area of rotor conductor $A_{RL}$, the resistance of the end-ring $R_{22}$, and the leakage inductance of the end ring $L_2$, can be computed. Fig. 3.5 shows the equivalent circuit for each layer of the rotor cage winding, where *J2*, *J3*, *J4*, *J5*,..., etc., denote successive rotor slots and end-ring sections of a particular layer.

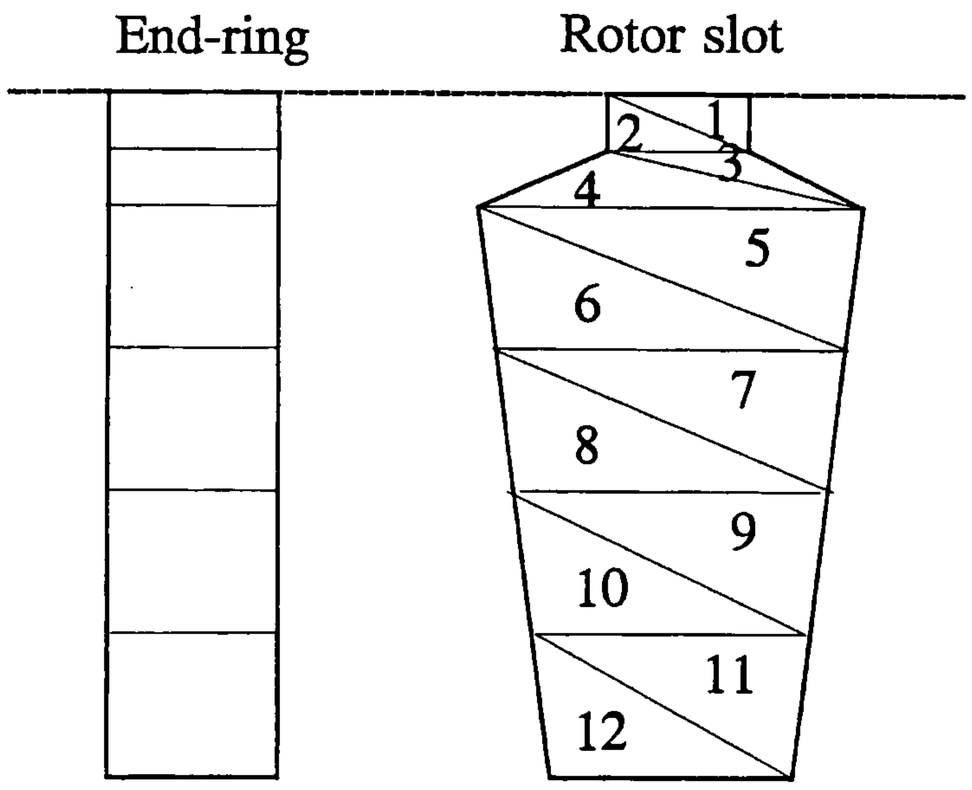


Fig. 3.4 Shape of rotor conductor and end ring: each rotor conductor is partitioned into 12 elements in six layers for field computation.

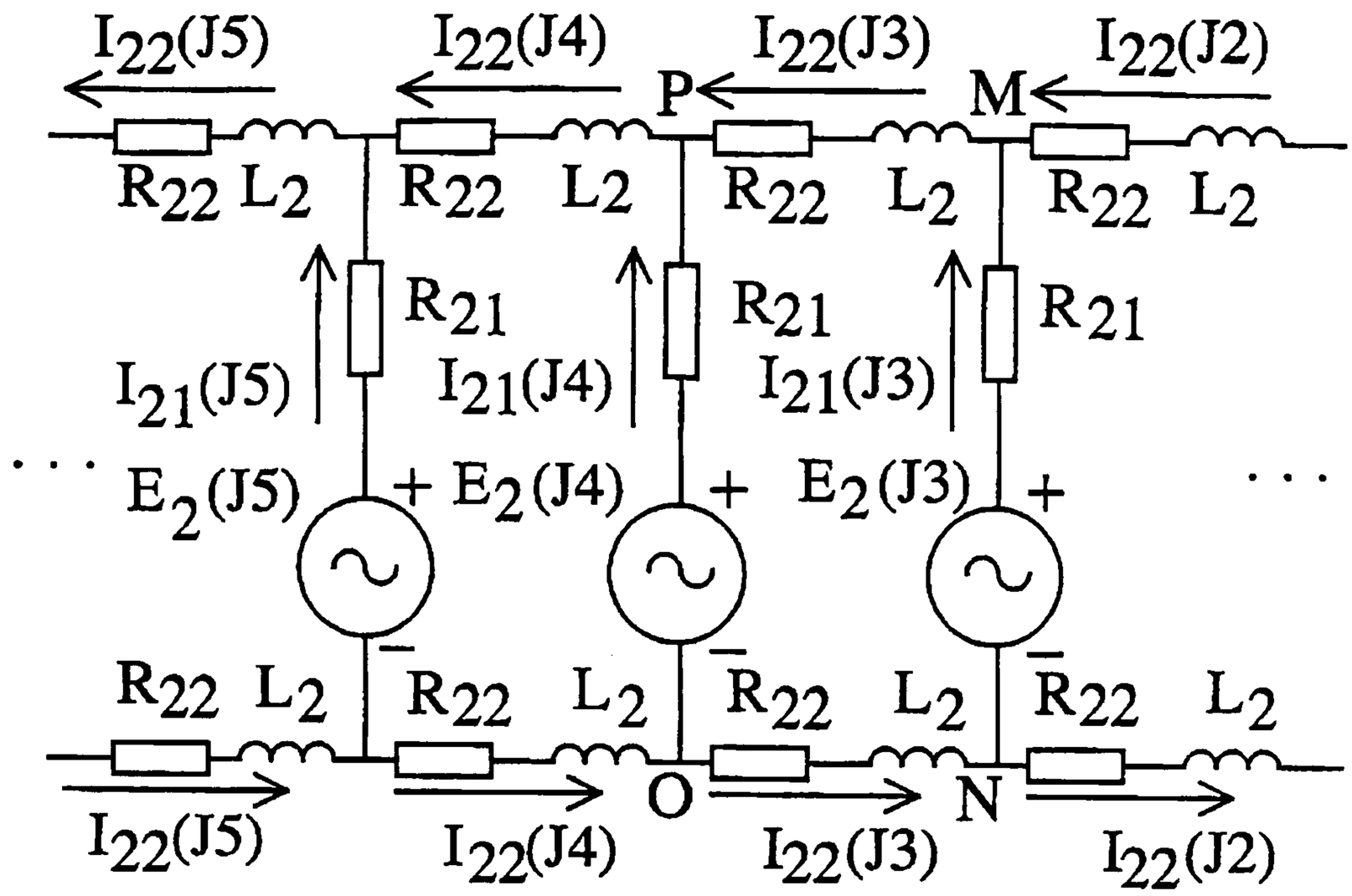


Fig. 3.5 Circuit model for each layer of rotor cage winding.

Consider the mesh MNOP in a typical rotor conductor layer as shown in Fig. 3.5., i.e., the one with generated e.m.f.s $E_2(J3)$ and $E_2(J4)$. Three new circuit variables are introduced, namely the current density in the layer $\delta(J3)$, end-winding current $I_{22}(J3)$, and conductor e.m.f. $E_2(J3)$.

Applying Kirchhoff's Current Law to node M,

$$I_{22}(J2) + I_{21}(J3) = I_{22}(J3)\,. \tag{3.18}$$

The rotor bar layer current $I_{21}(J3)$ can be expressed as:

$$I_{21} = \delta(J3).\, A_{RL}\,. \tag{3.19}$$

Applying Kirchhoff's Voltage Law to mesh MNOP in Fig. 3.5,

$$\begin{aligned} E_2(J3) - E_2(J4) &= I_{21}(J3).R_{21} + 2\,I_{22}(J3).R_{22} \\ &+ 2\,L_2.\frac{d}{dt} I_{22}(J3) - I_{21}(J4).R_{21}. \end{aligned} \tag{3.20}$$

Re-writing (3.20) as a difference equation,

$$\begin{aligned} E_2(J3) - E_2(J4) - \delta(J3).A_{RL}.R_{21} - 2\,I_{22}(J3).R_{22} \\ - 2\,L_2.I_{22}(J3)/\Delta t + \delta(J4).A_{RL}.R_{21} = -2\,L_2.I_{22}'(J3)/\Delta t \end{aligned}\,. \tag{3.21}$$

In (3.21), $I_{22}'$ $(J3)$ is the value of $I_{22}(J3)$ in the previous time step and becomes a known quantity for the current FEM computation.

The rotor e.m.f. $E_2(J3)$ is taken to be the average value of the induced e.m.f. in the two elements (say $e$ and $e$+1) in a rotor conductor layer, i.e.

$$E_2(J3) = \frac{E(e) + E(e+1)}{2}. \tag{3.22}$$

For element $e$, the e.m.f. $E(e)$ is the sum of transformer e.m.f. and motional e.m.f., i.e.

$$E(e) = -\frac{\partial A}{\partial t}.l_{fe} + \vec{v} \times \vec{B}.l_{fe} \tag{3.23}$$

where $\vec{v}$ and $\vec{B}$ are the rotor velocity and flux density vectors at element $e$.

To evaluate the first term in (3.23), the derivative may be approximated by

$$\frac{\partial A}{\partial t} = \frac{A_e - A_e'}{\Delta t} \tag{3.24}$$

where

$A_e =$ average value of magnetic vector potential of element $e$ at time $t$;

$A_e' =$ average value of magnetic vector potential of element $e$ at time $t$ - $\Delta t$.

Fig. 3.6 shows an arbitrary conductor element at radius $R$ from the axis of rotation. If the rotor rotates at a speed $n$ r/s, the linear velocity of the element is

$$v = 2\pi R.n\ . \tag{3.25}$$

The components of flux density at the rotor element is

$$B_x = \frac{\partial A}{\partial y} = \frac{CL(1).A_i + CL(2).A_j + CL(3).A_k}{2\Delta_e} \tag{3.26}$$

$$B_y = -\frac{\partial A}{\partial x} = \frac{-BL(1).A_i - BL(2).A_j - BL(3).A_k}{2\Delta_e} \tag{3.27}$$

where $CL(\kappa)$ and $BL(\kappa)$ ($\kappa$ = 1,2,3), are constants pertaining to the element being considered and $\Delta_e$ = area of element.

Component of flux density normal to the linear velocity of the element is

$$B_n = B_x.\cos\theta + B_y.\sin\theta = \gamma_i.A_i + \gamma_j.A_j + \gamma_k.A_k \tag{3.28}$$

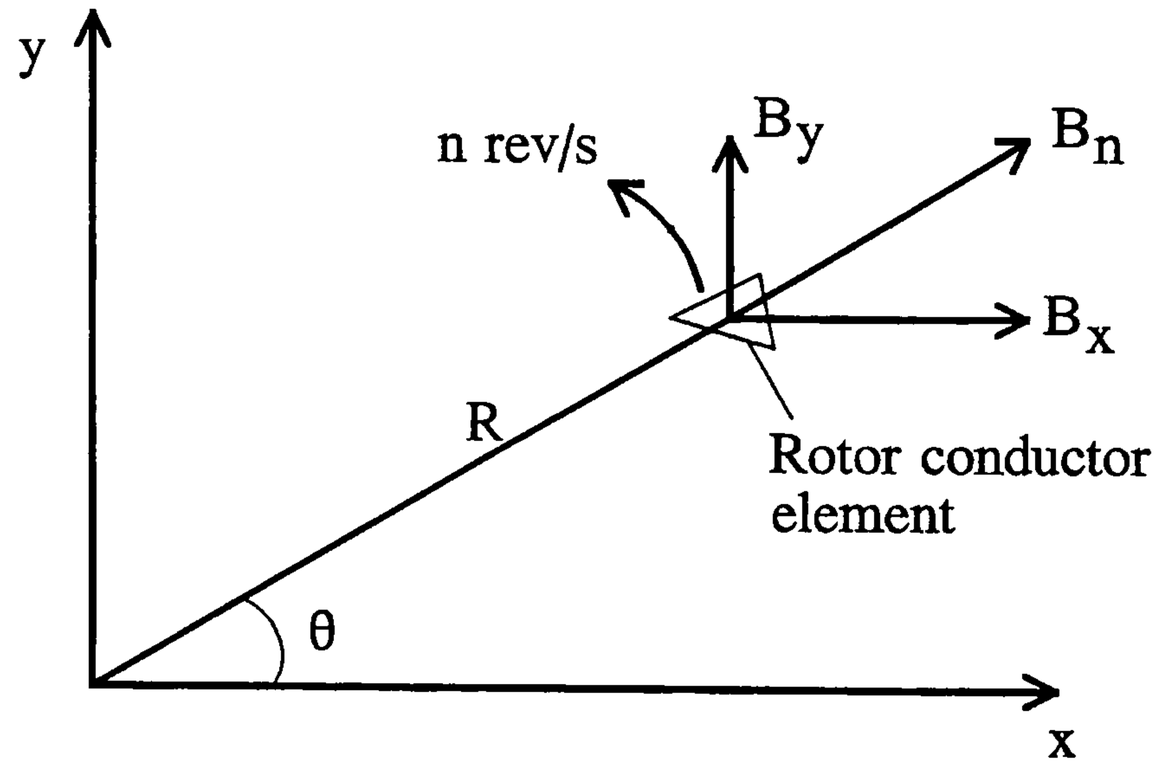


Fig. 3.6 Computation of flux density and generated e.m.f. in rotor conductor element.

where

$$\left.\begin{aligned}\gamma_i &= CL(1).\cos\theta - BL(1).\sin\theta;\\ \gamma_j &= CL(2).\cos\theta - BL(2).\sin\theta;\\ \gamma_k &= CL(3).\cos\theta - BL(3).\sin\theta.\end{aligned}\right\} \tag{3.29}$$

### 3.4.5 Comments on the Proposed Method

A time-stepping FEM coupled with external circuit equations for performance analysis of an IG with the Steinmetz connection has been developed. The capacitance in the stator circuit and end-winding leakage reactance in the rotor circuit both involve differential equations, and hence a time-varying transient circuit model is adopted. In this respect, the proposed approach is not fundamentally different from the time-stepping coupled finite element–state space (TSCFE-SS) algorithm [87], [91], [92] used by other researchers. In the TSCFE-SS method, inductance profiles have to be generated for each time step in order to determine the excitation currents for the subsequent time step. The proposed

method, however, aims to compute the machine performance directly from the field solution. Another salient feature of the proposed method is the use of a refined rotor circuit model that enables the complex current distribution in the rotor circuit to be considered.

In the present IG configuration, the grid voltage $V$ (= $V_A$) is known and is assumed to be a time-varying sinusoidal quantity. For the other phase voltages and currents, the magnitudes and the waveforms are obtained from the FEM solver and hence the effects of time and space harmonics on the generator performance are automatically accounted for.

The present FEM solver could be adapted for dynamic performance studies, such as turbine speed changes and switching operations. This requires the coupling of the electromechanical equation [90] with the matrix equations developed earlier in this paper and the rotor speed will then be one of the machine variables.

As far as possible the proposed method avoids the use of induction machine equivalent circuit parameters, defined conventionally under sinusoidal current and voltage conditions. The only assumption made is the omission of the stator end-winding leakage reactance, which simplifies the stator circuit equations with only a slight loss in accuracy.

## 3.5 Computational Aspects

A FORTRAN computer program was developed for the performance analysis of the three-phase IG with the Steinmetz connection. The computations referred to the experimental machine IG2 whose technical data are given in Appendix D.2. Program runs were conducted on a Pentium 586 computer with a clock speed of 333 MHz, 128 MB of RAM and 8 GB hard disk. In view of the constraints on the computing facilities, a

compromise had to be made among the computational accuracy, run time, and the memory requirements. Fig. 3.7 shows the finite element mesh used for the field analysis, the number of nodes and elements being equal to 2120 and 4068, respectively. Since 172 nodes fall on the boundaries with constant values of magnetic vector potential, the number of nodal magnetic vector potentials to be evaluated is 1948. Table 4.1 shows the number of variables used in the FEM solver.

TABLE 3.1
DISTRIBUTION OF VARIABLES IN FEM PROGRAM

| Circuit/Field Variables | Number |
|---|---|
| Nodal magnetic vector potentials *A* | 1948 |
| Stator phase e.m.f.s | 3 |
| Stator phase currents | 3 |
| Rotor circuit variables | 576 |
| Total | 2530 |

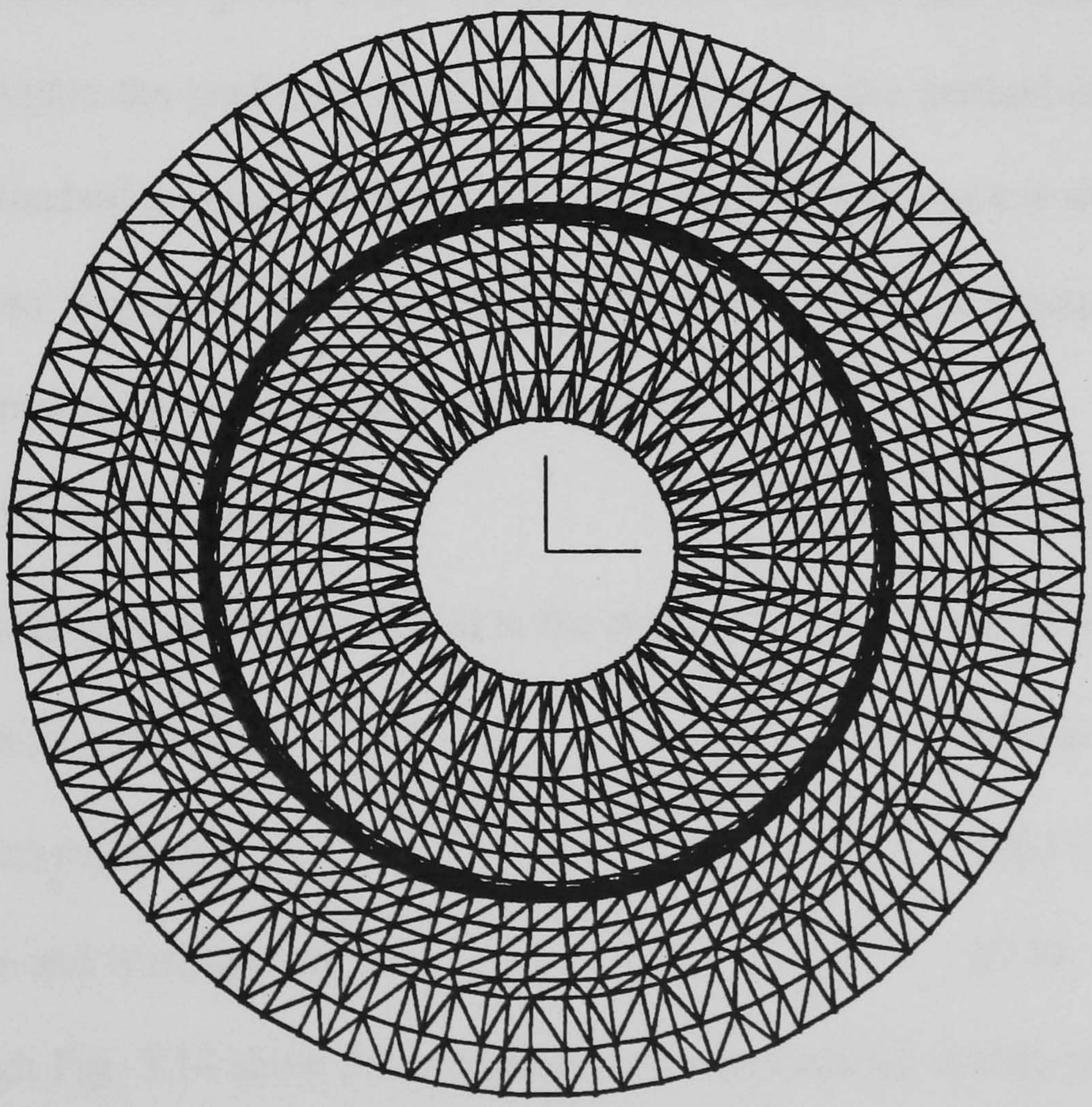

Fig. 3.7 Finite element mesh for experimental machine.

The time for solution of the matrix equation was approximately 45 seconds. For the electromagnetic quantities to settle to a steady state, the computation had to be extended to ten complete electrical cycles and the number of time steps (each corresponding to one electrical degree) required was over 1500. The total time for computing an operating point therefore amounted to 7 to 8 hours.

## 3.6 Results and Discussion

### 3.6.1 Computed and Experimental Results

Laboratory tests were conducted on the delta-connected experimental machine referred to in the previous section. The IG was operated on a 220-V, 50 Hz single-phase supply. A phase-converter capacitance of 93.6 μF was used to give approximately balanced operation at a speed of 1540 r/min and a phase current of 4.0 A. Instruments were arranged to measure the speed, phase currents, phase voltages, line current and output power. To compare the performance of the IG obtained by the method of symmetrical components, standard no-load test, locked-rotor test and dc resistance test were separately conducted, from which the following parameters were determined (assuming that the stator and referred rotor leakage reactances are equal):

| | | |
|---|---|---|
| Stator leakage impedance | = | (3.08 + j5.68) Ω |
| Rotor leakage impedance referred to the stator | = | (2.85 + j5.68) Ω |
| Magnetizing reactance | = | 80.8 Ω |
| Core loss resistance | = | 1463 Ω |
| Friction and windage loss | = | 27 W |

Fig. 3.8 through Fig. 3.14 show the computed and experimental results obtained on the IG with the Steinmetz connection. From Fig. 3.8 and Fig. 3.9, it is observed that the method of symmetrical components gives an accurate prediction of the variation of $V_B$

and $V_C$. In comparison, the FEM gives good prediction of $V_C$ but rather poor prediction of $V_B$, especially at low speeds.

From Fig. 3.10 to Fig. 3.12, it is found that both the FEM and method of symmetrical components give correct prediction of the trend of the phase currents. At high speeds, the FEM gives a more accurate prediction of $I_A$ and $I_C$, whereas the method of symmetrical components gives a better prediction of $I_B$.

Fig. 3.13 and Fig. 3.14 show the variation of line current and output power of the IG with rotor speed. Over the entire operating speed range, the FEM gives more accurate results compared with the method of symmetrical components.

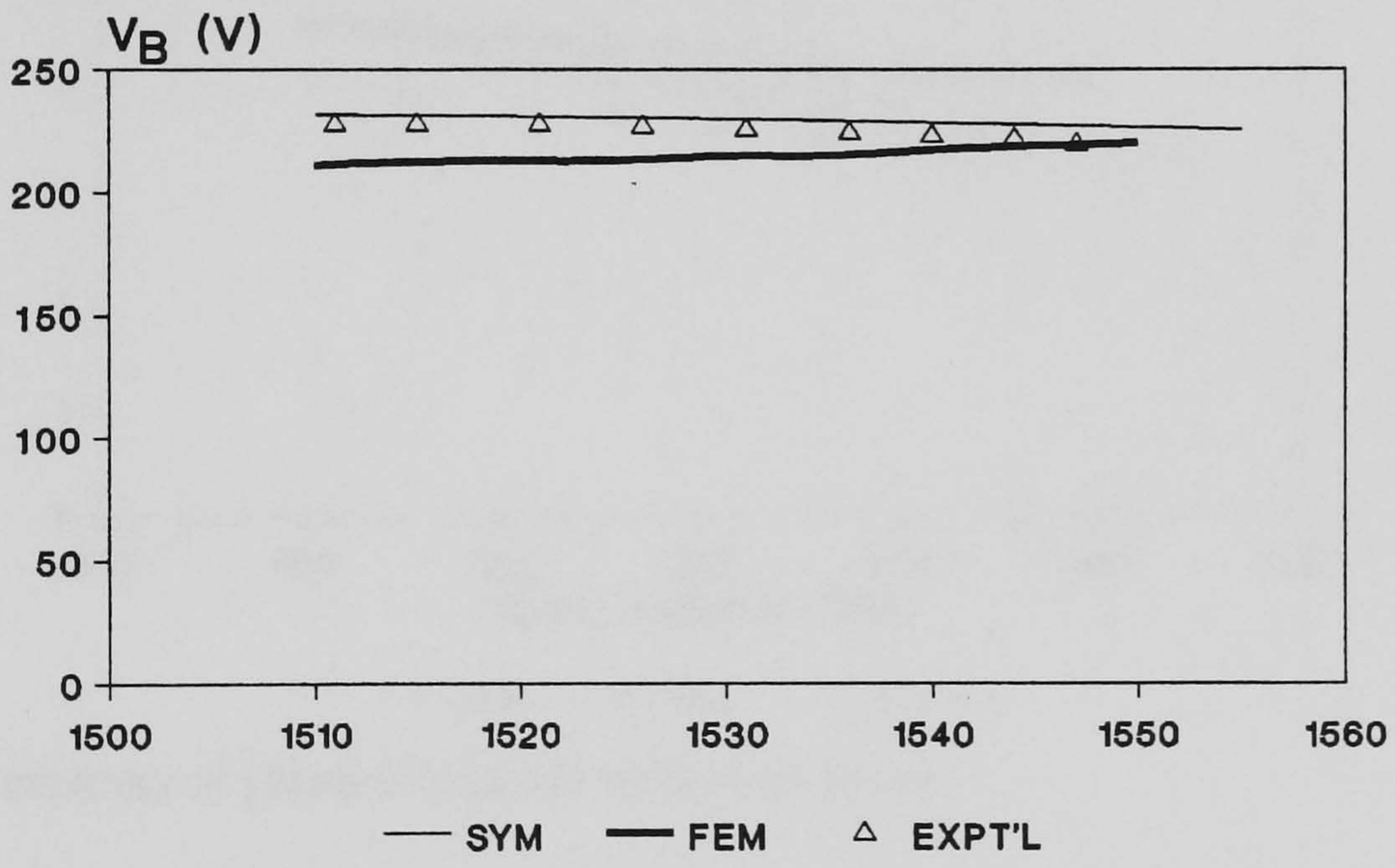


Fig. 3.8 Variation of phase-B voltage with rotor speed.

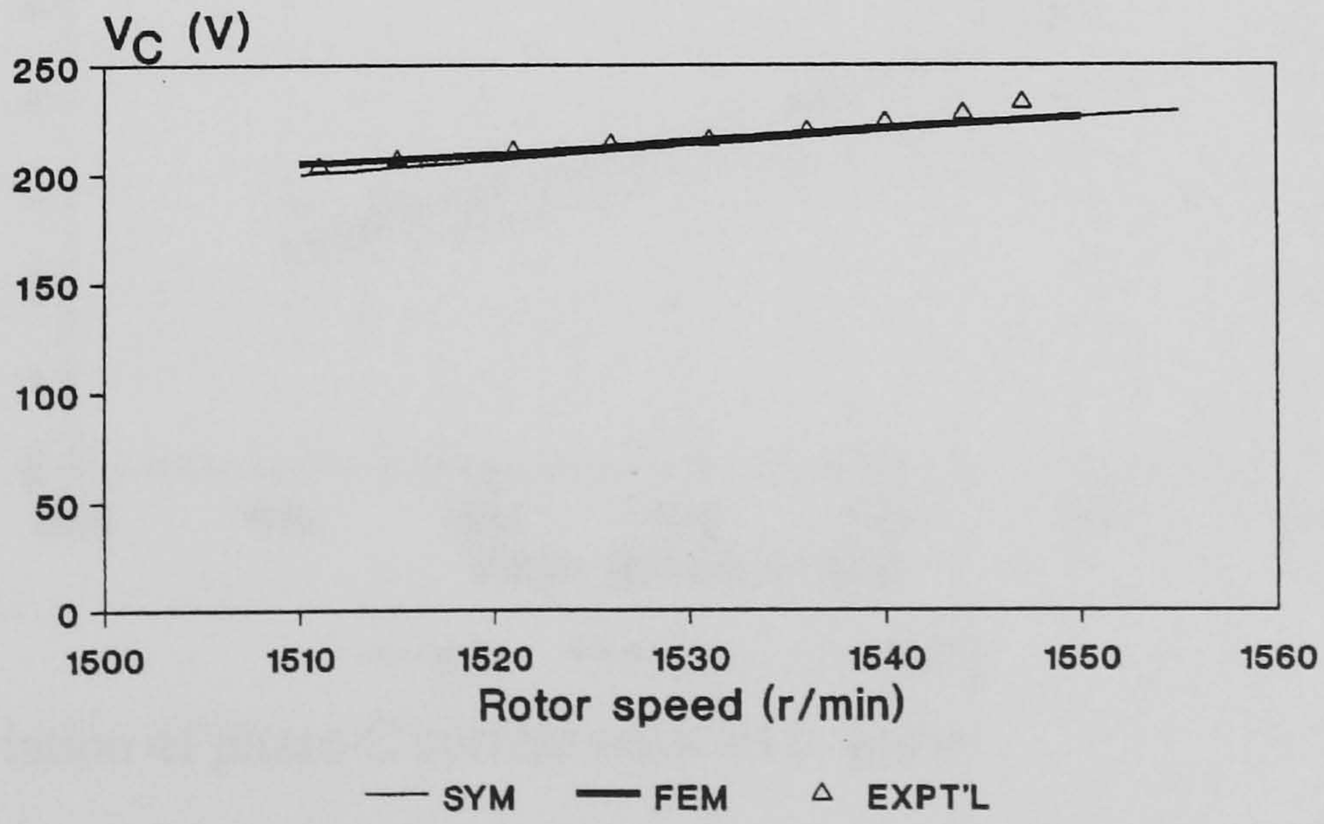


Fig. 3.9 Variation of phase-C voltage with rotor speed.

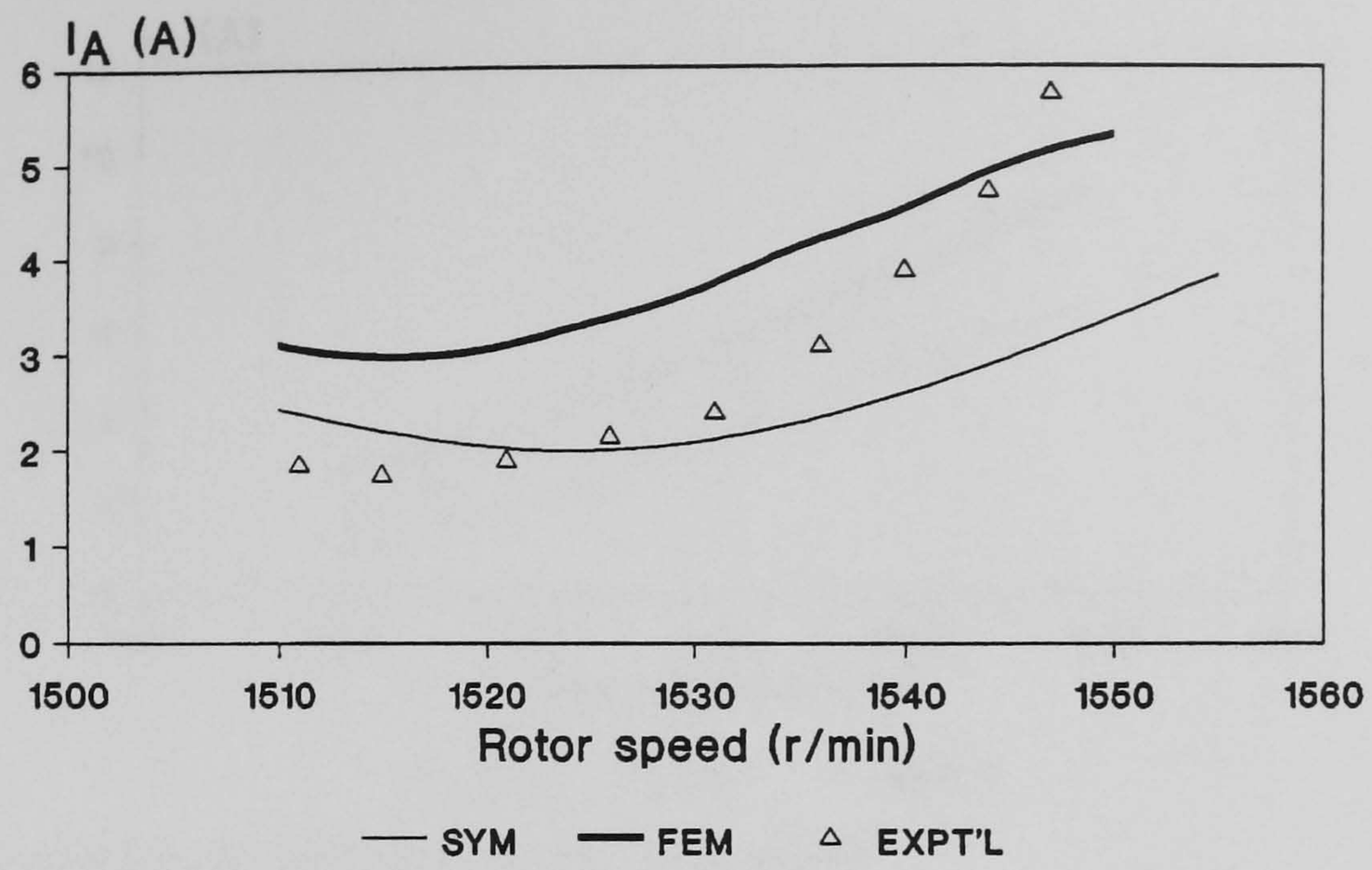


Fig. 3.10 Variation of phase-A current with rotor speed.

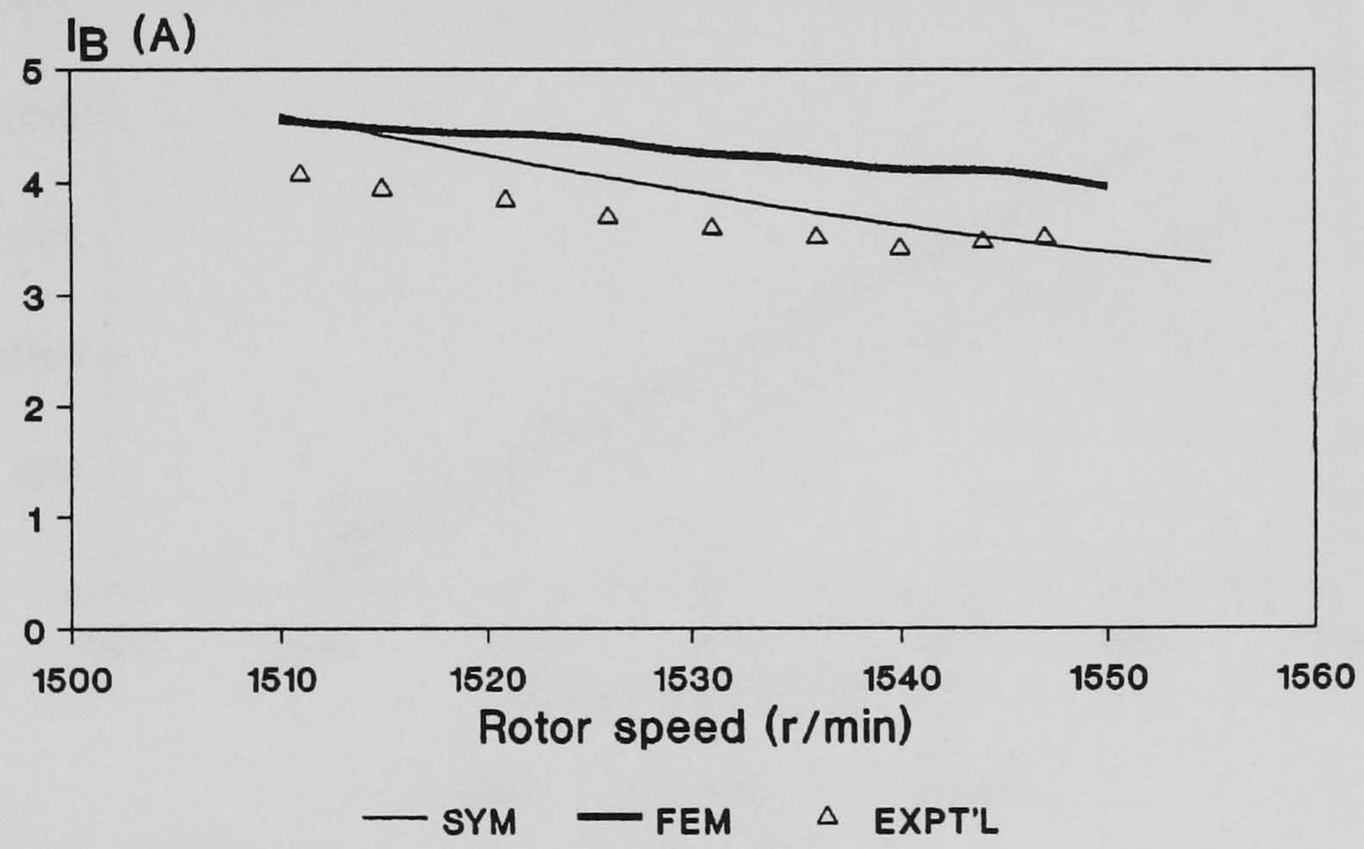


Fig. 3.11 Variation of phase-B current with rotor speed.

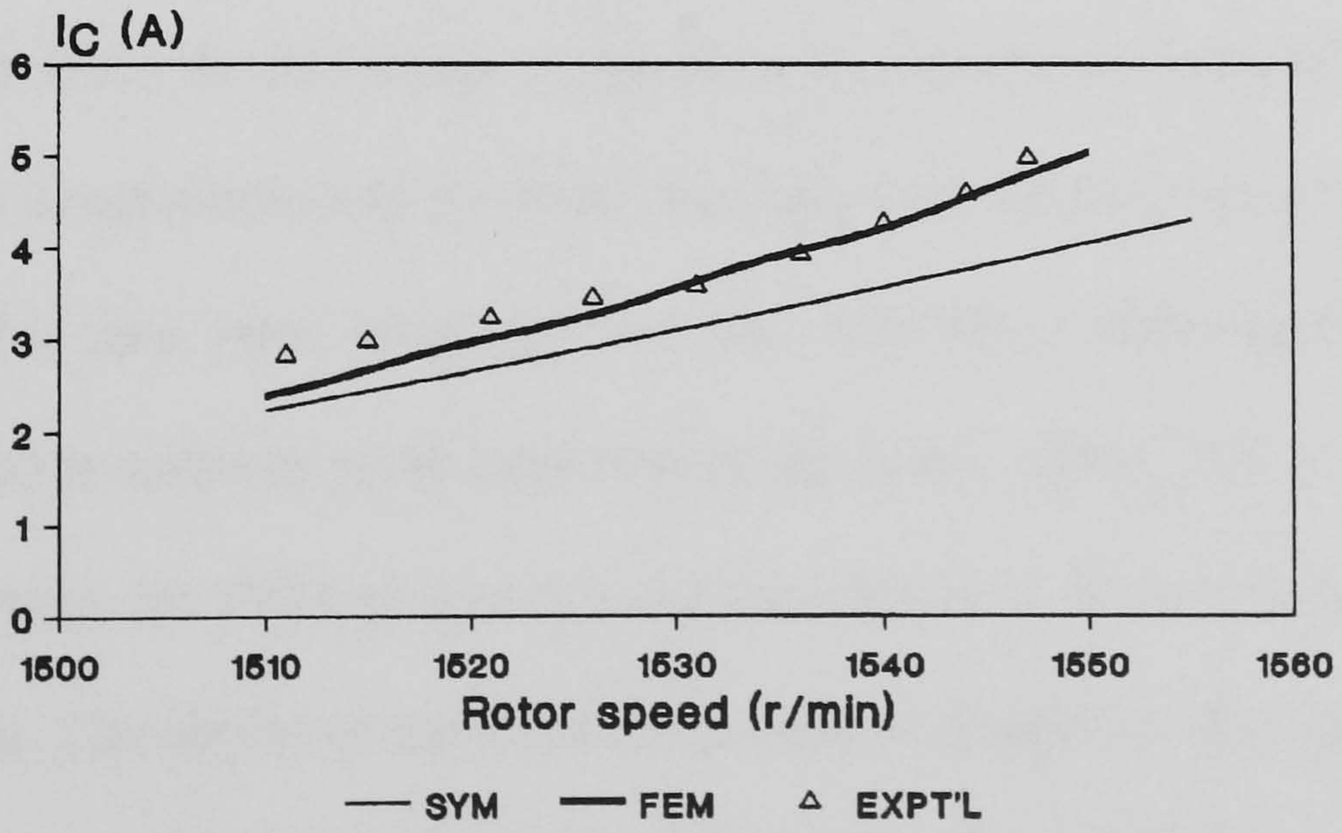


Fig. 3.12 Variation of phase-C current with rotor speed.

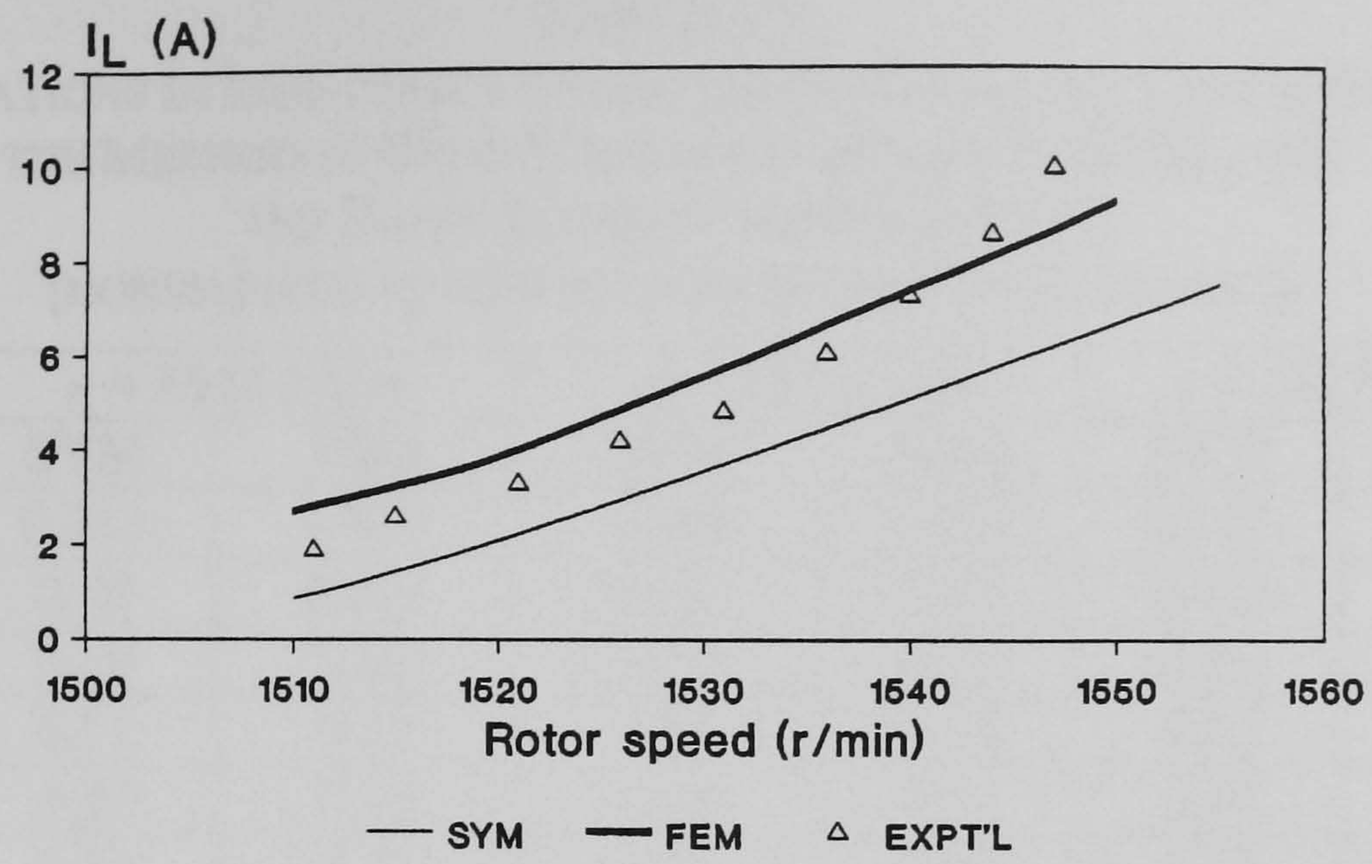


Fig. 3.13 Variation of line current with rotor speed.

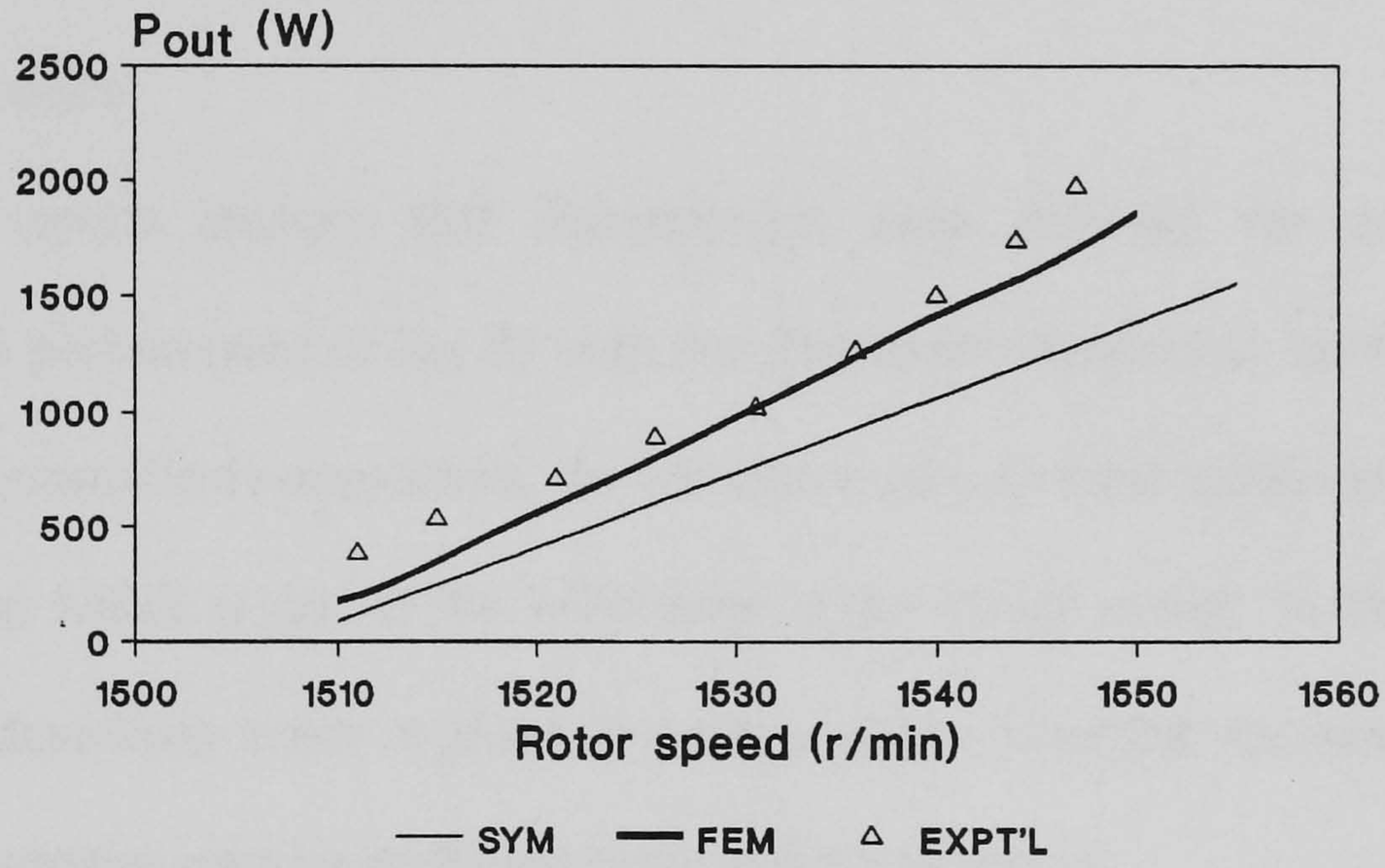


Fig. 3.14 Variation of output power with rotor speed.

Table 3.2 summarizes the deviations in generator performance computed by the method of symmetrical components and the FEM. For easy comparison, the deviation for each machine variable has been normalized to the respective experimental value. It is observed that both methods yield large deviations at low speed (1511 r/min). At high speed (1547 r/min), the FEM gives more accurate results in all the variables except the phase-B current. The ability of the FEM to account for magnetic saturation and change in effective rotor resistance due to loading and circuit imbalance is thus confirmed.

TABLE 3.2

DEVIATIONS IN INDUCTION GENERATOR PERFORMANCE COMPUTED BY THE METHOD OF SYMMETRICAL COMPONENTS (SYM) AND THE FINITE ELEMENT METHOD (FEM) (NORMALIZED TO RESPECTIVE EXPERIMENTAL VALUES)

| Variables | $n$ = 1511 r/min | | $n$ = 1536 r/miin | | $n$ = 1547 r/min | |
|---|---|---|---|---|---|---|
| | SYM | FEM | SYM | FEM | SYM | FEM |
| $V_B$ | 0.011 | 0.077 | 0.013 | 0.038 | 0.027 | 0.005 |
| $V_C$ | 0.02 | 0.007 | 0.016 | 0.01 | 0.043 | 0.039 |
| $I_A$ | 0.29 | 0.62 | 0.23 | 0.32 | 0.45 | 0.11 |
| $I_B$ | 0.11 | 0.11 | 0.06 | 0.19 | 0.02 | 0.15 |
| $I_C$ | 0.20 | 0.15 | 0.14 | 0.01 | 0.21 | 0.032 |
| $I_L$ | 0.54 | 0.51 | 0.25 | 0.09 | 0.38 | 0.15 |
| $P_{out}$ | 0.74 | 0.56 | 0.26 | 0.03 | 0.34 | 0.14 |

### 3.6.2 Discussion

The above results indicate that discrepancies exist between the computed and experimental performance of the IG with the Steinmetz connection. In the case of the method of symmetrical components, the deviations mainly exist in the currents and the output power, which is due to the limitations in the circuit model. In the case of the FEM, large deviations occur in phase-B voltage, phase-A current and phase-B current. These discrepancies may be attributed to the following factors:

1) Numerical solution of the circuit differential equations requires their transformation to the corresponding difference equations which involves the time step $\Delta t$. A smaller $\Delta t$ reduces the discretization error. At the same time more air gap nodes must be used, which is beneficial in reducing the error caused by distortion of the air gap elements as a result of the rotor rotation (time stepping).

2) Numerical solution of a high-order matrix equation incurs considerable cumulative errors. This problem may be resolved by using double precision in the FEM solver, but the memory requirement will be increased significantly.

3) Thermal effects on the machine parameters, particularly on the rotor resistance, are difficult to account for. In the FEM computations, the rotor resistance was corrected to that corresponding to the average operating temperature under experimental conditions, but there might be hot spots where the temperatures deviate from the average value and hence causing the generator performance to change. For a more accurate analysis, an appropriate thermal model has to be incorporated with the FEM field analysis model [88].

4) Use of a three-dimensional (3-D) FEM will yield a better modelling of the skewed rotor cage and hence will improve the computational accuracy, particularly when stray losses and efficiency are to be considered [96].

5) In the present rotor circuit model, each rotor cage bar and end ring is partitioned into six layers in order to account for the rotor current distribution. The accuracy will be improved if more layers are used, but more circuit variables will be introduced, thereby increasing the computer memory required.

## 3.7 Summary

A new approach for analyzing the performance of a grid-connected single-phase IG with the Steinmetz connection has been presented in this chapter. A coupled circuit and field approach based on two-dimensional finite element method is adopted in order to account for the asymmetrical stator winding connection as well as the complex magnetic field in the machine and the distribution of current in the rotor winding. Detailed derivation of the stator and rotor circuit equations suitable for coupling with the FEM field equations is given. Experimental results obtained on a small induction machine have also been presented to check the accuracy of both FEM and symmetrical component analysis. To improve the computational accuracy, a larger number of nodes and elements have to be

used for the FEM mesh, in particular for the air gap region. Since the proposed method is based on rigorous machine modelling and is very general, it can be applied to other asymmetrical IG configurations, with appropriate modification in accordance with specific circuit constraints. With the increasing availability of powerful computers at modest cost, the proposed method should be a better alternative for the analysis of single-phase IGs.

# Chapter 4

# SEIGS FOR AUTONOMOUS POWER SYSTEMS

## 4.1 Introduction

This chapter discusses the various circuit configurations for self-excited induction generators (SEIGs) used in autonomous (also known as stand-alone or isolated) power systems. The Steinmetz connection as shown in Fig. 4.1 is first considered in order to set forth the basic method of analysis that can be readily extended to more complicated circuit configurations, in particular the general case of asymmetrically-connected excitation capacitances and load impedances.

Since the SEIG supplies isolated loads, the frequency of the output voltage is variable even when the rotor speed is maintained constant. To simplify the analysis, all the circuit parameters have been referred to the base (rated) frequency $f_{base}$ by introducing the per-unit frequency $a$ and the per-unit speed $b$, as explained in Appendix A.2. Thus, the per-unit slip of the SEIG is $(a - b)/a$ and each voltage shown in Fig. 4.1 has to be multiplied by $a$ in order to give the actual value. The *motor* convention will be adopted for the direction of currents in the equivalent circuits.

To illustrate the feasibility of the proposed analysis method and solution technique, a number of case studies were carried out on a 2.2-kW, delta-connected induction machine whose technical data are given in Appendix D.1. All the equivalent circuit parameters are assumed to be constant except the magnetizing reactance $X_m$, which varies with the positive-sequence air gap voltage $E_1$. The variation of $X_m$ with $E_1$ is piecewise linearized using the describing function given by (D.1).

## 4.2 Three-Phase SEIG with the Steinmetz Connection

### 4.2.1 Circuit Connection and Analysis

Fig. 4.1 shows the Steinmetz connection for a delta-connected three-phase induction generator self-excited with a single capacitance and supplying a single-phase load, the capacitance being connected across the lagging phase [67]. The single-phase load is connected across phase A (the reference phase), while the excitation capacitance $C$ is connected across phase B (the lagging phase). Besides providing the reactive power for initiating and sustaining self-excitation, $C$ (or the corresponding complex admittance $Z_C$ ) also acts as a phase balancer by injecting a line current $I_2$ into the 'free' terminal of the stator winding. Voltage build-up in the single-phase SEIG is easily initiated by first switching off the load and using a sufficiently large value of $C$. The stator phase voltages and currents are unbalanced due to the asymmetrical winding configuration, but the phase balance is improved as the load is increased. In case the generator voltage fails to build up due to a previous de-magnetization operation, the residual flux should first be re-established by circulating a direct current momentarily through the stator winding. The self-excitation performance is also improved by operating the generator initially at a higher speed or by using a larger value of excitation capacitance.

With reference to Fig. 4.1, the 'inspection equations' may be written as follows:

$$V = V_A \tag{4.1}$$

$$V_A + V_B + V_C = 0 \tag{4.2}$$

$$I_2 = V_B / Z_C = I_C - I_B \tag{4.3}$$

$$I = I_A - I_C = -V / Z_L \tag{4.4}$$

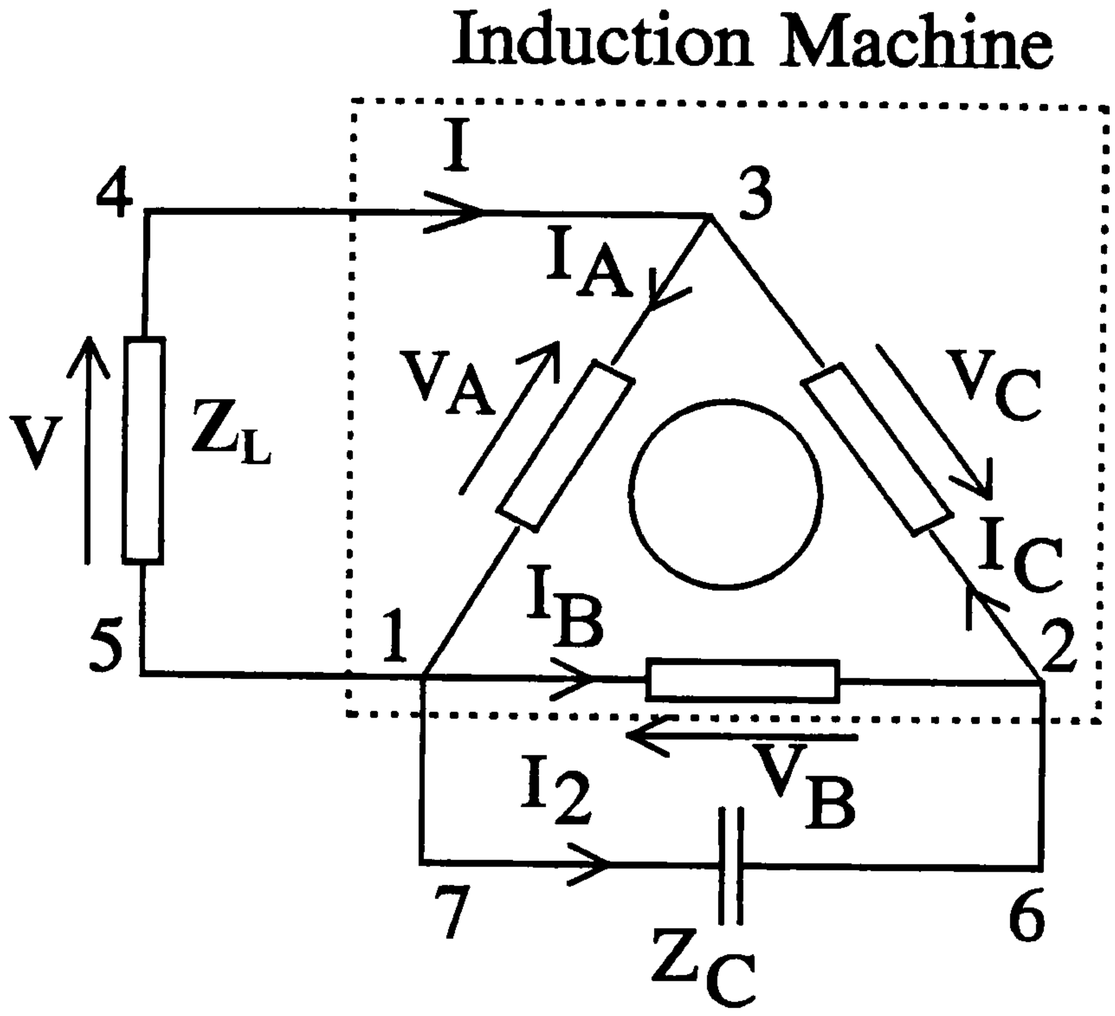


Fig. 4.1 Steinmetz connection for a three-phase SEIG supplying a single-phase load.

where

$$Z_L = \frac{R_L}{a} + jX_L . \tag{4.5}$$

The inspection equations may be solved using the method of symmetrical components to give the positive- and negative-sequence voltages:

$$V_p = \sqrt{3}V . \frac{Z_p\left(Z_C + \frac{e^{j\pi/6}}{\sqrt{3}} Z_n\right)}{Z_p Z_n + Z_p Z_C + Z_n Z_C} \tag{4.6}$$

$$V_n = \sqrt{3}V . \frac{Z_n\left(Z_C + \frac{e^{-j\pi/6}}{\sqrt{3}} Z_p\right)}{Z_p Z_n + Z_p Z_C + Z_n Z_C} \tag{4.7}$$

where $Z_p$ and $Z_n$ are respectively the positive- and negative-sequence impedances of the generator and $Z_C = 1/(j2\pi f_{base} C.a^2)$ is the complex impedance of the excitation capacitance at the base frequency. Details of $Z_p$ and $Z_n$ are given in Fig. A.3 and Fig. A.4 of Appendix A.2.

From (4.6) and (4.7) and referring to Fig. 4.1, the input impedance of the induction generator across terminals 1 and 3 is given by

$$Z_{in} = R_{in} + j\,X_{in} = \frac{Z_p Z_n + Z_p Z_C + Z_n Z_C}{3 Z_C + Z_p + Z_n}. \tag{4.8}$$

The derivation of (4.6), (4.7) and (4.8) is given in Appendix A.5.

From (4.8), the SEIG system of Fig. 4.1 may be reduced to the simple circuit shown in Fig. 4.2.

Applying Kirchhoff's voltage law to the latter circuit,

$$I.(Z_L + Z_{in}) = 0. \tag{4.9}$$

For successful voltage build-up, $I \neq 0$, hence

$$Z_{in} + Z_L = 0 \tag{4.10}$$

i.e., the impedances in loop 1345 in Fig. 4.2 must sum to zero.

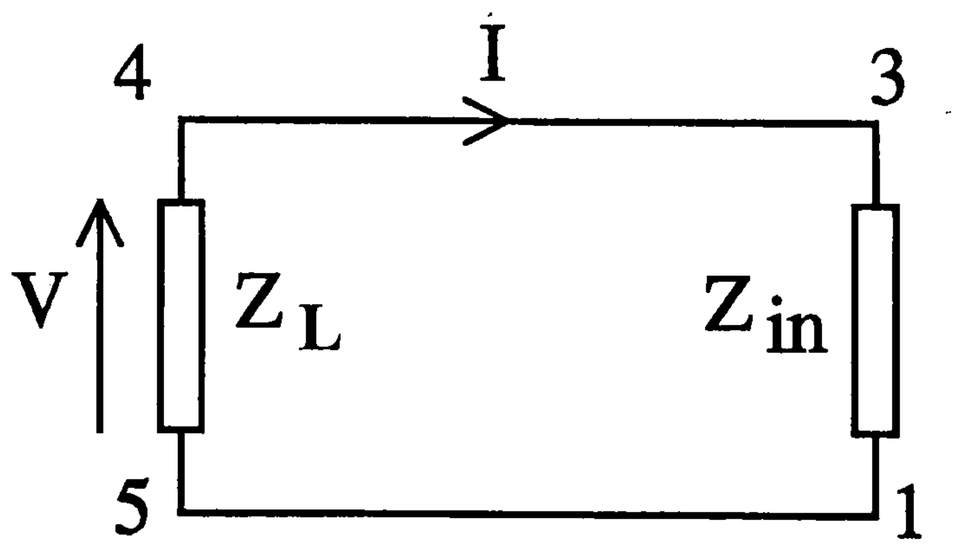


Fig. 4.2 Simplified circuit of three-phase SEIG with Steinmetz connection.

The complex equation (4.10) must be solved in order to give the excitation frequency *a* and the magnetizing reactance $X_m$. After *a* and $X_m$ have been determined, the positive-sequence air gap voltage is found from the magnetization curve. The generator performance can then be computed using (4.1) to (4.7) together with the symmetrical component equations.

### 4.2.2 Solution Technique

For a given per-unit speed $b$ and a given excitation capacitance, $Z_{in}$ is a highly nonlinear function of $a$ and $X_m$, implying that (4.10) is a complex equation in these two variables and hence is extremely difficult to solve using conventional techniques such as the Newton-Raphson method [26] or the polynomial method [28]. To avoid the lengthy mathematical manipulations involved, the solution of (4.10) is formulated as the following optimization problem:

$$\textbf{Minimize} \quad Z(a, X_m) = \sqrt{\left(R_{in} + \frac{R_L}{a}\right)^2 + \left(X_{in} + X_L\right)^2} \tag{4.11}$$

**subject to the constraints:**

$$0 < a < b$$

**and**

$$0 < X_m < X_{mu}$$

where $X_{mu}$ is the unsaturated value of the magnetizing reactance. This approach is based on the fact that, for given values of $a$ and $X_m$, the input impedance $Z_{in}$ can be computed readily.

It is easy to show that (4.10) is satisfied when the scalar impedance function $Z(a, X_m)$ given by (4.11) assumes a minimum value of zero. For function minimization, a classical search algorithm such as the Hooke and Jeeves method [97] or a commercial optimization package [98] may be employed.

In this and subsequent sections, the pattern search method of Hooke and Jeeves will be used for function minimization for the following reasons:

1) It is a well-proven and robust method that suits a wide range of mathematical functions.

2) This method does not involve derivatives of functions and as such is suitable for problems in which the derivatives of functions do not exist or are difficult to evaluate.

3) The method is relatively simple to program.

This method employs two search strategies, namely *exploratory moves* and *pattern moves*, in order to arrive at the optimum point. A function evaluation is required each time an exploratory move or pattern move is to be made. Details of the method are given in Appendix B. For normal operation of an SEIG, $a$ is slightly less than the per-unit speed $b$ while $X_m$ is less than the unsaturated value $X_{mu}$, hence $b$ and $X_{mu}$ could in general be chosen as initial estimates for $a$ and $X_m$ for starting the search procedure. After $a$ and $X_m$ have been determined, the steady-state performance can be calculated using the circuit equations and the magnetization curve of the IG.

### 4.2.3 Capacitance Requirement

This section addresses the capacitor sizing problem of the three-phase SEIG with the Steinmetz connection. A solution method is developed for computing the generator performance and capacitance requirement, taking into account the effect of load impedance, power factor and the rotor speed. The solution technique is further extended to the computation of capacitance required to maintain the terminal voltage at a preset value when the generator is on load. The theoretical results are validated by experiments on machine IG1 whose data are given in Appendix D.1.

For a given rotor speed, load impedance and power factor, the value of excitation capacitance must lie within certain limits for an induction generator to self-excite and to secure a stable operating point. The limiting conditions are obtained when the magnetizing reactance $X_m$ is equal to the unsaturated value $X_{mu}$ [33], [34]. For the

Steinmetz connection shown in Fig. 4.1, a simple method to determine the capacitance for initiating self-excitation is to consider the impedances in mesh 1267. Using the symmetrical components analysis presented in Section 4.2.1, the input impedance of the generator $Z'_{in}$ when viewed across terminals 1 and 2 is determined as follows:

$$Z'_{in} = R'_{in} + j\,X'_{in} = \frac{Z_p Z_n + Z_p Z_L + Z_n Z_L}{3Z_L + Z_p + Z_n} \tag{4.12}$$

where $Z_L$ is given by (4.5). For a given speed and load, both $R'_{in}$ and $X'_{in}$ are functions of the per-unit frequency $a$ only.

Successful voltage build-up requires the sum of impedances in mesh 1267 to be equal to zero, i.e.,

$$Z'_{in} + Z_C = 0\,. \tag{4.13}$$

The complex equation (4.13) can be split into two algebraic equations by equating the sum of real and imaginary terms respectively to zero:

$$R'_{in}(a) = 0 \tag{4.14}$$

$$X'_{in}(a) - \frac{X_C}{a^2} = 0 \tag{4.15}$$

where $X_C = 1/(j2\pi f_{base}C)$.

Eqn. (4.14) may be solved to yield the per-unit frequency $a$. The corresponding value of excitation capacitance can then be determined from (4.15).

Eqn. (4.14) is a high-order polynomial in $a$. Although the coefficients of the polynomial could be evaluated by systematic algebraic manipulations, the effort required is tremendous. To overcome this difficulty, the Secant method [99] is employed in the solution procedure. This method involves the evaluation of function values only and hence is easy to implement. The Secant formula as applied to the present problem is:

$$a_{n+1} = a_n - \frac{(a_n - a_{n-1})\, R'_{in}(a_n)}{R'_{in}(a_n) - R'_{in}(a_{n-1})} \tag{4.16}$$

where $a_{n-1}$, $a_n$, and $a_{n+1}$ are the values of the per-unit frequency at the end of the $(n-1)$th, $n$th and $(n+1)$th iteration respectively. The convergence criterion is that the value of per-unit frequency in successive iterations is less than a specified value, say 1.0e-6.

Two initial estimates of $a$ are required for starting the Secant method. To ascertain the appropriate initial values, the function $R'_{in}$ is computed and plotted in Fig. 4.3 for the experimental machine. It is assumed that the generator is driven at rated speed and is supplying a single-phase load at a power factor (p.f.) of unity. For a given load impedance, there are in general two roots to (4.14). Both roots are less than the per-unit speed $b$. The lower root $a_{min}$ lies between $0.75b$ to $0.83b$, while the upper root $a_{max}$ lies between $0.83b$ and $b$. To compute $a_{min}$, the initial estimates of $a$ can conveniently be chosen as $0.65b$ and $0.7b$. To compute $a_{max}$, the initial estimates can be chosen as $b$ and $0.99b$.

When the load impedance is very small (e.g., $Z_L$ = 0.01 p.u.), the input resistance $R'_{in}$ is always positive and no solution to (4.14) exists. There is thus a critical value of load impedance below which self-excitation is impossible, irrespective of the value of the excitation capacitance.

Fig. 4.4 shows the corresponding variations of $X'_{in}$ with $a$. A comparison between Fig. 4.3 and Fig. 4.4 shows that, for a given load impedance and speed, $X'_{in}$ is in general a monotonously increasing function over the interval $[a_{min}, a_{max}]$ ( if it exists). Thus, $a_{min}$ corresponds to $C_{max}$ while $a_{max}$ corresponds to $C_{min}$. $C_{min}$ is the minimum capacitance required for self-excitation, while $C_{max}$ is the capacitance above which self-excitation is not possible.

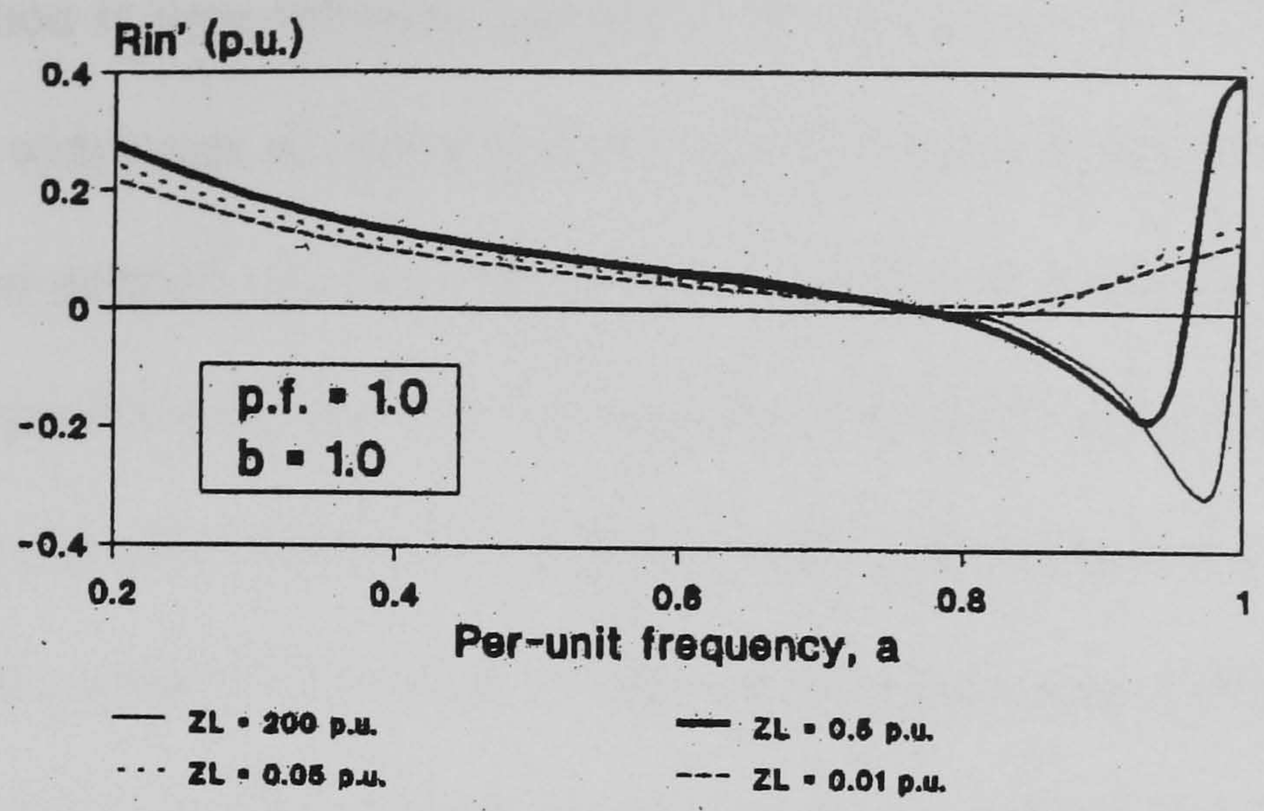


Fig. 4.3 Variation of $R'_{in}$ with per-unit frequency.

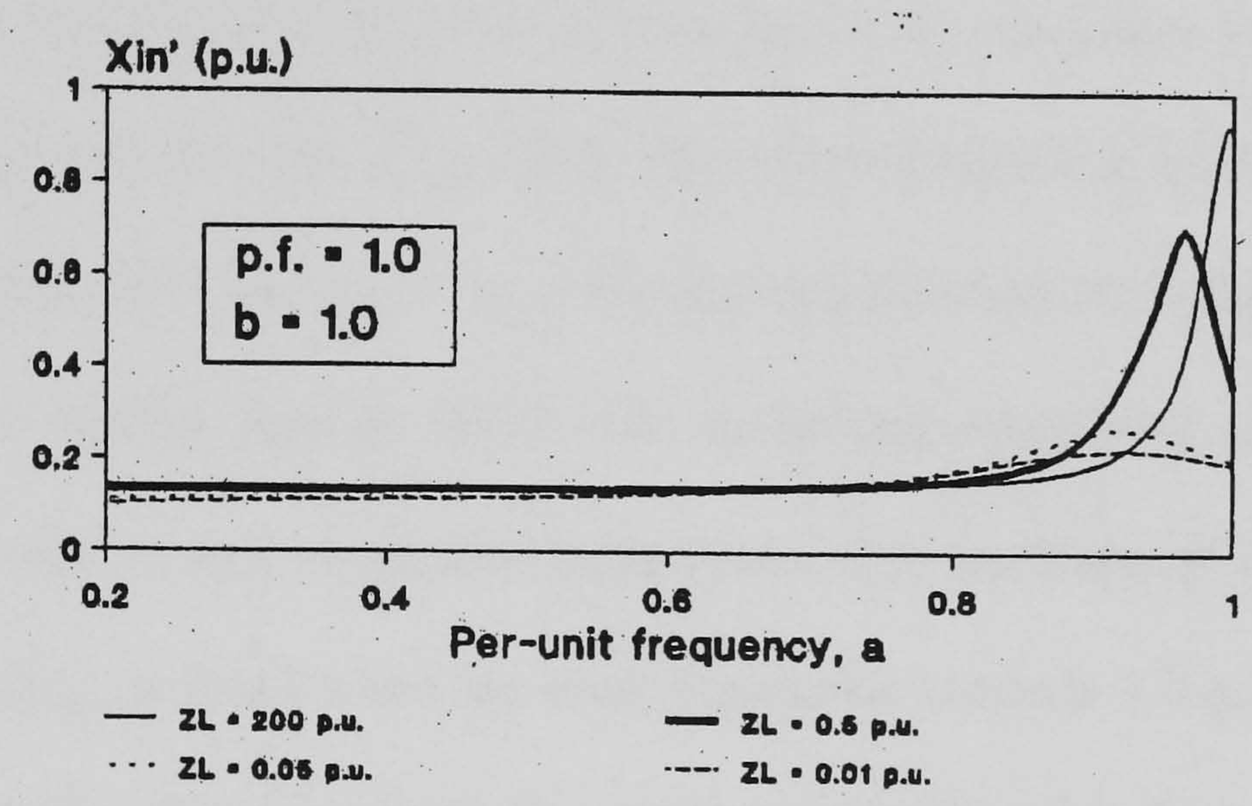


Fig. 4.4 Variation of $X'_{in}$ with per-unit frequency.

### 4.2.4 Computed and Experimental Results

A computer program was developed for computing the capacitance requirement of the experimental machine IG1 with Steinmetz connection. Typical computed results are listed in Table 4.1.

TABLE 4.1
COMPUTED RESULTS USING THE SECANT METHOD
$b = 1.0$; p.f. = 1.0; $a_o = 1.0$; $a_1 = 0.99$

| $Z_L$ (p.u.) | $a_{max}$ | $C_{min}$ (μF) | Number of iterations | Function Minimum |
|---|---|---|---|---|
| 200 | 0.994886 | 85.27 | 4 | -3.678e-6 |
| 20 | 0.993951 | 85.57 | 4 | -2.225e-6 |
| 5 | 0.990879 | 86.81 | 3 | -1.196e-6 |
| 2 | 0.984949 | 90.35 | 5 | 1.184e-8 |
| 1 | 0.975696 | 98.98 | 7 | -3.631e-6 |

The Secant method is very efficient: convergence can in general be obtained in 3 to 7 iterations over a wide range of load impedance and the function minima are very close to zero. It should be pointed out, however, that the number of iterations and convergence depend on the circuit conditions. For low speeds or small load impedances, the initial values may need to be adjusted in order to speed up the convergence process.

Fig. 4.5 shows the computed variation of per-unit frequency and excitation capacitance with load impedance at rated speed. As explained in Section 4.2.3, there are two frequencies $a_{max}$ and $a_{min}$ for a given load impedance $Z_L$ and speed, provided that $Z_L$ is greater than some critical value $Z_{L,crit}$. When the load impedance is equal to $Z_{L,crit}$, there is only one solution to (4.9) and $a_{max} = a_{min}$. For the experimental machine, $Z_{L,crit}$ is equal to 0.0415 p.u. This implies that an SEIG with Steinmetz connection is capable of self-excitation even with a very small load impedance. The variation of $a_{max}$ and $a_{min}$, and hence $C_{min}$ and $C_{max}$, is small when the load impedance exceeds 1.0 p.u. But for smaller load impedances, $C_{min}$ increases while $C_{max}$ decreases rapidly with decrease in $Z_L$.

The experimental results for $C_{min}$ are also given in Fig. 4.5. In all cases, the experimental values are slightly higher than the theoretical values but correlation is good.

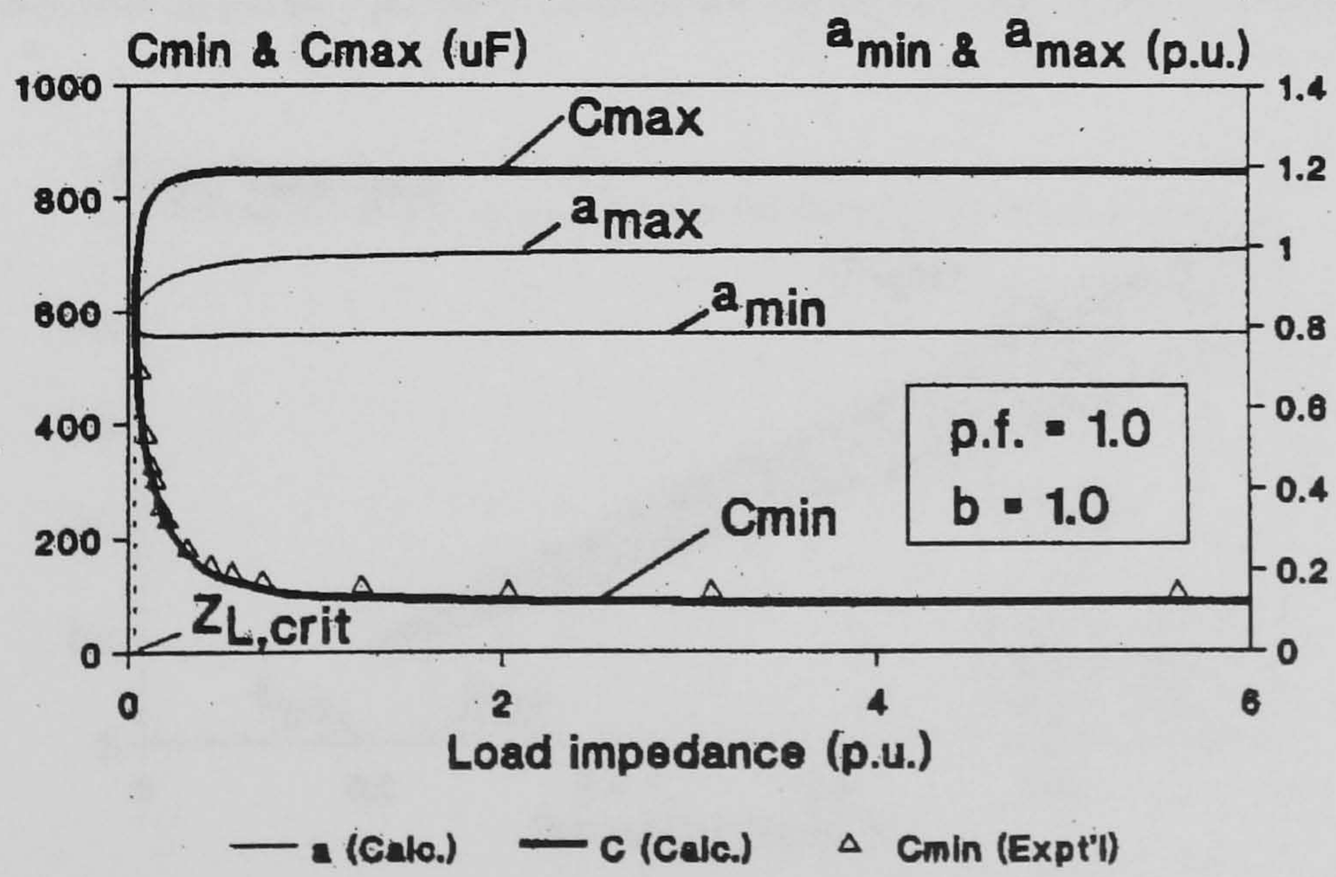


Fig. 4.5 Variation of per-unit frequency and excitation capacitance with load impedance.

Fig. 4.6 and Fig. 4.7 show the computed variation p.u. frequency and excitation capacitance with the per-unit speed for given load impedances. The following observations can be made:

1) For a given load impedance, there exists a critical speed $b_{crit}$ below which self-excitation is impossible. The value of $b_{crit}$ increases with decrease in load impedance. When $Z_L$ is varied from 200 p.u. to 0.1 p.u., $b_{crit}$ increases from 0.2 p.u. (point $b_{c1}$ in Fig. 4.5) to 0.25 p.u. (point $b_{c2}$).

2) $C_{min}$ in general increases with decrease in the per-unit speed $b$.

3) At higher speeds, $C_{max}$ also increases with decrease in $b$, but below a certain speed (e.g. point P on the computed curve for $Z_L$ = 200 p.u. in Fig. 4.7), $C_{max}$ decreases with decrease in $b$.

4) The self-excitation region bounded by $C_{min}$ and $C_{max}$ decreases with decrease in load impedance.

5) The effect of load impedance on $C_{min}$ is much more pronounced than that on $C_{max}$.

The experimental values of $C_{min}$ as a function of per-unit speed are also shown in Fig. 4.7. The close agreement between the computed and experimental results in Fig. 4.5 and Fig. 4.7 confirms the accuracy of the theoretical analysis and solution method.

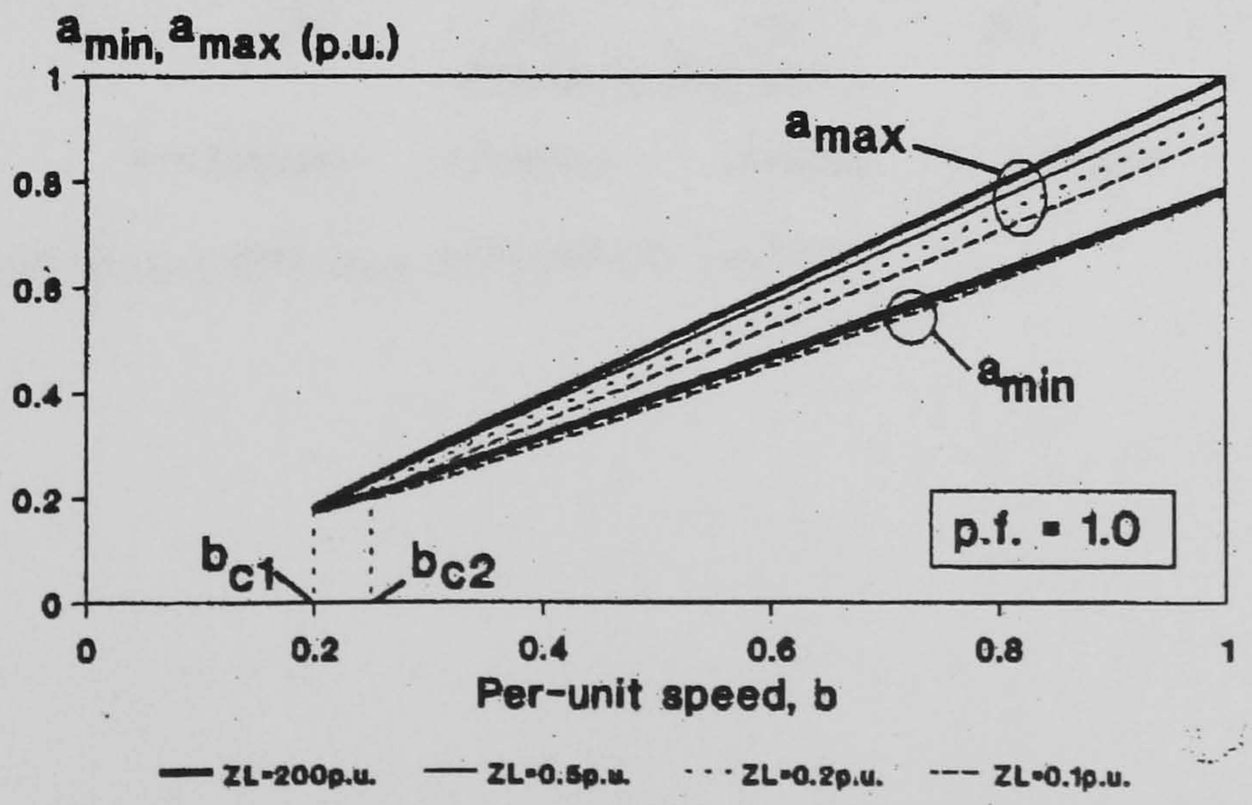


Fig. 4.6 Variation of $a_{min}$ and $a_{max}$ with speed for given load impedances.

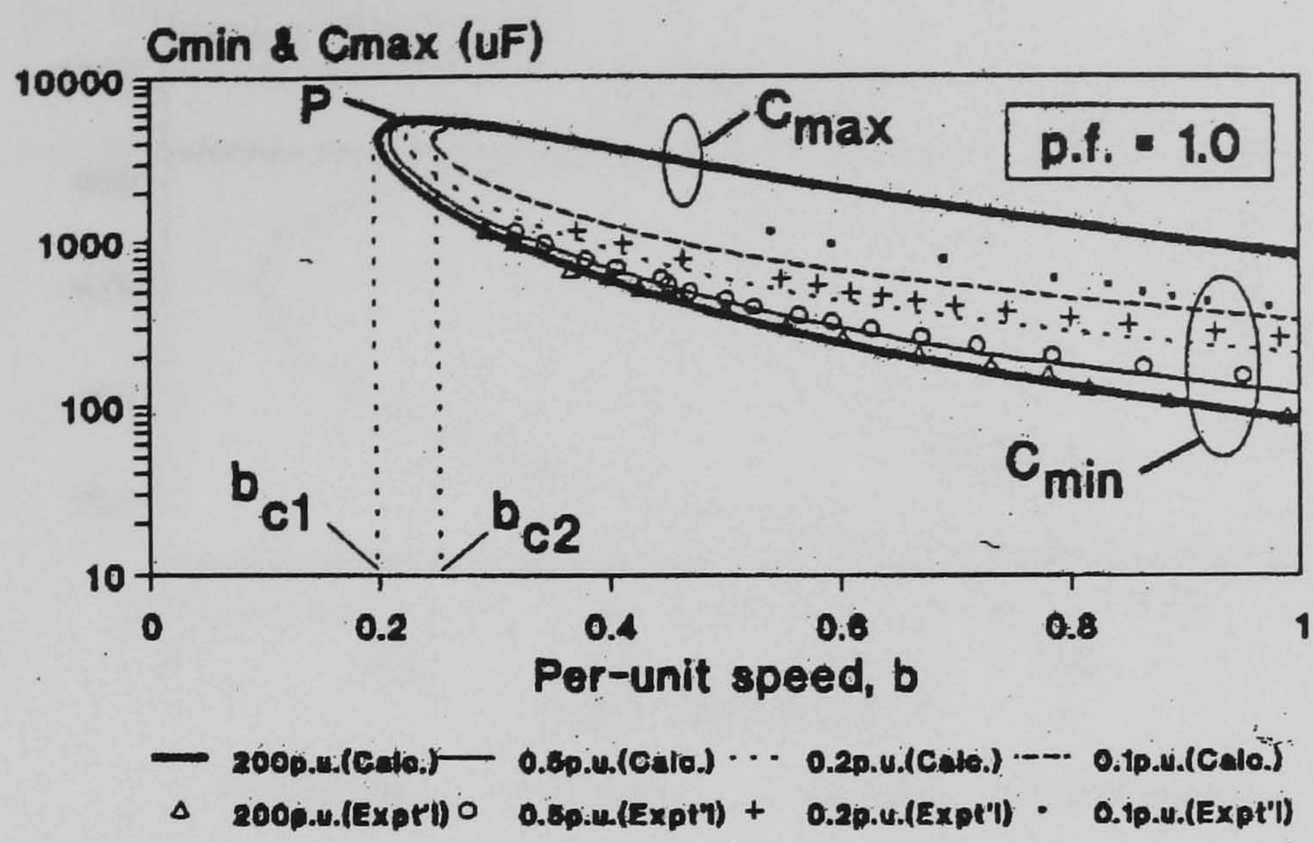


Fig. 4.7 Variation of $C_{min}$ and $C_{max}$ with speed for given load impedances.

Fig. 4.8 and Fig. 4.9 show the computed variation of per-unit frequency and excitation capacitance with load power factor. Critical values of power factor, below which the SEIG fails to self-excite, are found to exist. When the load impedance is small, a high load power factor is beneficial in securing voltage build-up.

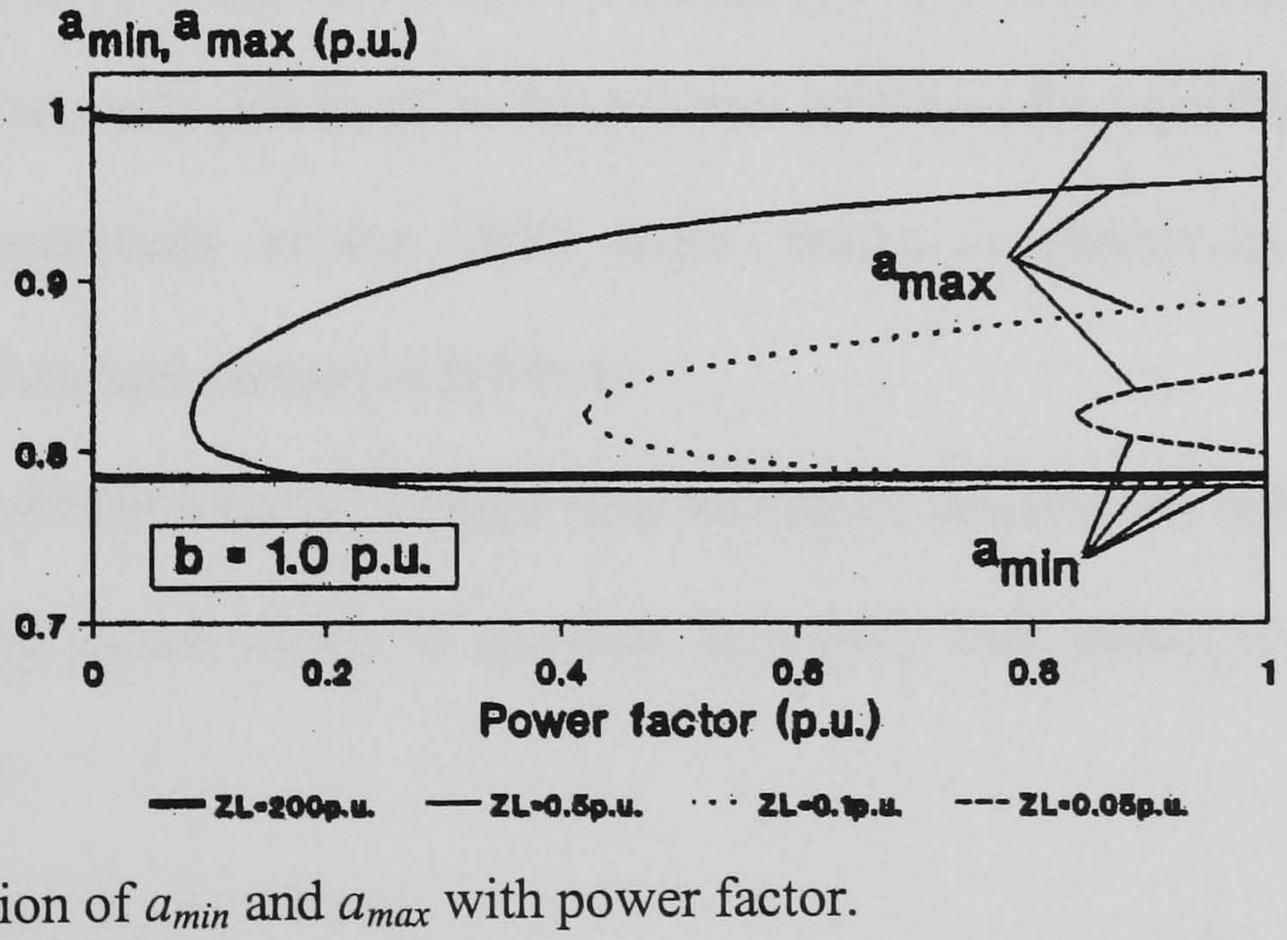


Fig. 4.8 Variation of $a_{min}$ and $a_{max}$ with power factor.

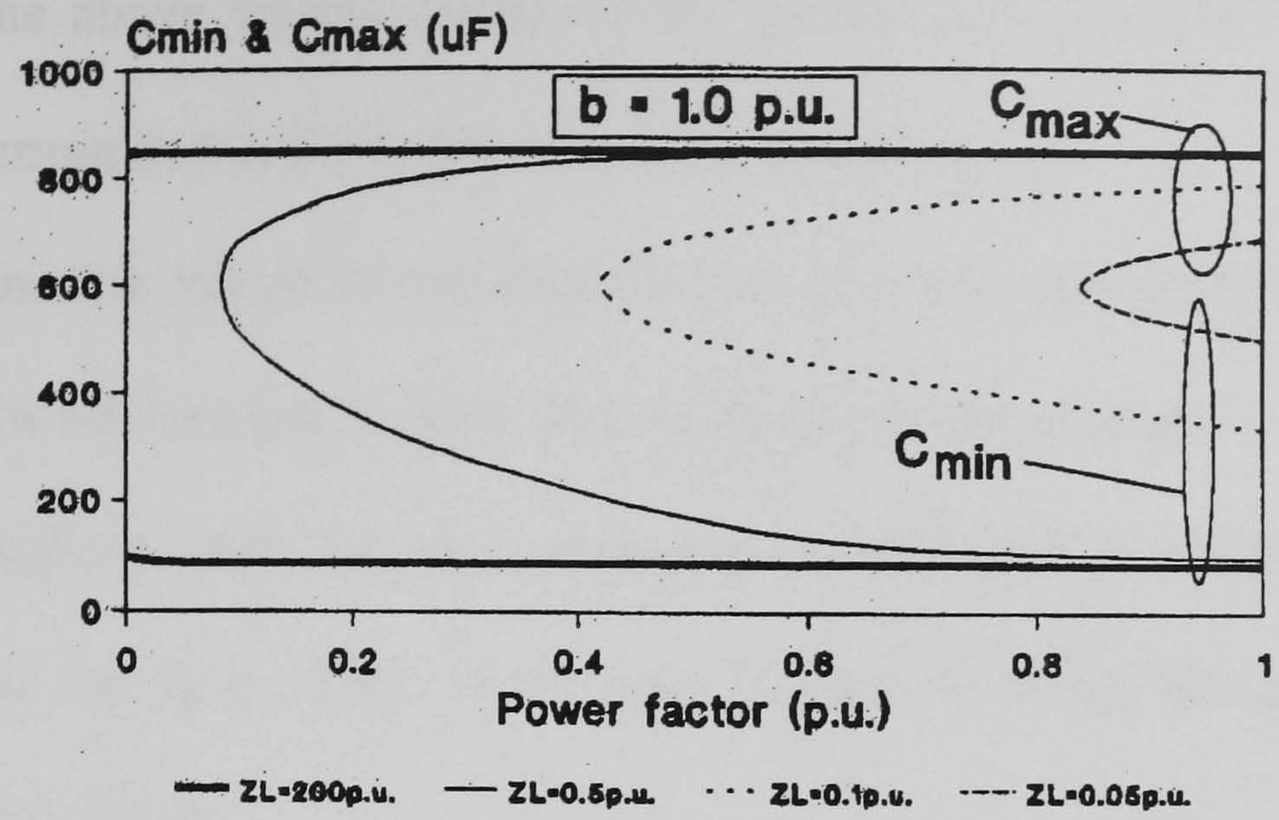


Fig. 4.9 Variation of $C_{min}$ and $C_{max}$ with power factor.

### 4.2.5 Capacitance Requirement on Load

The capacitances computed in the previous sections are those that mark the onset of self-excitation. When the SEIG is loaded, the load current produces a demagnetizing effect on the air gap field and the terminal voltage drops. To maintain the terminal voltage constant, the excitation capacitance has to be increased as the load current increases. On the basis of the analysis presented in the previous sections, it is possible to compute the capacitance requirement of the SEIG under loaded conditions using an iterative procedure which is summarized as follows:

1) For a specified terminal voltage $V$, power factor and per-unit speed $b$, assume the following initial values of per-unit frequency and positive-sequence air gap voltage:

$$a_o = b;\ E_1 = V / a_o$$

2) Obtain the corresponding value of magnetizing reactance using the $X_m$–$E_1$ curve which can be derived from the magnetization characteristic determined in a synchronous speed test.

3) Using the above values, determine the generator impedance $Z'_{in} = R'_{in} + jX'_{in}$ across terminals 4 and 5 in the circuit shown in Fig. 4.1.

4) Determine the values of per-unit frequency $a$ and capacitive reactance $X_c$ that satisfy the self-excitation conditions using the Secant method.

5) Compute the positive-sequence component of voltage $V_p$ using (4.6).

6) Compute the new value of air gap voltage $E_1$ from the positive-sequence equivalent circuit.

7) Repeat steps 1) to 6) until the difference in $V_p$ in successive iterations is sufficiently small.

8) Compute the excitation capacitance and the generator performance using the final values of $a$ and $X_C$.

Since only $a_{max}$ needs to be computed, initial values of $a$ required to start the Secant method can be chosen as $0.99b$ and $0.98b$. In general, the number of iterations increases with decrease in load impedance. For the experimental machine IG1 and with a tolerance of 1.0e-4 as the convergence criterion (step 7)), the number of iterations varies from 7 to 15, showing that the above iterative procedure converges quite rapidly.

Fig. 4.10 shows the excitation capacitance required to maintain a specified terminal voltage when the SEIG is supplying a unity power factor load at rated speed. There is good agreement between the computed and experimental results when the terminal voltage is 0.8 p.u. For a terminal voltage of 1.0 p.u., however, the discrepancy between computed and experimental results increases with the load current. This could be attributed to the more pronounced saturation and hence more complicated magnetic conditions within the machine.

Fig. 4.11 shows the computed capacitance required to maintain the terminal voltage at 1.0 p.u. at different load power factors. The capacitance required increases rapidly when the power factor is lower than 0.8 lagging.

Fig. 4.10 and Fig. 4.11 suggest that a controller for varying the excitation capacitance should be incorporated in the SEIG system for stabilization of the load voltage.

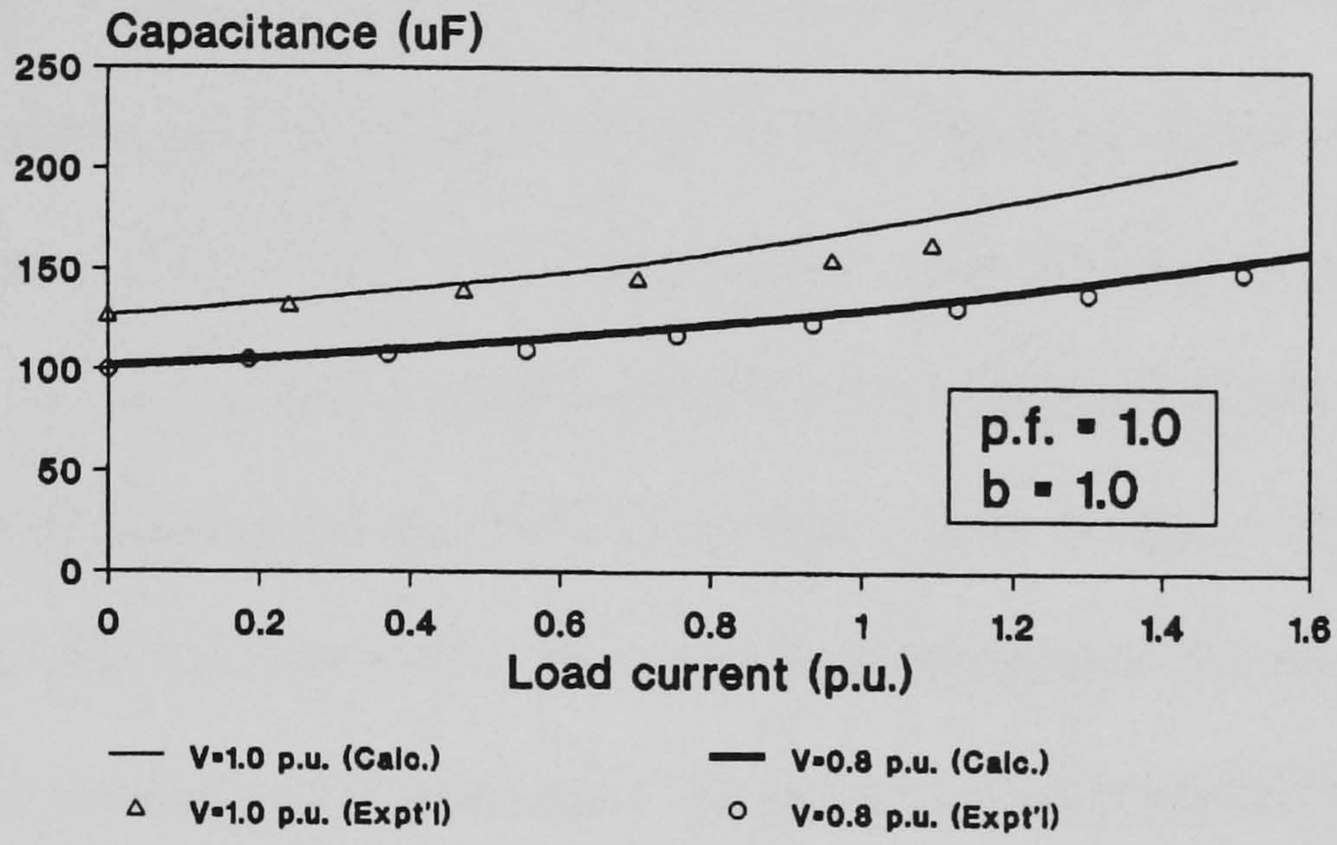


Fig. 4.10 Excitation capacitance required to maintain the terminal voltage at preset values.

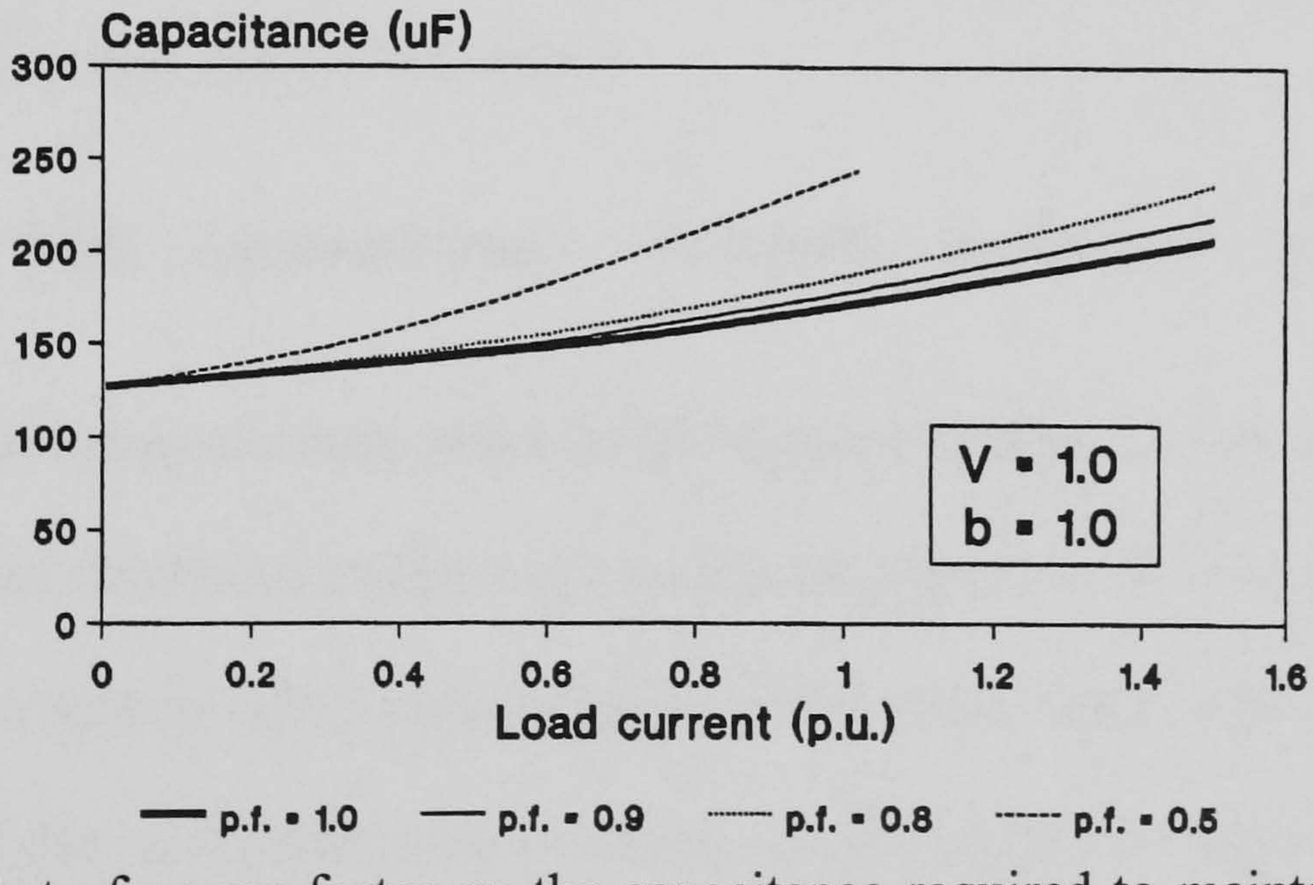


Fig. 4.11 Effect of power factor on the capacitance required to maintain the terminal voltage at rated value.

### 4.2.6 Summary

This section has presented the analysis of a three-phase SEIG with the Steinmetz connection. The method of symmetrical components is used in association with a

function optimization method in order to account for the circuit asymmetry and the variation of machine parameters. Based on this approach, a simple method for capacitor sizing has been developed. The method involves the derivation of the generator input impedance and the formulation of two nonlinear equations from a consideration of the self-excitation conditions. Solving one of the equations using the Secant method, the per-unit frequency is determined and the excitation capacitance can subsequently be computed using the second equation. Effects of load impedance, speed and power factor on the capacitance requirement have been studied. Critical values of load impedance, speed and power factor, below which the SEIG fails to self-excite, are found to exist. Compared with the single-phasing mode of operation, however, the SEIG with Steinmetz connection can self-excite even with very small load impedance. An iterative procedure is developed for computing the capacitance required to maintain a preset terminal voltage when the SEIG is on load. Where possible, the theoretical analysis has been verified by experiments on a small induction machine.

## 4.3 SEIG with Asymmetrically Connected Impedances and Excitation Capacitances

When the power rating of a three-phase SEIG becomes smaller, it is increasingly difficult to ensure an even distribution of the loads among the phases, which means that in general the SEIG has to operate with a certain degree of phase imbalance. Unbalanced operation may also result due to manufacturing tolerances of the excitation capacitances, failure of some excitation capacitance modules or the disconnection of loads by the consumers. Autonomous power systems often employ single-phase distribution schemes for reasons of low cost, ease of maintenance and simplicity in protection [7]. When a three-phase SEIG is used to supply single-phase loads, the inherent phase imbalance in the machine

will result in poor generator performance, such as overcurrent, overvoltage, poor efficiency, excessive temperature rise and machine vibration. These undesirable effects can be alleviated to a large extent by the use of the Steinmetz connection as discussed in Section 4.2. For isolated operation, however, perfect phase balance cannot be achieved for a pure resistive load [67] or a series R-L load [100].

The objectives of this section are to develop a general method for analyzing the steady-state performance of a three-phase SEIG under various unbalanced operating conditions and to investigate a novel phase-balancing scheme for the SEIG when supplying single-phase loads. Theoretical and experimental results will be compared in order to validate the analysis and the principle of phase-balancing.

### 4.3.1 Circuit Model

Fig. 4.12 shows the circuit connection of a symmetrical, delta-connected IG with asymmetrically connected terminal impedances. At least one of the terminal impedances $Z_1$, $Z_2$, and $Z_3$ must contain a capacitive element in order to furnish the reactive power necessary for initiating self-excitation.

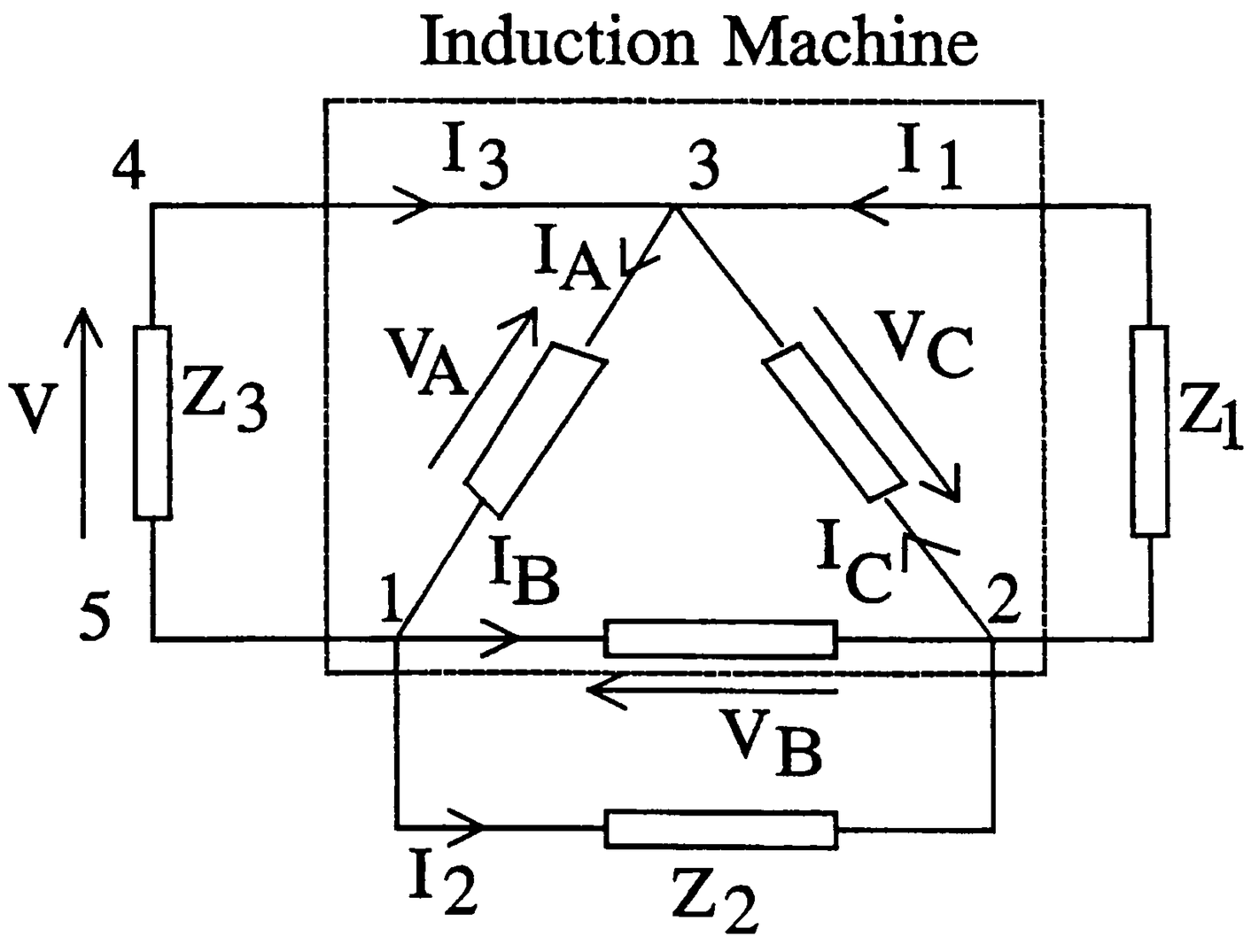


Fig. 4.12 Three-phase SEIG with asymmetrically connected terminal impedances.

The circuit model shown in Fig. 4.12 can be used to study practically all modes of unbalanced operation of the SEIG in which zero-sequence quantities are absent. By assigning appropriate values to the terminal impedances, a specific unbalanced operating condition can be simulated.

A star-connected SEIG with symmetrical stator windings can also be analyzed by first transforming the generator to an equivalent delta-connected machine whose per-phase impedance is three-times the actual star-connected value. In the case of star-connected load impedances and excitation capacitances with isolated neutral points, star-delta transformation can likewise be applied to yield the equivalent delta-connected impedance values. After these transformation procedures, the circuit will be reduced to the generic form as shown in Fig. 4.12.

For loads to be supplied by a four-wire system, a delta-star connected transformer can be placed between the generator and the loads so that zero-sequence currents are excluded from the SEIG. With appropriate impedance transformations, the system is again reduced to that as shown in Fig. 4.12.

### 4.3.2 Performance Analysis

The method of symmetrical components is employed in order to account for the unbalanced circuit conditions. All the equivalent circuit parameters are assumed to be constant except the magnetizing reactance which is a function of the positive-sequence air gap voltage. To facilitate performance analysis, the SEIG system may be regarded as a passive circuit when viewed across any two stator terminals. For convenience, phase A is chosen as the reference and the input impedance of the IG across terminals 1 and 3 in Fig. 4.12 will be considered. If the impedance $Z_3$ is replaced by the voltage $V$, the system

is identical to that shown in Fig. 2.1 and hence can be analyzed in the same manner as in Section 2.2.

From the analysis, the voltage across terminals 1 and 3 in Fig. 4.12 is determined as follows:

$$V = \frac{V_p}{\sqrt{3}}(h - h^2).\frac{Y_1 + Y_2 + Y_p + Y_n}{hY_2 + (h - h^2)Y_n - h^2 Y_1} \tag{4.17}$$

where $h$ is the complex operator exp(j2π/3).

The input current $I_3$ is given by

$$I_3 = \frac{V_p}{\sqrt{3}}(h - h^2)\frac{(Y_1 + Y_2)(Y_p + Y_n) + 3Y_pY_n + Y_1Y_2}{hY_2 + (h - h^2)Y_n - h^2 Y_1}. \tag{4.18}$$

From (4.17) and (4.18), the input impedance $Z_{in}$ of the IG when viewed across terminals 1 and 3 is given by

$$Z_{in} = \frac{V}{I_3} = \frac{Y_1 + Y_2 + Y_p + Y_n}{(Y_1 + Y_2)(Y_p + Y_n) + 3Y_pY_n + Y_1Y_2}. \tag{4.19}$$

Both $Y_p$ and $Y_n$ are functions of the per-unit frequency $a$ and the magnetizing reactance $X_m$, hence the input impedance of the IG may be written as:

$$Z_{in} = R_{in}(a, X_m) + j\,X_{in}(a, X_m). \tag{4.20}$$

From (4.20), the SEIG system of Fig. 4.12 may also be reduced to the simple circuit shown in Fig. 4.2, with $Z_L$ replaced by $Z_3$. For successful voltage build-up,

$$Z_3 + Z_{in} = 0. \tag{4.21}$$

The complex equation (4.21) may be solved using the solution technique described in Section 4.2.2. The scalar impedance function to be minimized is:

$$Z(a, X_m) = \sqrt{(R_3 + R_{in})^2 + (X_3 + X_{in})^2} \tag{4.22}$$

where $R_3$ and $X_3$ are respectively the equivalent series resistance and reactance of the terminal impedance $Z_3$. After $a$ and $X_m$ have been determined, the positive-sequence air gap voltage is found from the magnetization curve. The generator performance can then be computed using the circuit equations together with the symmetrical component equations.

### 4.3.3 Computed and Experimental Results

A number of case studies were carried out on the experimental machine IG1 whose data are given in Appendix D.1. Appropriate numerical values are assigned to the terminal impedances in order to simulate a particular unbalanced operating condition. For example, a zero capacitance value implies the absence of an excitation capacitance while a very large resistance value, say 1.0e5 p.u., is equivalent to the absence of a connected load resistance. Operation at rated speed is assumed in each case investigated.

To simplify the calculations and for easy comparison, all the parameters are expressed in per-unit values, using the rated phase voltage, rated phase current, and rated power per phase of the induction machine as bases. Over a wide range of load and for various unbalanced cases, convergence can be obtained in 350 to 450 function evaluations for the experimental machine. Table 4.2 summarizes the cases studied and shows the typical circuit parameters used. As shown in Table 4.3, very good agreement between the computed and experimental results is obtained for most of the unbalanced cases, hence the accuracy of the analysis and solution procedure is verified. Larger discrepancies exist, however, for case 5. The severe phase imbalance for plain single-phasing operation results in nonlinearity in the magnetic circuit of the SEIG. The principle of superposition, which is the basis of symmetrical component analysis, is therefore less valid.

TABLE 4.2

CASE STUDIES OF THREE-PHASE SEIG WITH ASYMMETRICALLY CONNECTED TERMINAL IMPEDANCES

| Case | $Z_1 = R_{L1} // C_1$ | | $Z_2 = R_{L2} // C_2$ | | $Z_3 = R_{L3} // C_3$ | | Remarks |
|---|---|---|---|---|---|---|---|
| | $R_{L1}$ (p.u.) | $C_1$ (μF) | $R_{L2}$ (p.u.) | $C_2$ (μF) | $R_{L3}$ (p.u.) | $C_3$ (μF) | |
| 1 | 2.10 | 60 | 1.10 | 60 | 5.0 | 60 | Balanced capacitances; unbalanced load resistance |
| 2 | 2.15 | 30 | 2.15 | 60 | 2.15 | 60 | Unbalanced capacitance; balanced load resistance |
| 3 | 2.95 | 60 | 3.30 | 62 | 2.15 | 72 | Unbalanced capacitance; unbalanced load resistance |
| 4 | ∞ | 60 | ∞ | 60 | 0.97 | 60 | Balanced capacitance; single-phase load resistance |
| 5 | ∞ | 0 | ∞ | 0 | 1.65 | 125 | Plain single-phasing operation |
| 6 | ∞ | 0 | ∞ | 125 | 0.90 | 0 | Steinmetz connection |

TABLE 4.3

PERFORMANCE OF SEIG FOR THE CIRCUIT CONFIGURATIONS LISTED IN TABLE 4.2 (NORMAL: EXPERIMENTAL VALUES; BRACKETED: COMPUTED VALUES)

| Case | Phase voltages (p.u.) | | | Phase currents (p.u.) | | | * VUF | $*P_{out}$ (p.u.) | Efficiency (p.u.) |
|---|---|---|---|---|---|---|---|---|---|
| | $V_A$ | $V_B$ | $V_C$ | $I_A$ | $I_B$ | $I_C$ | | | |
| 1 | 1.0091 (1.0507) | 0.9545 (0.9808) | 0.9545 (0.9686) | 0.9574 (0.9736) | 1.046 (1.0648) | 0.713 (0.7141) | 0.0486 (0.0518) | 1.47 (1.545) | 0.7998 (0.7747) |
| 2 | 0.9045 (0.9197) | 0.8818 (0.8875) | 0.8727 (0.8733) | 0.7204 (0.7103) | 0.7796 (0.7933) | 0.6167 (0.5926) | 0.0288 (0.0309) | 1.0968 (1.115) | 0.8174 (0.7905) |
| 3 | 1.0818 (1.0902) | 1.075 (1.0781) | 1.0909 (1.1046) | 1.0278 (1.0154) | 0.9074 (0.9032) | 1.011 (0.9709) | 0.0095 (0.0141) | 1.299 (1.3197) | 0.7616 (0.7447) |
| 4 | 0.9909 (1.0057) | 1.0364 (1.0438) | 1.1182 (1.1618) | 1.0057 (1.0192) | 0.4852 (0.4739) | 1.1667 (1.1716) | 0.0878 (0.0896) | 1.0093 (1.0396) | 0.7133 (0.6934) |
| 5 | 0.824 (0.9261) | 0.6727 (0.7337) | 0.8368 (0.9272) | 0.9444 (1.0352) | 0.4407 (0.5176) | 0.4407 (0.5176) | 0.1321 (0.145) | 0.4209 (0.5204) | 0.6241 (0.6096) |
| 6 | 0.8291 (0.8633) | 0.9045 (0.9547) | 0.8355 (0.867) | 0.3296 (0.3521) | 0.6741 (0.7443) | 0.7778 (0.7812) | 0.0573 (0.0681) | 0.7357 (0.8256) | 0.7675 (0.7521) |

* VUF = Voltage unbalance factor; $P_{out}$ = Total electrical power output

### 4.3.4 Modified Steinmetz Connection (MSC)

Many autonomous electric power systems employ single-phase generation and distribution for reasons of simplicity and reduced cost. An examination of cases 4 and 5 in Tables 4.2 and 4.3, however, reveals that poor generator performance, such as phase imbalance and poor efficiency, will result when single-phase loads are supplied by a three-phase SEIG. These disadvantages are overcome to a large extent by the use of the Steinmetz connection which has been investigated in considerable detail in Section 4.2. By connecting the excitation capacitance and load across different phases, better phase

balance and higher efficiency could be obtained and the minimum voltage unbalance factor was about 5% for a pure resistive load.

Subsequent research on the Steinmetz connection for SEIGs reveals that additional circuit elements are required in order to achieve perfect phase balance. Based on this result, a modified Steinmetz connection (MSC) for a three-phase SEIG is proposed in this section. Fig. 4.13 shows the circuit connection of the MSC, where all circuit parameters have been referred to the base frequency. The impedance $Z_3$ across phase A (the reference phase) consists of the main load resistance $R_{L3}$ and the auxiliary excitation capacitance in parallel. The impedance $Z_2$ across phase B (the lagging phase) consists of the main excitation capacitance $C_2$ and auxiliary load resistance $R_{L2}$ in parallel. Compared with the original Steinmetz connection in Fig. 4.1, it is seen that the auxiliary resistance $R_{L2}$ and the auxiliary excitation capacitance $C_3$ have been introduced. For a practical SEIG system, $R_{L2}$ could be local loads such as lighting, storage heating, or battery charging. Alternatively, $R_{L2}$ could be a portion of the remote loads.

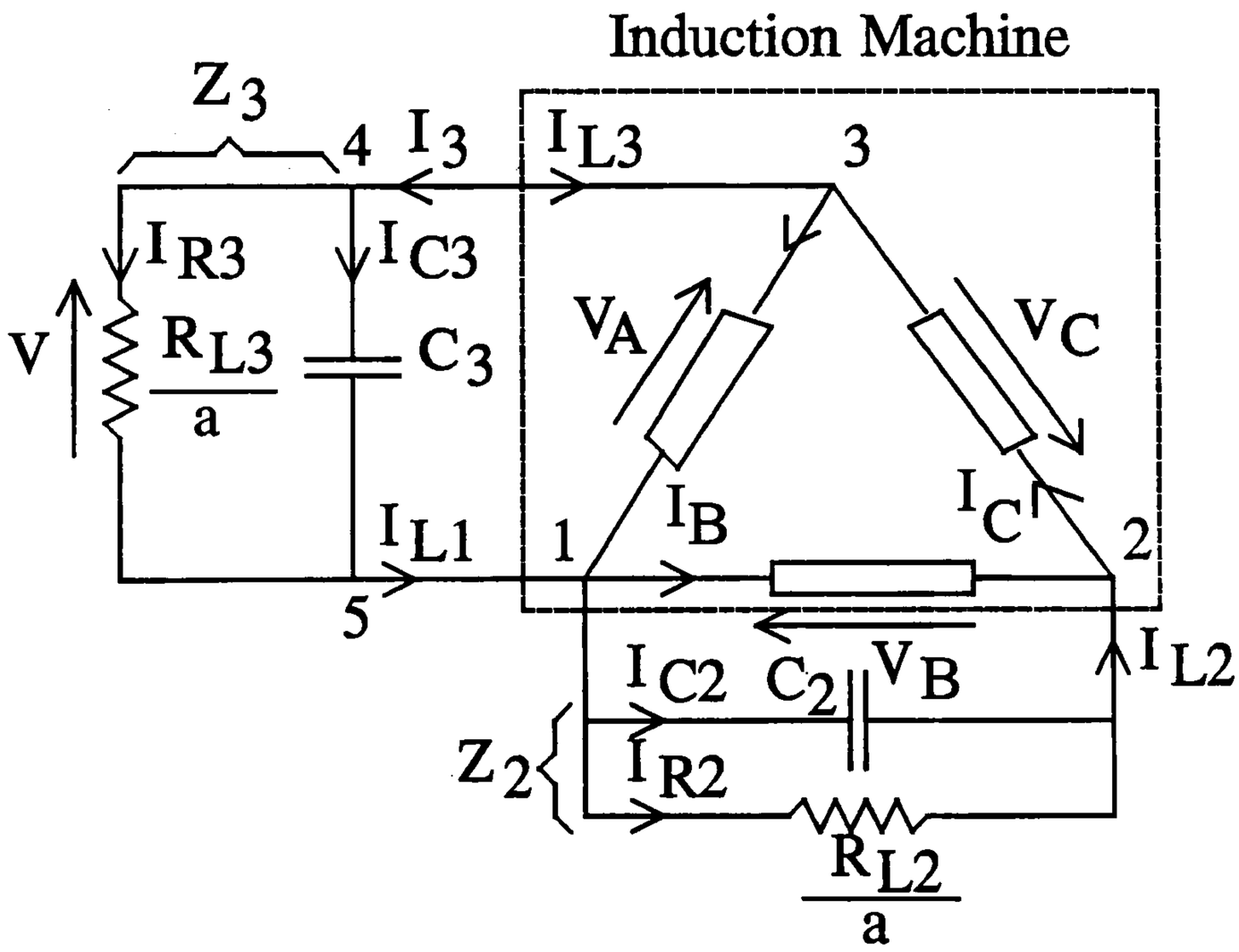


Fig. 4.13 Modified Steinmetz connection (MSC) for three-phase SEIG.

The three-phase SEIG with MSC can also be analyzed using the general method described in Sections 4.3.2 and 4.3.3. In this case, $Y_1$ is equal to zero while $Y_2$ and $Y_3$ are the resultant admittances connected across phase B and phase A respectively.

*A) Conditions for Perfect Phase Balance*

Fig. 4.14 shows the phasor diagram of the three-phase SEIG with MSC under balanced conditions, it being assumed that the positive-sequence impedance angle $\phi_p$ is greater than $2\pi/3$ rad. The line current $I_{L2}$ flowing into terminal 2 consists of the current $I_{C2}$ through the main excitation capacitance $C_2$ and the current $I_{R2}$ through the auxiliary resistance $R_{L2}$. Meanwhile, the line current $I_{L3}$ flowing into terminal 3 is contributed by $-I_{R3}$ (where $I_{R3}$ is the main load current) as well as $-I_{C3}$ (where $I_{C3}$ is the current through the auxiliary capacitance $C_3$). The current components $I_{R2}$ and $I_{C3}$ enable balanced line currents of the SEIG to be synthesized.

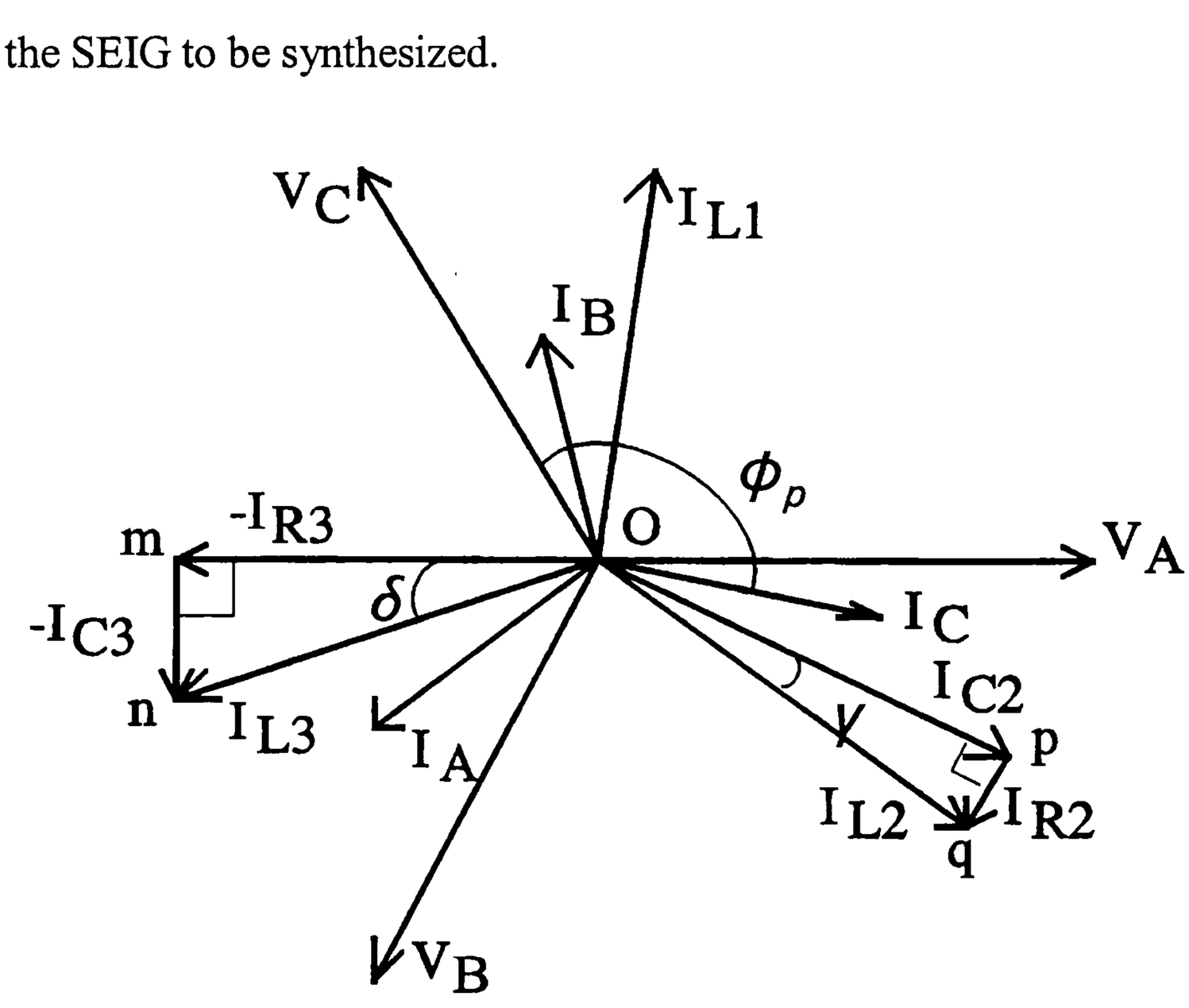


Fig. 4.14 Phasor diagram for SEIG with MSC under perfect phase balance.

A careful study of the relationship between the voltage and current phasors in Fig. 4.14 shows that, under perfect phase balance, the angle $\gamma$ between $I_{C2}$ and $I_{L2}$ is equal to ($\phi_p$ - $2\pi/3$) rad while the angle $\delta$ between $-I_{R3}$ and $I_{L3}$ is equal to ($5\pi/6$ - $\phi_p$) rad. Since each current in the phasor triangles Opq and Omn may be expressed in terms of the phase voltage and the associated admittance, conductance or susceptance, the following relationships can be derived:

$$G_2 = \sqrt{3}\,|Y_p|\sin(\phi_p - 2\pi/3) \tag{4.23}$$

$$B_2 = \sqrt{3}\,|Y_p|\cos(\phi_p - 2\pi/3) \tag{4.24}$$

$$G_3 = \sqrt{3}\,|Y_p|\cos(5\pi/6 - \phi_p) \tag{4.25}$$

$$B_3 = \sqrt{3}\,|Y_p|\sin(5\pi/6 - \phi_p) \tag{4.26}$$

where $G_2 = a/R_{L2}$, $B_2 = a^2.2\pi f_{base}.C_2$, $G_3 = a/R_{L3}$, and $B_3 = a^2.2\pi f_{base}.C_3$.

When $\phi_p$ is greater than $2\pi/3$ rad (which corresponds to a heavy load condition), $G_2$ is positive and perfect balance can be obtained with all four circuit elements in Fig. 4.13 present. When $\phi_p$ is equal to $2\pi/3$ rad, $G_2$ vanishes showing that phase balance can be achieved with the auxiliary load resistance removed. Under this condition, $B_2 = \sqrt{3}Y_p$, $B_3 = \sqrt{3}Y_p/2$ and $G_3 = 3Y_p/2$. When $\phi_p$ is less than $2\pi/3$ rad, however, $G_2$ is negative and perfect phase balance cannot be obtained with passive circuit elements.

Eqn. (4.26) shows that $B_3$ vanishes when $\phi_p = 5\pi/6$ rad, which implies that the auxiliary capacitance $C_3$ can be dispensed with. When $\phi_p$ exceeds $5\pi/6$ rad, $B_3$ becomes negative, implying that perfect balance can be achieved with an auxiliary inductance across phase A. In practice, however, the full-load power factor angle of an SEIG ranges from $2\pi/3$ rad to $4\pi/5$ rad, hence it is very unlikely that an inductive element need to be used.

To investigate the phase-balancing capability of the modified Steinmetz connection, experiments were performed on the 2.2 kW induction machine. The rotor speed is maintained at rated value throughout the tests. The values of $R_{L2}$, $C_2$, $R_{L3}$, and $C_3$ were carefully adjusted to give perfect phase balance in the SEIG for specific values of phase current. Typical results are summarized in Table 4.4. The good agreement between the computed and experimental values of the circuit parameters verifies the principle of phase balancing for a three-phase SEIG using the MSC.

TABLE 4.4
CIRCUIT CONDITIONS TO GIVE BALANCED OPERATION OF THREE-PHASE SEIG WITH MODIFIED STEINMETZ CONNECTION
(NORMAL: EXPERIMENTAL VALUES; BRACKETED: COMPUTED VALUES)

| $V_{ph}$ (p.u.) | $I_{ph}$ (p.u.) | $Y_p$ (p.u.) | $\phi_p$ (deg.) | $Z_2 = R_{L2} // C_2$ | | $Z_3 = R_{L3} // C_3$ | |
|---|---|---|---|---|---|---|---|
| | | | | $R_{L2}$ (p.u.) | $C_2$ (μF) | $R_{L3}$ (p.u.) | $C_3$ (μF) |
| 0.805 | 0.954 | 1.214 | 134.7 | 1.775<br>(1.873) | 168<br>(167) | 0.5069<br>(0.493) | 49<br>(46) |
| 0.899 | 0.878 | 0.975 | 130.8 | 2.88<br>(3.1) | 133<br>(132) | 0.641<br>(0.614) | 45<br>(44) |
| 0.999 | 1.006 | 1.007 | 125.6 | 4.91<br>(5.7) | 141<br>(139) | 0.644<br>(0.615) | 58<br>(57) |
| 0.985 | 0.768 | 0.779 | 120 | ∞<br>(∞) | 104<br>(107) | 0.872<br>(0.843) | 56<br>(54) |
| 1.064 | 1.019 | 0.957 | 120 | ∞<br>(∞) | 134<br>(134) | 0.675<br>(0.722) | 67<br>(67) |

Figs. 4.15 – 4.17 show the performance characteristics of the SEIG in which $C_2$ = 146 μF, $C_3$ = 47 μF and $R_{L2}$ = 94 Ω (2.3 p.u.). These values of phase converter elements result in perfect phase balance at an experimental load current of 1.52 p.u. and a phase current of 0.93 p.u. When the load is reduced, $I_B$ increases rapidly while $I_C$ decreases. On the other hand, $I_A$ remains substantially constant for load currents down to 0.8 p.u. Provided that the load does not vary too widely from that corresponding to perfect phase balance, satisfactory performance of the SEIG can still be obtained. Under no-load conditions,

however, there will be severe overcurrent and overvoltage in phase A and phase B, hence the excitation capacitances need to be reduced. Fig. 4.17 shows that, under perfect phase balance, the SEIG delivers a power of 1.31 p.u. and 0.323 p.u. (experimental values) to the main load and auxiliary load respectively. In other words, about 80% of the electrical power output is delivered to the main load. The total load is 1.63 p.u. (1940 W), which is 88% of the rated power of the induction machine. An experimental efficiency of 80% is obtainable at and close to the load corresponding to perfect phase balance. Very good agreement between the computed and experimental characteristics has been obtained.

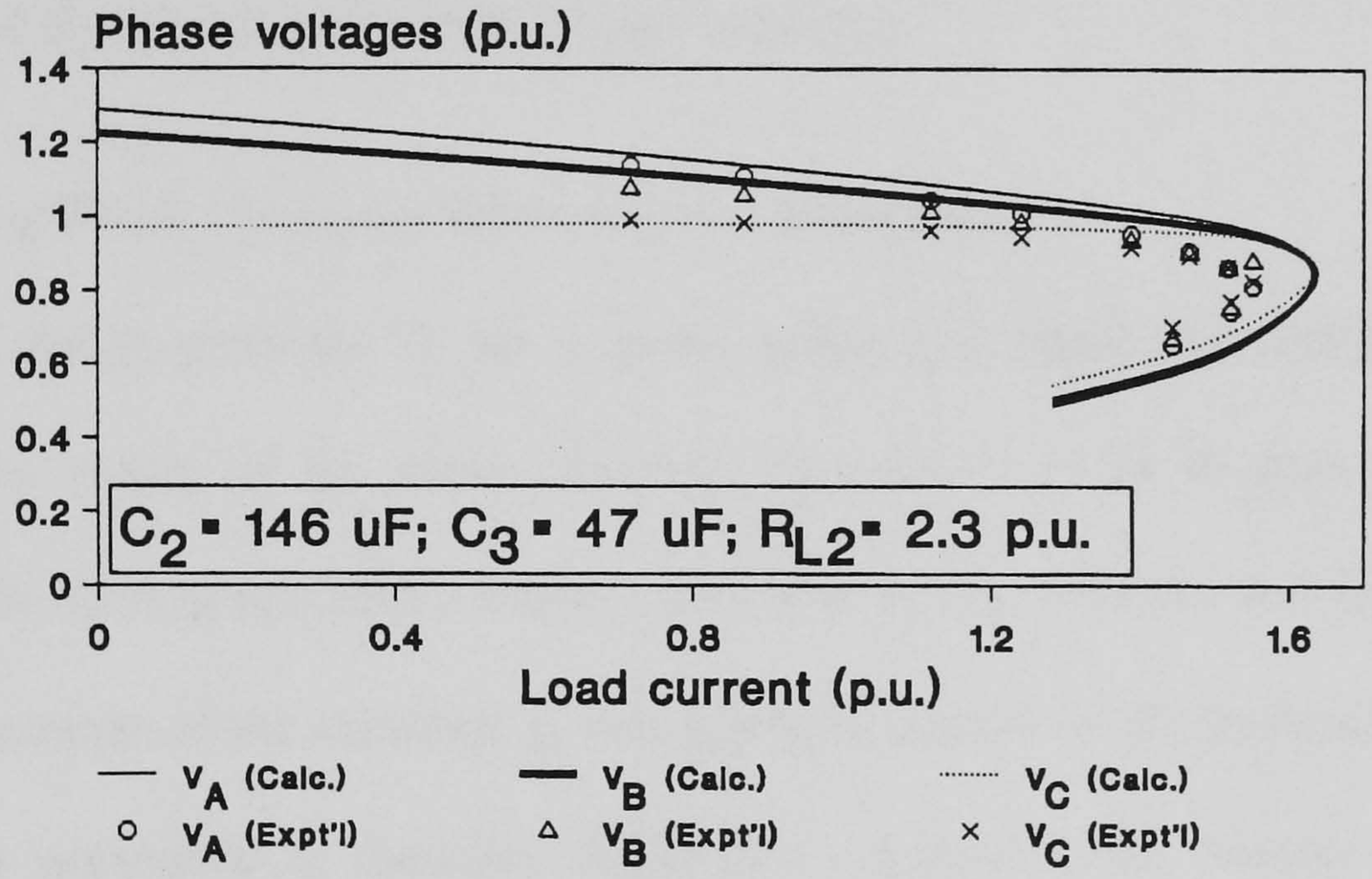


Fig. 4.15 Phase voltages of SEIG with MSC.

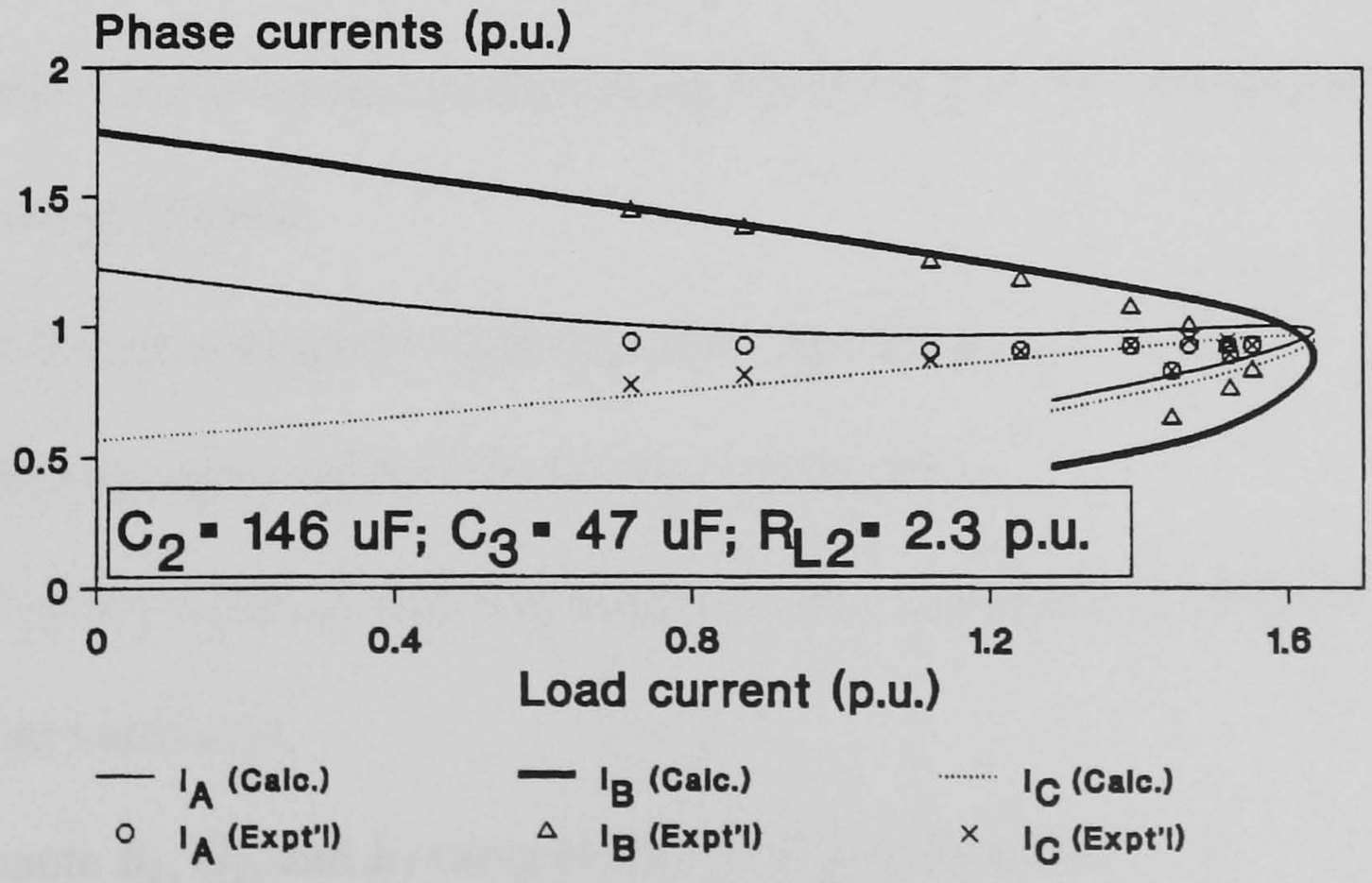


Fig. 4.16 Phase currents of SEIG with MSC.

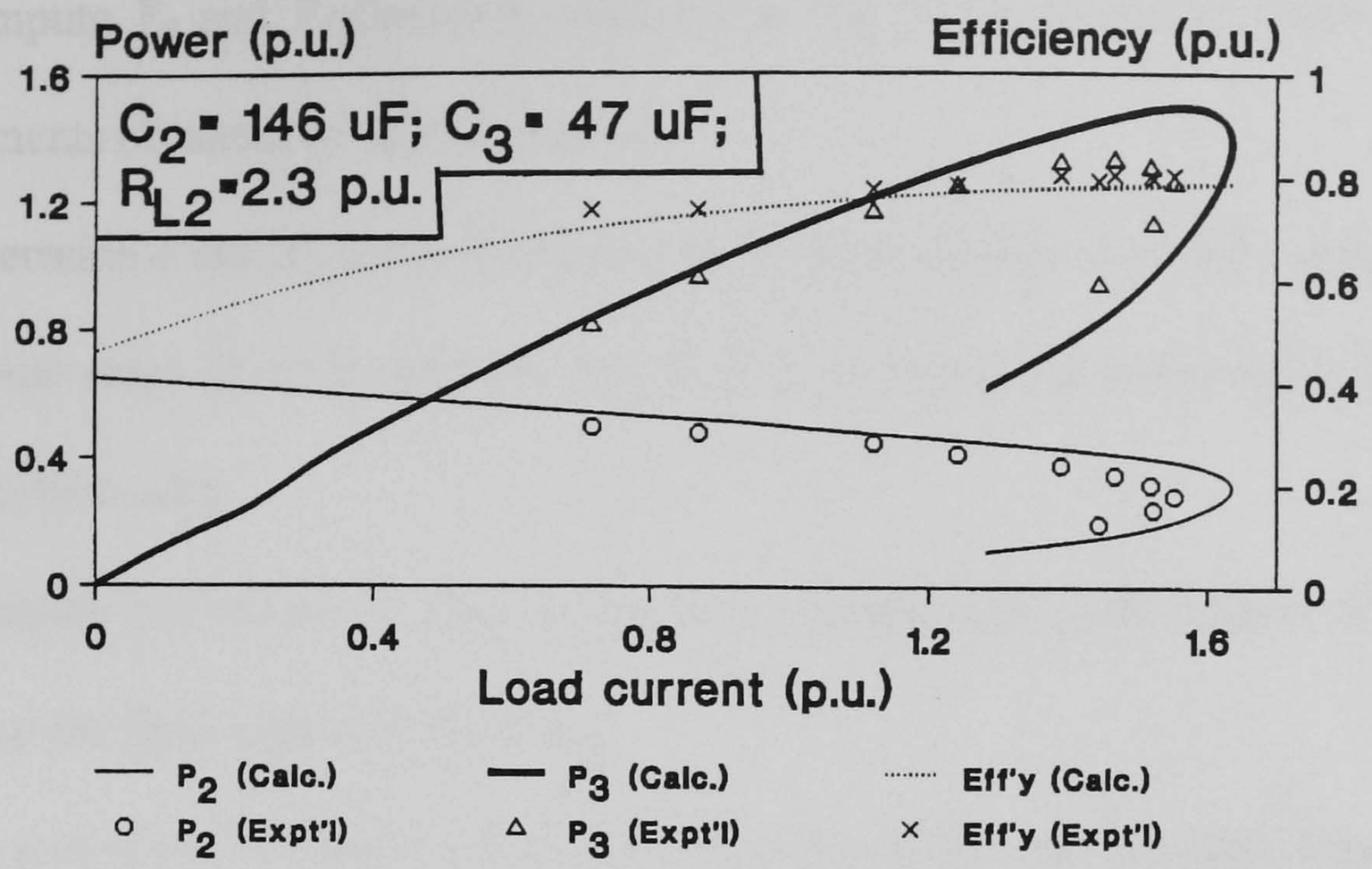


Fig. 4.17 Output power and efficiency of SEIG with MSC. ($P_2$: Output power to auxiliary load $R_{L2}$; $P_3$: Output power to main load $R_{L3}$)

*B) Selection of Phase Converter Elements for a Given Load*

A practical design problem is, for a given speed and main load resistance $R_{L3}$, to determine the values of the phase converter elements in order to give perfect phase balance in the three-phase SEIG. From (4.23)-(4.26), it is observed that $G_2$, $B_2$, $G_3$, and $B_3$ are all functions of the variables $Y_p$ and $\phi_p$ which depend on the terminal impedances. An iterative procedure is therefore required to determine the values of the phase converter elements that give perfect phase balance. For convenience, $\phi_p$ can first be specified while $Y_p$ is to be determined during the iterations. The iterative procedure may be summarized as follows:

1) Input the per-unit speed $b$ and specified value of $\phi_p$.

2) Assume an initial value of the per-unit frequency $a$.

3) For a given value of main load resistance $R_{L3}$, compute $|Y_p|$ from (4.25) using the current value of $a$.

4) Compute $B_2$, $G_2$, and $B_3$ using (4.23), (4.24), and (4.26).

5) Compute $Y_2$ and $Y_3$ (hence $R_3$ and $X_3$) in Fig. 4.13, using the values of circuit elements obtained in steps 3) and 4).

6) Determine $a$ and $X_m$ using the Hooke and Jeeves method outlined in Appendix B.

7) Repeat steps 3) to 6) until the values of $a$ in successive iterations is less than a specified value.

8) Compute the values of phase converter elements and performance of the SEIG using the final values of $a$ and $X_m$.

The above procedure has been tested with reference to the experimental machine IG1. Convergence can usually be obtained in three to five iterations. Fig. 4.18 and Fig. 4.19 show the computed values of $C_2$, $C_3$, and $R_{L2}$ to give perfect phase balance in the SEIG for given values of main load conductance $G_{L3}$. From Fig. 4.20, it is observed that both the phase voltage and phase current increase with decrease in $\phi_p$ until the limiting value of 120 electrical degrees is reached. The SEIG is thus more likely to experience overvoltage and overcurrent at small values of $\phi_p$.

Fig. 4.21 shows the total output power and efficiency of the SEIG with MSC under balanced conditions. At $\phi_p$ = 120 electrical degrees, rated current occurs when $G_{L3}$ = 1.4 p.u., and the total output power is 1.6 p.u. At $\phi_p$ = 135 electrical degrees, rated current occurs when $G_{L3}$ = 1.88 p.u. and the total output power is 1.86 p.u. From voltage, current, output power and efficiency considerations, it is desirable to operate the SEIG at higher values of $\phi_p$.

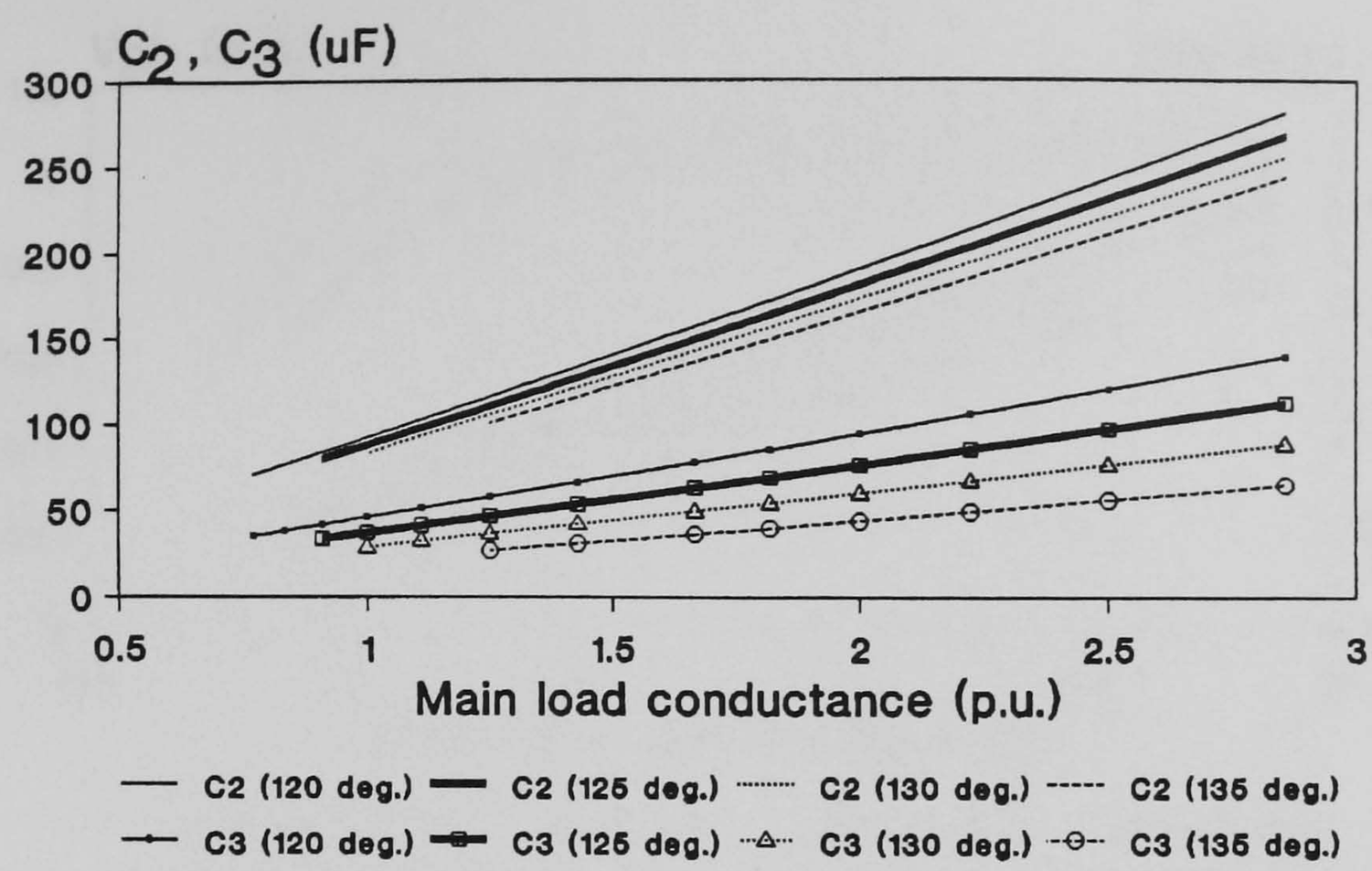


Fig. 4.18 Main and auxiliary excitation capacitances for perfect phase balance in SEIG with MSC.

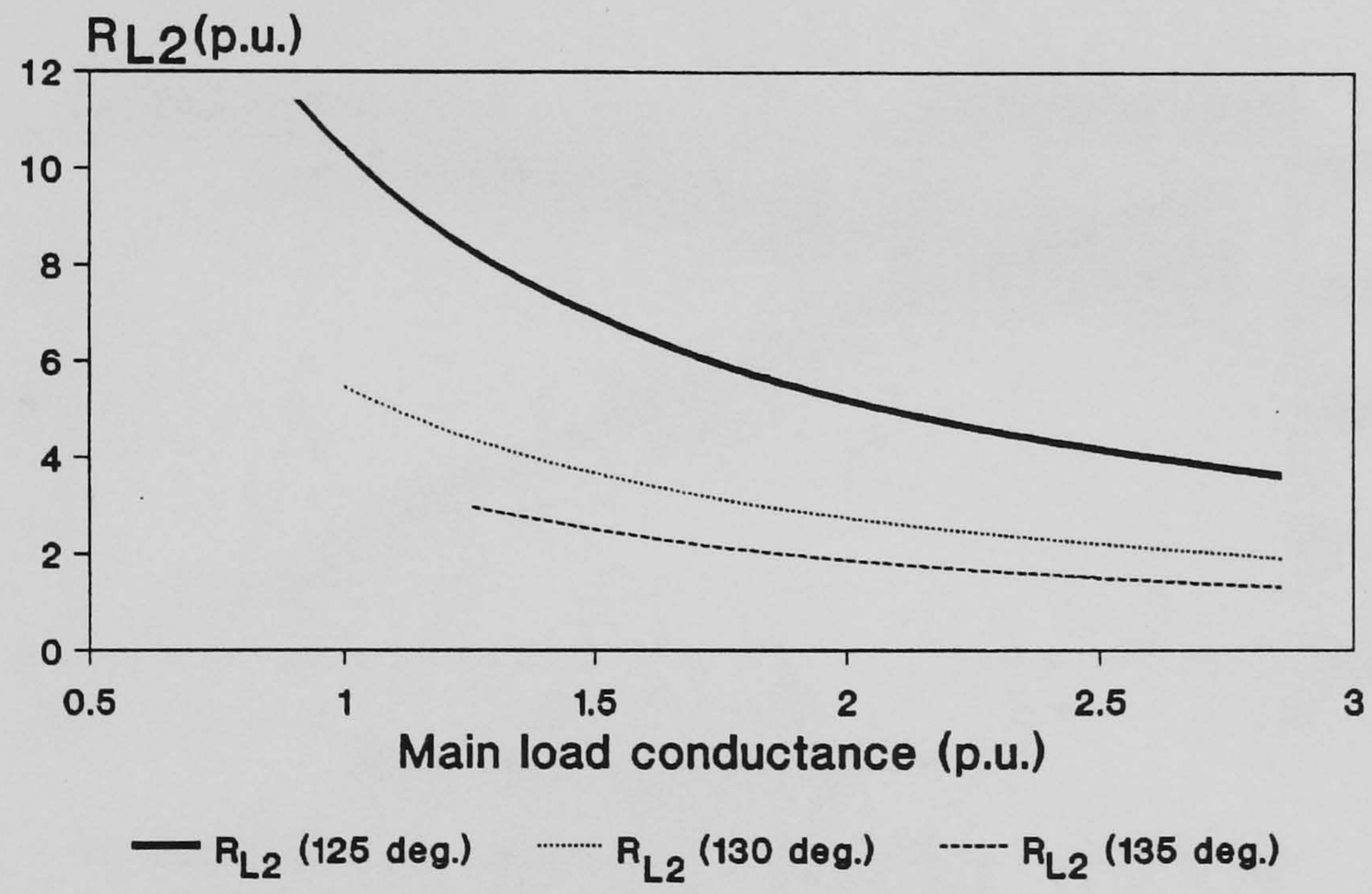


Fig. 4.19 Auxiliary load resistance for perfect phase balance in SEIG with MSC.

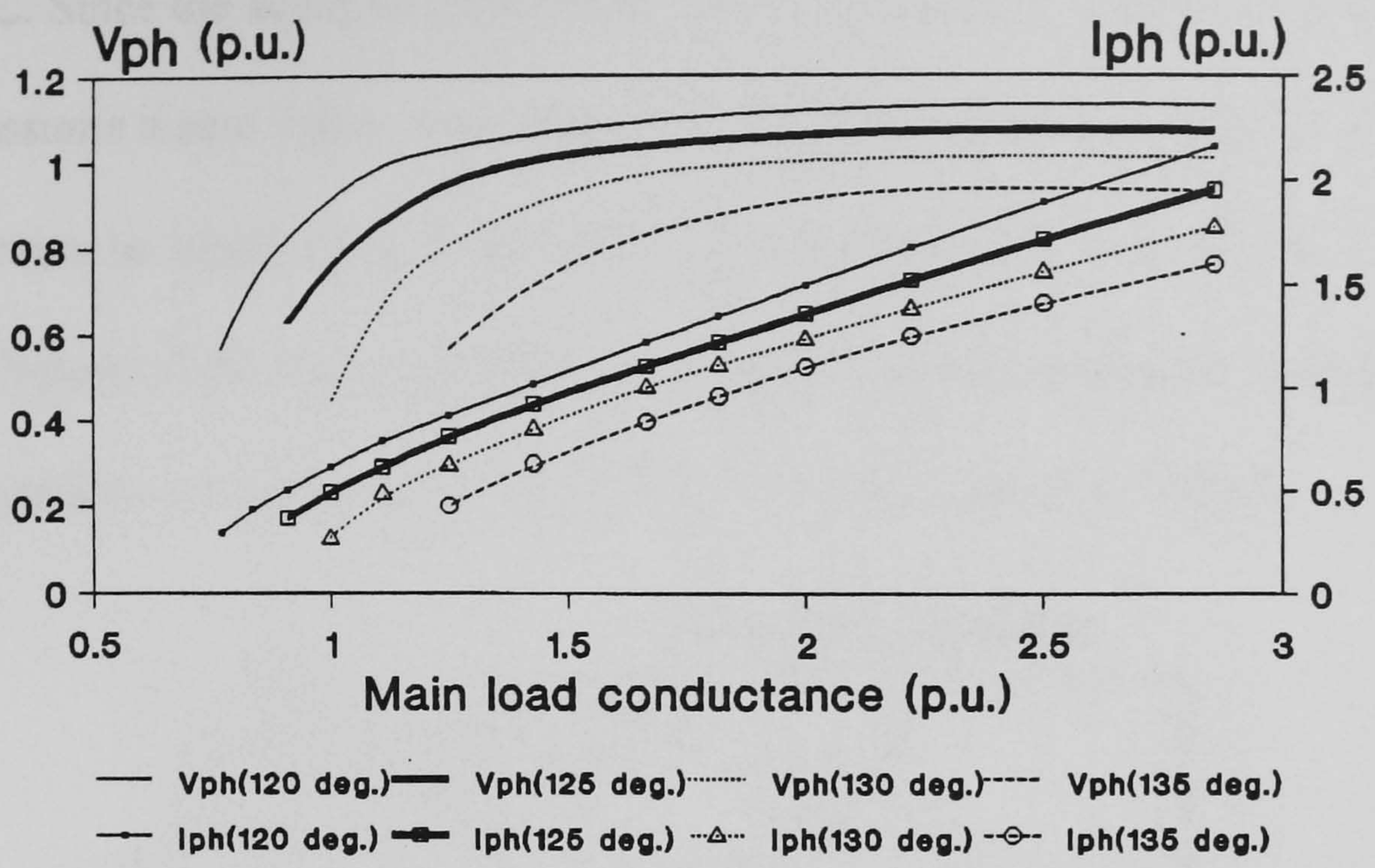


Fig. 4.20 Phase voltage and phase current of SEIG with MSC under perfect phase balance.

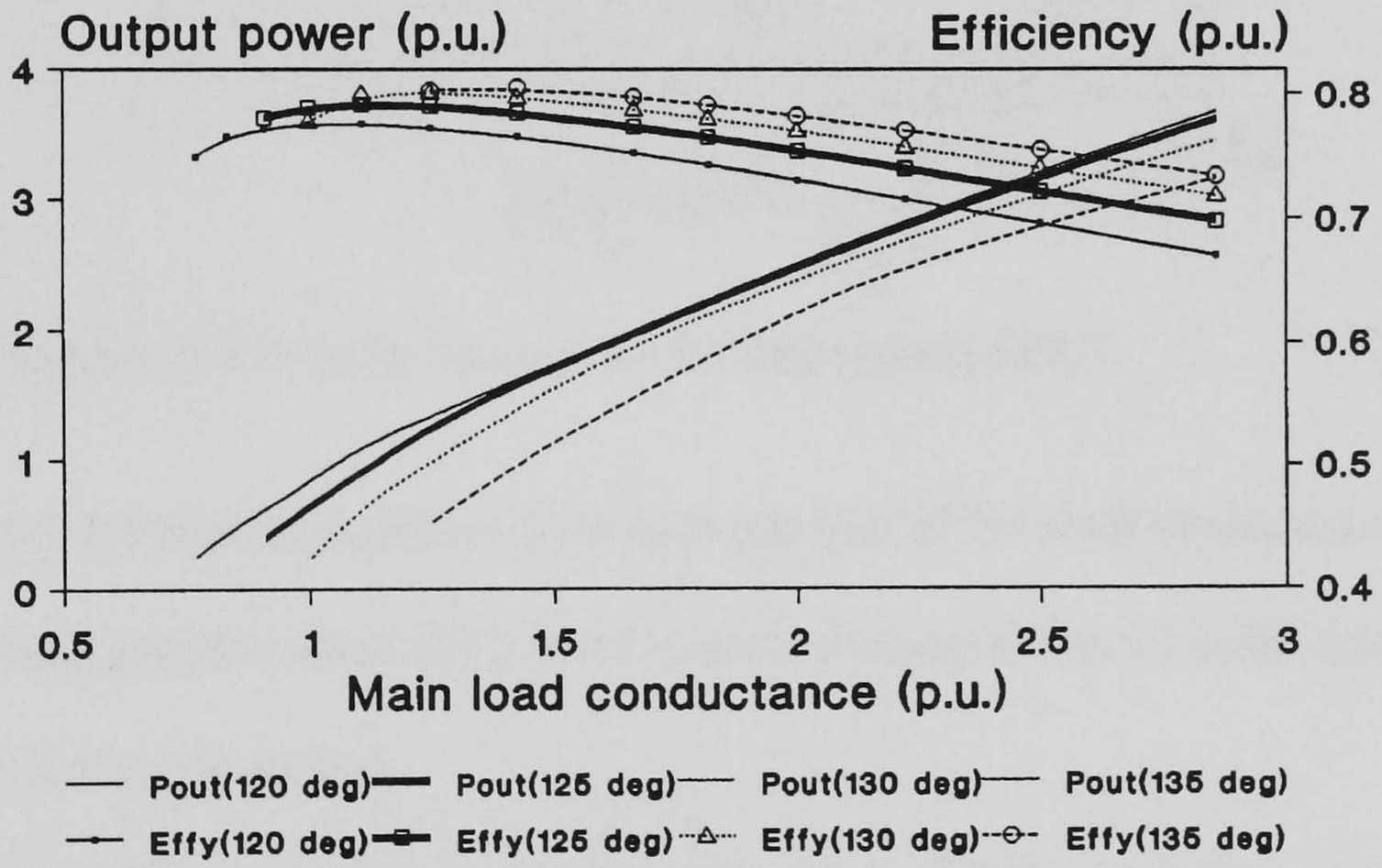


Fig. 4.21 Output power and efficiency of SEIG with MSC under perfect phase balance.

### 4.3.5 Simplified Steinmetz Connection (SSC)

In circumstances where it is not practicable to provide auxiliary loads, or when auxiliary loads need not be supplied, the simplified Steinmetz connection (SSC) shown in Fig. 4.22 may be employed. In this case, all the electrical power output of the SEIG is delivered to the single-phase load $R_{L3}$. The phasor diagram for MSC (Fig. 4.13) and the corresponding equations (4.23)-(4.26) may be used to identify the conditions for perfect phase balance

for the SSC. Since the auxiliary load resistance $R_{L2}$ is absent, the value of $G_2$ in (4.23) is forced to assume a zero value. Accordingly the positive-sequence impedance angle $\phi_p$ of the SEIG must be equal to $2\pi/3$ rad for (4.23) to be satisfied. From (4.24), (4.25) and (4.26), the values of the load conductance and phase-converter susceptances that result in balanced operation of the SEIG are: $B_2 = \sqrt{3}Y_p$, $G_3 = 3Y_p/2$, and $B_3 = \sqrt{3}Y_p/2$.

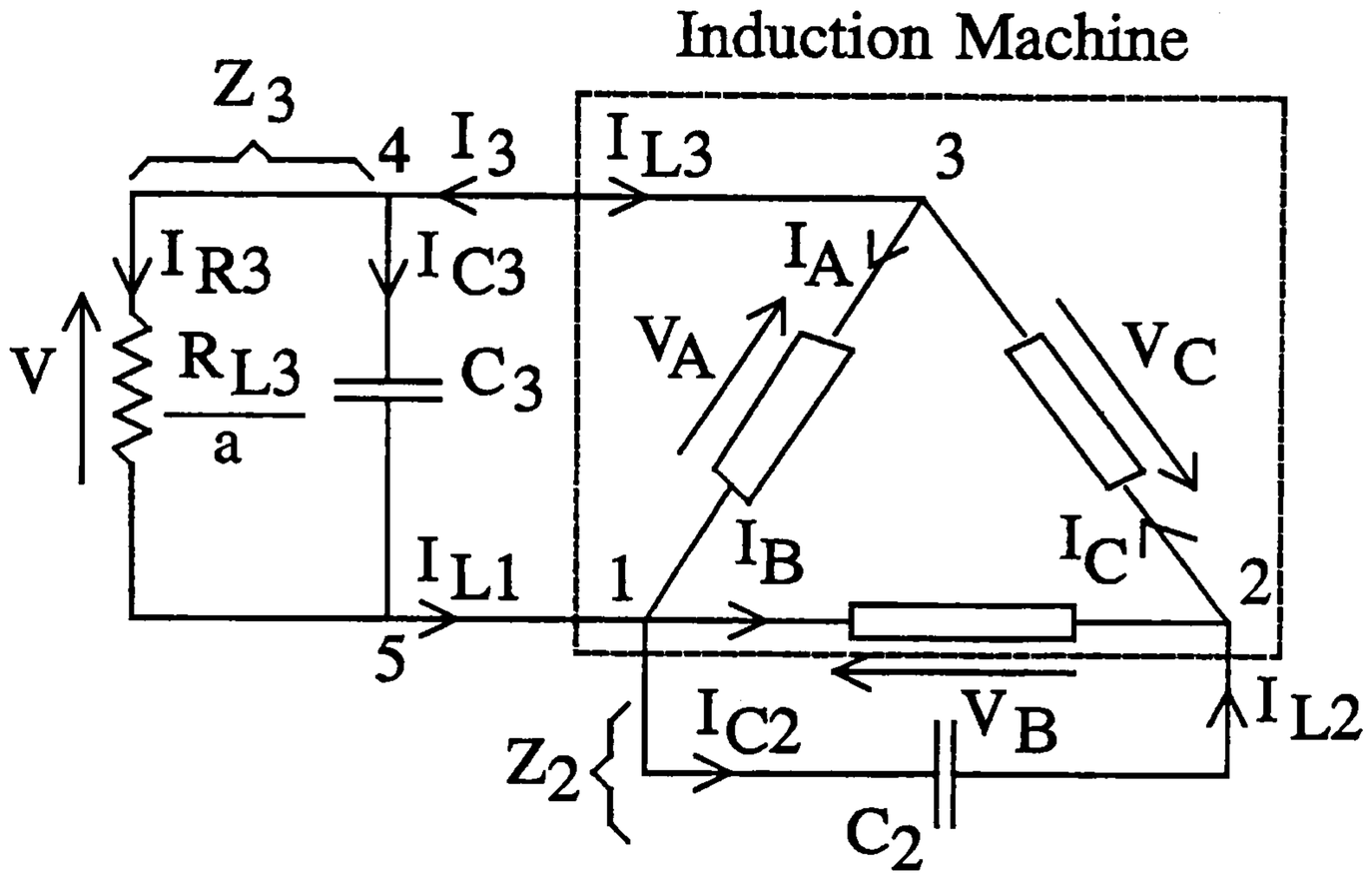


Fig. 4.22 Simplified Steinmetz connection for three-phase SEIG.

The auxiliary excitation capacitance $C_3$ is thus one half of the main excitation capacitance $C_2$. By selecting proper values of $C_2$ and $C_3$, perfect phase balance can be achieved for a specific value of stator current.

Analysis of the SEIG with SSC is similar to that for the SEIG with MSC, except that the admittance $Y_2$ is now equal to $(0 + jB_2)$.

Figs. 4.23 to 4.25 show the computed and experimental performance of the SEIG with SSC at rated speed. With main and auxiliary excitation capacitances fixed at 110 μF and 55 μF respectively, the SEIG is balanced at a load current (experimental value) of 1.13 p.u, which corresponds to a phase voltage of 0.985 p.u. and a phase current of 0.77 p.u. Under this condition, a power of 1.11 p.u. (1320 W) is delivered to the load and the

efficiency of the SEIG is 79.6%. Again very good agreement between the computed and experimental results is observed.

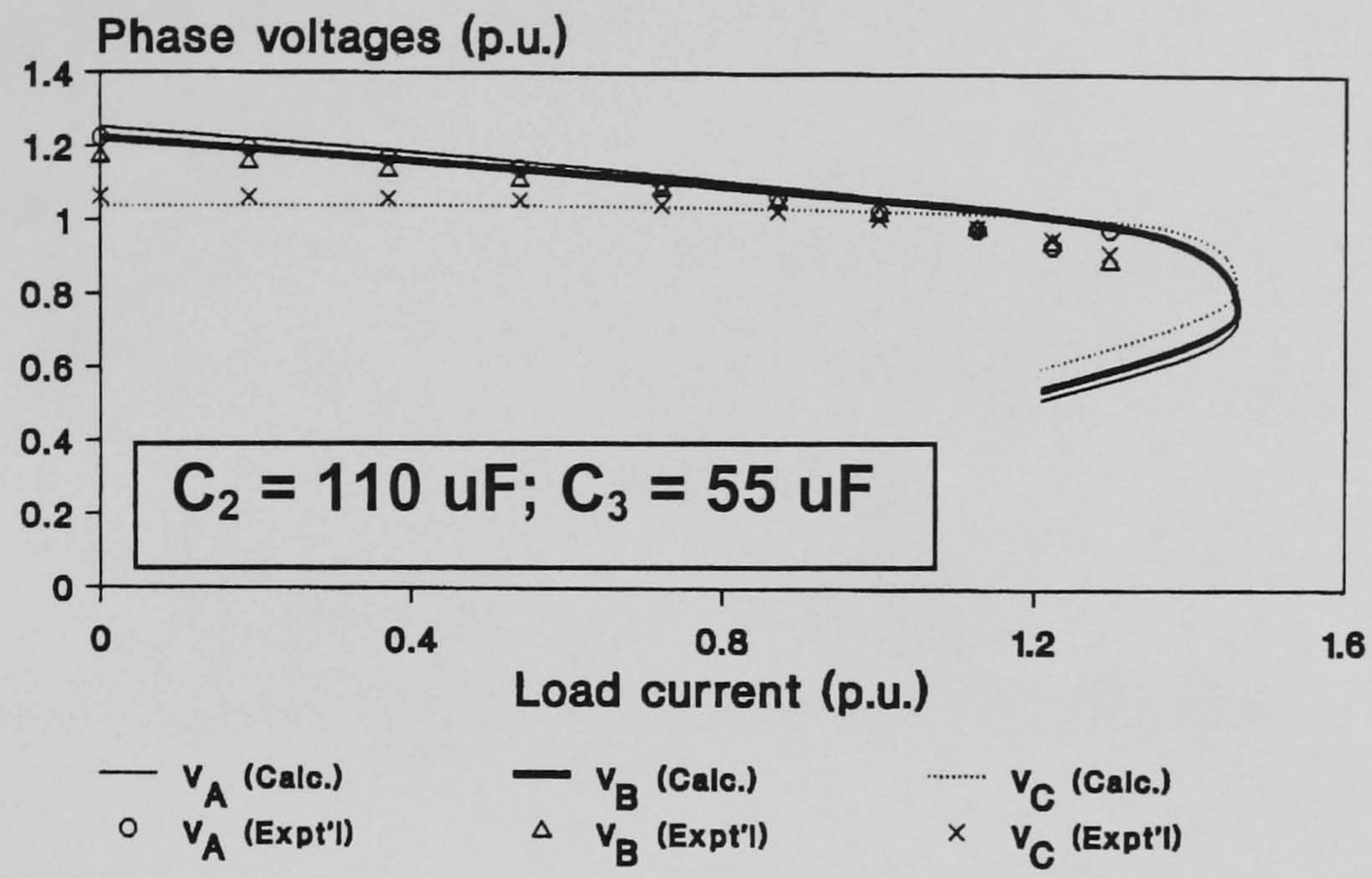


Fig. 4.23 Phase voltages of three-phase SEIG with SSC.

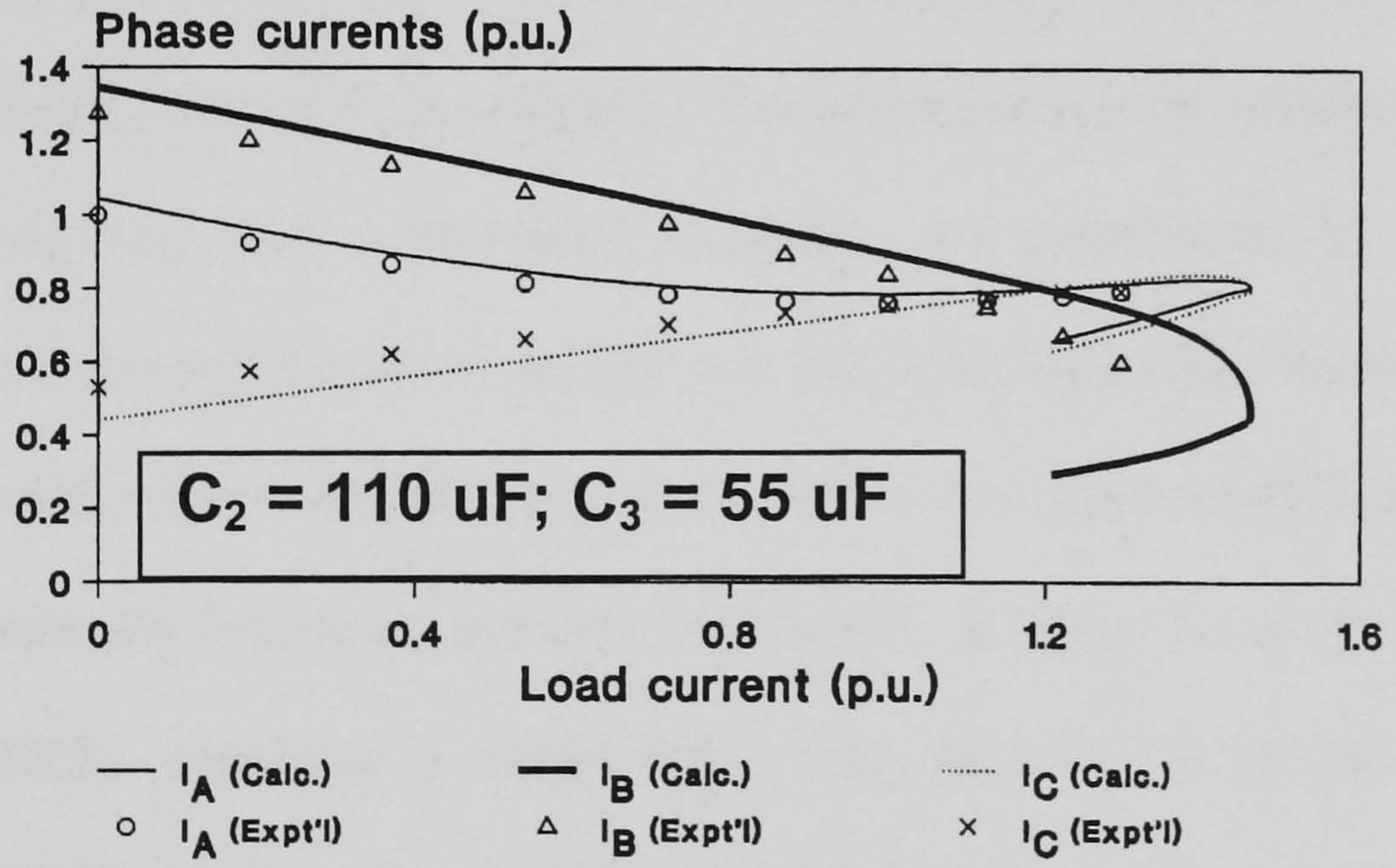


Fig. 4.24 Phase currents of three-phase SEIG with SSC.

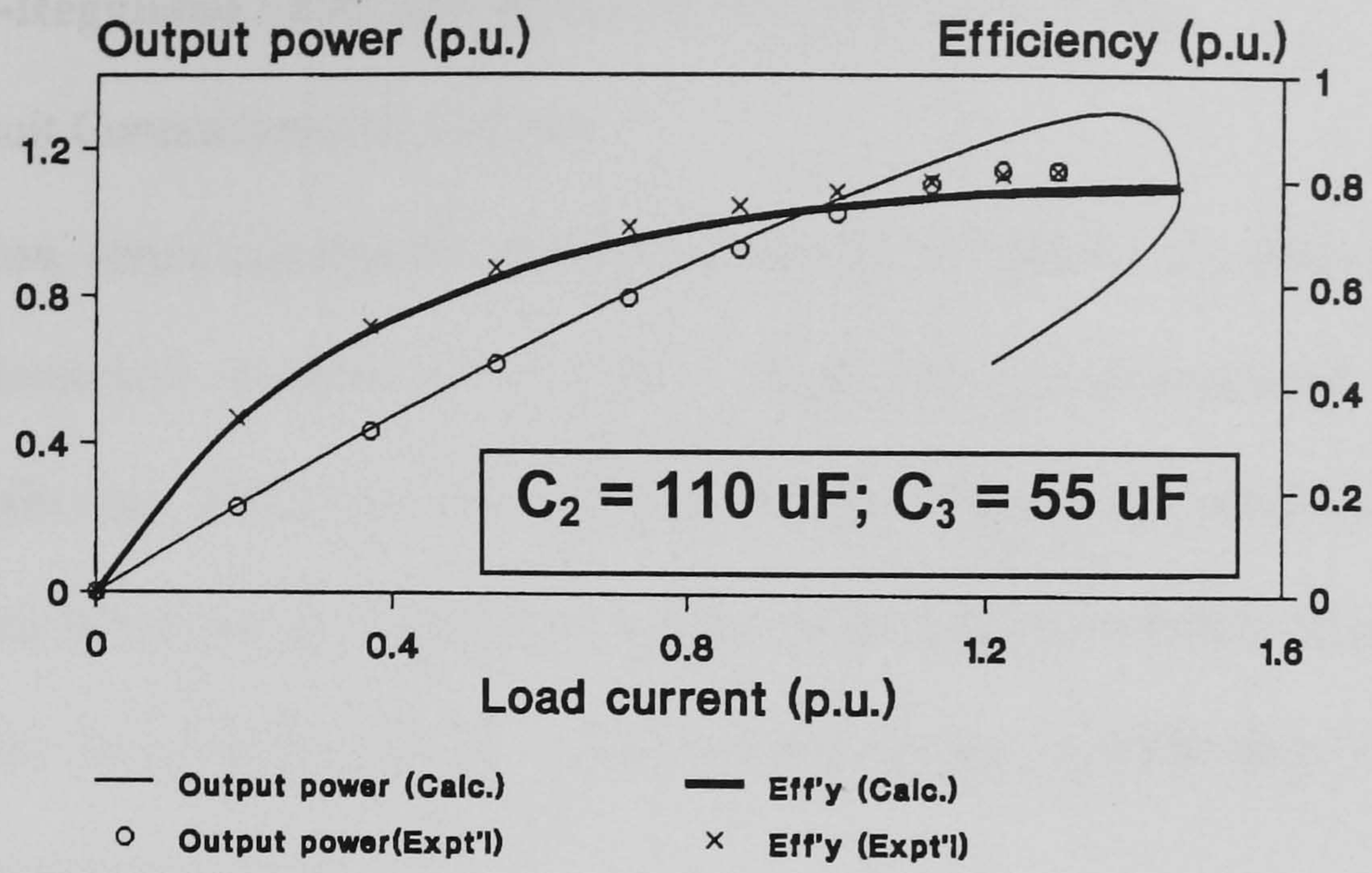


Fig. 4.25 Output power and efficiency of three-phase SEIG with SSC.

### 4.3.6 Summary

A general analysis for a three-phase SEIG with asymmetrically connected load and excitation capacitances has been presented. The equivalent circuit variables, namely the excitation frequency and magnetizing reactance, are determined by the function minimization method presented in Section 4.2. The close agreement between computed and experimental results obtained verifies the theory and solution method for an SEIG with asymmetrically connected terminal impedances. A phase-balancing scheme for a three-phase SEIG supplying a single-phase load, namely the modified Steinmetz connection (MSC), has also been investigated. From the voltage/current relationship in the phasor diagram, the conditions for balanced operation are deduced and an iterative method to determine the corresponding values of the phase converter elements for a given load has been developed. When there is no auxiliary load resistance, perfect phase balance can still be achieved provided that the auxiliary excitation capacitance is half of the main excitation capacitance. Since the MSC or the SSC scheme involves only passive circuit elements, it is an economical and effective method for achieving perfect phase balance in a three-phase SEIG that supplies single-phase loads.

## 4.4 Self-Regulated SEIG (SRSEIG) for Single-Phase Loads

### 4.4.1 Circuit Connection and Analysis

In this section, series capacitance compensation will be applied to a three-phase SEIG with the Steinmetz connection to give a single-phase self-regulated self-excited induction generator (SRSEIG) with reduced voltage regulation, better phase balance and increased power output. Besides, it will be shown that a condition of perfect phase balance in the three-phase machine could be achieved over a wide range of load with this new excitation scheme.

Fig. 4.26 shows the circuit connection of the single-phase SRSEIG for a delta-connected induction machine. The shunt excitation capacitance $C_{sh}$ is selected to give the desired no-load voltage, while the series compensation capacitance $C_{se}$ provides additional reactive power when the load current increases, resulting in a reduced voltage drop.

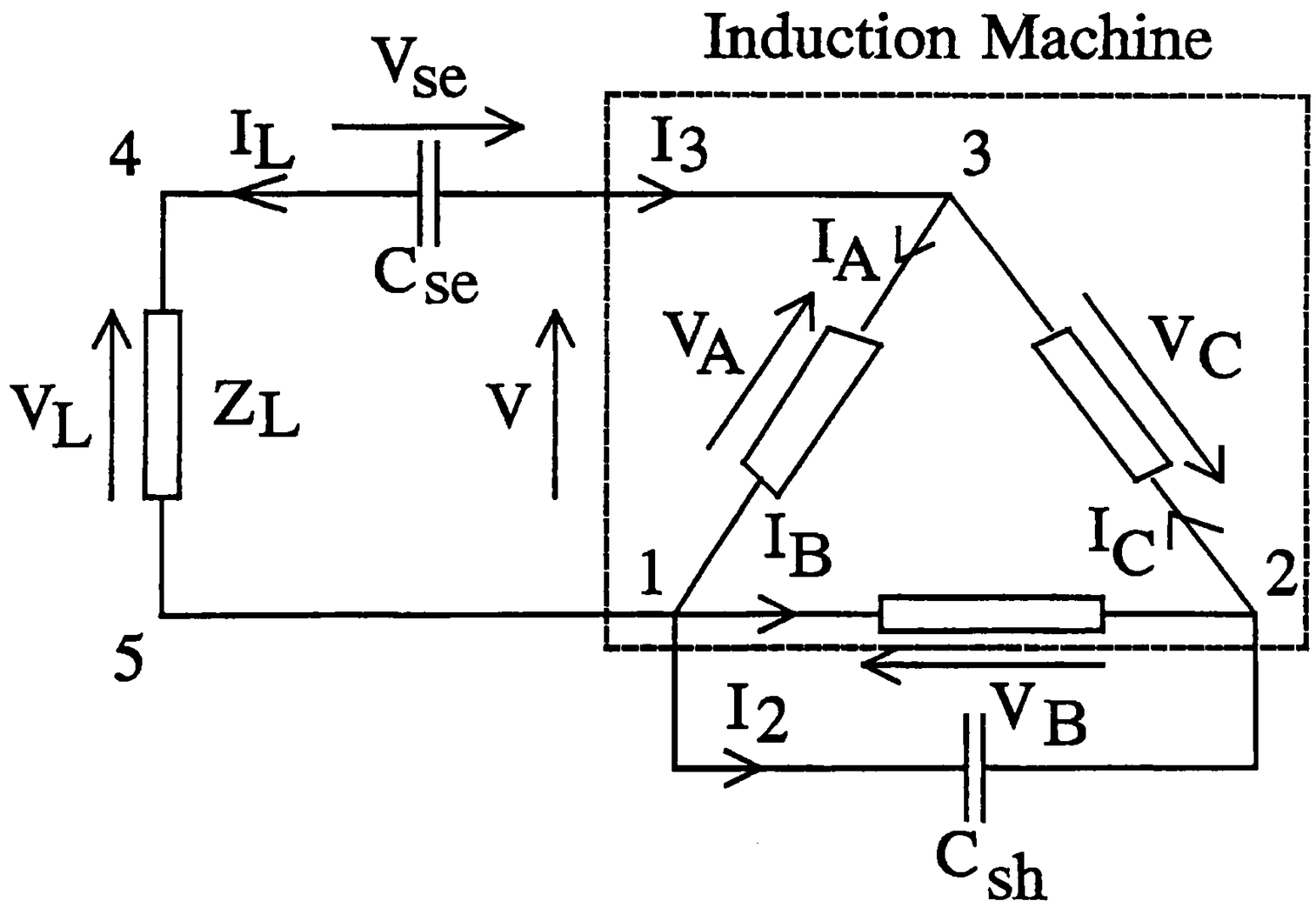


Fig. 4.26 Circuit connection of single-phase SRSEIG using a three-phase delta-connected induction machine.

A general analysis of the single-phase SRSEIG can be carried out using the method presented in Section 4.2. For the SRSEIG system, the input impedance $Z_{in}$ as viewed across terminals 1 and 3 is given by:

$$Z_{in} = \frac{Z_p Z_n + Z_p Z_{sh} + Z_n Z_{sh}}{3 Z_{sh} + Z_p + Z_n} \tag{4.27}$$

where

$$Z_{sh} = \frac{1}{j2\pi f_{base} \cdot C_{sh} \cdot a^2} = -j X_{sh} \,. \tag{4.28}$$

The complex impedance of the series capacitance $C_{se}$ is

$$Z_{se} = \frac{1}{j2\pi f_{base} \cdot C_{se} \cdot a^2} = -j X_{se} \,. \tag{4.29}$$

The following scalar impedance function should thus be minimized for solution of the SRSEIG circuit:

$$Z(a, X_m) = \sqrt{\left( R_{in} + \frac{R_L}{a} \right)^2 + ( X_{in} + X_L - X_{se} )^2} \,. \tag{4.30}$$

To simplify the calculations and for easy comparison, all the machine parameters are expressed in per-unit values using the rated phase voltage and rated phase current as bases. Table 4.5 shows the computed results for machine IG1 (technical details of which are given in Appendix D.1), with an excitation capacitance of 125 μF and a series compensation capacitance of 350 μF. The per-unit speed and the load power factor are both equal to unity. It is observed that, over a wide range of load impedance, the number of function evaluations $N$ required for a solution varies from 330 to 550. The results here indicate that the Hooke and Jeeves method is computationally efficient and is suitable for solving the single-phase SRSEIG performance analysis problem. The accuracy is very good as observed from the function minima obtained in Table 4.5.

TABLE 4.5
COMPUTED RESULTS FOR SINGLE-PHASE SRSEIG USING THE HOOKE AND JEEVES METHOD
$C_{sh}$ = 125 μF; $C_{se}$ = 350 μF; $b$ = 1.0, P.F. = 1.0
$a_0 = 0.97b$; $X_{m0} = X_{mu}$ = 2.48 p.u.

| $R_L$ (p.u.) | $a$ | $X_m$ (p.u.) | Number of function evaluations $N$ | $Z(a,X_m)$ (p.u.) |
|---|---|---|---|---|
| 50 | 0.9916 | 1.6226 | 381 | 9.06e-4 |
| 10 | 0.9900 | 1.6329 | 332 | 1.32e-4 |
| 5 | 0.9880 | 1.6443 | 390 | 6.24e-5 |
| 2 | 0.9823 | 1.6686 | 396 | 1.32e-5 |
| 1 | 0.9737 | 1.6771 | 356 | 6.43e-7 |
| 0.5 | 0.9593 | 1.5982 | 417 | 8.53e-7 |
| 0.3 | 0.9455 | 1.4056 | 509 | 2.92e-7 |
| 0.1 | 0.9240 | 0.8335 | 386 | 4.0 e-7 |

### 4.4.2 Effect of Series Compensation Capacitance

It is of interest to investigate the effect of $C_{sh}$ and $C_{se}$ on the performance of the single-phase SRSEIG. In practice, $C_{sh}$ is chosen so as to secure self-excitation and a stable operating point without causing excessive phase voltages and currents at no load. Depending on the voltage regulation and phase balance requirements, different values of $C_{se}$ could be chosen. To facilitate the subsequent discussion, a parameter called the compensation factor $K$ is defined as follows:

$$K = \frac{X_{se}}{X_{sh}} = \frac{C_{sh}}{C_{se}} \tag{4.31}$$

where $X_{sh}$ and $X_{se}$ have been defined in (4.28) and (4.29), respectively.

For the purpose of comparison, it is assumed in this section that the single-phase SRSEIG is operating at rated speed and is supplying a unity-power-factor load.

*A) Voltage regulation*

When choosing the value of the series compensation capacitance $C_{se}$, one should consider the voltage drop across $C_{se}$ as well as the amount of compensating reactive power available. A large value of $C_{se}$ results in a smaller voltage drop, but the reactive

power ($I_L^2 X_{se}$) generated is also small. On the other hand, a small value of $C_{se}$ results in a larger voltage drop but provides more reactive power for voltage compensation.

Fig. 4.27 shows the computed variation of magnetizing reactance $X_m$ of the experimental SRSEIG (for which $X_{mu}$ = 2.48 p.u.) with the load admittance $Y_L$ for different values of $K$ when a shunt excitation capacitance of 125 μF is used. Without series compensation ($K$ = 0), $X_m$ increases rapidly with load conductance and reaches the unsaturated value of 2.48 p.u. when $Y_L$ is equal to 2.05 p.u. At larger values of $K$, the range of $Y_L$ over which $X_m$ is less than the unsaturated value is extended. This implies that the SRSEIG is capable of maintaining a high terminal voltage over a wider range of load. At $K$ = 0.357, $X_m$ remains substantially constant over the practical range of $Y_L$, i.e. the saturation level of the machine is only slightly affected by the load.

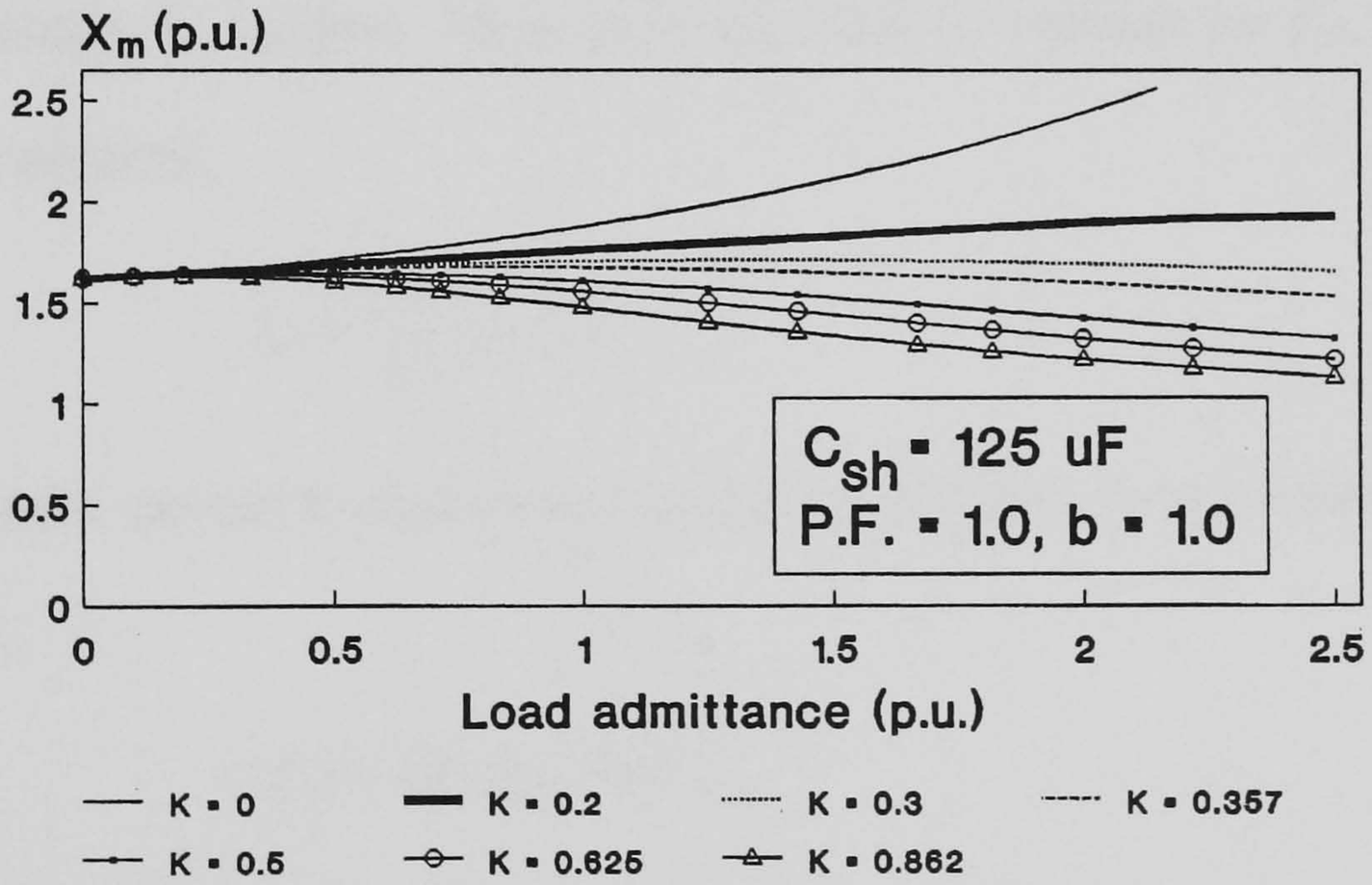


Fig. 4.27 Variation of magnetizing reactance with load admittance.

Fig. 4.28 shows the computed variation of load voltage with $Y_L$ under the above operating conditions. Best voltage regulation characteristics are obtained when $K$ is between 0.3 and 0.5. When $K$ is less than 0.25 or greater than 0.8, the load voltage decreases significantly.

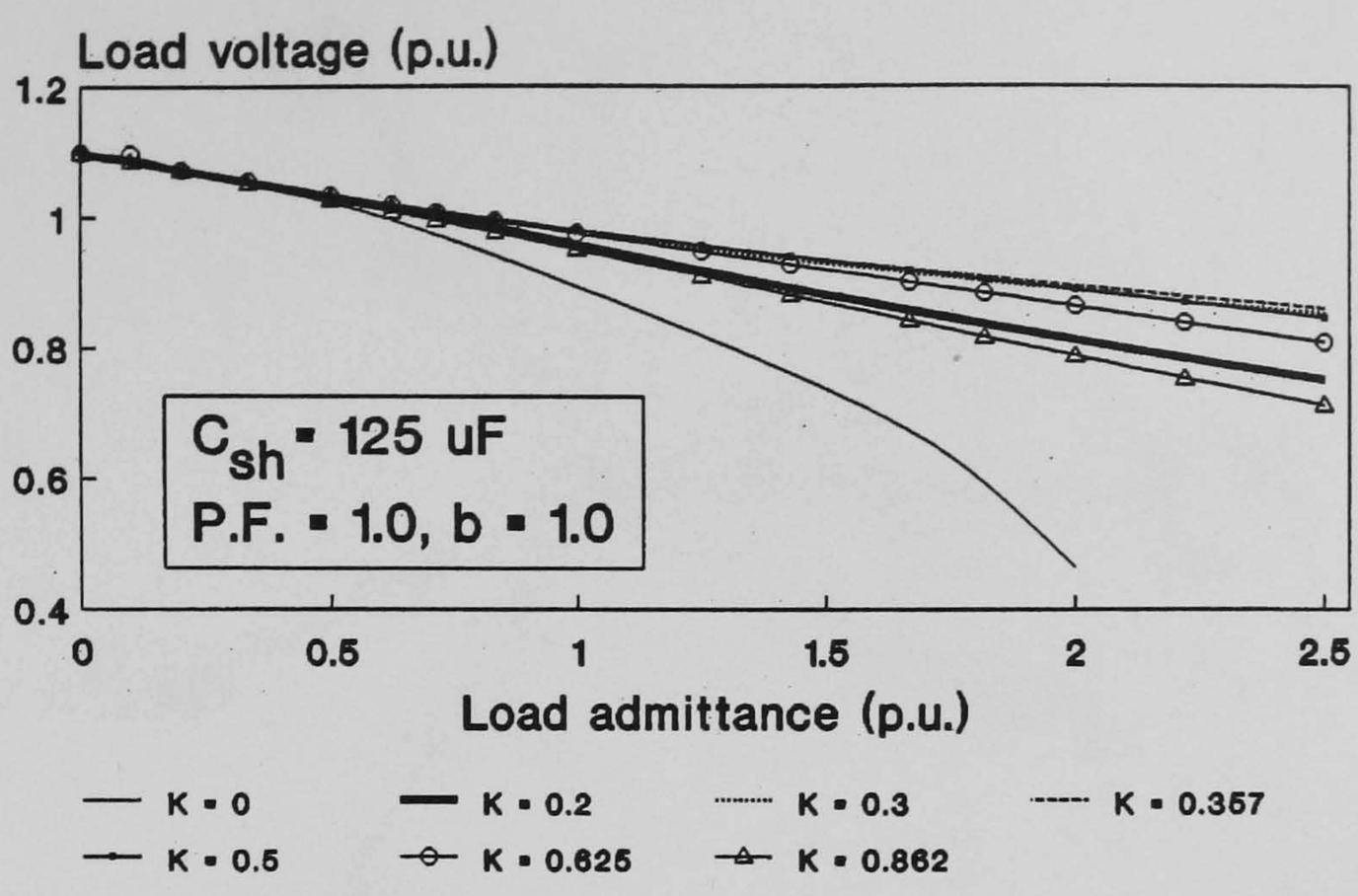


Fig. 4.28 Variation of load voltage with load admittance.

*B) Phase balancing capability*

One novel feature of the single-phase SRSEIG is that it can operate with balanced phase voltages and currents in the three-phase machine. This occurs when the negative-sequence voltage $V_n$ vanishes. From (4.7) and with $Z_C$ replaced by $Z_{sh}$, the following condition is deduced:

$$Z_{sh} + \frac{e^{-j\pi/6}}{\sqrt{3}} . Z_p = 0 . \tag{4.32}$$

Since the shunt excitation capacitance may be considered to be lossless, from (4.32) one obtains,

$$|Z_p| = \sqrt{3}\,|Z_{sh}| = \sqrt{3}\,X_{sh} \tag{4.33}$$

and

$$\phi_p = \frac{2\pi}{3} \tag{4.34}$$

where $\phi_p$ is the positive-sequence impedance angle of the three-phase induction machine.

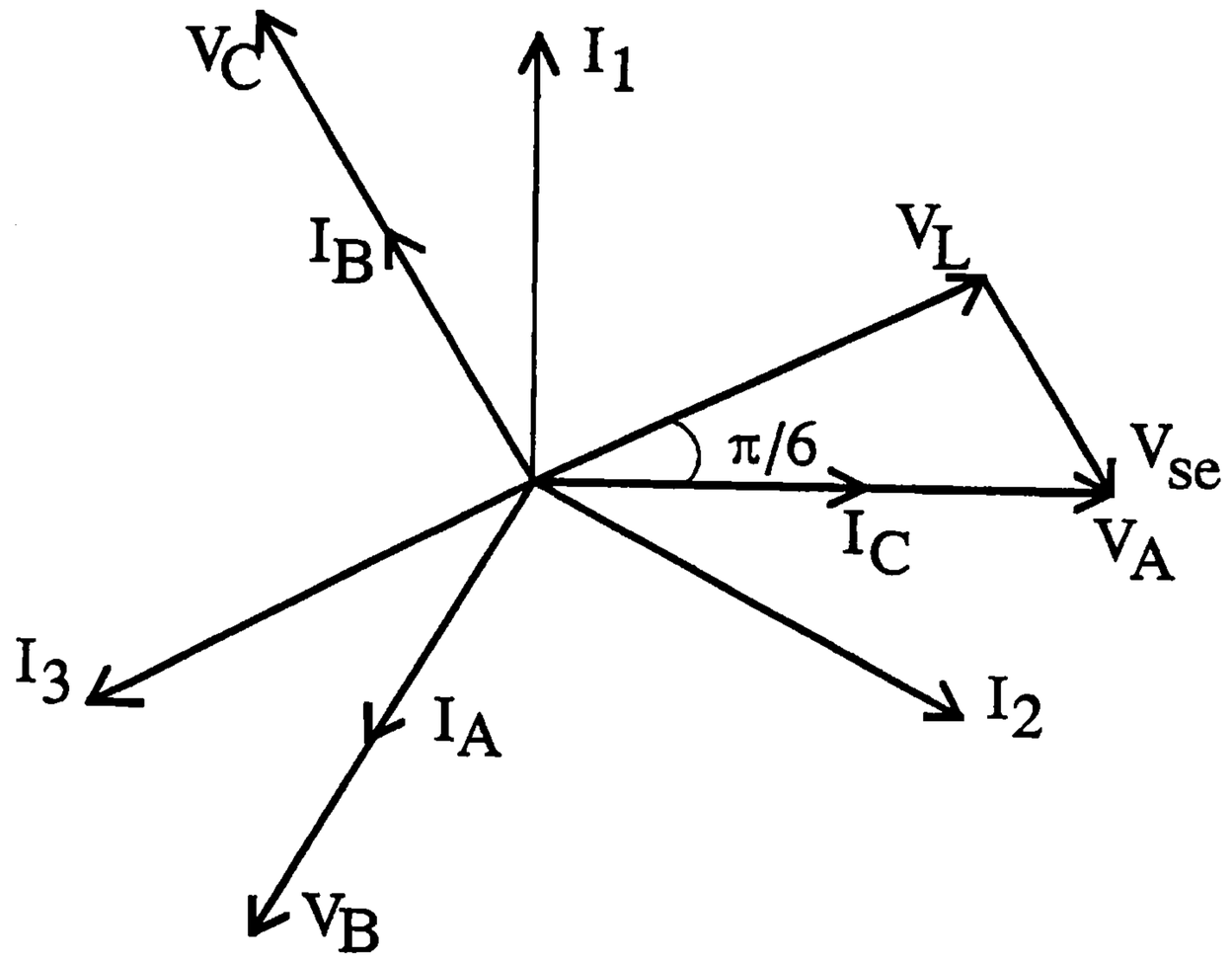


Fig. 4.29 Phasor diagram of single-phase SRSEIG when the three-phase machine is balanced at a unity-power-factor load.

Fig. 4.29 shows the phasor diagram of the SRSEIG under perfect phase balance conditions. From the diagram, the following relationships can be deduced:

$$|Z_{se}| = X_{se} = \frac{Z_p}{2\sqrt{3}} \tag{4.35}$$

$$\frac{R_L}{a} = \sqrt{3}\, X_{se} = \frac{|Z_p|}{2} \tag{4.36}$$

and

$$V_L = \frac{\sqrt{3}}{2} . V_A . \tag{4.37}$$

From (4.33) and (4.35),

$$X_{sh} = 2\, X_{se} \tag{4.38}$$

or

$$C_{se} = 2\, C_{sh} . \tag{4.39}$$

Eqns. (4.36), (4.38) and (4.39) imply that perfect phase balance in the three-phase induction machine can be achieved when a compensation factor of 0.5 is used and the

load resistance (referred to the base frequency) is numerically equal to one-half of the positive-sequence impedance. Under these conditions, the load voltage is 0.866 times the terminal voltage of the three-phase machine, while the generator impedance angle is equal to $2\pi/3$ electrical radians.

*C) Capacitances for perfect phase balance*

A practical design problem is the selection of $C_{sh}$ and $C_{se}$ to give perfect phase balance for a given load resistance $R_L$. When the speed of the IG is regulated to give a constant frequency in the output voltage, $C_{sh}$ and $C_{se}$ can be determined directly from (4.33) and (4.35). For constant-speed operation, however, the per-unit frequency is a function of the load and the excitation capacitances, which are not known until the SRSEIG circuit is completely solved. To overcome this difficulty, the following iterative solution procedure is proposed:

1) Input the values of per-unit speed and load resistance $R_L$.

2) Assume an initial value of the per-unit frequency $a$.

3) Compute $X_{sh}$ and $X_{se}$ from eqns. (4.33) and (4.35).

4) Solve the SRSEIG circuit for $a$, $X_m$, and $Z_p$ using the above values of $X_{se}$ and $X_{sh}$.

5) Repeat steps 3) and 4) until the per-unit frequency $a$ in successive iterations differ by a sufficiently small value (say 1.0e-6).

6) Determine $C_{sh}$ and $C_{se}$ using the final values of $a$ and $X_m$.

7) Compute the generator performance.

Fig. 4.30 shows the computed and experimental values of the shunt and series capacitances to give balanced operation for the experimental machine. The values of $C_{sh}$ and $C_{se}$ required increase approximately linearly with the load admittance. At light

loads, the combination of $R_L$, $C_{sh}$ and $C_{se}$ may force the magnetizing reactance of the IG to exceed the unsaturated value, implying that the operating point does not exist.

The results in Fig. 4.30 show that, by a proper selection of the excitation capacitance, compensation capacitance and load resistance, it is possible to obtain perfect balance in the three-phase machine over a wide range of load.

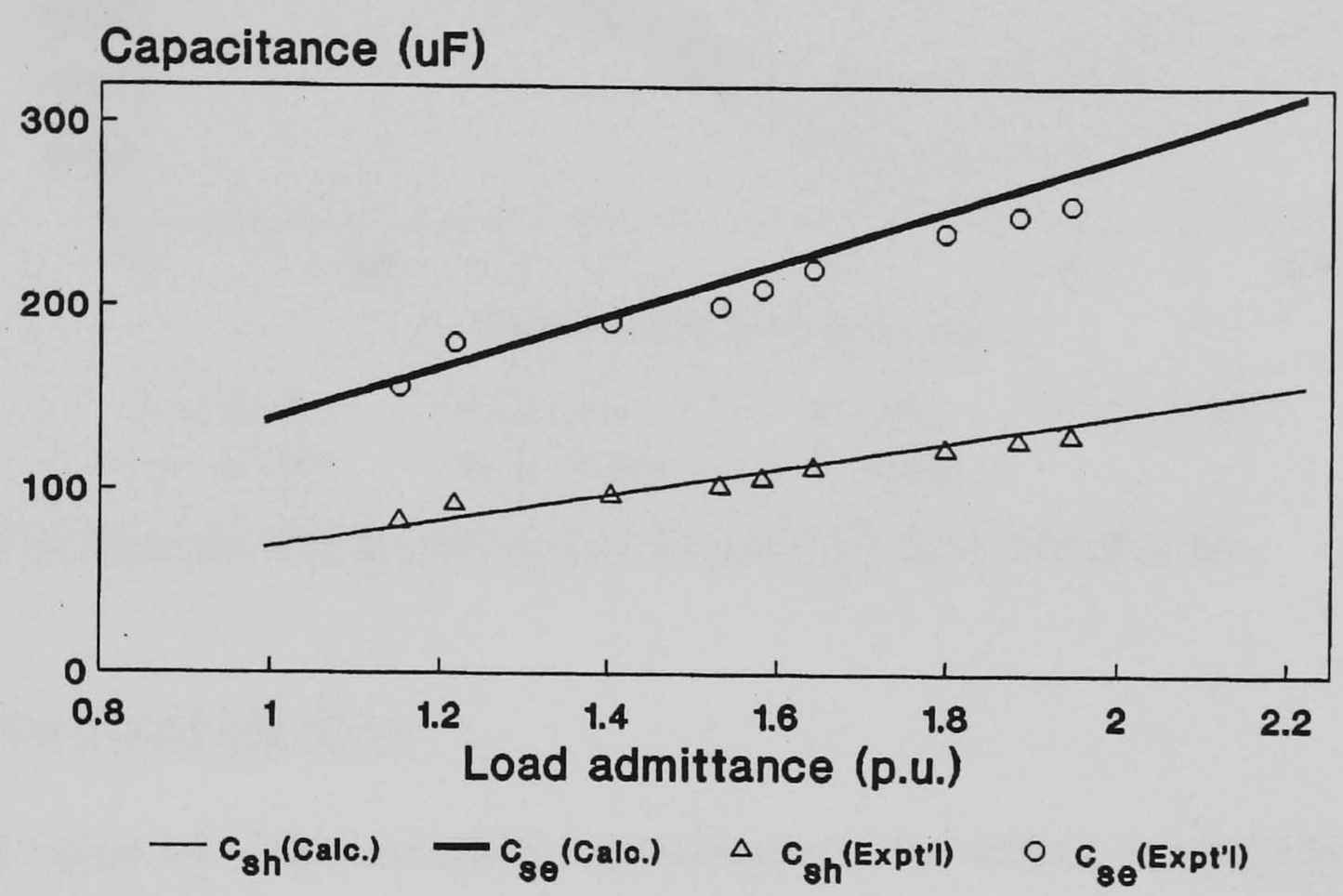


Fig. 4.30 Computed and experimental values of capacitances to give balanced operation in the three-phase machine at unity-power-factor loads.

*D) Voltage unbalance factor*

Balanced operation can only be achieved for a given combination of $R_L$, $C_{sh}$ and $C_{se}$. When the load or the compensation factor changes, the three-phase machine will again be unbalanced. The degree of unbalance is conveniently described in terms of voltage unbalance factor (VUF) which is defined as the ratio of the negative-sequence voltage $V_n$ to the positive-sequence voltage $V_p$. Fig. 4.31 shows the effect of compensation factor $K$ on the VUF when the shunt excitation capacitance is constant at 125 μF. It is interesting to note that for each value of $K$, the variation of VUF with load admittance is a V-shaped curve. Besides, the VUF becomes smaller as the value of $K$ is closer to

0.5. When $K$ is equal to 0.5, the minimum phase imbalance in the three-phase machine is obtained, with zero VUF occurring at a load admittance of 1.82 p.u.

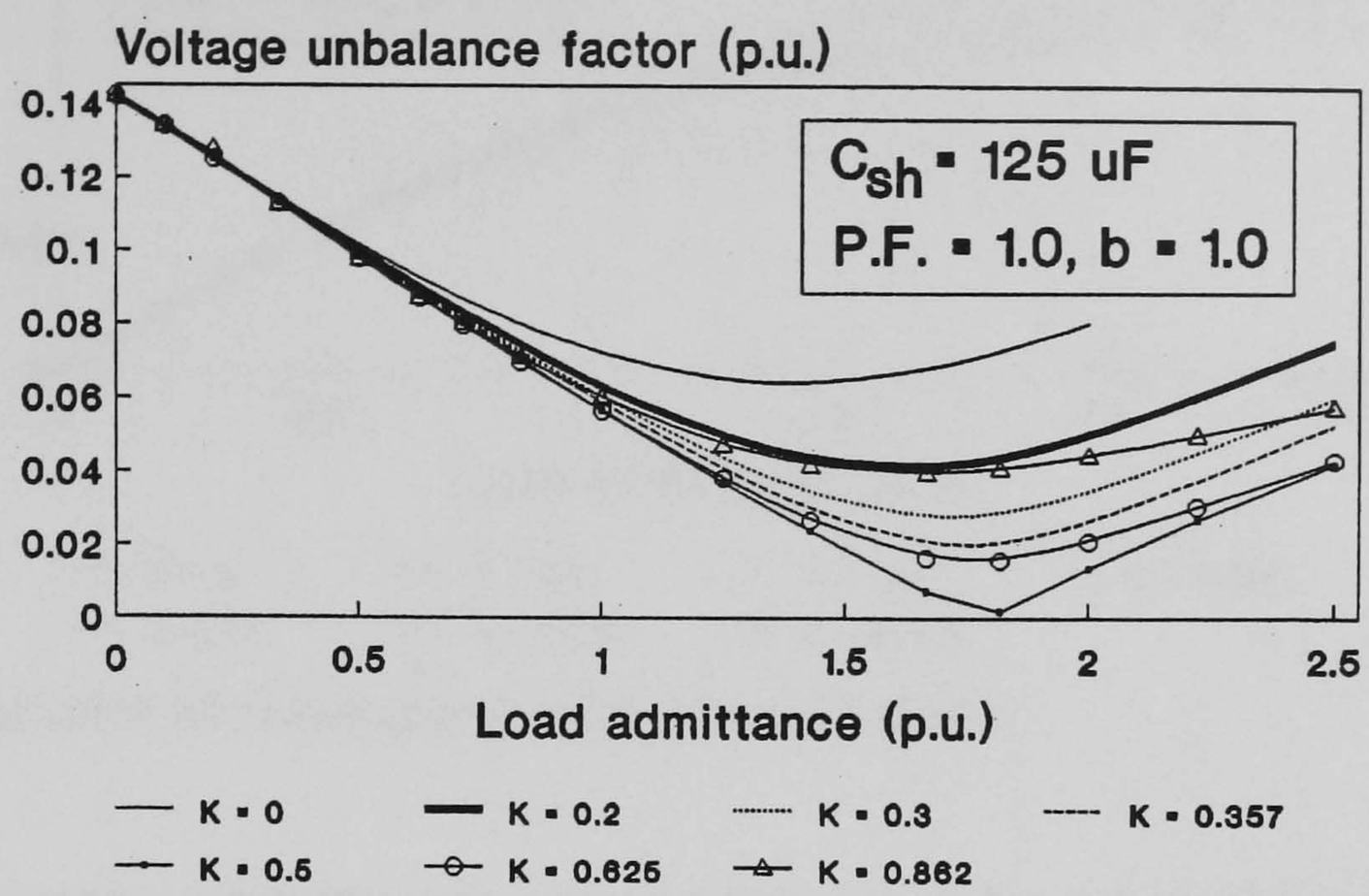


Fig. 4.31 Variation of voltage unbalance factor with load admittance.

*E) Output power and efficiency*

For a given value of shunt excitation capacitance, the output power from the single-phase SRSEIG depends on the series compensation capacitance used. Fig. 4.32 shows the computed variation of output power of the experimental machine with load admittance when $C_{sh}$ is equal to 125 μF. With no compensation (i.e. $K = 0$), a power limit occurs at a load admittance of about 1.3 p.u and loss of excitation occurs when the load admittance is equal to 2.05 p.u. When $K$ exceeds 0.2, a marked increase in the output power is obtained and stable operation of the single-phase SRSEIG is possible even with very large values of load admittance. The output power from the machine is large when $K$ is between 0.3 and 0.5, the best power output being obtained when $K$ is equal to 0.357. This observation suggests that the use of very large values of compensation capacitance is unnecessary and should be avoided.

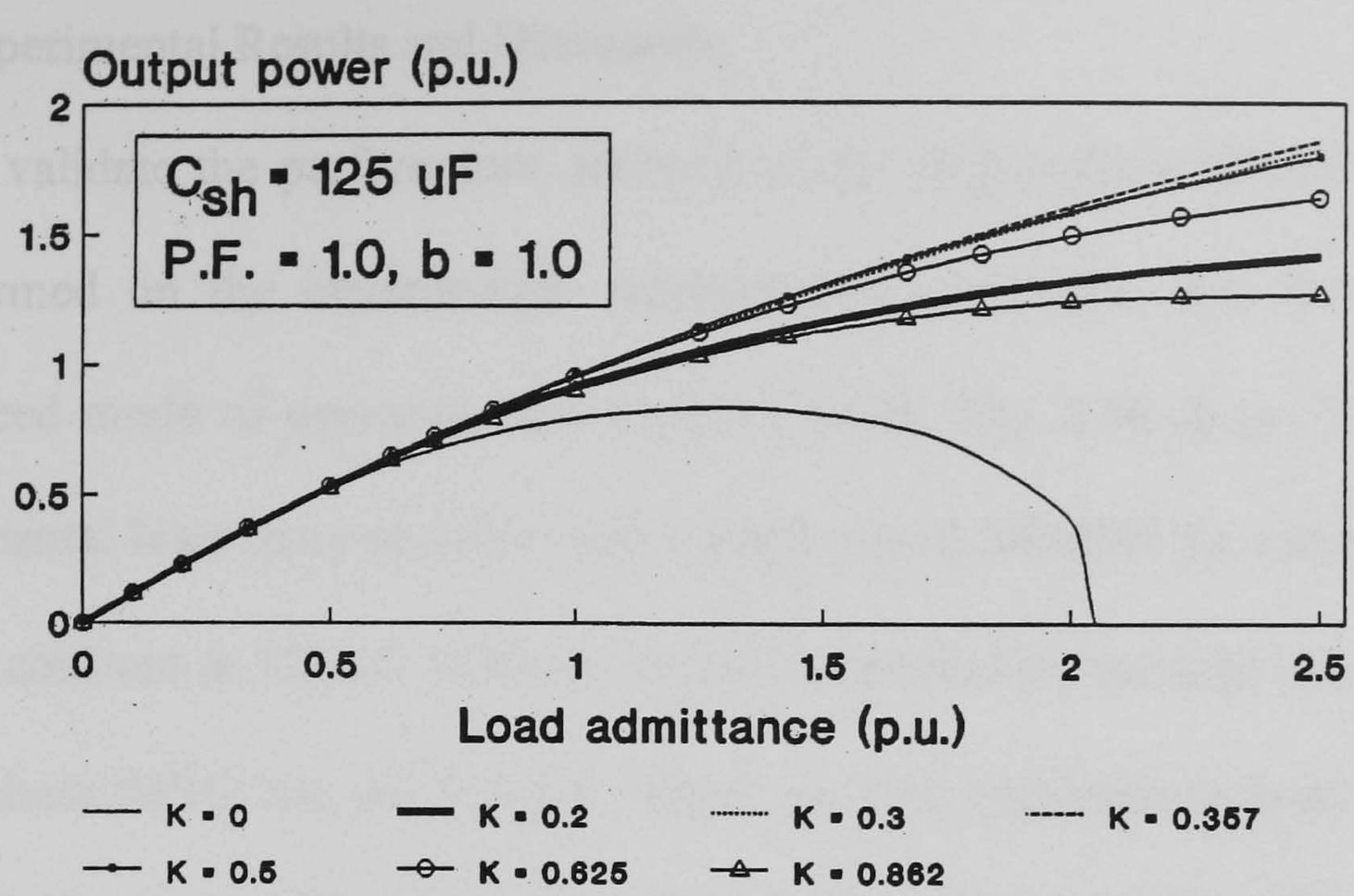


Fig. 4.32 Variation of output power with load admittance.

Fig. 4.33 shows the computed variation of efficiency of the single-phase SRSEIG with load admittance for various values of $K$. The efficiency is highest when $K$ is equal to 0.2 and it decreases monotonously as $K$ increases. Efficiency of the uncompensated machine is comparable with that of the SRSEIG when $K$ is between 0.2 and 0.357, up to a load admittance of 2.0 p.u. at which it drops abruptly due to the rapid decrease in the output voltage.

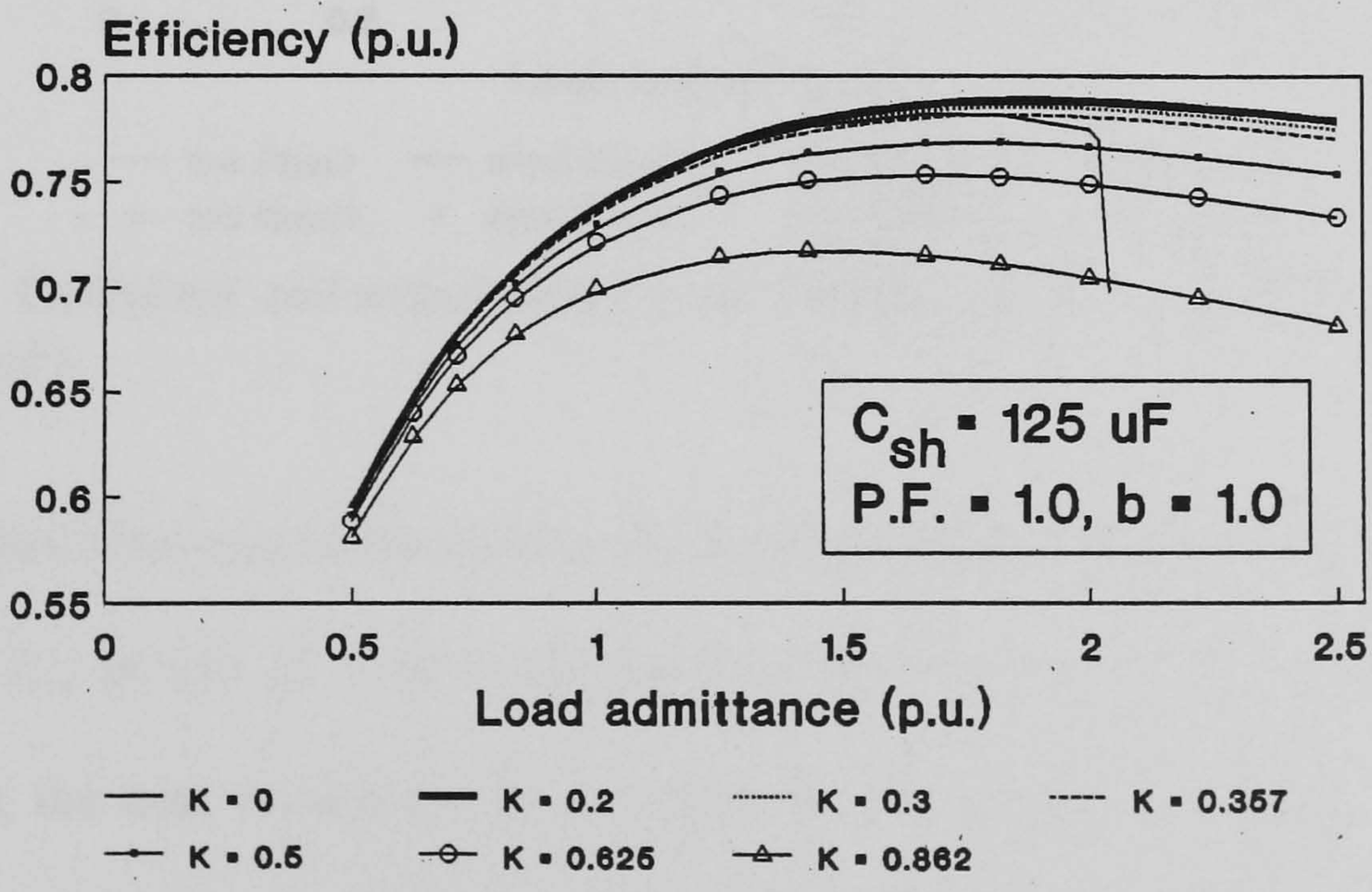


Fig. 4.33 Variation of efficiency with load admittance.

### 4.4.3 Experimental Results and Discussion

In order to validate the performance analysis of the single-phase SRSEIG, load tests were performed on the experimental machine IG1. Attention was focused on the constant-speed mode of operation and resistive loads. Fig. 4.34 shows the computed and experimental load characteristics of the single-phase SRSEIG for various values of $K$, with $C_{sh}$ constant at 125 μF. Without series compensation, the load characteristic of the single-phase SEIG has the familiar 'bend' and the maximum current that can be supplied is 1.14 p.u., at which the voltage drop is approximately 40%. With $K$ equal to 0.5, the load characteristic of the single-phase SRSEIG is practically linear up to a load current of 2.0 p.u. at which the voltage drop is 22%.

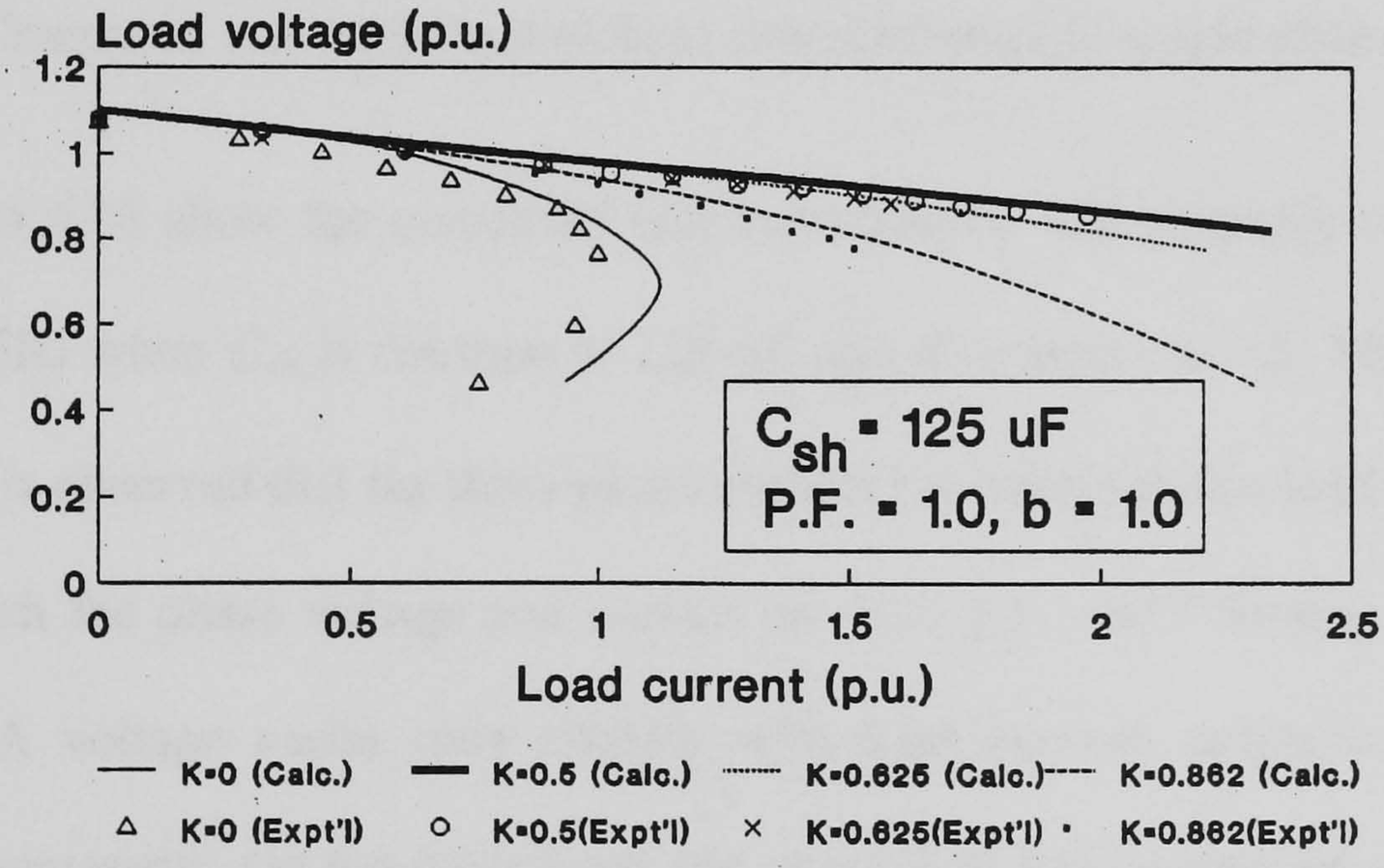


Fig. 4.34 Computed and experimental load characteristics of single-phase SRSEIG ($C_{sh}$ = 125 μF).

Fig. 4.35 shows the load characteristics of the single-phase SRSEIG for various values of $K$, with $C_{se}$ at 250 μF. The results indicate that, by varying the shunt excitation capacitance, the load voltage can be regulated. By selecting proper values of $C_{sh}$, it is possible to obtain different degrees of compounding in the load characteristic. When $K$ is equal to 0.38, for example, a nearly level-compounded characteristic is obtained,

with zero voltage regulation occurring at a load current of 1.3 p.u. A reduction of $K$ (or $C_{sh}$) results in a lower output voltage as well as a reduction in VUF, but perfect phase balance cannot be achieved when $K$ deviates from 0.5.

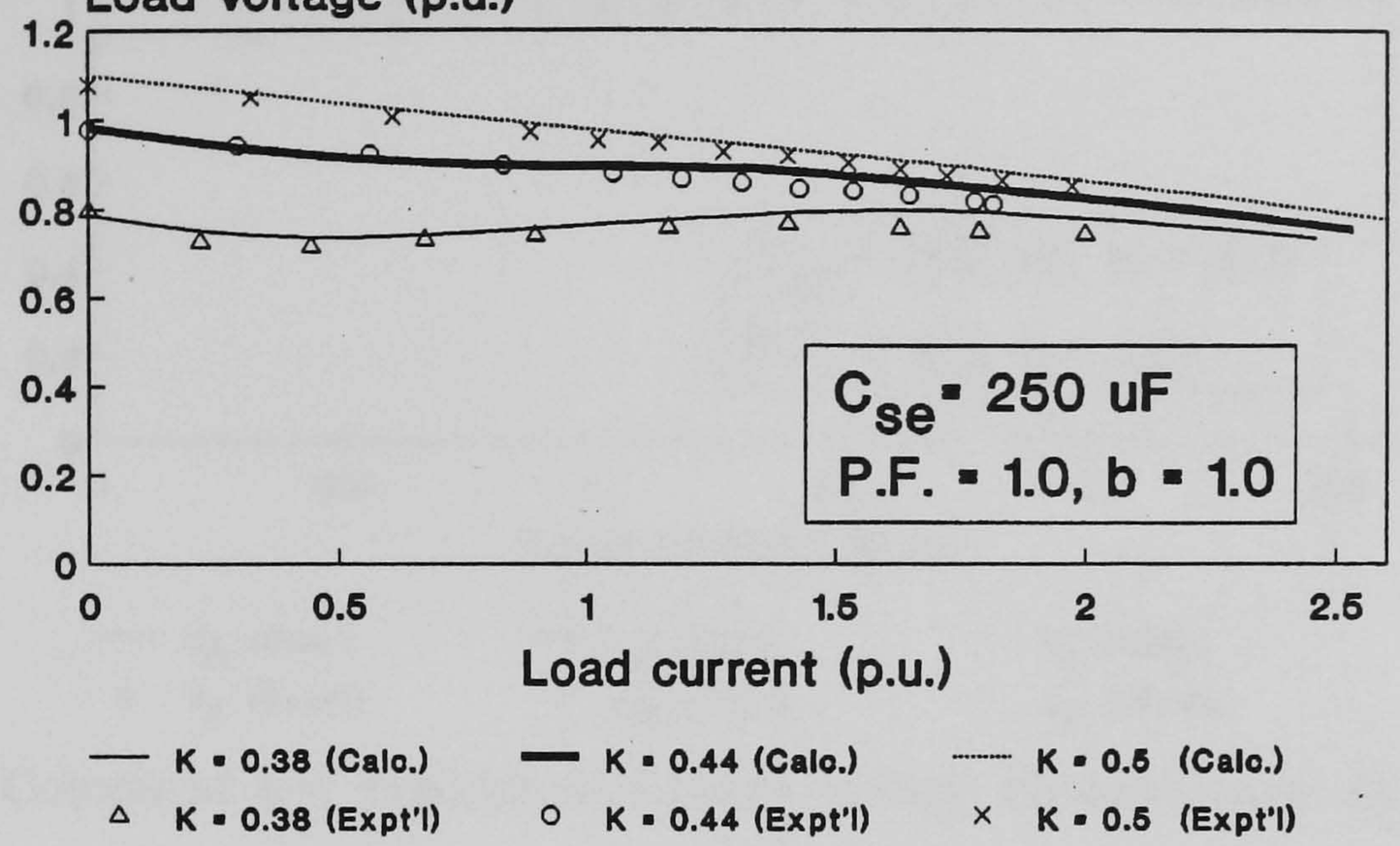


Fig. 4.35 Computed and experimental load characteristics of single-phase SRSEIG.

Figs. 4.36 to 4.38 show the computed and experimental characteristics of the single-phase SRSEIG when $C_{sh}$ is constant at 125 μF and $K$ is equal to 0.5. From Figs. 4.36 and 4.37, it is observed that the three-phase machine is balanced at a load current of 1.6 p.u., at which the phase voltage and current are 1.05 p.u. and 0.94 p.u., respectively. The phase-A voltage varies only slightly with load current, exhibiting a concave-upward characteristic. On the other hand, the phase-B voltage decreases and the phase-C voltage increases monotonously with load current. Fig. 4.37 also shows that, under light load conditions, overcurrent occurs in phase B. When the load current exceeds that corresponding to perfect phase balance, overcurrent will first occur in phase A and phase C. At very large load currents, all three phases of the induction generator will be overloaded. Provided that the load current varies between 1.0 p.u. to 2.0 p.u., the phase imbalance in the three-phase machine should be acceptable. When prolonged operation at light load is required, however, it is recommended that smaller values of $C_{sh}$ and $C_{se}$

be used in order to balance the machine at a lower load current, thereby reducing the VUF at light load.

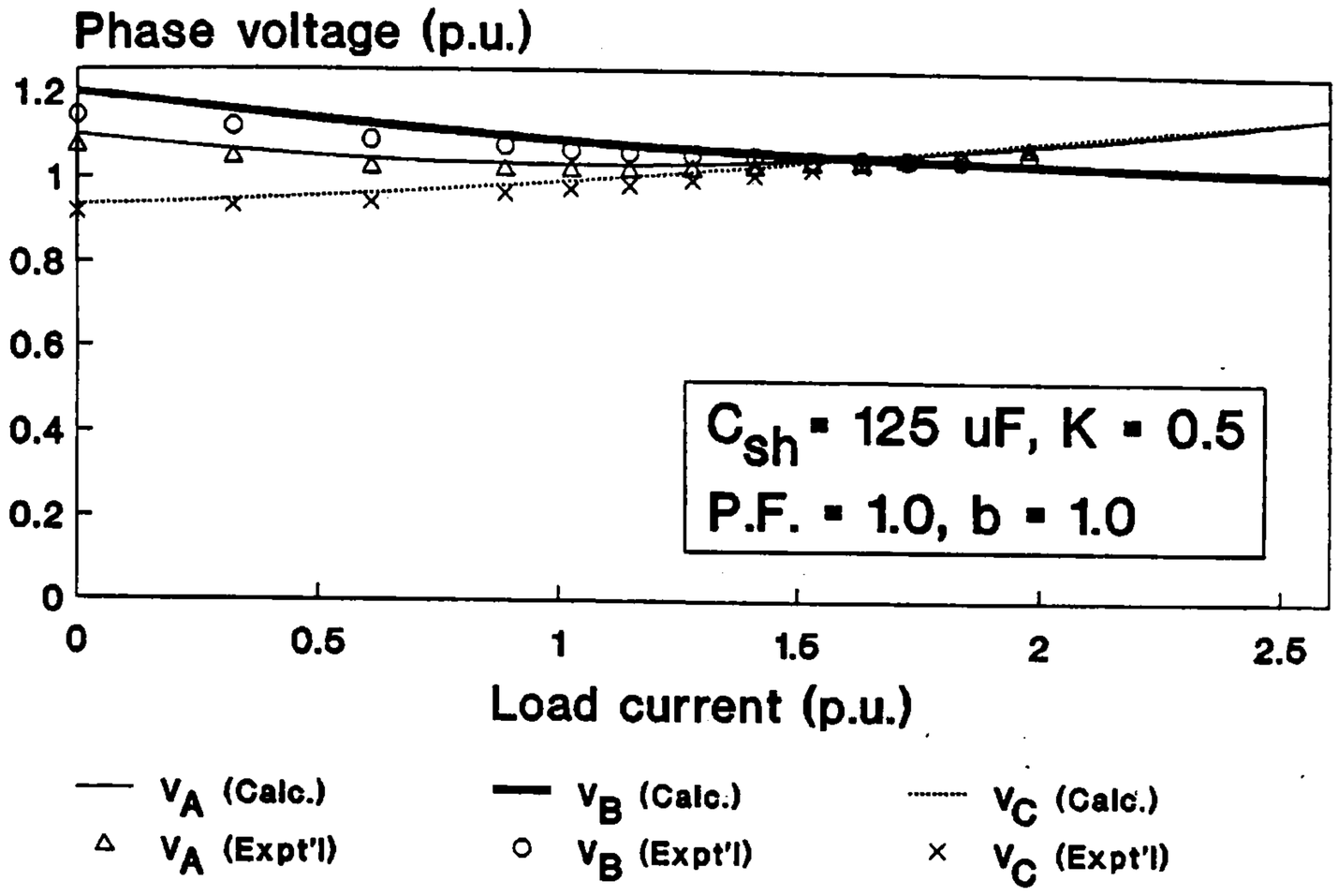


Fig. 4.36 Computed and experimental phase voltage characteristics of single-phase SRSEIG.

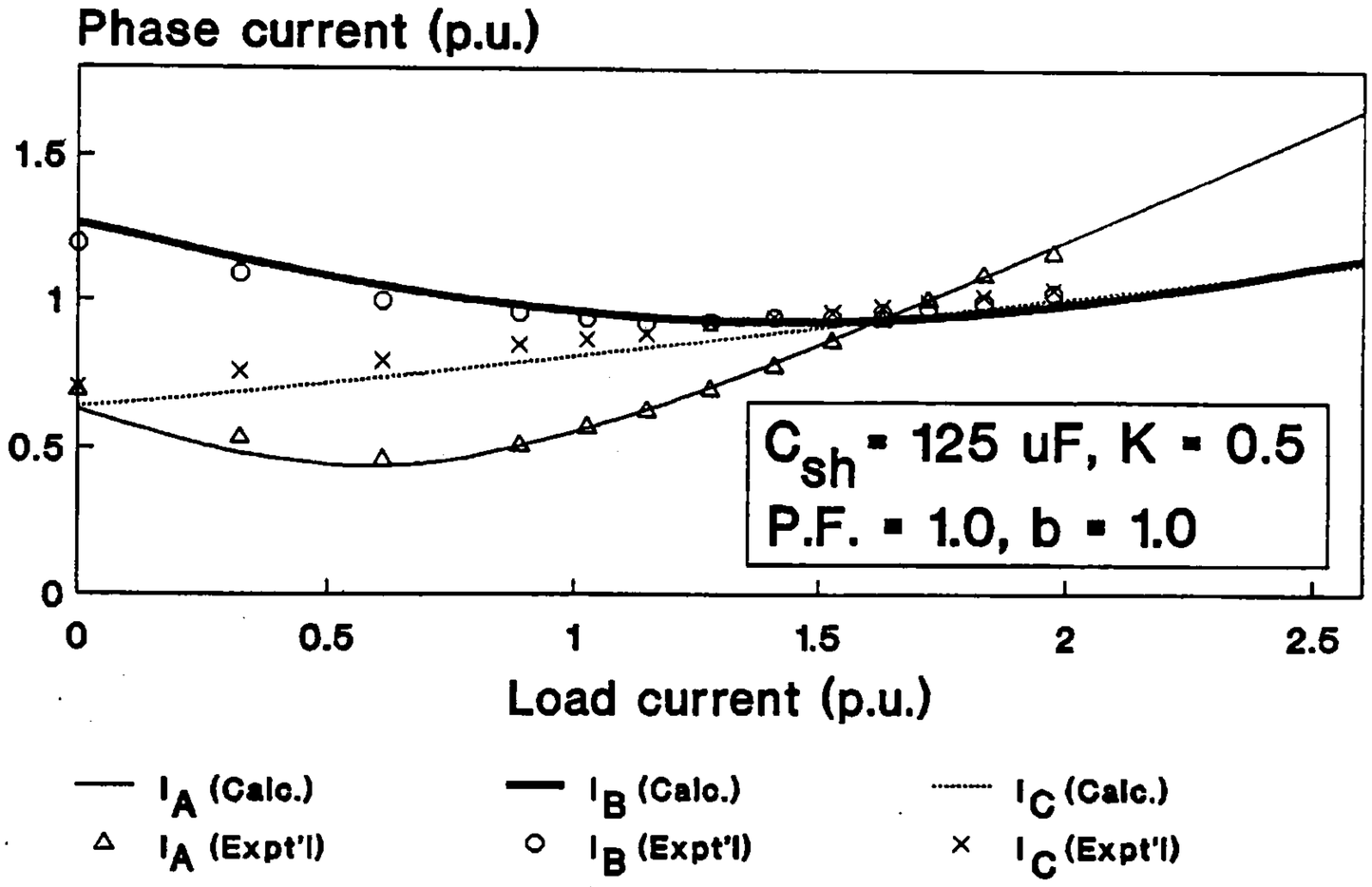


Fig. 4.37 Computed and experimental phase current characteristics of single-phase SRSEIG.

Fig. 4.38 shows the output power, efficiency and frequency characteristics of the single-phase SRSEIG. Due to the self regulation in the load voltage, the power output increases almost linearly as the load current increases. A high efficiency is obtained when the load current exceeds 0.8 p.u. Under perfect phase balance condition, the machine delivers an output power of 1.48 p.u. (1760 W) at an efficiency of 0.77 p.u.

The per-unit frequency $a$ drops slightly with increase in load current: at perfect phase balance, the p.u. frequency is equal to 0.964.

The above results confirm that very satisfactory machine operation at unity load power factor is obtained when $K = 0.5$.

Good correlation between the computed and experimental characteristics is observed from Fig. 4.30 and from Figs. 4.34 to 4.38. The validity of the theoretical analysis and the feasibility of the proposed single-phase SRSEIG are thus verified.

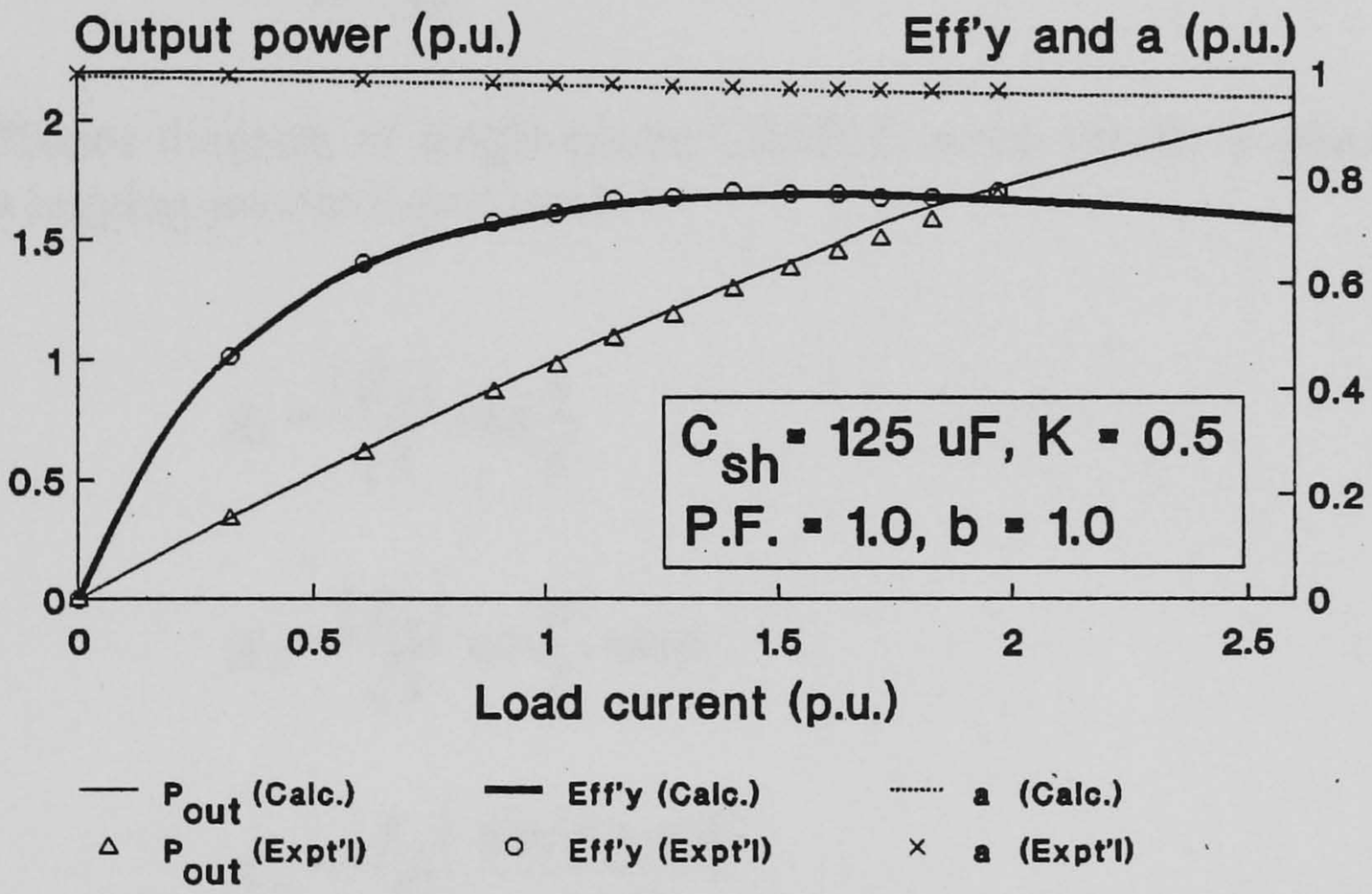


Fig. 4.38 Computed and experimental output power, efficiency and frequency characteristics of single-phase SRSEIG.

### 4.4.4 Effect of Load Power Factor

Autonomous power systems supply typically lighting and storage heating loads with power factors equal to or close to unity. For these applications, the analysis and results presented in Sections 4.4.2 and 4.4.3 are generally applicable. Special consideration should be given, however, to the case when the load power factor differs from unity.

Fig. 4.39 shows the phasor diagram of the single-phase SRSEIG (Fig. 4.26) under perfect phase balance and the load power factor angle is $\phi$ lagging. From the diagram, the following relationships can readily be deduced:

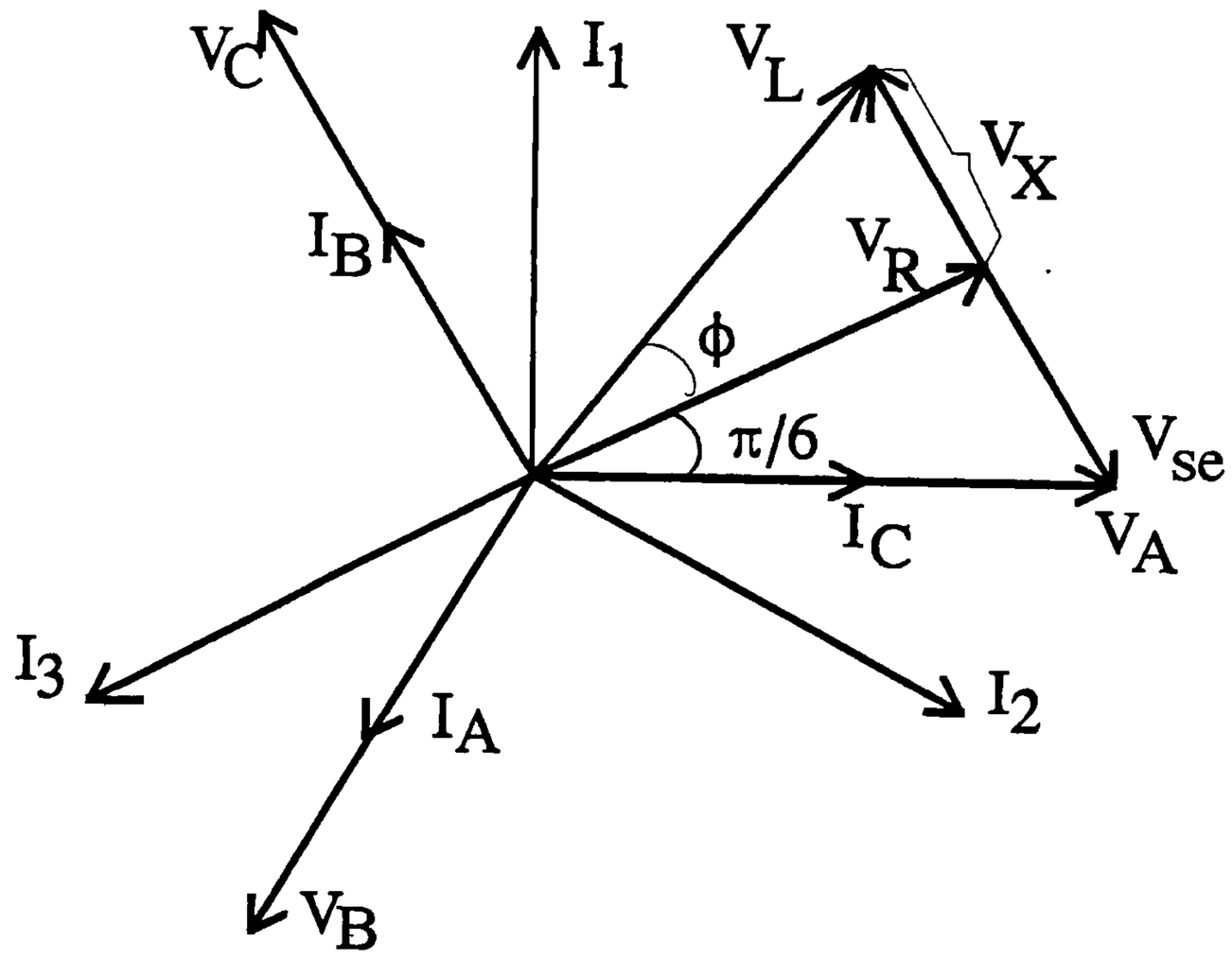


Fig. 4.39 Phasor diagram of single-phase SRSEIG when the three-phase machine is balanced at a lagging-power-factor load.

$$R_L = \frac{|Z_p|}{\sqrt{3}}.\cos\frac{\pi}{6} \tag{4.40}$$

$$X_L = \frac{|Z_p|}{\sqrt{3}}.\cos\frac{\pi}{6}.\tan\phi \tag{4.41}$$

$$X_{se} = \frac{|Z_p|}{\sqrt{3}}.\frac{\sin(\phi + \pi/6)}{\cos\phi}. \tag{4.42}$$

The compensation factor $K$ that results in perfect phase balance in the three-phase IG is

$$K = \frac{X_{se}}{X_{sh}} = \frac{\sin(\phi + \pi/6)}{\cos\phi}. \tag{4.43}$$

The load voltage $V_L$ and the voltage drop $V_{se}$ across the series compensation capacitance $C_{se}$ are given by:

$$V_L = V_{ph}.\cos\frac{\pi}{6}.\sec\phi \tag{4.44}$$

$$V_{se} = V_{ph}.\frac{\sin(\phi + \pi/6)}{\cos\phi}. \tag{4.45}$$

From Fig. 4.39 and (4.43), it is observed that $X_{se}$ is larger when the load power factor angle is increased, implying that a higher value of $K$ is required. At a power factor angle of $\pi/6$ rad lagging, $K$ must be equal to unity for perfect phase balance. Under this condition, both $V_L$ and $V_{se}$ are equal to the phase voltage of the IG.

A smooth variation of $K$ is required for achieving perfect balance at different load power factor angles, but this would significantly increase the complexity and capital cost of the generator system. In practice, provision of discrete values of $C_{se}$ and $K$ suffices to give satisfactory generator performance. Fig. 4.40 shows the load characteristics of the single-phase SRSEIG at different power factors when $C_{sh}$ = 125 μF and $K$ = 1.0. It is observed that the load voltage exhibits an interesting double-peak characteristic when the load power factor is lagging. The undulation in the load voltage characteristics is larger as the load power factor decreases, but the load voltage remains substantially constant at light and medium loads.

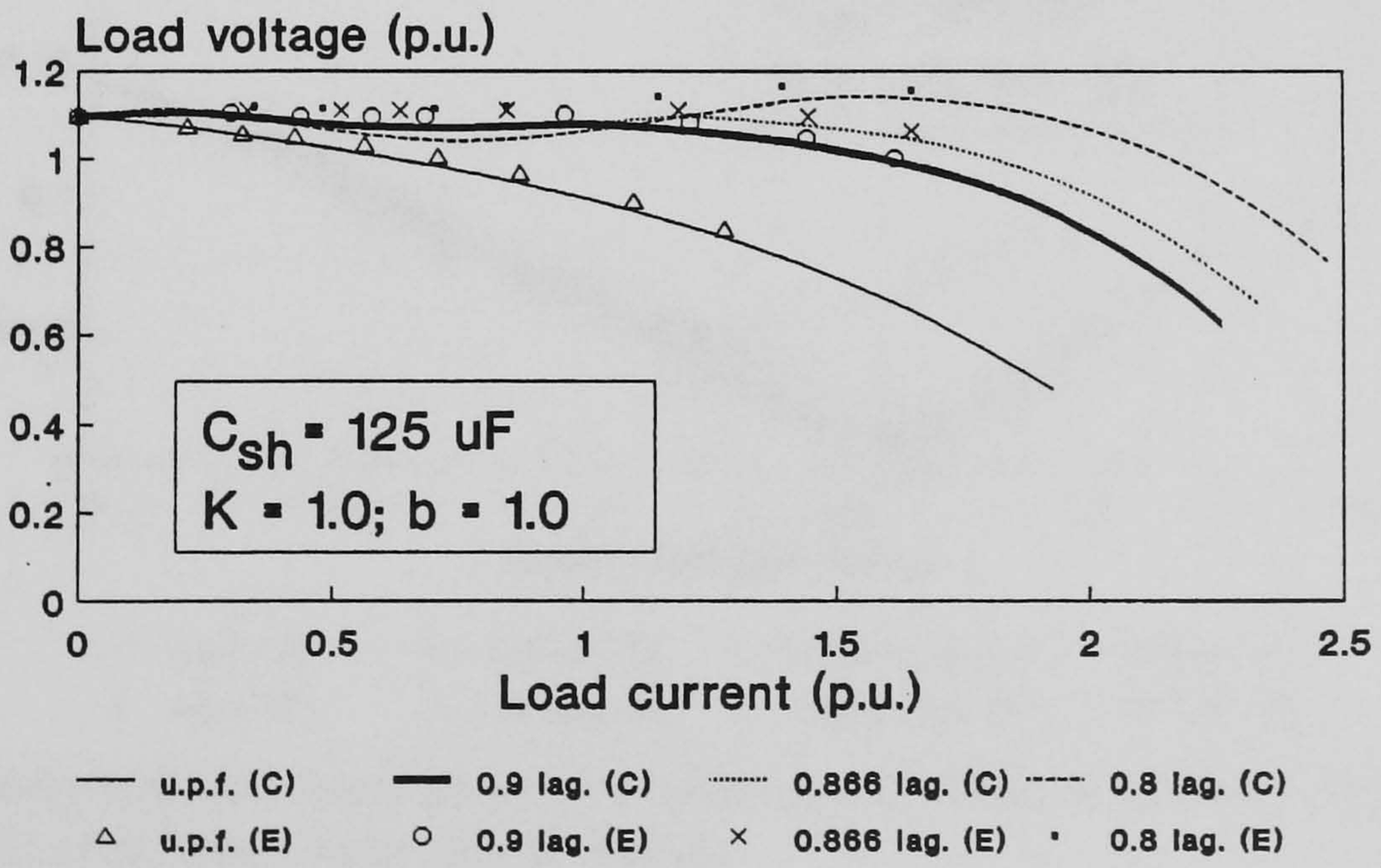


Fig. 4.40 Computed and experimental load voltage characteristics of single-phase SRSEIG at different load power factors.

At a power factor of 0.8 lagging, zero voltage regulation occurs at three different values of load current, but the computed results indicate that for load currents not exceeding 1.5 p.u., the voltage regulation is smallest when the load power factor is 0.866 lagging. With unity-power-factor loads, however, the voltage regulation is much larger compared with that obtaining when a compensation factor of 0.5 is used, as shown in Fig. 4.34.

Fig. 4.41 shows the computed and experimental VUF characteristics of the single-phase SRSEIG at different power factors when $K$ = 1.0. At a load power factor of 0.866 lagging, perfect phase balance is obtained at a load current of 1.65 p.u., which is very close to the rated value. At a load power factor of 0.8 lagging and 0.9 lagging, the minimum values of VUF are 0.018 and 0.01, respectively. At unity load power factor, the VUF for heavy loads is considerably higher.

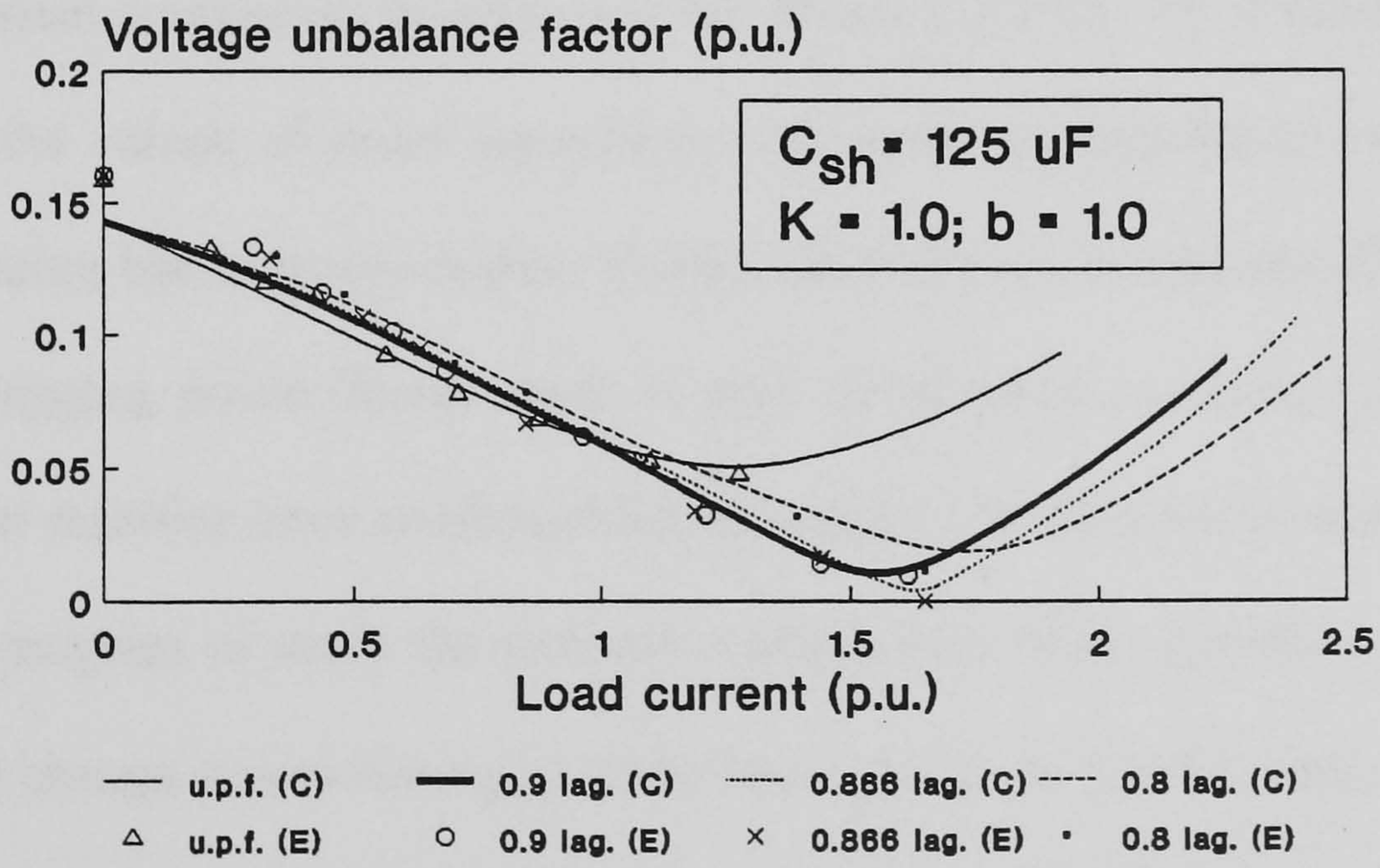


Fig. 4.41 Computed and experimental variations of voltage unbalance factor of single-phase SRSEIG at different load power factors.

For practical applications, the value of $K$ may be changed by a simple switching operation on $C_{se}$ which comprises two identical units, each equal to $C_{sh}$. For load power factors close to unity, the two capacitor units are connected in parallel to yield a

compensation factor of 0.5. As the load power factor becomes more lagging, one of the capacitor units may be switched out to yield a compensation factor of unity.

### 4.4.5 Summary

In this section, the steady-state performance of a single-phase self-regulated SEIG using a three-phase machine has been analyzed. The effect of compensation factor on the generator performance has been investigated in detail with reference to a small experimental machine. Very good phase balance is obtained over a wide range of load by virtue of the Steinmetz connection and the phase-shifting effect of the series compensation capacitance on the load current. Other advantages of the single-phase SRSEIG include good winding utilization, large power output, high efficiency, and a small voltage regulation. The conditions for achieving perfect phase balance in the three-phase machine, which supplies single-phase loads, have also been deduced from the symmetrical component analysis and the phasor diagram. An iterative method for computing the values of shunt capacitance and series compensation capacitance for phase balancing has been developed. Performance of the single-phase SRSEIG when supplying lagging power factor loads is also investigated. Laboratory tests on the experimental machine have confirmed the accuracy of the theoretical analysis. Further work is in progress to study the transient performance of the generator, for example sudden load change and switching of motor loads. Since the circuit configuration of the proposed single-phase SRSEIG is extremely simple and only static capacitors are required, the generator can be conveniently implemented for use in low-cost single-phase autonomous power generation schemes.

## 4.5 SEIG with the Smith Connection (SMSEIG)

Application of the Smith connection to a three-phase IG connected to a single-phase grid has been studied in Section 2.3. In this section, it will be shown that this connection can be used in a novel excitation scheme for a three-phase SEIG that supplies isolated single-phase loads. Good phase balance in the generator can be achieved, resulting in a high efficiency and a large power output.

### 4.5.1 Circuit Connection and Operating Principle

Fig. 4.42 shows the proposed excitation scheme. When viewed into terminals 1 and 3 across which the single-phase load $Z_L$ is connected, the stator phases and the excitation capacitances are in the form of the Smith connection discussed in Section 2.3. For easy reference in the subsequent discussion, this new excitation scheme will be abbreviated as the SMSEIG. In order to suppress the zero-sequence current, the capacitance $C_3$ must be equal to twice of the capacitance $C_2$.

Self-excitation in the SMSEIG takes place in a similar manner as a three-phase SEIG with symmetrical winding connection and balanced capacitances. Residual flux must be present in the rotor, and the capacitances must be sufficiently large for the terminal voltage to build up [26]. As in other SEIG schemes, the frequency and magnetizing reactance of the SMSEIG are not constant but vary with the rotor speed and the load impedance.

The phasor diagrams for the SMSEIG is the same as that for the SMIG, as illustrated in Fig. 2.13(a) and Fig. 2.13(b). Provided that the generator impedance angle $\phi_p$ lies between $2\pi/3$ rad and $5\pi/6$ rad, $I_B$ can be synthesized with the proper magnitude and phase angle as to yield perfect phase balance in the SMSEIG. Under this condition the IG operates with balanced phase currents and phase voltages and its performance is

similar to a three-phase SEIG with balanced excitation capacitances and balanced load impedances. The currents $I_1$, $I_2$ and $I_3$ can be adjusted easily by varying the capacitances $C_1$, $C_2$ and $C_3$. Fig. 2.13 also suggests that the SMSEIG is best suited for supplying high power factor (e.g., resistive) loads.

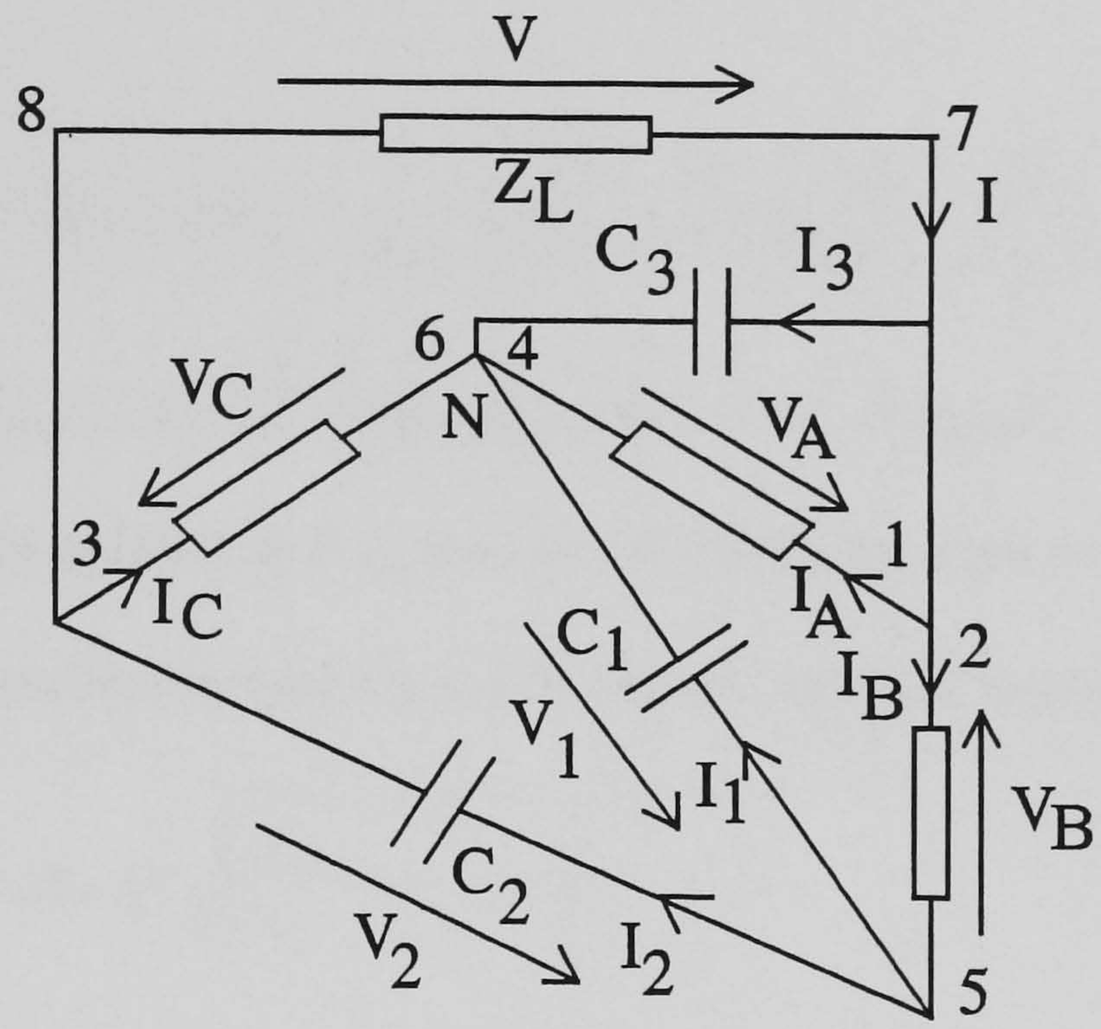


Fig. 4.42 Circuit connection of proposed excitation scheme for three-phase induction generator supplying an isolated single-phase load.

### 4.5.2 Performance Analysis

To determine the steady-state performance of the SMSEIG, the analysis presented in Section 2.3 for the grid-connected SMIG is used in association with the solution method for a single-phase SEIG, presented in Section 4.2.

For the SMSEIG, it can be shown that the input impedance $Z_{in}$ across terminals 1 and 3 is given by:

$$Z_{in} = R_{in} + j\,X_{in} = \frac{Y_p + Y_n + 3Y_1 + 2Y_2}{2Y_1Y_2 + (Y_p + Y_n)(Y_1 + 2Y_2) + Y_pY_n} \tag{4.46}$$

where $Y_1 = ja^2.2\pi f_{base}C_1$, $Y_2 = ja^2.2\pi f_{base}C_2$, and $Y_3 = ja^2.2\pi f_{base}C_3$.

For a given per-unit speed $b$ and a given set of excitation capacitances, the values of $a$ and $X_m$ may be determined by minimizing the following scalar impedance function:

$$Z(a, X_m) = \sqrt{\left(\frac{R_L}{a} + R_{in}\right)^2 + (X_L + X_{in})^2}\,. \tag{4.47}$$

After $a$ and $X_m$ have been determined, the steady-state performance of the SMSEIG can be obtained from the appropriate circuit equations.

### 4.5.3 Balanced Operation

*A) Conditions for phase balance*

As in the SMIG, the capacitive admittances for perfect phase balance are given by:

$$|Y_1| = \frac{2}{\sqrt{3}}|Y_p|\sin\left(\frac{5\pi}{6} - \phi_p\right) \tag{4.48}$$

$$|Y_2| = |Y_p|\sin\left(\phi_p - \frac{2\pi}{3}\right) \tag{4.49}$$

$$|Y_3| = 2|Y_p|\sin\left(\phi_p - \frac{2\pi}{3}\right) \tag{4.50}$$

while the load admittance $Y_L$, referred to the base frequency, is given by

$$|Y_L| = -\frac{|I|}{|V|} = \frac{|Y_p|}{\sqrt{3}} \cdot \sqrt{1 + 8\sin^2\left(\phi_p - \frac{2\pi}{3}\right)}. \tag{4.51}$$

Eqns. (4.48) to (4.50) may be simplified when the load is purely resistive. Since the load power factor angle is now π rad, it can be shown that the generator impedance angle $\phi_p$ is

$$\phi_p = \tan^{-1}\left(-\frac{2}{\sqrt{3}}\right) = 2.2845\ rad\ . \tag{4.52}$$

The IG thus operates with an output power factor of 0.655 leading when perfectly balanced and supplying a pure resistive load.

Substitution of (4.52) into (4.48) to (4.50) yields

$$|Y_1| = \frac{|Y_2|}{2} = |Y_3| = \frac{1}{\sqrt{7}}|Y_p|. \tag{4.53}$$

The capacitances $C_1$ and $C_3$ are thus equal, while the currents are related by

$$|I| = \sqrt{3}|I_1| = 3|I_2| = 3|I_3| = \frac{3}{\sqrt{7}} I_{ph}. \tag{4.54}$$

*B) Capacitances for perfect phase balance*

It is of interest to determine, for a given load impedance and per-unit speed, the values of excitation capacitances that give perfect phase balance in the SMSEIG. Since $Y_p$ and $\phi_p$ are functions of $a$ and $X_m$, both being unknown to start with, an iterative procedure has to be used. The steps are outlined as follows:

1) Assume appropriate initial values of $a$ and $X_m$.

2) For the given value of load impedance, compute the load admittance $|Y_L|$ and the operating load power factor angle $\phi$.

3) Determine the corresponding generator impedance angle $\phi_p$ using an iterative method.

4) Compute $|Y_p|$ from (4.51), using the current values of $|Y_L|$ and $\phi_p$.

5) Compute the capacitive admittances $|Y_1|$, $|Y_2|$, and $|Y_3|$ from (4.48) to (4.50).

6) Determine the new values of $a$ and $X_m$, using the solution technique outlined in Section 4.2.2.

7) Update the values of $\phi$ and $|Y_L|$ using the new values of $a$ and $X_m$.

8) Repeat steps 3) to 7) until the values of $a$ in successive iterations is less than the prescribed tolerance, say 1.0e-6.

9) Compute the excitation capacitances $C_1$, $C_2$, and $C_3$ using the final values of $a$ and $X_m$, hence obtain the performance of the SMSEIG under balanced conditions.

### 4.5.4 Results and Discussion

*A) Computed Results: Constant-Speed Operation*

Computed results were obtained for experimental machine IG1 whose data are given in Appendix D.1, the emphasis being placed on the performance when the SMSEIG is operated at constant speed and is supplying unity-power-factor loads.

Fig. 4.43 shows the computed variations of $a$ and $X_m$ with load admittance $Y_L$ when the SMSEIG operates with perfect phase balance. Reduction in $Y_L$ causes $X_m$ to increase, implying that the induction machine becomes less saturated. When $Y_L$ = 0.403 p.u., $X_m$ is equal to the unsaturated value $X_{mu}$ (= 2.48 p.u.). There is thus a value of load admittance below which perfect phase balance cannot be achieved for the SMSEIG.

Fig. 4.44 shows the variation of $C_1$ with $Y_L$ to give perfect phase balance and the corresponding phase voltage of the induction generator. The capacitance required for giving perfect phase balance decreases as $Y_L$ is reduced, hence the decrease in $X_m$.

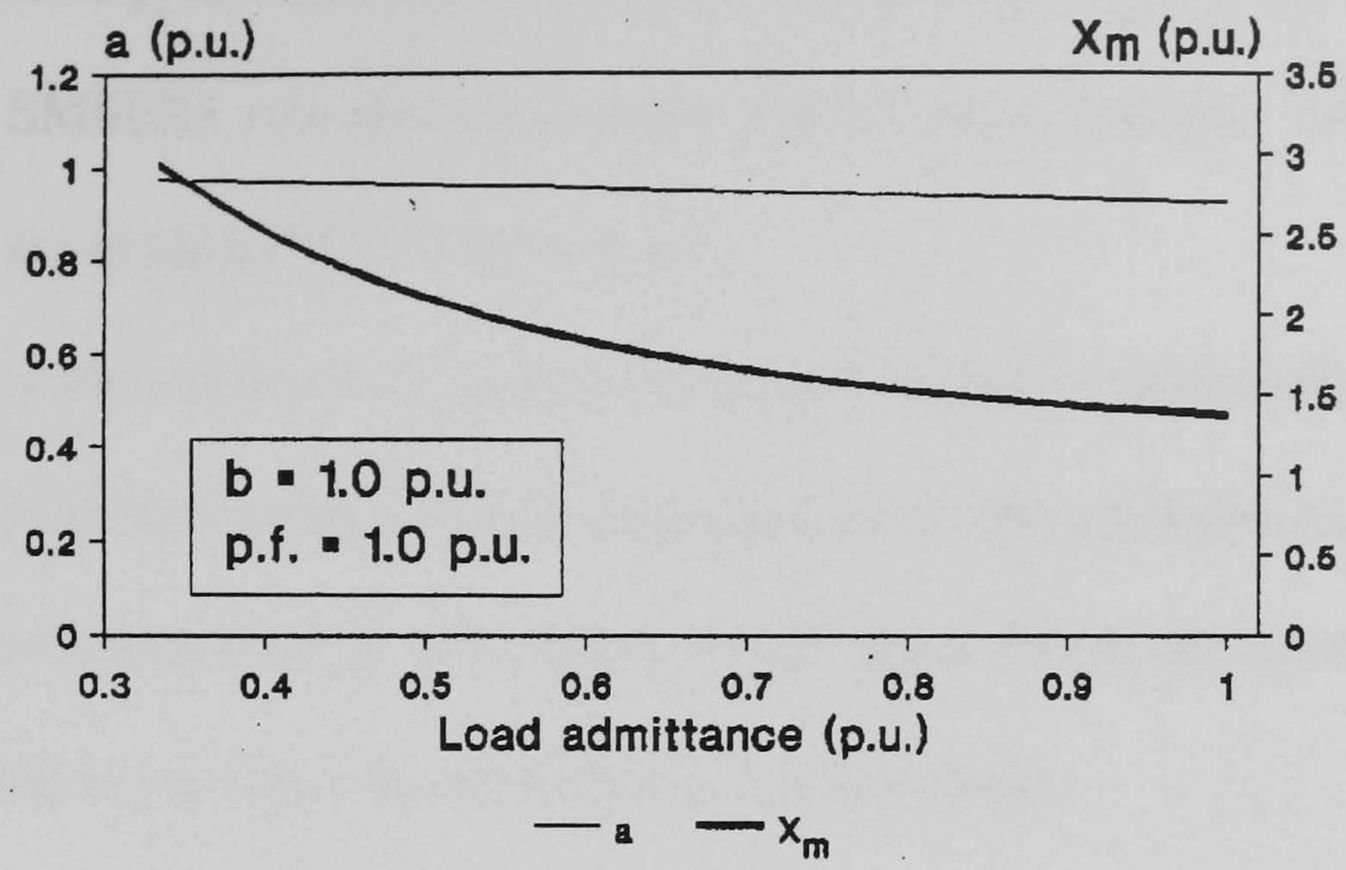


Fig. 4.43 Computed variation of per-unit frequency and magnetizing reactance under perfect phase balance.

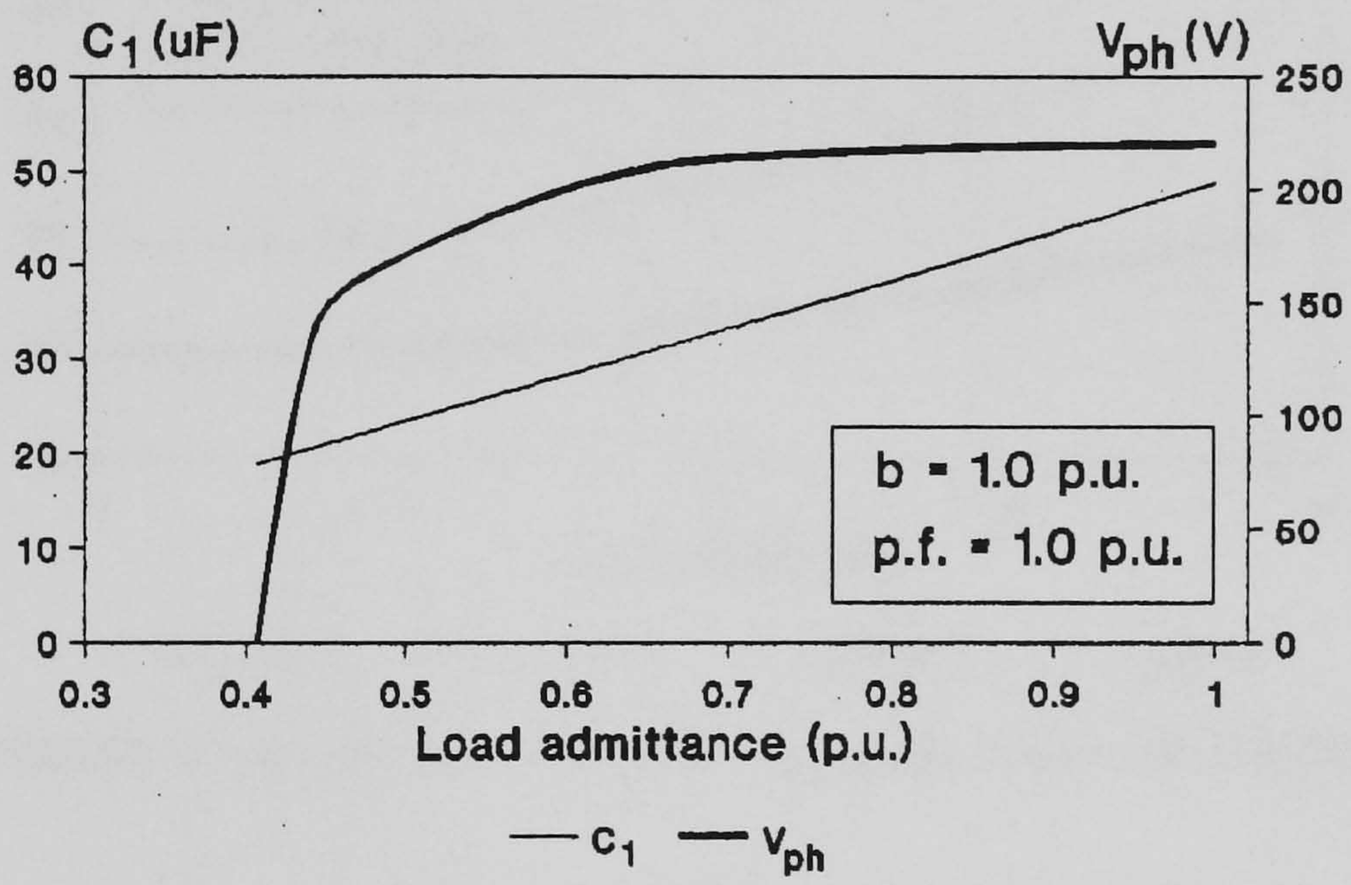


Fig. 4.44 Computed variation of capacitance $C_1$ and phase voltage under perfect phase balance.

*B) Experimental Results: Constant-Speed Operation*

To verify the phase-balancing capability of the SMSEIG, laboratory tests were performed on the experimental machine. The speed of the SMSEIG was maintained at rated value (i.e. $b$ = 1.0 p.u.) and the capacitances were increased until self-excitation occurred. The load resistance was then switched in and the capacitances were adjusted until the phase voltages and currents were balanced. Since the load was resistive, the balance point could be obtained quite easily by varying the capacitances simultaneously

in the proportion as prescribed by (4.53). Both machine noise and vibration levels were low when the SMSEIG was operating under perfect phase balance. The performance characteristics are given in Figs. 4.45 to 4.47.

Fig. 4.45 shows the values of $C_1$ and $C_2$ that result in perfect phase balance. The good correlation between the computed and experimental results confirms the feasibility of the proposed excitation scheme. It is observed that larger values of capacitances need to be used for achieving perfect phase balance at heavier loads.

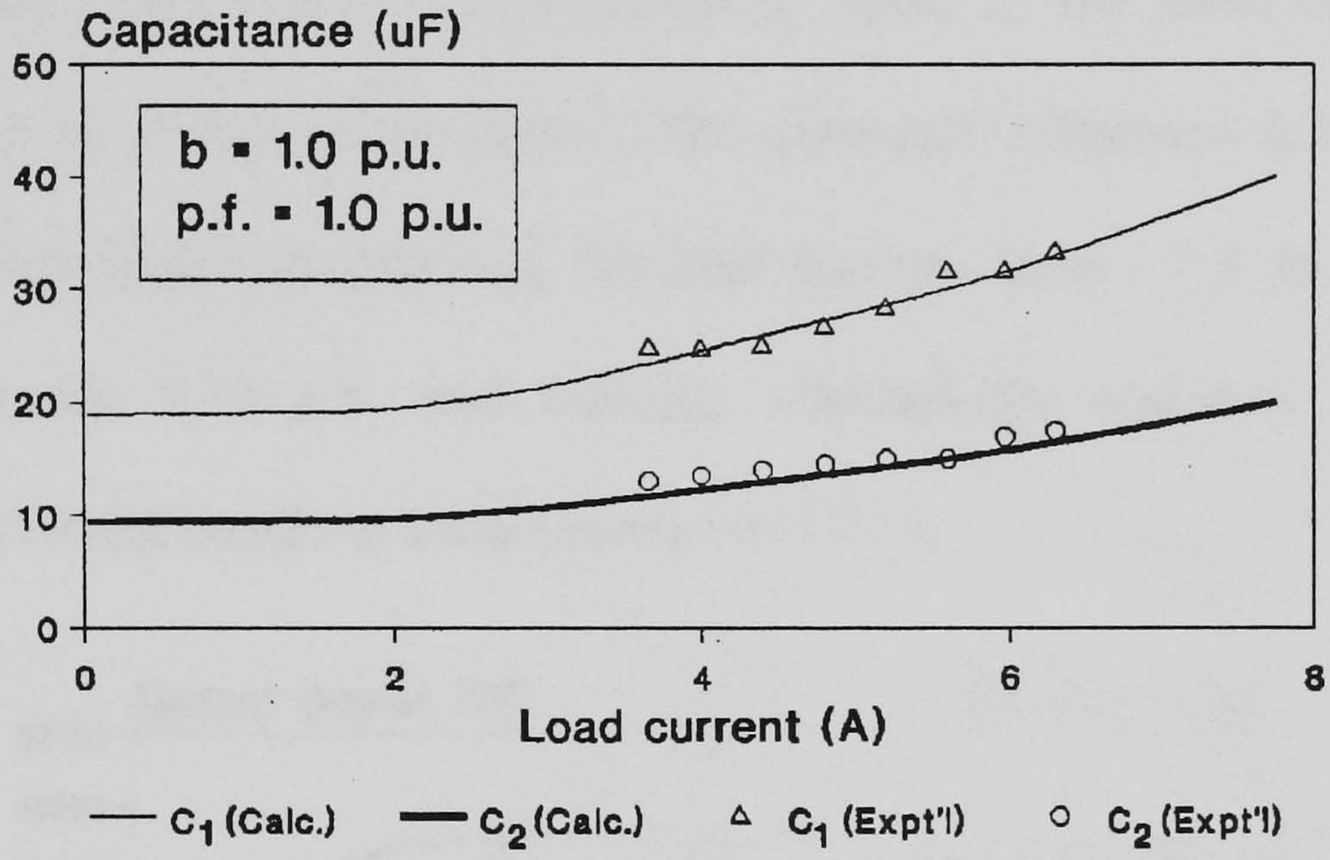


Fig. 4.45 Excitation capacitances to give perfect phase balance in SMSEIG.

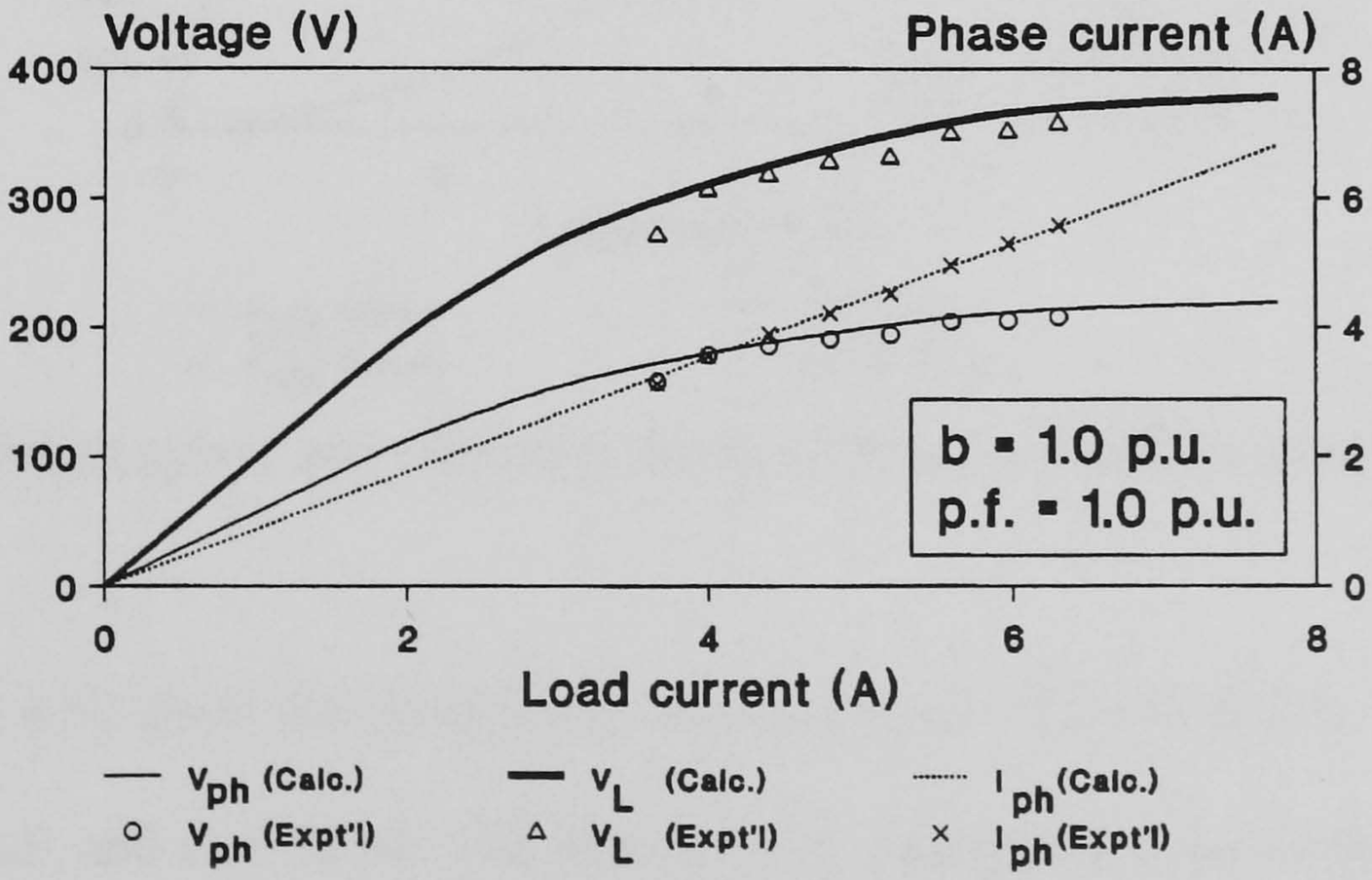


Fig. 4.46 Variation of load voltage, phase voltage and phase current of SMSEIG under perfect balance.

Fig. 4.46 shows the corresponding variations of load voltage, generator phase voltage, and generator phase current with load current. Due to the increased reactive power from the capacitances, the generator is driven into heavier saturation and the output voltage increases. When delivering a rated load current of 6.2 A, the phase voltage is 213 V (0.97 p.u.). This shows that the generator rating has been fully utilized.

Fig. 4.47 shows the output power and efficiency characteristics of the SMSEIG under balanced conditions. At rated load current, the generator delivers a power of 2250 W to the single-phase load, which is approximately equal to the rated output when the machine is run as a three-phase motor. The generator efficiency is high since only positive-sequence losses are incurred. For load currents from 1.7 A to rated value, the efficiency exceeds 0.75 p.u. and remains substantially constant. The maximum efficiency is 0.79 and occurs at a load current of 3.5 A.

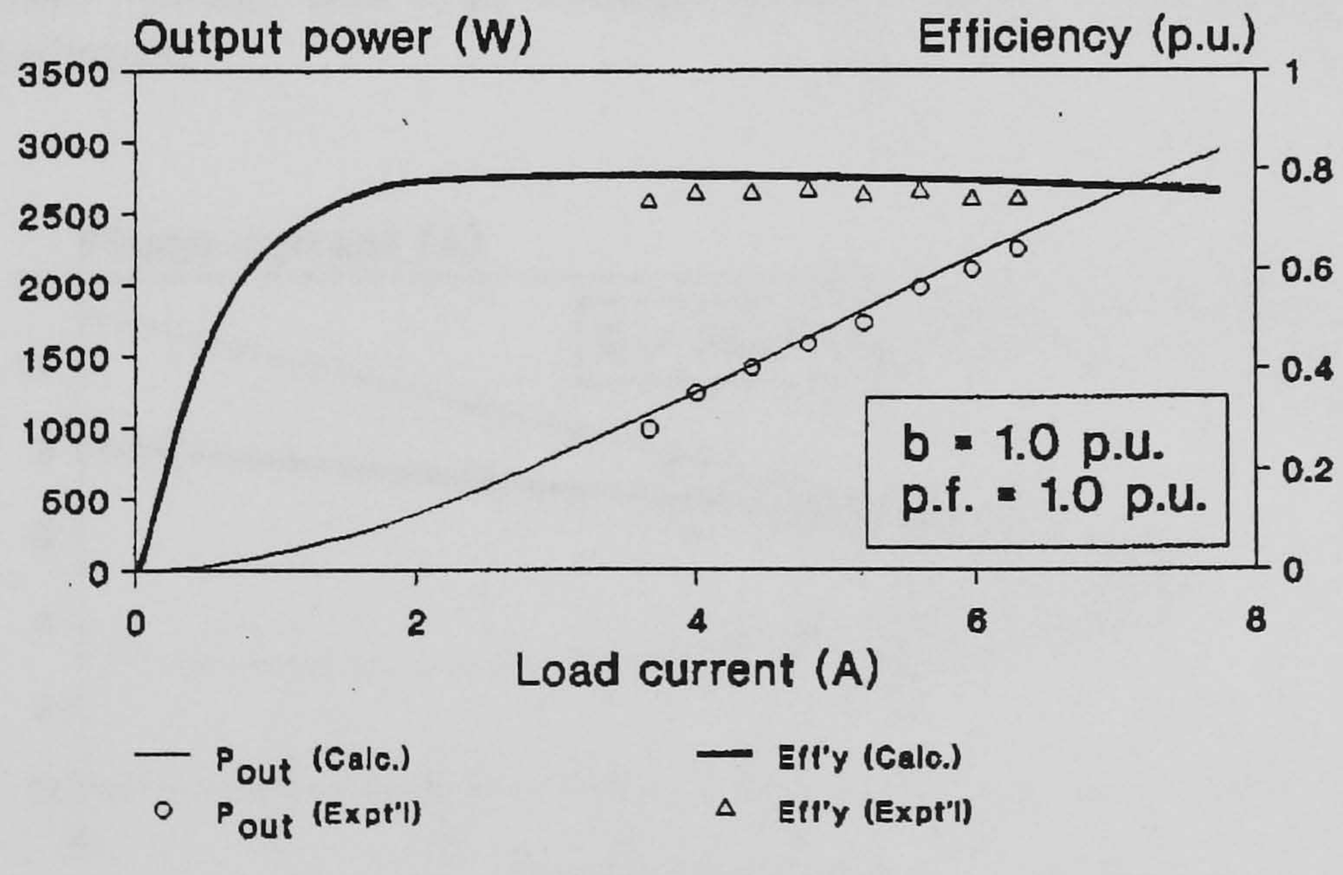


Fig. 4.47 Output power and efficiency characteristics of SMSEIG under perfect phase balance.

Figs. 4.48 to 4.50 show the performance characteristics of the SMSEIG when $C_1$ = 32 μF, $C_2$ = 16 μF, and $C_3$ = 32 μF. The rotor speed is maintained at rated value and a unity-power-factor load is supplied. With these excitation capacitances, the three-phase

machine is balanced experimentally at a load current of 5.8 A, the corresponding phase voltage and phase current being 203 V and 5.2 A, respectively. Since the excitation capacitances remain unchanged, they will generate excessive magnetizing reactive power when the load current decreases, causing the phase voltages to increase (Fig. 4.48). At no load, $V_A$, $V_B$ and $V_C$ are equal to 324 V, 243 V and 256 V, respectively.

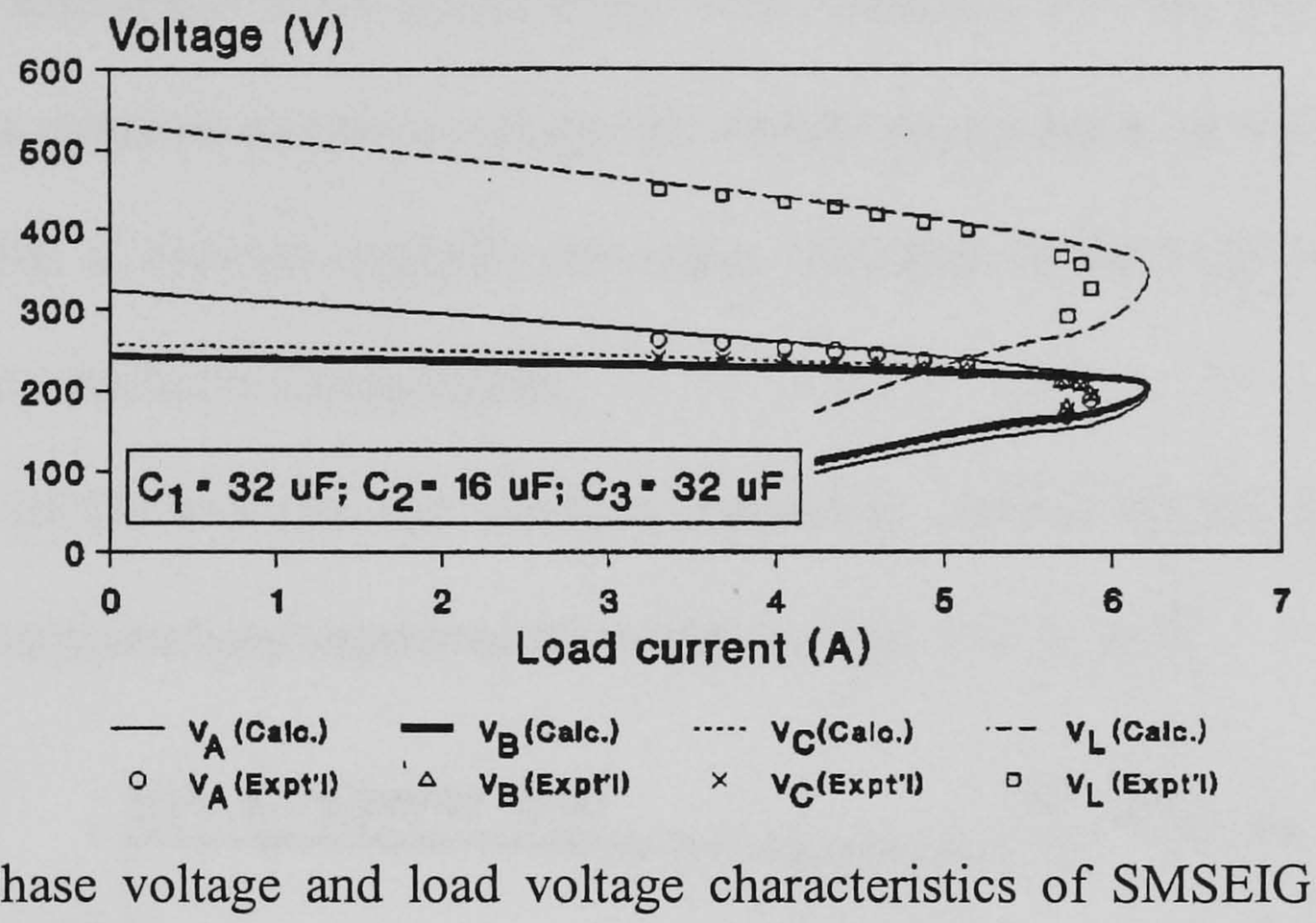


Fig. 4.48 Phase voltage and load voltage characteristics of SMSEIG with constant excitation capacitances.

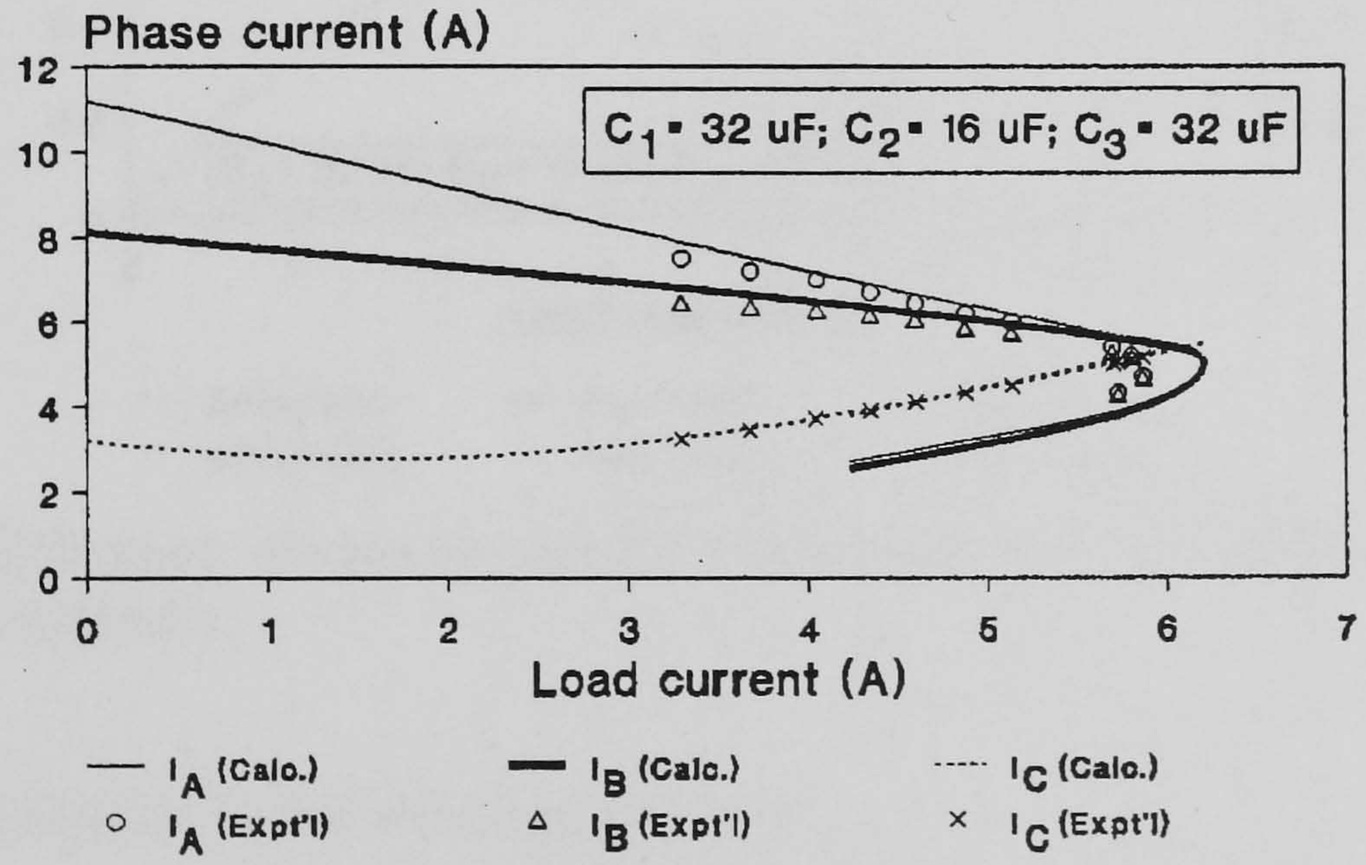


Fig. 4.49 Phase current characteristics of SMSEIG with constant excitation capacitances.

Fig. 4.49 shows the phase current characteristics of the SMSEIG. When the load current decreases from the value corresponding to perfect phase balance, both phase-A and

phase-B currents increase, whereas phase-C current decreases. At light load, all the phase currents increase with reduction in load current. At no load, $I_A$ and $I_B$ are equal to 11.2 A and 8.1 A, respectively.

Fig. 4.50 shows the variation of per-unit frequency, efficiency and VUF of the SMSEIG with load current. For operation at rated speed, the output frequency is 0.95 p.u. at rated current. The efficiency drops significantly with reduction of load current due to the increase in the negative-sequence voltage and current components, as well as the increase in iron loss due to heavier magnetic saturation. Variation in the VUF is approximately linear from no load to the balance point.

The validity of the analysis and solution method is verified by the close agreement between the computed and experimental results in Figs. 4.45 to 4.50.

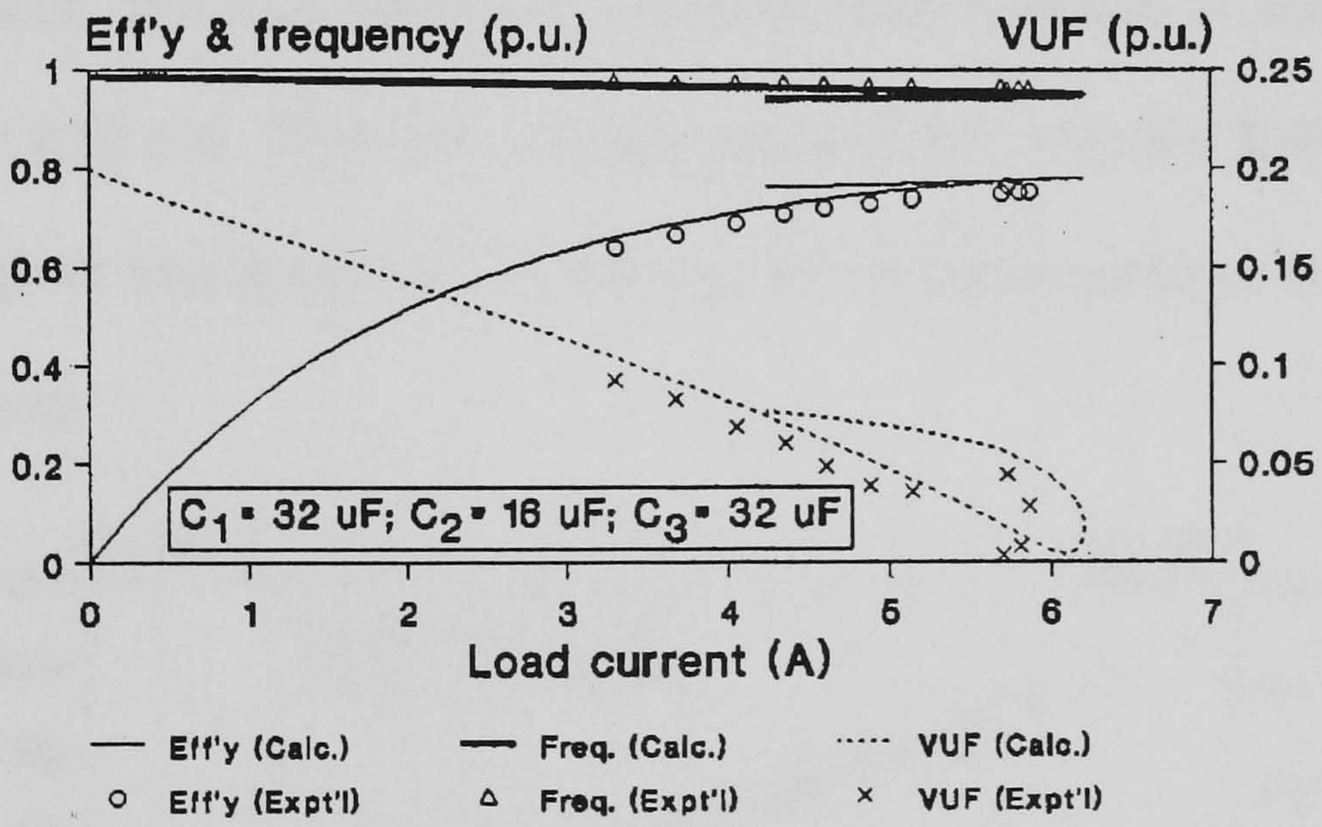


Fig. 4.50 Efficiency, frequency and VUF characteristics of SMSEIG with constant excitation capacitances.

*C) Computed Results: Variable-Speed Operation*

Pertinent characteristics of the SMSEIG were also computed for variable-speed operation. Fig. 4.51 shows the computed values of $C_1$ required for balanced operation of the SMSEIG at different operating speeds and the corresponding values of the phase voltage. For a given load impedance, $C_1$ (and also $C_2$ and $C_3$) decreases with increase in

the per-unit speed $b$. There is also a minimum value of $b$ below which stable operation is not possible while maintaining perfect balance. The phase voltage (and hence the load voltage) increases with $b$, thereby imposing an upper limit to the permissible operating speed.

Fig. 4.52 shows the computed performance of the SMSEIG as a function of speed when $C_1$ = 32 μF, $C_2$ = 16 μF and $C_3$ = 32 μF, and a constant load impedance of 1.48 p.u. at unity power factor is being supplied. This combination of excitation capacitances and load impedance results in perfect phase balance at rated speed. The VUF characteristic is a nearly flat V-shaped curve, implying that the phase imbalance is very slight despite a large change in the rotor speed. Over a wide speed range, the efficiency of the SMSEIG remains practically constant at 0.78 p.u., while the per-unit frequency $a$ varies almost linearly with speed. The load voltage $V_L$ decreases with reduction in rotor speed and it collapses at $b$ = 0.83 p.u. The above results indicate that, once the SMSEIG has been balanced for a given load impedance at rated speed, its performance at other speeds will also be satisfactory.

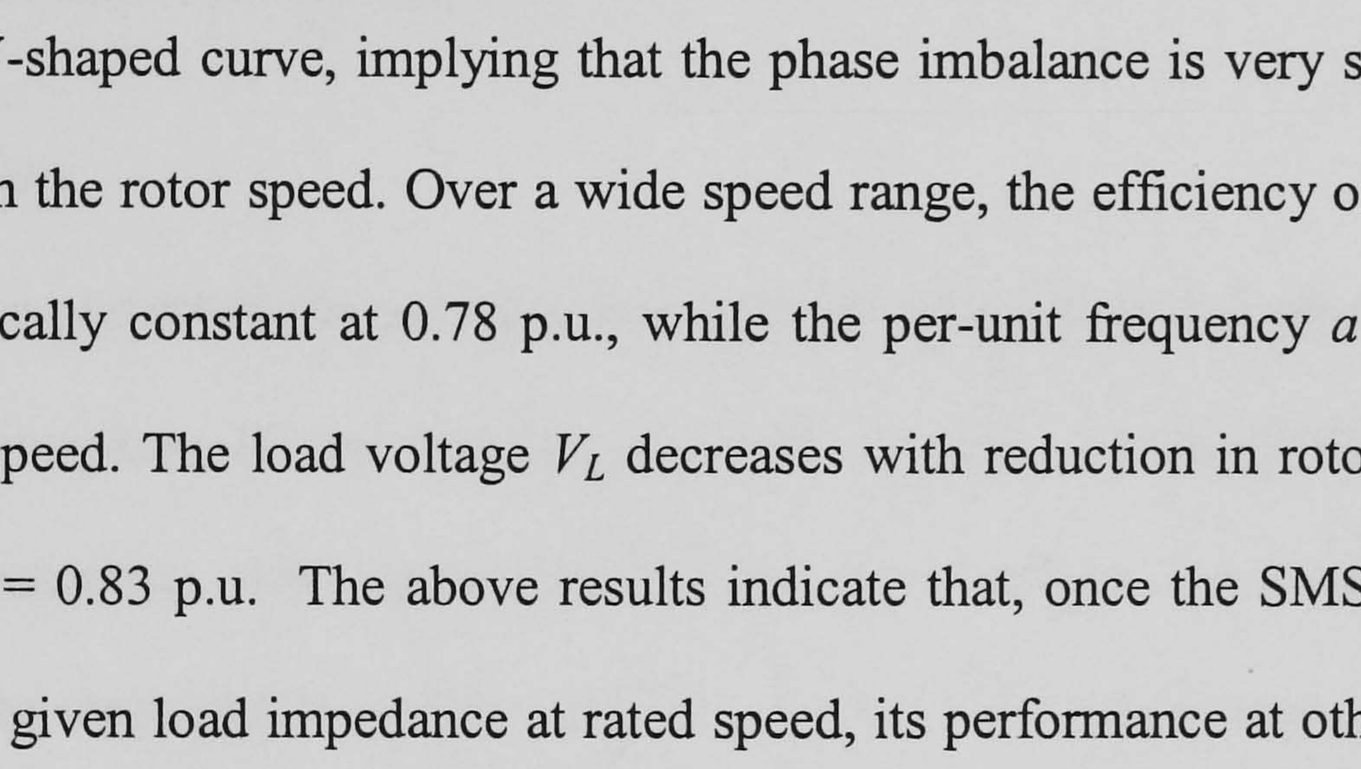


Fig. 4.51 Computed variations of $C_1$ and phase voltage of SMSEIG with rotor speed under perfect phase balance.

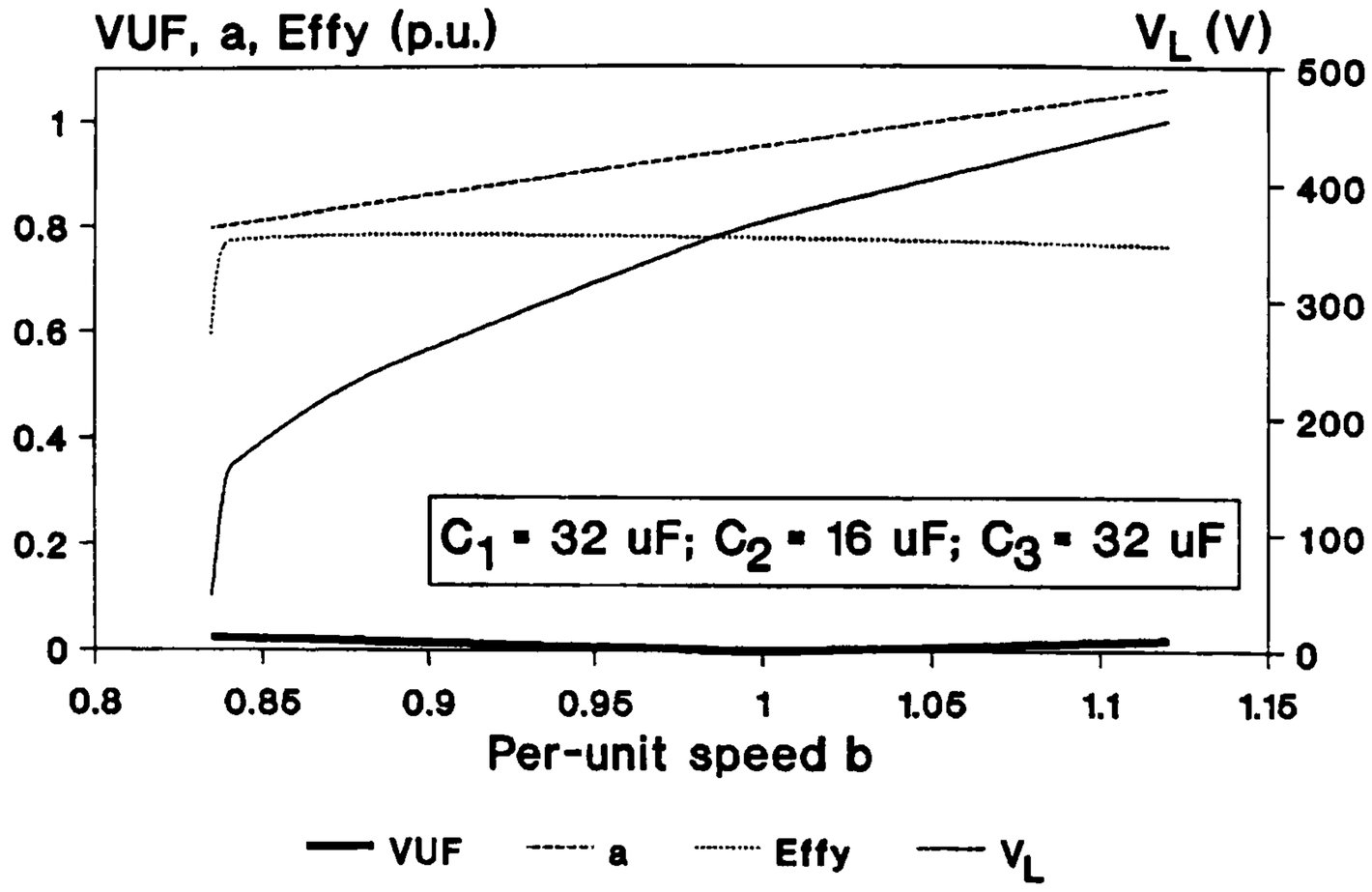


Fig. 4.52 Computed variations of VUF, per-unit frequency, efficiency and load voltage of SMSEIG with rotor speed.

### 4.5.5 Summary

Section 4.5 has presented the principle and analysis of a novel excitation scheme for a stand-alone three-phase IG that supplies single-phase loads, viz. the SMSEIG. Adopting the Smith connection with appropriate values of excitation capacitances, balanced operation of the three-phase machine can be achieved. The steady-state performance of the SMSEIG is analyzed using the method of symmetrical components in association with an optimization procedure. A method to determine the capacitances to give perfect phase balance is also presented. Experimental investigations have confirmed the feasibility of the proposed excitation scheme. Although only results of the resistive load case have been reported, the analysis set forth can readily be applied to different load power factor conditions. The SMSEIG has the advantages of low cost, high efficiency and large power output, and as such is an economical choice when developing autonomous single-phase power systems in remote regions.

# Chapter 5

# VOLTAGE AND FREQUENCY CONTROL OF SEIG WITH SLIP-RING ROTOR (SESRIG)

## 5.1 Introduction

A major disadvantage of an SEIG is that the output voltage and frequency are speed and load dependent. An increase in the rotor speed, for example, will result in a proportionate increase in frequency, often accompanied by severe overvoltage and excessive current. Recently, there has been rigorous research on the voltage and frequency control of squirrel-cage type SEIGs [45]-[50], but relatively little research efforts have been devoted to the use of the slip-ring induction machine for generator applications. Although the slip-ring machine is more expensive and requires more maintenance, it permits rotor slip-power control when driven by a variable-speed turbine. The slip-ring machine may be operated as a double-output induction generator (DOIG) using the slip-energy recovery technique [101], [102]. In the case of a self-excited slip-ring induction generator (SESRIG), the system cost can be further reduced by the use of a simple rotor resistance controller [103], [104]. Since only a capacitor bank need to be connected to the stator terminals, the SESRIG provides a good quality ac source with little harmonic distortion to the stator load. Another advantageous feature of the SESRIG is that independent control of the voltage and frequency can be achieved easily. Even with a wide variation in speed, the generator frequency can be maintained reasonably constant by rotor resistance control, while the voltage can be controlled by varying the excitation capacitance. The rating of the rotor resistance controller is small compared with the generator rating, hence the cost saving is quite significant.

In this chapter, the voltage and frequency control of a three-phase SESRIG by variation of external rotor resistance will be investigated. Based on a normalized equivalent circuit model, the frequency and voltage control characteristics are deduced and experimental results are presented to verify the feasibility of the control method. Practical implementation of a closed-loop scheme that uses chopper-controlled rotor resistance will also be described.

## 5.2 Performance Analysis of SESRIG

Fig. 5.1 shows the circuit arrangement of a three-phase SESRIG which is supplying a balanced stator load. The excitation capacitance $C$ is required for initiating voltage build-up and maintaining the output voltage. It is noticed that the electrical output power is dissipated in both the stator impedance $Z_L$ as well as the external rotor resistance $R_x$, hence the machine may also be regarded as a DOIG if the power in $R_x$ is effectively utilized.

Fig. 5.2 shows the per-phase equivalent circuit of the SESRIG, where the rotor resistance $R_2$ is the sum of the rotor winding resistance and the external rotor resistance, both referred to the stator side.

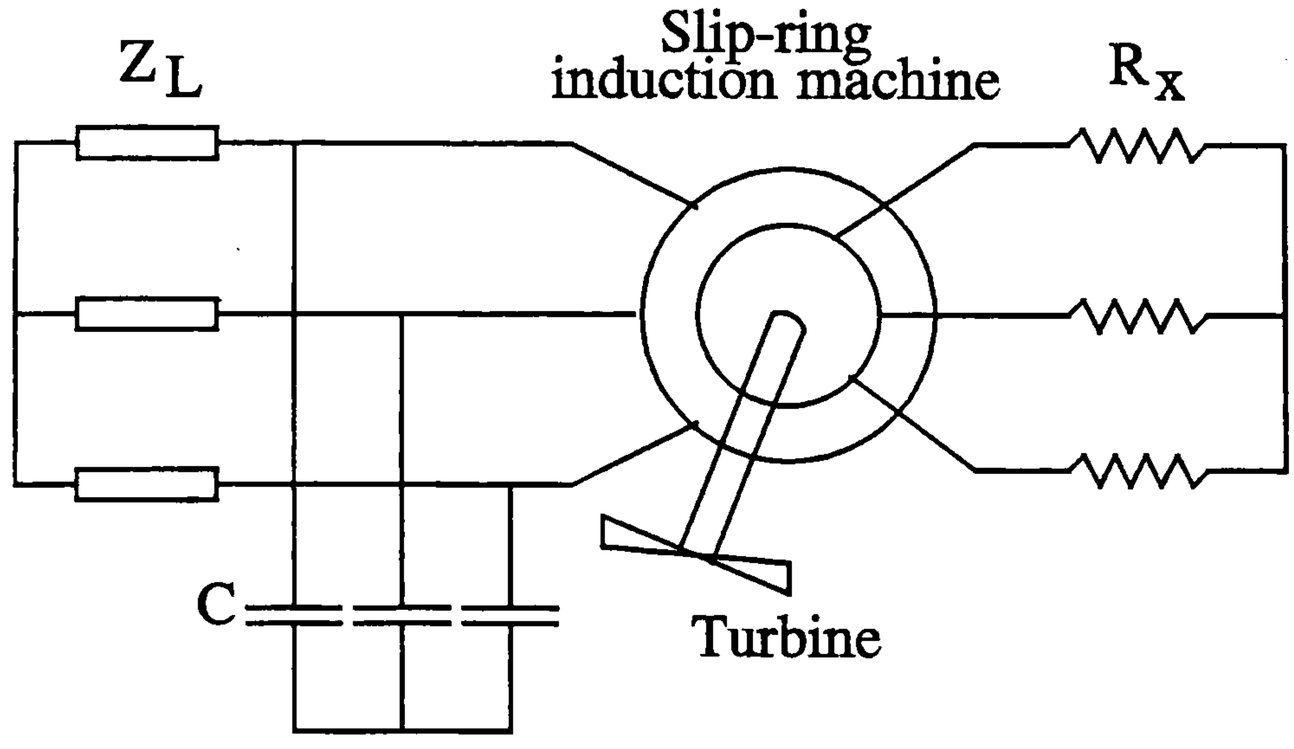


Fig. 5.1 Self-excited slip-ring induction generator (SESRIG).

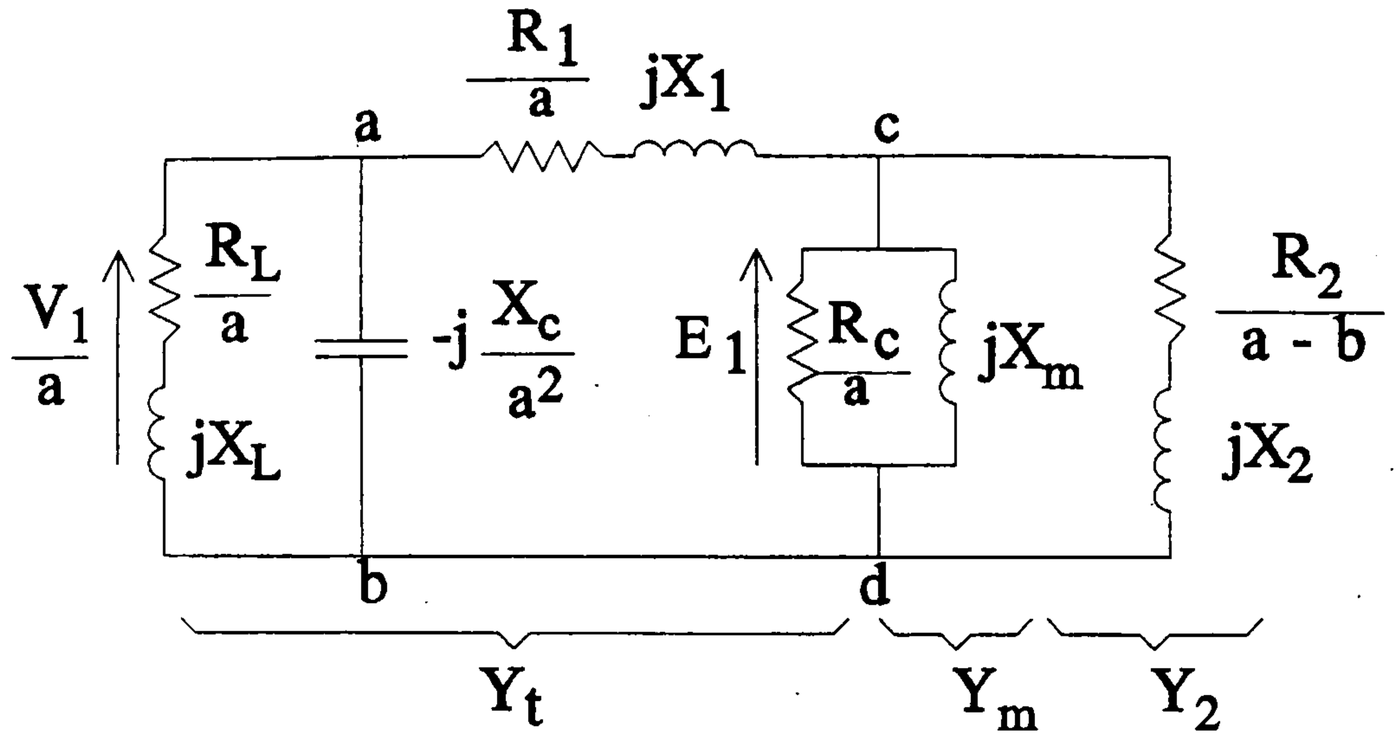


Fig. 5.2 Per-phase equivalent circuit of SESRIG.

Various methods have been developed for solution of the SEIG equivalent circuit. Adopting the nodal admittance method [28], the following relationship may be established for successful voltage build-up:

$$Y_t + Y_m + Y_2 = 0 \tag{5.1}$$

where

$$Y_t = \frac{1}{Z_t} = \frac{1}{Z_{ac} + Z_{ab}} = G_t + jB_t \tag{5.2}$$

$$Y_m = \frac{a}{R_c} - j.\frac{1}{X_m} = G_m - jB_m \tag{5.3}$$

$$Y_2 = \frac{1}{\frac{R_2}{a-b} + jX_2} = G_2 - jB_2 . \tag{5.4}$$

Equating the real and imaginary parts in (5.1) to zero respectively, the following equations in real numbers are obtained:

$$G_t + G_m + G_2 = 0 \tag{5.5}$$

$$B_t - B_m - B_2 = 0 . \tag{5.6}$$

For a given rotor speed, load impedance and excitation capacitance, (5.5) is a nonlinear equation in the variable $a$ only. Numerical solution of (5.5) using an iterative method [42] enables $a$ to be determined, and (5.6) can subsequently be used to calculate $X_m$. With the aid of the magnetization curve (plot of $E_1$ versus $X_m$), $E_1$ can be determined and the equivalent circuit is completely solved to yield the steady-state performance.

Performance analysis and experiments for variable-speed operation were conducted on a 3-phase, 4-pole, 50-Hz, 380-V, 4.5-A, 1.8-kW, star/star connected slip-ring induction machine whose per-unit equivalent circuit constants are: $R_1 = 0.0597$, $X_1 = 0.118$, $R_2 = 0.0982$, $X_2 = 0.118$. The magnetization curve was represented by the following set of describing equations:

$$E_1 = \begin{cases} 1.4613 - 0.3327\,X_m, & X_m < 1.7728 \\ 1.5294 - 0.3711\,X_m, & 1.7728 \le X_m < 2.045 \\ 3.0455 - 1.1125\,X_m, & 2.045 \le X_m < 2.213 \\ 185.1 - 83.37\,X_m, & 2.213 \le X_m < 2.22 \\ 0, & 2.22 \le X_m \end{cases} \cdot \tag{5.7}$$

Fig. 5.3, Fig. 5.4 and Fig. 5.5 show, respectively, the stator voltage, stator current and frequency characteristics of the SESRIG for different values of external rotor resistance $R_x$. For convenience, all the machine parameters, except the excitation capacitance, are expressed in per unit. It is observed that increasing $R_x$ has the effect of shifting the performance characteristics to the right-hand side of the speed axis. At a rotor speed of 1.05 p.u. or above, the generator voltage or frequency can be maintained at rated value (i.e. 1.0 p.u.) by varying $R_x$. This feature will be employed for voltage and frequency control of the SESRIG, to be discussed in the next section.

To achieve higher system efficiency, it is important that the power dissipated in $R_x$ be fully utilized. If $R_x$ takes the form of resistive heater elements, the slip power could

conveniently be used for storage heating which is a common load in an autonomous power system. The total power output of the SESRIG is then the sum of the stator load power and the power consumed by $R_x$.

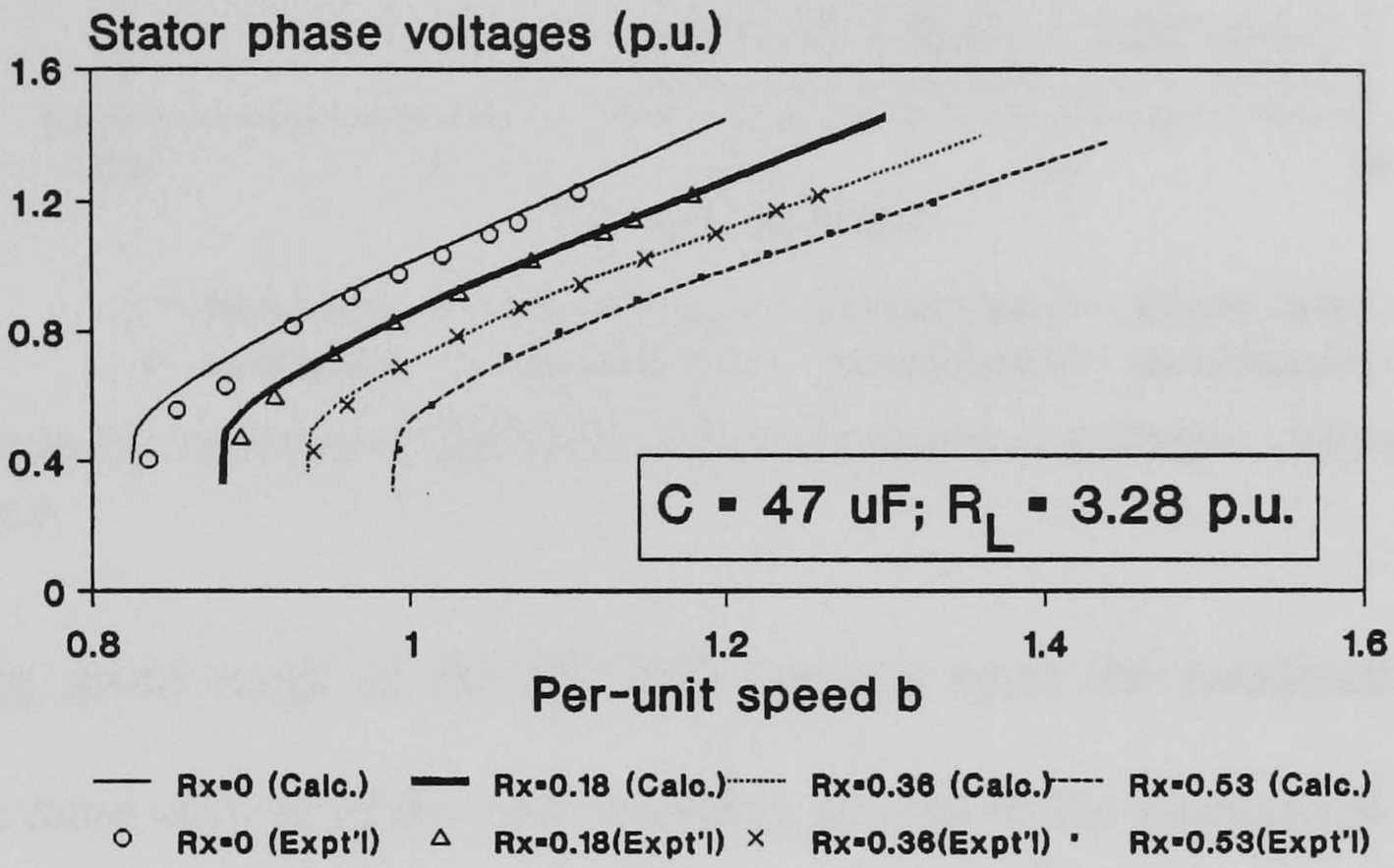


Fig. 5.3 Stator voltage variation of SESRIG with rotor speed at different values of external rotor resistance.

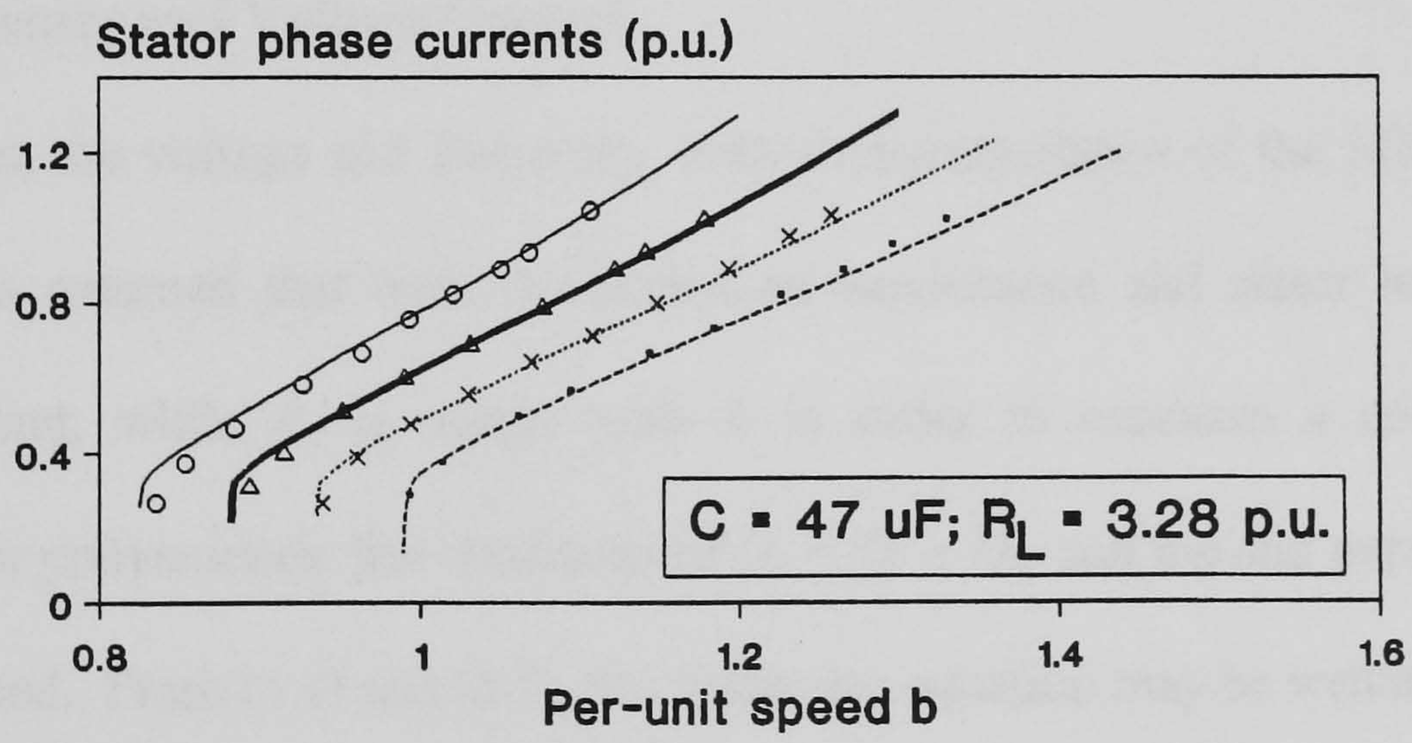


Fig. 5.4 Stator current variation of SESRIG with rotor speed at different values of external rotor resistance.

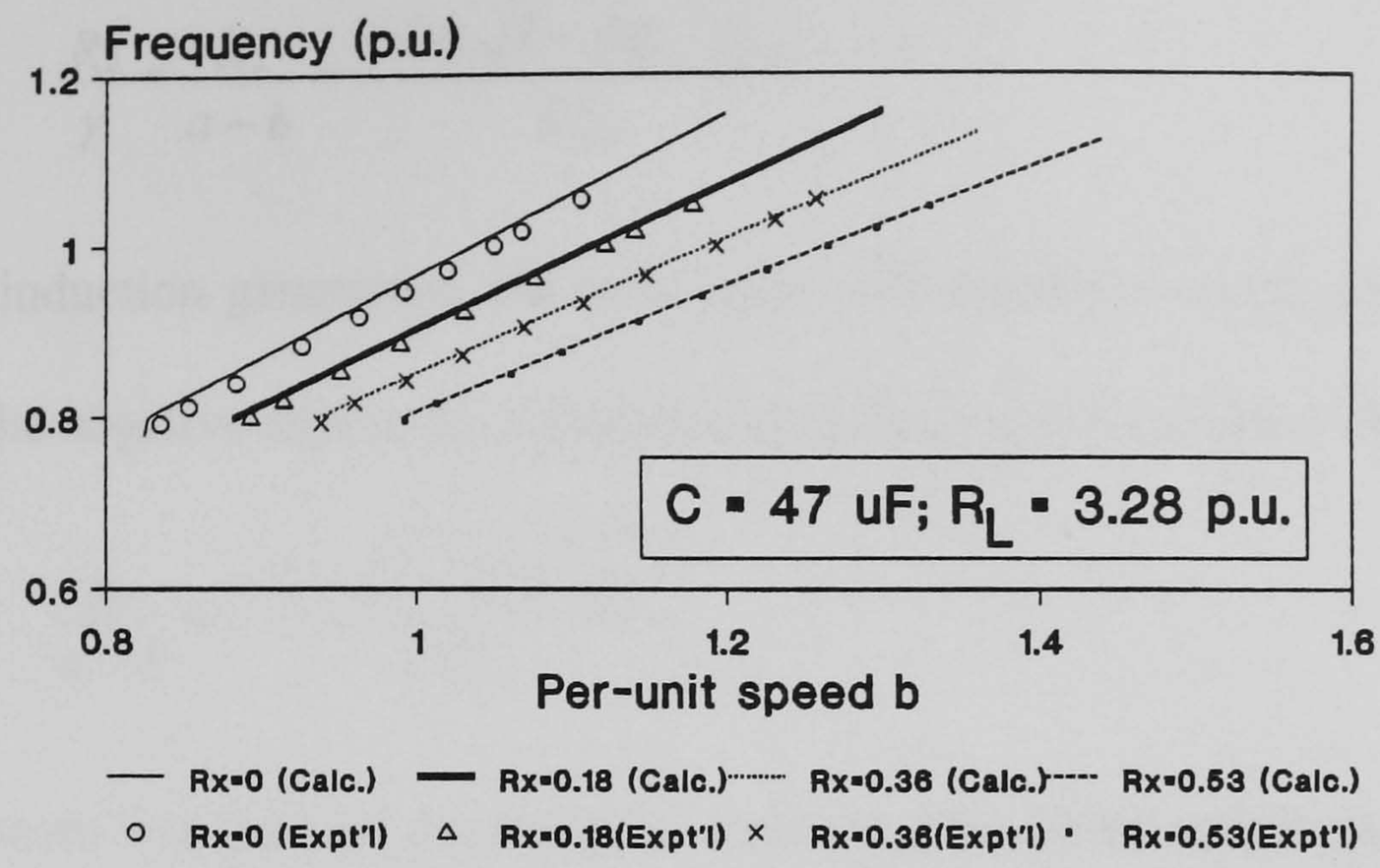


Fig. 5.5 Frequency variation of SESRIG with rotor speed at different values of external rotor resistance.

The operating speed range of the SESRIG depends upon the maximum value of $R_x$ available, the rated voltage of the rotor winding, as well as the mechanical constraints of the turbine-generator system.

## 5.3 Frequency and Voltage Control

In this section, the voltage and frequency control characteristics of the SESRIG will be deduced. It is assumed that both the excitation capacitance and stator load resistance remain constant, while $R_x$ is varied with $b$ in order to maintain a constant output frequency. For convenience, the conductance $G_e = G_t + G_m$ and the slip parameter $\gamma = a - b$ are introduced. From (5.4) and (5.5), the following equation may be written:

$$G_e + \frac{\gamma R_2}{R_2^2 + \gamma^2 X_2^2} = 0 . \tag{5.8}$$

It should be noted that, for a specified value of $a$, $G_e$ is a constant when the excitation capacitance and load resistance are both constant.

Solving (5.8) for $\gamma$, one obtains:

$$\frac{R_2}{\gamma} = \frac{R_2}{a-b} = \frac{-1 \pm \sqrt{1 - 4G_e^{\,2} X_2^{\,2}}}{2G_e} . \tag{5.9}$$

For practical induction generators, the term $R_2/(a - b)$ usually assumes a large negative value, hence the negative sign in the numerator of (5.9) should be chosen. Therefore,

$$\frac{R_2}{a-b} = \frac{-1 - \sqrt{1 - 4G_e^{\,2} X_2^{\,2}}}{2G_e} . \tag{5.10}$$

Eqn. (5.10) shows that the total rotor circuit resistance should be varied linearly with the per-unit speed $b$ in order to control the frequency at a given value.

Substituting (5.10) into (5.6),

$$\frac{1}{X_m} = B_t - \frac{2G_e^{\,2} X_2}{1 + \sqrt{1 - 4G_e^{\,2} X_2^{\,2}}} . \tag{5.11}$$

Eqn. (5.11) implies that, for a given per-unit frequency $a$, excitation capacitance and load resistance, the magnetizing reactance $X_m$ of the SESRIG, and hence the air gap voltage $E_1$, is independent of the rotor speed. It follows therefore that both the stator current and terminal voltage are constant.

Fig. 5.6 shows the variation of external rotor resistance and the resultant output voltage when the per-unit frequency of the SESRIG is maintained at 1.0 p.u. and the stator load resistance is 2.36 p.u. Over a wide range of speed, the stator voltage remains constant at 1.06 p.u. when $C = 47$ μF and 0.86 p.u. when $C = 37$ μF.

The close agreement between the computed and experimental results in Fig. 5.3 to Fig. 5.6 confirms the accuracy of the circuit model and solution method. Fig. 5.6, in addition, demonstrates the feasibility of voltage and frequency control of the SESRIG by varying the external rotor resistance. Either the frequency or the terminal voltage may be chosen as the feedback variable for voltage and frequency control.

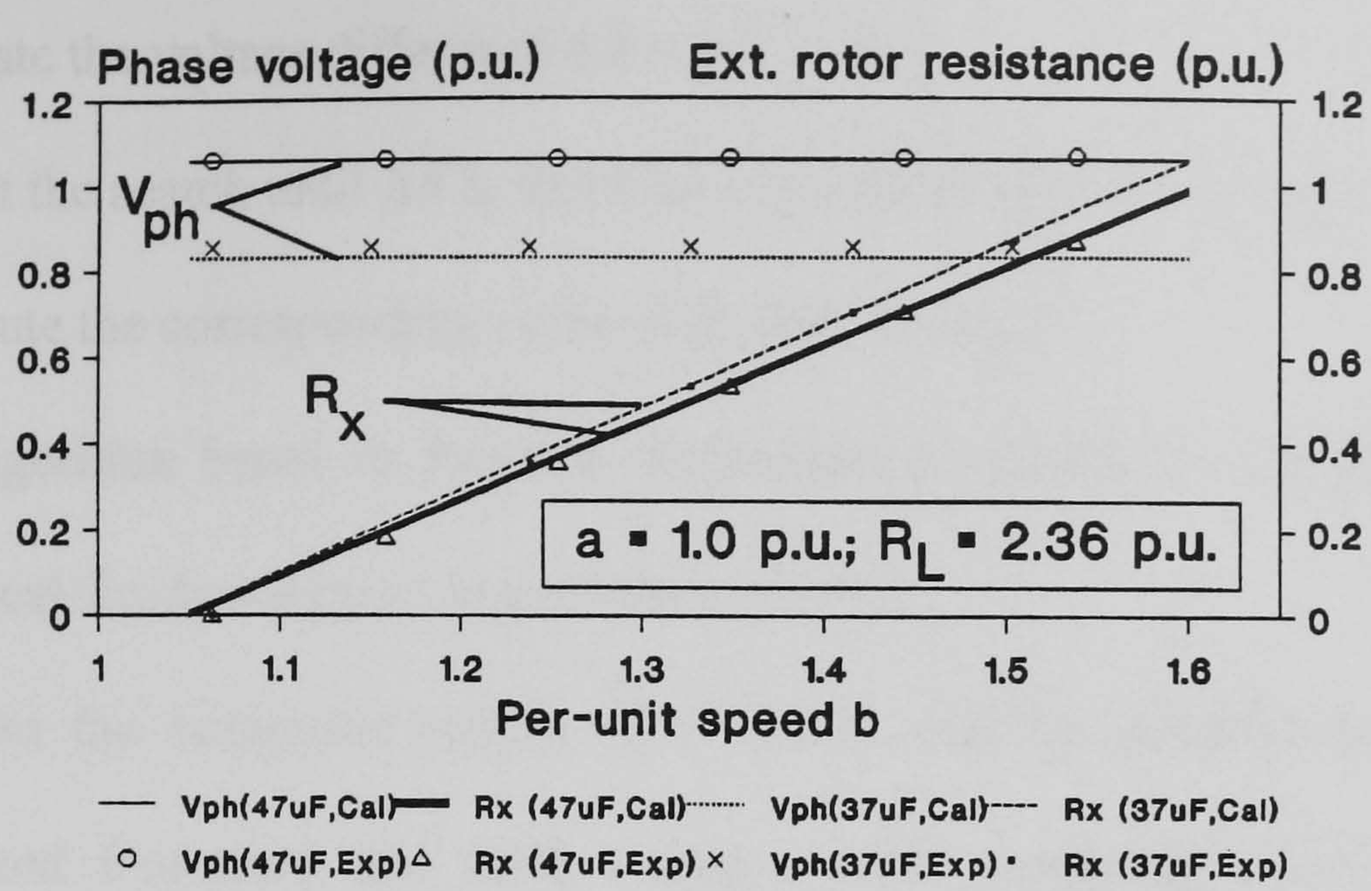


Fig. 5.6 External rotor resistance $R_x$ for the SESRIG to operate at rated frequency and the corresponding variation of stator phase voltage.

## 5.4 Control with Variable Stator Load

When the stator load impedance is changed, it is also possible to maintain the output frequency constant by varying $R_x$, but the stator terminal voltage will differ from the nominal value. In order to control the stator terminal voltage at the desired value, it is necessary to control the excitation capacitance $C$ simultaneously as $R_x$ is varied. The analysis can now be formulated as the following problem:

*For a given value of load impedance $Z_L$ and per-unit speed b, determine the values of C and $R_x$ that result in operation of the SESRIG at the specified voltage $V_1^*$ and per-unit frequency a.*

The above problem can be solved by using the following simple search algorithm, with $C$ as the variable:

1) Using the current value of search variable $C$, compute $R_2$ using (5.10).

2) Obtain the corresponding value of magnetizing reactance $X_m$ from (5.11), and, hence, the air gap voltage $E_1$ from the magnetization curve.

3) Compute the stator terminal voltage $V_1$.

4) Evaluate the voltage difference $\Delta V = |V_1^* - V_1|$.

5) Repeat the search until $\Delta V$ is less than a specified tolerance $\varepsilon$, say 1.0e-6.

6) Compute the corresponding value of $R_2$ and, hence, $R_x$.

Any search algorithm based on function evaluations is suitable for the present problem, e.g., the classical Golden-Section search method [105].

Fig. 5.7 shows the computed values of $C$ and $R_x$ for the experimental SESRIG to operate at rated frequency and rated voltage, while supplying a unity-power-factor stator load. At a specific rotor speed, $C$ has to be increased when the output power increases, while $R_x$ has to be reduced. There is thus a value of output power at which $R_x$ is reduced to zero, which corresponds to operation with the slip-rings short-circuited. At $b$ = 1.1 p.u., for example, this condition prevails when the machine is delivering an output power of 0.84 p.u. When the output power exceeds this value, it is not possible to maintain the frequency and voltage simultaneously at the specified values. It is also observed from Fig. 5.7 that a smaller excitation capacitance and a larger external rotor resistance are required for maintaining constant voltage and frequency at a higher rotor speed.

Fig. 5.8 shows the computed variations of stator current and efficiency with output power when both the voltage and frequency of the SESRIG are maintained at rated values. At a higher rotor speed, more output power can be delivered without the rated stator current being exceeded. Because of the simultaneous control of $C$ and $R_x$, the maximum efficiency of the SESRIG now occurs at a stator current of 0.91 p.u., irrespective of the rotor speed. The maximum efficiency is 0.79 p.u. when $b$ = 1.1 p.u. and it increases to 0.83 p.u. when $b$ = 1.4 p.u. The efficiency is good when the output power exceeds 0.4 p.u.

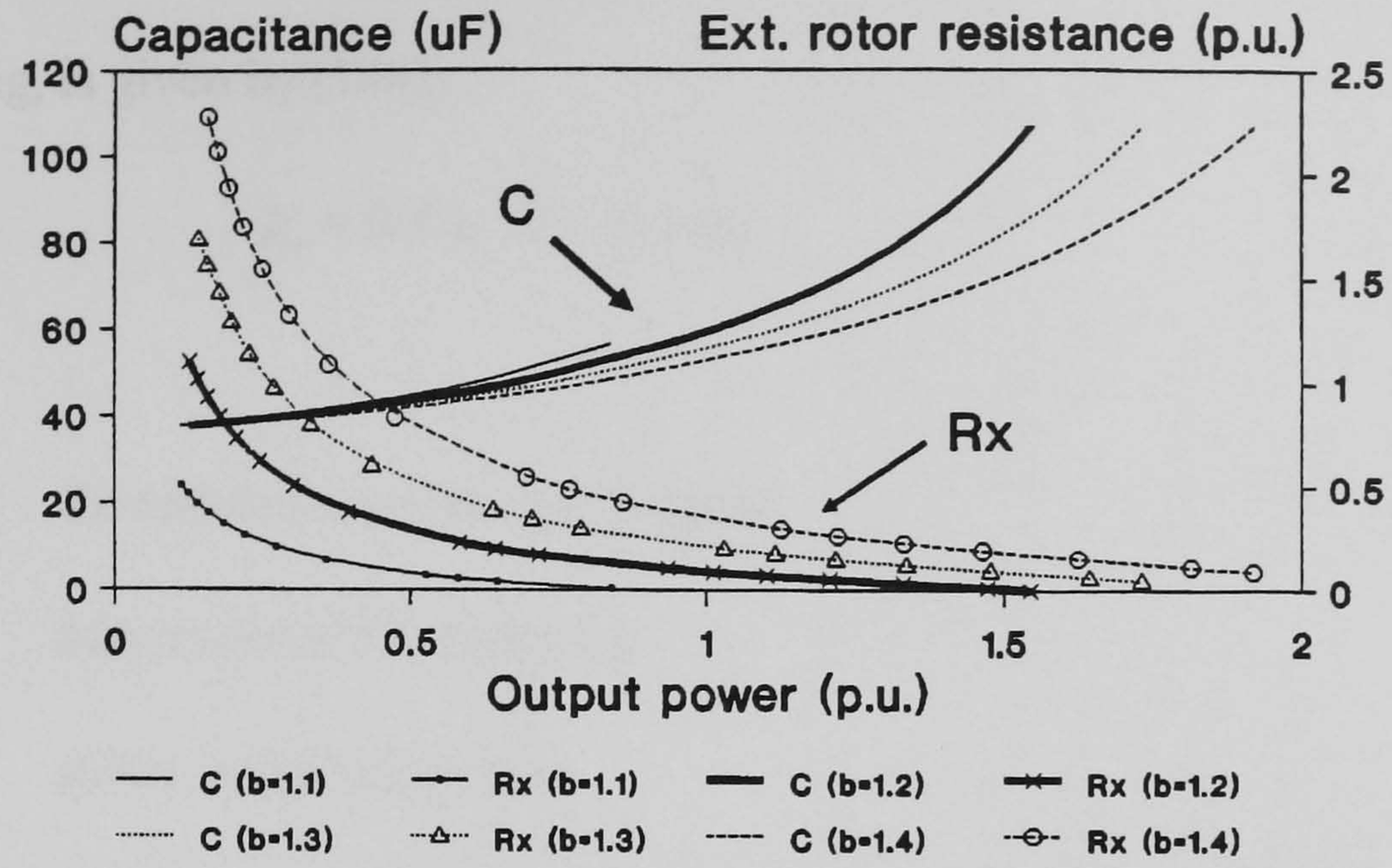


Fig. 5.7 Variation of $R_x$ and $C$ for the SESRIG to operate at rated voltage and rated frequency, a resistive load being supplied.

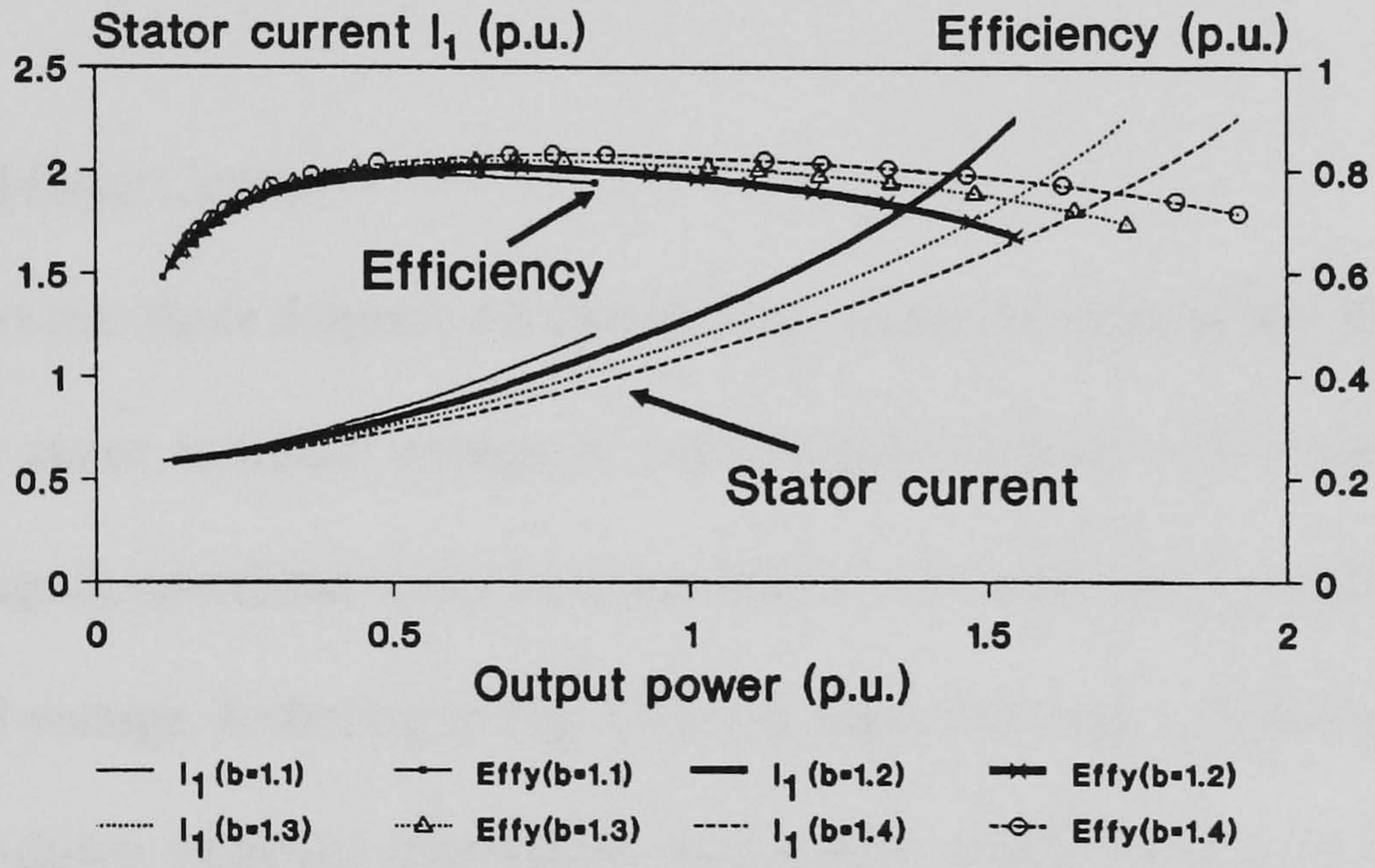


Fig. 5.8 Variation of stator current and efficiency when the SESRIG is controlled at rated voltage and rated frequency.

## 5.5 Practical Implementation

### 5.5.1 Chopper-Controlled Rotor External Resistance

It is desirable to have automatic control of the voltage and frequency when either the stator load impedance or the rotor speed changes. Instead of a variable three-phase rotor resistance, a chopper-controlled external resistance may be employed, as illustrated in Fig. 5.9. Assuming that the diodes in the rotor bridge rectifier are ideal and the choke is

lossless, the effective external resistance per phase $R_x$ in the rotor circuit, referred to the stator winding, is given by [106]:

$$R_x = 0.5\, a_t^{\,2}\,(1-\alpha)\,R_{dc} \tag{5.12}$$

where

$R_{dc}$ = dc resistance across the chopper;

$\alpha$ = duty cycle of the chopper;

$a_t$ = stator / rotor turns ratio.

A reduction in the duty cycle $\alpha$ of the chopper results in an increase in the effective rotor resistance of the SESRIG. A variable external resistance is thus presented to the rotor circuit.

### 5.5.2 Closed-Loop Control

Fig. 5.10 shows the block diagram for closed-loop control of voltage and frequency of the SESRIG. The stator terminal voltage is conveniently chosen as the feedback variable since any change in speed and stator load impedance will result in a corresponding change in the terminal voltage. Referring to Fig. 5.10, the stator terminal voltage signal $v_t$, derived from the step-down isolation transformer and signal conditioning circuit, is compared with the reference signal $v_{ref}$ that corresponds to the set-point voltage. The error signal $v_e$ is fed to a proportional-plus-integral (PI) controller that outputs a signal $v_0$ for controlling the duty cycle $\alpha$ of the chopper via pulse-width modulation (PWM), opto-isolation and gate drive circuits.

In the prototype controller implemented, the chopper main switch was a power MOSFET controlled by an LM3524 PWM circuit and an IR2132 driver circuit. The total cost of the components was approximately US$50, or one-tenth that of the SESRIG system.

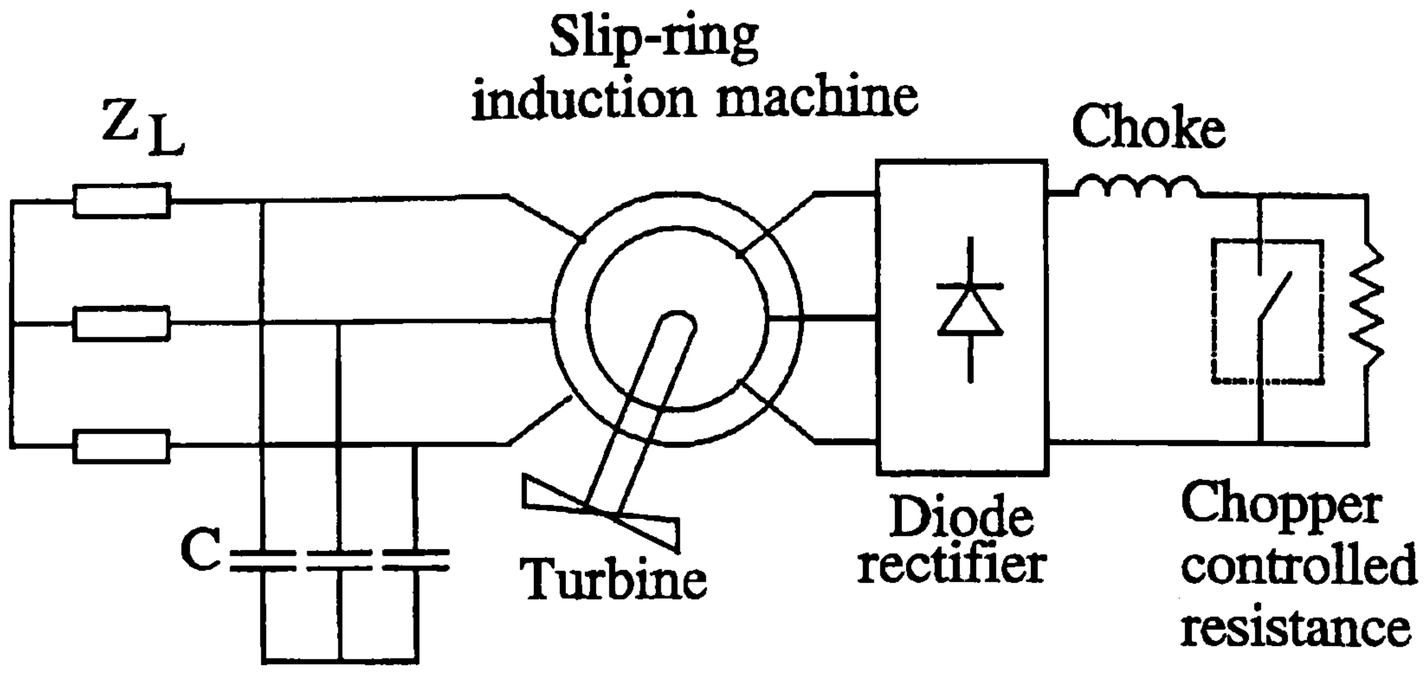


Fig. 5.9 SESRIG with chopper-controlled rotor external resistance.

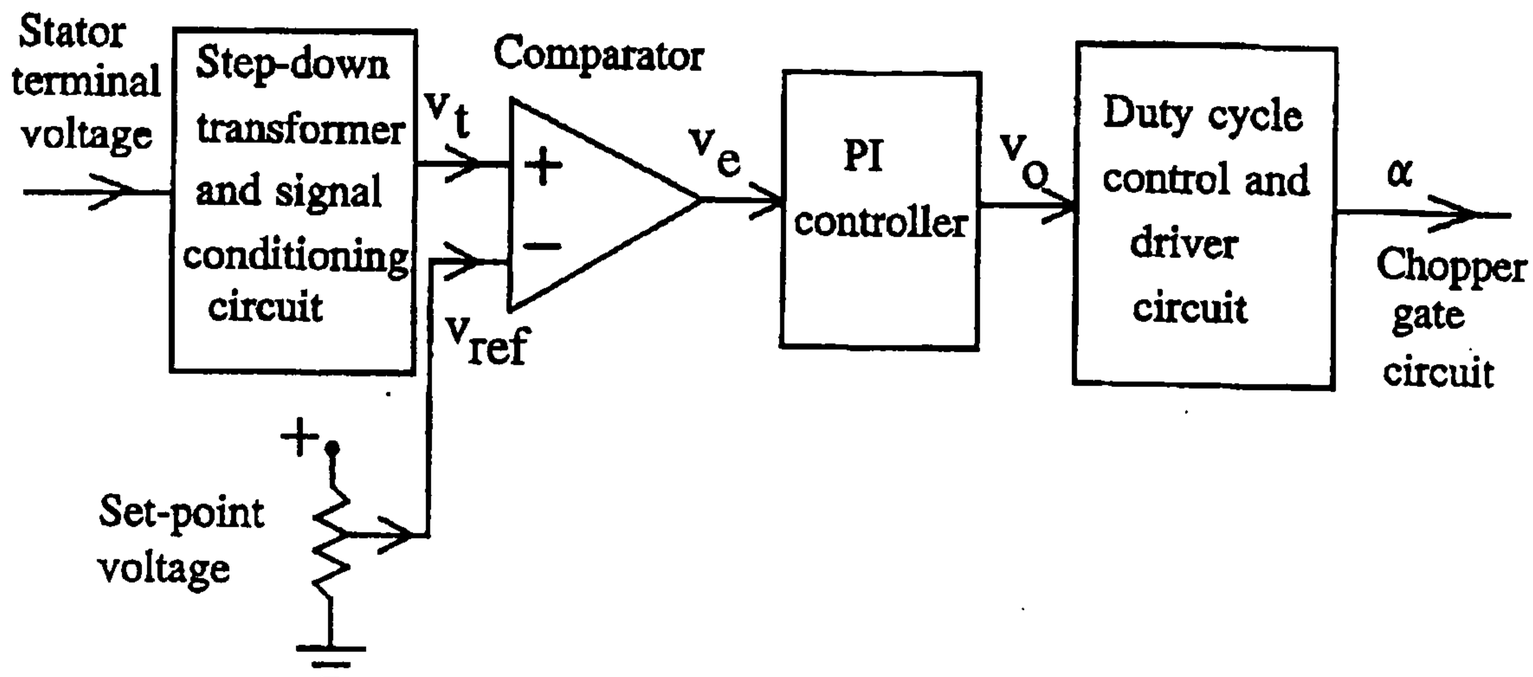


Fig. 5.10 Feedback circuit for voltage control of SESRIG.

### 5.5.3 Tuning of PI Controller

Proper tuning of the PI controller is required in order to give a satisfactory dynamic performance. For this purpose, the SESRIG may be approximated as a first-order system with the following transfer function:

$$G(s) = \frac{K.e^{-st_0}}{s\tau + 1} \tag{5.13}$$

where

$K$ = system gain;

$\tau$ = time constant of the system;

$t_0$ = time delay of the system.

The parameters of the transfer function may be determined using the open-loop step response method [107]. With the transfer function identified, the gain of the proportional controller $K_p$ and the gain of the integral controller $K_i$ can be determined using the Ziegler-Nichols open-loop tuning method [107]. For the prototype experimental system, the controller parameters were determined as follows:

$K = 1.15$; $\tau = 0.8$ s; $t_0 = 0.341$ s;

$K_p = 1.87$; $K_i = 1.13$

### 5.5.4 Dynamic Response

To study the dynamic response of the SESRIG with closed-loop control, the machine was driven by a separately-excited dc motor that emulated an unregulated, variable-speed turbine while a resistive load was being supplied. It was found that, with an excitation capacitance of 45 μF per phase, the terminal voltage could be maintained at the rated value over a wide speed range, the maximum rotor speed attained being limited primarily by the rated current of the dc motor. Under these conditions, the frequency of the stator voltage was found to be 48.1 Hz. Using the above value of excitation capacitance, dynamic load tests were performed on the generator system, with the reference voltage signal set to give rated stator terminal voltage. For easy comparison, the stator voltage signal from the signal conditioning circuit and the PWM control signal were monitored using a digital storage oscilloscope during the dynamic tests.

Fig. 5.11 and Fig. 5.12 show the dynamic response of the SESRIG subsequent to a speed change, the stator load resistance being kept constant at 4.29 p.u. The PI controller took effect as soon as the speed started to change, outputting a corresponding PWM control signal. The stator voltage was restored to the set-point value in approximately 2.7 s when the speed was increased from 1561 r/min to 1623 r/min (Fig. 5.11), and 3.2 s when the

speed was decreased from 1761 r/min to 1618 r/min (Fig. 5.12). The dynamic response characteristics displayed very little overshoot, showing that the controller had been properly designed, with minimal overshoot and small steady-state error. It should be noted that the inherent dynamic speed-torque characteristic of the motor drive contributed partly to the delay in the voltage restoration.

Fig. 5.13 shows the dynamic response of the SESRIG system after the stator load resistance was switched from 4.29 p.u. to 3.73 p.u. The load change was accompanied by a speed drop from 1645 r/min to 1590 r/min as the speed of the simulated turbine was not regulated. Again the voltage was restored in about 2.7 s.

The experimental dynamic responses of the SESRIG shown in Fig. 5.11 to Fig. 5.13 are comparable with other cage-type SEIG voltage and frequency control schemes that employ PI controllers [46], [47].

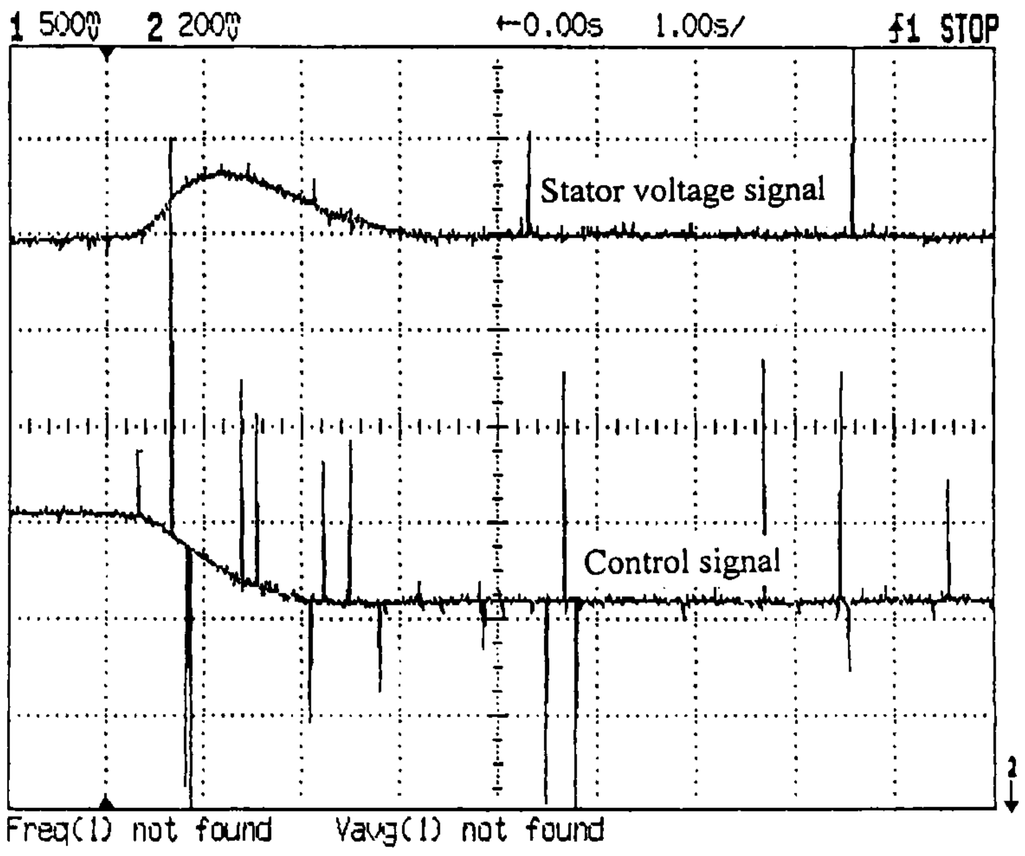


Fig. 5.11 Dynamic response of SESRIG following a speed change from 1561 r/min to 1623 r/min, $R_L = 4.29$ p.u. (Time scale: 1 s /div).

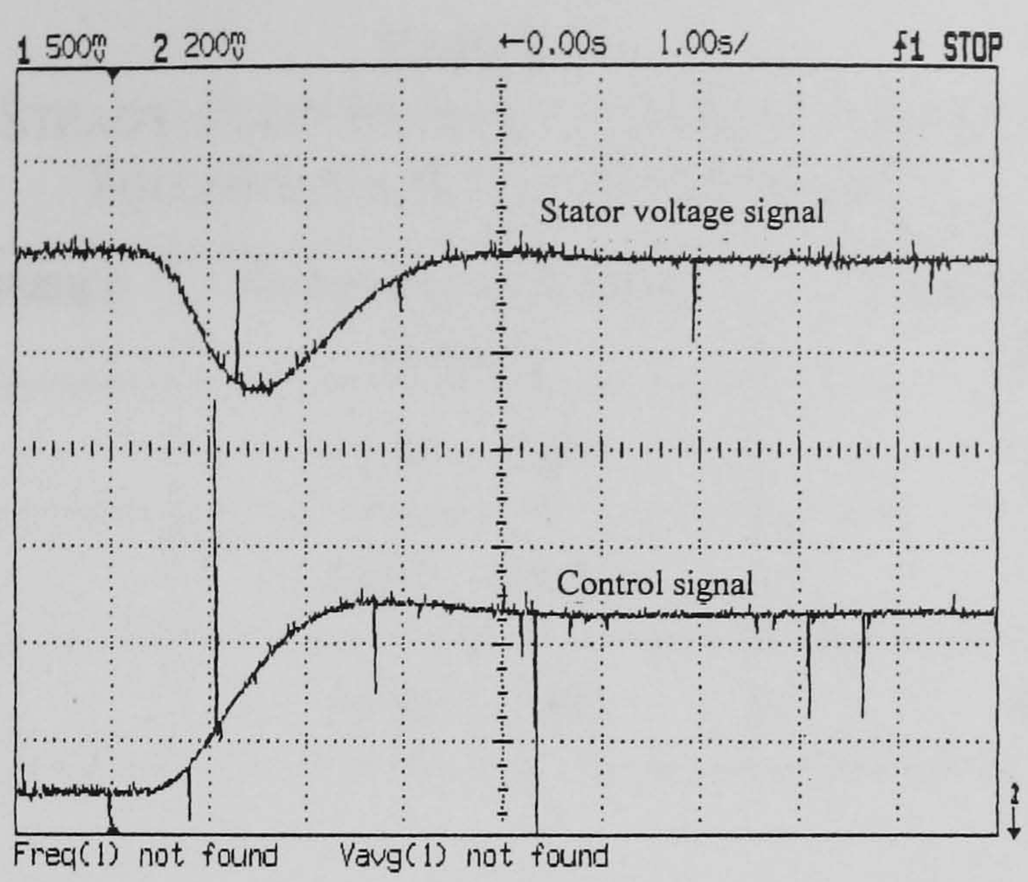


Fig. 5.12 Dynamic response of SESRIG following a speed change from 1761 r/min to 1618 r/min, $R_L$ = 4.29 p.u. (Time scale: 1 s/div).

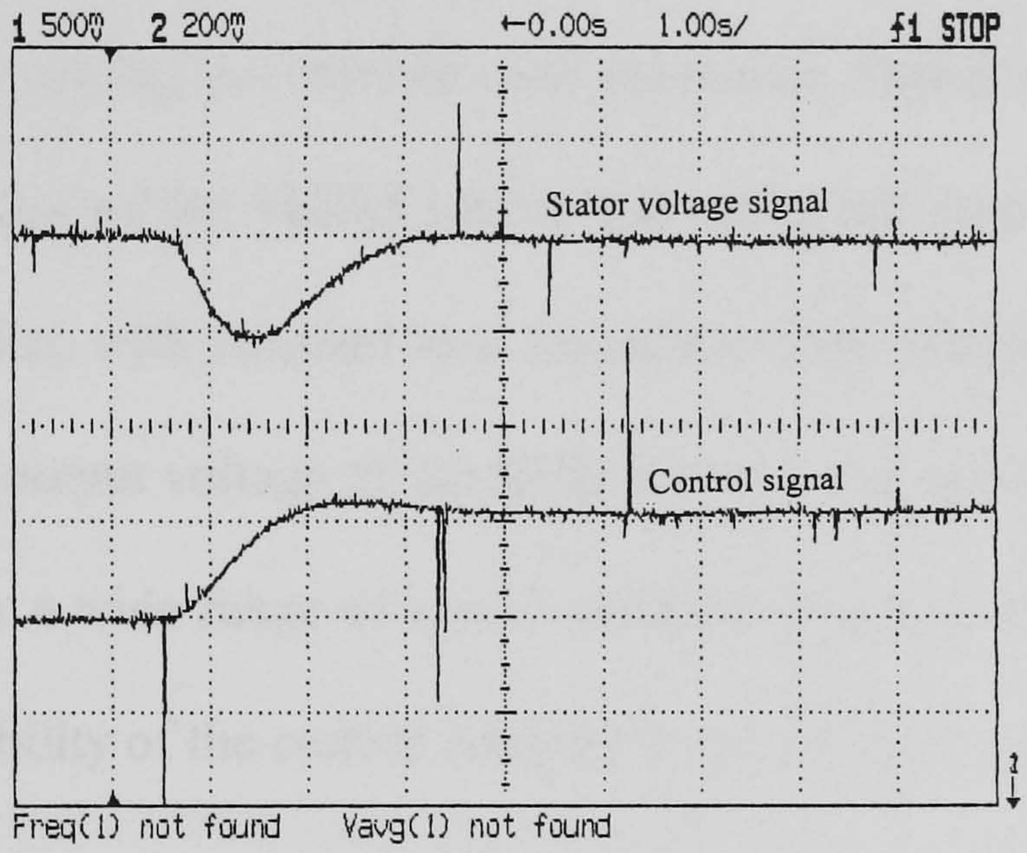


Fig. 5.13 Dynamic response of SESRIG following a change of stator load resistance from 4.29 p.u. to 3.73 p.u., accompanied by a speed change from 1645 r/min to 1590 r/min. (Time scale: 1 s/div).

Table 5.1 shows the steady-state frequency error when the SESRIG with the feedback controller was subjected to a rotor speed change. It is observed that, despite the change in rotor speed being considered, the maximum frequency deviation after the transient period is only 0.1 Hz for different stator load resistances.

The above observations confirm that both the voltage and frequency can be controlled using the proposed method.

TABLE 5.1
STEADY-STATE FREQUENCY ERROR OF SESRIG
FOLLOWING A ROTOR SPEED CHANGE

| Stator load resistance $R_L$ (p.u.) | Rotor speed change (r/min) | Frequency error (Hz) |
|---|---|---|
| 4.93 | 1530 – 1809 | 0.1 |
| 4.29 | 1561 – 1623 | 0 |
| 3.73 | 1588 – 1680 | 0.1 |

## 5.6 Summary

This chapter has presented the voltage and frequency control for a self-excited slip-ring induction generator by varying the external rotor resistance. Steady-state performance and the control characteristics of the SESRIG have been obtained from an equivalent circuit analysis. It is shown that, with constant load impedance and excitation capacitance, both the frequency and the output voltage of the SESRIG can be maintained constant by rotor resistance control over a wide range of speed without exceeding the stator current limit. The analysis and feasibility of the control method have been verified by experiments on a 1.8-kW slip-ring machine. Practical implementation of a low-cost, closed-loop rotor resistance controller for the SESRIG has also been described. A properly tuned PI controller enables good steady-state accuracy and satisfactory dynamic response to be obtained on the generator system. The control method can also be implemented for single-phase SEIG schemes, such as the MSC, SSC, and the SMSEIG discussed in Chapter 4. The proposed scheme may be used in a low-cost variable-speed wind energy system for providing good-quality electric power to remote regions.

# Chapter 6

# PERMANENT-MAGNET SYNCHRONOUS GENERATORS FOR AUTONOMOUS POWER SYSTEMS

## 6.1 Introduction

As mentioned in Chapter 1, the permanent-magnet synchronous generator (PMSG) is also suitable for small-scale, isolated power system applications. Compared with the SEIG, the PMSG is more efficient and has no risk of loss of excitation, but it has the disadvantage that the output voltage cannot be regulated. A PMSG that possesses an inherent voltage compensation capability is desirable for maintaining a constant load voltage. In this chapter, it is demonstrated that the inverse saliency feature of a synchronous generator with an inset PM rotor can be exploited for improving the voltage regulation. Performance of the generator is computed based on the two-axis theory, and the conditions for achieving zero voltage regulation are deduced for the case of unity-power-factor loads as well as lagging-power-factor loads. The open-circuit voltage, direct-axis synchronous reactance and quadrature-axis synchronous reactance required in the analysis are accurately determined from the finite element method. A coupled circuit and field method will also be used for computing the generator load characteristic directly. Computed and experimental performance of a small prototype PMSG will be presented to validate the theoretical analysis.

## 6.2 Principle and Construction of PMSG with Inset Rotor

In an ac generator with a surface-magnet rotor, the direct-axis (d-axis) synchronous reactance $X_d$ and the quadrature-axis (q-axis) synchronous reactance $X_q$ are approximately equal. Fig. 6.1(a) shows the phasor diagram for unity-power-factor operation of a synchronous generator with a surface-magnet rotor, where $E$ is the open-

circuit voltage, $V$ is the terminal voltage, $I$ is the armature current, $R$ is the armature resistance and $X_s$ ($= X_d = X_q$) is the synchronous reactance. It is obvious that $V$ is less than $E$ when the generator is on load. Fig. 6.1(b) shows the phasor diagram of a synchronous generator that exhibits inverse saliency, i.e., a machine in which $X_q$ is larger than $X_d$. It should be noted that the d-axis current $I_d$ and q-axis current $I_q$, and hence the d-axis synchronous reactance drop $I_dX_d$ and q-axis synchronous reactance drop $I_qX_q$, depend upon the load impedance. In general, a larger $I_qX_q$ drop causes the terminal voltage phasor $V$ to fall further behind the open-circuit voltage phasor $E$. Under certain favourable conditions, the magnitude of $V$ may be equal to, or even greater than, the magnitude of $E$. With a suitable ratio of $X_q$ to $X_d$, it is possible to achieve zero voltage regulation at a particular load.

Fig. 6.2 shows the cross-sectional view of a prototype PMSG with an inset rotor, the technical details of which being given in Appendix D.3. Each permanent magnet is arch-shaped and is surface-mounted on the rotor yoke using a suitable bonding material, while soft-iron pole pieces occupy the interpolar regions. The edges of each rotor magnet are tapered in such a way that its inner pole arc is wider than the outer pole arc. This design results in a better air gap flux density distribution and hence a more sinusoidal output voltage waveform. The gap between each magnet and the adjacent soft-iron pole piece is filled with epoxy for better mechanical strength. The rotor magnets are made of neodymium-iron-boron (NdFeB), a high-energy PM material whose recoil permeability is very close to that of air. This property results in a suppression of the d-axis flux linkage and hence $X_q$ is larger than $X_d$, i.e., the generator exhibits inverse saliency. The desired $X_q/X_d$ ratio can be obtained by an appropriate choice of the interpolar air gap length, the pole arcs of the permanent magnets and the widths of the interpolar soft-iron pole pieces.

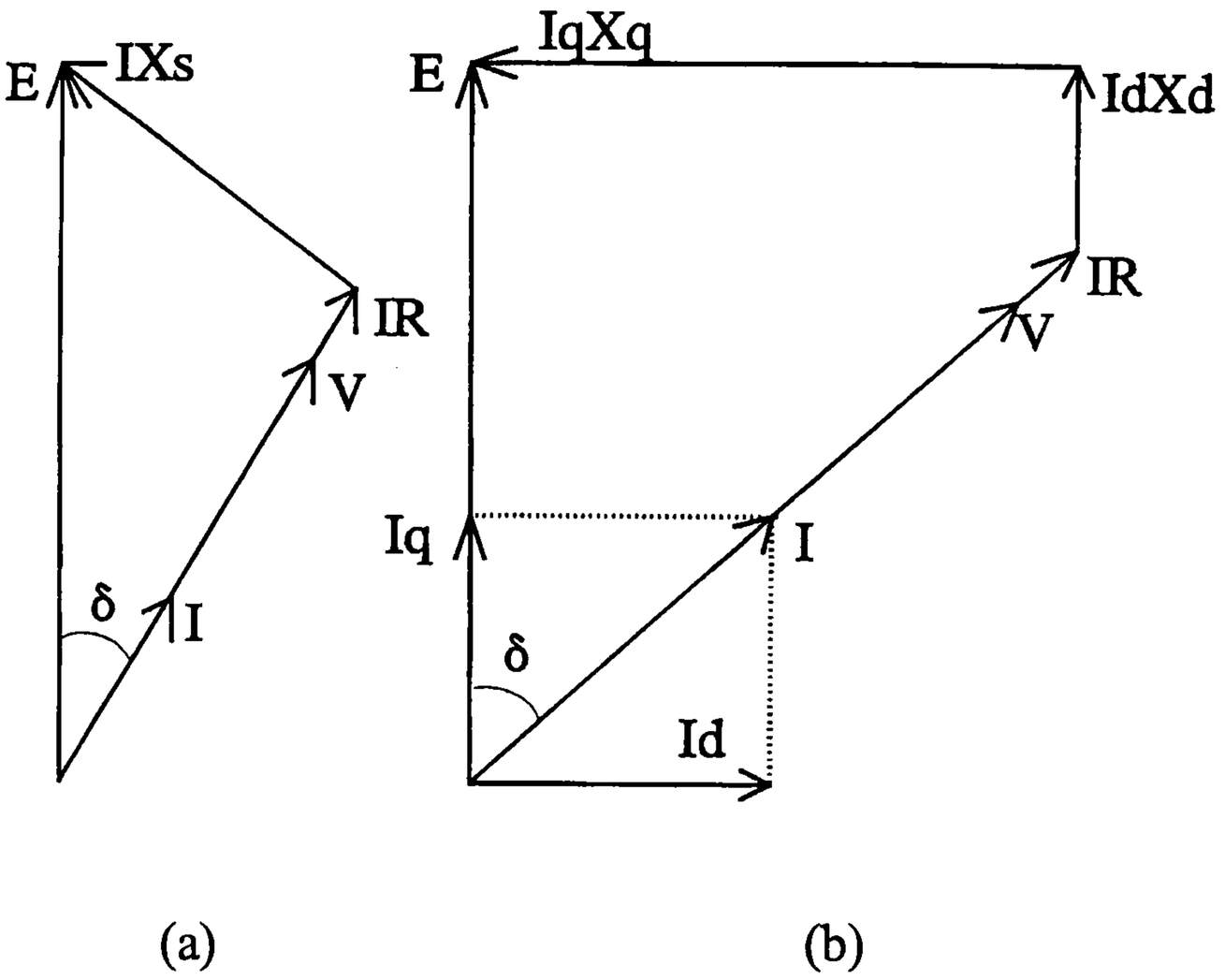


(a) (b)

Fig. 6.1 Phasor diagram of PMSG when supplying a unity-power-factor load: (a) surface-magnet rotor type; (b) generator with inverse saliency.

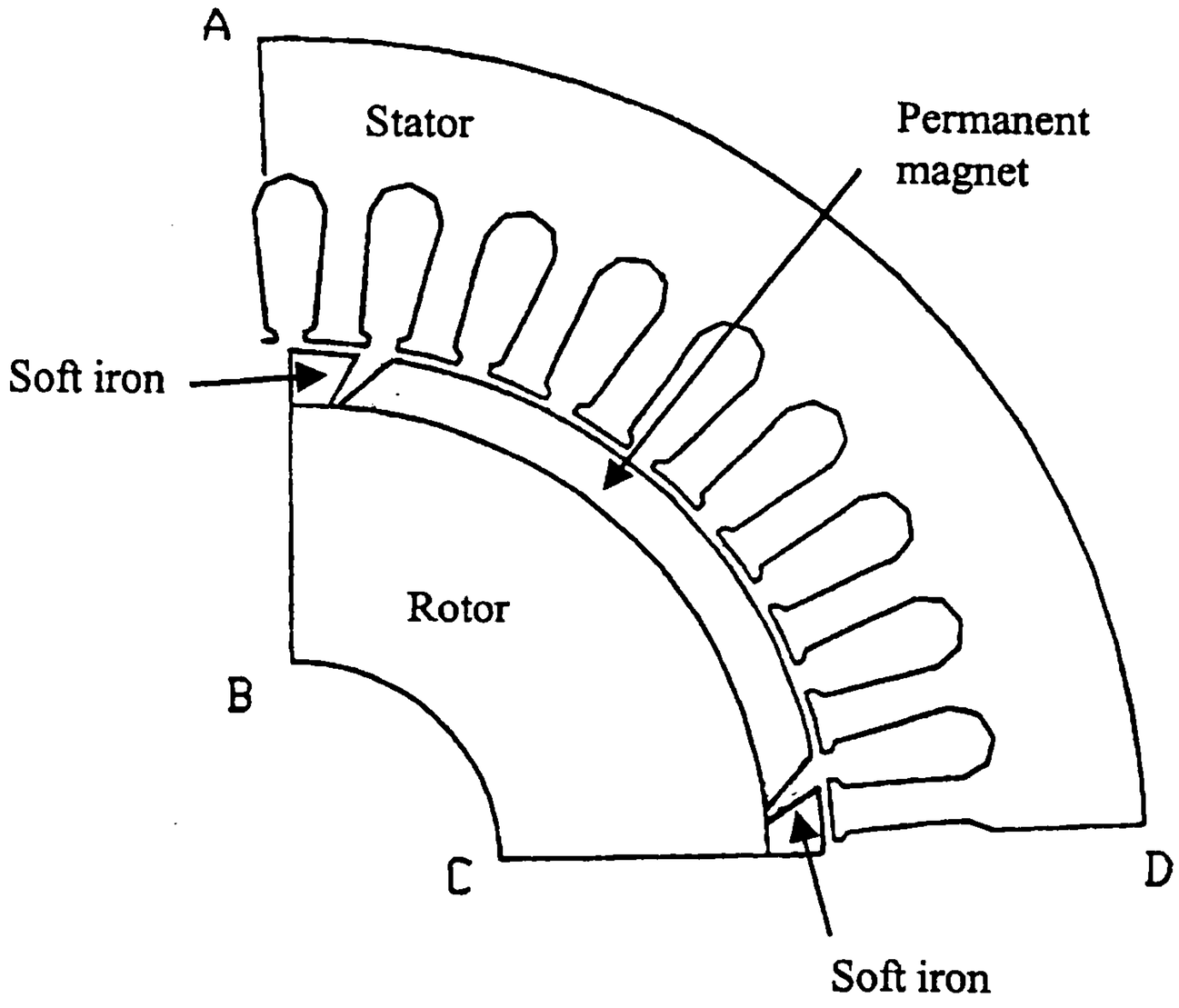


Fig. 6.2 Construction of a four-pole prototype PMSG with inset rotor, a quarter cross-section being shown.

## 6.3 Analysis for Unity-Power-Factor Loads

### 6.3.1 Analysis Using the Two-Axis Model

Heating and lighting loads usually predominate in autonomous power systems. In this section, this mode of operation is analyzed for the prototype PMSG based on the two-axis model [71], [73]. Besides the prediction of the load characteristics, it is of interest to investigate the conditions at which the generator terminal voltage on load is equal to the open-circuit voltage, i.e., the generator operates with zero voltage regulation. Two cases will be considered: analysis with armature resistance neglected and analysis with armature resistance taken into consideration.

*A) Armature resistance neglected*

The armature resistance may be neglected when the machine rating is large. Referring to Fig. 6.1(b), the following equations can be written:

$$V\cos\delta = E - I_d X_d \tag{6.1}$$

$$V\sin\delta = I_q X_q \tag{6.2}$$

$$I_d = I\sin\delta \tag{6.3}$$

$$I_q = I\cos\delta \tag{6.4}$$

$$I = \frac{V}{R_L} \tag{6.5}$$

$$I = \sqrt{I_d^{\,2} + I_q^{\,2}} \tag{6.6}$$

where $R_L$ is the load resistance and $\delta$ is the load angle (i.e. the angle between $E$ and $V$).

Solving (6.1) to (6.6), the terminal voltage $V$ is given by

$$V = \frac{E.R_L\sqrt{R_L^{\,2} + X_q^{\,2}}}{R_L^{\,2} + X_d X_q}. \tag{6.7}$$

The load characteristic can be computed from (6.5) and (6.7).

From (6.7), the load resistance $R_L$ at which zero voltage regulation occurs (i.e. $V = E$) is,

$$R_L = \frac{X_q}{\sqrt{r(r-2)}} \tag{6.8}$$

where $r$ = inverse saliency ratio = $X_q / X_d$.

Eqn. (6.8) indicates that when the inverse saliency ratio $r$ exceeds 2, there exists a value of $R_L$ that gives zero voltage regulation.

It can also be shown that the load angle $\delta$ at which zero voltage regulation occurs is given by

$$\tan\left(\frac{\delta}{2}\right) = \sqrt{\frac{r-2}{r}}\,. \tag{6.9}$$

*B) Armature resistance considered*

When the armature resistance cannot be neglected, a similar analysis can be carried out with reference to Fig. 6.1(b). It can be shown that the load angle is given by

$$\tan\delta = \frac{I X_q}{V + IR} \tag{6.10}$$

while the terminal voltage $V$ and the open-circuit voltage $E$ are related by the following equation:

$$E = \frac{(V + IR)^2 + I^2 X_d X_q}{\sqrt{(V + IR)^2 + (IX_q)^2}}\,. \tag{6.11}$$

The load angle at which zero voltage regulation occurs is now given by

$$\tan\left(\frac{\delta}{2}\right) = \frac{R + X_d \tan\delta}{X_q - R\tan\delta}\,. \tag{6.12}$$

Eqn. (6.12) may be solved numerically to give the load angle $\delta$. This approach, however, requires suitable initial estimates of $\delta$ to be selected in order to start the numerical procedure.

If the parameter $k = \tan(\delta/2)$ is introduced, (6.12) can be expanded to give the following cubic equation:

$$X_q k^3 + R k^2 + (2 X_d - X_q).k + R = 0 . \tag{6.13}$$

Standard closed forms of solution for (6.13) are available, e.g. by using Cardan's method [108]. Only positive real values of $k$ give feasible operating points. After $k$ (and hence $\delta$) is known, the load current at which zero voltage regulation occurs can be determined from (6.10).

As an example, consider a PMSG with the following parameters at rated speed [71]: $E$ = 51.7 V, $X_d$ = 14 Ω, $X_q$ = 55 Ω, and $R$ = 3.5 Ω. Solution of (6.12) with these numerical values substituted yields the following positive real roots: $k_1$ = 0.1374 and $k_2$ = 0.5875. For root $k_1$, the load angle and armature current are $15.6^0$e and 0.268 A, respectively. For root $k_2$, the corresponding values are $60.9^0$e and 1.9 A, respectively. There are thus two different loads at which zero voltage regulation is obtained. In practice, however, operation with the larger load would give more output power and a higher efficiency.

The solutions of (6.12) can also be determined graphically by the points of intersection between the functions $f_1$ and $f_2$, where $f_1 = \tan(\delta/2)$ and $f_2 = (R + X_d \tan\delta)/(X_q - R \tan\delta)$, as illustrated in Fig. 6.3 for the PMSG in reference [71]. When $R$ = 3.5 Ω, $f_1$ and $f_2$ intersect at two points. It is apparent that the function $f_2$ is displaced upward with an increase in $R$, causing the separation between the intersection points to decrease. When $R$ = 8 Ω, $f_2$ is larger than $f_1$ for all values of $\delta$. There is no point of intersection and hence zero voltage regulation cannot be achieved. At some critical value of $R$, the two roots are equal, implying that zero voltage regulation is obtained at only one value of load current. For the given machine, the critical value of $R$ was found to be 6.34 Ω using a simple search method.

Fig. 6.4 shows the load characteristics of the generator for different values of $R$.

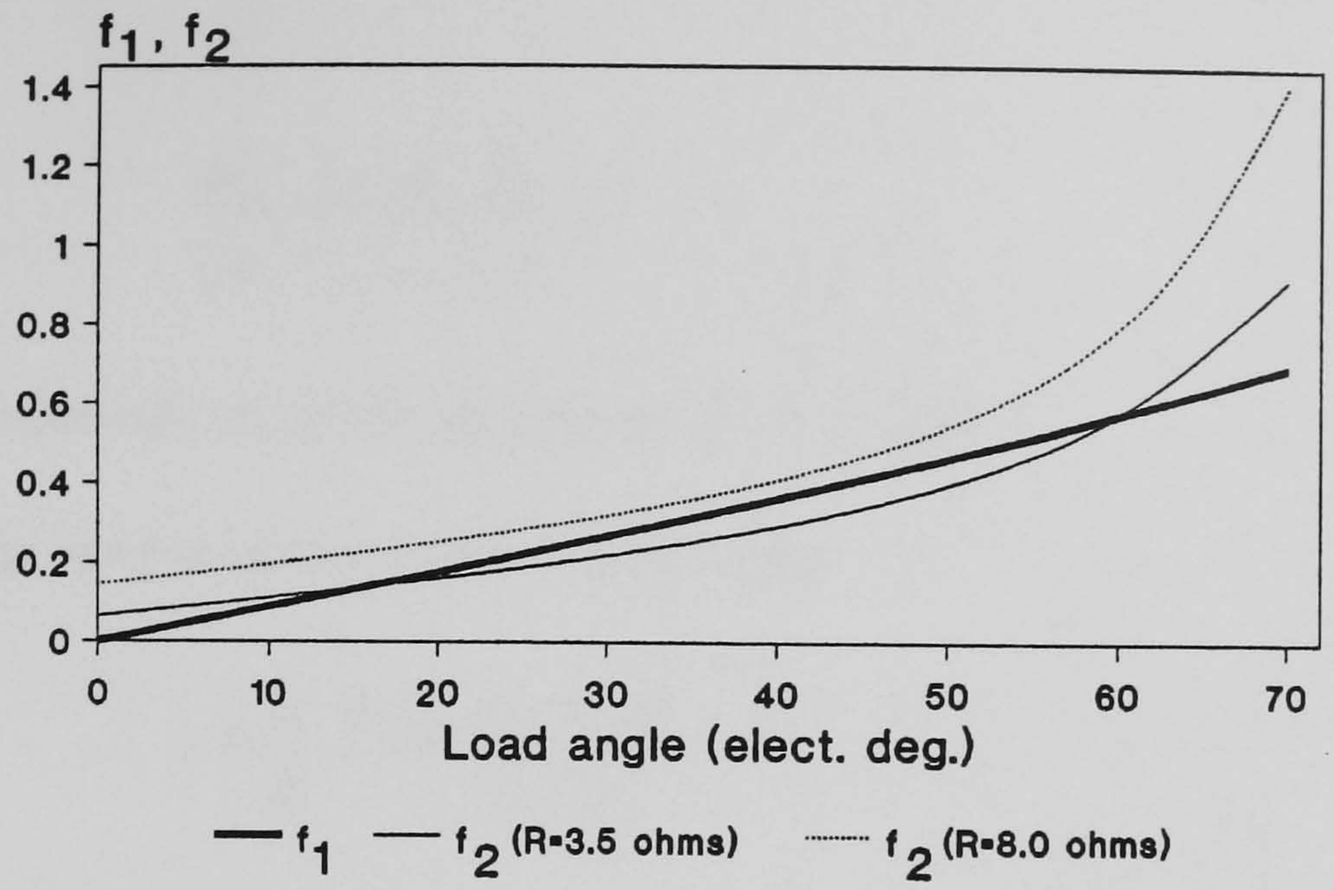


Fig. 6.3 Graphical solution of (6.12) for determining the load angle $\delta$.

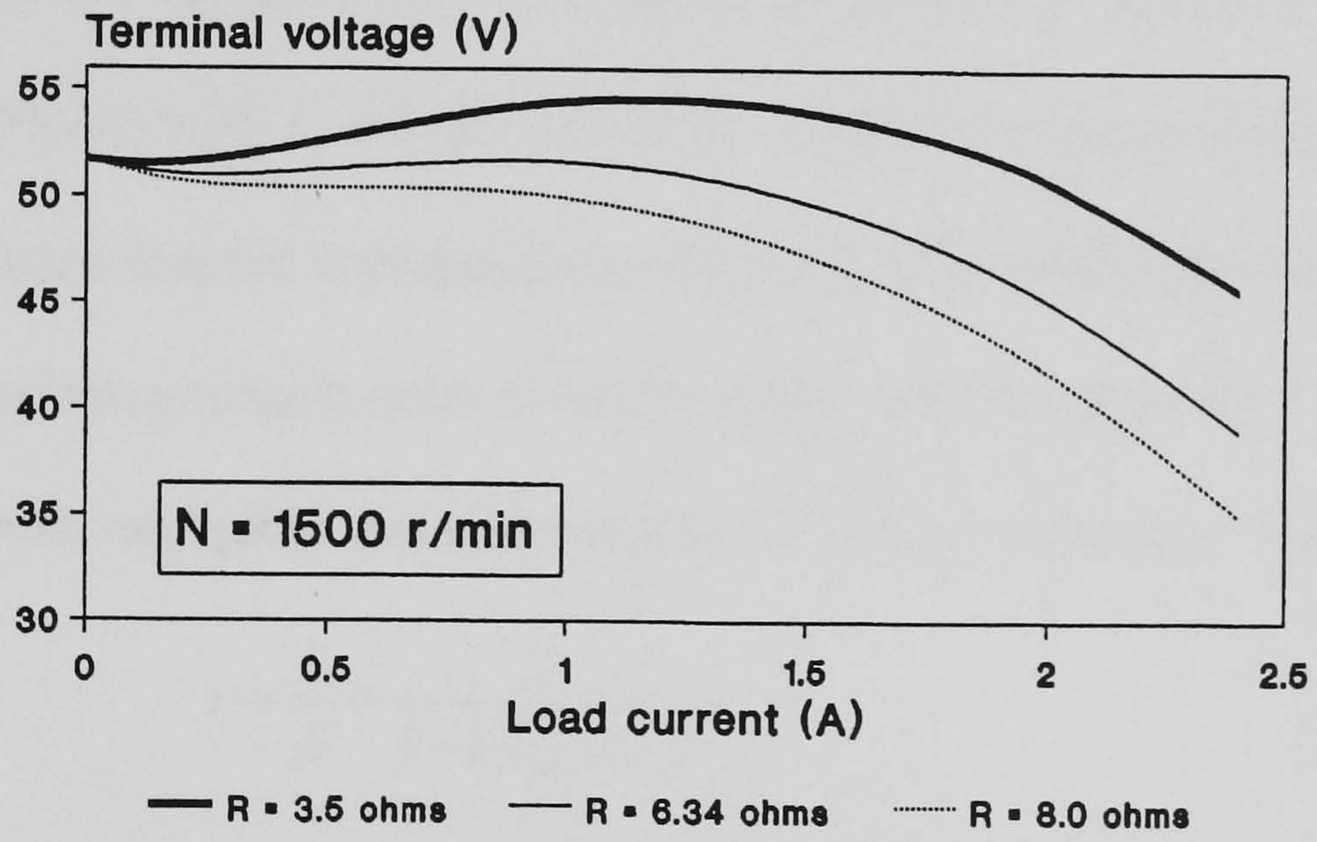


Fig. 6.4 Effect of armature resistance $R$ on the load characteristics of PMSG with $E$ = 51.7 V, $X_d$ = 14 Ω, $X_q$ = 55 Ω.

### 6.3.2 Design Considerations

For the electrical machine designer, it is of interest to determine, for a given speed, armature resistance $R$ and d-axis synchronous reactance $X_d$, the value of q-axis synchronous reactance $X_q$ (or $r$) such that zero voltage regulation occurs at a specific armature current. To simplify the derivation, (6.11) is re-written in per-unit form, the no-

load voltage $E$ being taken as unity. Thus, with $V = E = 1.0$ p.u., the following equation is obtained:

$$\frac{\alpha^2 + I_{pu}^{\ 2} X_d X_q}{\sqrt{\alpha^2 + (I_{pu} X_q)^2}} = 1 \tag{6.14}$$

where $I_{pu}$ is the per-unit armature current and $\alpha = 1 + I_{pu}R$.

From (6.14), the inverse saliency ratio $r$ is given by

$$r = \frac{\alpha}{\beta} \cdot \frac{\alpha . I_{pu} X_d + \sqrt{\alpha^2 - \beta}}{I_{pu} X_d} \tag{6.15}$$

where $\beta = 1 - (I_{pu}X_d)^2$.

Fig. 6.5 shows the variation of $r$ with speed to yield zero voltage regulation at rated current for a PMSG with $R = 0.295\ \Omega$ and $X_d = 0.88\ \Omega$ (at the nominal frequency of 50 Hz). It is apparent that for low-speed operation, the generator has to be designed with a large inverse saliency ratio in order to achieve zero voltage regulation.

For a PMSG with negligible armature resistance, (6.15) is reduced to the following:

$$r = \frac{2}{\beta} = \frac{2}{1 - (I_{pu} X_d)^2}. \tag{6.16}$$

Since the per-unit value of $X_d$ is independent of speed, the value of $r$ to give zero voltage regulation is the same for all speeds.

It is also of interest to study the effect of speed on the armature resistance to yield zero voltage regulation. Solving (6.14) for $\alpha$, one obtains:

$$\alpha^2 = \frac{1}{2}\left[-(2rI_{pu}^2 X_d^2 - 1) \pm \sqrt{1 + 4r^2 I_{pu}^2 X_d^2 - 4rI_{pu}^2 X_d^2}\right]. \tag{6.17}$$

The per-unit resistance is given by

$$R = \frac{\alpha - 1}{I_{pu}}. \tag{6.18}$$

But

$$R = \frac{R_{actual}}{Z_{base,n}.b} \tag{6.19}$$

where $R_{actual}$ is the ohmic value of the armature resistance, $Z_{base,n}$ is the base impedance at nominal frequency and $b$ is the ratio of actual speed to the base speed.

The ohmic value of the armature resistance is thus

$$R_{actual} = \frac{\alpha - 1}{I_{pu}} . Z_{base,n} . b . \tag{6.20}$$

Eqn. (6.20) implies that, for zero voltage regulation at a specific current, a larger armature resistance can be tolerated when the generator operates at a higher speed.

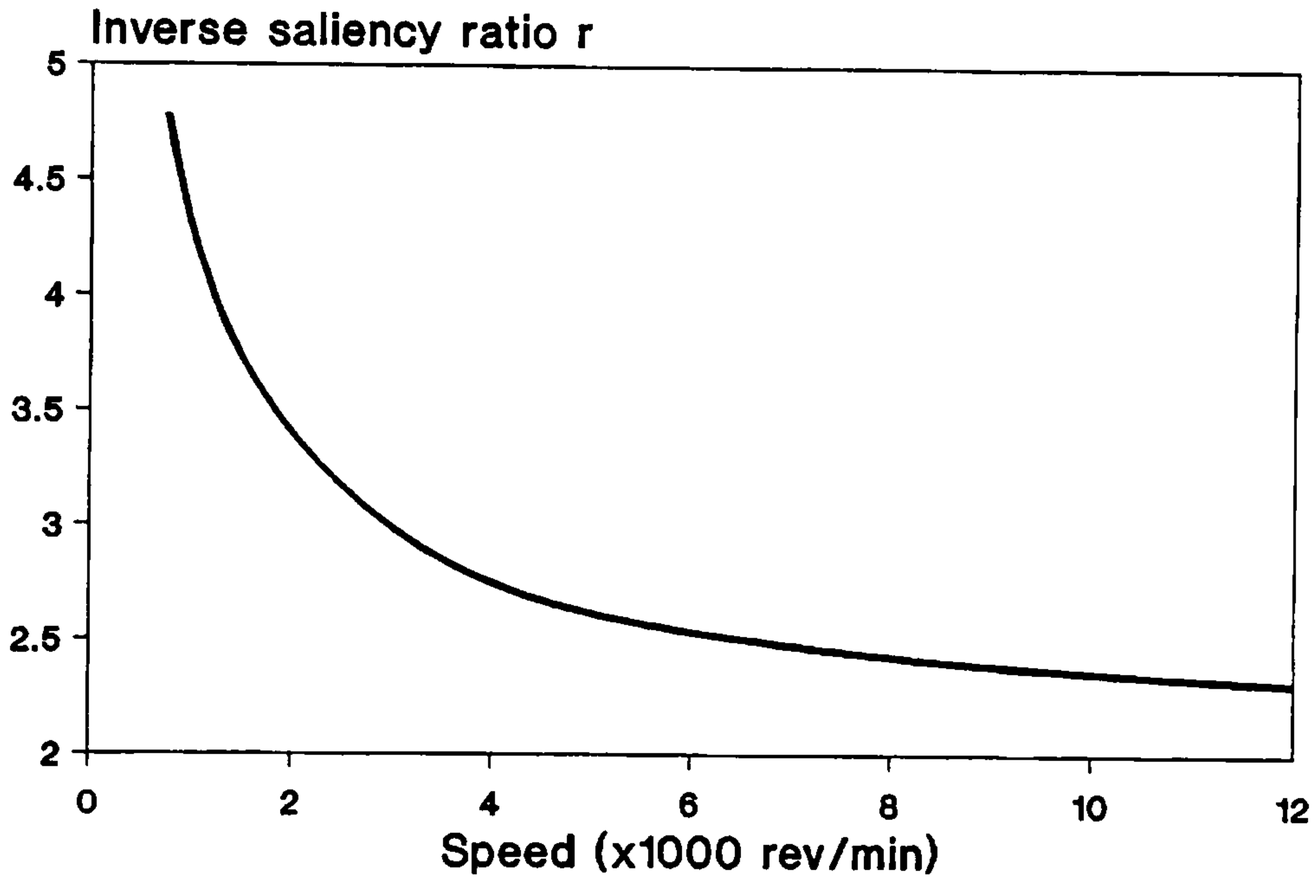


Fig. 6.5 Inverse saliency ratio $r$ to give zero voltage regulation in PMSG at different speeds.

### 6.3.3 Computed Results

For comparison purpose, the load current characteristics of the prototype PMSG with inset rotor and a surface-magnet PMSG with similar design were computed using the two-axis model. The machine parameters required were determined from FEM (Section 6.5) and are listed in Table 6.1. For easy comparison, the voltages have been normalized to the corresponding no-load voltages. At the nominal speed of 1500 r/min, the full-load

voltage drops in the generators with inset PM rotor and surface-mounted PM rotor are 4.4% and 8.4% respectively. At a speed of 6000 r/min, the generator with inset PM rotor exhibits a nearly level voltage characteristic, with zero voltage drop occurring at full load. The computed results have confirmed that the inset PM rotor construction is effective in improving the voltage regulation.

Fig. 6.7 shows the computed voltage-current characteristics of the prototype generator when operating at different speeds. It is observed that the voltage compensation due to inverse saliency increases with speed, which is consistent with the derivation in Section 6.3.2. Above 6000 r/min, the terminal voltage rises with increase of load, i.e. negative voltage regulation can be obtained.

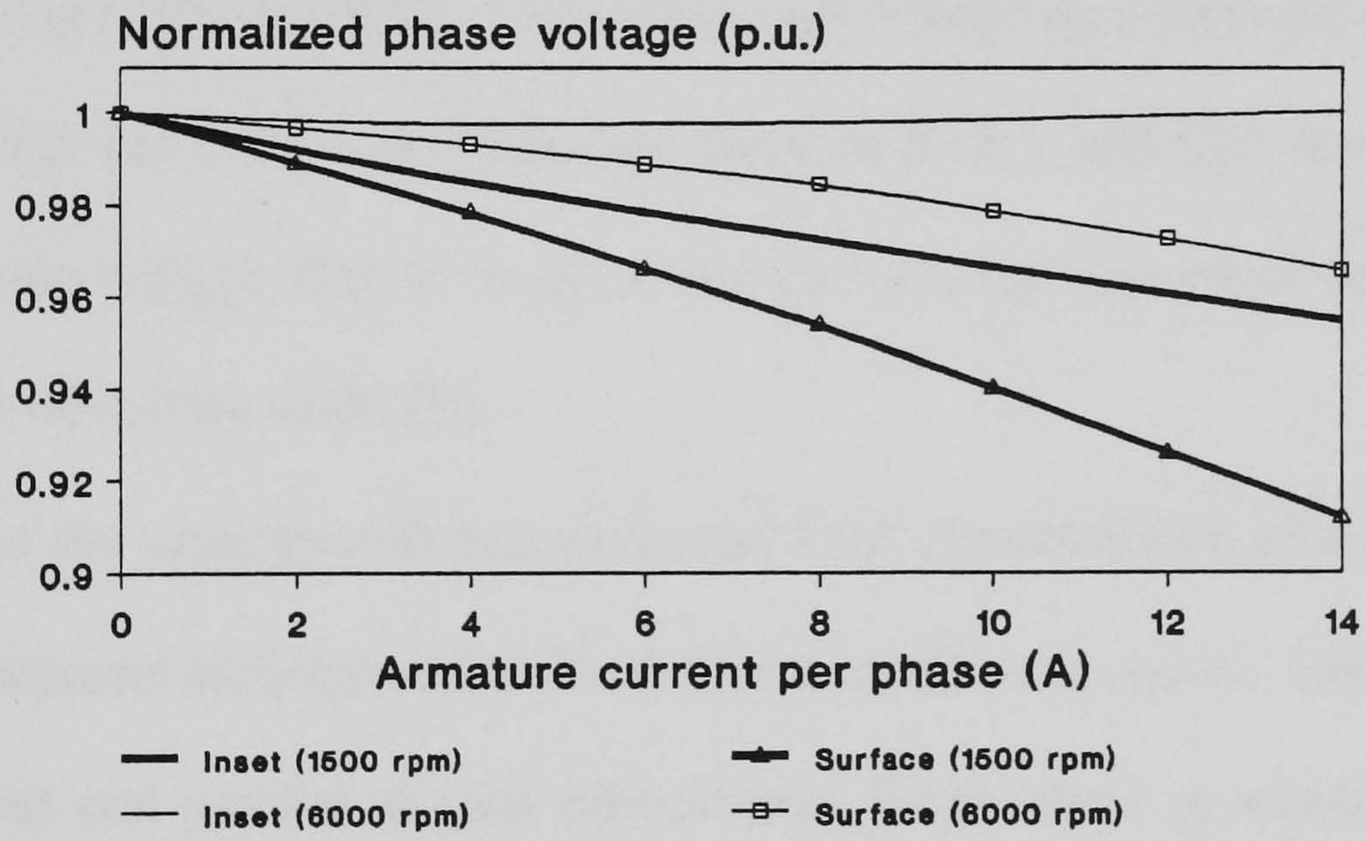


Fig. 6.6 Computed load characteristics of synchronous generators with inset and surface-mounted PM rotors.

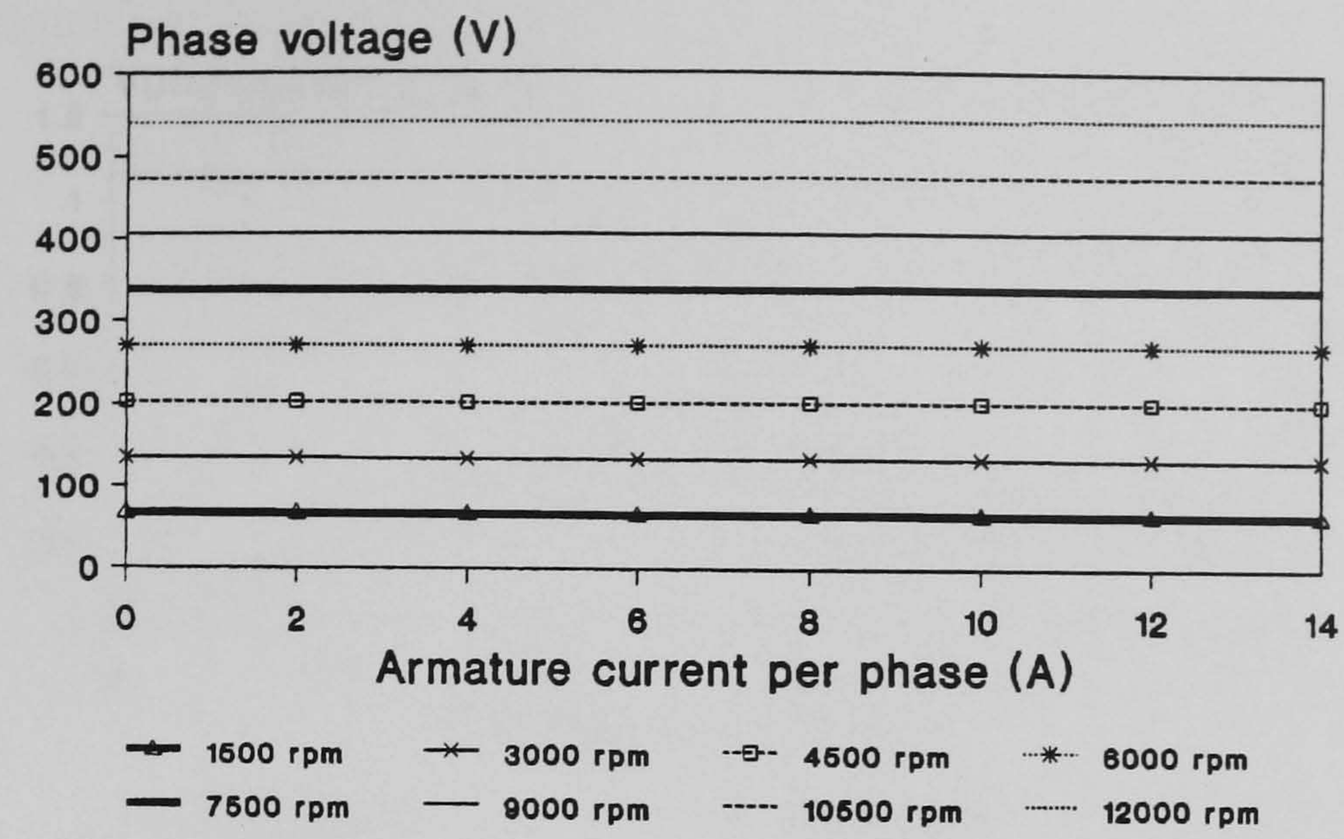


Fig. 6.7 Computed load characteristics of prototype PMSG with inset rotor.

### 6.3.4 Experimental Results

Fig. 6.8 shows the experimental performance characteristics of the prototype PMSG when driven at the nominal speed (1500 r/min) and supplying a unity-power-factor load. The base voltage and current per phase are taken as 63.5 V and 13.3 A respectively. At rated current, the voltage drop of the generator is 5.9% and the power output is 1.0 p.u. (2.5 kW) at an efficiency of 86.2%.

Fig. 6.9 shows the experimental and computed load characteristics of the PMSG when supplying a balanced unity-power-load and driven at different speeds. The characteristics are nearly level and parallel to each other, hence the machine is suitable for use as a constant-voltage generator. The close agreement between the computed and experimental results in Fig. 6.9 confirms the accuracy of the parameters obtained from the finite element method.

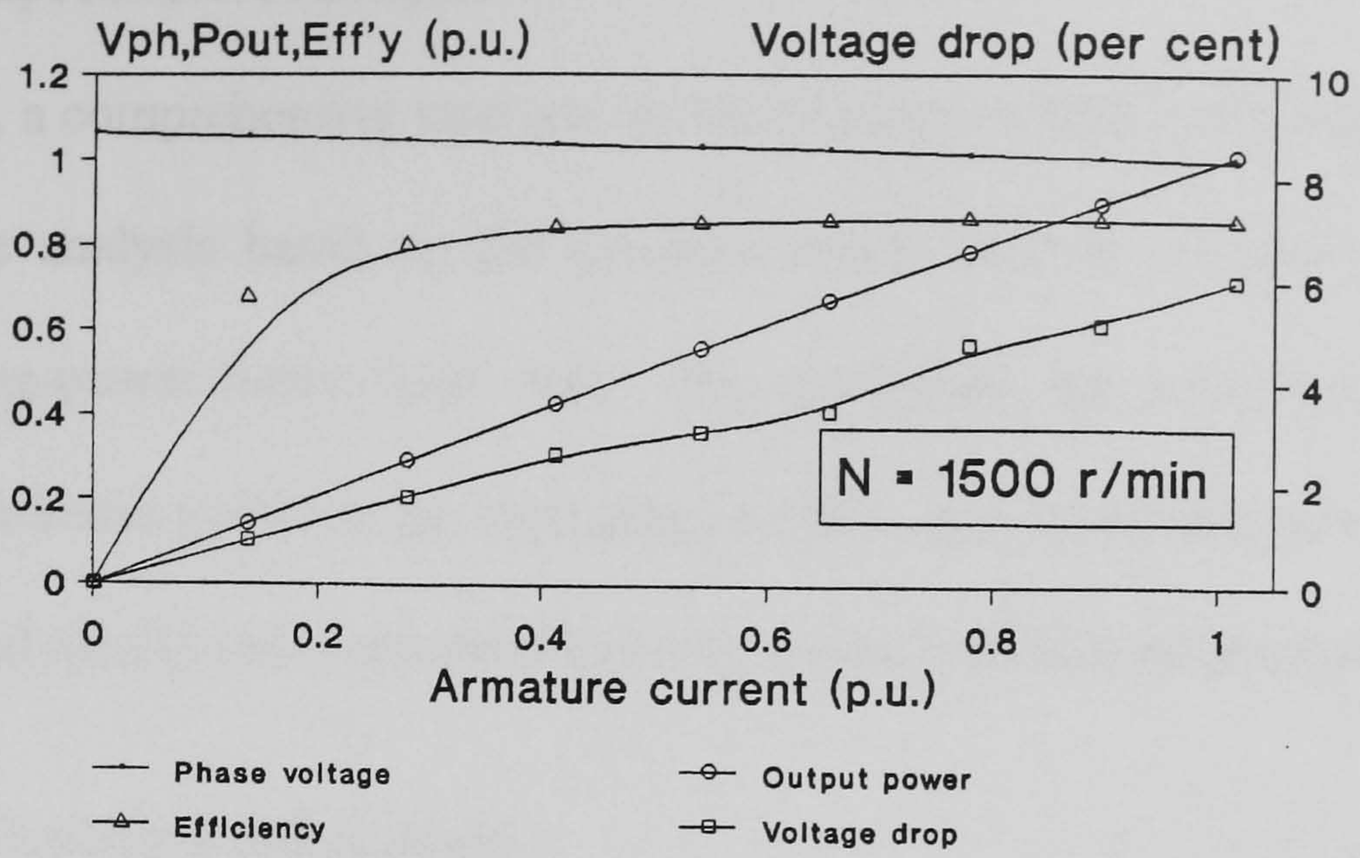


Fig. 6.8 Experimental performance characteristics of prototype PMSG at rated speed.

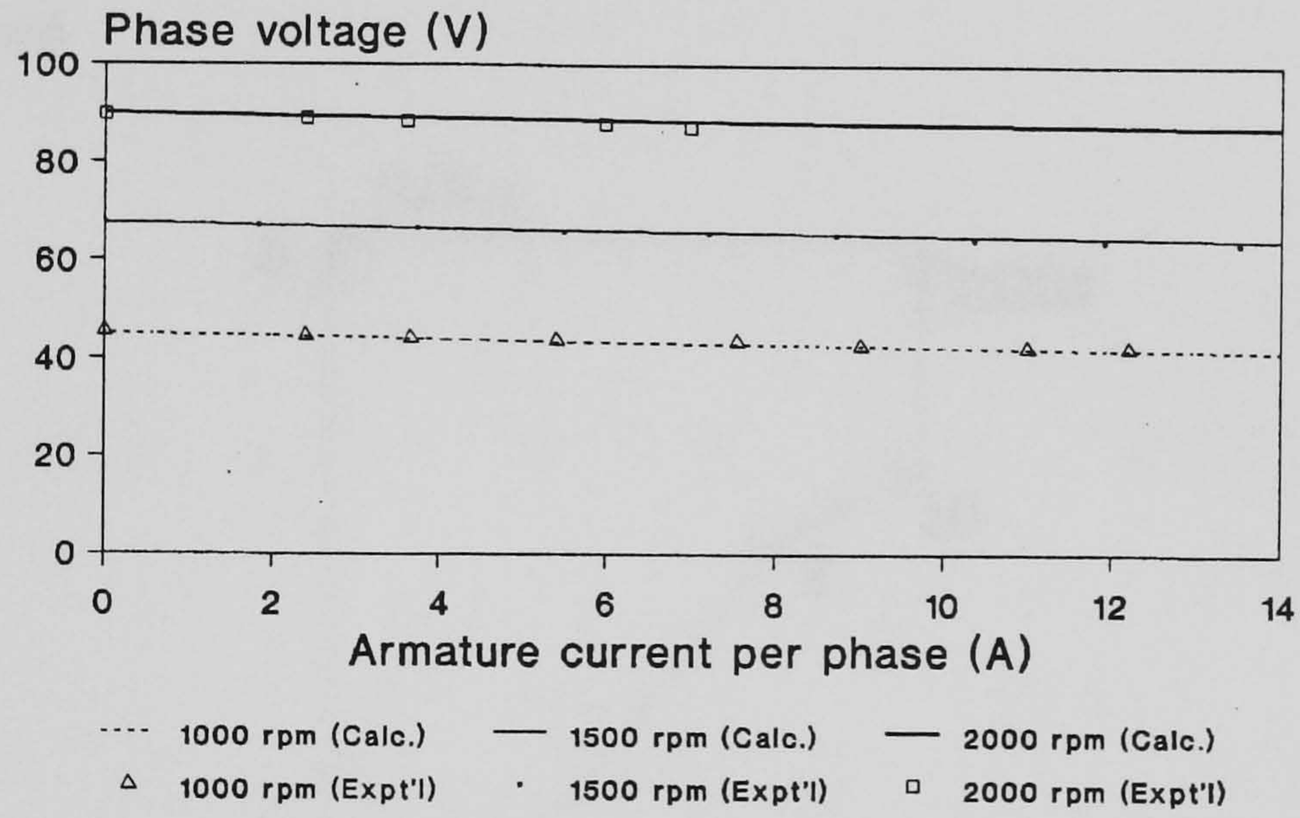


Fig. 6.9 Load characteristics of prototype PMSG at different speeds.

### 6.3.5 Summary

The analysis and performance of a three-phase synchronous generator with inset permanent-magnet rotor have been presented in this section. Particular emphasis has been placed on the conditions for achieving zero voltage regulation when the generator is supplying an isolated resistive load. It is demonstrated that the voltage regulation is significantly improved as a result of the inverse saliency feature of the inset PM rotor construction. Experiments performed on a 2.5-kVA prototype generator have confirmed the accuracy of the theoretical analysis.

## 6.4 A Comprehensive Analysis

In this section, a comprehensive analysis on the prototype PMSG with inset rotor will be presented. The analysis based on the two-axis model will be extended to include the general lagging-power-factor load case. The conditions for achieving zero voltage regulation, extremum points in the load characteristic, and maximum power output, will be deduced analytically and a saturated two-axis model will also be proposed.

### 6.4.1 Basic Equations and Analysis

Fig. 6.10 shows the phasor diagram of the PMSG when it is supplying a lagging-power-factor load.

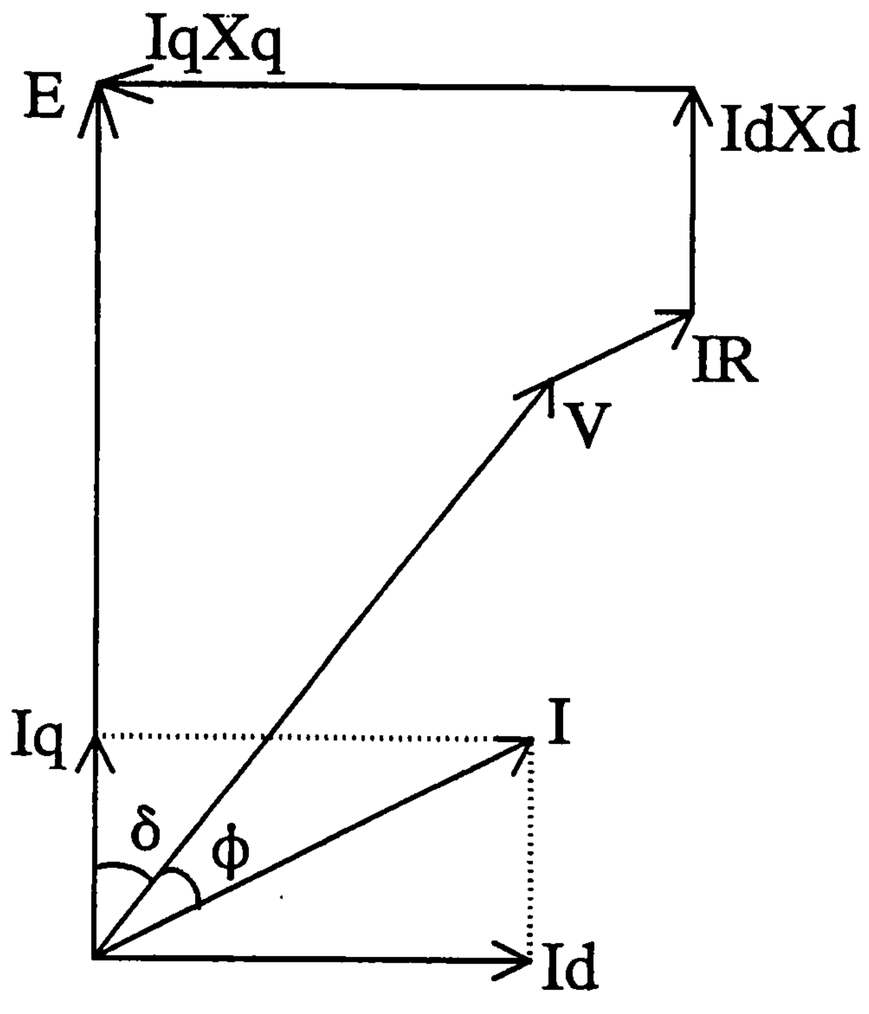


Fig. 6.10 Phasor diagram of PMSG when supplying a lagging-power-factor load.

It is convenient to use the load impedance $Z_L$ as variable in the performance analysis for isolated operation. With reference to Fig. 6.10, the following equations may be written for generator operation with a lagging-power-factor load:

$$V\cos\delta = E - I_d X_d - I_q R \tag{6.21}$$

$$V\sin\delta = I_q X_q - I_d R \tag{6.22}$$

$$I_d = I\sin(\delta+\phi) \tag{6.23}$$

$$I_q = I\cos(\delta+\phi) \tag{6.24}$$

$$V = I.Z_L \tag{6.25}$$

where $Z_L$ is the load impedance and $\phi$ is the load power factor angle.

Substituting (6.23), (6.24) and (6.25) into (6.22),

$$Z_L\sin\delta = X_q\cos(\delta+\phi) - R\sin(\delta+\phi) \tag{6.26}$$

Expanding the right-hand-side of (6.26) and rearranging terms, the following equation may be deduced:

$$\tan\delta = \frac{X_q\cos\phi - R\sin\phi}{Z_L + X_q\sin\phi + R\cos\phi}. \tag{6.27}$$

For a given load impedance $Z_L$ and load impedance angle $\phi$, the load angle $\delta$ can be computed from (6.27). Substitution of the value of $\delta$ into (6.21) gives the terminal voltage $V$ as follows:

$$V = \frac{E\,Z_L}{Z_L\cos\delta + R\cos(\delta+\phi) + X_d\sin(\delta+\phi)}. \tag{6.28}$$

The load current (or armature current) $I$ is given by:

$$I = \frac{E}{Z_L\cos\delta + R\cos(\delta+\phi) + X_d\sin(\delta+\phi)}. \tag{6.29}$$

Eqns. (6.28) and (6.29) enable the load characteristics of the PMSG to be evaluated.

It is also possible to express the terminal voltage $V$ directly in terms of the load impedance $Z_L$. Eliminating $\delta$ from (6.27) and (6.28), the following equation is obtained:

$$V = E.\frac{Z_L\sqrt{Z_L^{\,2} + g_1.Z_L + g_2}}{Z_L^{\,2} + g_3.Z_L + g_4} \tag{6.30}$$

where

$$g_1 = 2(X_q \sin\phi + R\cos\phi),\ g_2 = R^2 + X_q^2,\ g_3 = 2R\cos\phi + (X_d + X_q)\sin\phi,\ g_4 = R^2 + X_d X_q.$$

The load characteristic can therefore be computed using (6.25) and (6.30) without having to determine $\delta$ first.

Fig. 6.11 shows the computed load characteristics of the prototype PMSG at nominal speed (1500 r/min) and four times of nominal speed (6000 r/min). It is apparent that the voltage compensation effect of the PMSG is weaker when the load power factor is lagging. At the nominal speed (1500 r/min), the full-load voltage drop is 4.7% when the load power factor is unity and 15.7% when the load power factor is 0.8 lagging. At a speed of 6000 r/min, the generator exhibits a nearly level load characteristic when the load power factor is unity, with zero voltage drop occurring at full load. At 0.8 power factor lagging, the corresponding voltage drop is 11%.

Fig. 6.12 shows the effect of inverse saliency ratio $r$ on the load characteristics of the PMSG when supplying a unity-power-factor load. For this investigation, it is assumed that $E$, $R$ and $X_d$ of the generator are the same as the corresponding values of the prototype generator. It is observed that the optimum value of $r$ is 4, at which a nearly level load characteristic is obtained. For values of $r$ exceeding 4, the terminal voltage increases with load current over most of the practical current range.

Fig. 6.13 shows the effect of armature resistance $R$ on the load characteristics of the prototype PMSG when supplying a unity-power-factor load. A reduction in $R$ results in a smaller voltage drop. A comparison between Fig. 6.12 and Fig. 6.13 shows that reducing $R$ to a quarter of the original value has approximately the same effect as increasing $r$ by four times. When $R$ is smaller than one-quarter of the original value, negative voltage regulation can also be obtained.

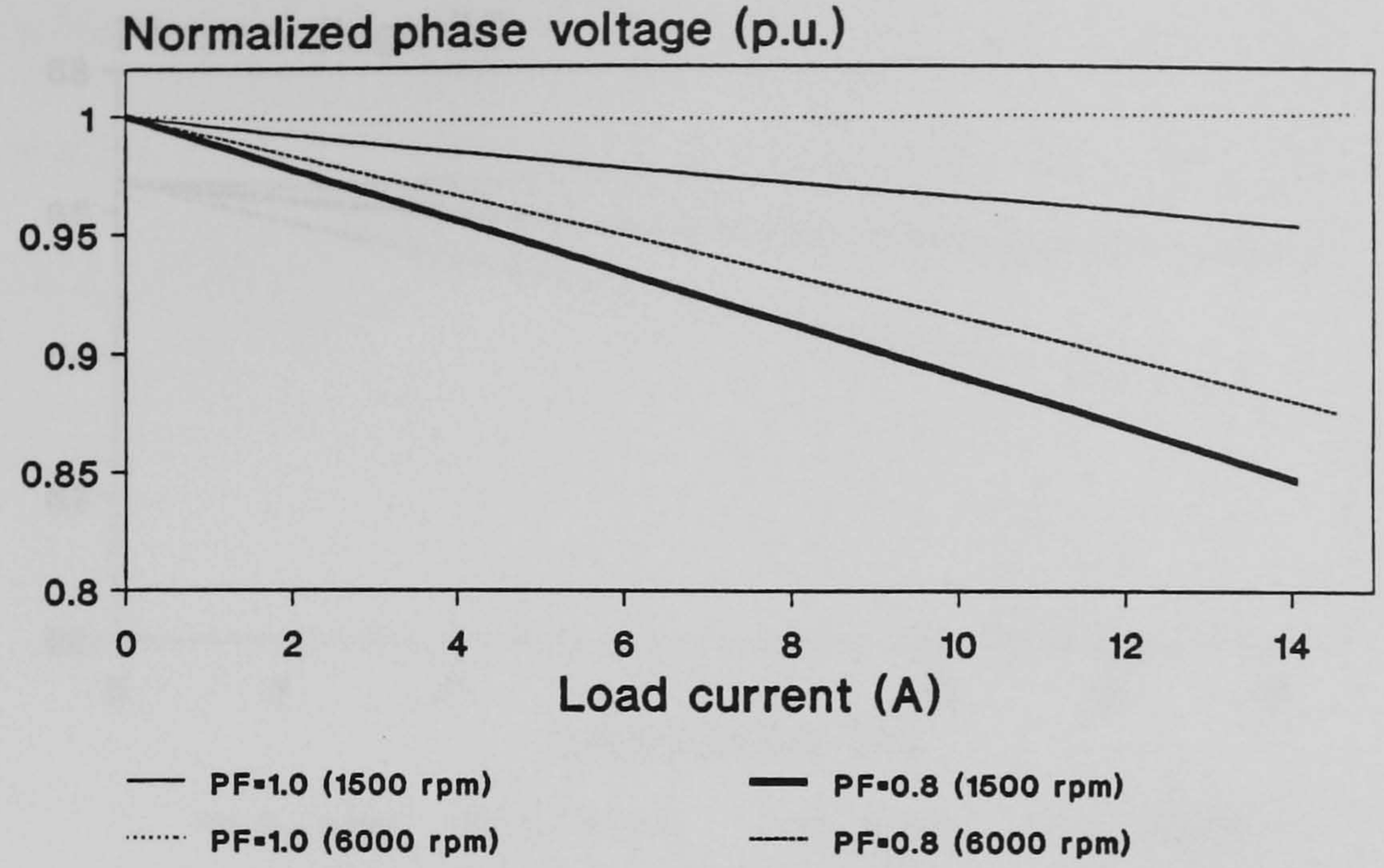


Fig. 6.11 Computed load characteristics of PMSG with the following machine parameters at nominal speed: $E = 66.44$ V, $R = 0.295\ \Omega$, $X_d = 0.88\ \Omega$, $X_q = 2.23\ \Omega$.

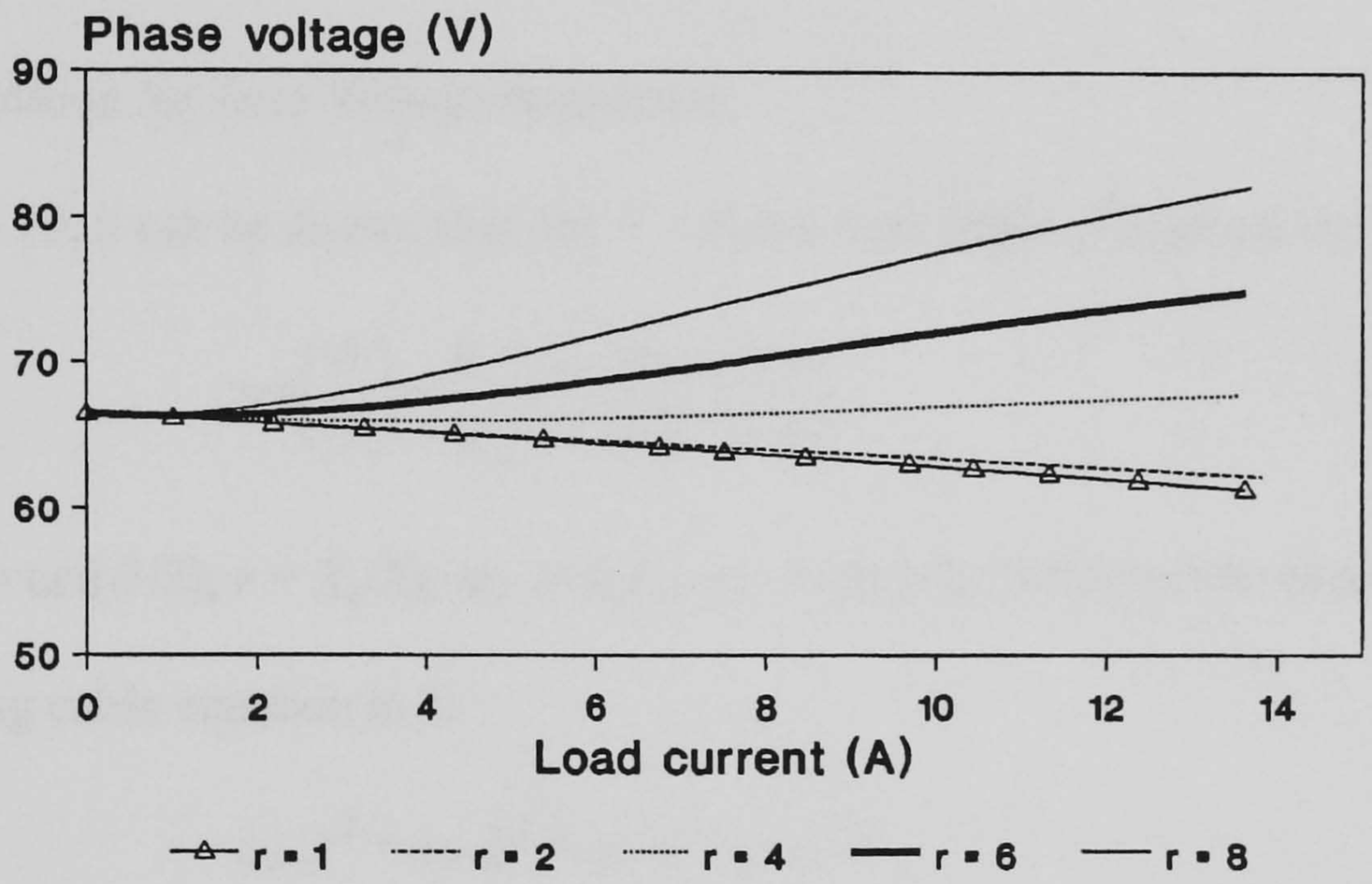


Fig. 6.12 Effect of inverse saliency ratio $r$ on the load characteristics of a PMSG operating at nominal speed and supplying a unity-power-factor load: $E = 66.44$ V, $R = 0.295\ \Omega$, $X_d = 0.88\ \Omega$.

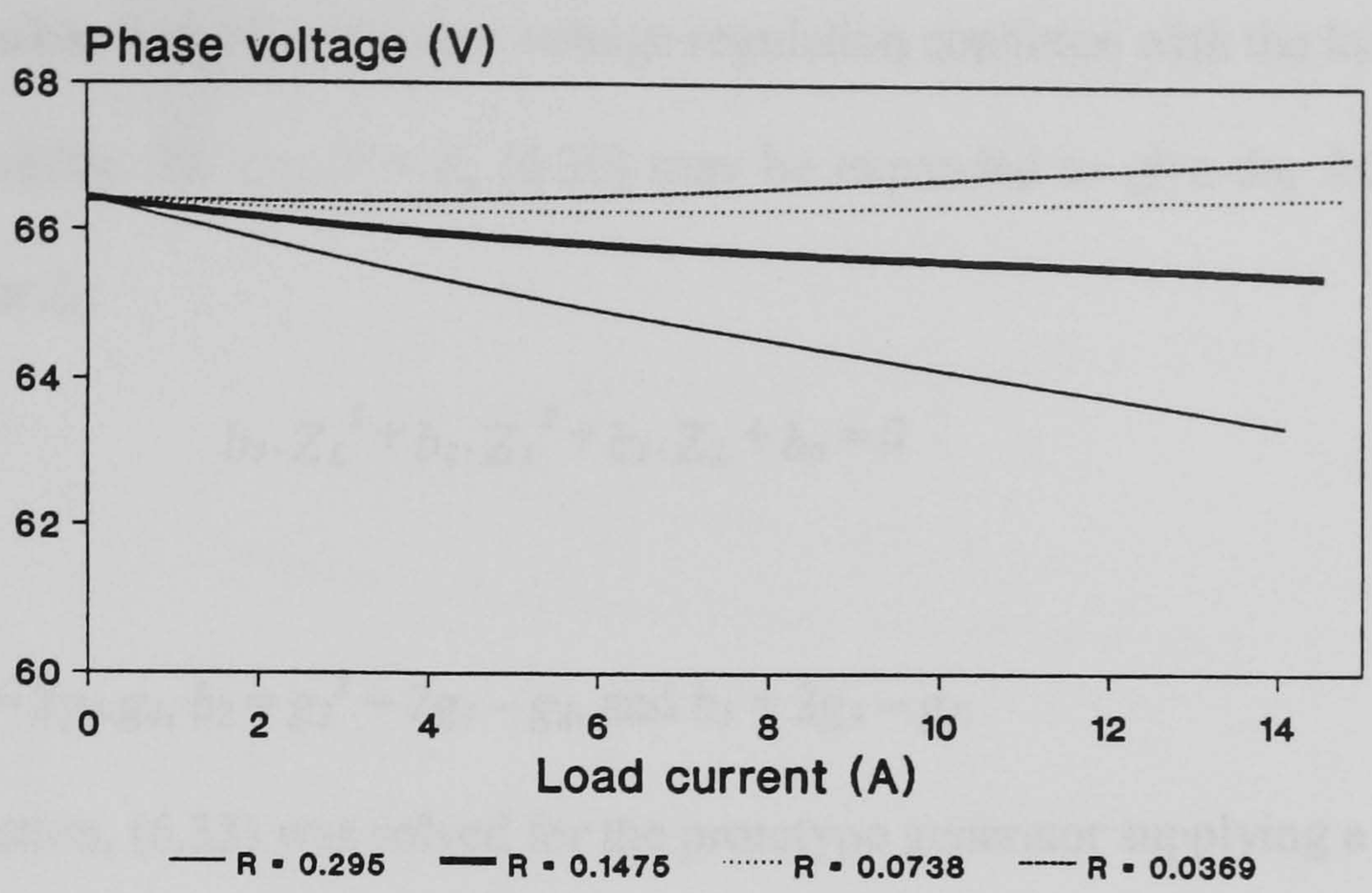


Fig. 6.13 Effect of armature resistance $R$ on the load characteristics of a PMSG operating at nominal speed and supplying a unity-power-factor load: $E = 66.44$ V, $X_d = 0.88\ \Omega$, $X_q = 2.23\ \Omega$.

### 6.4.2 Condition for Zero Voltage Regulation

From Fig. 6.10, it can be shown that, for $V = E$, the load angle $\delta$ is given by:

$$\tan\left(\frac{\delta}{2}\right) = \frac{R + X_d \tan(\delta + \phi)}{X_q - R \tan(\delta + \phi)}. \tag{6.31}$$

If we let $k = \tan(\delta/2)$, $r = X_q/X_d$, $m_1 = R/X_d$, $m_2 = \tan(\phi)$, (6.31) can be expanded to give the following cubic equation in $k$:

$$a_3 . k^3 + a_2 . k^2 + a_1 . k + a_0 = 0 \tag{6.32}$$

where

$a_0 = m_1 + m_2$, $a_1 = 2 - r - m_1 . m_2$, $a_2 = m_1 + m_2 . (2r - 1)$, and $a_3 = r - m_1 . m_2$.

Eqn. (6.32) is similar in form to (6.13) and hence may also be solved using the Cardan's method [108]. Positive-real roots to (6.32), if they exist, indicate that zero voltage regulation may be achieved. The corresponding value of $\delta$ and load current can subsequently be computed.

It is also possible to deduce the zero voltage regulation condition with the load impedance $Z_L$ as the variable. Putting $V = E$, (6.30) may be expanded to give the following cubic polynomial in $Z_L$:

$$b_3 \cdot Z_L^{\,3} + b_2 \cdot Z_L^{\,2} + b_1 \cdot Z_L + b_0 = 0 \tag{6.33}$$

where

$b_0 = g_4^{\,2}$, $b_1 = 2g_3.g_4$, $b_2 = g_3^{\,2} + 2g_4 - g_2$, and $b_3 = 2g_3 - g_1$.

As an illustration, (6.33) was solved for the prototype generator supplying a unity-power-factor load at 6000 r/min. Under this condition, $E = 265.6$ V, $R = 0.295\ \Omega$, $X_d = 3.52\ \Omega$, $X_q = 8.92\ \Omega$, $\cos\phi = 1.0$. Solution of (6.33) gave two positive roots, viz. 20.74 and 13.1. When $Z_L = 20.74\ \Omega$, $\delta = 22.98^0$e and $I = 12.8$ A; when $Z_L = 13.1\ \Omega$, $\delta = 33.62^0$e and $I =$ 20.24 A.

Fig. 6.14 shows the effect of rotor speed on the load angle that gives zero voltage regulation and the corresponding load current $I$ when the prototype generator is supplying a unity-power-factor load. When the rotor speed is higher than the critical value of 5687 r/min, there are two values of $\delta$ (or $I$) at which zero voltage regulation occurs. When the rotor speed is less than the critical value, no positive real roots to (6.32) or (6.33) exist and hence a zero voltage regulation condition does not exist. It should be noted that at the critical speed, (6.32) or (6.33) gives repeated positive roots.

Fig. 6.15 shows the effect of inverse saliency ratio on the load angle that gives zero voltage regulation. At nominal speed (1500 r/min), zero voltage regulation is achieved when $r$ exceeds 3.5. At four times nominal speed (6000 r/min), the critical value of $r$ is reduced to 2.51. These results are consistent with the load characteristics shown in Fig. 6.12.

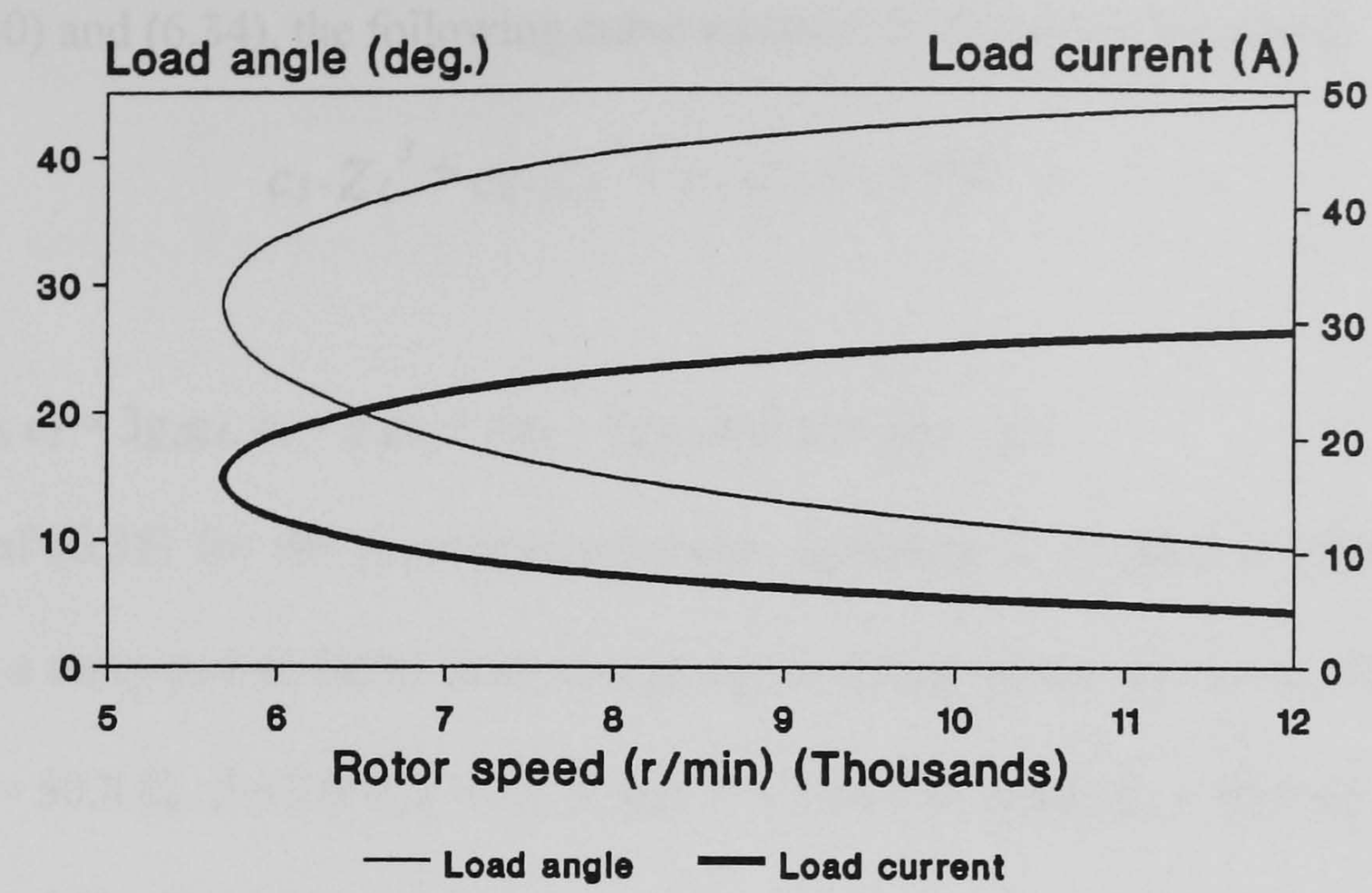


Fig. 6.14 Effect of rotor speed on the load angle that gives zero voltage regulation when the prototype generator is supplying a unity-power-factor load and the corresponding load current.

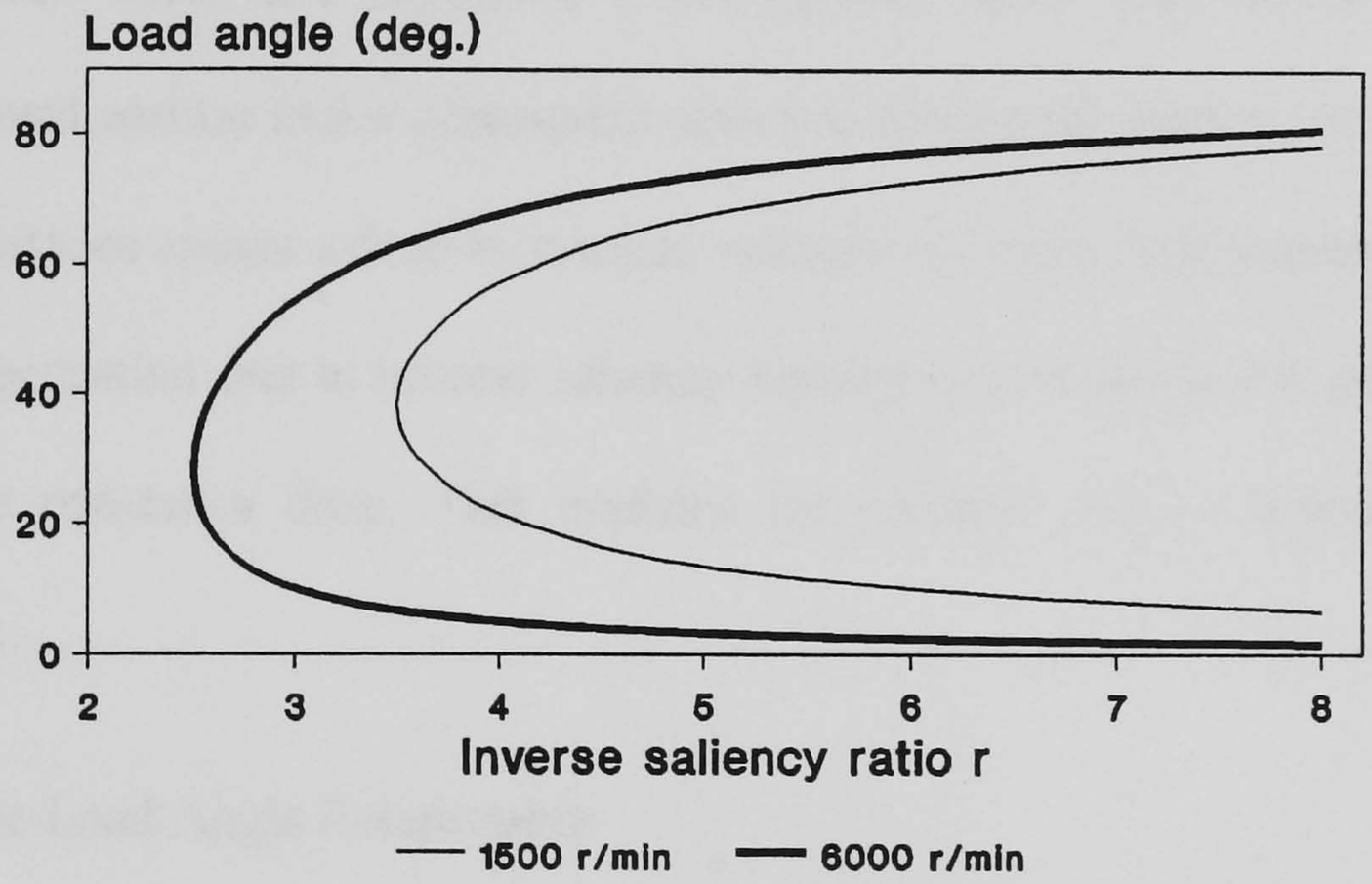


Fig. 6.15 Effect of inverse saliency ratio $r$ on the load angle that gives zero voltage regulation at nominal speed for a generator with $R = 0.295\Omega$, $X_d = 0.88\Omega$.

### 6.4.3 Extremum Points in the Load Characteristic

The results in Fig. 6.11 through Fig. 6.13 also suggest that extremum points might exist in the load characteristic of the PMSG. If $Z_L$ is used as a variable, this condition will occur when the derivative of $V$ with respect of $Z_L$ is equal to zero, i.e.:

$$\frac{dV}{dZ_L} = 0 \,. \tag{6.34}$$

From (6.30) and (6.34), the following cubic equation in $Z_L$ may be deduced:

$$c_3 \cdot Z_L^{\,3} + c_2 \cdot Z_L^{\,2} + c_1 \cdot Z_L + c_0 = 0 \qquad (6.35)$$

where

$c_0 = 2g_2g_4$, $c_1 = 3g_1g_4$, $c_2 = g_1g_3 + 4g_4 - 2g_2$, and $c_3 = 2g_3 - g_1$.

Solution of (6.35) for the prototype generator operating at a speed of 6000 r/min and supplying a unity-power-factor load also gives two positive real roots, viz. 50.8 and 15.8. When $Z_L = 50.8\ \Omega$, $\delta = 9.9^0$e, $I = 5.2$ A and $V = 264.9$ V; when $Z_L = 15.8\ \Omega$, $\delta = 29.0^0$e, $I = 16.9$ A and $V = 265.9$ V.

The results in Sections 6.4.2 and 6.4.3 suggest that the load characteristic of the prototype PMSG at 6000 r/min and supplying a unity-power-factor load comprises an initial concave-upward section and a subsequent concave-downward section. At light loads the armature resistance causes a drop in terminal voltage; but as the load current increases, the voltage compensation due to inverse saliency becomes dominant and it gradually offsets the armature resistance drop. This explains the presence of a 'saddle' in the load characteristic.

### 6.4.4 Power-Load Angle Relationship

Since the terminal voltage $V$ varies with load, the power-load angle characteristic of a PMSG under isolated operation is different from that under infinite busbar operation. For a three-phase generator supplying an isolated load, the total output power is given by:

$$P = \frac{3V^2}{Z_L}.\cos\phi\,. \qquad (6.36)$$

Substituting (6.26) and (6.28) into (6.36), the power-load angle equation for the PMSG can be deduced:

$$P = \frac{3E^2 \cos\phi.[X_q \cos(\delta+\phi) - R\sin(\delta+\phi)]\sin\delta}{[X_q \cos\delta.\cos(\delta+\phi) - R\sin\phi + X_d \sin\delta.\sin(\delta+\phi)]^2}. \quad (6.37)$$

Fig. 6.16 shows the effect of inverse saliency ratio $r$ on the power-load angle characteristics of a PMSG with $E$ = 66.44 V, $R$ = 0.295 Ω, $X_d$ = 0.88 Ω at nominal speed (1500 r/min) and supplying a unity-power-factor load. For a given value of $r$, a maximum power condition occurs at a load angle which is less than $90^0$e. The maximum power output from the generator increases with increase in $r$, but at light loads the value of $\delta$ for a given output power is larger.

The maximum power condition cannot be easily deduced from (6.37). To simplify the mathematical derivation, the power is first expressed in terms of $Z_L$ as follows:

$$P = 3E^2 \cos\phi.\frac{Z_L(Z_L^2 + g_1 \cdot Z_L + g_2)}{(Z_L^2 + g_3 \cdot Z_L + g_4)^2}. \quad (6.38)$$

For a given power factor angle $\phi$, maximum power output occurs when

$$\frac{dP}{dZ_L} = 0. \quad (6.39)$$

From (6.38) and (6.39), the following quartic polynomial equation is obtained:

$$d_4 \cdot Z_L^4 + d_3 \cdot Z_L^3 + d_2 \cdot Z_L^2 + d_1 \cdot Z_L + d_0 = 0 \quad (6.40)$$

where $d_0 = -g_2 g_4$, $d_1 = g_2 g_3 - 2g_1 g_4$, $d_2 = 3(g_2 - g_4)$, $d_3 = 2g_1 - g_3$, and $d_4 = 1$.

Eqn. (6.40) may be solved in a straightforward manner using Ferrari's method [108].

Again only positive real roots yield feasible extremum points.

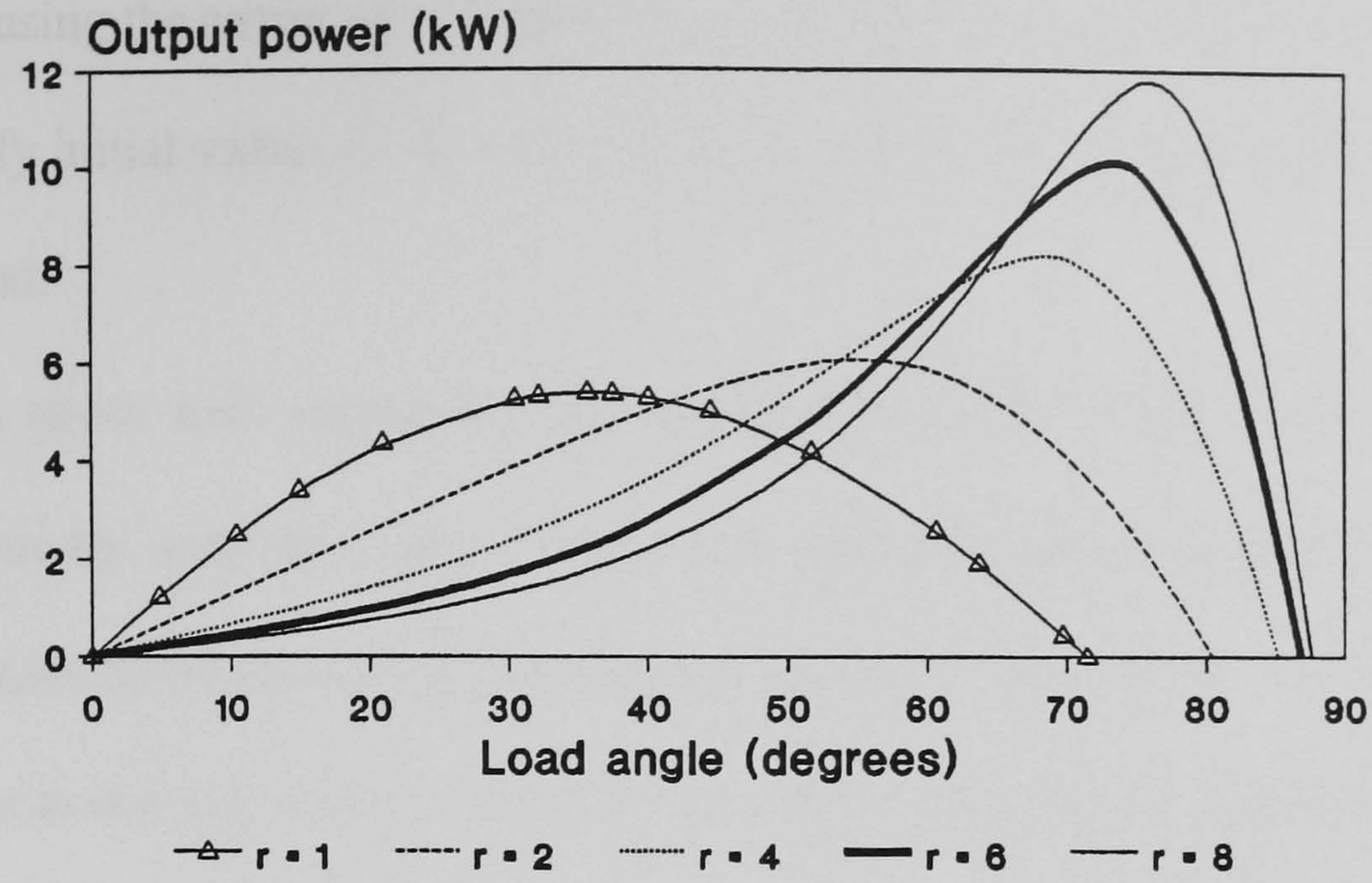


Fig. 6.16 Effect of inverse saliency ratio $r$ on the power-load angle characteristics of a PMSG operating at nominal speed and supplying a unity-power-factor load: $E = 66.44$ V, $R = 0.295\ \Omega$, $X_d = 0.88\ \Omega$.

### 6.4.5 The Saturated Two-Axis Model

A saturated two-axis model for the PMSG with inset rotor is now proposed based on the results obtained from a 2-D FEM (to be elaborated in Section 6.5). Fig. 6.24 shows the computed variations $X_d$ and $X_q$ as a function of the exciting currents $I_d$ and $I_q$. For representation in a computer program, the variations may be approximated by the following describing functions:

$$X_d = \begin{cases} 0.86 + 0.003\, I_d\,, & I_d < 10 \\ 0.89\,, & I_d \geq 10 \end{cases} \tag{6.41}$$

$$X_q = \begin{cases} 2.23\,, & I_q < 6 \\ 2.605 - 0.0625\, I_q\,, & I_q \geq 6 \end{cases} . \tag{6.42}$$

The analysis using the saturated two-axis model can be summarized as follows:

1) Specify initial values of $X_d$ and $X_q$. For convenience, the unsaturated values could be used.

2) For a given load impedance $Z_L$, load power factor angle $\phi$ and rotor speed, evaluate the terminal voltage $V$ using the method presented in Section 6.4.1.

3) Compute the d-axis current $I_d$ and q-axis current $I_q$, using (6.23) and (6.24).

4) Compute the new values of $X_d$ and $X_q$ from (6.41) and (6.42), respectively.

5) Repeat steps 2) to 4) until the difference between the values of $V$ in successive iterations is less than a specified value, say 0.000001.

6) Compute the load voltage and generator performance using the final value of terminal voltage and the corresponding load angle.

Fig. 6.17 shows the computed and experimental load characteristics of the prototype PMSG when driven at the nominal speed (1500 r/min). At heavy loads, the voltage compensation effect due to inverse saliency is partly offset by saturation in the q-axis magnetic circuit. For unity-power-factor loads, saturation effect is noticeable for load currents exceeding 6 A. It is observed that the analysis based on the saturated two-axis model gives a more accurate prediction of the load characteristic compared with the two-axis model with fixed parameters, especially under heavy load conditions. For loads at 0.8 power factor lagging, however, both methods give practically the same results. This is due to the fact that $I_q$ is smaller and hence the effect of q-axis saturation is less pronounced.

The good correlation between the computed and experimental results confirms the validity of the analysis based on the saturated two-axis model.

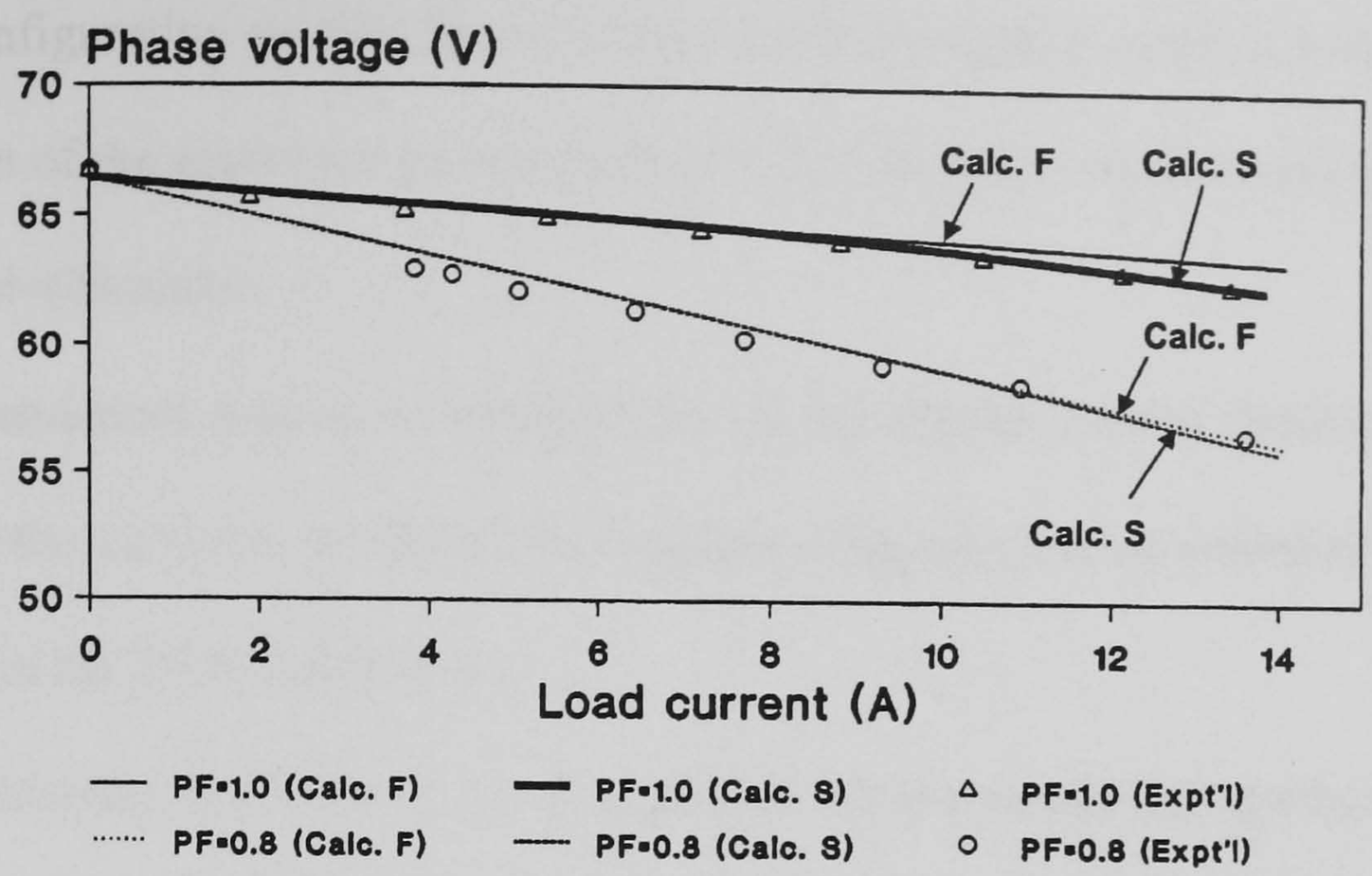


Fig. 6.17 Load characteristics of prototype PMSG at nominal speed (Calc. F — calculated using fixed values of $X_d$ and $X_q$; Calc. S — calculated using saturated two-axis model).

### 6.4.6 Summary

This section has presented a comprehensive analysis of a three-phase PMSG with inset rotor. Relevant equations for lagging-power-factor loads are developed based on the two-axis model. The conditions for achieving zero voltage regulation, extremum points on the load characteristic, and maximum power output, have been deduced analytically. It is shown that the saturated two-axis model gives a more accurate prediction of the load characteristic at heavy loads.

## 6.5 Computation of Synchronous Reactances

### 6.5.1 Analysis Based on FEM

The synchronous reactances $X_d$ and $X_q$ may be computed from an analysis based on a two-dimensional finite element method (2D FEM). To compute the magnetic field distribution, eight-noded, quadrilateral elements [95] are used in the mesh formation and FEM computations in order to reduce the number of elements required while maintaining a reasonably high computational accuracy. Advantage is taken of the symmetry in the

machine configuration so that the solution region need only cover one-quarter of the cross-section of the prototype generator (Fig. 6.2). The FEM mesh used consists of 108 elements and 429 nodes.

The rotor permanent magnet is modelled by an equivalent current density $J_c$ that also accounts for the curvature effects of the magnets. Magnetic vector potential $A$ is taken as the variable in the FEM formulation.

Magnetic hysteresis in the iron cores is neglected, i.e. the nominal magnetization curve is used for modelling magnetic saturation. Fig. 6.18 shows the magnetization curve for the ferromagnetic material of the prototype generator.

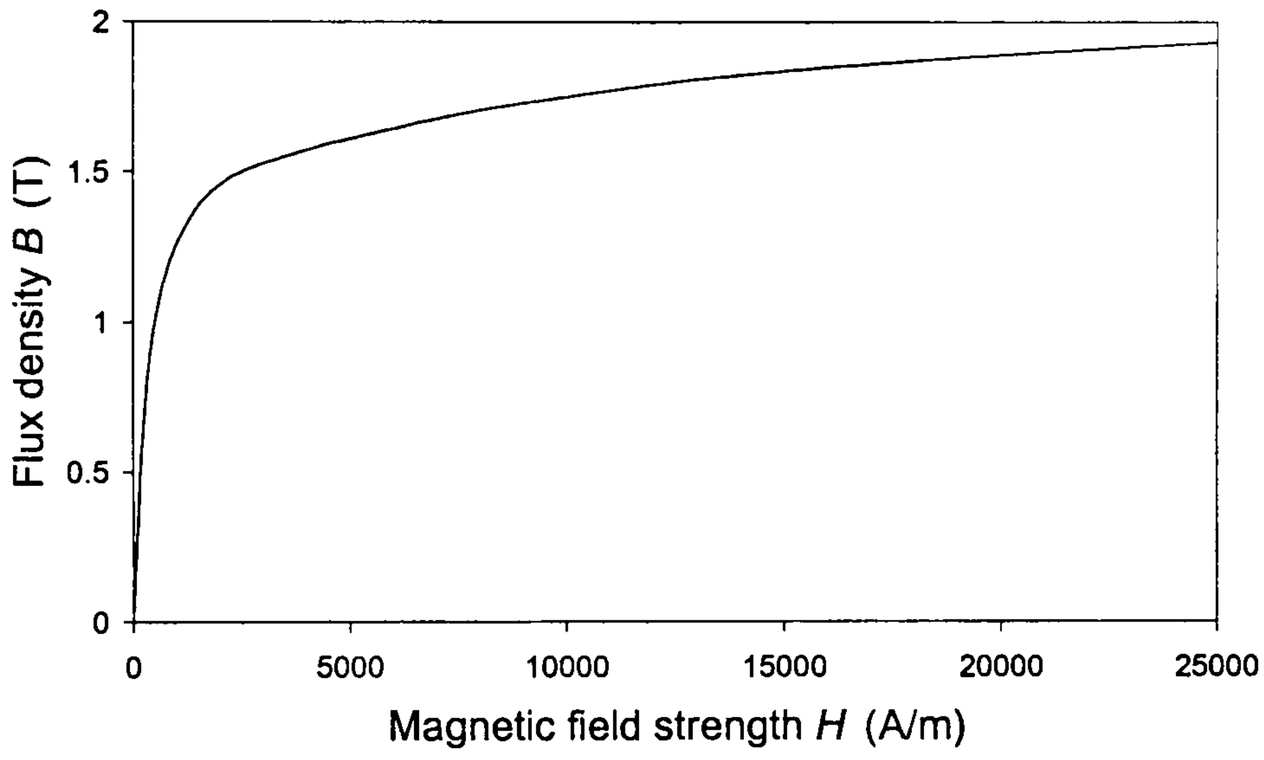


Fig. 6.18 Magnetization curve of prototype PMSG.

With reference to Fig. 6.2, the basic field equation and boundary conditions of the PMSG may be written as follows [95]:

$$\frac{\partial}{\partial x}\left(\frac{1}{\mu}\frac{\partial A}{\partial x}\right)+\frac{\partial}{\partial y}\left(\frac{1}{\mu}\frac{\partial A}{\partial y}\right)=-J \tag{6.43}$$

$$\frac{1}{\mu_1}\frac{\partial A}{\partial n}\bigg|_{L^-}-\frac{1}{\mu_2}\frac{\partial A}{\partial n}\bigg|_{L^+}=J_c \tag{6.44}$$

$$A|_{AD}=A|_{BC} \tag{6.45}$$

$$A|_{AB}=-A|_{DC} \tag{6.46}$$

where

$ABCD$ = boundary surface defined in Fig. 6.2;

$J$ = externally impressed current density;

$J_c$ = equivalent surface current density of PM material;

$L$ = surface of permanent magnet along the direction of the magnetization;

$L^+$ = edge adjacent to $L$ and outside the permanent magnet material;

$L^-$ = edge adjacent to $L$ and inside the permanent magnet material;

$\mu$ = permeability;

$\mu_1$ = permeability of permanent-magnet material;

$\mu_2$ = permeability of air.

Depending upon the region being considered, (6.43) need to be slightly modified. In sourceless regions, as in the case of the stator core and the rotor yoke, $J$ should be equated to zero.

The energy functional is

$$E(A) = \iint_{\Omega} \left( \int_0^B \frac{B}{\mu}.dB - A.J \right) dx.dy - \int_L J_c.A.dl' \tag{6.47}$$

where $B$ is the flux density and $dl'$ is an infinitesimal segment along edge $L$.

After discretization and functional minimization as discussed in Appendix C, the following matrix equation is obtained:

$$[K].[A] = [R] \tag{6.48}$$

where

$[K]$ = $n \times n$ coefficient (stiffness) matrix;

$[A]$ = $n \times 1$ column vector of nodal magnetic vector potentials;

$[R]$ = $n \times 1$ right-hand side column vector containing known terms;

and $n$ = number of nodes.

After solving (6.48) to give $A$, the flux density at any point $(x, y)$ may be computed as follows:

$$B = \sqrt{B_x^2 + B_y^2} \tag{6.49}$$

$$\begin{bmatrix} B_x \\ B_y \end{bmatrix} = [J]^{-1} \begin{bmatrix} \frac{\partial N_1}{\partial \eta} & \cdots & \frac{\partial N_8}{\partial \eta} \\ \\ \frac{\partial N_1}{\partial \xi} & \cdots & \frac{\partial N_8}{\partial \xi} \end{bmatrix} \begin{bmatrix} A_1 \\ \cdot \\ \cdot \\ A_8 \end{bmatrix} \tag{6.50}$$

where

$[J]^{-1}$ = inverse of Jacobian matrix;

$N_1,...N_8$ = shape functions;

$\xi$ , $\eta$ = local coordinates.

### 6.5.2 Computation of $X_d$ and $X_q$

For computing $X_d$ or $X_q$, the usual definition of air gap magnetizing reactance is used, but the effect of rotor magnets on the flux produced by the exciting current in each axis has to be accounted for.

To compute $X_d$, d-axis of the rotor is aligned with the resultant magnetomotive force (m.m.f.) axis of the armature winding and a specified balanced three-phase current is allowed to flow. With the surface current density $J_c$ set to that corresponding to the remanent flux density, the magnetic field distribution is computed and the values of permeability in the elements are determined. Using these values of magnetic permeability, the magnetic field distribution is re-calculated with $J_c$ set to zero and the resultant flux linkage is evaluated. $X_d$ is then determined from the ratio of the induced

e.m.f. to the armature current, plus the leakage reactance of the end winding $X_e$. The value of $X_d$ computed in this manner has thus included the effect of the rotor magnets. The flux linkage in the $i$th coil in the d-axis winding is

$$\Psi_i = w.\phi_i \tag{6.51}$$

where

$$\phi_i = \int_{S_i} \overline{B}.d\,\overline{s} = \int \nabla \times \overline{A}.d\,\overline{s} = \int_{l} \overline{A}.d\,\overline{l} = (A_i - A_i').l_{fe}. \tag{6.52}$$

The induced e.m.f. in the d-axis is

$$E_d = 4.44\, f\,(\sum_{i=1}^{p\,g} \psi_i)/c. \tag{6.53}$$

$X_d$ is then computed as the ratio of the induced e.m.f. in the winding to the corresponding current, i.e.

$$X_d = \frac{E_d}{I_d} + X_e \tag{6.54}$$

where

$A_i, A_i'$ = equivalent vector potential at the coil sides of the $i$th coil;

$c$ = number of parallel paths;

$B$ = flux density;

$E_d$ = induced e.m.f. in the d-axis winding;

$f$ = frequency of induced e.m.f.;

$g$ = number of slots per pole per phase;

$I_d$ = d-axis armature current;

$l$ = boundary of plane $S_i$;

$l_{fe}$ = effective length of the iron core;

$p$ = number of poles;

$S_i$ = area formed by the coil sides of the $i$th coil;

$w$ = turns per coil;

$X_e$ = leakage reactance of the end winding;

$\psi_i$ = flux linkage in the $i$th coil;

$\phi_i$ = flux in the $i$th coil.

$X_q$ can be computed in a similar manner, but the q-axis of the rotor should be aligned with the resultant m.m.f. axis of the armature winding.

### 6.5.3 Computed Results

The above algorithms were implemented in a FORTRAN program with reference to the prototype generator shown in Fig. 6.2. Computations were also performed on an identical generator with a surface-magnet rotor (i.e. one without the interpolar soft-iron pole pieces). The per-phase machine parameters, computed for an exciting current of 6 A, are listed in Table 6.1.

TABLE 6.1
PER-PHASE PARAMETERS OF PROTOTYPE GENERATOR
$X_d$ and $X_q$ COMPUTED AT A CURRENT OF 6 A

| Rotor type | $X_d$ (Ω) | $X_q$ (Ω) | $E$ (V) |
|---|---|---|---|
| Inset PM rotor | 0.88 | 2.23 | 66.44 |
| Surface-magnet rotor | 0.73 | 0.74 | 67.67 |

Fig. 6.19 shows the flux plot of the prototype PMSG on no load. Since there is no armature current, all the flux is contributed by the rotor magnets. It is observed that the presence of soft-iron pole pieces in the interpolar axis results in an additional leakage rotor flux, hence the no-load voltage is slightly less than that of an equivalent generator with surface-magnet rotor.

Fig. 6.20 shows the flux density distribution due to the d-axis current alone. Most of the d-axis flux traverses a large effective air gap, either through the radial length of the magnet or through the stator slots, hence the d-axis flux linkage is naturally suppressed. On the other hand, the q-axis flux plot in Fig. 6.21 shows that a large portion of the q-axis flux traverses the low-reluctance path provided by the soft-iron pole pieces. The origin of inverse saliency in the inset rotor is thus clearly demonstrated. In Fig. 6.21, regions of high flux density can be identified, implying that local magnetic saturation is prominent in the q-axis.

Fig. 6.22 and Fig. 6.23 show respectively the composite flux plot (i.e. flux plot with combined rotor and stator excitation) of the PMSG when excited with d-axis and q-axis current. It is observed that the q-axis current gives rise to a more irregular flux density distribution and the flux density distribution is no-longer symmetrical as in the case of d-axis excitation.

By repeating the FEM computations presented in Section 6.5.2 over the practical range of stator exciting current, the variation of $X_d$ with $I_d$, as well as the variation of $X_q$ with $I_q$, can be obtained.

The computed values of $X_d$ and $X_q$ for the prototype generator are shown, respectively, by the triangular and circular symbols in Fig. 6.24. It is seen that the inset rotor construction results in a remarkable increase in $X_q$. The inverse saliency ratio $r$ of the generator is approximately equal to 2.53 under unsaturated conditions. Due to magnetic saturation in the q-axis, $X_q$ decreases as $I_q$ increases. $X_d$, on the other hand, increases slightly with $I_d$ due to the demagnetizing effect of $I_d$ on the rotor magnet. The computed results indicate that the saturation characteristic of the PMSG with inset rotor is different from that of an interior-type PM generator [71].

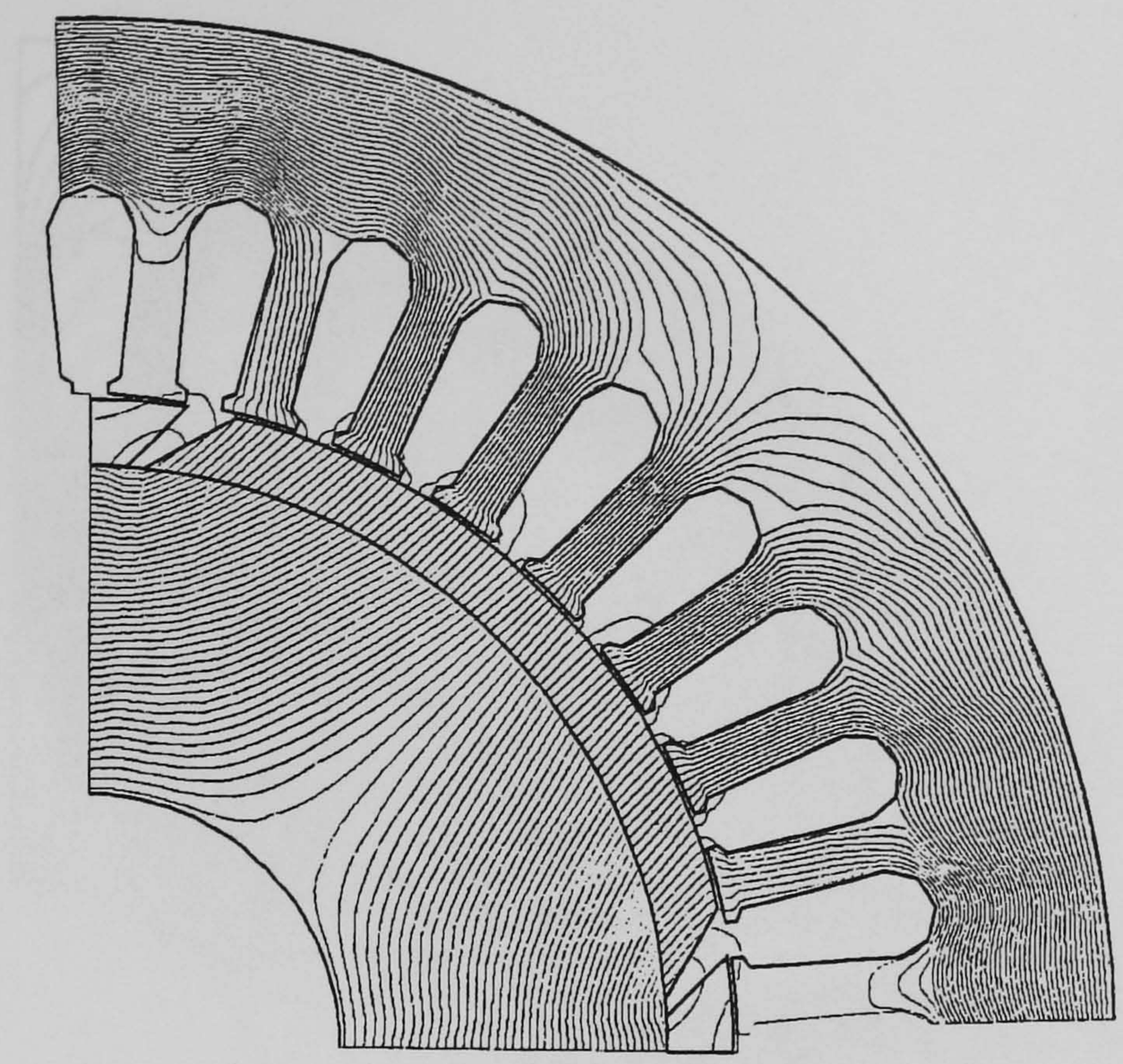

Fig. 6.19 Flux density distribution due to rotor permanent magnet alone.

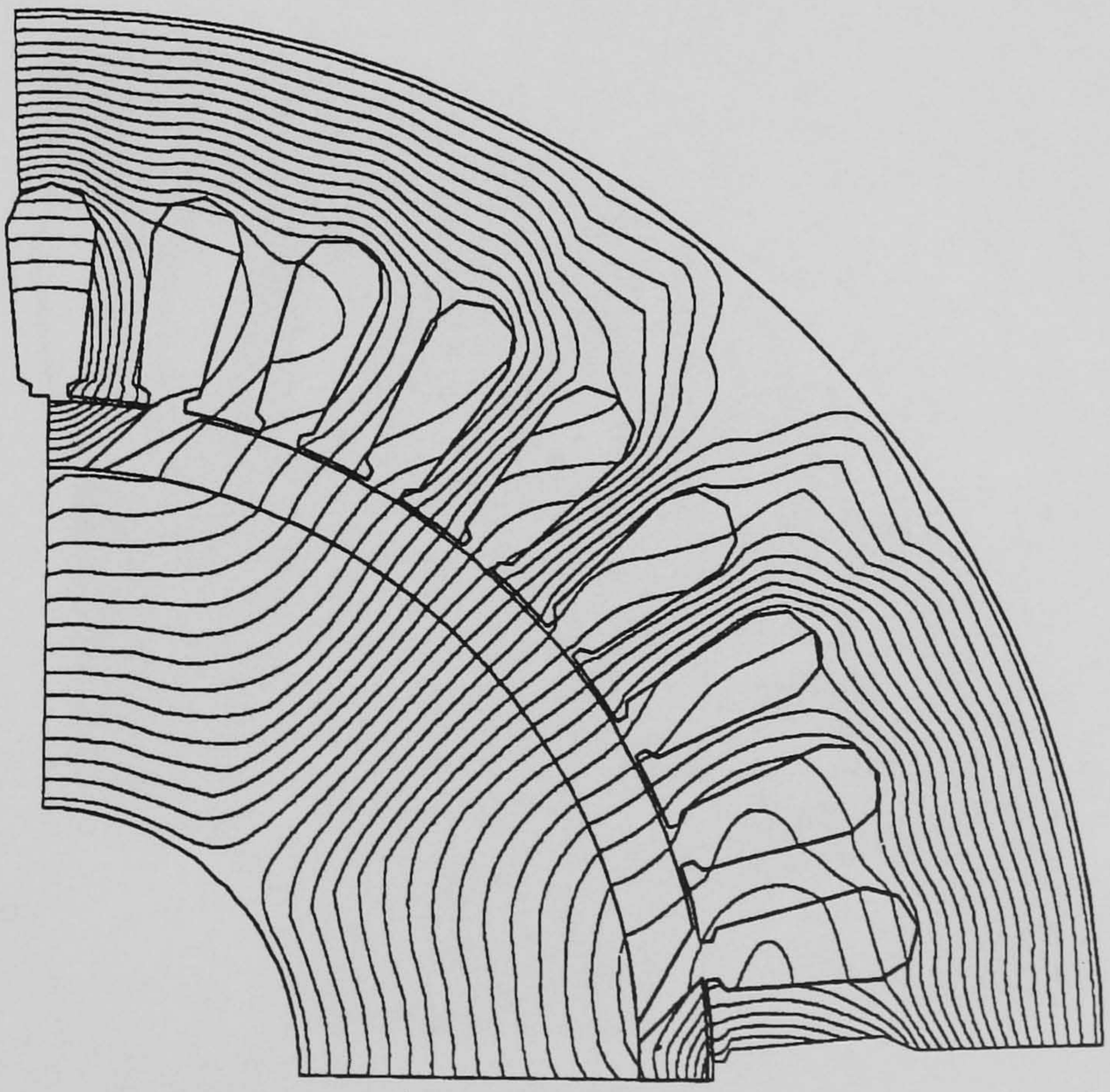

Fig. 6.20 Flux density distribution due to d-axis current alone.

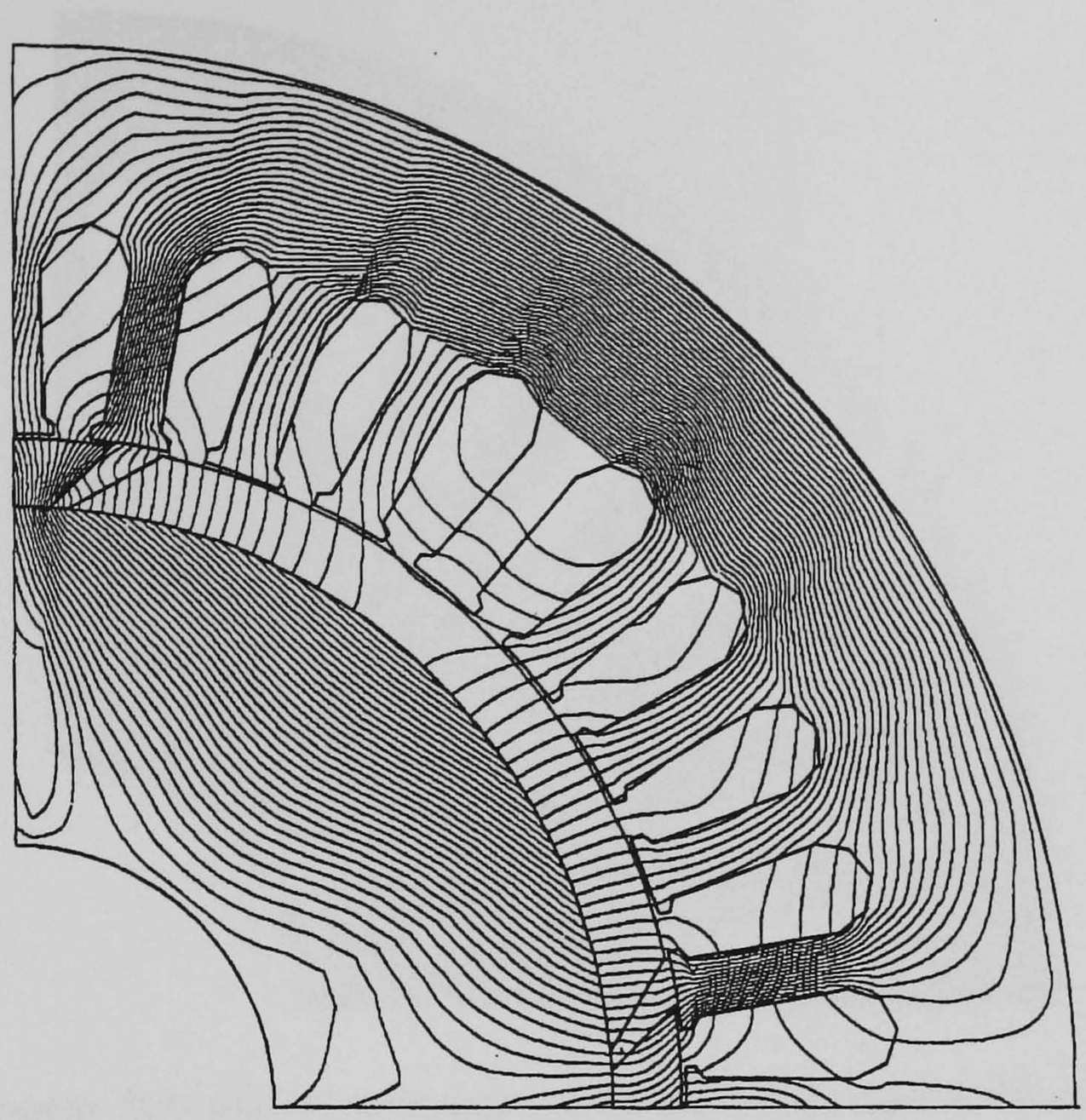

Fig. 6.21 Flux density distribution due to q-axis current alone.

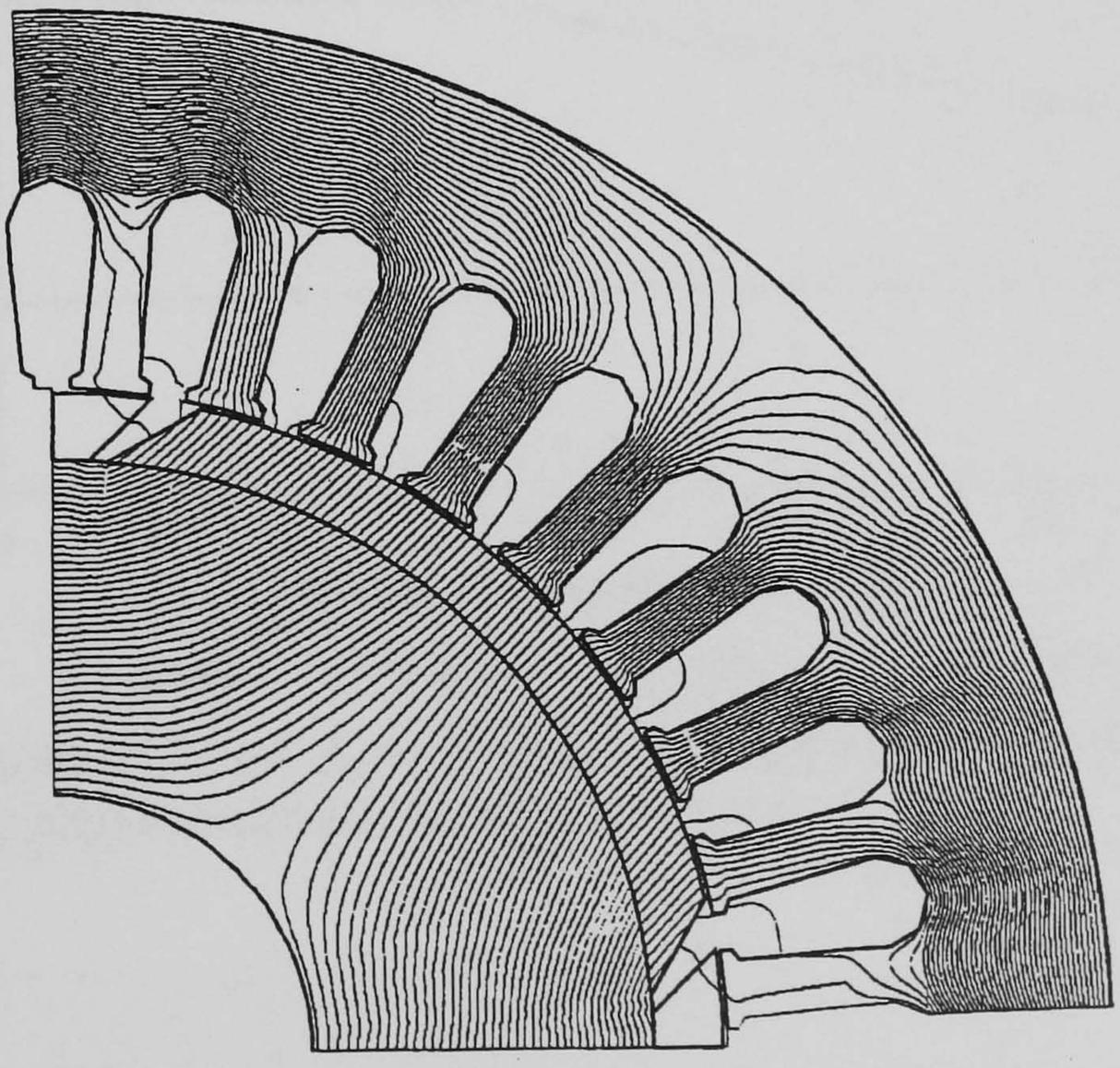

Fig. 6.22 Composite flux plot of prototype generator when excited by d-axis armature current.

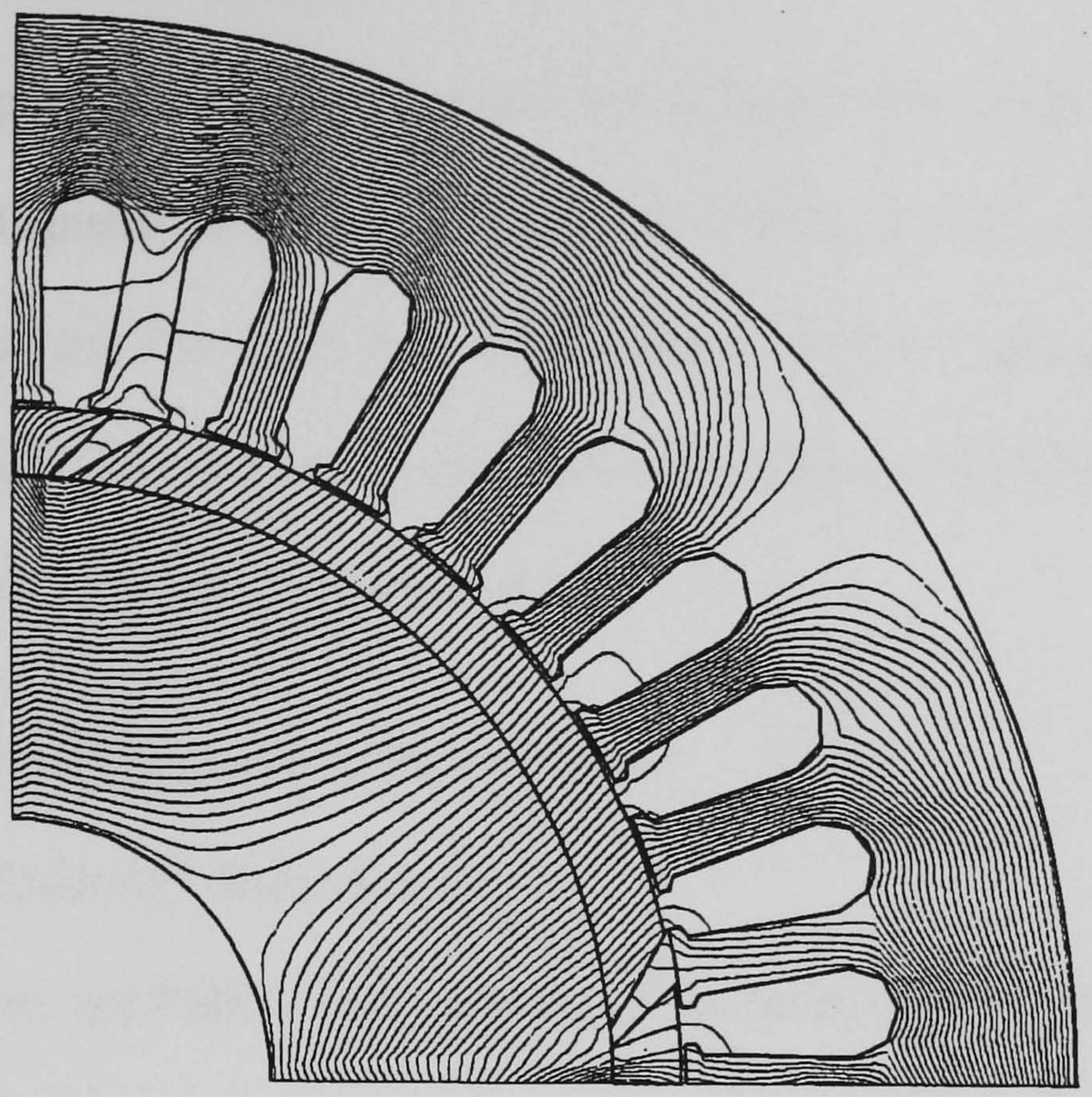

Fig. 6.23 Composite flux plot of prototype generator when excited by q-axis current.

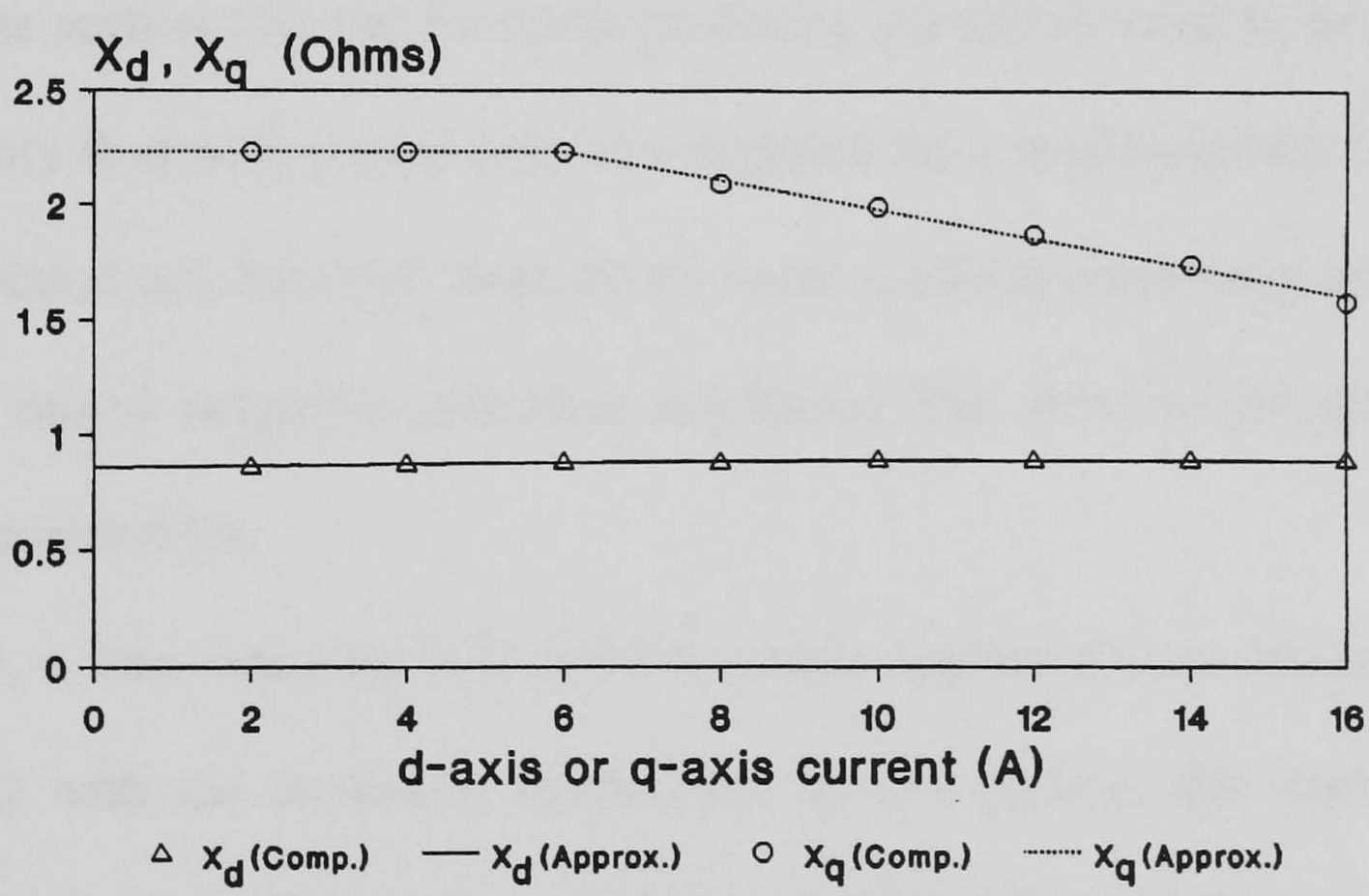


Fig. 6.24 Variations of $X_d$ and $X_q$ with stator exciting current computed from FEM, and the corresponding piecewise-linearized approximations.

### 6.5.4 Summary

A method for computing the d-axis and q-axis synchronous reactances for the PMSG has been presented. Magnetic saturation, including the effect of rotor magnets, has been included in the analysis. The origin of inverse saliency is clearly demonstrated from the flux plots. The results are useful for performance evaluation of the PMSG, especially in the development of a saturated two-axis model.

## 6.6 Analysis Using Time-Stepping 2-D FEM

### 6.6.1 Machine Model and Assumptions

In previous sections, the PMSG with inset rotor has been analyzed using the two-axis model, the values of $X_d$ and $X_q$ required being determined from a field analysis based on the FEM. This approach is computationally efficient since only one-quarter of the machine cross section (for the four-pole prototype generator) need to be modeled and the flux density distribution need only be computed for a single position of the rotor. It should be pointed out, however, that the two-axis model is essentially an approximate method and mixed magnetic saturation conditions that exist in the actual machine cannot be accounted for.

In Chapter 3, a time-stepping, 2-D FEM has been applied for the analysis of a grid-connected IG with the Steinmetz connection. In this section, this approach will be pursued again for the performance analysis of a PMSG with an inset rotor.

The solution region has to be extended to the complete cross-section of the PM generator since the axisymmetric boundary condition is no longer valid. As shown in Fig. 6.25, the field solution region $\Omega$ is bounded by the outer periphery $T1$ of the stator core and the inner periphery $T2$ of the rotor yoke (which coincides with the outer surface of the rotor shaft). It is assumed that all the flux is confined within the region $\Omega$.

As in Chapter 3, first-order triangular elements and linear interpolation functions are used, but only balanced operation at constant speed will be considered.

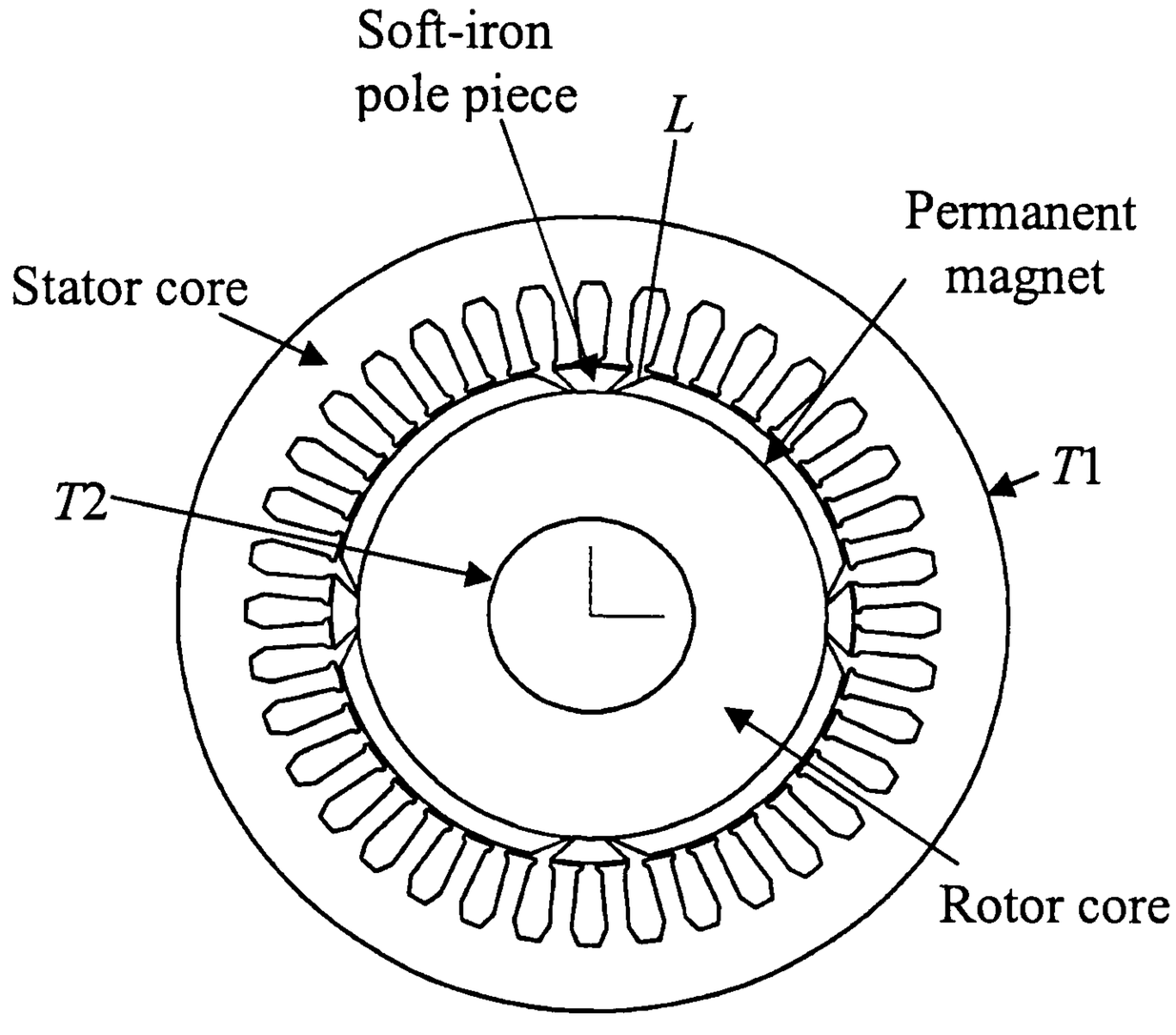


Fig. 6.25 Cross-sectional view of prototype PMSG with inset rotor construction.

### 6.6.2 Coupled Circuit and Field Analysis

The field equations given in Section 6.5 are also applicable for the present analysis, except for the boundaries with zero magnetic potential. With reference to Fig. 6.25, the boundary condition is given by:

$$A|_{T1} = A|_{T2} = 0 . \tag{6.55}$$

The matrix equation (6.48) in the field domain has to be coupled to the external circuit. For a PMSG supplying an isolated load, the external circuit comprises the armature resistance $R$, the armature end-winding leakage inductance $L_e$, the load resistance $R_L$, and the load inductance $L_L$. Fig. 6.26 shows the circuit connection of a star-connected PMSG which supplies a balanced, three-wire, star-connected load. Six circuit variables are introduced, namely the resultant generated e.m.f.s $E_A$, $E_B$, and $E_C$ and the phase currents $I_A$, $I_B$ and $I_C$. It should be noted that $E_A$, $E_B$, and $E_C$ can each be expressed in

terms of the nodal magnetic potentials, hence it remains to establish the equations for the phase currents.

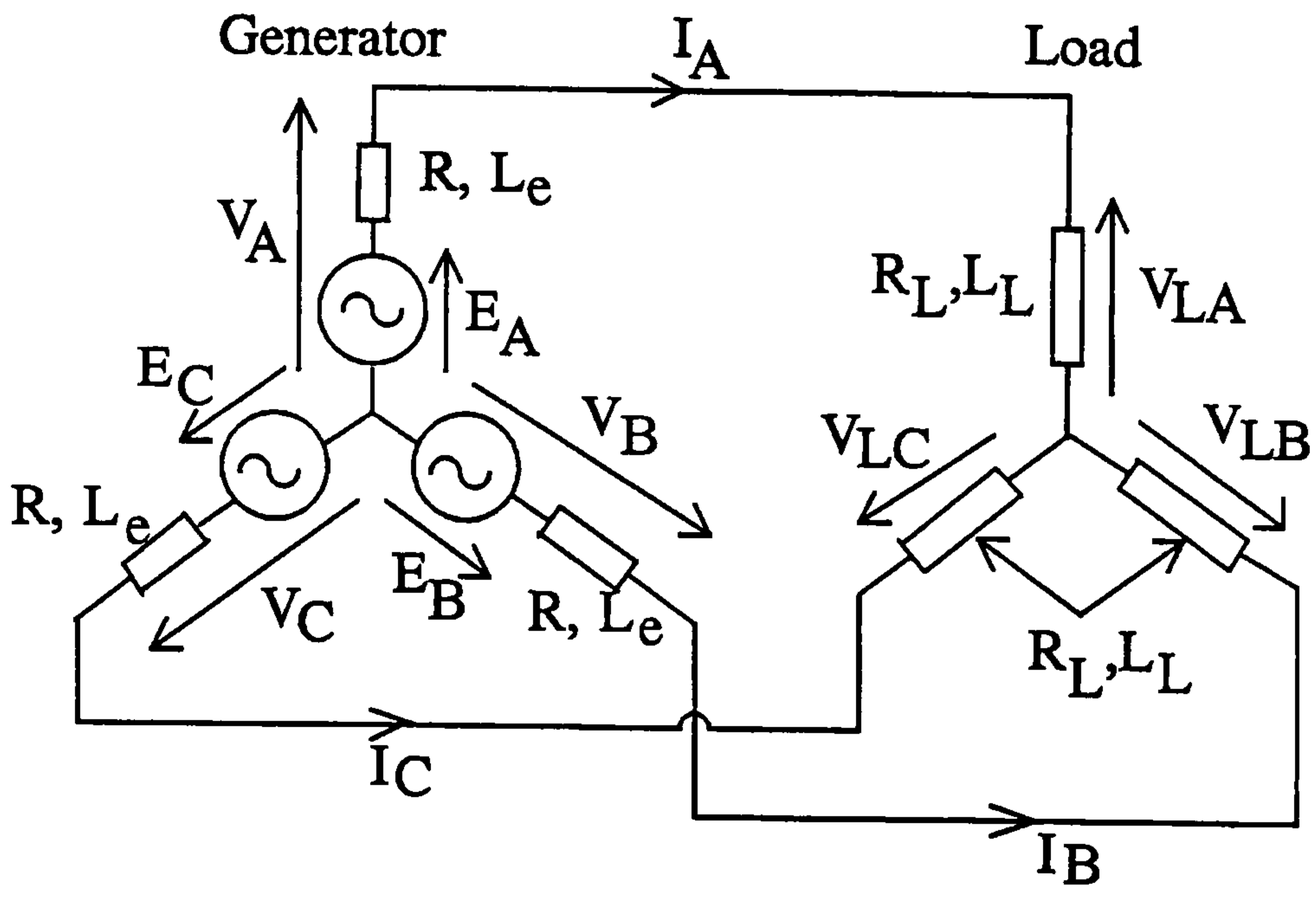


Fig. 6.26 PMSG supplying an isolated, balanced three-wire star-connected load.

For the mesh containing phase A and phase B in Fig. 6.26,

$$E_A - E_B = R_t I_A + L_t \frac{dI_A}{dt} - R_t I_B - L_t \frac{dI_B}{dt} \tag{6.56}$$

where $R_t = R + R_L$, and $L_t = L_e + L_L$.

Rewriting (6.56) in finite difference form:

$$E_A - E_B = R_t I_A + L_t \frac{(I_A - I'_A)}{\Delta t} - R_t I_B - L_t \frac{(I_B - I'_B)}{\Delta t} \tag{6.57}$$

where $I'_A$ = value of phase-A current in the previous time step;

$I'_B$ = value of phase-B current in the previous time step.

Eqn. (6.57) can further be expressed in the following form:

$$m_1 I_A - m_1 I_B - E_A + E_B = m_2 I'_A - m_2 I'_B \tag{6.58}$$

where $m_1 = R_t + L_t/\Delta t$; $m_2 = L_t/\Delta t$.

In a similar manner, for the mesh containing phase B and phase C,

$$m_1 I_B - m_1 I_C - E_B + E_C = m_2 I'_B - m_2 I'_C \,. \tag{6.59}$$

For a three-wire system, the line currents must satisfy the following constraint:

$$I_A + I_B + I_C = 0. \tag{6.60}$$

The phase-A voltage of the generator armature winding is

$$V_A = E_A - RI_A - m_2(I_A - I'_A) \tag{6.61}$$

and the phase-A load voltage is given by

$$V_{LA} = R_L I_A + m_3(I_A - I'_A) \tag{6.62}$$

where $m_3 = L_L/\Delta t$.

From (6.48), (6.58)-(6.60) and the three equations for the generated e.m.f.s, the following matrix equation may be established:

$$[K'].[A'] = [R'] \tag{6.63}$$

where

$[K']$ $n' \times n'$ modified stiffness matrix;

$[A']$ $n' \times 1$ column vector containing all the field and circuit variables;

$[R']$ $n' \times 1$ column vector containing known terms;

and $n' = n + 6$.

Solution of (6.63) enables the magnetic vector potentials $A$, flux density, stator e.m.f.s, stator currents, and the terminal voltage to be determined. It should be noted that the synchronous reactances need not be evaluated throughout the solution procedure.

Fig. 6.27 shows the mesh formation for the proposed analysis using time-stepping 2-D FEM. There are 2816 nodes and 5384 elements. The number of nodes with zero magnetic vector potential (i.e. nodes that fall on boundaries $T1$ and $T2$) total 248, hence the total number of field variables are 2816 – 248 = 2568. Since there are six additional circuit

variables, the total number of variables in the coupled circuit and field formulation are $2568 + 6 = 2574$.

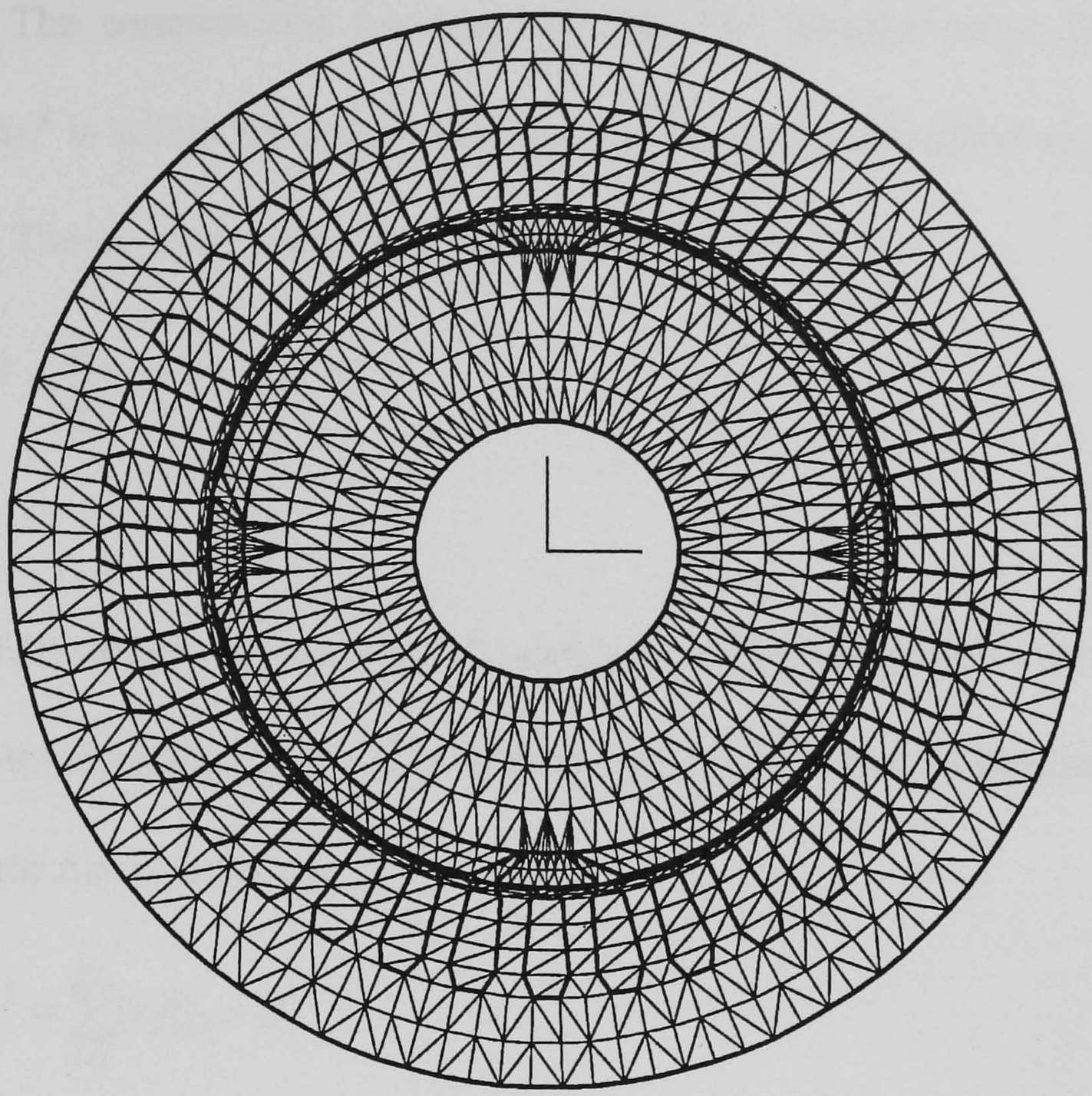

Fig. 6.27 Mesh formation for 2-D FEM analysis of PMSG with inset rotor.

### 6.6.3 Magnetic Saturation Consideration

In order to account for the effect of saturation, a magnetic nonlinearity sub-program has been incorporated in the FEM solver. For this purpose, the magnetization curve shown in Fig. 6.18 is used. Fig. 6.28 shows the flowchart of the proposed time-stepping 2-D FEM coupled with the external circuit equations. With the magnetic permeability $\mu$ of each element initialized to the appropriate value (for regions containing ferromagnetic material, the unsaturated value of $\mu$ is used), the stiffness matrix $[K]$ is formed and modified according to the boundary conditions and the external circuit configuration. For each time step, the modified system of equations is solved and the flux densities in all the elements

are evaluated from the nodal vector potentials. Using the magnetization curve of the magnetic material, the corresponding values of permeability $\mu$ (and hence the reluctivity $\upsilon$) are updated. The computations are repeated until the iteration error $\Delta\xi^2$ or the reluctivity error $\Delta\upsilon^2$ is within the specified values, or the specified number of iterations has been reached. The iteration error $\Delta\xi^2$ is defined as follows:

$$\Delta\xi^2 = \sum_{i=1}^{n'} [A_i'^{(k+1)} - A_i'^{(k)}]^2 \tag{6.64}$$

where

$A_i'^{(k+1)}$ = value of $i$th variable of the modified column vector $[A']$ in the $(k+1)$th iteration;

$A_i'^{(k)}$ = value of $i$th variable of the modified column vector $[A']$ in the $k$th iteration.

The reluctivity error $\Delta\upsilon^2$ is defined as:

$$\Delta\upsilon^2 = \sum_{i=1}^{n_e} [\upsilon_{i,new}^{(k)} - \upsilon_i^{(k)}]^2 \tag{6.65}$$

where

$\upsilon_i^{(k)}$ = value of reluctivity of the $i$th element at the beginning of the $k$th iteration;

$\upsilon_{i,new}^{(k)}$ = value of reluctivity at the end of the $k$th iteration;

$n_e$ = number of elements.

A relaxation factor may be applied for updating the values of $\upsilon$ for the next iteration:

$$\upsilon_i^{(k+1)} = \upsilon_i^{(k)} + W.(\upsilon_{i,new}^{(k)} - \upsilon_i^{(k)}) \tag{6.66}$$

where

$\upsilon_i^{(k+1)}$ value of reluctivity at the beginning of the $(k+1)$th iteration;

$W$ relaxation factor.

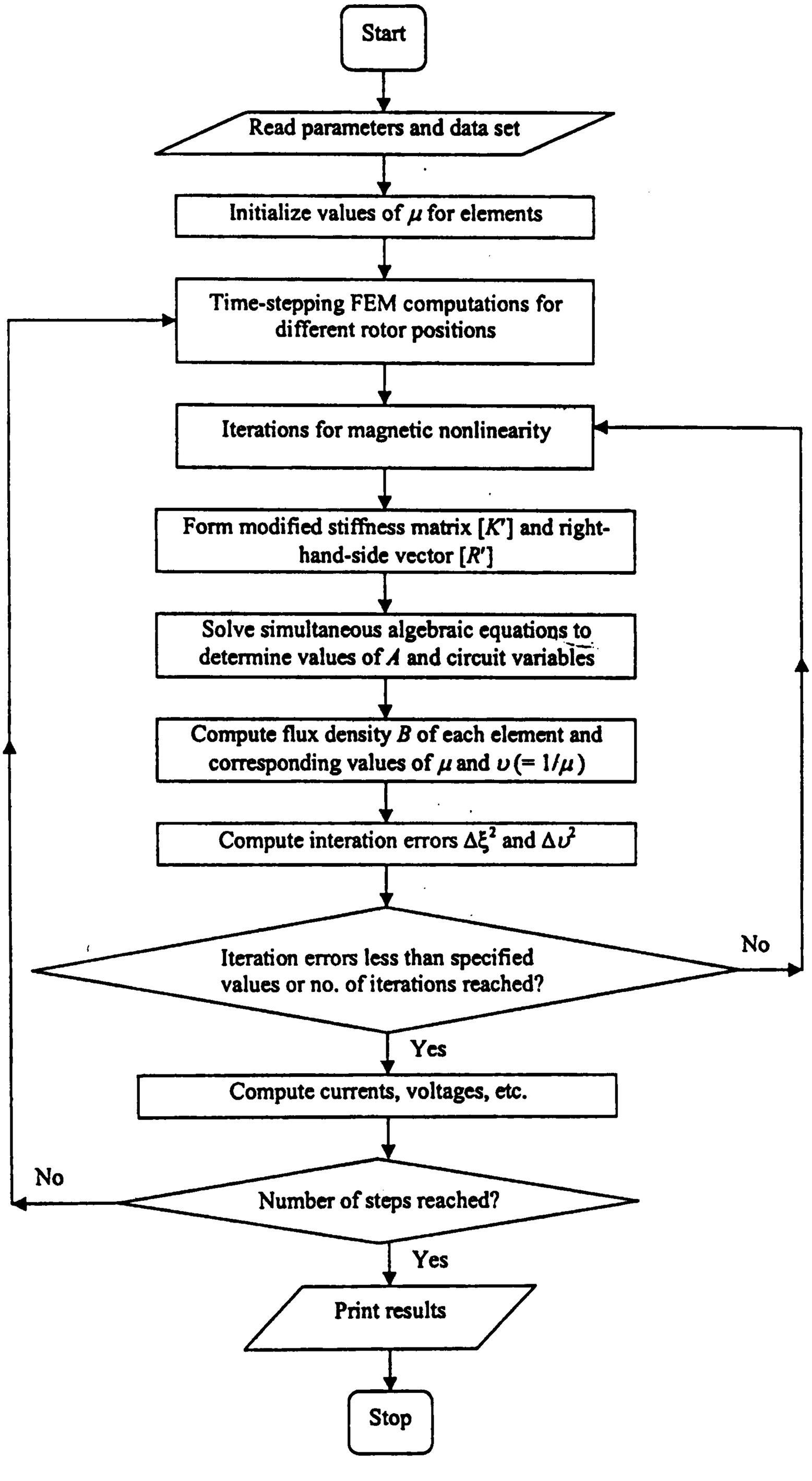


Fig. 6.28 Flowchart of time-stepping 2-D FEM for performance analysis of PMSG considering magnetic saturation.

### 6.6.4 Computed Results

The above algorithms were implemented in a FORTRAN program that incorporates the FEM computations, pre-processing and post-processing routines. In the solver, each time step was equivalent to one mechanical degree. For each load impedance or operating point, the FEM computations were performed over 1440 steps (i.e. four complete revolutions of the rotor) to allow the system quantities to reach the steady-state. For the magnetic nonlinearity sub-program, the maximum number of iterations was specified to be five. This choice was a compromise between the desired computational accuracy and the computation time required for a complete solution. An acceleration factor of 0.2 was found to give satisfactory convergence. The solution procedure was time-consuming due to the large number of variables and also the large number of steps involved. On a Pentium 4 personal computer with a clock speed of 1.6 GHz, the computation time for one operating point was approximately 30 h.

Fig. 6.29 shows the computed flux plot of the PMSG under no-load conditions. Since there is no armature current, all the flux is contributed by the rotor magnets. A small rotor leakage flux can be observed to flow across the soft-iron pole pieces, hence the no-load voltage is slightly less than that of an equivalent generator with surface-magnet rotor (i.e. one in which the interpolar pole pieces are removed.

Fig. 6.30 shows the computed flux plot of the PMSG when it is supplying a pure resistive load of 4.71 Ω per phase. Due to the presence of soft-iron pole pieces, there is considerable magnetic flux in the q-axis and magnetic saturation can be significant in the q-axis region, e.g. the base of each soft-iron pole piece and the stator teeth adjacent to it. This condition cannot be easily analyzed by using the two-axis model and hence the proposed time-stepping 2-D FEM that includes effect of magnetic saturation is justified.

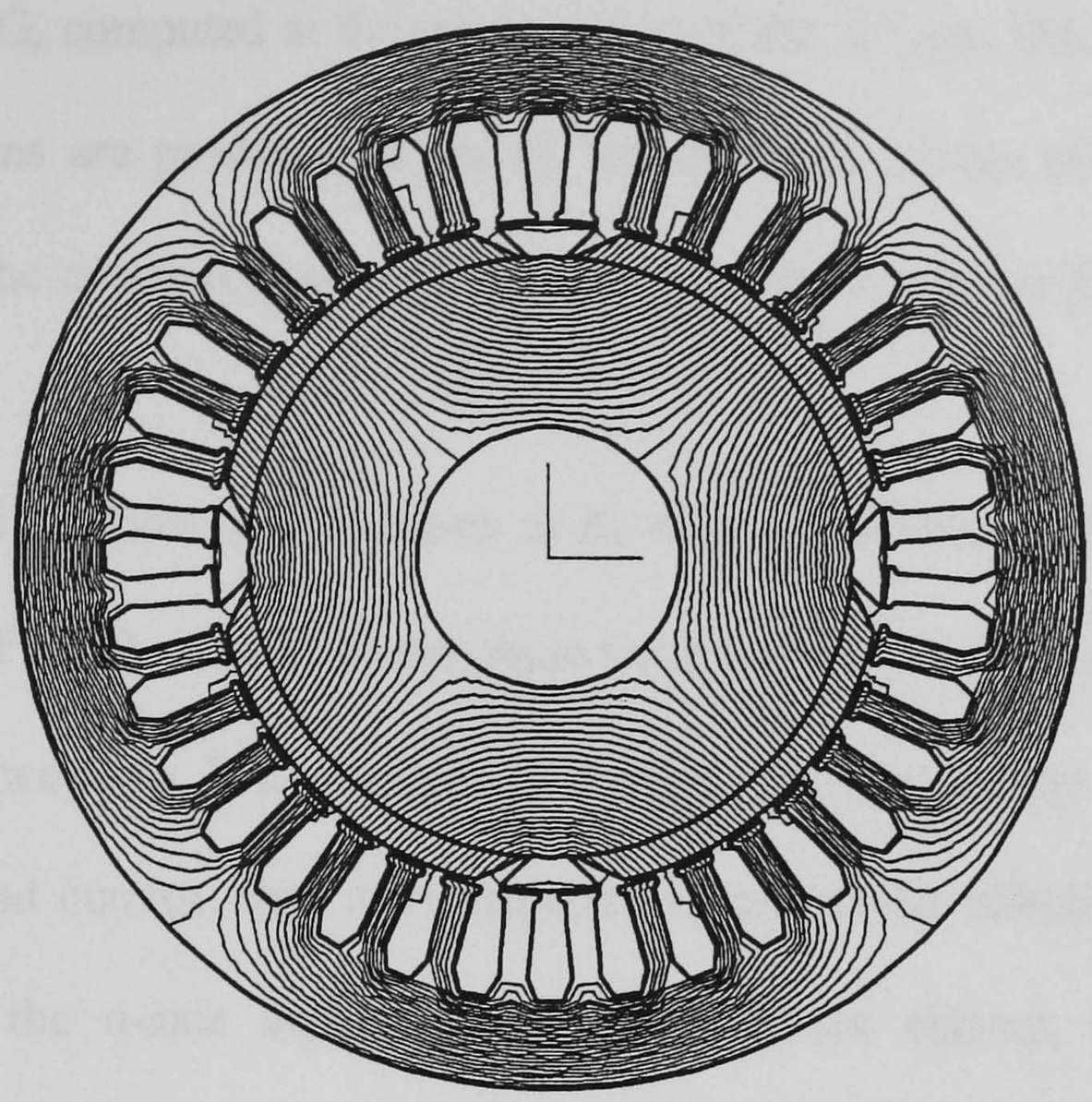

Fig. 6.29 Flux plot of PMSG with inset rotor under no-load condition.

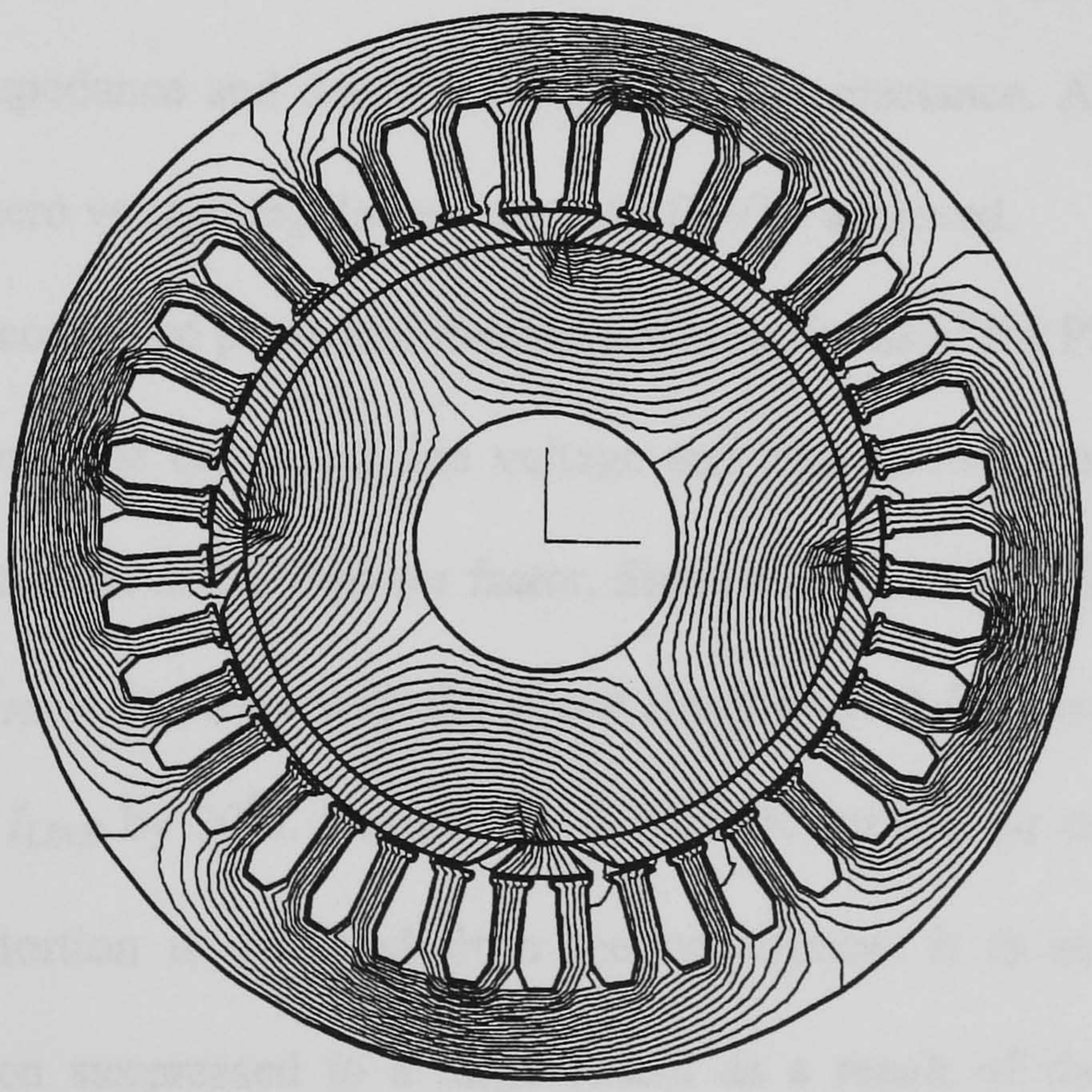

Fig. 6.30 Flux plot of PMSG with inset rotor when supplying a resistive load of 4.71 Ω per phase.

Fig. 6.31 shows the variation of the radial component $B_n$ of the no-load air gap flux density in the PMSG, computed at the mean radius of the air gap. Due to the stator slot openings, undulations are produced in the $B_n$ waveform. It is also observed that $B_n$ is practically zero in the q-axis region, which agrees with the computed flux plot shown in Fig. 6.29.

Fig. 6.32 and Fig. 6.33 show the variations in $B_n$ when the PMSG is supplying a unity-power-factor load of 9.1 Ω and 4.71 Ω per phase (which correspond to load currents of 7.1 A and 13.2 A), respectively. It is observed that the q-axis flux density increases almost linearly with the load current, with a consequent increase in the effective flux per pole. Since the flux in the q-axis depends upon the armature current, the flux density compensation effect increases with the load current. For a well designed generator, it is possible for the voltage compensation to partially offset the voltage drop due to the armature leakage impedance and d-axis armature reaction reactance. A reduced voltage regulation, or even zero voltage regulation, can therefore be achieved.

Fig. 6.34 shows the computed phase and line voltage waveforms of the PMSG on no load, while Fig. 6.35 shows the computed line voltage and line current when the PMSG is supplying full-load current at unity power factor. Since a resistive load is being supplied, the phase voltage $V_{PH}$ is in phase with the phase (line) current $I_{LINE}$ and hence the line voltage $V_{LINE}$ leads $I_{LINE}$ by $30^0$e. Despite the use of the inset rotor construction, very small harmonic distortion is observed from the waveforms. It is seen that the slot harmonics have been suppressed to a large extent as a result of the distribution of armature winding and the use of short-pitched coils.

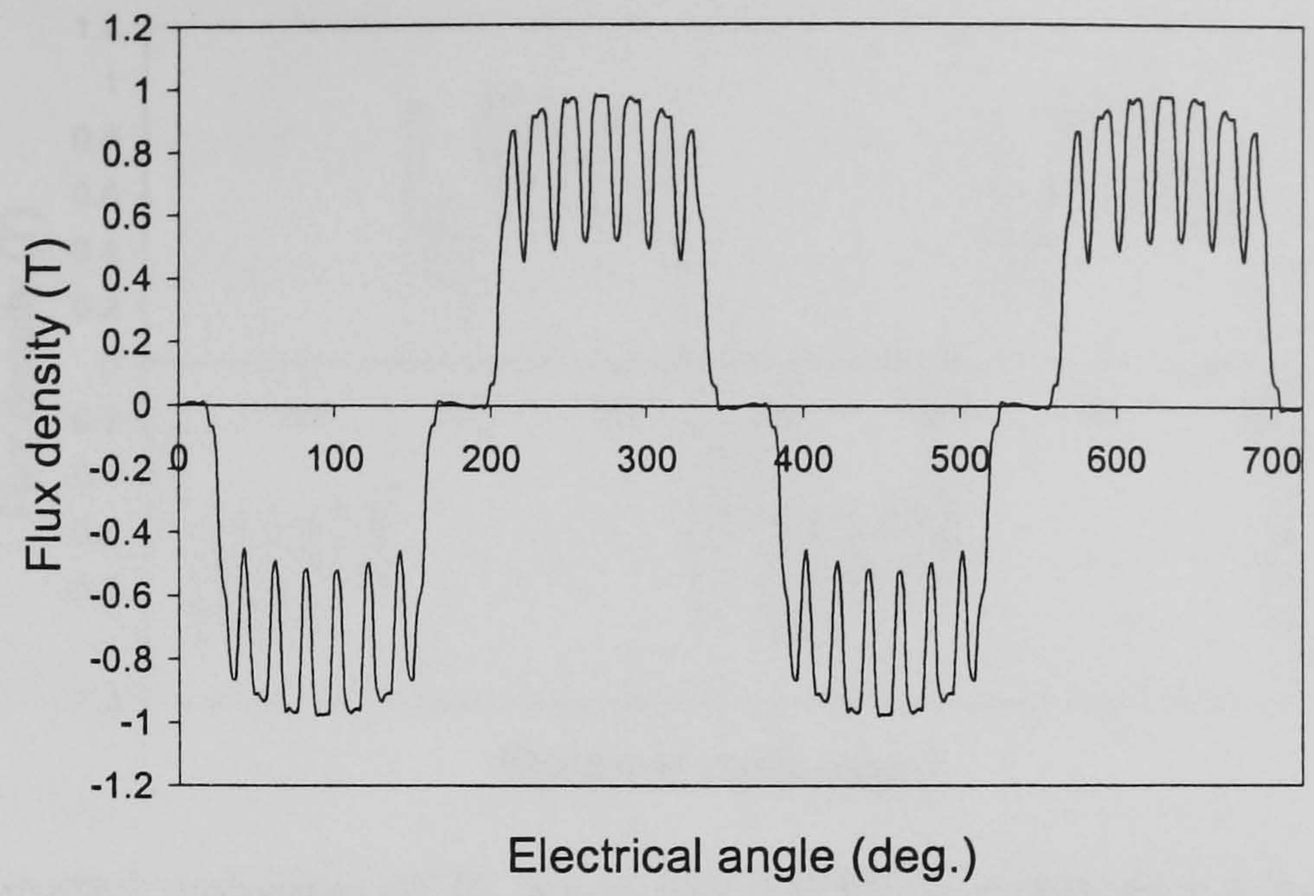


Fig. 6.31 Computed variation of $B_n$ when the PMSG is on no load.

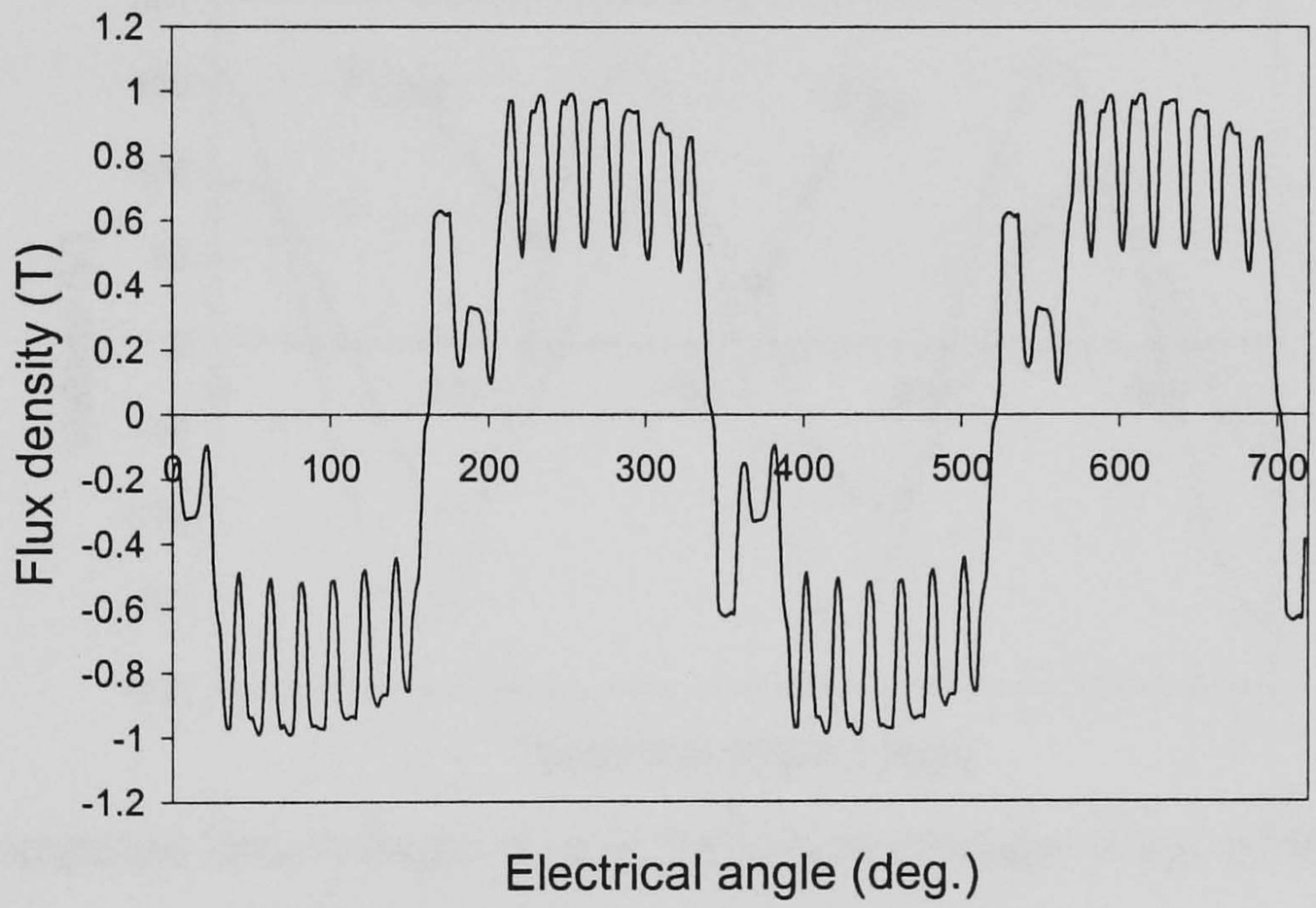


Fig. 6.32 Computed variation of $B_n$ when the PMSG is supplying a load resistance of 9.1 Ω per phase.

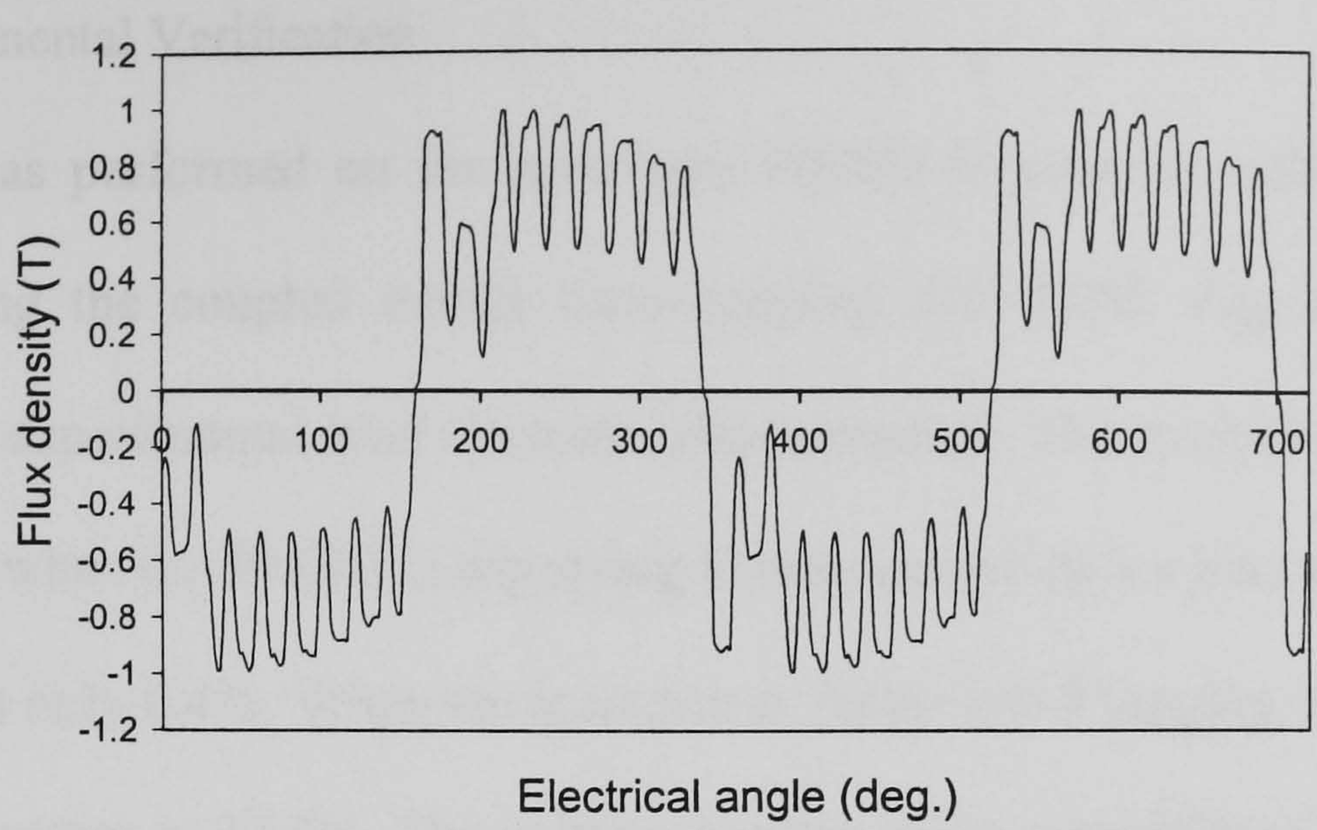


Fig. 6.33 Computed variation of $B_n$ when the PMSG is supplying a load resistance of 4.71 Ω per phase.

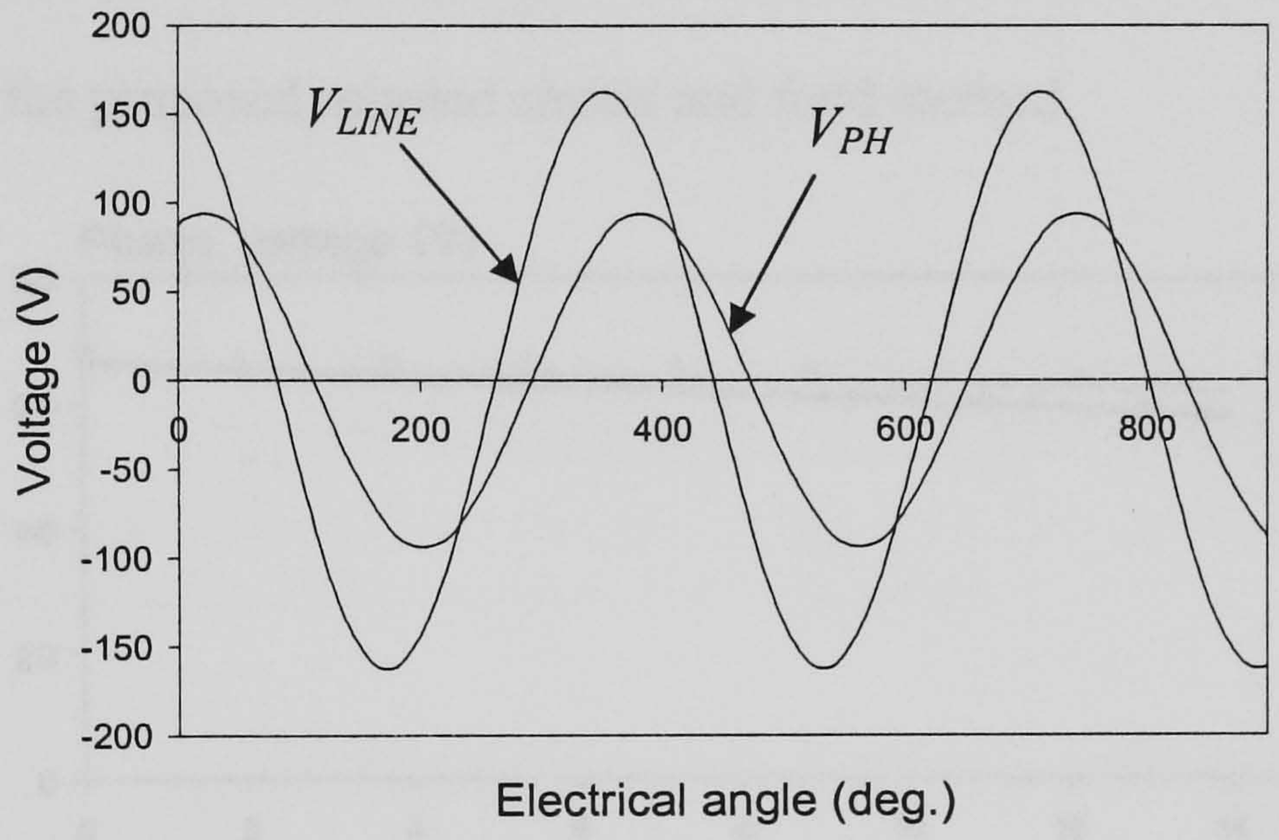


Fig. 6.34 Computed line-voltage ($V_{LINE}$) and phase-voltage ($V_{PH}$) of the PMSG at no load.

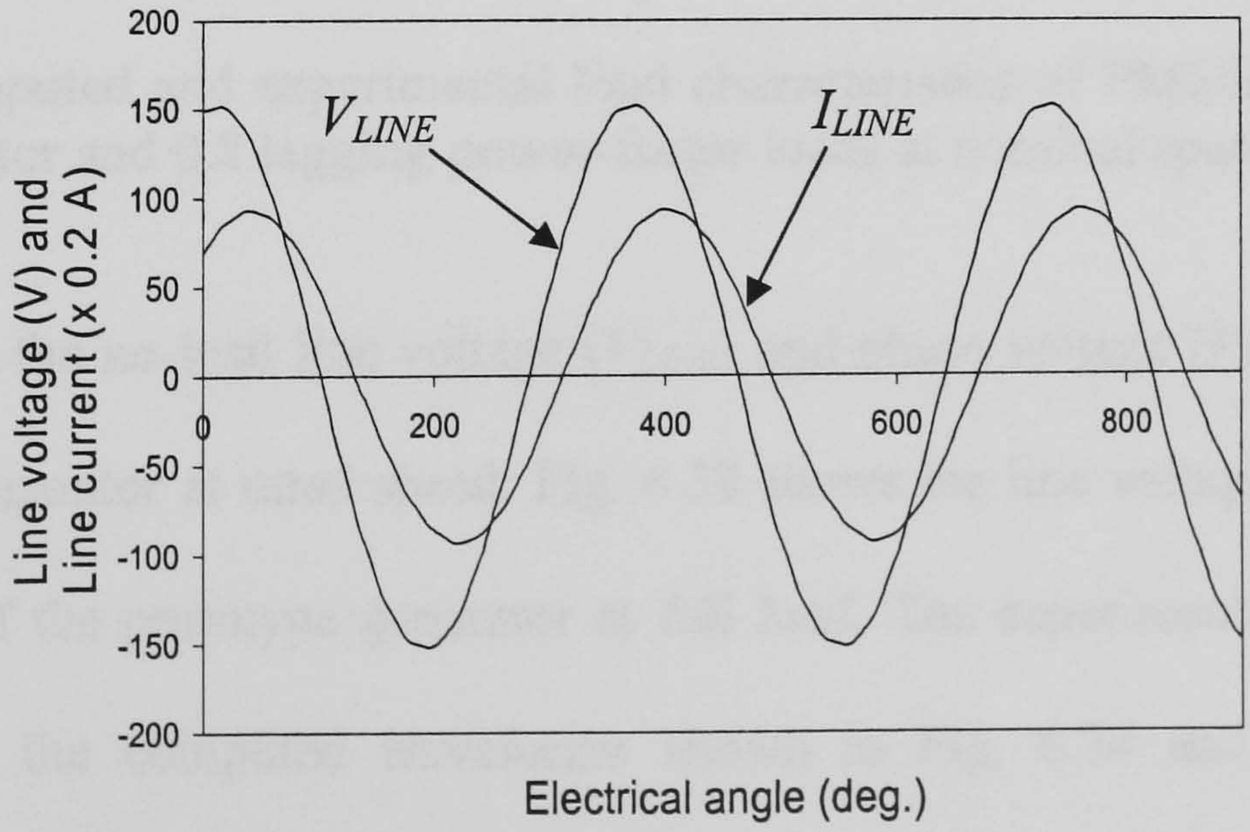


Fig. 6.35 Computed line-voltage ($V_{LINE}$) and line current ($I_{LINE}$) of the PMSG when supplying full-load current at unity power factor.

### 6.6.5 Experimental Verification

A load test was performed on the prototype PMSG in order to validate the results computed using the coupled circuit time-stepping 2-D FEM. Fig. 6.36 shows the computed and experimental load characteristics obtained. The computed characteristic is nearly level when the PMSG is supplying a unity-power-factor load and the full load voltage drop is only 6.4%. When the load power factor is 0.8 lagging, the voltage drop at full load increases to 12.7%. The voltage compensation capability of the PMSG with inset rotor is therefore better for unity-power-factor loads. Very good agreement between the computed and experimental characteristics has been obtained, confirming the accuracy of the proposed coupled circuit and field method.

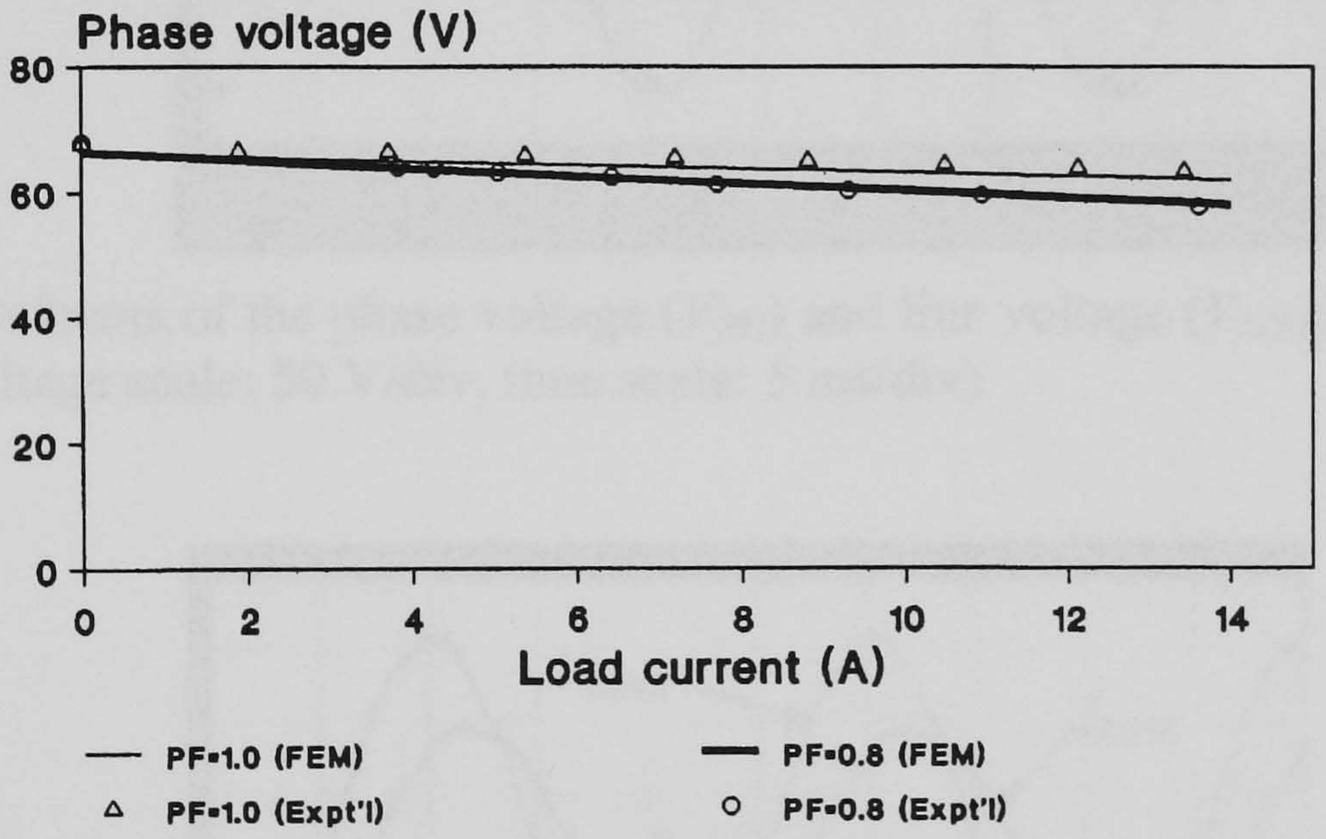


Fig. 6.36 Computed and experimental load characteristics of PMSG when supplying unity-power-factor and 0.8 lagging-power-factor loads at nominal speed.

Fig. 6.37 shows the no-load line voltage ($V_{LINE}$) and phase voltage ($V_{PH}$) waveforms of the prototype generator at rated speed. Fig. 6.38 shows the line voltage ($V_{LINE}$) and line current ($I_{LINE}$) of the prototype generator at full load. The experimental waveforms are very similar to the computed waveforms shown in Fig. 6.34 and Fig. 6.35. It is interesting to note that there is less harmonic distortion in the experimental waveforms

at full load, and the load current is practically sinusoidal. A harmonic analysis on the waveforms in Fig. 6.38 revealed that the total harmonic distortion (THD) in the line voltage was 2.1% only. The fifth and the seventh harmonics in the full-load line voltage waveform were dominant and were equal to 0.9% and 1.5%, respectively. The harmonic content of the PMSG is thus acceptable for practical applications.

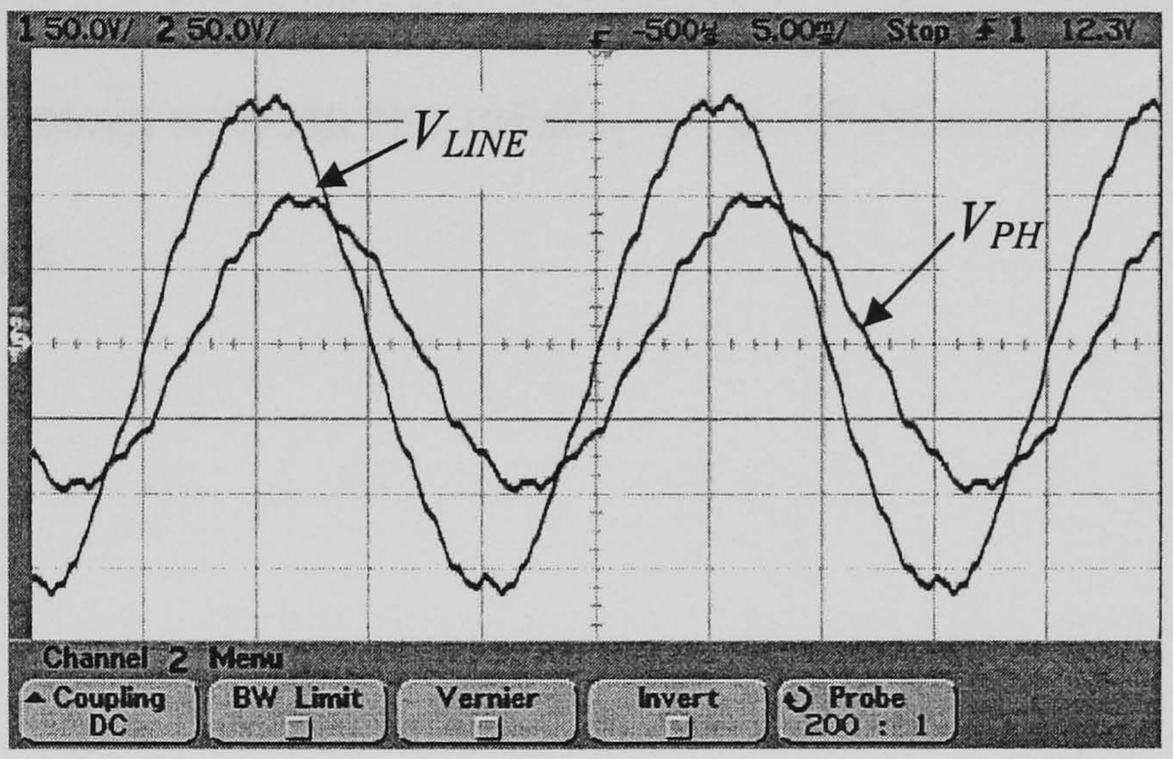


Fig. 6.37 Waveforms of the phase voltage ($V_{PH}$) and line voltage ($V_{LINE}$) of the PMSG on no load. (Voltage scale: 50 V/div; time scale: 5 ms/div)

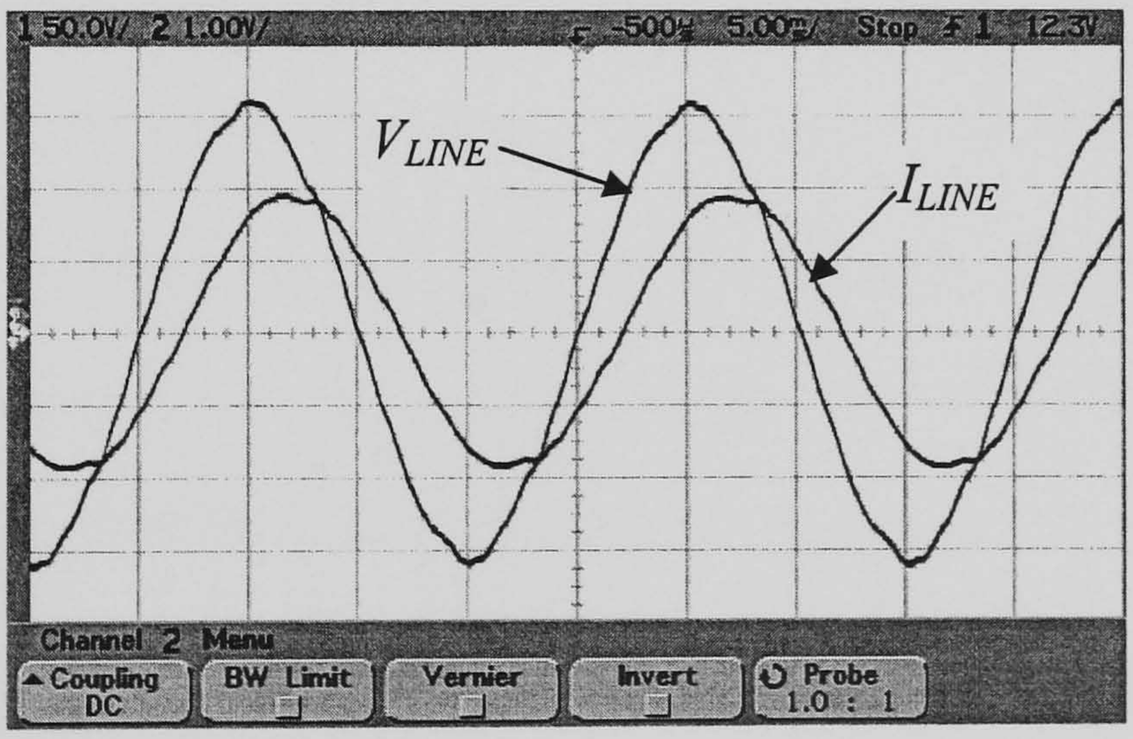


Fig. 6.38 Line voltage ($V_{LINE}$) and line current ($I_{LINE}$) waveforms of PMSG at full load. (Voltage scale: 50 V/div; current scale: 10 A /div; time scale: 5 ms/div)

### 6.6.6 Summary

A coupled circuit and field approach has been attempted for the performance analysis of a three-phase PMSG with inset rotor and a two-dimensional finite element method is used for the field solution. The solver developed has also accounted for the effect of saturation on the air gap flux density and the load characteristics. The experimental voltage and current waveforms are similar to those computed from the 2-D FEM, while good agreement between the computed and experimental load characteristics has been obtained. These observations confirm the validity of the FEM model and the accuracy of the solution procedure.

# Chapter 7

# CONCLUSIONS

## 7.1 Accomplishments of the Thesis

This thesis has explored the feasibility of using the induction generator and the permanent-magnet synchronous generator for distributed and autonomous power system applications.

The study of the IG has focused on single-phase operation of a three-phase machine. For the grid-connected IG, a systematic analysis based on the method of symmetrical components enables the steady-state performance of various phase-balancing schemes to be investigated. The analysis is subsequently extended to a three-phase IG with the Smith connection (SMIG) and Smith's Mode C circuit. The feasibility of microcontroller-based multi-mode operation of the SMIG is also studied.

A coupled circuit and field approach for analyzing a single-phase grid-connected IG with the Steinmetz connection is proposed. The thesis has presented the general methodology for coupling the asymmetrical stator circuit equations to the field equations based on a time-stepping 2-D FEM. A detailed rotor circuit model is also introduced in order to account for the non-uniform current distribution in the rotor winding. The results computed from the FEM and the symmetrical component method, are compared with the experimental data.

Another major accomplishment of the thesis is the development and analysis of practical SEIG schemes for asymmetrically connected and single-phase loads. By using the method of symmetrical components and an effective search algorithm, the steady-state performance of various SEIG schemes that employ three-phase machines can be

analyzed. For the special case of single-phase loads, the modified Steinmetz connection (MSC) and simplified Steinmetz connection (SSC) have been proposed and investigated. For improving the voltage regulation, an SRSEIG scheme that possesses automatic voltage-regulating as well as good phase-balancing capability is developed. By an appropriate choice of the shunt and series capacitances, a nearly level load characteristic of the SRSEIG may be obtained.

The capacitor sizing problem of an SEIG is also addressed with reference to the Steinmetz connection. The results throw light on the proper selection of excitation capacitance for securing self-excitation in other SEIG schemes.

The SMSEIG, namely an SEIG with the Smith connection, is proposed and investigated quantitatively for the first time. This scheme is particularly suitable for supplying single-phase unity-power-factor loads. It is demonstrated that the voltage unbalance factor of the SMSEIG is not sensitive to change in rotor speed. This suggests that, once the SMSEIG has been balanced at a particular speed, its performance over a wide speed range will remain satisfactory. The same argument may be extended to other SEIG schemes.

The use of a self-excited slip-ring induction generator (SESRIG) permits voltage and frequency control over a wide speed range and hence the excitation scheme is suitable for use with a variable-speed wind energy conversion system. The voltage and frequency control characteristics are deduced and practical implementation of a closed-loop control scheme using a rotor resistance chopper circuit is described. With a properly tuned PI controller, satisfactory dynamic response of the SESRIG to speed and load changes has been obtained. Balanced stator loads have been considered, but the analysis and control can be extended to other single-phase SEIG systems.

To address the recent developments in small-scale autonomous power systems, a prototype permanent-magnet synchronous generator with inset rotor is studied. Due to its inverse saliency characteristic, the generator is capable of automatic voltage compensation. The analysis is first developed for the resistive-load case but is subsequently extended to the general lagging-power-factor load case. Of particular interest is the deduction of the conditions for zero voltage regulation and the corresponding shape of the load characteristic. For the prototype generator, it is found that a nearly level load characteristic is obtained when it operates at around 6000 r/min, implying that the prototype generator is suitable for use in a direct-coupled, engine-driven power system. The parameters necessary for the two-axis model are obtained from a 2-D FEM and a saturated model is proposed in order to improve the computational accuracy. A coupled circuit and field approach that enables mixed d-axis and q-axis saturation conditions to be analyzed is also proposed. The computed flux density distribution shows clearly the effect of load on the interpolar flux density and hence the resulting load characteristic.

Experimental work on the prototype PMSG has confirmed the accuracy of the two-axis model and the parameters computed from FEM. Furthermore, the waveforms of voltages and currents are practically sinusoidal, a fact that renders the prototype PMSG a suitable machine for supplying isolated loads.

## 7.2 Future Work

The IG and SEIG schemes presented in the thesis are by no means exhaustive. The methodologies presented in Chapters 2 and 4 may readily be applied to other feasible phase-balancing schemes. A phasor diagram analysis, for example, has revealed that perfect phase balance in the SMIG could be realized with purely resistive phase

converters. The resulting system could be useful in applications where a large amount of local load has to be supplied. Variable-speed operation of the SMSEIG may also be extended to other SEIG schemes, such as the SESRIG, with the turbine characteristic duly included in the analysis. The various phase-balancing schemes for the IG and SEIG could also be applied to the reluctance generator (RG). A more refined analysis, however, need to be developed, particularly the accurate modeling and determination of negative-sequence circuit parameters.

The coupled circuit and field analysis for the IG has been studied with reference to a grid-connected machine with the Steinmetz connection. With appropriate modification of the circuit equations and the use of a proper magnetization curve, the analysis could be extended to other grid-connected IG schemes or SEIG schemes. The results of field analysis could also be processed to yield the transient performance, such as load changes, switching of phase converters, etc.

The rotor resistance controller for the SESRIG scheme presented in Chapter 5 could be replaced by a slip-energy recovery circuit that returns the slip energy to the stator side. Alternatively, the doubly-fed induction generator (DFIG) [109], in which the rotor is fed by a PWM inverter, may be employed. Various vector control methods (both sensorless or with rotor position sensors), could be developed for voltage and frequency control.

The coupled circuit and field analysis developed for the PMSG could be extended to certain operational problems, such as nonlinear loads, load switching, terminal short-circuits and unbalanced loads. New machine configurations for specific applications should also be studied, e.g., direct-coupled PMSGs for wind energy conversion systems.

With more and more renewable generation introduced into the existing power networks, system integration aspects need to be studied. These may include, for example, new converter topologies, power factor correction, reduction in harmonic distortion, system stability, generator-system dynamic interactions and plant economics.

# Appendix A

# Analysis for IG and SEIG

## A.1 Symmetrical Component Equations for IG

The symmetrical component equations for phase voltages and phase currents are [9]:

$$\begin{bmatrix} V_A \\ V_B \\ V_C \end{bmatrix} = \frac{1}{\sqrt{3}} \begin{bmatrix} 1 & 1 & 1 \\ 1 & h^2 & h \\ 1 & h & h^2 \end{bmatrix} \begin{bmatrix} V_0 \\ V_p \\ V_n \end{bmatrix} \tag{A.1}$$

$$\begin{bmatrix} I_A \\ I_B \\ I_C \end{bmatrix} = \frac{1}{\sqrt{3}} \begin{bmatrix} 1 & 1 & 1 \\ 1 & h^2 & h \\ 1 & h & h^2 \end{bmatrix} \begin{bmatrix} I_0 \\ I_p \\ I_n \end{bmatrix} \tag{A.2}$$

where $h$ is the complex operator $\exp(j2\pi/3)$.

It is assumed in the thesis that induction machines with symmetrical three-phase stator windings are used. For these machines, Wagner and Evans [110] have established that currents of different sequences do not react upon each other. It follows that when voltages of a given sequence are applied to the induction machine, only currents of the same sequence are produced. The sequence voltages and currents are therefore decoupled, and the following relationships are valid:

$$I_0 = V_0 / Z_0 = V_0 Y_0 \tag{A.3}$$

$$I_p = V_p / Z_p = V_p Y_p \tag{A.4}$$

$$I_n = V_n / Z_n = V_n Y_n . \tag{A.5}$$

In (A.3) to (A.5), $Z_0$, $Z_p$ and $Z_n$ are, respectively, the zero-, positive-, and negative-sequence impedance of the induction machine while $Y_0$, $Y_p$ and $Y_n$ are, respectively, the zero-, positive-, and negative-sequence admittance of the induction machine.

## A.2 Positive-Sequence and Negative-Sequence Circuits of IG

Zero-sequence quantities are absent in the IG schemes investigated in this thesis, hence only the positive-sequence and negative-sequence circuits need to be considered. Fig. A.1 and Fig. A.2 show, respectively, the positive-sequence and negative-sequence equivalent circuits of the grid-connected IG. For convenience, the *motor* convention has been adopted for the direction of current, i.e., the reference direction of current $I_p$ or $I_n$ is into the stator winding and the voltage $V_p$ or $V_n$ is considered to be applied to the machine. The advantage of this approach is that the symmetrical component analysis developed for induction motors could be applied directly. This convention will be used in the thesis whenever the method of symmetrical components is used.

In Fig. A.1 and Fig. A.2, $s_p$ and $s_n$ denote, respectively, the per-unit slip of the rotor with respect to the positive-sequence rotating field and the negative-sequence rotating field. It is obvious that $s_n = 2 - s_p$ .

From Fig. A.1, the positive-sequence impedance $Z_p$ and admittance $Y_p$ are given by

$$Z_p = |Z_p| \angle \phi_p = (R_1 + jX_1) + R_c \,//\, jX_m \,//\left(\frac{R_p}{s_p} + jX_2\right) \tag{A.6}$$

$$Y_p = \frac{1}{Z_p} = |Y_p| \angle -\phi_p \tag{A.7}$$

where $|Z_p|$ is the magnitude of $Z_p$, $|Y_p|$ is the magnitude of $Y_p$, and $\phi_p$ is the positive-sequence impedance angle. Both $|Z_p|$ and $\phi_p$ are functions of the per-unit slip $s_p$. For normal operation as an induction generator, $s_p$ is a small negative number, hence $\phi_p$ will in general vary between $\pi/2$ rad and $\pi$ rad. Accordingly, the positive-sequence current $I_p$ lags the positive-sequence voltage $V_p$ by an angle greater than $\pi/2$ rad. The *input* power is therefore negative, implying that the machine is delivering power to the stator circuit.

The negative-sequence impedance $Z_n$ and admittance $Y_n$ can likewise be computed from Fig. A.2.

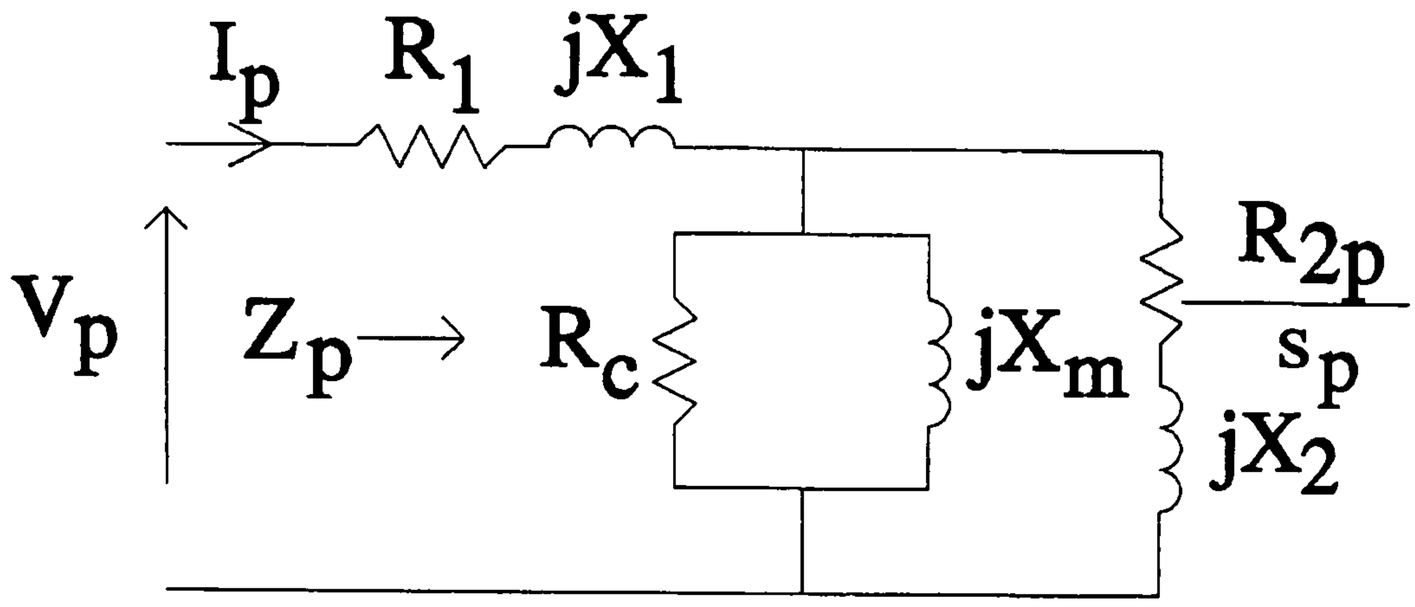


Fig. A.1 Positive-sequence equivalent circuit of grid-connected IG.

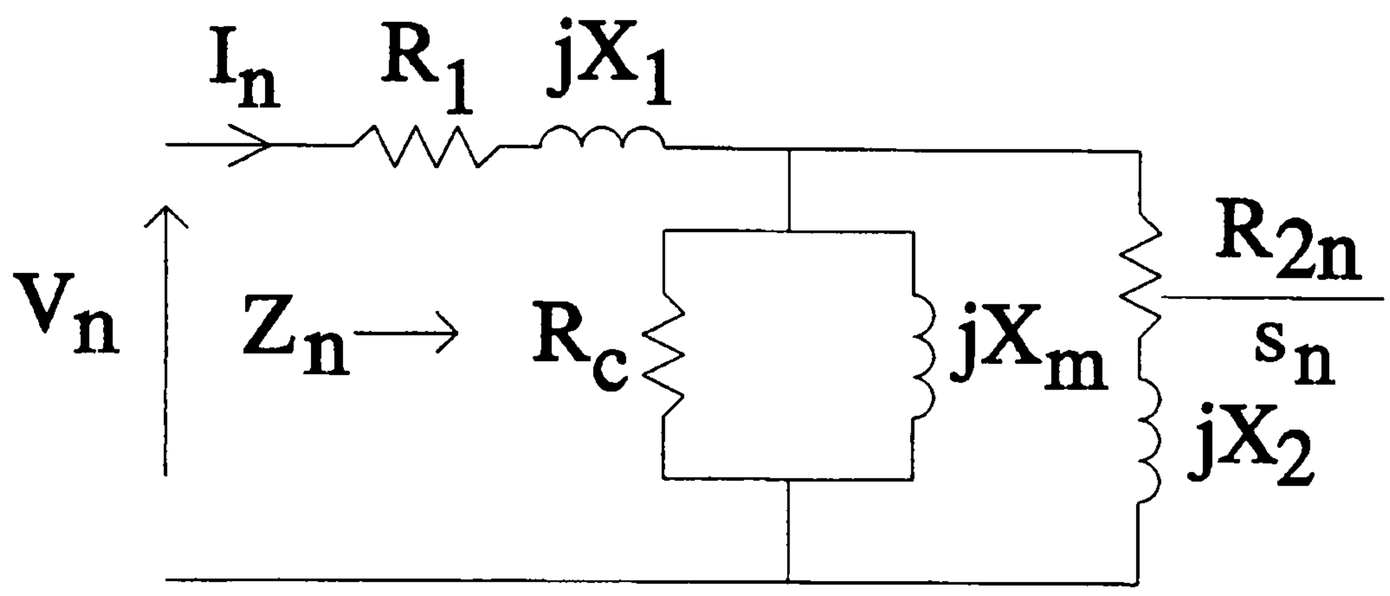


Fig. A.2 Negative-sequence equivalent circuit of grid-connected IG.

For isolated (or self-excited) operation, the frequency of generated e.m.f. of the IG may not be constant. To facilitate analysis, it is convenient to refer the circuit quantities to the base (rated) frequency $f_{base}$ by introducing the following parameters [23]:

1) Per-unit frequency $a$, defined by:

$a$ = (Actual frequency)/(Base frequency) = $f / f_{base}$

2) Per-unit speed $b$, defined by:

$b$ = (Actual rotor speed) / (Synchronous speed corresponding to base frequency)

$= n_r / n_{base} = n_r / (f_{base} / p)$

where $p$ is the number of pole-pairs and $n_r$ is the rotor speed.

The positive-sequence and negative-sequence impedances of the IG for isolated operation are shown in Fig. A.3 and Fig. A.4.

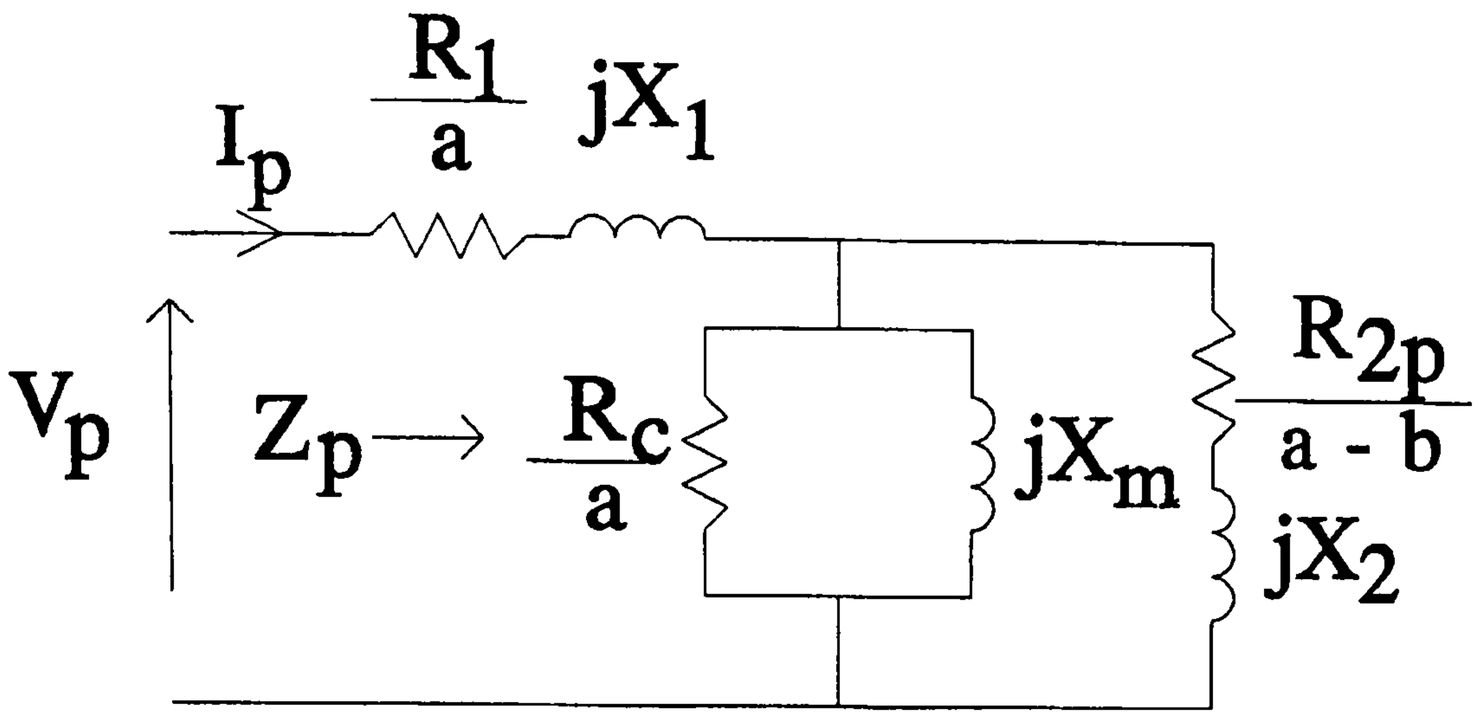


Fig. A.3 Positive-sequence equivalent circuit of IG for isolated operation.

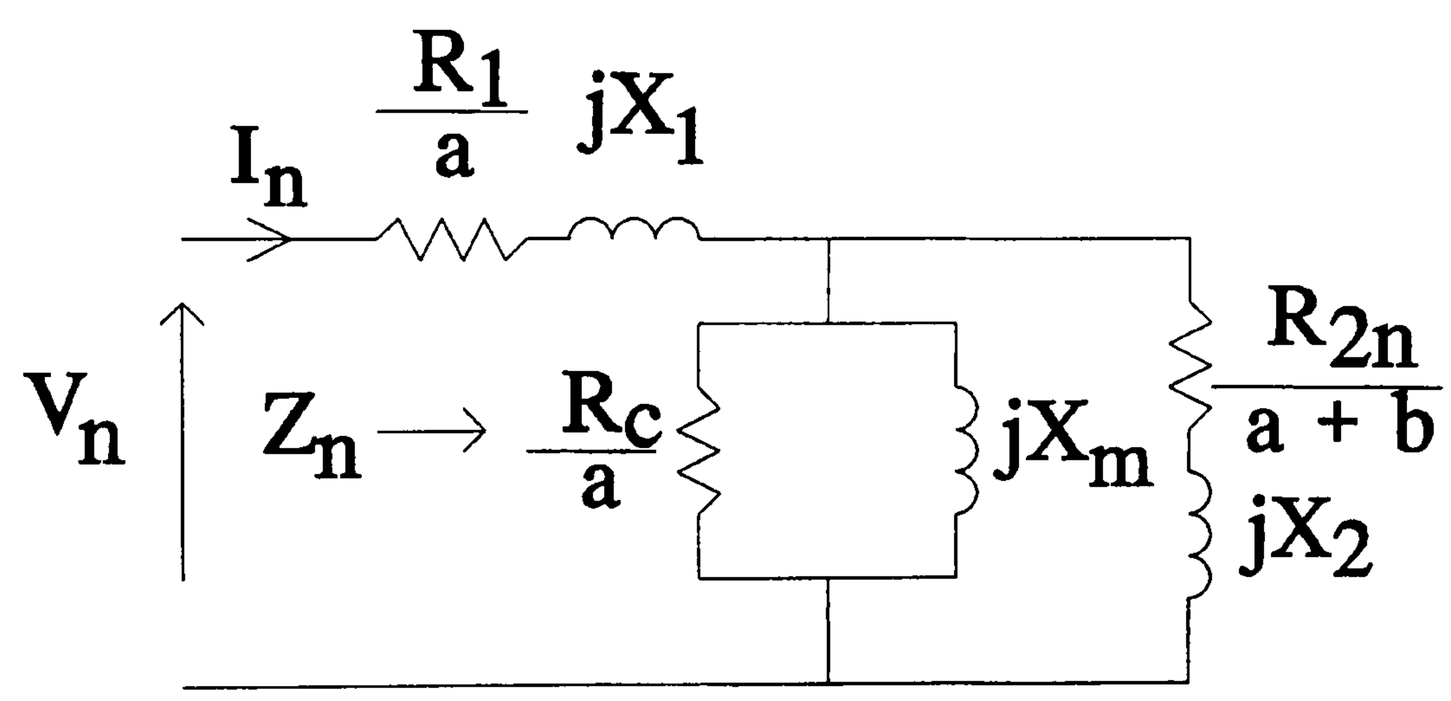


Fig. A.4 Negative-sequence equivalent circuit of IG for isolated operation.

## A.3 $V_p$ and $V_n$ for IG with Dual Phase Converters

From (2.2) and (A.1),

$$V_0 = 0 \text{ and } I_0 = 0 \tag{A.8}$$

i.e., zero sequence quantities are absent from the system.

Substituting (A.3) to (A.5) into (A.2), (2.3) and (2.4),

$$I_A = \frac{1}{\sqrt{3}}\left(I_p + I_n\right) = \frac{1}{\sqrt{3}}\left(V_p Y_p + V_n Y_n\right) \tag{A.9}$$

$$I_B = \frac{1}{\sqrt{3}}\left(h^2 I_p + h I_n\right) = \frac{1}{\sqrt{3}}\left(h^2 V_p Y_p + h V_n Y_n\right) \tag{A.10}$$

$$I_C = \frac{1}{\sqrt{3}}\left(h I_p + h^2 I_n\right) = \frac{1}{\sqrt{3}}\left(h V_p Y_p + h^2 V_n Y_n\right) \tag{A.11}$$

$$I_1 = \frac{1}{\sqrt{3}}\left(h V_p + h^2 V_n\right) Y_1 \tag{A.12}$$

$$I_2 = \frac{1}{\sqrt{3}}\left(h^2 V_p + h V_n\right) Y_2 . \tag{A.13}$$

Substituting (A.9) to (A.13) into (2.5) and rearranging terms, one obtains:

$$V_n = V_p . \frac{h Y_1 - h^2 Y_2 - (h^2 - h) Y_p}{-h^2 Y_1 + h Y_2 + (h - h^2) Y_n} . \tag{A.14}$$

The terminal voltage $V$ is given by

$$V = V_A = \frac{1}{\sqrt{3}}\left(V_p + V_n\right). \tag{A.15}$$

From (A.14) and (A.15),

$$V_p = \sqrt{3}\, V . \frac{Y_n - \frac{h}{1-h} Y_1 + \frac{1}{1-h} Y_2}{Y_1 + Y_2 + Y_p + Y_n} \tag{A.16}$$

or $$V_p = \sqrt{3}\,V.\frac{Y_n + \frac{e^{-j\pi/6}}{\sqrt{3}}Y_1 + \frac{e^{j\pi/6}}{\sqrt{3}}Y_2}{Y_1 + Y_2 + Y_p + Y_n}. \tag{2.6}$$

Substituting (A.16) into (A.14),

$$V_n = \sqrt{3}\,V.\frac{Y_p + \frac{1}{1-h}Y_1 - \frac{h}{1-h}Y_2}{Y_1 + Y_2 + Y_p + Y_n} \tag{A.17}$$

or $$V_n = \sqrt{3}\,V.\frac{Y_p + \frac{e^{j\pi/6}}{\sqrt{3}}Y_1 + \frac{e^{-j\pi/6}}{\sqrt{3}}Y_2}{Y_1 + Y_2 + Y_p + Y_n}. \tag{2.7}$$

## A.4 Derivation of (2.12)

Applying Sine Rule to the current phasor triangle in Fig. 2.7(a),

$$\frac{I_1}{\sin\theta_1} = \frac{I_{L2}}{\sin\theta_2}$$

or $$\frac{I_1}{\sin(2\pi/3 - \phi_p)} = \frac{I_{LINE}}{\sin(2\pi/3)}$$

where $I_{LINE}$ is the line current of the IG under perfect phase balance.

$$\therefore I_1 = \frac{2I_{LINE}}{\sqrt{3}}\sin(2\pi/3 - \phi_p) \tag{A.18}$$

Applying Sine Rule to the current phasor triangle in Fig. 2.7(b),

$$\frac{I}{\sin\theta_5} = \frac{I_1}{\sin\gamma}$$

or $$\frac{I}{\sin(2\pi/3 - \phi_p)} = \frac{I_1}{\sin\gamma}$$

$$\therefore \sin\gamma = \frac{I_1}{I}\sin(2\pi/3 - \phi_p) \tag{A.19}$$

Applying Cosine Rule to the current phasor triangle in Fig. 2.7(b),

$$I = \sqrt{I_{L3}^2 + I_1^2 - 2I_{L3}I_1\cos\theta_5}$$

$$= \sqrt{I_{LINE}^2 + \frac{4}{3}I_{LINE}^2.\sin^2(2\pi/3-\phi_p) - 2I_{LINE}^2\sin(2\pi/3-\phi_p).\cos(2\pi/3-\phi_p)} \quad \text{(A.20)}$$

$$= \frac{I_{LINE}}{\sqrt{3}}.\sqrt{3+4\sin^2(2\pi/3-\phi_p) - 2\sqrt{3}\sin 2(2\pi/3-\phi_p)}$$

Substituting (A.18) and (A.20) into (A.19),

$$\sin\gamma = \frac{2\sin^2(2\pi/3-\phi_p)}{\sqrt{3+4\sin^2(2\pi/3-\phi_p) - 2\sqrt{3}\sin 2(2\pi/3-\phi_p)}} \quad \text{(A.21)}$$

If we let $\alpha = 2\pi/3 - \phi_p$, then (A.21) is simplified to:

$$\sin\gamma = \frac{2\sin^2\alpha}{\sqrt{3+4\sin^2\alpha - 2\sqrt{3}\sin 2\alpha}} \quad \text{(2.12)}$$

## A.5 Input Impedance of SEIG with the Steinmetz Connection

From (4.2), it is obvious that (A.8) is also valid for the three-phase SEIG with the Steinmetz connection as shown in Fig. 4.1. The phase currents are also given by (A.9) and (A.11), while the terminal voltage $V$ is given by (A.15).

Substituting (A.6) to (A.11) into (4.3), one obtains

$$h^2\frac{V_p}{Z_C} + h\frac{V_n}{Z_C} = (h-h^2)\frac{V_p}{Z_p} + (h^2-h)\frac{V_n}{Z_n}$$

or
$$V_n = V_p.\frac{Z_C + \frac{e^{-j\pi/6}}{\sqrt{3}}Z_p}{Z_C + \frac{e^{j\pi/6}}{\sqrt{3}}Z_n}.\frac{Z_n}{Z_p}. \quad \text{(A.22)}$$

Substituting (A.22) into (A.15),

$$V_p = \sqrt{3}V.\frac{Z_p\left(Z_C + \frac{Z_n}{1-h}\right)}{(Z_pZ_n + Z_pZ_C + Z_nZ_C)} \quad \text{(A.23)}$$

or $$V_p = \sqrt{3}V.\frac{Z_p\left(Z_C + \frac{e^{j\pi/6}}{\sqrt{3}}Z_n\right)}{(Z_pZ_n + Z_pZ_C + Z_nZ_C)}. \tag{4.6}$$

Substituting (A.23) into (A.22),

$$V_n = \sqrt{3}V.\frac{Z_n\left(Z_C + \frac{e^{-j\pi/6}}{\sqrt{3}}Z_p\right)}{(Z_pZ_n + Z_pZ_C + Z_nZ_C)}. \tag{4.7}$$

From (4.6) and (4.7)

$$I_p = \frac{V_p}{Z_p} = \sqrt{3}V.\frac{Z_C + \frac{e^{j\pi/6}}{\sqrt{3}}Z_n}{(Z_pZ_n + Z_pZ_C + Z_nZ_C)} \tag{A.24}$$

$$I_n = \frac{V_n}{Z_n} = \sqrt{3}V.\frac{Z_C + \frac{e^{-j\pi/6}}{\sqrt{3}}Z_p}{(Z_pZ_n + Z_pZ_C + Z_nZ_C)}. \tag{A.25}$$

From (4.4) and (A.2), the input current $I$ is given by

$$I = I_A - I_C = \frac{1}{\sqrt{3}}\left[(1-h)I_p + (1-h^2)I_n\right]. \tag{A.26}$$

Substituting (A.24) and (A.25) into (A.26) and simplifying,

$$I = V.\frac{3Z_C + Z_p + Z_n}{Z_pZ_n + Z_pZ_C + Z_nZ_C}. \tag{A.27}$$

When viewed across terminals 1 and 3, the input impedance of the SEIG in Fig. 4.1 is given by

$$Z_{in} = \frac{V}{I} = \frac{Z_pZ_n + Z_pZ_C + Z_nZ_C}{3Z_C + Z_p + Z_n}. \tag{4.8}$$

# Appendix B

## The Method of Hooke and Jeeves

The pattern search method of Hooke and Jeeves [97] consists of a sequence of *exploratory moves* about a base point which, if successful, are followed by *pattern moves*. The procedure is summarized as follows:

*Exploratory Moves*

The purpose of an exploratory move is to acquire information about the function f(**x**) in the neighborhood of the current base point $\mathbf{b_k}$. Each variable $x_i$, in turn, is given an increment $\epsilon_i$ (first in the positive direction and then, if necessary, in the negative direction) and a check is made of the new function value. If any move is a success (i.e. results in a reduced function value), the new value of that variable will be retained. After all the variables have been considered, a new base point $\mathbf{b_{k+1}}$ will be reached. If $\mathbf{b_{k+1}} = \mathbf{b_k}$, no function reduction has been achieved. The step length $\epsilon_i$ is reduced (say to 1/10th of its current value) and the procedure is repeated. If $\mathbf{b_{k+1}} \neq \mathbf{b_k}$, a pattern move from $\mathbf{b_k}$ is made.

*Pattern Moves*

A pattern move attempts to speed up the search by using the information already acquired about f(**x**) so as to identify the best search direction. By intuition, a move is made from $\mathbf{b_{k+1}}$ in the direction $\mathbf{b_{k+1}} - \mathbf{b_k}$, since a move in this direction has led to a decrease in the function value. Thus, the function is evaluated at the next pattern point given by

$$p_k = b_k + 2(b_{k+1} - b_k)\,. \tag{B.1}$$

The search continues with a new sequence of exploratory moves about $\mathbf{p_k}$. If the lowest function value obtained is less than f($\mathbf{b_k}$), then a new base point $\mathbf{b_{k+2}}$ has been reached. In this case a second pattern move is made (using (B.1) with all suffixes increased by unity).

If not, the pattern move from $\mathbf{b}_{k+1}$ is abandoned and we continue with a new sequence of exploratory moves about $\mathbf{b}_{k+1}$.

The minimum is assumed to be obtained if the step length for each variable has been reduced to a specified small value.

For the SEIG problem, the two variables are the per-unit frequency $a$ and the magnetizing reactance $X_m$. After a successful voltage build-up, $a$ must be less than the per-unit speed $b$ and $X_m$ must be less than the unsaturated magnetizing reactance $X_{mu}$. To start the Hooke and Jeeves' pattern search procedure, initial estimates of $a$ and $X_m$ can be chosen to be $b$ and $X_{mu}$ , respectively. For small load impedances, however, it was found that an initial value of $0.97b$ for $a$ would give better convergence performance.

In the computer programs, an initial step length of 0.01 was chosen for both variables and convergence was assumed to be obtained if the step length was reduced to less than 1.0e-8. All the circuit parameters used were expressed in per-unit values.

# Appendix C

# A Note on the Finite Element Method [10]

## C.1 Energy Functional and Discretization

The solution of field problems using the finite element method involves the minimization of an energy functional, since the total energy in any physical system should be a minimum under steady-state conditions. In this thesis, the two-dimensional field problem is formulated in terms of magnetic vector potential $A$ and the coil currents (and hence the current densities $J$) are assumed to be known. The appropriate energy functional to be minimized is:

$$E(A) = \iint_{\Omega} \left( \int_{0}^{B} \frac{B}{\mu} . dB - A.J \right) dx.dy \,. \tag{3.3}$$

It will be assumed that the permeability $\mu$ at any point is constant at the value corresponding to the final flux density $B$. Eqn. (3.3) can then be written as:

$$E(A) = \iint_{\Omega} \left( \frac{B^2}{2\mu} - J.A \right) dx.dy = \iint_{\Omega} \left[ \frac{1}{2\mu} \left\{ \left( \frac{\partial A}{\partial x} \right)^2 + \left( \frac{\partial A}{\partial y} \right)^2 \right\} - J.A \right] dx.dy \,. \tag{C.1}$$

Consider the discretized solution region (Fig. 3.7) with $n_e$ elements and $n_p$ nodes. Because the energy of the functional is a scalar quantity, the energy in the global field region is considered to be the sum of energies in individual elements. Therefore, we aim to find the nodal potentials $A_1, A_2, \ldots A_{n_p}$, such that the following condition is satisfied:

$$E(A) = E(A_1, A_2, \ldots, A_{n_p}) = \min \,. \tag{C.2}$$

That is,

$$\frac{\partial E(A)}{\partial A_p} = 0 \qquad (p = 1, 2, 3, \ldots, n_p) \tag{C.3}$$

or,

$$\frac{\partial E_1(A)}{\partial A_p} + \frac{\partial E_2(A)}{\partial A_p} = 0 \qquad (p = 1, 2, 3, \ldots, n_p) \qquad \text{(C.4)}$$

where

$$E_1(A) = \iint_{\Omega} \left[ \frac{1}{2\mu} \left\{ \left( \frac{\partial A}{\partial x} \right)^2 + \left( \frac{\partial A}{\partial y} \right)^2 \right\} \right] dx.dy \qquad \text{(C.5)}$$

$$E_2(A) = - \iint_{\Omega} J.A \, dx.dy \, . \qquad \text{(C.6)}$$

## C.2 Shape Functions

Assume that the solution region has been divided into a number of triangular elements, or sub-regions, as shown in Fig. C.1. For a typical element *e*, the vertices *i*, *j* and *m* are assigned in the counterclockwise sense. The magnetic vector potential at any point (*x*,*y*) within element *e* is approximated by the following linear interpolating function:

$$A(x, y) = \beta_1 + \beta_2 x + \beta_3 y \qquad \text{(C.7)}$$

where $\beta_1$, $\beta_2$, and $\beta_3$ are the coefficients to be determined.

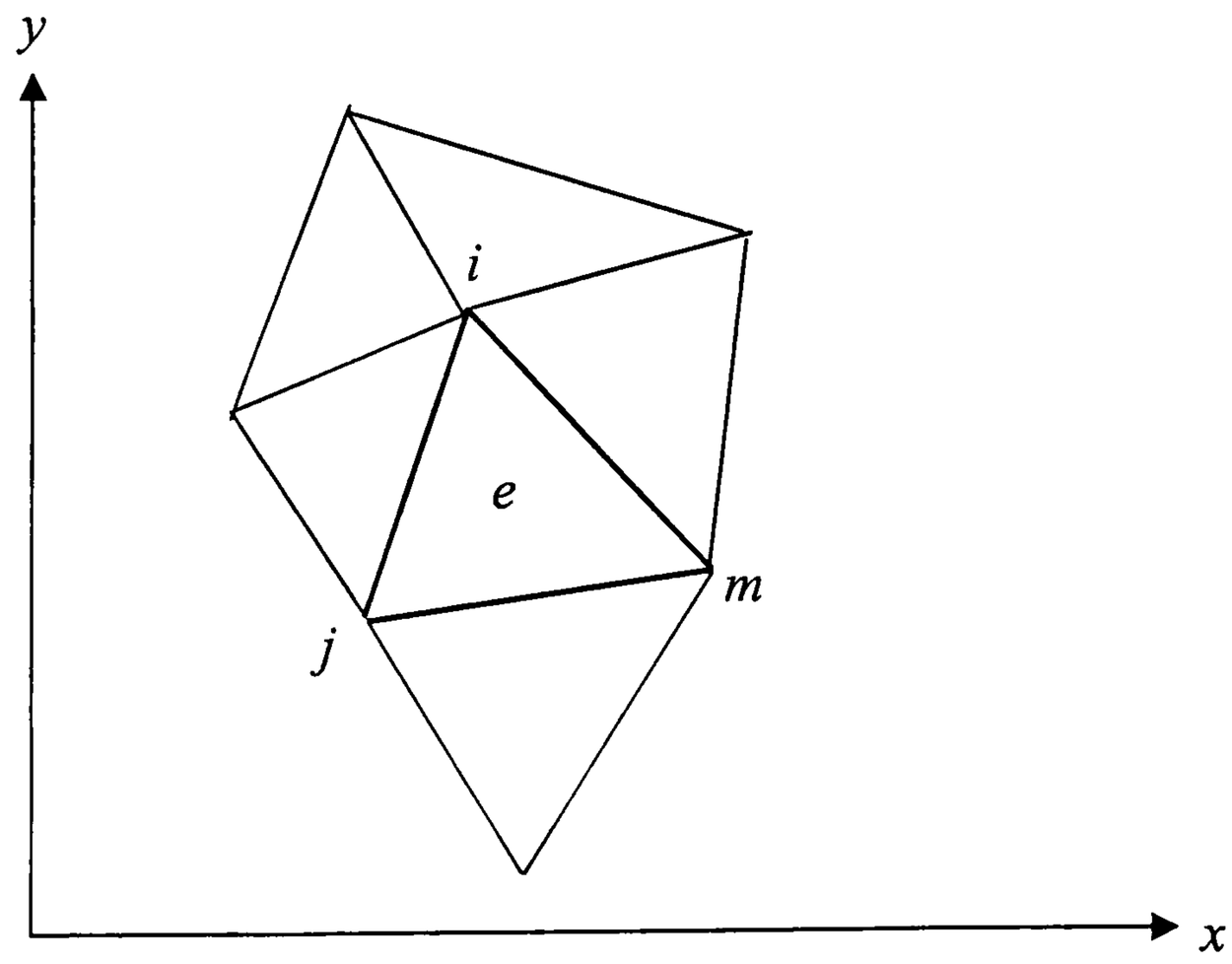


Fig. C.1 Discretization of field region by triangular elements.

If the coordinates of the vertices $i$, $j$ and $m$ are $(x_i, y_i)$, $(x_j, y_j)$ and $(x_m, y_m)$, while the magnetic vector potentials are $A_i$, $A_j$, and $A_m$, respectively, then from (C.7),

$$\left.\begin{aligned} A_i &= \beta_1 + \beta_2 x_i + \beta_3 y_i \\ A_j &= \beta_1 + \beta_2 x_j + \beta_3 y_j \\ A_m &= \beta_1 + \beta_2 x_m + \beta_3 y_m \end{aligned}\right\}. \tag{C.8}$$

The coefficients can be determined by solving (C.8):

$$\left.\begin{aligned} \beta_1 &= \frac{1}{2\Delta_e}(a_i A_i + a_j A_j + a_m A_m) \\ \beta_2 &= \frac{1}{2\Delta_e}(b_i A_i + b_j A_j + b_m A_m) \\ \beta_3 &= \frac{1}{2\Delta_e}(c_i A_i + c_j A_j + c_m A_m) \end{aligned}\right\} \tag{C.9}$$

where

$$\left.\begin{aligned} a_i &= x_j y_m - x_m y_j;\ \ a_j = x_m y_i - x_i y_m;\ \ a_m = x_i y_j - x_j y_i \\ b_i &= y_j - y_m;\ \ b_j = y_m - y_i;\ \ b_m = y_i - y_j; \\ c_i &= x_m - x_j;\ \ c_j = x_i - x_m;\ \ c_m = x_j - x_i; \end{aligned}\right\} \tag{C.10}$$

and $\Delta_e$ denotes the area of the triangular element $e$, i.e.,

$$\Delta_e = \frac{1}{2}\begin{vmatrix} 1 & x_i & y_i \\ 1 & x_j & y_j \\ 1 & x_m & y_m \end{vmatrix} = \frac{1}{2}(b_i c_j - b_j c_i) = \frac{1}{2}(a_i + a_j + a_m) \tag{C.11}$$

Substituting (C.9) into (C.7) and rearranging terms,

$$A(x,y) = \frac{1}{2\Delta_e}\left[(a_i + b_i x + c_i y)A_i + (a_j + b_j x + c_j y)A_j + (a_m + b_m x + c_m y)A_m\right] \tag{C.12}$$

or

$$A(x,y) = N_i.A_i + N_j A_j + N_m A_m \tag{C.13}$$

where

$$\left.\begin{aligned} N_i &= \frac{1}{2\Delta_e}(a_i + b_i x + c_i y) \\ N_j &= \frac{1}{2\Delta_e}(a_j + b_j x + c_j y) \\ N_m &= \frac{1}{2\Delta_e}(a_m + b_m x + c_m y) \end{aligned}\right\}. \qquad \text{(C.14)}$$

$N_i$, $N_j$ and $N_m$ are known as the shape functions and they all depend on the geometry of the triangular element $e$.

Taking the partial derivative on (C.12),

$$\left.\begin{aligned} \frac{\partial A}{\partial x} &= \frac{1}{2\Delta_e}(b_i A_i + b_j A_j + b_m A_m) \\ \frac{\partial A}{\partial y} &= \frac{1}{2\Delta_e}(c_i A_i + c_j A_j + c_m A_m) \end{aligned}\right\}. \qquad \text{(C.15)}$$

Consider first the contribution $E_{e1}$ of a typical element $e$ to the total energy functional $E_1$ in (C.5):

$$E_{e1}(A) = \iint_{\Omega_e}\left[\frac{1}{2\mu}\left\{\left(\frac{\partial A}{\partial x}\right)^2 + \left(\frac{\partial A}{\partial y}\right)^2\right\}\right]dx.dy\,. \qquad \text{(C.16)}$$

The terms in square brackets in (C.16) can be expressed as:

$$\left(\frac{\partial A}{\partial x}\right)^2 + \left(\frac{\partial A}{\partial y}\right)^2 = \begin{bmatrix}\frac{\partial A}{\partial x} & \frac{\partial A}{\partial y}\end{bmatrix}\begin{bmatrix}\frac{\partial A}{\partial x} \\ \frac{\partial A}{\partial y}\end{bmatrix}. \qquad \text{(C.17)}$$

$$= \frac{1}{4\Delta_e^2}\begin{bmatrix}A_i & A_j & A_m\end{bmatrix}\begin{bmatrix}b_i & c_i \\ b_j & c_j \\ b_m & c_m\end{bmatrix}\begin{bmatrix}b_i & b_j & b_m \\ c_i & c_j & c_m\end{bmatrix}\begin{bmatrix}A_i \\ A_j \\ A_m\end{bmatrix}$$

But

$$\iint_{\Omega_e} dx.dy = \Delta_e \qquad \text{(C.18)}$$

therefore (C.16) may be written as:

$$E_{el}(A) = \frac{1}{4\mu\Delta_e}.\frac{1}{2}\begin{bmatrix} A_i & A_j & A_m \end{bmatrix}\begin{bmatrix} b_i^2 + c_i^2 & b_ib_j + c_ic_j & b_ib_m + c_ic_m \\ b_jb_i + c_jc_i & b_j^2 + c_j^2 & b_jb_m + c_jc_m \\ b_mb_i + c_mc_i & b_mb_j + c_mc_j & b_m^2 + c_m^2 \end{bmatrix}\begin{bmatrix} A_i \\ A_j \\ A_m \end{bmatrix}$$

$$= \frac{1}{2}\begin{bmatrix} A_i & A_j & A_m \end{bmatrix}\begin{bmatrix} K_{ii}^e & K_{ij}^e & K_{im}^e \\ K_{ji}^e & K_{jj}^e & K_{jm}^e \\ K_{mi}^e & K_{mj}^e & K_{mm}^e \end{bmatrix}\begin{bmatrix} A_i \\ A_j \\ A_m \end{bmatrix}$$

$$= \frac{1}{2}[A]_e^T[K]_e[A]_e \qquad \text{(C.19)}$$

where $[A]_e = \begin{bmatrix} A_i \\ A_j \\ A_m \end{bmatrix}$,

and $[A]_e^T$ = the transpose of $[A]_e$.

The elements of matrix $[K]_e$ are given as follows:

$$K_{st}^e = \frac{1}{4\mu\Delta_e}(b_sb_t + c_sc_t) \qquad (s = i, j, m;\ \ t = i, j, m). \qquad \text{(C.20)}$$

## C.3 Functional Minimization and Global Assembly

If the global magnetic potential vector is denoted by $[A]$, then the local magnetic potential vector $[A]_e$ of element *e*, when expressed in the global system, is given by

$$[A]_e = [C]_e[A] \qquad \text{(C.21)}$$

where $[C]_e$ is known as the connection matrix.

From (C.19), the energy functional $E_{el}(A)$ can be expressed as:

$$E_{el}(A) = \frac{1}{2}[A]^T\left([C]_e^T[K]_e[C]_e\right)[A] = \frac{1}{2}[A]^T[K^*]_e[A] \qquad \text{(C.22)}$$

where

$$\left[K^*\right]_e = [C]_e^T [K]_e [C]_e \tag{C.23}$$

It should be noted that $\left[K^*\right]_e$ is an $(n_e \times n_e)$ matrix in which the elements are given by:

$$K_{st}^{*e} = \frac{1}{4\mu\Delta_e}(b_s b_t + c_s c_t) \qquad (s = i, j, m;\ \ t = i, j, m) \tag{C.24a}$$

$$K_{st}^{*e} = 0 \qquad (s \neq i, j, m;\ \ t \neq i, j, m) \tag{C.24b}$$

The total energy of the field region $\Omega$ can now be expressed as:

$$E_1(A) = \frac{1}{2}[A]^T \left( \sum_{e=1}^{n_e} \left[K^*\right]_e \right) [A] = \frac{1}{2}[A]^T [K][A] \tag{C.25}$$

where

$$[K] = \sum_{e=1}^{n_e} \left[K^*\right]_e \tag{C.26}$$

$[K]$ is known as the coefficient matrix, or the stiffness matrix.

From (C.25),

$$\frac{\partial E_1(A)}{\partial A_p} = [K][A] \tag{C.27}$$

Next consider the second derivative in (C.4). For element $e$,

$$E_{e2}(A) = -\iint_{\Omega_e} J.A\, dx.dy \tag{C.28}$$

With $J$ constant within the element, it can be shown that

$$\frac{\partial E_{e2}(A)}{\partial A_k} = -\iint_{\Omega_e} J.(a_k + b_k x + c_k y)dx.dy = -\frac{J.\Delta_e}{3} \qquad (k = i, j, m). \tag{C.29}$$

Considering the contributions from all the nodes,

$$\frac{\partial E_{e2}(A)}{\partial A_p} = -[R] \tag{C.30}$$

where $[R]$ is an $(n_p \times 1)$ column vector in which all the terms are known.

From (C.4), (C.26) and (C.29), the following matrix equation is obtained:

$$[K][A]=[R]. \tag{3.4}$$

The right-hand side vector $[R]$ is also known as the forcing function.

# Appendix D

# Technical Data of Experimental Machines

## D.1 Machine IG1

Three-phase, delta-connected, 2.2 kW, 220 V, 9.4 A, 4-pole, 50 Hz, cage type induction machine (Sections 2.2, 2.3, 4.2, 4.3, 4.4 and 4.5).

The machine parameters are (per-unit values given in brackets):

| | | |
|---|---|---|
| Stator resistance $R_1$ | = | 3.44 Ω (0.0844); |
| Stator leakage reactance $X_1$ | = | 4.56 Ω (0.112); |
| Positive-sequence rotor resistance $R_{2p}$ | = | 2.53 Ω (0.0621); |
| Negative-sequence rotor resistance $R_{2n}$ | = | 4.0 Ω (0.0981); |
| Rotor leakage reactance $X_2$ | = | 4.07 Ω (0.1); |
| Core loss resistance $R_c$ | = | 896 Ω (22.0); |
| Magnetizing reactance at nominal voltage | = | 71 Ω (1.74); |
| Friction and windage loss $P_{fw}$ | = | 47 W (0.013); |
| Stray-load loss | = | 1.8% of rated power. |

Variation of positive-sequence air-gap voltage $E_1$ with magnetizing reactance $X_m$ is modelled by the following describing equations expressed in per unit:

$$E_1 = \begin{cases} 1.345 - 0.203\,X_m, & X_m < 1.728 \\ 1.901 - 0.525\,X_m, & 1.728 \le X_m < 2.259 \\ 3.156 - 1.08\,X_m, & 2.259 \le X_m < 2.446 \\ 37.49 - 15.12\,X_m, & 2.446 \le X_m < 2.48 \\ 0, & 2.48 \le X_m \end{cases} . \qquad \text{(D.1)}$$

## D.2 Machine IG2

Three-phase, delta-connected, 2.2 kW, 220 V, 9.4 A, 50 Hz, four-pole, cage type induction machine (Chapter 3).

*Stator:*

| | | |
|---|---|---|
| Outer diameter | = | 155 mm; |
| Inner diameter | = | 98 mm; |
| Axial length | = | 101 mm; |
| Number of slots | = | 36; |
| Turns per coil | = | 43; |

| | | |
|---|---|---|
| Coil-span | = | 9 slots; |
| Number of parallel paths | = | 1. |

*Rotor:*

| | | |
|---|---|---|
| Outer diameter | = | 97.4 mm; |
| Inner diameter | = | 38 mm; |
| Number of slots | = | 32; |
| End-ring resistance | = | 0.1817e-4 Ω (per layer); |
| End-ring leakage inductance | = | 0.5784e-7 H (per layer). |

## D.3 Prototype PMSG with inset rotor

This machine is used for the investigations in Chapter 6. The specifications of the generator are as follows:

*General:*

3-phase, 4-pole, 1500 r/min, star-connected, 110 V, 2.5 kVA

*Stator:*

| | | |
|---|---|---|
| Outer diameter | = | 155 mm; |
| Inner diameter | = | 98 mm; |
| Number of slots | = | 36; |
| Coil span | = | 7 slots; |
| Axial core length | = | 100 mm; |
| Turns per coil | = | 6; |
| Cross-sectional area of conductors | = | 2.65 $mm^2$; |
| Armature resistance per phase | = | 0.295 Ω. |

*Rotor:*

| | | |
|---|---|---|
| Permanent magnet material | = | NdFeB; |
| Outer diameter of soft-iron pole pieces | = | 97.3 mm; |
| Outer diameter of magnets | = | 96.4 mm; |
| Inner diameter of magnets | = | 87.4 mm; |
| Inner diameter of rotor core | = | 38 mm; |
| Average pole arc of magnets | = | 144°e; |
| Average arc of interpolar soft-iron pole pieces | = | 12°e; |
| Space between magnet and soft-iron pole piece | = | 6°e; |
| Remanence of NdFeB magnets | = | 1.128 T; |
| Coercive force of NdFeB magnet | = | 880 kA/m. |

# Appendix E

# List of Publications

## E.1 Journal Papers


[1] T.F. Chan and L.L. Lai, "Steady-state analysis of a three-phase induction motor with the Smith connection," *IEEE Power Engineering Review*, Vol. 20, No. 10, pp. 45-46, October 2000.

[2] T.F. Chan and L.L. Lai, "A novel single-phase self-regulated induction generator using a three-phase machine," *IEEE Transactions on Energy Conversion*, Vol. 16, No. 2, pp. 204-208, June 2001.

[3] T.F. Chan and Loi Lei Lai, "Steady-state analysis and performance of a stand-alone three-phase induction generator with asymmetrically connected load impedances and excitation capacitances," *IEEE Transactions on Energy Conversion*, Vol. 16, No. 4, pp. 327-333, December 2001.

[4] T.F. Chan and Loi Lei Lai, "Capacitance requirements of a three-phase induction generator self-excited with a single capacitance and supplying a single-phase load," *IEEE Transactions on Energy Conversion*, Vol. 17, No. 1, pp. 90-94, March 2002.

[5] T.F. Chan and Loi Lei Lai, "Single-phase operation of a three-phase induction generator with the Smith connection," *IEEE Transactions on Energy Conversion*, Vol. 17, No. 1, pp. 47-54, March 2002.

[6] T.F. Chan and L.L. Lai, " Steady-state analysis and performance of a single-phase self-regulated self-excited induction generator," *IEE Proceedings – Generation, Transmission and Distribution*, Vol. 149, No. 2, pp. 233-241, March 2002.

[7] T.F. Chan, L.L. Lai and Lie-Tong Yan, "Finite element analysis of a single-phase grid-connected induction generator with the Steinmetz connection," *IEEE Transactions on Energy Conversion*, Vol. 18, No. 2, pp. 321-329, June 2003.

[8] T.F. Chan, K.A. Nigim and L.L. Lai, "Voltage and frequency control of self-excited slip-ring induction generators," *IEEE Transaction on Energy Conversion*, Vol. 19, No. 1, pp. 81-87, March 2004.

[9] T.F. Chan and L.L. Lai, "A novel excitation scheme for a stand-alone three-phase induction generator supplying single-phase loads," *IEEE Transactions on Energy Conversion*, Vol. 19, No. 1, pp. 136-143, March 2004.

[10] T.F. Chan, L.L. Lai and Lie-Tong Yan, "Performance of a three-phase a.c. generator with inset NdFeB permanent-magnet rotor," *IEEE Transactions on Energy Conversion*, Vol. 19, No. 1, pp. 88-94, March 2004.

[11] T.F. Chan and L.L. Lai, "Single-phase operation of a three-phase induction generator using a novel line current injection method," Accepted for publication in *IEEE Transactions on Energy Conversion*. (Paper TEC-00169-2003.R1).

[12] T.F. Chan, L.T. Yan and L.L. Lai, "Permanent-magnet synchronous generator with inset rotor for autonomous power-system applications," *IEE Proceedings – Generation, Transmission and Distribution*, Vol. 151, No. 5, September 2004, pp. 597-603.

## E.2 Conference Papers

[1] T.F. Chan and L.L. Lai, "Phase balancing for an induction generator operating on a single-phase power system," *Proceedings of the IEEE Power Engineering Society Winter Meeting 2000*, January 23-27, 2000, Singapore, Vol. 1, pp. 165-170.

[2] T.F. Chan and L.L. Lai, "Phase balancing for a self-excited induction generator," *Proceedings of the International Conference on Electrical Utility Deregulation and Structuring, and Power Technologies 2000*, April 4-7, 2000, City University, London, U.K, pp. 602-607.

[3] T.F. Chan and L.L. Lai, "Single-phase operation of a three-phase induction motor with the Smith connection," *Proceedings of 2000 IEEE Power Engineering Society Summer Meeting*, July 18-20, 2000, Seattle, Washington, USA, Vol. 4, pp. 2453-2458.

[4] T.F. Chan, Lie-Tong Yan and L.L. Lai, "Analysis and performance of a three-phase a.c. generator with inset permanent-magnet rotor," *Proceedings of the 5th International Conference on Advances in Power System Control, Operation and Management, APSCOM 2000*, October 30 - November 1, 2000, Hong Kong, pp. 436-440.

[5] T.F. Chan, Lie-Tong Yan and L.L. Lai, "Performance of a three-phase a.c. generator with inset NdFeB permanent-magnet rotor," *Proceedings of IEEE International Electric Machines and Drives Conference (IEMDC 2001)*, June 17-20, 2001, Cambridge, U.S.A., pp. 652-657.

[6] T.F. Chan, K.A. Nigim and L.L. Lai, "Voltage and frequency control of self-excited slip-ring induction generators," *Proceedings of IEEE International Electric Machines and Drives Conference (IEMDC 2001)*, June 17-20, 2001, Cambridge, U.S.A., pp. 410-414.

[7] T.F. Chan and L.L. Lai, "Single-phase operation of a three-phase induction generator using a novel line current injection method," *Proceedings of IEEE International Electric Machines and Drives Conference (IEMDC 2003)*, June 1-4, 2003, Madison, U.S.A., pp. 715-720.

[8] T.F. Chan and L.L. Lai, "Microcontroller based multi-mode operation of a three-phase induction generator with the Smith connection," *Proceedings of IEEE International Electric Machines and Drives Conference (IEMDC 2003)*, June 1-4, 2003, Madison, U.S.A., pp. 1623-1628.

[9] T.F. Chan, Lie-Tong Yan and L.L. Lai, "Performance of a permanent-magnet a.c. generator with rotor inverse saliency," *Proceedings of the 6th International Conference on Electrical Machines and Systems (ICEMS 2003)*, November 8-11, 2003, Beijing, China, Vol. I, pp. 45-48.

[10] T.F. Chan, Lie-Tong Yan and L.L. Lai, "Analysis of an A.C. generator with inset permanent-magnet rotor including effects of saturation," *Proceedings of the 6th International Conference on Advances in Power System Control, Operation and Management (APSCOM 2003)*, November 11-14, 2003, Hong Kong, Vol. 1, pp. 372-377.

## References


[1] R. Ramakumar, "Emerging options for integrated renewable energy systems," in *Proceedings of IEEE Power Engineering Society Winter Power Meeting 2000*, 23-27 January 2000, Singapore.

[2] Loi Lei Lai (Editor), *Power System Restructuring and Deregulation: Trading, Performance and Information Technology*. London: John Wiley & Sons, August 2001.

[3] N. Jenkins, "Embedded generation," *IEE Power Engineering Journal*, Vol. 9, No. 3, pp. 145-150, June 1995.

[4] R.L. Nailen, "Watts from waste heat - induction generators for the process industries," *IEEE Transactions on Industry Applications*, Vol. IA-19, No. 3, pp. 470-475, May/June 1983.

[5] P.G. Holmes, "Single- to 3-phase transient phase conversion in induction motor drives," *IEE Proceedings*, Part B, Vol. 132, No. 5, pp. 289-296, September 1985.

[6] M.O. Durham and R. Ramakumar, "Power system balancers for an induction generator," *IEEE Transactions on Industry Applications*, Vol. IA-23, No. 6, pp. 1067-1072, November/December 1987.

[7] R. Holland, "Appropriate technology - rural electrification in developing countries," *IEE Review*, Vol. 35, No. 7, pp. 251-254, August 1989.

[8] A. Doig, "Off-grid electricity for developing countries," *IEE Review*, Vol. 45, No. 1, pp. 25-28, January 1999.

[9] J.E. Brown and O.I. Butler, "A general method of analysis of 3-phase induction motors with asymmetrical primary connections," *IEE Proceedings*, Vol. 100, Part II, pp. 25-34, February 1953.

[10] S.J. Salon, *Finite Element Analysis of Electric Machines*. Boston: Kluwer Academic Publishers, 1995.

[11] O.J.M. Smith, "High-efficiency single-phase motor," *IEEE Transactions on Energy Conversion*, Vol. 7, No. 3, pp. 560-569, September 1992.

[12] O.J.M. Smith, "Large low-cost single-phase SEMIHEX™ motors," *IEEE Transactions on Energy Conversion*, Vol. 14, No. 4, pp. 1353-1358, December 1999.

[13] O.J.M. Smith, "High-efficiency large single-phase adapters and motors," *IEEE Power Engineering Review*, Vol. 18, No. 12, pp. 58-59, December 1998.

[14] J. F. Gieras and M. Wing, *Permanent-Magnet Motor Technology*. NY: Marcel Dekker, Inc., 1997.

[15] T.E. Abdel-Kader, "The reluctance machine as a self-excited generator," *Electric Machines and Power Systems*, Vol. 73, No. 10, pp. 144-148, October 1985.

[16] A.L. Mohamadein, Y.H.A. Rahim and A.S. Al-Khalaf, "Steady-state performance of self-excited reluctance generators," *IEE Proceedings*, Part B, Vol. 137, No. 5, pp. 293-298, September 1990.

[17] T.F. Chan, "Steady-state analysis of a three-phase self-excited reluctance generator," *IEEE Transactions on Energy Conversion*, Vol. 7, No. 1, pp. 223-230, March 1992.

[18] I. Boldea, Z.X. Fu and S.A. Nasar, "High-performance reluctance generator," *IEE Proceedings*, Part B, Vol. 140, No. 2, pp. 124-130, March 1993.

[19] Y.S. Wang and L. Wang, "Minimum loading resistance and its effects on performance of an isolated self-excited reluctance generator," *IEE Proceedings – Generation, Transmission and Distribution*, Vol. 148, No. 3, pp. 251-256, May 2001.

[20] T.J.E. Miller. *Brushless Permanent-Magnet and Reluctance Drives*. Oxford Science Publications, 1989.

[21] I. Husain, A. Radun and J. Nairus, "Fault analysis and excitation requirements for switched reluctance generators," *IEEE Transactions on Energy Conversion*, Vol. 17, No. 1, pp. 67-72, March 2002.

[22] B. Fahimi, "A switched reluctance machine based starter/generator for more electric cars," in *Proceedings of IEEE International Electric Machines and Drives Conference, (IEMDC2001)*, Cambridge, Massachusetts, 17-20 June 2001, pp. 73-78.

[23] M.G. Say, *Alternating Current Machines*. London: Pitman (ELBS), 5th Ed., pp. 333-336, 1983.

[24] E.D. Bassett and F.M. Potter, "Capacitance excitation for induction generators," *Transactions of AIEE*, Vol. 54, pp. 540-545, May 1935.

[25] C.F. Wagner, "Self-excitation of induction motors with series capacitors," *Transactions of AIEE*, Vol. 60, pp. 1241-1247, 1941.

[26] S.S. Murthy, O.P. Malik and A.K. Tandon, "Analysis of self-excited induction generators," *IEE Proceedings*, Part C, Vol. 129, No. 6, pp. 260-265, November 1982.

[27] N.H. Malik and S.E. Hague, "Steady state analysis and performance of an isolated self-excited induction generator," *IEEE Transactions on Energy Conversion*, Vol. EC-1, No. 3, pp. 134-139, September 1986.

[28] L. Ouazene and G. McPherson, Jr., "Analysis of the isolated induction generator," *IEEE Transactions on Power Apparatus and Systems*, Vol. PAS-102, No. 8, pp. 2793-2798, August 1983.

[29] J.M. Elder, J.T. Boys and J.L. Woodward, "Self-excited induction machine as a small low-cost generator," *IEE Proceedings*, Part C, Vol. 131, No. 2, pp. 33-41, March 1984.

[30] C. Grantham, D. Sutanto and B. Mismail, "Steady-state and transient analysis of self-excited induction generators," *IEE Proceedings*, Part B, Vol. 136, No. 2, pp. 61-68, March 1989.

[31] L. Wang, "A novel analysis on the performance of an isolated self-excited induction generator," *IEEE Transactions on Energy Conversion*, Vol. 12, No. 2, pp. 109-115, June 1997.

[32] N.H. Malik and A.A. Mazi, "Capacitance requirements for isolated self excited induction generators," *IEEE Transactions on Energy Conversion*, Vol. EC-2, No. 1, pp. 62-68, March 1987.

[33] A.K. Jabri and A.I. Alolah, "Capacitance requirement for isolated self-excited induction generator," *IEE Proceedings*, Part B, Vol. 137, No. 3, pp. 154-159, May 1990.

[34] T.F. Chan, "Capacitance requirements of self-excited induction generator," *IEEE Transactions on Energy Conversion*, Vol. 8, No. 2, pp. 304-311, June 1993.

[35] R. Bonert and G. Hoops, "Standalone induction generator with terminal impedance controller and no turbine control," *IEEE Transactions on Energy Conversion*, Vol. EC-5, No. 1, pp. 28-31, March 1990.

[36] T.F. Chan, "Self-excited induction generators driven by regulated and unregulated turbines," *IEEE Transactions on Energy Conversion*, Vol. 11, No. 2, pp. 338-343, June 1996.

[37] S.M. Alghuwainem, "Steady-state analysis of an isolated self-excited induction generator driven by regulated and unregulated turbines," *IEEE Transactions on Energy Conversion*, Vol. 14, No. 2, pp. 718-723, June 1999.

[38] N. Ammasaigounden, M. Subbiah and M.R. Krishnamurthy, "Wind-driven self-excited pole-changing induction generators," *IEE Proceedings*, Part B, Vol. 133, No. 5, pp. 315-321, September 1986.

[39] D.B. Watson, J. Arrillaga and T. Densem, "Controllable d.c. power supply from wind driven self-excited induction machines," *IEE Proceedings*, Vol. 126, No. 12, pp. 1245-1248, December 1979.

[40] G. Raina and O.P. Malik, "Wind energy conversion using a self-excited induction generator," *IEEE Transactions on Power Apparatus and Systems*, Vol. PAS-102, No. 12, pp. 3933-3936, December 1983.

[41] E. Bim, J. Szajner and Y. Burian, "Voltage compensation of an induction generator with long-shunt connection," *IEEE Transations on Energy Conversion*, Vol. EC-4, No. 3, pp. 526-530, September 1989.

[42] T.F. Chan, "Analysis of self-excited induction generators using an iterative method," *IEEE Transactions on Energy Conversion*, Vol. 10, No. 3, pp. 502-507, September 1995.

[43] L. Wang and J.Y. Su, "Effects of long-shunt and short-shunt connections on voltage variations of a self-excited induction generator," *IEEE Transactions on Energy Conversion*, Vol. 12, No. 4, pp. 368-374, December 1997.

[44] L. Wang and C.H. Lee, "Long-shunt and short-shunt connections on dynamic performance of a SEIG feeding an induction motor load," *IEEE Transactions on Energy Conversion*, Vol. 15, No. 1 pp. 1-7, March 2000.

[45] E. Profumo, B. Colombo and F. Mocci, "A frequency controller for induction generators in stand-by minihydro power plants," in *Proceedings of 4th International Conference on Electrical Machines and Drives*, IEE Conference Publication No. 310, 13-15 September 1989, London, UK.

[46] M.A. Al-Saffa, Eui-Cheol Nho, and T.A. Lipo, "Controlled shunt capacitor self-excited induction generator," in *Thirty-Third IEEE Industry Applications Society Annual Meeting Conference Record,* Vol. 2, pp. 1486-1490, 1998.

[47] R. Bonert and S. Rajakaruna, "Self-excited induction generator with excellent voltage and frequency control," *IEE Proceedings–Generation, Transmission and Distribution*, Vol. 145, No. 1, pp. 33-39, January 1998.

[48] O. Chtchetinine, "Voltage stabilization system for induction generator in stand alone mode," *IEEE Transactions on Energy Conversion*, Vol. 14, No. 3, pp. 298-303, September 1999.

[49] E. Suarez and G. Bortolotto, "Voltage-frequency control of a self-excited induction generator," *IEEE Transactions on Energy Conversion*, Vol. 14, No. 3, pp. 394-401, September 1999.

[50] E.G. Marra and J.A. Pomilio, "Induction-generator-based system providing regulated voltage with constant frequency," *IEEE Transactions on Industrial Electronics*, Vol. 47, No. 4, pp. 908-914, August 2000.

[51] E.C. Boardman, S.S. Venkata and N.G. Butler, "The effect of rotational direction in single-phase induction generators," *IEEE Transactions on Power Apparatus and Systems*, Vol. PAS-103, No. 8, pp. 2222-2229, August 1984.

[52] G.L. Johnson, *Wind Energy Systems*. Engelwood Cliffs, NJ: Prentice-Hall, 1985.

[53] O.J.M. Smith, "Three-phase induction generator for single-phase line," *IEEE Transactions on Energy Conversion*, Vol. EC-2, No. 3, pp. 382-387, September 1987.

[54] T.F. Chan, "Performance analysis of a three-phase induction generator connected to a single-phase power system," *IEEE Transactions on Energy Conversion*, Vol. 13, No. 3, pp. 205-211, September 1998.

[55] S.S. Murthy, "A novel self-excited self-regulated single phase induction generator Part 1: Basic system and theory," *IEEE Transactions on Energy Conversion*, Vol. 8, No. 3, pp. 377-382, September 1993.

[56] S.S. Murthy, H.C. Rai and A.K. Tandon, "A novel self-excited self-regulated single phase induction generator Part 2: Experimental investigation," *IEEE Transactions on Energy Conversion*, Vol. 8, No. 3, pp. 383-388, September 1993.

[57] Y.H.A. Rahim, A.I. Alolah and R.I. Al-Mudaiheem, "Performance of single phase induction generators," *IEEE Transactions on Energy Conversion*, Vol. 8, No. 3, pp. 389-395, September 1993.

[58] T.F. Chan, "Analysis of a single-phase self-excited induction generator," *Electric Machines and Power Systems*, Vol. 23, No. 2, pp. 149-162, March 1995.

[59] B. Singh and L.B. Shilpkar, "Steady-state analysis of the single-phase self-excited induction generator," *IEE Proceedings–Generation, Transmission and Distribution*, Vol. 146, No. 5, pp. 421-427, September 1999.

[60] O. Ojo, "The transient and qualitative performance of a self-excited single-phase induction generator," *IEEE Transactions on Energy Conversion*, Vol. 10, No. 3, pp. 493-501, September 1995.

[61] B. Singh, R.B. Saxena, S.S. Murthy and B. P. Singh, "A single-phase self-excited induction generator for lighting loads in remote areas," *International Journal of Electrical Engineering Education*, Vol. 25, No. 3, pp. 269-275, July 1988.

[62] D.B. Watson and R.M. Watson, "Microprocessor control of a self-excited induction generator," *International Journal of Electrical Engineering Education*, Vol. 22, No. 1, pp. 83-92, January 1985.

[63] O. Ojo, O. Omozusi, A. Ginart and G. Gonoh, "The operation of a stand-alone, single-phase induction generator using a single-phase, pulse-width modulated inverter with a battery supply," *IEEE Transactions on Energy Conversion*, Vol. 14, No. 3, pp. 526-531, September 1999.

[64] A.H. Al-Bahrani, and N.H. Malik, "Steady state analysis and performance characteristics of a three-phase induction generator self-excited with a single capacitor," *IEEE Transactions on Energy Conversion*, Vol. 5, No. 4, pp. 725-732, December 1990.

[65] Y.H.A. Rahim, "Excitation of isolated three-phase induction generator by a single capacitor," *IEE Proceedings*, Part B, Vol. 140, No. 1, pp. 44-50, January 1993.

[66] T. Fukami, Y. Kaburaki, S. Kawahara and T. Miyamoto, "Performance analysis of a self-regulated self-excited single-phase induction generator using a three-phase machine," *IEEE Transactions on Energy Conversion*, Vol. 14, No. 3, pp. 622-627, September 1999.

[67] T.F. Chan, "Performance analysis of a three-phase induction generator self-excited with a single capacitance," *IEEE Transactions on Energy Conversion*, Vol. 14, No. 4, pp. 894-900, December 1999.

[68] K.J. Binns and Kurdali, "Permanent-magnet a.c. generators," *IEE Proceedings*, Vol. 126, No. 7, pp. 690-696, July 1979.

[69] K.J. Binns and T.S. Low, "Performance and application of multi-stacked imbricated permanent-magnet generators," *IEE Proceedings*, Part B, Vol. 130, No. 6, pp. 407-414, November 1983.

[70] E. Spooner, and Chalmers, "TORUS: a slotless toroidal stator permanent-magnet generator," *IEE Proceedings*, Vol. 139, No. 6, pp. 497-506, November 1992.

[71] B.J. Chalmers, "Performance of interior type permanent-magnet alternator," *IEE Proceedings–Electric Power Applications*, Vol. 141, No. 4, pp. 186-190, July 1994.

[72] W. Wu, E. Spooner and B.J. Chalmers, "Design of slotless torus generators with reduced voltage regulation," *IEE Proceedings–Electric Power Applications*, Vol. 142, No. 5, pp. 337-343, September 1995.

[73] M.A. Rahman, A.M. Osheiba, T.S. Radwan and E.S. Abdin, "Modelling and controller design of an isolated diesel engine permanent magnet synchronous generator," *IEEE Transactions on Energy Conversion*, Vol. 11, No. 2, pp. 324-330, June 1996.

[74] N. Naoe, "Voltage compensation of permanent-magnet generator with capacitors," in *1997 IEEE International Electric Machines and Drives Conference Record*, May 18-21, 1997, Milwaukee, Wisconsin, U.S.A.

[75] O. Ojo and John Cox, and Zhiqing Wu, "DC power generation using interior permanent-magnet machines," *IEEE Transactions on Energy Conversion*, Vol. 12, No. 4, pp. 351-356, December 1997.

[76] T.F. Chan and Lie-Tong Yan, "Analysis and performance of a surface-mounted NdFeB permanent-magnet a.c. generator," in *Proceedings of Conference on Advances in Power System Control, Operation and Management (APSCOM-97)*, 11-14 November 1997, Hong Kong.

[77] B.J. Chalmers, W. Wu and E. Spooner, "An axial-flux permanent-magnet generator for a gearless wind energy system," *IEEE Transactions on Energy Conversion*, Vol. 14, No. 2, pp. 251-257, June 1999.

[78] E. Muljadi, C.P. Butterfield and Y.H. Wan, "Axial-flux modular permanent-magnet generator with a toroidal winding for wind-turbine applications," *IEEE Transactions on Industry Applications*, Vol. 35, No. 4, pp. 831-836, July/August 1999.

[79] Ping Zhou, Thomas E. McDermott, Zoltan J. Cendes and M.A. Rahman, "Steady-state analysis of synchronous generators by a coupled field-circuit method," Paper No. WC2-2, in *1997 IEEE International Electric Machines and Drives Conference Record*, 18-21 May 1997, Milwaukee, Wisconsin, U.S.A.

[80] C.E. Tindall and W. Monteith, "Balanced operation of 3-phase induction motors connected to single-phase supplies," *IEE Proceedings*, Vol. 123, No. 6, pp. 517-522, June 1976.

[81] V. Ostovic, *Dynamics of Saturated Electric Machines*. New York: Springer-Verlag, 1989.

[82] T.F. Chan and L.L. Lai, "Steady-state analysis of a three-phase induction motor with the Smith connection," *IEEE Power Engineering Review*, Vol. 20, No. 10, pp. 45-46, October 2000.

[83] T.F. Chan and L.L. Lai, "Single-phase operation of a three-phase induction motor with the Smith connection," in *Proceedings of 2000 IEEE Power Engineering Society Summer Meeting*, 18-20 July 2000, Seattle, Washington, USA, Vol. 4, pp. 2453-2458.

[84] L.S. MacKenzie, *The 8051 Microcontroller*. Englewood Cliffs, CA: Prentice-Hall Inc., 1995.

[85] S. Yeralan and A. Ahluwalia, *Programming and Interfacing the 8051 Microcontroller*. Reading, MA: Addison-Wesley Publishing Company, 1995.

[86] http://www.iguanalabs.com/8952pin.htm.

[87] N.A. Demerdash and P. Baldassari, "A combined finite element state space modeling environment for induction motors in the ABC frame of reference: The no load condition," *IEEE Transactions on Energy Conversion*, Vol. 7, No. 4, pp. 698-709, December 1992.

[88] C.C. Chan, Lie-Tong Yan, Pi-Zhang Chen, Ze-Zhong Wang and K. T. Chau, "Analysis of electromagnetic and thermal fields for induction motors during starting," *IEEE Transactions on Energy Conversion*, Vol. 9, No. 1, pp. 53-60, March 1994.

[89] J. Brauer, H. Sadeghi and R. Oesterlei, "Polyphase induction motor performance computed directly by finite elements," *IEEE Transactions on Energy Conversion*, Vol. 14, No. 3, pp. 583-588, September 1999.

[90] T.H. Pham, P.F. Wendling, S.J. Salon and H. Acikgoz, "Transient finite element analysis of an induction motor with external circuit connections and electromechanical coupling," *IEEE Transactions on Energy Conversion*, Vol. 14, No. 4, pp. 1407-1412, December 1999.

[91] N.A. Demerdash, J.F. Bangura, and A.A. Arkadan, "A time-stepping coupled finite element - state space model for induction motor drives - Part 1: Model formulation and machine parameter computation," *IEEE Transactions on Energy Conversion*, Vol. 14, No. 4, pp. 1465-1471, December 1999.

[92] N.A. Demerdash and T.W. Nehl, "Electric machinery parameters and torques by current and energy perturbations from field computations — Part I: theory and formulation," *IEEE Transactions on Energy Conversion*, Vol. 14, No. 4, pp. 1507-1513, December 1999.

[93] A. Domijan, Jr. and Y. Yin, "Single phase induction machine simulation using the electromagnetic transients program: theory and test cases," *IEEE Transactions on Energy Conversion*, Vol. 9, No. 3, pp. 535-542, September 1994.

[94] R. Hung and H.W. Dommel, "Synchronous machine models for simulation of induction motor transients," *IEEE Transactions on Energy Conversion*, Vol. 11, No. 2, pp. 833-838, May 1996.

[95] Pi-Zhang Chen, Lie-Tong Yan and Ruo-Ping Yao. *Theory and Computation of Electromagnetic Fields in Electrical Machines*. Science Press, China, 1986.

[96] S.L. Ho, W.N. Fu, and H.C. Wong, "Estimation of stray losses of skewed induction motors using coupled 2-D and 3-D time stepping finite element methods," *IEEE Transactions on Magnetics*, Vol. 34, No. 5, pp. 3102-3105, September 1998.

[97] Byron S. Gottfried and Joel Weisman, *Introduction to Optimization Theory*. Prentice Hall Inc., Englewood Cliffs, New Jersey, 1973.

[98] A.I. Alolah and M.A. Alkanhal, "Optimization-based steady state analysis of three-phase self-excited induction generator," *IEEE Transactions on Energy Conversion*, Vol. 15, No. 1, pp. 61-65, March 2000.

[99] A. Balfour and W.T. Beveridge, *Basic Numerical Analysis with Fortran*. London: Heinemann, pp. 138-144, 1977.

[100] A.I. Alolah and M.A. Alkanhal, "Excitation requirements of three phase self excited induction generator under single phase loading with minimum unbalance," in *Proceedings of IEEE Power Engineering Society 2000 Winter Meeting*, 23-27 January 2000, Singapore.

[101] Z.M. Salameh and L.F. Kazda, "Analysis of the steady state performance of the double output induction generator," *IEEE Transactions on Energy Conversion*, Vol. EC-1, No. 1, pp. 26-32, March 1986.

[102] B.T. Ooi and R.A. David, "Induction-generator/synchronous-condenser system for wind-turbine power," *IEE Proceedings*, Vol. 126, No. 1, pp. 69-74, January 1979.

[103] K.A. Nigim, "Static exciter for wound rotor induction machine," in *Conference Record of 16th IAS Annual Meeting*, Vol. 2, pp. 934-937, 1990.

[104] F. Giraud and Z.M. Salameh, "Wind-driven, variable-speed, variable-frequency, double-output, induction generator," *Electric Machines and Power Systems*, Vol. 26, No. 3, pp. 287-297, April 1998.

[105] B.D. Bunday, *Basic Optimisation Methods*. London: Edward Arnold, 1984.

[106] G.K. Dubey, *Power Semiconductor Controlled Drives*. NJ: Englewood Cliffs, Prentice-Hall, 1989.

[107] K.J. Astrom and T. Hagglund, *PID Controllers: Theory, Design and Tuning*. Research Triangle Park, N.C.: Instrument Society of America, 1995.

[108] M.V. Sweet, *Algebra, Geometry and Trigonometry in Science, Engineering and Mathematics*. Chichester, UK: Ellis Horwood Limited, 1984.

[109] R.S. Pena, G.M. Asher and J.C. Clare, "A doubly fed induction generator using back to back PWM converters supplying an isolated load from a variable speed wind turbine," *IEE Proceedings – Electric Power and Applications*, Vol. 143, No. 5, pp. 380-387, September 1996.

[110] C.F. Wagner and R.D. Evans, *Symmetrical Components*. NY: McGraw Hill, 1933.